SynerCrete'18: Interdisciplinary Approaches for Cement-based Materials and Structural Concrete: Synergizing Expertise and Bridging Scales of Space and Time
Vol. 1

SynerCrete'18 International Conference on Interdisciplinary Approaches
for Cement-based Materials and Structural Concrete

24-26 October 2018, Funchal, Madeira Island, Portugal

Published by RILEM Publications S.A.R.L.
4 avenue du Recteur Poincaré 75016 Paris - France
Tel : + 33 1 42 24 64 46 Fax : + 33 9 70 29 51 20
http://www.rilem.net E-mail: dg@rilem.net

ISBN Vol. 1:978-2-35158-211-4 ISBN Vol. 2: 978-2-35158-212-1
ISBN Vol. 1&2: 978-2-35158-202-2 e-ISBN Vol. 1&2: 978-2-35158-203-9
DOI: 10.5281/zenodo.1405563 Legal deposit n. (Portugal):
Printed by Canto Redondo / VASP DPS http://www.cantoredondo.eu
Cover design by: Boutik Studio http://boutik.pt/

RILEM, The International Union of Laboratories and Experts in Construction Materials, Systems and Structures, is a non-profit-making, non-governmental technical association whose vocation is to contribute to progress in the construction sciences, techniques and industries, essentially by means of the communication it fosters between research and practice. RILEM's activity therefore aims at developing the knowledge of properties of materials and performance of structures, at defining the means for their assessment in laboratory and service conditions and at unifying measurement and testing methods used with this objective.

RILEM was founded in 1947, and has a membership of over 900 in some 70 countries. It forms an institutional framework for co-operation by experts to:

- optimise and harmonise test methods for measuring properties and performance of building and civil engineering materials and structures under laboratory and service environments,
- prepare technical recommendations for testing methods,
- prepare state-of-the-art reports to identify further research needs,
- collaborate with national or international associations in realising these objectives.

RILEM members include the leading building research and testing laboratories around the world, industrial research, manufacturing and contracting interests, as well as a significant number of individual members from industry and universities. RILEM's focus is on construction materials and their use in building and civil engineering structures, covering all phases of the building process from manufacture to use and recycling of materials.

RILEM meets these objectives through the work of its technical committees. Symposia, workshops and seminars are organised to facilitate the exchange of information and dissemination of knowledge. RILEM's primary output consists of technical recommendations. RILEM also publishes the journal *Materials and Structures* which provides a further avenue for reporting the work of its committees. Many other publications, in the form of reports, monographs, symposia and workshop proceedings are produced.

SynerCrete'18: Interdisciplinary Approaches for Cement-based Materials and Structural Concrete: Synergizing Expertise and Bridging Scales of Space and Time
Vol. 1

Funchal, Madeira, Portugal
24-26 October 2018

Edited by
Miguel Azenha
Dirk Schlicke
Farid Benboudjema
Agnieszka Jędrzejewska

RILEM Publications S.A.R.L.

National Support (Portugal)

International Support

Sponsors

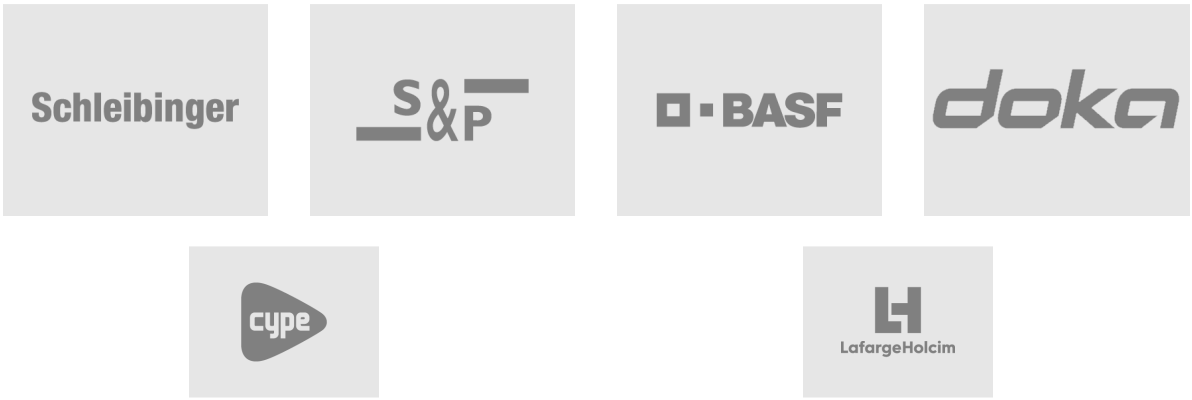

RILEM Publications

The following list is presenting the global offer of RILEM Publications, sorted by series. Each publication is available in printed version and/or in online version.

RILEM PROCEEDINGS (PRO)

PRO 1: Durability of High Performance Concrete (ISBN: 2-912143-03-9); *Ed. H. Sommer*

PRO 2: Chloride Penetration into Concrete (ISBN: 2-912143-00-04); *Eds. L.-O. Nilsson and J.-P. Ollivier*

PRO 3: Evaluation and Strengthening of Existing Masonry Structures (ISBN: 2-912143-02-0); *Eds. L. Binda and C. Modena*

PRO 4: Concrete: From Material to Structure (ISBN: 2-912143-04-7); *Eds. J.-P. Bournazel and Y. Malier*

PRO 5: The Role of Admixtures in High Performance Concrete (ISBN: 2-912143-05-5); *Eds. J. G. Cabrera and R. Rivera-Villarreal*

PRO 6: High Performance Fiber Reinforced Cement Composites - HPFRCC 3 (ISBN: 2-912143-06-3); *Eds. H. W. Reinhardt and A. E. Naaman*

PRO 7: 1st International RILEM Symposium on Self-Compacting Concrete (ISBN: 2-912143-09-8); *Eds. Å. Skarendahl and Ö. Petersson*

PRO 8: International RILEM Symposium on Timber Engineering (ISBN: 2-912143-10-1); *Ed. L. Boström*

PRO 9: 2nd International RILEM Symposium on Adhesion between Polymers and Concrete ISAP '99 (ISBN: 2-912143-11-X); *Eds. Y. Ohama and M. Puterman*

PRO 10: 3rd International RILEM Symposium on Durability of Building and Construction Sealants (ISBN: 2-912143-13-6); *Eds. A. T. Wolf*

PRO 11: 4th International RILEM Conference on Reflective Cracking in Pavements (ISBN: 2-912143-14-4); *Eds. A. O. Abd El Halim, D. A. Taylor and El H. H. Mohamed*

PRO 12: International RILEM Workshop on Historic Mortars: Characteristics and Tests (ISBN: 2-912143-15-2); *Eds. P. Bartos, C. Groot and J. J. Hughes*

PRO 13: 2nd International RILEM Symposium on Hydration and Setting (ISBN: 2-912143-16-0); *Ed. A. Nonat*

PRO 14: Integrated Life-Cycle Design of Materials and Structures - ILCDES 2000 (ISBN: 951-758-408-3); (ISSN: 0356-9403); *Ed. S. Sarja*

PRO 15: Fifth RILEM Symposium on Fibre-Reinforced Concretes (FRC) - BEFIB'2000 (ISBN: 2-912143-18-7); *Eds. P. Rossi and G. Chanvillard*

PRO 16: Life Prediction and Management of Concrete Structures (ISBN: 2-912143-19-5); *Ed. D. Naus*

PRO 17: Shrinkage of Concrete – Shrinkage 2000 (ISBN: 2-912143-20-9); *Eds. V. Baroghel-Bouny and P.-C. Aïtcin*

PRO 18: Measurement and Interpretation of the On-Site Corrosion Rate (ISBN: 2-912143-21-7); *Eds. C. Andrade, C. Alonso, J. Fullea, J. Polimon and J. Rodriguez*

PRO 19: Testing and Modelling the Chloride Ingress into Concrete (ISBN: 2-912143-22-5); *Eds. C. Andrade and J. Kropp*

PRO 20: 1st International RILEM Workshop on Microbial Impacts on Building Materials (CD 02) (e-ISBN 978-2-35158-013-4); *Ed. M. Ribas Silva*

PRO 21: International RILEM Symposium on Connections between Steel and Concrete (ISBN: 2-912143-25-X); *Ed. R. Eligehausen*

PRO 22: International RILEM Symposium on Joints in Timber Structures (ISBN: 2-912143-28-4); *Eds. S. Aicher and H.-W. Reinhardt*

PRO 23: International RILEM Conference on Early Age Cracking in Cementitious Systems (ISBN: 2-912143-29-2); *Eds. K. Kovler and A. Bentur*

PRO 24: 2nd International RILEM Workshop on Frost Resistance of Concrete (ISBN: 2-912143-30-6); *Eds. M. J. Setzer, R. Auberg and H.-J. Keck*

PRO 25: International RILEM Workshop on Frost Damage in Concrete (ISBN: 2-912143-31-4); *Eds. D. J. Janssen, M. J. Setzer and M. B. Snyder*

PRO 26: International RILEM Workshop on On-Site Control and Evaluation of Masonry Structures (ISBN: 2-912143-34-9); *Eds. L. Binda and R. C. de Vekey*

PRO 27: International RILEM Symposium on Building Joint Sealants (CD03); *Ed. A. T. Wolf*

PRO 28: 6th International RILEM Symposium on Performance Testing and Evaluation of Bituminous Materials - PTEBM'03 (ISBN: 2-912143-35-7; e-ISBN: 978-2-912143-77-8); *Ed. M. N. Partl*

PRO 29: 2nd International RILEM Workshop on Life Prediction and Ageing Management of Concrete Structures (ISBN: 2-912143-36-5); *Ed. D. J. Naus*

PRO 30: 4th International RILEM Workshop on High Performance Fiber Reinforced Cement Composites - HPFRCC 4 (ISBN: 2-912143-37-3); *Eds. A. E. Naaman and H. W. Reinhardt*

PRO 31: International RILEM Workshop on Test and Design Methods for Steel Fibre Reinforced Concrete: Background and Experiences (ISBN: 2-912143-38-1); *Eds. B. Schnütgen and L. Vandewalle*

PRO 32: International Conference on Advances in Concrete and Structures 2 vol. (ISBN (set): 2-912143-41-1); *Eds. Ying-shu Yuan, Surendra P. Shah and Heng-lin Lü*

PRO 33: 3rd International Symposium on Self-Compacting Concrete (ISBN: 2-912143-42-X); *Eds. Ó. Wallevik and I. Níelsson*

PRO 34: International RILEM Conference on Microbial Impact on Building Materials (ISBN: 2-912143-43-8); *Ed. M. Ribas Silva*

PRO 35: International RILEM TC 186-ISA on Internal Sulfate Attack and Delayed Ettringite Formation (ISBN: 2-912143-44-6); *Eds. K. Scrivener and J. Skalny*

PRO 36: International RILEM Symposium on Concrete Science and Engineering – A Tribute to Arnon Bentur (ISBN: 2-912143-46-2); *Eds. K. Kovler, J. Marchand, S. Mindess and J. Weiss*

PRO 37: 5th International RILEM Conference on Cracking in Pavements – Mitigation, Risk Assessment and Prevention (ISBN: 2-912143-47-0); *Eds. C. Petit, I. Al-Qadi and A. Millien*

PRO 38: 3rd International RILEM Workshop on Testing and Modelling the Chloride Ingress into Concrete (ISBN: 2-912143-48-9); *Eds. C. Andrade and J. Kropp*

PRO 39: 6th International RILEM Symposium on Fibre-Reinforced Concretes - BEFIB 2004 (ISBN: 2-912143-51-9); *Eds. M. Di Prisco, R. Felicetti and G. A. Plizzari*

PRO 40: International RILEM Conference on the Use of Recycled Materials in Buildings and Structures (ISBN: 2-912143-52-7); *Eds. E. Vázquez, Ch. F. Hendriks and G. M. T. Janssen*

PRO 41: RILEM International Symposium on Environment-Conscious Materials and Systems for Sustainable Development (ISBN: 2-912143-55-1); *Eds. N. Kashino and Y. Ohama*

PRO 42: SCC'2005 - China: 1st International Symposium on Design, Performance and Use of Self-Consolidating Concrete (ISBN: 2-912143-61-6); *Eds. Zhiwu Yu, Caijun Shi, Kamal Henri Khayat and Youjun Xie*

PRO 43: International RILEM Workshop on Bonded Concrete Overlays (e-ISBN: 2-912143-83-7); *Eds. J. L. Granju and J. Silfwerbrand*

PRO 44: 2nd International RILEM Workshop on Microbial Impacts on Building Materials (CD11) (e-ISBN: 2-912143-84-5); *Ed. M. Ribas Silva*

PRO 45: 2nd International Symposium on Nanotechnology in Construction, Bilbao (ISBN: 2-912143-87-X); *Eds. Peter J. M. Bartos, Yolanda de Miguel and Antonio Porro*

PRO 46: ConcreteLife'06 - International RILEM-JCI Seminar on Concrete Durability and Service Life Planning: Curing, Crack Control, Performance in Harsh Environments (ISBN: 2-912143-89-6); *Ed. K. Kovler*

PRO 47: International RILEM Workshop on Performance Based Evaluation and Indicators for Concrete Durability (ISBN: 978-2-912143-95-2); *Eds. V. Baroghel-Bouny, C. Andrade, R. Torrent and K. Scrivener*

PRO 48: 1st International RILEM Symposium on Advances in Concrete through Science and Engineering (e-ISBN: 2-912143-92-6); *Eds. J. Weiss, K. Kovler, J. Marchand, and S. Mindess*

PRO 49: International RILEM Workshop on High Performance Fiber Reinforced Cementitious Composites in Structural Applications (ISBN: 2-912143-93-4); *Eds. G. Fischer and V.C. Li*

PRO 50: 1st International RILEM Symposium on Textile Reinforced Concrete (ISBN: 2-912143-97-7); *Eds. Josef Hegger, Wolfgang Brameshuber and Norbert Will*

PRO 51: 2nd International Symposium on Advances in Concrete through Science and Engineering (ISBN: 2-35158-003-6; e-ISBN: 2-35158-002-8); *Eds. J. Marchand, B. Bissonnette, R. Gagné, M. Jolin and F. Paradis*

PRO 52: Volume Changes of Hardening Concrete: Testing and Mitigation (ISBN: 2-35158-004-4; e-ISBN: 2-35158-005-2); *Eds. O. M. Jensen, P. Lura and K. Kovler*

PRO 53: High Performance Fiber Reinforced Cement Composites - HPFRCC5 (ISBN: 978-2-35158-046-2); *Eds. H. W. Reinhardt and A. E. Naaman*

PRO 54: 5th International RILEM Symposium on Self-Compacting Concrete (ISBN: 978-2-35158-047-9); *Eds. G. De Schutter and V. Boel*

PRO 55: International RILEM Symposium Photocatalysis, Environment and Construction Materials (ISBN: 978-2-35158-056-1); *Eds. P. Baglioni and L. Cassar*

PRO56: International RILEM Workshop on Integral Service Life Modelling of Concrete Structures (ISBN 978-2-35158-058-5); *Eds. R. M. Ferreira, J. Gulikers and C. Andrade*

PRO57: RILEM Workshop on Performance of cement-based materials in aggressive aqueous environments (e-ISBN: 978-2-35158-059-2); *Ed. N. De Belie*

PRO58: International RILEM Symposium on Concrete Modelling - CONMOD'08 (ISBN: 978-2-35158-060-8); *Eds. E. Schlangen and G. De Schutter*

PRO 59: International RILEM Conference on On Site Assessment of Concrete, Masonry and Timber Structures - SACoMaTiS 2008 (ISBN set: 978-2-35158-061-5); *Eds. L. Binda, M. di Prisco and R. Felicetti*

PRO 60: Seventh RILEM International Symposium on Fibre Reinforced Concrete: Design and Applications - BEFIB 2008 (ISBN: 978-2-35158-064-6); *Ed. R. Gettu*

PRO 61: 1st International Conference on Microstructure Related Durability of Cementitious Composites 2 vol., (ISBN: 978-2-35158-065-3); *Eds. W. Sun, K. van Breugel, C. Miao, G. Ye and H. Chen*

PRO 62: NSF/ RILEM Workshop: In-situ Evaluation of Historic Wood and Masonry Structures (e-ISBN: 978-2-35158-068-4); *Eds. B. Kasal, R. Anthony and M. Drdácký*

PRO 63: Concrete in Aggressive Aqueous Environments: Performance, Testing and Modelling, 2 vol., (ISBN: 978-2-35158-071-4); *Eds. M. G. Alexander and A. Bertron*

PRO 64: Long Term Performance of Cementitious Barriers and Reinforced Concrete in Nuclear Power Plants and Waste Management - NUCPERF 2009 (ISBN: 978-2-35158-072-1); *Eds. V. L'Hostis, R. Gens, C. Gallé*

PRO 65: Design Performance and Use of Self-consolidating Concrete - SCC'2009 (ISBN: 978-2-35158-073-8); *Eds. C. Shi, Z. Yu, K. H. Khayat and P. Yan*

PRO 66: 2nd International RILEM Workshop on Concrete Durability and Service Life Planning - ConcreteLife'09 (ISBN: 978-2-35158-074-5); *Ed. K. Kovler*

PRO 67: Repairs Mortars for Historic Masonry (e-ISBN: 978-2-35158-083-7); *Ed. C. Groot*

PRO 68: Proceedings of the 3rd International RILEM Symposium on 'Rheology of Cement Suspensions such as Fresh Concrete (ISBN 978-2-35158-091-2); *Eds. O. H. Wallevik, S. Kubens and S. Oesterheld*

PRO 69: 3rd International PhD Student Workshop on 'Modelling the Durability of Reinforced Concrete (ISBN: 978-2-35158-095-0); *Eds. R. M. Ferreira, J. Gulikers and C. Andrade*

PRO 70: 2nd International Conference on 'Service Life Design for Infrastructure' (ISBN set: 978-2-35158-096-7, e-ISBN: 978-2-35158-097-4); *Ed. K. van Breugel, G. Ye and Y. Yuan*

PRO 71: Advances in Civil Engineering Materials - The 50-year Teaching Anniversary of Prof. Sun Wei' (ISBN: 978-2-35158-098-1; e-ISBN: 978-2-35158-099-8); *Eds. C. Miao, G. Ye, and H. Chen*

PRO 72: First International Conference on 'Advances in Chemically-Activated Materials – CAM'2010' (2010), 264 pp, ISBN: 978-2-35158-101-8; e-ISBN: 978-2-35158-115-5, *Eds. Caijun Shi and Xiaodong Shen*

PRO 73: 2nd International Conference on 'Waste Engineering and Management - ICWEM 2010' (2010), 894 pp, ISBN: 978-2-35158-102-5; e-ISBN: 978-2-35158-103-2, *Eds. J. Zh. Xiao, Y. Zhang, M. S. Cheung and R. Chu*

PRO 74: International RILEM Conference on 'Use of Superabsorsorbent Polymers and Other New Addditives in Concrete' (2010) 374 pp., ISBN: 978-2-35158-104-9; e-ISBN: 978-2-35158-105-6;
Eds. O.M. Jensen, M.T. Hasholt, and S. Laustsen

PRO 75: International Conference on 'Material Science - 2nd ICTRC - Textile Reinforced Concrete - Theme 1' (2010) 436 pp., ISBN: 978-2-35158-106-3; e-ISBN: 978-2-35158-107-0; *Ed. W. Brameshuber*

PRO 76: International Conference on 'Material Science - HetMat - Modelling of Heterogeneous Materials - Theme 2' (2010) 255 pp., ISBN: 978-2-35158-108-7; e-ISBN: 978-2-35158-109-4; *Ed. W. Brameshuber*

PRO 77: International Conference on 'Material Science - AdIPoC - Additions Improving Properties of Concrete - Theme 3' (2010) 459 pp., ISBN: 978-2-35158-110-0; e-ISBN: 978-2-35158-111-7; *Ed. W. Brameshuber*

PRO 78: 2nd Historic Mortars Conference and RILEM TC 203-RHM Final Workshop – HMC2010 (2010) 1416 pp., e-ISBN: 978-2-35158-112-4; *Eds J. Válek, C. Groot, and J. J. Hughes*

PRO 79: International RILEM Conference on Advances in Construction Materials Through Science and Engineering (2011) 213 pp., e-ISBN: 978-2-35158-117-9; *Eds Christopher Leung and K.T. Wan*

PRO 80: 2nd International RILEM Conference on Concrete Spalling due to Fire Exposure (2011) 453 pp., ISBN: 978-2-35158-118-6, e-ISBN: 978-2-35158-119-3; *Eds E.A.B. Koenders and F. Dehn*

PRO 81: 2nd International RILEM Conference on Strain Hardening Cementitious Composites (SHCC2-Rio) (2011) 451 pp., ISBN: 978-2-35158-120-9, e-ISBN: 978-2-35158-121-6; *Eds R.D. Toledo Filho, F.A. Silva, E.A.B. Koenders and E.M.R. Fairbairn*

PRO 82: 2nd International RILEM Conference on Progress of Recycling in the Built Environment (2011) 507 pp., e-ISBN: 978-2-35158-122-3; *Eds V.M. John, E. Vazquez, S.C. Angulo and C. Ulsen*

PRO 83: 2nd International Conference on Microstructural-related Durability of Cementitious Composites (2012) 250 pp., ISBN: 978-2-35158-129-2; e-ISBN: 978-2-35158-123-0; *Eds G. Ye, K. van Breugel, W. Sun and C. Miao*

PRO 85: RILEM-JCI International Workshop on Crack Control of Mass Concrete and Related issues concerning Early-Age of Concrete Structures – ConCrack 3 – Control of Cracking in Concrete Structures 3 (2012) 237 pp., ISBN: 978-2-35158-125-4; e-ISBN: 978-2-35158-126-1; *Eds F. Toutlemonde and J.-M. Torrenti*

PRO 86: International Symposium on Life Cycle Assessment and Construction (2012) 414 pp., ISBN: 978-2-35158-127-8, e-ISBN: 978-2-35158-128-5; *Eds A. Ventura and C. de la Roche*

PRO 87: UHPFRC 2013 – RILEM-fib-AFGC International Symposium on Ultra-High Performance Fibre-Reinforced Concrete (2013), ISBN: 978-2-35158-130-8, e-ISBN: 978-2-35158-131-5; *Eds F. Toutlemonde*

PRO 88: 8th RILEM International Symposium on Fibre Reinforced Concrete (2012) 344 pp., ISBN: 978-2-35158-132-2, e-ISBN: 978-2-35158-133-9; *Eds Joaquim A.O. Barros*

PRO 89: RILEM International workshop on performance-based specification and control of concrete durability (2014) 678 pp, ISBN: 978-2-35158-135-3, e-ISBN: 978-2-35158-136-0; *Eds. D. Bjegović, H. Beushausen and M. Serdar*

PRO 90: 7th RILEM International Conference on Self-Compacting Concrete and of the 1st RILEM International Conference on Rheology and Processing of Construction Materials (2013) 396 pp, ISBN: 978-2-35158-137-7, e-ISBN: 978-2-35158-138-4; *Eds. Nicolas Roussel and Hela Bessaies-Bey*

PRO 91: CONMOD 2014 - RILEM International Symposium on Concrete Modelling (2014), ISBN: 978-2-35158-139-1; e-ISBN: 978-2-35158-140-7; *Eds. Kefei Li, Peiyu Yan and Rongwei Yang*

PRO 92: CAM 2014 - 2nd International Conference on advances in chemically-activated materials (2014) 392 pp., ISBN: 978-2-35158-141-4; e-ISBN: 978-2-35158-142-1; *Eds. Caijun Shi and Xiadong Shen*

PRO 93: SCC 2014 - 3rd International Symposium on Design, Performance and Use of Self-Consolidating Concrete (2014) 438 pp., ISBN: 978-2-35158-143-8; e-ISBN: 978-2-35158-144-5; *Eds. Caijun Shi, Zhihua Ou, Kamal H. Khayat*

PRO 94 (online version): HPFRCC-7 - 7th RILEM conference on High performance fiber reinforced cement composites (2015), e-ISBN: 978-2-35158-146-9; *Eds. H.W. Reinhardt, G.J. Parra-Montesinos, H. Garrecht*

PRO 95: International RILEM Conference on Application of superabsorbent polymers and other new admixtures in concrete construction (2014), ISBN: 978-2-35158-147-6; e-ISBN: 978-2-35158-148-3; *Eds. Viktor Mechtcherine, Christof Schroefl*

PRO 96 (online version): XIII DBMC: XIII International Conference on Durability of Building Materials and Components (2015), e-ISBN: 978-2-35158-149-0; *Eds. M. Quattrone, V.M. John*

PRO 97: SHCC3 – 3rd International RILEM Conference on Strain Hardening Cementitious Composites (2014), ISBN: 978-2-35158-150-6; e-ISBN: 978-2-35158-151-3; *Eds. E. Schlangen, M.G. Sierra Beltran, M. Lukovic, G. Ye*

PRO 98: FERRO-11 – 11th International Symposium on Ferrocement and 3rd ICTRC - International Conference on Textile Reinforced Concrete (2015), ISBN: 978-2-35158-152-0; e-ISBN: 978-2-35158-153-7; *Ed. W. Brameshuber*

PRO 99 (online version): ICBBM 2015 - 1st International Conference on Bio-Based Building Materials (2015), e-ISBN: 978-2-35158-154-4; *Eds. S. Amziane, M. Sonebi*

PRO 100: SCC16 - RILEM Self-Consolidating Concrete Conference (2016)**,** ISBN: 978-2-35158-156-8; e-ISBN: 978-2-35158-157-5

PRO 101 (online version): III Progress of Recycling in the Built Environment (2015), e-ISBN: 978-2-35158-158-2; *Eds I. Martins, C. Ulsen and S. C. Angulo*

PRO 102 (online version): RILEM Conference on Microorganisms-Cementitious Materials Interactions (2016), e-ISBN: 978-2-35158-160-5; *Eds. Alexandra Bertron, Henk Jonkers, Virginie Wiktor*

PRO 103 (online version): ACESC'16 - Advances in Civil Engineering and Sustainable Construction (2016), e-ISBN: 978-2-35158-161-2

PRO 104 (online version): SSCS'2015 - Numerical Modeling - Strategies for Sustainable Concrete Structures (2015), e-ISBN: 978-2-35158-162-9

PRO 105: 1st International Conference on UHPC Materials and Structures (2016), ISBN: 978-2-35158-164-3, e-ISBN: 978-2-35158-165-0

PRO 106: AFGC-ACI-fib-RILEM International Conference on Ultra-High-Performance Fibre-Reinforced Concrete – UHPFRC 2017 (2017), ISBN: 978-2-35158-166-7, e-ISBN: 978-2-35158-167-4; *Eds. François Toutlemonde & Jacques Resplendino*

PRO 107 (online version): XIV DBMC – 14th International Conference on Durability of Building Materials and Components (2017), e-ISBN: 978-2-35158-159-9; *Eds. Geert De Schutter, Nele De Belie, Arnold Janssens, Nathan Van Den Bossche*

PRO 108: MSSCE 2016 - Innovation of Teaching in Materials and Structures (2016), ISBN: 978-2-35158-178-0, e-ISBN: 978-2-35158-179-7; *Ed. Per Goltermann*

PRO 109 (two volumes): MSSCE 2016 - Service Life of Cement-Based Materials and Structures (2016), ISBN Vol. 1: 978-2-35158-170-4, Vol. 2: 978-2-35158-171-4, Set Vol. 1&2: 978-2-35158-172-8, e-ISBN : 978-2-35158-173-5; *Eds. Miguel Azenha, Ivan Gabrijel, Dirk Schlicke, Terje Kanstad and Ole Mejlhede Jensen*

PRO 110: MSSCE 2016 - Historical Masonry (2016), ISBN: 978-2-35158-178-0, e-ISBN: 978-2-35158-179-7; *Eds. Inge Rörig-Dalgaard and Ioannis Ioannou*

PRO 111: MSSCE 2016 - Electrochemistry in Civil Engineering (2016), ISBN: 978-2-35158-176-6, e-ISBN: 978-2-35158-177-3; *Ed. Lisbeth M. Ottosen*

PRO 112: MSSCE 2016 - Moisture in Materials and Structures (2016), ISBN: 978-2-35158-178-0, e-ISBN: 978-2-35158-179-7; *Eds. Kurt Kielsgaard Hansen, Carsten Rode and Lars-Olof Nilsson*

PRO 113: MSSCE 2016 - Concrete with Supplementary Cementitious Materials (2016), ISBN: 978-2-35158-178-0, e-ISBN: 978-2-35158-179-7; *Eds. Ole Mejlhede Jensen, Konstantin Kovler and Nele De Belie*

PRO 114: MSSCE 2016 - Frost Action in Concrete (2016), ISBN: 978-2-35158-182-7, e-ISBN: 978-2-35158-183-4; *Eds. Marianne Tange Hasholt, Katja Fridh and R. Doug Hooton*

PRO 115: MSSCE 2016 - Fresh Concrete (2016), ISBN: 978-2-35158-184-1, e-ISBN: 978-2-35158-185-8; *Eds. Lars N. Thrane, Claus Pade, Oldrich Svec and Nicolas Roussel*

PRO 116: BEFIB 2016 – 9th RILEM International Symposium on Fiber Reinforced Concrete (2016), ISBN: 978-2-35158-187-2, e-ISBN: 978-2-35158-186-5;

PRO 117: 3rd International RILEM Conference on Microstructure Related Durability of Cementitious Composites (2016), ISBN: 978-2-35158-188-9, e-ISBN: 978-2-35158-189-6; *Eds. Changwen Miao, Wei Sun, Jiaping Liu, Huisu Chen, Guang Ye and Klaas van Breugel*

PRO 118 (4 volumes): International Conference on Advances in Construction Materials and Systems (2017), ISBN Set: 978-2-35158-190-2, Vol. 1: 978-2-35158-193-3, Vol. 2: 978-2-35158-194-0, Vol. 3: ISBN:978-2-35158-195-7, Vol. 4: ISBN:978-2-35158-196-4, e-ISBN: 978-2-35158-191-9; *Ed. Manu Santhanam*

PRO 119 (online version): ICBBM 2017 - Second International RILEM Conference on Bio-based Building Materials, (2017), e-ISBN: 978-2-35158-192-6; *Ed. Sofiane Amziane*

PRO 120 (2 volumes): EAC-02 - 2nd International RILEM/COST Conference on Early Age Cracking and Serviceability in Cement-based Materials and Structures, (2017), Vol. 1: 978-2-35158-199-5, Vol. 2: 978-2-35158-200-8, Set: 978-2-35158-197-1, e-ISBN: 978-2-35158-198-8; *Eds. Stéphanie Staquet and Dimitrios Aggelis*

RILEM REPORTS (REP)

Report 19: Considerations for Use in Managing the Aging of Nuclear Power Plant Concrete Structures (ISBN: 2-912143-07-1); *Ed. D. J. Naus*

Report 20: Engineering and Transport Properties of the Interfacial Transition Zone in Cementitious Composites (ISBN: 2-912143-08-X); *Eds. M. G. Alexander, G. Arliguie, G. Ballivy, A. Bentur and J. Marchand*

Report 21: Durability of Building Sealants (ISBN: 2-912143-12-8); *Ed. A. T. Wolf*

Report 22: Sustainable Raw Materials - Construction and Demolition Waste (ISBN: 2-912143-17-9); *Eds. C. F. Hendriks and H. S. Pietersen*

Report 23: Self-Compacting Concrete state-of-the-art report (ISBN: 2-912143-23-3); *Eds. Å. Skarendahl and Ö. Petersson*

Report 24: Workability and Rheology of Fresh Concrete: Compendium of Tests (ISBN: 2-912143-32-2); *Eds. P. J. M. Bartos, M. Sonebi and A. K. Tamimi*

Report 25: Early Age Cracking in Cementitious Systems (ISBN: 2-912143-33-0); *Ed. A. Bentur*

Report 26: Towards Sustainable Roofing (Joint Committee CIB/RILEM) (CD 07) (e-ISBN 978-2-912143-65-5); *Eds. Thomas W. Hutchinson and Keith Roberts*

Report 27: Condition Assessment of Roofs (Joint Committee CIB/RILEM) (CD 08) (e-ISBN 978-2-912143-66-2); *Ed. CIB W 83/RILEM TC166-RMS*

Report 28: Final report of RILEM TC 167-COM 'Characterisation of Old Mortars with Respect to Their Repair (ISBN: 978-2-912143-56-3); *Eds. C. Groot, G. Ashall and J. Hughes*

Report 29: Pavement Performance Prediction and Evaluation (PPPE): Interlaboratory Tests (e-ISBN: 2-912143-68-3); *Eds. M. Partl and H. Piber*

Report 30: Final Report of RILEM TC 198-URM 'Use of Recycled Materials' (ISBN: 2-912143-82-9; e-ISBN: 2-912143-69-1); *Eds. Ch. F. Hendriks, G. M. T. Janssen and E. Vázquez*

Report 31: Final Report of RILEM TC 185-ATC 'Advanced testing of cement-based materials during setting and hardening' (ISBN: 2-912143-81-0; e-ISBN: 2-912143-70-5); *Eds. H. W. Reinhardt and C. U. Grosse*

Report 32: Probabilistic Assessment of Existing Structures. A JCSS publication (ISBN 2-912143-24-1); *Ed. D. Diamantidis*

Report 33: State-of-the-Art Report of RILEM Technical Committee TC 184-IFE 'Industrial Floors' (ISBN 2-35158-006-0); *Ed. P. Seidler*

Report 34: Report of RILEM Technical Committee TC 147-FMB 'Fracture mechanics applications to anchorage and bond' Tension of Reinforced Concrete Prisms – Round Robin Analysis and Tests on Bond (e-ISBN 2-912143-91-8); *Eds. L. Elfgren and K. Noghabai*

Report 35: Final Report of RILEM Technical Committee TC 188-CSC 'Casting of Self Compacting Concrete' (ISBN 2-35158-001-X; e-ISBN: 2-912143-98-5); *Eds. Å. Skarendahl and P. Billberg*

Report 36: State-of-the-Art Report of RILEM Technical Committee TC 201-TRC 'Textile Reinforced Concrete' (ISBN 2-912143-99-3); *Ed. W. Brameshuber*

Report 37: State-of-the-Art Report of RILEM Technical Committee TC 192-ECM 'Environment-conscious construction materials and systems' (ISBN: 978-2-35158-053-0); *Eds. N. Kashino, D. Van Gemert and K. Imamoto*

Report 38: State-of-the-Art Report of RILEM Technical Committee TC 205-DSC 'Durability of Self-Compacting Concrete' (ISBN: 978-2-35158-048-6); *Eds. G. De Schutter and K. Audenaert*

Report 39: Final Report of RILEM Technical Committee TC 187-SOC 'Experimental determination of the stress-crack opening curve for concrete in tension' (ISBN 978-2-35158-049-3); *Ed. J. Planas*

Report 40: State-of-the-Art Report of RILEM Technical Committee TC 189-NEC 'Non-Destructive Evaluation of the Penetrability and Thickness of the Concrete Cover' (ISBN 978-2-35158-054-7);
Eds. R. Torrent and L. Fernández Luco

Report 41: State-of-the-Art Report of RILEM Technical Committee TC 196-ICC 'Internal Curing of Concrete' (ISBN 978-2-35158-009-7); *Eds. K. Kovler and O. M. Jensen*

Report 42: 'Acoustic Emission and Related Non-destructive Evaluation Techniques for Crack Detection and Damage Evaluation in Concrete' - Final Report of RILEM Technical Committee 212-ACD (e-ISBN: 978-2-35158-100-1); *Ed. M. Ohtsu*

Report 45: Repair Mortars for Historic Masonry - State-of-the-Art Report of RILEM Technical Committee TC 203-RHM (e-ISBN: 978-2-35158-163-6); *Eds. Paul Maurenbrecher and Caspar Groot*

Report 46: Surface delamination of concrete industrial floors and other durability related aspects guide - Report of RILEM Technical Committee TC 268-SIF (e-ISBN: 978-2-35158-201-5); *Ed. Valérie Pollet*

Conference Chairs

Miguel Azenha, Dirk Schlicke

Scientific Committee Chairs

Farid Benboudjema, Agnieszka Jędrzejewska

National Organizing Committee

Paulo Lobo, José Sena Cruz, Eduardo Júlio, Rui Faria, Manuel Pipa, Romeu Vicente

COST Organizing Committee

Violeta Bokan-Bosiljkov, Laurie Lacarrière, Terje Kanstad, Sreejith Nanukuttan, Emmanuel Rozière, Marijana Serdar, Stéphanie Staquet, François Toutlemonde, Mateusz Wyrzykowski

Scientific Committee

Farid Benboudjema (Chair)
Agnieszka Jędrzejewska (Chair)
Ouali Amiri
Sofiane Amziane
Shingo Asamoto
Miguel Azenha
Nele de Belie
Violeta Bokan Bosiljkov
Alexandra Bourdot
Matthieu Briffaut
Tomo Cerovšek
Özlem Cizer
Gianluca Cusatis
Aveline Darquennes
Szymon Dawczyński
Eduardo Fairbairn
Rui Faria
Ivan Gabrijel
Erez Gal
Dariusz Gawin
Ole Jensen
Joachim Juhart
Terje Kanstad
Eduardus Koenders
Barbara Klemczak
Laurie Lacarrière
Paulo B. Lourenço
Ippei Maruyama
Kyuichi Maruyama
Enrico Masoero
Hadi Mazaheripour
Sreejith Nanukuttan
Małgorzata Pająk
Arnaud Perrot
Bernhard Pichler
Manuel Pipa
John Provis
Vlastimir Radonjanin
Marta Roig
Emmanuel Rozière
Mercedes Sanchez Moreno
Ryoichi Sato
José Sena-Cruz
Dirk Schlicke
Geert De Schutter
Giuseppe Sciumè
Marijana Serdar
Carlos Serra
Ioannis Sfikas
Paulo Silva Lobo
Mohammed Sonebi
Carlos Sousa
Tayfun Altuğ Söylev
Maria Stefanidou
Stéphanie Staquet
Aljoša Šajna
Vít Šmilauer
Luping Tang
Katrin Turner
Jean-Michel Torrenti
François Toutlemonde
Jörg F. Unger
Neven Ukrainczyk
Mateusz Wyrzykowski
Guang Ye
Ismail Yurtdas
Xiangming Zhou
Mariusz Zych

Preface

The focus of the conference is set to communicating, discussing and arousing progress in research, development and application of Cement-based Materials and Structural Concrete, which have been attained through combination of expertise from distinct fields of knowledge. Indeed, in the words of Federico Capasso, a renowned Physicist who was one of the inventors of the quantum cascade laser:

> "*... we must not think of science in a disciplinary way, by making boxes. Nature does not know what physics, chemistry or biology is! It is a question of putting an end to the positivist philosophy of Auguste Comte, fortunately in decline of speed, which classified the disciplines and despised the experimental activity.*"

The intent of this conference was therefore to provide added value through collaboration and by bringing together researchers and practitioners with similar views in regard to interdisciplinary approaches in the fields of Cement-based Materials and Structural Concrete: it is about **Syner**gizing expertise on the ultimate goal of Structural Conc**Crete**, hence the acronym **SynerCrete**, was chosen for the conference. Exciting fields of research such as performance-based design, 3D modelling for analysis/design, Building Information Modelling and even robotics (e.g. digital fabrication or robotics design) were included, while retaining focus on multi-scale approaches at time and spatial levels.

SynerCrete'18 also marks the end of COST Action TU1404 "Towards the next generation of standards for service life of cement-based materials and structures" (www.tu1404.eu), offering a final forum to the discussions raised during the funded period of the Action, that started 4 years ago in 2014. The conference is an opportunity for the 304 COST Action members to deepen their collaboration and to focus on activities that allow the continuation of the networking which was established by the Action. A sense of accomplishment is felt by all the members of the Action, in the view of the important achievements of networking tools that were brought about by the extended Round Robin Testing Programme (RRT+), the Numerical Benchmarking Activities and 24 Short Term Scientific Missions (STSMs). Indeed, a remarkable number of papers that have been published in the two volumes of these Conference Proceedings are directly a result of one of the aforementioned networking tools.

The conference has consisted of 8 key-note speakers and 180 regular papers presented over 3 days. It is also relevant to emphasize the collaboration of another COST Action in SynerCrete: COST Action CA15202 "Self-healing As preventive Repair of COncrete Structures – SARCOS", which has an important contribution to the purposes of COST TU1404.

A further remark in regard to the wide international institutional support that this conference attained, is about the direct support of RILEM, fib, JCI and ACI. Specifically, with regard to the Japanese Concrete Institute, a mention is given to the special session dedicated to the most recent version of "JCI Guidelines for Control of Cracking of Mass Concrete", as it was indeed one of the most inspiring documents that influenced the genesis of COST Action TU1404.

A final word is given in regard to the location of the conference which combines implicit symbolisms. Firstly, this is the only event of COST Action TU1404 taking place in Portugal, which is the home country of the Grant Holder and Chairman of the Action. Secondly, the conference venue is the island of Madeira, therefore not in mainland Portugal, putting attention to one of the remotest regions of Europe, officially classified as one of the eight ultra-peripheral regions of the European Union.

Miguel Azenha **Dirk Schlicke** **Farid Benboudjema** **Agnieszka Jędrzejewska**

October 2018, Funchal, Portugal

Acknowledgements

This publication is based upon work from COST Action TU1404 'Towards the next generation of standards for service life of cement-based materials and structures', supported by COST (European Cooperation in Science and Technology).

COST (European Cooperation in Science and Technology) is a pan-European intergovernmental framework. Its mission is to enable break-through scientific and technological developments leading to new concepts and products and thereby contribute to strengthening Europe's research and innovation capacities. It allows researchers, engineers and scholars to jointly develop their own ideas and take new initiatives across all fields of science and technology, while promoting multi- and interdisciplinary approaches. COST aims at fostering a better integration of less research intensive countries to the knowledge hubs of the European Research Area. The COST Association, an International not-for-profit Association under Belgian Law, integrates all management, governing and administrative functions necessary for the operation of the framework. The COST Association has currently 37 Member Countries.

Funded by the Horizon 2020 Framework Programme
of the European Union

www.tu1404.eu
www.cost.eu

VOLUME 1

KEYNOTE LECTURES

COST ACTION TU1404 - RRT+, NUMERICAL BENCHMARKING AND RECOMMENDATIONS

CONCRETE TECHNOLOGY AND ADVANCED MATERIAL TESTING

FIBRE-REINFORCED CONCRETE AND NON-METALLIC REINFORCEMENT

SELF-HEALING AND REPAIR OF CONCRETE STRUCTURES (COST CA15202 - SARCOS)

KEYNOTE LECTURES

SynerCrete'18 International Conference on Interdisciplinary Approaches
for Cement-based Materials and Structural Concrete
24-26 October 2018, Funchal, Madeira Island, Portugal

INNOVATION IN RESEARCH ON NEW BINDERS

John L. Provis [(1)]

(1) University of Sheffield, Sheffield S1 3JD, UK

Abstract
The development and uptake of new cementitious binders is always a slow process, in a global industry which is both very large and necessarily very conservative. However, the drivers for diversification of the world's "toolkit" of cements are growing stronger, as we appreciate that it is not possible to meet the construction and infrastructure needs of global society with a "one-size-fits-all" material solution, as we seek sustainable development at both local and worldwide levels. This is fundamentally because human society is the sum (not the average) of a very diverse set of local scenarios, each with its own particular set of needs, and each with its own portfolio of resources. If we were to consider the average, there would potentially be a single best option that is valid worldwide - but this is not the case, and a technology (cement, concrete or any other material) which is sustainable and optimal in one location will often not be appropriate in another. This leads to the absolute requirement for development of a toolkit of cements, each of which is sustainable and fit for purpose in its own scenario and context. This presentation will give some examples of such cements, with a particular focus on alkali-activated binders, and will outline how innovation in materials science research is intrinsically interlinked with innovation in use and uptake of new materials.

1. The role of alternative binders in the future cements landscape

As global society seeks sustainability in every aspect of its activities, following international treaties, commitments and pledges to protect the planet for future generations, the construction materials industry faces deep and fundamental challenges. As the largest-volume manufactured product worldwide other than drinking water, Portland cement is used almost ubiquitously, and is valued for its technical characteristics (strength and durability), its ease of use, and most of all its versatility and robustness. This brings the ability to 'mistreat' a material in many practical senses through improper formulation, mixing, casting and curing,

yet still obtaining sufficient technical performance for general usage in non-structural applications. However, as society aims to reduce anthropogenic influence on the global environment, and thus the intrinsic carbon dioxide emissions profile of Portland cement receives increasing scrutiny, it is increasingly becoming clear that there are important roles to play within a broader construction materials 'toolkit', for alternative materials that can offer sufficient (or outstanding) technical characteristics in specified applications, without these necessarily needing to be as broadly applicable or universally available as is Portland cement.

Examples of attractive members of this cements toolkit include calcium aluminate cements [1, 2], various magnesia-based cements (silicates, phosphates, carbonates, oxysalts, and others) [3-7], and alternative clinker types including those containing hydraulic calcium sulfoaluminate or sulfosilicate phases [8-10], as well as those which more closely resemble the chemistry of conventional Portland cement, such as belitic clinkers [11-13] and high-volume blends of latent hydraulic or pozzolanic supplementary cementitious materials (SCMs) with Portland cement [14-18]. In the early period of cement usage through the 1800s – and before Portland cement became established as the near-universal cement deployed in construction – there was a much broader range of cement types available [19], and it is in fact debatable whether the first "Portland cements" (including those described by the 1824 patent of Aspdin) bear any real resemblance to those which were produced even 100 years later [20], let alone those used in current engineering practice.

Having seen the global growth and domination of Portland cement extend to every part of the globe in the past decades, with over 100 million tonnes of cement and clinker now transported internationally by ship per annum (and at least a similar quantity transported domestically by ship) [21], there is growing emphasis on "local solutions to local needs" as a pathway to reducing the environmental impact of the global construction materials industry. Much of the long-distance transport of cements is required because local production facilities are not sufficient to meet demand – for example, in parts of sub-Saharan Africa which import cement – but many of these regions do have locally-available mineral or by-product resources which can be eminently suited to the production of non-Portland cements. A particular example of this is the tropical belt of lateritic clay soils, which are found in locations such as western Africa and northern Brazil which have high demand for construction and relatively low levels of industrialisation, have been used effectively in the development of alkali-activated binders [22, 23]. Similarly, nations such as South Africa and Australia which have very high levels of fly ash generation from coal combustion provide obvious and attractive scope for the use of alkali-activation in valorising this material [24, 25].

The utilisation of local resources offers the possibility for large-scale improvement in the selection and use of construction materials in local contexts, through diversification and the adoption of a materials toolkit approach. The value of such an approach becomes particularly evident when we consider what is really meant by the "global construction industry". Most national and international roadmapping and planning exercises are conducted on the basis of averaging across local situations, with weighting factors applied as needed, to distil a large and complex body of data into readily comprehensible information. However, such an approach will inevitably lead to recommendations of a one-size-fits-all approach, as local variations are smoothed out, and the apparent 'best' overall solution for a globally averaged

calculation is unlikely to be locally optimal in regions which have very different needs and materials availability. The alternative approach – and the one which is likely to strongly highlight the value of the toolkit approach to materials selection – is to change the methodology by which local scenarios are aggregated: instead of considering the *average* of all local scenarios, it is better to consider their *sum*. So, rather than attempting to homogenise all of the details and special circumstances which prevail locally, these can be considered and an appropriate toolkit designed and made available to account for them. Using the strengths, opportunities and resources in each location, to make available appropriate and fit-for-purposes materials and processes, also opens the possibility for vernacular expertise and skills to be fully incorporated into future sustainable development paradigms, rather than an externally-driven, externally-imposed, uniform solution.

It should also be noted that there is a strong possibility that such a local analysis will result in the recommendation that a particular material (e.g. an alkali-activated binder) turns out not to be the most appropriate selection for a particular location. This raises a further point around the design of a materials toolkit approach: it is essential that advocates of sustainable construction as a whole, can decouple this from the (often financially based) drive to advocate a single material above all others regardless of context. An attitude shift is needed: instead of asking "*can* this material be used in this application?", a more valuable question to ask (and far more difficult to answer holistically) is "*should* this material be used in this application?". This question requires a combination of technical or scientific insight (to be addressed in the following section), linked with economic, social and environmental insights, to generate an answer which can realistically be used as the basis of decision-making in materials selection at a large scale. This is generally not something that can be achieved by a single researcher, specifier, producer, designer, engineer, technologist or policy-maker, but requires multi-disciplinary combinations of insight to justify and support materials selection which is technically sound, environmentally responsible, and economically feasible.

2. The importance of materials science in developing and validating new cements

The development of a deeper understanding of the materials science of cements – both Portland and non-Portland based – is fundamental and essential to proving their serviceability and durability [26-28]. This is particularly important in applications where very long term durability is critical, and where the timescales of importance are far beyond those which are accessible in the laboratory; for example, in major infrastructure projects in demanding environments which are designed for a service life of centuries or more [26, 29, 30], and in the long-term storage and disposal of nuclear waste, which may require cementitious materials to serve their designed purpose for hundreds of millennia in preventing the release of contaminants [31-33]. The particular needs of this latter application are one of the reasons why so much of the fundamental science of cements has been developed and published by organisations and research programmes linked to the nuclear energy sector, but the availability of this information brings obvious and essential benefits in other usages of cements as well.

The work of cement chemists (and cement materials scientists more broadly) has on occasion been criticised for being apparently esoteric in nature, and not always fully connected to civil engineering applications [34]. While this is certainly true in some instances, with high-profile research programmes having generated (and widely disseminated) research outputs which are demonstrably incorrect regarding, for example, the fundamental science and chemical nature of cement hydrate gels, alkali-activated binders, and solid-fluid reaction processes, this should not be extended to discarding the essential – and correct – research findings of those who have conducted careful and detailed research to generate new physicochemical insight from advanced modelling and experimental investigations. Rather, any apparent mis-steps that may appear in the scientific record need to be openly discussed (see e.g. documents such as [35, 36], as well as numerous 'Discussion' or 'Letter to the Editor' documents published in journals, although at a decreasing rate in recent years compared to the historical practice), any useful information that can be gleaned from the work extracted in any case, and the results used to build 'more correct' theoretical foundations for our understanding. The field of cements science is – fortunately – one in which fundamental and important questions remain the topic of evolving discussion, analysis and improvement [29]; there are many key scientific advances still remaining to be made in this field, and many points upon which leading experts have not yet reached consensus regarding the underlying chemical and physical processes and molecular structures that control the reactivity and performance of cementitious materials, both novel and "traditional".

This also raises the need for advances in the application of modern materials science characterisation techniques to the study of cements [37, 38]. Cementitious binders are almost invariably complex in chemical and mineralogical characteristics, often dominated by crystallographically disordered phases, and are dynamic materials which evolve significantly as a function of time (unless hydration is halted – which is a potentially intrusive procedure in and of itself). The presence of water in most cement reaction products raises additional difficulty in applying techniques that may require vacuum conditions for analysis, e.g. surface-sensitive spectroscopic and many microscopic techniques, the binder phases are often prone to atmospheric carbonation during sample preparation, transfer and analysis, and the brittle and porous nature of cementitious specimens can also make sample preparation challenging. However, through appropriately careful sample preparation, the application of advanced analytical techniques can bring insight, understanding and advancement in the field which more than justifies the difficulties involved in obtaining, analysing and interpreting the data. There are certainly cases where the application of highly advanced analytical approaches brings essentially the same information as can be obtained from more 'everyday' experimentation – and often in a more time-consuming and expensive manner – leading to criticisms that researchers are seeking a "beautiful answer to a stupid question". However, if experimental campaigns are more intelligently designed to make use of the unique capabilities of specific tools, techniques and instruments, some truly unique (and valuable) scientific studies, and important engineering insight, can certainly be gained.

3. Conclusions

The value that can be derived from the broader uptake and use of innovative types of cements, as a component of a future sustainable global built environment, must be motivated by a real industrial or societal demand. Technology push will never be enough to bring a new cement into large scale use; something which appears to be a solution in search of a problem is much less attractive than the ability to develop a tailored solution to solve a clearly identified problem. In some cases, the problem must first be highlighted as end-users are not necessarily aware that the performance of the existing material or design solution is below desirable levels, but there are many cases – for example, related to the need to reduce global carbon emissions, or to improve the acid resistance of concrete sewer pipes – where the problem is well understood and the industry is actively seeking a solution (or set of solutions). In such cases, it is extremely valuable for a scientist, engineer or technologist to hold a 'toolkit' of materials, understanding the strengths and limitations of each, to enable them to generate and validate recommendations for the selection of the best material for each task. In current practice, the 'best' is generally assumed to be Portland cement, simply because it is the ubiquitous answer to almost every question of cement selection. However, in a sustainable future society where a materials toolkit is truly available, this need not always be the case. Portland cement, and its blends, will certainly continue to play a major role in global construction for the foreseeable future. However, the availability of a validated toolkit of fit-for-purpose alternative cements will add value and bring outstanding opportunities to improve technical, environmental and economic performance in the industry, and this more than justifies the continued effort in research, development and deployment of alternative cements.

Acknowledgements
The research leading to these results has received funding from the European Research Council under the European Union's Seventh Framework Programme (FP7/2007-2013)/ ERC grant agreement n° 335928 "GeopolyConc", and from the Engineering and Physical Sciences Research Council (UK), grants EP/M003272/1 and EP/P013171/1.

References

[1] K.L. Scrivener, J.-L. Cabiron, R. Letourneux, High-performance concretes from calcium aluminate cements, Cem Concr Res, 29 (1999) 1215-1223.
[2] C. Evju, S. Hansen, Expansive properties of ettringite in a mixture of calcium aluminate cement, Portland cement and β-calcium sulfate hemihydrate, Cem Concr Res, 31 (2001) 257-261.
[3] S.A. Walling, J.L. Provis, Magnesia based cements – a journey of 150 years, and cements for the future?, Chem Rev, 116 (2016) 4170-4204.
[4] C. Roosz, S. Grangeon, P. Blanc, V. Montouillout, B. Lothenbach, P. Henocq, E. Giffaut, P. Vieillard, S. Gaboreau, Crystal structure of magnesium silicate hydrates (M-S-H): The relation with 2:1 Mg–Si phyllosilicates, Cem Concr Res, 73 (2015) 228-237.
[5] S. Sorel, Sur un nouveau ciment magnésien (On a new magnesium cement), C R Hebd Acad Sci (Paris), 65 (1867) 102-104.

[6] T. Zhang, L.J. Vandeperre, C.R. Cheeseman, Magnesium-silicate-hydrate cements for encapsulating problematic aluminium containing wastes, J Sust Cem-Based Mater, 1 (2012) 34-45.
[7] A.S. Wagh, Chemically Bonded Phosphate Ceramics, Elsevier, Oxford, UK, 2004.
[8] E. Gartner, T. Sui, Alternative cement clinkers, Cem Concr Res, (2018) in press, DOI 10.1016/j.cemconres.2017.1002.1002.
[9] T. Hanein, I. Galan, F.P. Glasser, S. Skalamprinos, A. Elhoweris, M.S. Imbabi, M.N. Bannerman, Stability of ternesite and the production at scale of ternesite-based clinkers, Cem Concr Res, 98 (2017) 91-100.
[10] F. Bullerjahn, D. Schmitt, M. Ben Haha, Effect of raw mix design and of clinkering process on the formation and mineralogical composition of (ternesite) belite calcium sulphoaluminate ferrite clinker, Cem Concr Res, 59 (2014) 87-95.
[11] C.D. Popescu, M. Muntean, J.H. Sharp, Industrial trial production of low energy belite cement, Cem Concr Compos, 25 (2003) 689-693.
[12] L. Kacimi, A. Simon-Masseron, S. Salem, A. Ghomari, Z. Derriche, Synthesis of belite cement clinker of high hydraulic reactivity, Cem Concr Res, 39 (2009) 559-565.
[13] J.J. Thomas, S. Ghazizadeh, E. Masoero, Kinetic mechanisms and activation energies for hydration of standard and highly reactive forms of β-dicalcium silicate (C2S), Cem Concr Res, 100 (2017) 322-328.
[14] E. Gartner, H. Hirao, A review of alternative approaches to the reduction of CO2 emissions associated with the manufacture of the binder phase in concrete, Cem Concr Res, 78 (2015) 126-142.
[15] M.C.G. Juenger, R. Siddique, Recent advances in understanding the role of supplementary cementitious materials in concrete, Cem Concr Res, 78 (2015) 71-80.
[16] B. Lothenbach, K. Scrivener, R.D. Hooton, Supplementary cementitious materials, Cem Concr Res, 41 (2011) 1244-1256.
[17] R. Snellings, G. Mertens, J. Elsen, Supplementary cementitious materials, Rev Miner Geochem, 74 (2012) 211-278.
[18] K. Scrivener, F. Martirena, S. Bishnoi, S. Maity, Calcined clay limestone cements (LC3), Cem Concr Res, (2018) in press, DOI 10.1016/j.cemconres.2017.1008.1017.
[19] G.R. Redgrave, C. Spackman, Calcareous Cements: Their Nature, Manufacture, and Uses, with some Observations upon Cement Testing (2nd Ed.), Charles Griffin & Company, London, 1905.
[20] A.C. Davis, A Hundred Years of Portland Cement, 1824-1924, Concrete Publications Limited, London, 1924.
[21] A. Ligthart, Cement and clinker trade and risk of a Chinese slowdown, Global Cement, http://www.globalcement.com/magazine/articles/995-cement-and-clinker-trade-and-risk-of-a-chinese-slowdown, 2016.
[22] P.N. Lemougna, A.B. Madi, E. Kamseu, U.C. Melo, M.-P. Delplancke, H. Rahier, Influence of the processing temperature on the compressive strength of Na activated lateritic soil for building applications, Contr Build Mater, 65 (2014) 60-66.
[23] K.C. Gomes, G.S.T. Lima, S.M. Torres, S. De Barros, I.F. Vasconcelos, N.P. Barbosa, Iron distribution in geopolymer with ferromagnetic rich precursor, Mater Sci Forum, 643 (2010) 131-138.

[24] J. Shekhovtsova, I. Zhernovsky, M. Kovtun, N. Kozhukhova, I. Zhernovskaya, E. Kearsley, Estimation of fly ash reactivity for use in alkali-activated cements - A step towards sustainable building material and waste utilization, J Cleaner Prod, 178 (2018) 22-33.
[25] Beyond Zero Emissions, Zero Carbon Industry Plan - Rethinking Cement, Melbourne, 2017.
[26] M. Alexander, M. Thomas, Service life prediction and performance testing — Current developments and practical applications, Cem Concr Res, 78 (2015) 155-164.
[27] R.D. Hooton, J.A. Bickley, Design for durability: The key to improving concrete sustainability, Constr Build Mater, 67C (2014) 422-430.
[28] H.M. Jennings, J.W. Bullard, From electrons to infrastructure: Engineering concrete from the bottom up, Cem Concr Res, 41 (2011) 727-735.
[29] J.J. Biernacki, J.W. Bullard, G. Sant, K. Brown, Fredrik P. Glasser, S. Jones, T. Ley, R. Livingston, L. Nicoleau, J. Olek, F. Sanchez, R. Shahsavari, P.E. Stutzman, K. Sobolev, T. Prater, Cements in the 21st century: challenges, perspectives, and opportunities, J Am Ceram Soc, 100 (2017) 2746-2773.
[30] J.R. Clifton, Predicting the service life of concrete, ACI Mater J, 90 (1993) 611-617.
[31] A.S. Aloy, J.R. Harbour, E.W. Holtzscheiter, C.A. Langton, Evaluation of durability of mortars and concretes used in ancient structures, MRS Symp Proc, 1107 (2008).
[32] N.B. Milestone, Reactions in cement encapsulated nuclear wastes: Need for toolbox of different cement types, Adv Appl Ceram, 105 (2006) 13-20.
[33] F.P. Glasser, Mineralogical aspects of cement in radioactive waste disposal, Miner Mag, 65 (2001) 621-633.
[34] A.M. Neville, Neville on Concrete (2nd Ed), Booksurge, Charleston, SC, 2006.
[35] I.G. Richardson, The importance of proper crystal-chemical and geometrical reasoning demonstrated using layered single and double hydroxides, Acta Cryst B, 69 (2013) 150-162.
[36] J.L. Provis, On the use of the Jander equation in cement hydration modelling, RILEM Techn Lett 1 (2016) 62-67.
[37] J.L. Provis, A. Hajimohammadi, C.E. White, S.A. Bernal, R.J. Myers, R.P. Winarski, V. Rose, T.E. Proffen, A. Llobet, J.S.J. van Deventer, Nanostructural characterization of geopolymers by advanced beamline techniques, Cem Concr Compos, 36 (2013) 56-64.
[38] S.R. Chae, J. Moon, S. Yoon, S. Bae, P. Levitz, R. Winarski, P.J.M. Monteiro, Advanced nanoscale characterization of cement based materials using X-ray synchrotron radiation: A review, Int J Concr Struct Mater, 7 (2013) 95-110.

SynerCrete'18 International Conference on Interdisciplinary Approaches
for Cement-based Materials and Structural Concrete
24-26 October 2018, Funchal, Madeira Island, Portugal

UNDERSTANDING MATERIAL-DEPENDENT STRUCTURAL BEHAVIOUR FOR THE AGING MANAGEMENT OF CONCRETE STRUCTURES

Ippei Maruyama [(1)]

(1) Nagoya University, Nagoya, Japan

Abstract
The structural performance of concrete structures constantly changes due to the chemical and physical reactions of concrete components in a given environment. For the long-term use of concrete structures, such aging phenomena should be understood and controlled. Herein, the most common environmental drying impacts on concrete structures are discussed with regards to the cement paste, aggregate and their mutual interactions; the roles of these elements on structural performance are clarified. The alteration of calcium silicate hydrate in Portland cement paste during the first drying significantly impacts the strength and shrinkage of cement paste and concrete. The rock-forming mineral composition of the aggregate used plays a significant role in the volume stability. Damage caused by an imbalance of volumetric change between aggregates and cement paste significantly contributes to the compressive strength and Young's modulus of concrete. Structural performance changes of a shear reinforced concrete wall due to drying are explained by examining the roles of concrete components.

1. Introduction

For the continuous use of concrete structures after disasters, the monitoring of the health of concrete structures by using sensors is one of the promising technologies. Recently, many public buildings have been installed with accelerators and velocimeters. These sensors can evaluate the dynamic motion of building structures; the accelerator results as a function of deformation (obtained by the second-order integration of the accelerator) represent the relationship between force and deformation. Based on this relationship, the structural damage can be obtained by a difference of tangents. As is shown in Fig. 1, all the concrete structures showed natural frequency changes with time [1]. These trends are not yielded during mid- or

small- earthquakes, instead they take place during in-between earthquakes [2]. The general environmental condition, namely, drying, mostly likely has an impact on concrete and concrete structures.

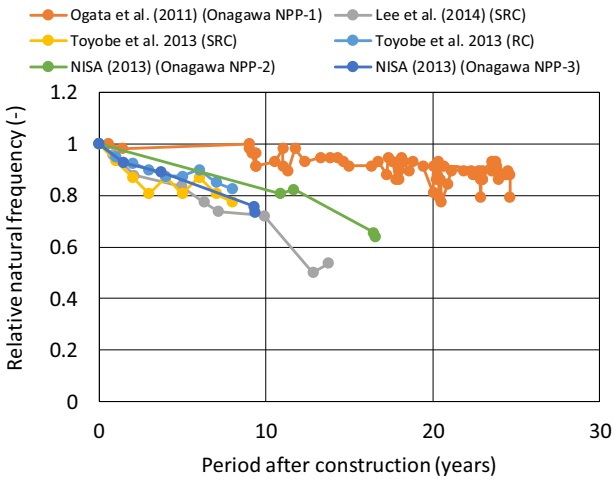

Figure 1: Natural frequency changes of concrete buildings [1].

2. Hardened cement paste

Hardened cement paste (hcp) is considered a porous and colloidal material [3]. The colloidal nature has been confirmed by sorption measurements [4,5], small-angle scattering measurements [6,7], and visual observations [8]. To understand the nature of hcp, especially for the first desorption process, the physical properties [10], microstructure [10, 11] as well as shrinkage behaviour [10, 12] have been studied. As shown in Figure 2, the bending strength and Young's modulus of matured hcp showed dramatic changes under different relative humidity (RH) conditions. At the same time, the microstructure of hcp changed during this drying process, as shown in Figure 3. Due to the colloidal nature of calcium silicate hydrate (C-S-H), which is the major hydrate of Portland cement paste, the capillary pores in hcp increased during the drying; therefore, the trend of decreasing general strength has been confirmed, especially from 90% to 40% RH, due to the stress concentration mechanism caused by an increase in capillary pores. At the same time, the solid portion agglomerated [11] and the interlayer distance of C-S-H reduced when the RH was less than or equal to 40% RH [11]. The strength and Young's modulus of C-S-H increased by this solid phase alteration in the corresponding RH range, as shown in Figure 2. Interestingly, as confirmed by the leftmost inset in Figure 3, in the case of the 11% RH condition, meso-pores, which are pores corresponding to the water sorption from 40% RH to 95% RH, were re-created; these meso-pores were minimized at the drying condition of 40% RH.

On the contrary, the shrinkage of hardened cement paste occurred largely between 80% and 40% RH, and the incremental shrinkage from 40% RH to 11% RH was not large [12]. This behaviour also reflects the microstructural changes during drying, as shown in Figure 4. The hcp samples dried at different RH conditions were tested for short-term length-change isotherms by using a thermal mechanical analyser coupled with a RH generator. When the sample was dried, the total shrinkage tended to be small. As shown in the rightmost inset of Figure 4, the incremental strain from 40% RH to 98% RH reduced when the drying condition

for the samples changed from 90% RH to 40% RH.

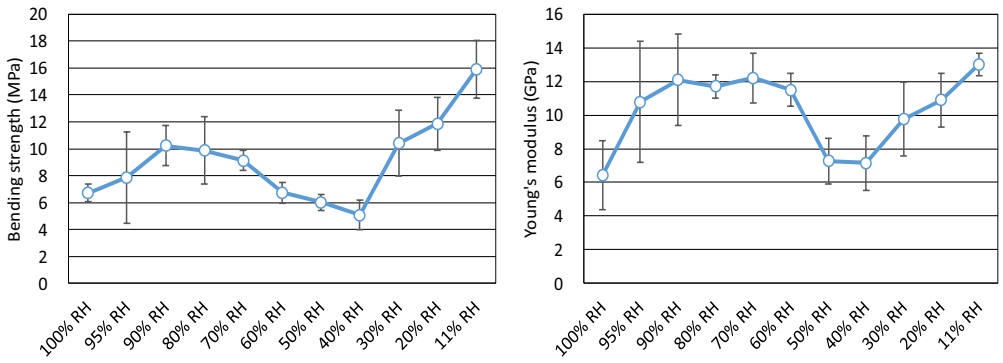

Figure 2: Change of bending strength (left) and Young's modulus (right) of matured hardened cement paste under different equilibrium relative humidity conditions [9].

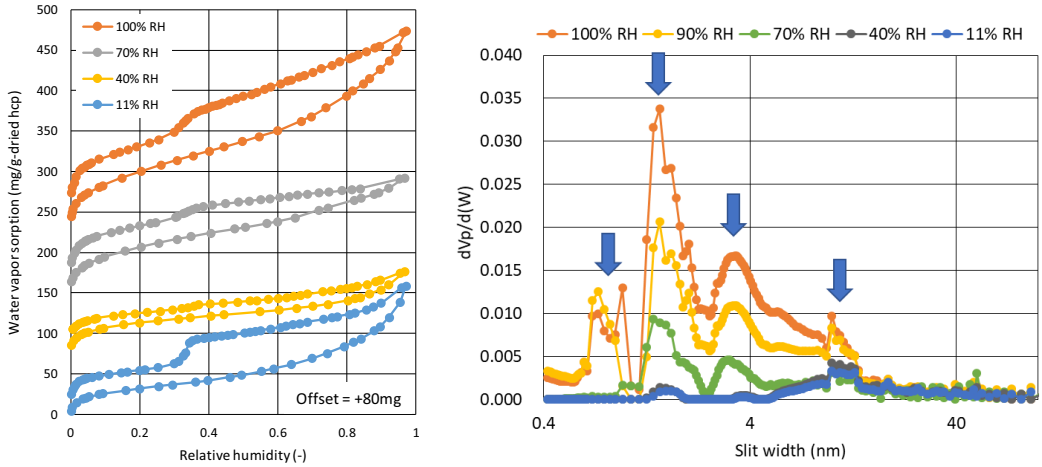

Figure 3: Microstructural changes of matured hardened cement under different equilibrium relative humidity conditions through water vapour sorption isotherms at 293 K (left) and slit size distribution obtained by the Grand Canonical Monte Carlo method (GCMC) for nitrogen sorption isotherms at 77 K.

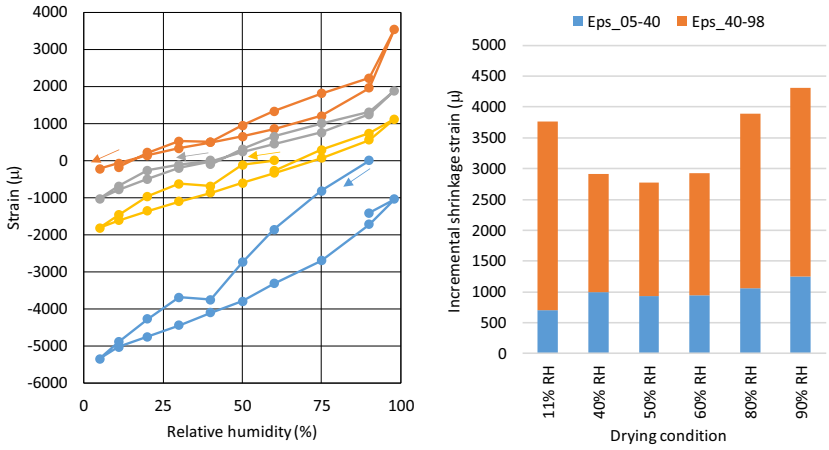

Figure 4: Shrinkage of hcp dried at different RH conditions (left [12]) and incremental shrinkage of hcp (right [12]).

Therefore, the microstructural changes during the first desorption are very crucial factors of the physical properties of hcp.

3. Concrete

The physical properties of concrete change with drying. Figure 5 shows an example of the compressive strength ratio (normalized to the compressive strength for the sealed condition) of concrete and mortar after reaching an equilibrium at different RH conditions as well as the bending strength ratio (normalized to the bending strength at the 95% RH condition) of hcp. The basic trend of the strength ratio was similar: a slight increase from the sealed condition to 80% RH, a decrease from 80% RH to 40% RH, and an increase from 40% RH to more intense drying conditions. Based on this figure, it can be concluded that compressive strength change of concrete is determined by the nature of hcp. It should be noted that the compressive strength of concrete was initiated from the failure of hcp under the compressive-shear mechanism, and this failure mode is close to the tensile strength (or the bending strength) rather than the compressive strength of hcp. In addition, when the type of coarse aggregate is changed for the same volumetric mixture proportion, the behaviour of the compressive strength ratio changes. When a low shrinkage aggregate was used, the reduction ratio increased. Therefore, it was elucidated experimentally that the nature of the aggregate also influences the compressive strength change due to drying. When the concrete was dried, there was a difference in the volumetric stability of the aggregate and cement paste, and the aggregate restrained the shrinkage of the cement paste. Consequently, damage due to the inhomogeneous shrinkage of aggregate and cement paste was reduced when a shrinking aggregate was used in the concrete. The example of crack development, visualized with the digital image correlation method, during drying is shown in Fig. 6 (right).

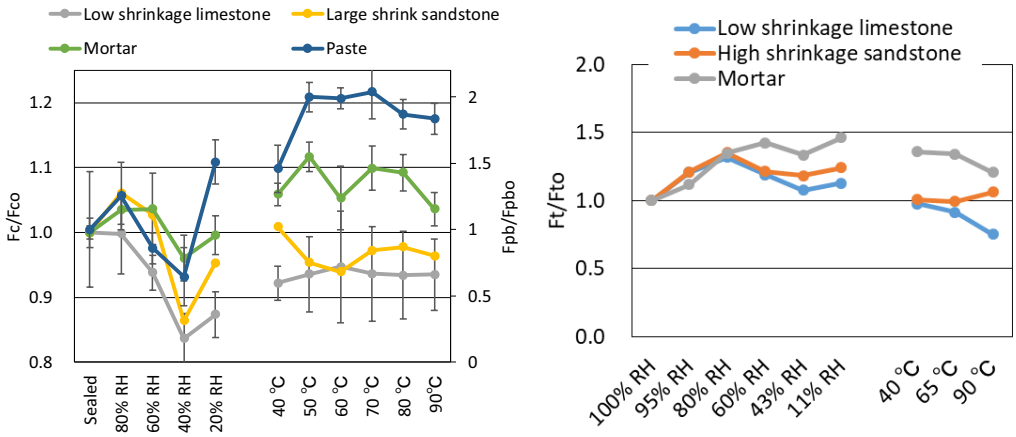

Figure 5: Compressive strength (left [9, 13]) and splitting tensile strength (right [14]) of matured concrete after reaching equilibrium at different RH conditions.

A similar trend was confirmed for tensile cracking, as shown in Fig. 5 (right). The splitting tensile strength of mortar, concrete with high shrinkage sandstone and concrete with low

shrinkage limestone were compared. Like the compressive strength, the strength increased from the high RH range to 80% RH. Then, the tensile strength decreased in cases of concrete. However, the decreasing trend is affected by the coarse aggregate; in cases where the concrete contains high-shrinkage sandstone coarse aggregate, the reduction becomes small. This also suggests that the inhomogeneous shrinkage behaviour between aggregate and hcp and the resultant cracking around aggregates impact the reduction of the change in splitting tensile strength.

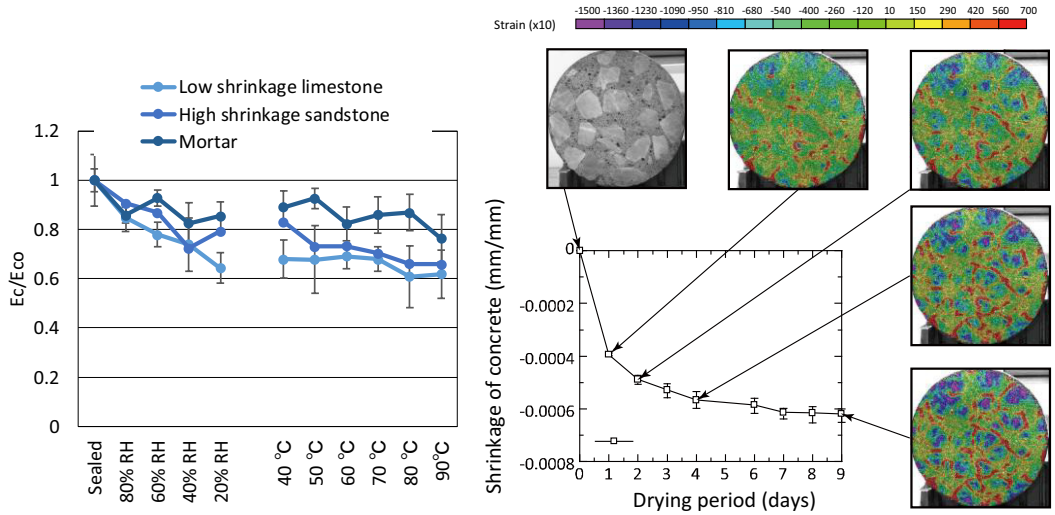

Figure 6: Young's modulus of matured concrete after reaching equilibrium at different RH conditions (left [9, 13]) and cracking around aggregates in concrete under drying conditions [15].

Young's modulus of concrete decreases when the concrete dries, as confirmed in the leftmost inset of Fig. 6. This reduction trend is also determined by the type of aggregate. When a low-shrinkage aggregate was used in the concrete, a large decrease in Young's modulus was observed. This result reveals that the inhomogeneous shrinkage behaviour between the aggregate and hcp as well as the opening of cracks around aggregates cause stress concentration, which reduces Young's modulus.

When the concrete shrinkage is restrained, the restraining role of the aggregate in terms of the shrinkage of hcp is changed. The crack development behaviours of concrete with high or low shrinkage coarse aggregates were confirmed experimentally (experimental setup is shown in the leftmost inset of Fig. 7) by using the digital image correlation method, as shown in the rightmost inset of Fig. 7.

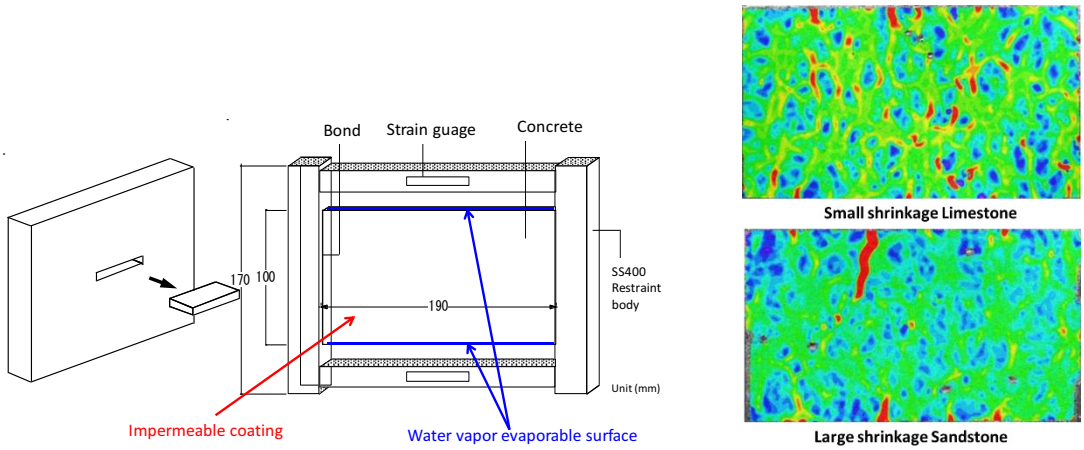

Figure 7: Restrained condition of concrete (left) and cracking behaviour of concrete with small shrinkage limestone (top right) and large shrinkage sandstone (bottom right) [16].

In the case of low-shrinkage limestone aggregate, when the concrete surface cracked due to water evaporation and the resultant shrinkage of the surface region occurred, the cracks did not propagate inwards because of the high bond strength between the aggregate and cement paste and the low shrinkage property of the aggregate. Softening due to this small crack was trivial and subsequent multiple small cracks occurred in other surface regions. Small cracks gradually proceeded into the inner part. On the contrary, when large-shrinkage sandstone was used, the small crack at the surface was connected to the surface cracking on the aggregate surface, and the first small crack abruptly proceeded internally. This is due to the smaller bond strength between the aggregate and cement paste, and the large shrinkage nature of the coarse aggregate, which contributes to the opening of cracks. Therefore, this crack propagation released the accumulated stress in other parts of the concrete; subsequently, one large (and probably visible) crack occurred in concrete, which became a through crack. Therefore, it was concluded that surface properties and the shrinkage nature of aggregate has a large influence on the concrete cracking.

4. Reinforced concrete member

The shrinkage of concrete induces stiffness changes of reinforced concrete structures [17]; it decreases in the flexural cracking moment and increases in the curvature and maximum crack width of beams [18-21]. This has been explained by the tensile stress of concrete induced by the restraining shrinkage and strain differences before and after the cracking of concrete. In this regard, the creep strain of concrete in RC columns under axial compressive loads plays the same role as that of shrinkage [22]. Creep strain and shrinkage strain in columns cause the re-distribution of stress among concrete and rebars, and in the case of the un-loading process, such as in seismic response, cracks are easily produced in tension [22]. This re-distribution of stress caused by shrinkage also reduces the moment capacity when the failure of covering concrete occurs [23].

For the shear cracking and shear failure, the diagonal cracking moment of the RC beam as well as the shear capacity of the RC beam is affected by shrinkage [24-26]. This is simply

because the stress, position and direction of diagonal cracking are altered by the shrinkage-induced stress and the enlarged crack width. The wider diagonal cracks also affect the performance of the RC column; the loading capacity in the cyclic loading process after the formation of diagonal cracking is decreased by the width of diagonal cracks [27]. Aoyama [29] concluded that self-induced stress will not affect the ultimate strength of reinforced concrete members if the failure mode is not changed.

The impact on drying of the reinforced concrete shear wall has been experimentally investigated recently [29]. The specimen details are shown in the leftmost inset of Figure 8. The specimens were well cured for about 3 months, and one was investigated. The other specimen was then subjected to drying for about a year, and after confirming that the shrinkage strain of the dummy wall specimen reached an equilibrium state (Figure 8, top right), the specimen was investigated. The comparison of the envelope of the load–deformation relationship is summarized in the bottom right inset of Figure 8.

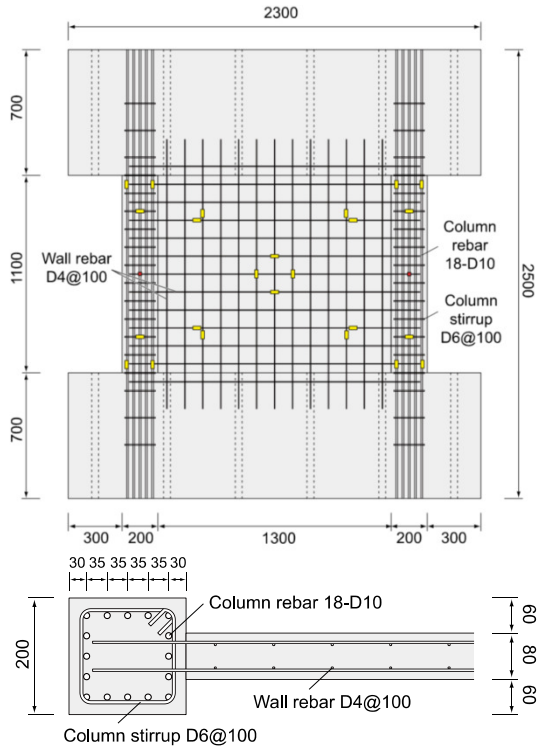

(a) Details of specimen

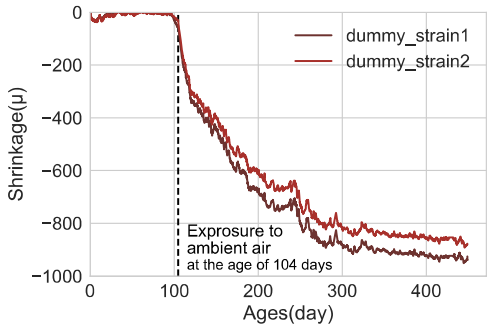

(b) Shrinkage of dummy concrete wall

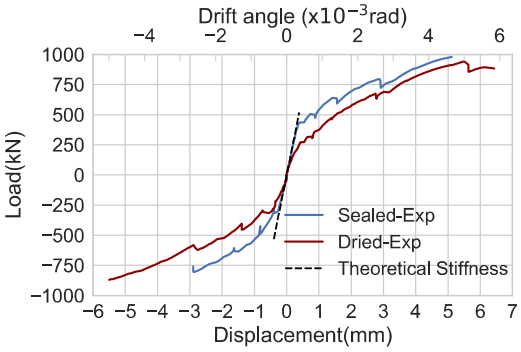

(c) Load-deformation relationships

Figure 8: Experimental results of the impact of drying on the structural performance of reinforced concrete shear wall: (a) details of the specimen, (b) shrinkage of concrete, and (c) load–deformation relationship of shear walls before and after drying [17].

One of the remarkable results was that the initial stiffness of the concrete wall after drying became about half that of the non-dried state. This value is quite consistent to the value obtained in Fig. 1. This means that this stiffness change of the reinforced structure needs special attention, especially for the earthquake response of high-rise buildings and vibration

resonance between buildings and installed equipment, from a viewpoint of aging management.
The other point worth mentioning is that the ultimate strength of the shear wall was not affected by drying, even though the deformation at the failure was increased by 25%. However, considering this difference in the ultimate strength using numerical analysis, it was found that this is attained by an increase in the material strength (about a 10% increase of the compressive strength for cylinder specimen) and a decrease in the structural concrete strength due to cracks opening normal to the strut compressive load in the wall, which can be analysed using the equation proposed by Vecchio and Collins [30]. As the compressive strength can be reduced by 15% due to drying and this behaviour is not monotonic, there is a risk of the ultimate shear strength of the concrete wall changing due to drying; RH conditions, the water-to-cement ratio of concrete and the type of coarse aggregate greatly influence this phenomenon. The risks of the ultimate shear strength change are also determined by the shape of the wall and reinforcement ratio.

5. Conclusion

The physical property changes of concrete during the first drying cannot be ignored from the viewpoint of the aging management of concrete structures. Structural stiffness changes and the potential ultimate strength of reinforced concrete members are crucial and determined by environmental conditions as well as material properties. This contribution has exhibited a research pathway from the material knowledge to the structural response. Now, a multiscale experimental campaign based on an appropriate research strategy would contribute to evaluating the current performance, and predict and control the future performance of concrete structures.

Acknowledgements
The experimental results shown in this contribution were supported by JSPS-KAKENHI 18H03804, 16H06363, 15H04077, and a research project of the Japanese Nuclear Regulatory Authority (JAMPSS). The author wishes to express his sincere gratitude to Prof. M. Teshigawa (Nagoya University), Dr A. Nakamura (Japanese Housing Authority), Dr G. Igarashi (Tohoku university), Ms. Y. Nishioka (Takenaka co.), Mr. H. Sasano, Mr. R. Kurihara, Mr. Jiri Rymes and Mr. H. Sugimoto (Nagoya University) for their contributions to the experiments and fruitful discussions.

References
[1] Maruyama, I., Multi-scale Review for Possible Mechanisms of Natural Frequency Change of Reinforced Concrete Structures under an Ordinary Drying Condition, J Adv Conc Tech 14(11) (2016), 691-705
[2] Li, L. et al, Earthquake damage evaluation of an 8-story steel-reinforced concrete building using Sa-Sd curves, J Struct Constr Eng 79(702) (2014), 1107-1115
[3] Jesser, L., Kolloide Chemische Reaktionen des Tonerdezementmörtels, Zement 16 (1927), 741

[4] Tomes, A. et al, Some Factors Affecting the Surface Area of Hydrated Portland Cement as Determined by Water-Vapor and Nitrogen Adsorption, Journal of Research of the National Bureau of Standards 59(6) (1957), 357-364
[5] Hunt, M. et al, Some Effects of Aging on the Surface Area of Portland Cement Paste, Journal of Research of the National Bureau of Standards 64A(2) (1960), 163-169
[6] Kropp, J. et al, Characterization of the microstructure of hydrated cement paste by small angle X-ray scattering. In: Arrowsmith JW, editor. Principles and Applications of Pore Structural Characterization, Bristol (1985), 83-96
[7] Völkl, J. et al, The specific surface of hardened cement paste by small-angle X-ray scattering effect of moisture content and chlorides, Cem Conc Res 17(1) (1987), 81-88
[8] Fonseca, P., and Jennings, H., The effect of drying on early-age morphology of C–S–H as observed in environmental SEM, Cem Conc Res 40(12) (2010), 1673-1680
[9] Maruyama, I., et al., Development of Soundness Assessment Procedure for Concrete Members Affected by Neutron and Gamma-Ray Irradiation, J Adv Conc Tech 15(9) (2017), 440-523
[10] Maruyama, I., et al., Microstructural and bulk property changes in hardened cement paste during the first drying process, Cem Conc Res 58 (2014), 20-34
[11] Maruyama, I., et al., Microstructural changes in white Portland cement paste under the first drying process evaluated by WAXS, SAXS, and USAXS, Cem Conc Res 91 (2016), 24-32
[12] Maruyama, I., et al., Bimodal behavior of C-S-H interpreted from short-term length change and water vapor sorption isotherms of hardened cement paste, Cem Conc Res 73 (2015), 158-168
[13] Maruyama, I., et al., Strength and Young's modulus change in concrete due to long-term drying and heating up to 90°C, Cem Conc Res 66 (2014), 48-63
[14] Lin, M., et al., Mechanism of Change in Splitting Tensile Strength of Concrete during Heating or Drying up to 90°C, J Adv Conc Tech 13(2) (2015), 94-102
[15] Maruyama, I. and Sasano, H., Strain and crack distribution in concrete during drying, Mater Struct 47(3) (2014), 517-532
[16] Maruyama, I., et al., Impact of aggregate properties on the development of shrinkage-induced cracking in concrete under restraint conditions. Cem Conc Res 85 (2016), 82-101
[17] Sasano, H., et al., Impact of drying on structural performance of reinforced concrete shear walls, J Adv Conc Tech 16(5) (2018), 210-232
[18] Okada, T., et al., Model tests for evaluation of restoring force characteristics of reactor buildings. Part 6: Scale effect test, Summaries of technical papers of Annual Meeting Architectural Institute of Japan. B, Structures I, 1986, 1089-1090 (in Japanese)
[19] Rusch, H. et al., Creep and shrinkage, NewYork, Springer-Verlag (1983)
[20] Bischoff, H., Effects of shrinkage on tension stiffening and cracking in reinforced concrete, Can J Civil Eng 28(3) (2001), 363-374
[21] Iso, M., et al., Experimental study on bending-shear behavior of reinforced concrete columns after subjected to seismic load, Proc. JCI (1993), 15(2), 525-530 (in Japanese)
[22] Tanimura, M. et al, Serviceability performance evaluation of RC flexural members improved by using low-shrinkage high-strength concrete, J Adv Conc Tech 5(2) (2007), 149-160
[23] Komuro, T., et al., Study on long term performance of reinforced concrete columns using high strength concrete, Proc. JCI (2008), 30(3) 223-228, (in Japanese)

[24] Collins, et al., Structural design considerations for high-strength concrete, Conc Int 15(5) (1993), 27-34
[25] Maruta, M. and Yamazaki, M., Study on the shear behavior of RC beams subjected to high temperature for long time, Proc. JCI (1990), 12(1), 603-608 (in Japanese)
[26] Sato, R. and Kawakane, H., A new concept for the early age shrinkage effect on diagonal cracking strength of reinforced HSC beams, J Adv Conc Tech 6(1) (2008), 45-67
[27] Nakarai, K., et al., Shear Strength of Reinforced Concrete Beams: Concrete Volumetric Change Effects. J Adv Conc Tech 14(5) (2016), 229-244
[28] Maruyama, I. et al., Effect of autogenous shrinkage on the structural performance of short rc column., Proc. AIJ, C-2, Structures IV, 107-108 (in Japanese)
[29] Aoyama, H., Impact of self-induced stress of reinforced concrete buildings (translated), PhD Thesis, University of Tokyo (1960)
[29] Sasano, H., et al., Impact of drying on structural performance of reinforced concrete shear walls, J Adv Conc Tech 16(5) (2018), 210-232
[30] Vecchio, F.J. and Collins, M.P., The modified compression-field theory for reinforced concrete elements subjected to shear, ACI J March-April (1986), 219-231

SynerCrete'18 International Conference on Interdisciplinary Approaches
for Cement-based Materials and Structural Concrete
24-26 October 2018, Funchal, Madeira Island, Portugal

INNOVATIVE WAYS IN CONDITION ASSESSMENT OF CONCRETE BRIDGE DECKS: DATA COLLECTION USING ROBOTICS, AND ADVANCED DATA INTERPRETATION AND VISUALIZATION

Nenad Gucunski [(1)], Jinyoung Kim [(2)], Kien Dinh [(3)], Jie Gong [(1)], Fei Liu [(1)], Seong-Hoon Kee [(4)], Basily Basily [(1)]

(1) Rutgers University, Piscataway, New Jersey, USA
(2) Ajou University, Suwon-si, Gyeonggi-do, Republic of Korea
(3) Marshall University, Huntigton, West Virginia, USA
(3) Dong-A University, Busan, Republic of Korea

Abstract
Concrete bridge decks deteriorate faster than other bridge components due to their direct exposure to traffic and environmental loads. Therefore, the ability to assess their condition and deterioration progression in a reliable and consistent manner is essential for implementation of appropriate maintenance and rehabilitation strategies and, ultimately, their economic management. A fully automated system named RABIT (Robotics Assisted Bridge Inspection Tool) integrates multiple nondestructive evaluation (NDE) technologies for a comprehensive and rapid assessment of concrete bridge decks. The system concentrates on the characterization of internal deterioration and damage, in particular three most common deterioration types in concrete bridge decks: rebar corrosion, delamination, and concrete degradation. RABIT implements four NDE technologies: electrical resistivity (ER), impact echo (IE), ultrasonic surface waves (USW) and ground-penetrating radar (GPR). ER enables characterization of the concrete's corrosive environment, while IE detection and characterization of delamination in the deck. The USW test concentrates on the assessment of concrete quality by measuring the concrete elastic modulus. Finally, GPR provides a qualitative assessment of concrete deck deterioration, mapping of rebars and measurement of concrete cover. The NDE technologies are used in a complementary way to enhance the overall condition assessment and certainty regarding the detected deterioration. The benefits stemming from periodical NDE surveys, along with several innovative ways of data interpretation and visualization are presented.

1. RABIT description and data collection

RABIT is a robotic system that can fully autonomously collect bridge deck data. The system was developed at Rutgers University with the support from Federal Highway Administration's (FHWA's) Long Term Bridge Performance (LTBP) Program. The system's NDE, imaging and navigation components are shown in Fig. 1. On the front end of RABIT there are two acoustic arrays and four Wenner type ER probes. Acoustic arrays are used in detection and characterization of delamination by impact echo (IE) method [1], and concrete quality through the modulus measurement using ultrasonic surface waves (USW) method [2]. Each of the acoustic arrays incorporates multiple solenoid type impact sources and receivers (accelerometers). Individual impact sources and nearby receivers are used in IE testing, while single sources and sets of nearby sensor pairs are used in USW measurements. The ER probes are used in the characterization of the concrete's corrosive environment by measuring electrical resistivity of concrete. The ER results can be correlated to the anticipated corrosion rates [3]. Two GPR arrays, placed in the rear of the robotic platform, provide a qualitative deck assessment [4]. Each array contains eight pairs of GPR antennas of dual polarization. Finally, two cameras on the front end are taking images of the deck surface, which are later stitched into high resolution images of larger deck sections.

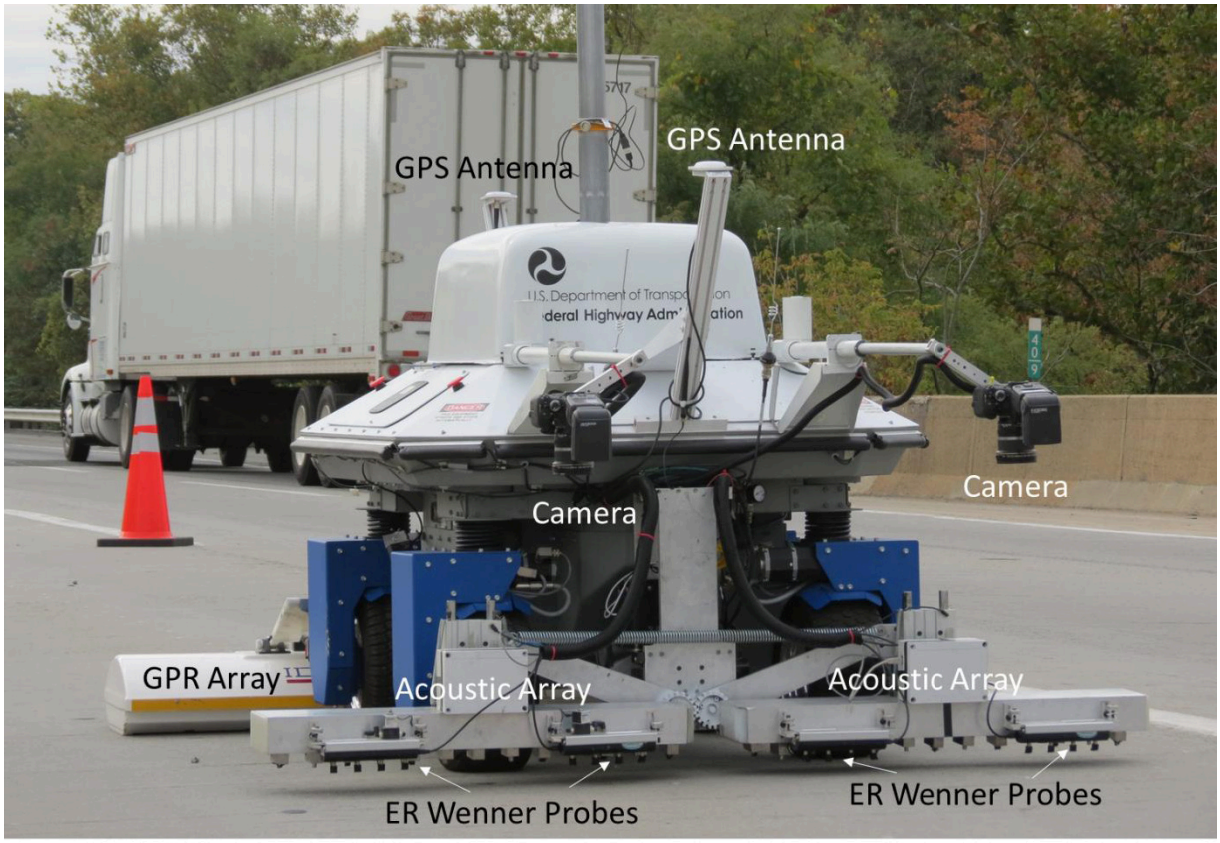

Figure 1: RABIT and NDE, imaging and navigation components.

Accurate and reliable robot localization and navigation is achieved through a fusion of three navigation systems. The first system is the differential global positioning system (DGPS) with

real-time kinematic (RTK) correction. The DGPS consists of a base-station GPS receiver, placed at any point on or near the bridge, and two GPS receivers located at the front and back of the robot (Fig. 1). After very precise GPS coordinates are obtained for the base station, a small portable cart with a GPS antenna is used to take GPS coordinates at three points on the deck. Those will be sufficient to fully define the path of RABIT data collection. The second navigation component is an inertial measurement unit (IMU), which are measuring the rotational position. Finally, the third system is wheel odometry that enables accurate distance measurement. The information coming from the three navigation components is fused using an extended Kalman filter (EKF) [5]. RABIT collects data at production rates of about 350 m^2 of deck area per hour.

2. Deck condition data presentation

The results from NDE RABIT surveys are presented in terms of condition maps and condition indices. As an example, delamination, concrete modulus and electrical resistivity maps obtained from three NDE technologies: IE, USW and ER, respectively, are shown in Fig. 2. Hot and warm colours indicate detected defects or deterioration, or lower material properties. In the case of delamination, the serious condition describes a fully developed delamination, while fair and poor conditions describe signs of delamination development. In the case of ER measurement, the resistivity results are correlated to the anticipated corrosion rates [6].

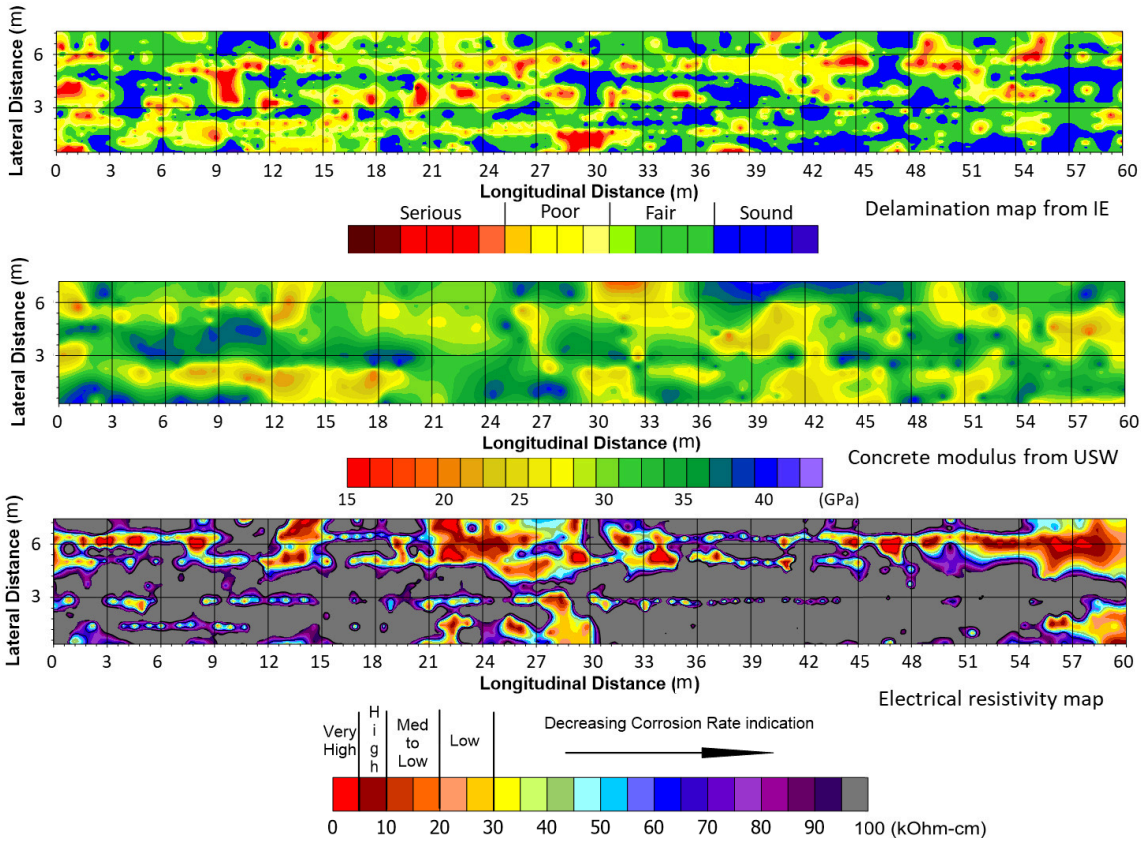

Figure 2: Delamination (top), concrete modulus (middle) and electrical resistivity maps (bottom) for Bridge no. 1328153, New Jersey.

Condition indices are used to present the overall condition of a deck. The condition index for each individual technology represents a weighted average of percentages of deck area in various states/conditions. The condition index (CI) is on a scale of 0 to 100, where 0 represents a fully deteriorated condition, and 100 a perfectly sound condition. The weight for any of the states are assigned based on their significance in the agency's decision making. For example, the FHWA's LTBP Program uses the following formula for the delamination CI:

$$Delamination\ \ Index\ \ (IE) = \frac{A_{Sound}\ \times 100 + A_{Fair}\ \times 50 + A_{Poor}\ \times 50 + A_{Serious}\ \times 0}{A_{Total}} \quad (1)$$

where A_{Sound}, A_{Fair}, A_{Poor}, and $A_{Serious}$ are the areas in "Sound", "Fair", "Poor", and "Serious" conditions. A 100 weight factor is given to the sound condition, 50 to fair and poor, and a 0 weight factor to the serious state. Table 1 summarizes the results for three delamination surveys for the same bridge conducted in 2013, 2015 and 2017.

Table 1: Delamination CI and percentages of deck area in various states for Bridge no. 1328153.

Year	Condition Index	Distribution (%)			
		Sound	Fair	Poor	Serious
2013	74.1	56	30	5	8
2015	65.9	44	32	9	13
2017	59.4	34	31	20	15

Images taken by the front end cameras are stitched into images of larger sections of the deck surface and become permanent "visual inspection" records. An example of a section of a stitched deck image is shown in Fig. 3. The image represents a record of the joint condition of a skewed bridge, which in this case is clearly filled with debris. Looking into the future, comparisons of images from multiple years will provide an insight into progression of visible deterioration and defects, and repairs conducted during the same period.

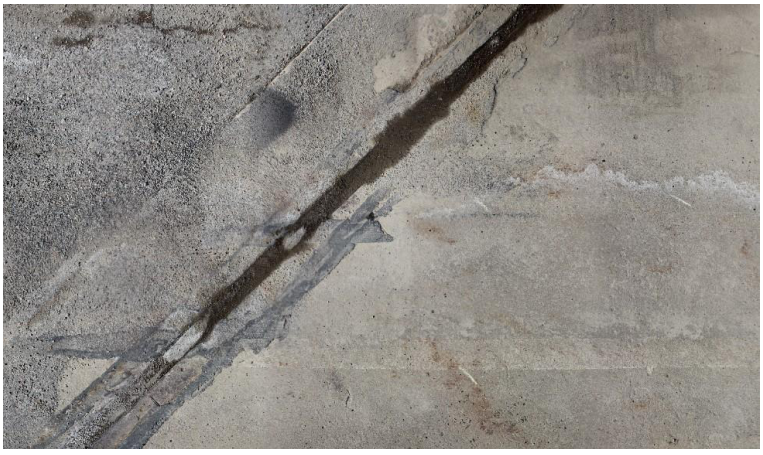

Figure 3. Image of a deck section around the joint of a bridge over Pohatcong River, Pohatcong Township, New Jersey.

3. Complementary forms of data presentation

The results from NDE surveys by RABIT can be merged with results from other technologies and data presentation platforms to provide a more intuitive presentation of the results. An example of one of approaches is merging of LiDAR (Light Detection and Ranging) point cloud data and a GPR condition map image from a RABIT survey is shown in Fig. 4. Condition maps from different NDE technology surveys, and for different years of surveys, can be superimposed on the LiDAR map and easily reviewed from different viewing positions.

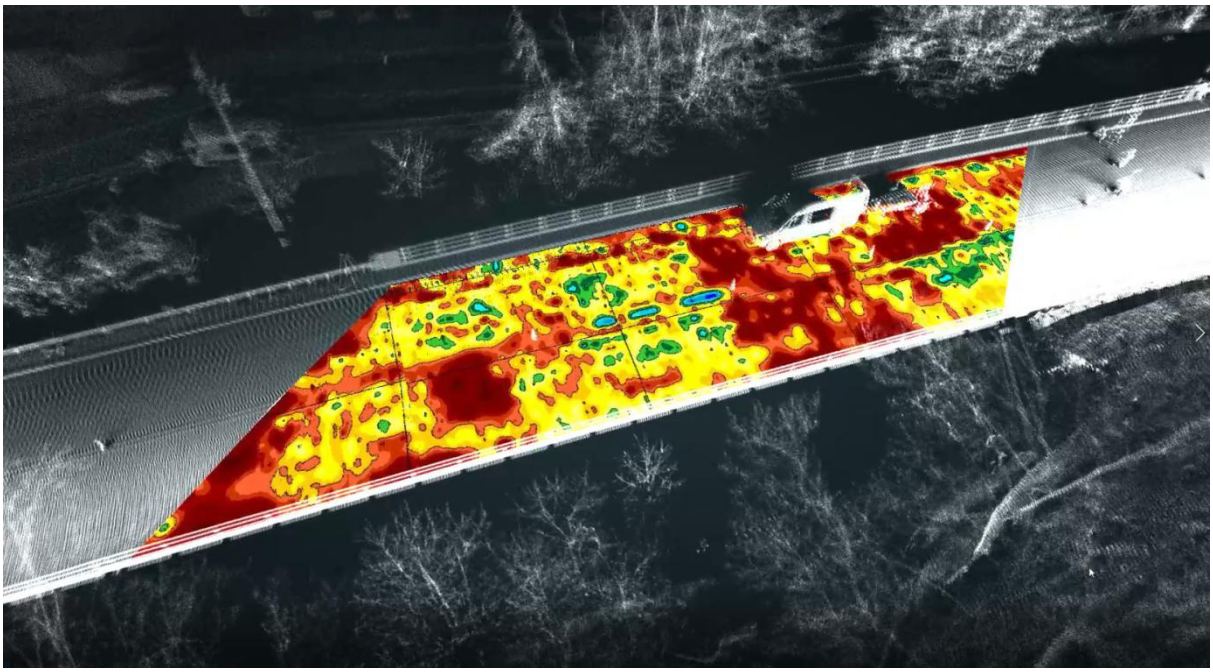

Figure 4: GPR condition map for Pohatcong Bridge superimposed on the LiDAR map.

Similarly, the NDE condition maps can be displayed in Google Earth. An example of it are the ER maps for a deck of the bridge on State Route 15 over Interstate 66 in Haymarket, Virginia, shown in Figure 5. The bridge was surveyed four times using manual NDE technologies, and once by RABIT, between 2009 and 2015. As it can be clearly observed, there was significant progression, in the size of the area affected and aggressiveness, of the concrete's corrosive environment. Similar to the ER results, results from other NDE technologies for any of the four surveys can be invoked.

4. Deterioration and predictive modeling using NDE results

Very important benefits from NDE surveys are stemming from the quantitative nature of the NDE results, which can be used in the development of more realistic deterioration and predictive models. As described earlier and illustrated in Tab. 1, the condition of a bridge deck can be quantified and expressed in terms of a condition index (CI) for a particular

deterioration or defect type. The indices in Tab. 1 for the assessments between 2013 and 2017 clearly point to a worsening of condition with respect to delamination.
A more comprehensive example of the use of CIs in describing progression of deterioration is shown in Fig. 6 for the Haymarket Bridge. Results for four NDE technologies: IE, ER, GPR and half-cell potential (HCP) are presented. The HCP is used to assess the probability of active corrosion in the deck reinforcement. Results from all four technologies describe a rapid progression of deterioration during the four year period.

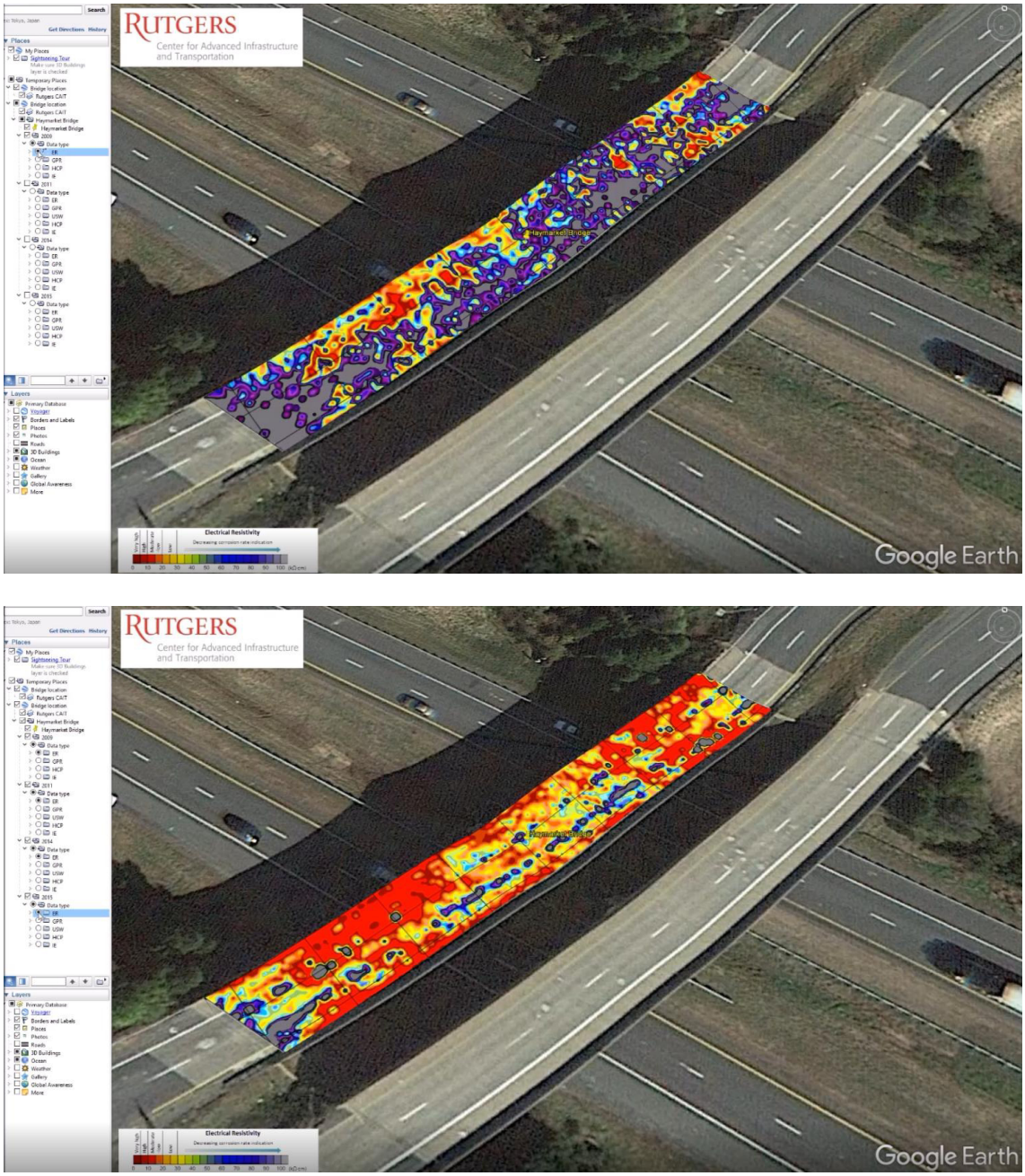

Figure 5: ER maps for 2009 (top) and 2015 (bottom) for State Route 15 over Interstate 66 bridge in Haymarket, Virginia.

In addition to the individual NDE technology indices, a combined condition index is also presented in the figure. In this case, the combined CI was calculated as a simple average of the four technology indices. In practice, the combined CI should be calculated as a weighted average of multiple technology indices based on the significance of a deterioration type in the deck maintenance decision making. Finally, to emphasize the benefit of the NDE evaluation in capturing deterioration progression, the condition rating from the National Bridge Inventory, which is based on the visual inspection, is presented in the same graph. As shown, the condition rating did not change during the same period. In fact, the data show that it did not change since 1992.

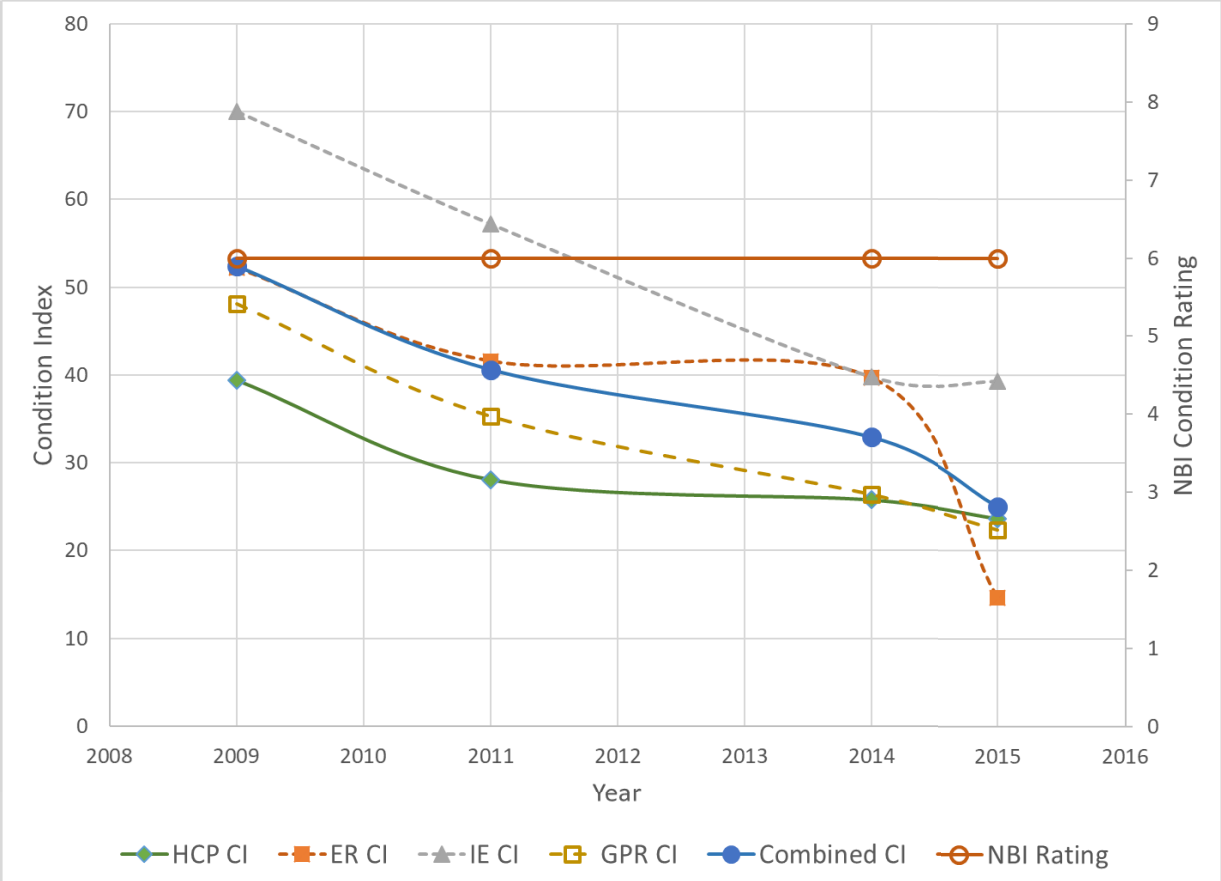

Figure 6: NDE condition indices and NBI condition ratings for the Haymarket Bridge for a period 2009-2015.

5. Conclusions

Accurate condition assessment of concrete bridge decks is essential for an effective bridge management. The robotic platform RABIT builds on the best practices of NDE and visual inspection for concrete bridge decks to improve the speed and cost of data collection, and accuracy of the obtained results. The improvements stem from the deployment of a large number of sensors and sensor arrays, and fully autonomous RABIT motion. Multi NDE technology data collection, including imaging, enables detection and characterization of all

primary deterioration types, and improves correlation between those to identify the primary causes of deterioration. Periodically collected data open opportunities for the development of more realistic deterioration and predictive models. Ultimately, it is expected that all the described advances will encourage bridge owners to pursue robotic bridge inspections on the network level.

References

[1] Sansalone, M., Impact-echo: The complete story. ACI Materials Journal, 94(6), (1997), 777-786.
[2] Nazarian, S., M. R. Baker, Crain, K., Report SHRP-H-375: Development and testing of a Seismic Pavement Analyzer, Report, Transportation Research Board, National Research Council, Washington, D.C. (1993).
[3] Gowers, K. R., Millard, S. G.: Measurement of concrete resistivity for assessment of corrosion severity of steel using Wenner technique." ACI Materials Journal, 96(5), (1999), 536-542.
[4] Barnes, C. L., Trottier, J.-F.: Ground penetrating radar for network level concrete deck repair management. Journal of Transportation Engineering, ASCE, 126(3), (2000), 257-262.
[5] Gucunski, N., Basily, B., Kim, J., Dinh, K., Duong, T., Kee, S.H., and Maher, A., RABIT: Implementation, performance validation and integration with other robotic platforms for improved management of bridge decks, International Journal of Intelligent Robotics and Applications, 1(3), (2017), 271-286.
[6] Pailes, B.M. and Gucunski, N., Understanding multi-modal nondestructive testing data through the evaluation of twelve deteriorating reinforced concrete bridge decks, Journal of Nondestructive Testing, 34(4), (2015), 34: 30.

SynerCrete'18 International Conference on Interdisciplinary Approaches
for Cement-based Materials and Structural Concrete
24-26 October 2018, Funchal, Madeira Island, Portugal

DEMONSTRATION PROJECTS WITH SELF-HEALING CAPSULE-BASED AND BACTERIA-BASED CONCRETE

Nele De Belie [(1)], Maria Araujo [(1)], Tim Van Mullem [(1)], Elke Gruyaert [(2)]

(1) Ghent University, Ghent, Belgium
(2) KU Leuven, Ghent, Belgium

Abstract
To reduce downtime, costs and labour for repair of concrete structures, self-healing concrete has been proposed as a solution. Over the last decade, the efficiency of different self-healing mechanisms has been tested at laboratory scale. Lately, the first demonstrators have been made in order to test the self-healing efficiency at real scale and in actual service conditions.
At the one hand our team has cast real-scale concrete beams, containing previously selected polymeric capsules. As capsule wall material, poly(methyl methacrylate) (PMMA) was chosen due to its high chemical stability in contact with concrete, high survival ratio during the concrete mixing process and ability to rupture when crossed by cracks of small width. The self-healing efficiency of the concrete elements with randomly dispersed PMMA capsules was determined after crack creation by 3-point-bending tests.
Secondly, an in situ demonstration project was established with microbial self-healing concrete. A mixed ureolytic culture of bacterial spores (MUC+) and the nutrients urea and calcium nitrate were mixed into the concrete in a real concrete plant. With this self-healing concrete the roof plate of a sewer inspection pit was cast. From the same batch of concrete, prisms were taken to the laboratory for crack creation and evaluation of the self-healing efficiency. For cracks with an average width of 348 μm, created after 6 weeks of curing, a sealing efficiency against water flow of more than 90% was measured after 24 weeks of water immersion.

1. Introduction

While natural materials such as bone or skin are able to heal themselves in an autonomous manner after mechanical damage, traditional man-made materials generally lack this intrinsic capacity for self-healing. In 1969, self-healing properties were for the first time built-in inside

polymeric materials [1] and in the following decades publications about self-healing in thermoplastic and cross-linked systems and concrete appeared [2]. Nevertheless, it was only in 2001, through an article about self-healing in polymer based materials published in Nature, that research in the field of self-healing materials was really triggered [3]. By restoring their functional properties autonomously after damage, self-healing materials would offer tremendous advantages over traditional materials in many application areas.
An extensive review on self-healing in cementitious materials was published in 2013 [2]. This has been updated recently in three review publications by the members of the COST action CA15202 SARCOS "Self-healing as preventive repair of concrete structures". The first paper of this series [4] focuses on the methodologies to realize self-healing concrete for damage management of structures. The second paper [5] gives insights in the experimental characterization of the self-healing capacity of cement based materials and its effects on the material performance, while the third paper [6] deals with research progress on numerical models for self-healing cementitious materials. The previously mentioned review [4] provides a state-of-the-art of recent developments of self-healing concrete, covering autogenous or intrinsic healing of traditional concrete followed by stimulated autogenous healing via use of mineral additions, crystalline admixtures or (superabsorbent) polymers, and subsequently autonomous self-healing mechanisms, i.e. via application of micro-, macro- or vascular encapsulated polymers, minerals or bacteria. The (stimulated) autogenous mechanisms are generally limited to healing crack widths of about 100-150 μm, take several weeks or even months to heal cracks completely and heavily rely on the environmental conditions (mainly presence of water). In contrast, most autonomous self-healing mechanisms can heal cracks of 300 μm, even sometimes up to more than 1 mm, and usually act faster (complete healing obtained in a time span of 1 day up to 3-4 weeks depending on the system). Two of these techniques, being polymeric macro-capsules with healing agent and mixed cultures of ureolytic bacteria, have been developed in our laboratory up to a level where they could be incorporated in concrete demonstration elements.

In recent years, self-healing of concrete cracks using macro-encapsulated healing agents has attracted quite some attention. However, most of the research has mainly been performed at a laboratory scale using small-scale mortar samples. Furthermore, the experiments using this self-healing approach generally involve manual placement of the capsules in the concrete matrix in strategic locations to ensure crack propagation through the capsules. The self-healing efficiency of concrete with randomly dispersed capsules is seldom investigated and it is limited to a few studies. Van Tittelboom et al. [7] evaluated the crack healing efficiency of concrete containing randomly distributed capsules filled with polyurethane. The authors concluded that a higher amount of capsules is needed to obtain the same probability of cracks hitting capsules compared to other placement methods in which capsules were strategically positioned (i.e. ideally positioned compared to the crack orientation). Although in this study some attempts have been made to increase the chance that the glass and ceramic capsules survive casting and mixing, it was observed that half of the capsules broke during mixing. In his PhD, Feiteira [8] has prepared self-healing concrete with randomly dispersed glass capsules (filled with polyurethane) with a wall thickness of 0.8 mm and a length of 3 cm. It was found that when a capsule dosage of 13 capsules per liter was used, the amount of capsules intersected by a crack was 4. This value was doubled by increasing the capsule dosage up to 36 capsules per liter. Higher dosage of capsules (up to 50 capsules per liter) are

suggested in order to achieve consistent healing efficiencies. Hilloulin et al. [9] investigated the potential of using brittle polymeric materials with a relatively low glass transition temperature (T_g) as protection materials in self-healing concrete and found that the capsule survival probability could be improved if the capsules were heated (above T_g) prior to mixing. Gruyaert et al. [10] explored the use of ethyl cellulose capsules containing different plasticizers to increase the survival of the capsules during concrete mixing. These plasticizing agents would make the capsules more flexible in an early stage and increase the resistance of the capsules during the mixing. Then, due to leaching out of the plasticizers, the capsules would become more brittle during concrete hardening and break more easily when a crack would form. The tested capsules could survive the concrete mixing; however, they did not break when cracks with a width of 0.4 mm were created.

In our latest work, poly(methyl methacrylate) (PMMA) with a low molecular weight was selected as the polymeric encapsulation material to test in real-scale concrete elements, based on previous results regarding the durability of the polymeric capsules in different environments (demineralized water, salt water and simulated concrete pore solution) and their compatibility with various healing agents and survival tests [11, 12]. Positive results with regard to strength regain and regain in liquid-tightness using encapsulated one-component polyurethane were obtained in lab-scale proof-of-concept tests [13]. Since compatibility tests showed that PMMA capsules are compatible with PU, this healing agent seemed to be the preferential choice. However, when capsules were filled with a polyurethane pre-polymer, it was noticed that the healing agent cured prematurely inside the capsules within a few days. The reason is that the polyurethane pre-polymer polymerizes in the presence of moisture/air and the capsules are not completely impermeable. Therefore, a water repellent agent finally was selected as agent to be encapsulated in the PMMA tubes for the larger scale experiments. A water repellent agent will not physically block the cracks, but will prevent ingress of water containing aggressive agents into the concrete matrix. Hence the main goal of self-healing concrete, i.e. to restore the durability of the concrete element after cracking, can be reached.

Based on the results of the EC FP7 project HEALCON, a second demonstrator was cast in situ, incorporating a bacterial healing agent. The HEALCON project, which was completed at the end of 2016, aimed to bring the self-healing concrete one step closer to the market. The most promising self-healing agents were further developed and upscaled, applied in large-scale concrete elements and tested with regard to the self-healing performance [14]. In 2017, one of the upscaled healing agents, a mixed ureolytic culture (MUC^+) developed by the HEALCON partner Avecom, was incorporated in a roof plate of an inspection pit. This inspection pit is part of the preparatory works for the Oosterweel link in the city of Antwerp, Belgium. MUC^+ consists of a mixture of MUC (mixed ureolytic culture derived from microbial biomass from a vegetable treatment plant with high ureolytic activity and no need of encapsulation [14]) and anaerobic granular bacteria with high CO_2 production and $CaCO_3$ precipitation capability. In comparison to axenic cultures, these non-axenic cultures can be produced at a low cost. Through their metabolism, ureolytic bacteria enzymatically transform the urea that is provided as nutrient into ammonium and carbonate ions and the latter will combine with calcium from the concrete matrix and/or an added calcium source to form calcium carbonate which heals formed cracks.

2. Materials and methods

2.1 Concrete beam with macro-capsule based self-healing system

The poly(methyl methacrylate) (PMMA) was supplied by Evonik Performance Materials (Plexiglas 8909, M_n = 38000 g/mol). Hollow tubes were extruded on a Bradender extruder equipped with a single screw and a tubular die (OD: 10 mm; ID: 8 mm). The processing temperature was 225-235 ºC and the screw speed was 10 min^{-1}. The wall thickness of the tubes was controlled by adjusting the conveyor speed (0.2 – 1 m/min): $Ø_{outer}$ = 6.5 mm, wall thickness = 0.7 mm. The capsules used in the large scale experiments were filled with a water repellent agent (WRA, Sikagard 750L) supplied by Sika Belgium nv [12].

Two real-scale concrete beams (250 cm × 40 cm × 20 cm) were made with self-compacting concrete. One of them contained PMMA capsules, another one was a reference beam without capsules. All mixes had the same composition (853 kg/m³ sand 0/5, 370 kg/m³ gravel 2/8, 328 kg/m³ gravel 8/16, 300 kg/m³ CEM I 52.5 N, 300 kg/m³ limestone filler, 165 l/m³ water and 2.5 l/m³ superplasticizer). For the beam with self-healing properties, PMMA capsules were added during the last minutes of the mixing process. A vertical shaft mixer (200 L) with a rotating pan was used to mix all components. As PMMA capsules tend to float due to their relatively low density, the concrete was cast in 2 layers. First, a concrete mix containing the capsules (approximately 22 capsules per liter of concrete) was prepared and poured into the mould (layer of 12 cm). Then, another mix (without capsules) was made and placed into the mould on top of the previous layer (Fig. 1).

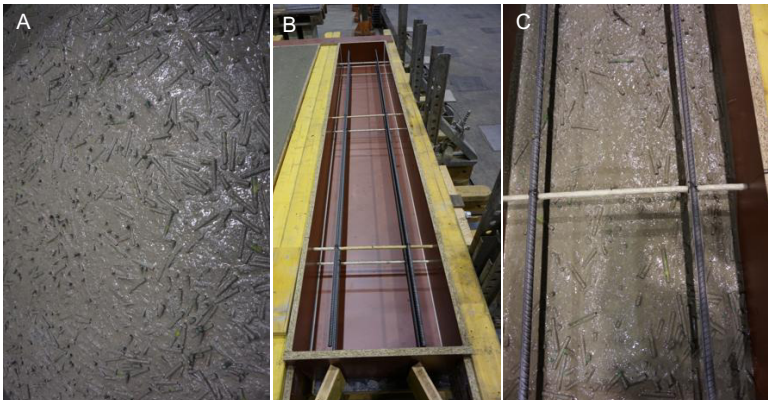

Figure 1: Concrete beam with self-healing properties. (A) Concrete mix with dispersed PMMA capsules; (B) Position of the reinforcement bars within the mould; (C) Concrete mix with randomly dispersed capsules poured into the mould, forming a layer of 12 cm.

At the age of 14 days, 6 cracks with varying crack widths (0.3 till 0.6 mm) were created in each beam by means of consecutive 3-point-bending tests. To create localized cracks, a notch was sawn at the corners of the beam in the middle of the span for the 3-point bending. One crack per day was created by moving the 3-point-bending set-up along the length of the beam. Immediately after cracking, the notches were filled with a shrinkage-free repair mortar to fix the crack opening. The load was only removed after sufficient hardening of the repair mortar. The final crack widths of each crack were measured at 6 positions using an optical microscope.

The self-healing efficiency of the concrete beams was evaluated by determining the resistance of the self-healed concrete against chloride ingress. The beams were positioned slightly tilted with the cracks in the upper surface and a 3 wt% NaCl solution was flown over the beams during 24 uninterrupted hours per week (Fig. 2). This 1 day wet – 6 days dry cycle was repeated during 6 consecutive weeks. Prior to exposure, all sides of the beams except the top and bottom surfaces were covered with a waterproof aluminium foil so that only the top surface was exposed to the chloride solution.

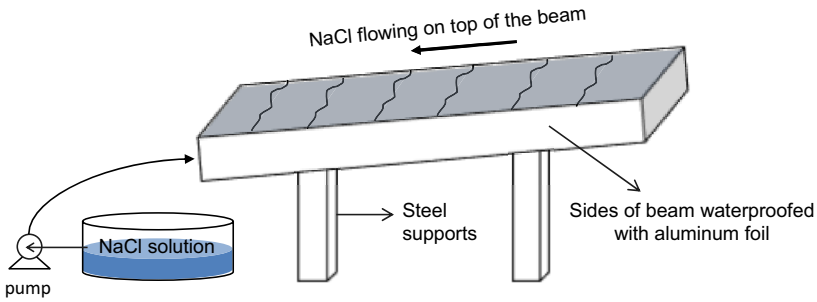

Figure 2: Schematic representation of a concrete beam exposed to 3 wt% NaCl solution.

To determine the chloride ingress, 2 cores with a diameter of 150 mm, with a crack inside, were extracted from each beam. Subsequently, each core was split along the crack surface and one half was then used to measure the chloride ingress. This was done by grinding off material at various depths (5, 25, 50 and 85 mm) in 2 mm layers perpendicular to the crack face. In addition, material was ground from the exposed surface downwards. Concrete powders were collected from ten layers for each zone and dried in an oven at 95 ºC for at least 7 days. The total chloride concentration per ground layer was determined by an acid-soluble extraction in a nitric acid (HNO_3) solution followed by a potentiometric titration against silver nitrate. More details about the test procedure can be found in [15].

2.2 Concrete slab with self-healing properties through incorporation of mixed ureolytic bacterial cultures

Bacterial self-healing concrete was produced at a concrete plant in Merksem, nearby the location of the inspection pit in which the concrete would be applied. A cement type CEM III/B 42.5N was used (430 kg/m³) and a water-to-cement ratio of 0.46. The self-healing agent, MUC^+ provided in powder form, was added in a dosage of 1% vs. cement mass in the concrete mix. Additionally, a precipitation precursor (urea) and a calcium source (calcium nitrate tetrahydrate), which function as bacterial nutrients, were added to the concrete mixture in a dosage of 1 m% vs. cement mass. These products were dissolved in a part of the mixing water and were separately added to the concrete mix, together with the MUC^+, via an inspection opening above the mixer. About 3.5 m³ of this bacterial self-healing concrete was produced. The fresh concrete properties measured at the mixing plant showed that the slump amounted to 90 mm and the air content was 4.5%.

The roof plate (Fig. 3) was prefabricated on the construction site near the inspection pit and installed on the pit 5 weeks after fabrication. Visual inspection 6 months after casting (and before filling of the pit with earth) showed that the surface was at that time still free of cracks.


Figure 3: Inspection pit (left) and roof plate made of self-healing concrete with MUC+ (right)

In order to test the sealing capacity of the concrete, 5 prisms (150 x 150 x 550 mm) were cast on site. These prisms contained 2 reinforcement bars (Ø 6 mm) located at 30 mm from the bottom side and 3 glass tubes (Ø 10 mm) located at 60 mm from the top side. After 6 weeks of curing the beams were cracked in a three point bending setup with a span of 450 mm aiming at a final crack width around 350 µm. After sealing the cracks at the sides of the specimens, the prisms were saturated for 5 days in tap water, after which an initial water flow test was performed (see [8] for a more detailed description). In short, one side of the glass tubes was sealed, while the other side was connected to a water reservoir under 1 bar pressure. Water would flow from the reservoir to the broken glass tubes, into the crack and leak out at the bottom side of the cracks. The water leakage in function of healing time was quantified by capturing the water over a 15 minutes test duration in a container on a scale with automatic logging. Water flow measurements were performed on the initially unhealed specimens (immediately after crack formation) and then once every 3 weeks during the healing period. During this period the specimens were submersed in tap water and measurements were taken until a 24 weeks healing period was reached. The sealing efficiency SE after different healing times can then be calculated based on Eq. (1).

$$\mathrm{SE} = \frac{WF_{initial} - WF_t}{WF_{initial}} \cdot 100\% \qquad (1)$$

in which $WF_{initial}$ is the initial water flow (g/min) and WF_t is the water flow after t weeks of healing.

3. Results

3.1 Concrete beam with macro-capsule based self-healing system

During loading of the beams containing encapsulated healing agent, leaking of the healing agent was detected, indicating that some capsules were crossed by the crack and broke. From previous results the PMMA capsules are expected to rupture when crossed by cracks of around 100 µm in width [16].

While exposing the concrete beams to the chloride solution, spots where the WRA leaked out could be clearly identified on the concrete beams, as shown in Fig. 4. This also confirms that some of the randomly dispersed capsules broke during crack formation and release their content. A reduction in the ingress of aggressive liquids is therefore expected for the concrete beams with self-healing properties.

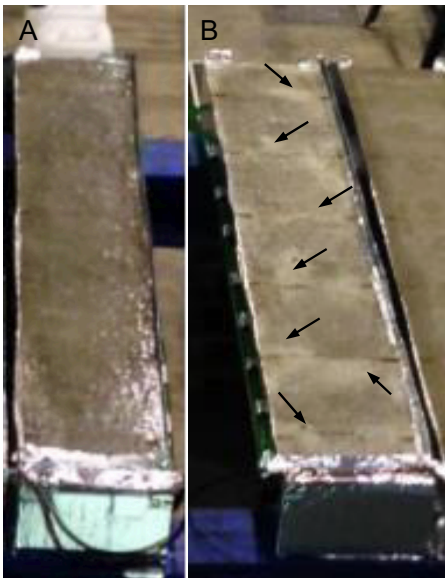

Figure 4: Concrete beams exposed to the chloride solution: (A) Reference beam without capsules; (B) Beam with self-healing properties provided by PMMA capsules. Arrows indicate the spots where leakage of WRA was visible.

The experimentally determined chloride profiles for all cracked (REF) and healed (PMMA) samples in the crack zone, when drilling down from the exposed surface, are shown in Fig. 5.

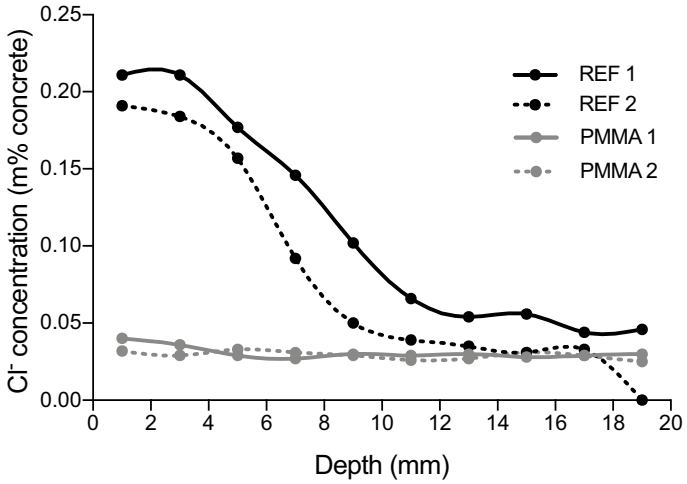

Figure 5: Chloride profiles taken near the cracks after 6 weeks of wet-dry cycles including 5 days dry period and 1 day exposure to a 3 wt% NaCl solution.

For the samples taken from the beam with PMMA capsules, the chloride concentration is approximately constant at every depth. When comparing with cracked concrete it is clear that the chloride content is considerably reduced due to release of healing agent from the capsules. For the reference samples, the highest chloride concentrations at every depth are found near the exposed surface. The chlorides have not only penetrated from the surface, but also through and perpendicular to the crack. The chloride profiles taken perpendicular to the crack face can be found in [17]. Here it is obvious that for the specimens containing PMMA capsules, the chloride concentration in the layer at 5 mm below the exposed surface may be more elevated, while the profiles taken deeper down (at 25, 50 and 85 mm from the exposed surface) show low chloride concentrations. For the reference cracked concrete, however, it was clear that the chloride concentration increased when approaching the crack wall. These results show that the ingress of chlorides is considerably reduced in areas where WRA was released from the capsules. This stresses the importance of having a uniform distribution of the capsules to achieve the highest possible sealing efficiencies.

3.2 Concrete slab with self-healing properties through incorporation of mixed ureolytic bacterial cultures

The results of the crack width measurements performed prior to saturation of the prisms that were cast alongside the slab, as well as the water flow results are given in Tab. 1. The average crack width of the specimens is equal to 348 µm with a coefficient of variance of 6.7%. During the healing period deposition of $CaCO_3$ crystals was noticed at the crack mouth. Evaluation of the crack widths and the initial water flows in Tab. 1 makes clear that the internal geometry of the cracks will have a large effect on the water flow. Specimens 3 and 5 for instance have the same mean crack width, however they show clearly different water flow values. Tab. 1 indicates that some healing is already obtained after 3 weeks in submersed conditions (average SE above 50%). The healing keeps increasing with time and the SE reaches an average value of 96% after 24 weeks.

Table 1: Overview of water flow and initial crack width measurements, as well as the calculated sealing efficiency after 3, 12 and 24 weeks submersed healing.

	Mean crack width [µm]	Initial water flow [g/min]	SE after 3 wk healing [-]	SE after 12 wk healing [-]	SE after 24 wk healing [-]
1	335	60.9	39%	65%	97%
2	320	33.4	49%	97%	100%
3	352	45.7	74%	81%	98%
4	383	26.9	50%	73%	86%
5	352	7.1	72%	100%	100%
Mean	348		57%	83%	96%

4. Conclusions

Two demonstrators were prepared to evaluate the self-healing efficiency of two different self-healing methodologies for concrete.
First a real-scale concrete beam (250 cm × 40 cm × 20 cm) was made with self-compacting concrete containing PMMA macro-capsules filled with a water repellent agent. Since PMMA capsules tend to float, the concrete was cast in 2 layers. At the age of 14 days, 6 cracks of 0.3-0.6 mm in width were created. When exposing the beams to a 3 wt% NaCl solution it was clear that WRA was released from the capsules and made also part of the concrete surface water repellent. When comparing the self-healing beam with a reference beam it was clear that the chloride ingress was considerably reduced due to release of WRA from the capsules.
Secondly, a mixed ureolytic culture of bacteria (MUC^{+}) was incorporated in a roof plate of an inspection pit in a dosage of 1% vs. cement mass. Additionally, urea and calcium nitrate tetrahydrate were added to the concrete mixture in a dosage of 1 m% vs. cement mass. Visual inspection 6 months after casting showed that the surface of the plate was at that time still free of cracks. Water flow tests were executed on prisms (150 x 150 x 550 mm) cast on site and cracked in a three point bending setup aiming at a final crack width around 350 µm. This allowed to illustrate that, if cracks appear, some healing is already obtained after 3 weeks in submersed conditions (average SE above 50%), and reaches on average values of 96% after 24 weeks.

Acknowledgements
The research leading to these results has received funding from the European Union Seventh Framework Programme (FP7/2007-2013) under grant agreement n° 309451 (HEALCON) and from VLAIO (Flanders Innovation & Entrepreneurship) for the project "Encapsulation of polymeric healing agents in self-healing concrete: capsule design". T. Van Mullem acknowledges the grant (17SCIP-B103706-03) from the Construction Technology Research Program funded by Ministry of Land, Infrastructure and Transport of Korean Government.

References

[1] Malinskii, Y.M et al, Investigation of self-healing of cracks in polymers, Mekhanika Polim. 2 (1969), 271-275
[2] Van Tittelboom, K. and De Belie, N., Self-healing in cementitious materials - a review, Materials 6 (2013), 2182-2217
[3] White, S.R. et al, Autonomic healing of polymer composites, Nature 409 (2001), 794-797
[4] De Belie, N. et al, A review of self-healing concrete for damage management of structures. Advanced Materials Interfaces (2018), 1800074, in press
[5] Ferrara, L. et al, Experimental characterization of the self-healing capacity of cement based materials and its effects on the material performance: A state of the art report by COST Action SARCOS WG2, Construction and building materials 167 (2018), 115-142.
[6] Jefferson, A.D. et al, Research progress on numerical models for self-healing cementitious materials. Advanced Materials Interfaces (2018), 1701378, 19 p

[7] Van Tittelboom K, et al, The efficiency of self-healing concrete using alternative manufacturing procedures and more realistic crack patterns. Cement and Concrete Composites 57 (2015),142-152
[8] Feiteira, J., Self-healing concrete encapsulated polymer precursors as healing agents for active cracks, PhD thesis, Ghent University (2017)
[9] Hilloulin, B. et al, Design of polymeric capsules for self-healing concrete. Cement and Concrete Composites 55 (2015), 298-307
[10] Gruyaert, E. et al, Capsules with evolving brittleness to resist the preparation of self-healing concrete. Materials de Construcción 66 (323) (2016), e092, 13 p
[11] Gruyaert, E. et al, Test method to assess the survival probability of capsules in self-healing concrete, 6th International Conference on Self-Healing Materials. Graf-Zeppelin-Haus, Friedrichshafen, Germany (2017)
[12] Araújo, M. et al, Design and testing of tubular polymeric capsules for self-healing of concrete, 3rd International conference "Innovative Materials, Structures and Technologies" IMST2017, Riga, Latvia (2017). Journal of Physics: IOP Conference Series: Material Science Engineering 251, 012003.
[13] Van Tittelboom, K et al, Self-healing efficiency of cementitious materials containing tubular capsules filled with healing agent. Cement and Concrete Composites, 33(4) (2011), 497-505
[14] Gruyaert, E. et al, Evaluation of the performance of self-healing concrete at small and large scale under laboratory conditions, Proceeding of the XIV DBMC - 14th International Conference on durability of building materials and components, PRO 107, Ghent (2017), 203-204, paper 203, 12 p
[15] Araújo, M. Design of novel polymeric healing agents and cylindrical capsules for self-healing concrete, PhD thesis, Ghent University (2018)
[16] Šavija, B. et al, Simulation aided design of tubular carriers for self-healing concrete. Materials 10 (10) (2017), 13 p
[17] Araújo, M. et al, Poly(methyl methacrylate) capsules as an alternative to the ''proof-of-concept'' glass capsules used in self-healing concrete, Cement and concrete composites, 89 (2018), 260-271.

COST ACTION TU1404

RRT^{+}, NUMERICAL BENCHMARKING AND RECOMMENDATIONS

SynerCrete'18 International Conference on Interdisciplinary Approaches
for Cement-based Materials and Structural Concrete
24-26 October 2018, Funchal, Madeira Island, Portugal

COMPILED COST ACTION RRT+ RESULTS FROM NTNU: DETERMINATION OF PARAMETERS REQUIRED FOR EARLY AGE CRACK ASSESSMENT

Anja Estensen Klausen [(1)], Terje Kanstad [(1)], Emmanuel Roziere [(2)]

(1) Norwegian University of Science and Technology (NTNU), Trondheim, Norway
(2) CENTRALE NANTES, Nantes, France

Abstract
Volume changes of concrete in the hardening phase and the associated cracking risk can be predicted by using calculation methods to assess the early age structural behaviour of the concrete. Based on such calculations and corresponding material parameters determined from laboratory experiments, proper choice of concrete type, mineral additives and execution methods on-site can be taken to minimize or avoid cracking. The current article constitutes a compilation of the Cost Action TU1404 RRT results from NTNU, and it aims to provide a set of parameters necessary to perform early age crack assessment of the investigated concrete. A vital part of the current test program was the Temperature-Stress Testing Machine (TSTM) at NTNU, which measures the restrained stress development of concrete through the hardening phase.

1. Introduction

Concrete in the hardening phase is subjected to volume changes caused by thermal dilation (TD) and autogenous deformation (AD). If these volume changes are restrained, they may lead to cracking and further to functionality, durability, and esthetical issues. The volume changes of concrete and the associated cracking risk can be predicted by using calculation methods to assess the early age structural behaviour of the concrete. Based on such calculations and corresponding material parameters determined from laboratory experiments, proper choice of concrete type, mineral additives and execution methods on-site can be taken to minimize or avoid cracking.
An extensive RRT program was initiated by the Cost Action TU1404 [1], and involved testing of properties of concrete by various European laboratories using both standardised and non-

standardised methods. The current article constitutes a compilation of the RRT results from NTNU, and aims to provide a set of parameters necessary to perform early age crack assessment of the investigated concrete. A vital part of the current test program was the Temperature-Stress Testing Machine (TSTM) at NTNU [2].

2. Experimental set-up

2.1 Property development

Compressive strength, direct uniaxial tensile strength and E-modulus in compression were tested under 20 °C isothermal conditions.

Compressive strength tests were performed on ø100x200 mm cylinders according to NS-EN 12390-3:2009.

Uniaxial tensile tests were performed by the standard method at SINTEF/NTNU in Norway: a uniaxial load was applied the100x100x600 mm specimen until it developed failure in tension. During testing, the deformation was measured over the 100 mm mid-section by two displacement transducers placed on opposite side of the prism. The strain rate was approximately $100x10^{-6}$ per min.

Modulus of elasticity in compression tests were performed on ø100x200 cylinders according to the Norwegian standard NS3676.

2.2 TSTM-System

The Temperature-Stress Testing Machine (TSTM) System at NTNU consists of a Dilation Rig and a TSTM, Fig. 1. The Dilation Rig measures free deformation, i.e. thermal dilation (TD) and autogenous deformation (AD), while the TSTM is constructed to measure the stress generation of concrete through the hardening phase. The TSTM-system is temperature controlled, i.e. it is possible to prescribe and apply realistic or isothermal temperature histories to the two concrete specimens.

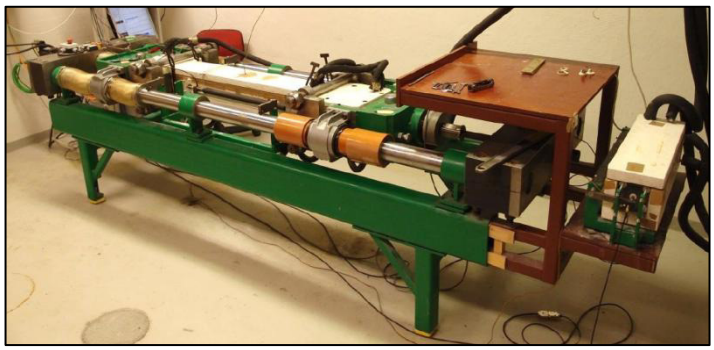

Figure 1: The TSTM-system at NTNU

The TSTM is both deformation-controlled and load-controlled. By applying a given degree of restraint and a chosen temperature history, the TSTM can directly simulate the stress development in a selected section of a concrete structure. During testing, a comprehensive stress-strain relation for each TSTM regulation is obtained. This stress-strain relation provides

an incremental E-modulus development (i.e. obtained from incremental loading) over time for the concrete in question. The stress development from the TSTM tests was also used to determine the start time for stress calculations, t_0 [2]. After testing, temperature steps of ±3 °C around an initial temperature of 20 °C was applied to the TSTM-system to determine the Coefficient of Thermal Expansion (CTE).

3. Materials and experimental program

All tests were performed on the ordinary concrete mixture (OC) as defined by TU1404 [1]. The mix design is presented in Tab. 1 a), and the test program is given in Tab. 1 b). During the realistic-temperature TSTM test, the concrete was subjected to a temperature history provided by Vercors project [1], Fig. 2.

Table 1: a) Concrete mix-design and b) Test program

a)

Cement CEM I 52,5 N-SR3	320
Sand 0-4	830
Gravel 4-11	449
Gravel 8-16	564
Admixture	1.44
Added water	172.4

b)

Test method	*Test age [Days]*
Compressive strength	7, 28
Tensile strength	7, 28
E-modulus in compression	7, 28
TSTM – isothermal, $R = 1.0^*$	0 - 62
TSTM – realistic temp., $R = 0.5^*$	0 - 15

*) *R = degree of restraint*

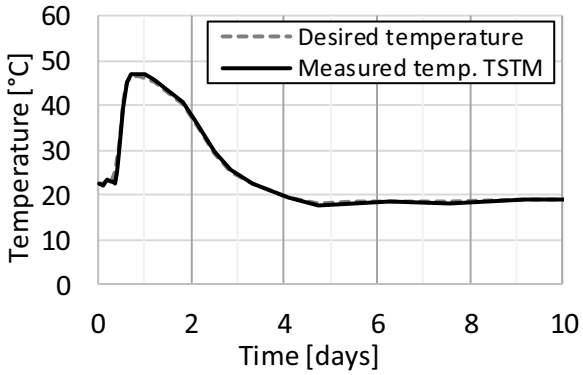

Figure 2: Temperature in the TSTM during testing

4. Material models and stress development calculations

The compressive strength, tensile strength and E-modulus were modelled by Eq. 1, which is a modified version of the CEB-FIP MC 1990-model, see [3] and [4]. The *s*-parameter is the

same for all properties, while the *n*-parameter is varying. The 28-days properties as well as the curve-fitting parameters were determined by parallel mechanical testing.

$$X(t_e) = X(28) \cdot \left\{ exp\left[s \cdot \left(1 - \sqrt{\frac{672 - t_0}{t_e - t_0}} \right) \right] \right\}^n \quad (1)$$

where $X(t_e)$ is the property as a function of maturity t_e. X(28) is the property at 28 days, s and n are curve-fitting parameters, and t_0 is the start time for stress development [maturity time]

The stress development measured in the TSTM was also calculated by a calculation routine in Excel and Visual Basic. The stress calculations were based on linear viscoelasticity with age adjusted effects, using the degree of restraint, the measured temperature and free deformation from the dilation rig as input data [2].

5. Test results and discussion

Material parameters for the OC was determined by fitting the material model described in the previous section to the results from the mechanical test series by using the method of least squares. The *s*-parameter was determined based on the measured incremental E-modulus development during the realistic TSTM-test, while the *n*-parameters and the property values at 28 days were found from the 7-day and 28-day values determined by the test program, see Tab. 2. The creep parameters were estimated based on previous experience, and then adjusted by fitting the calculated stress development to the measured stress development. The obtained model parameters are presented in Tab. 3.

Measured and modelled property developments are presented in Fig. 3. The two E-modulus test set-ups, i.e. the TSTM and the mechanical tests, provided good agreement.

Table 2: Test results, average values

Time [Days]	f_c^* [MPa]	f_t [MPa]	E_c [GPa]	E_{TSTM} [GPa]	t_0 [h]	CTE [MPa]
7	34.0	2.9	30.5	30.4	-	-
28	48.4	3.8	31.9	33.0	-	-
-	-	-	-	-	10.3	8.9**

**) Cylinder strength*

***) Average value of 15.8 days (CTE = 8.7) and 62.5 days (CTE = 9.1)*

Table 3: Deduced model parameters (where f_{c28} = cylinder strength)

Property development						Deduced creep parameters		
s	n_t	n_E	f_{c28} [MPa]	f_{t28} [MPa]	E_{28} [GPa]	Φ_0	*p*	*d*
0.342	0.754	0.321	48.4	3.8	33.0	0.65	0.20	0.40

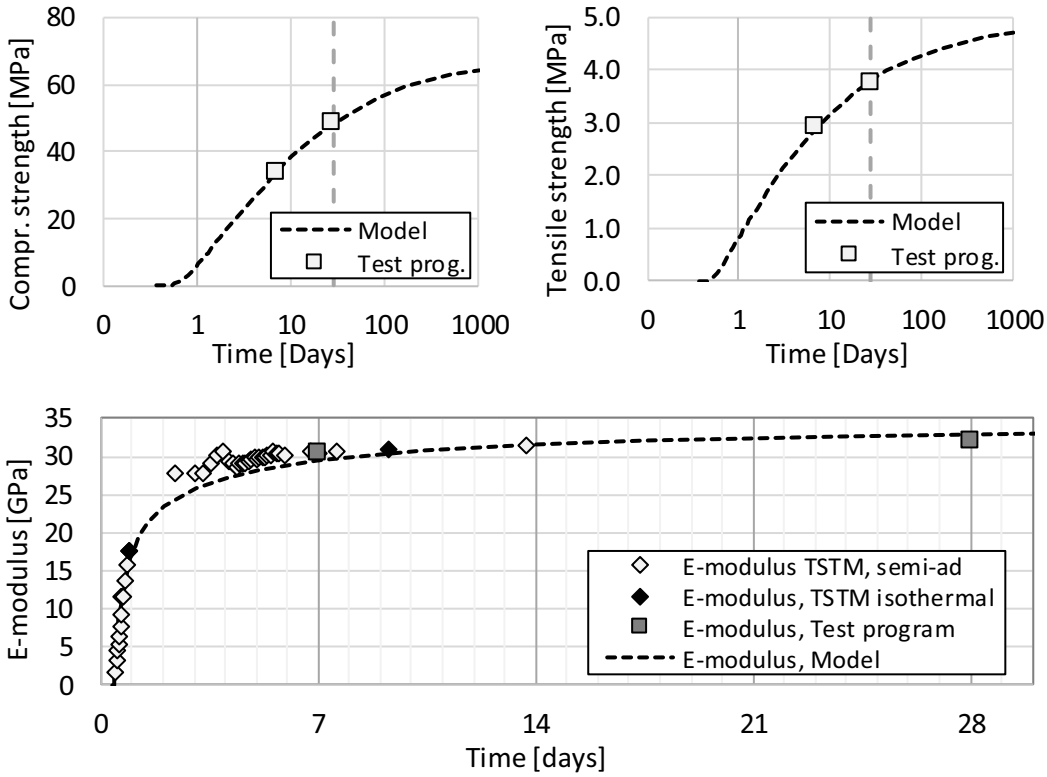

Figure 3: Property development

The AD developments were deduced by subtracting the TD from the total measured free deformation. The results are presented in Fig. 4a, and show that the concrete experiences a rather limited AD development under both isothermal and realistic temperature curing conditions.

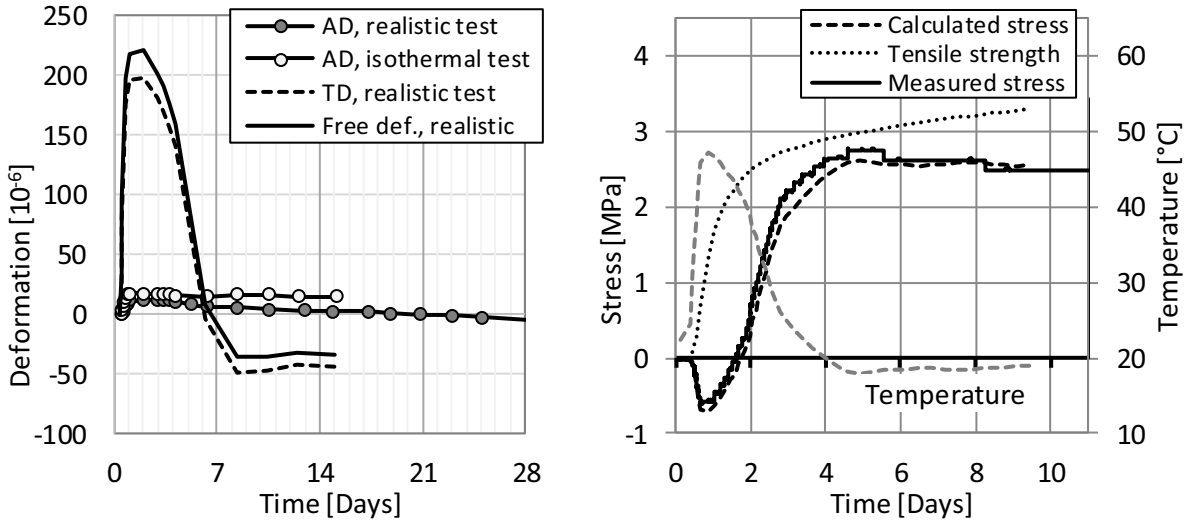

Figure 4: a) Measured deformation b) Measured and calculated stress development

The measured and calculated stress developments for the TSTM-test at realistic temperature conditions and a degree of restraint of 50% are presented in Fig. 4b. The agreement between measured and calculated stress is obviously good, as the creep parameters were deduced by fitting the calculated stress curve to the measured stress development. No dedicated creep tests were included in the current test program, however, previous experience has shown good agreement between creep parameters deduced from 1) stress development tests in the TSTM and 2) dedicated creep tests in the TSTM [2, 5].

6. Summary and conclusion

The current article constitutes a compilation of the Cost Action TU1404 RRT results from NTNU. Based on these results, the article proposes a set of parameters necessary to perform early age crack assessment of the investigated concrete. By using these model parameters combined with dedicated calculation methods to assess the early age structural behavior of the concrete, the volume changes of the concrete and the associated cracking risk can be predicted. Based on such calculations, proper choice of concrete type, mineral additives and execution methods on-site can be taken to minimize or avoid early age cracking.

Acknowledgements
The article is based on work performed in the User-driven Research-based Innovation project DaCS (Durable advanced Concrete Solutions, 2015 - 2019) and the COST Action TU1404 (www.tu1404.eu).

References

[1] Cost Action TU1404, RRT+, Main phase of the Extended Round Robin Testing programme for TU1404, TESTING PROTOCOLS, 2016.
[2] Anja Estensen Klausen, Early age crack assessment of concrete structures: experimental determination of decisive parameters, PhD Thesis, ISBN 978-82-326-1850-7 [printed ver.], ISBN 978-82-326-1851-4 [electronic ver.], Norwegian University of Science and Technology (NTNU), Trondheim, Norway, 2016.
[3] Terje Kanstad, Tor Arne Hammer, Øyvind Bjøntegaard, Erik J. Sellevold, Mechanical properties of young concrete: Part II: Determination of model parameters and test program proposals, Materials and Structures 36 (2003) pp. 226-230.
[4] Jan-Erik Jonasson, Peter Fjellström, Henrik Bäckström, Inverkan av variabel härdningstemperatur på betongens hållfasthetsutvikling (The influence of variable curing temperature on the strength development of concrete - only available in Swedish), Bygg & Teknik (2010)
[5] Anja Estensen Klausen, Terje Kanstad, Øyvind Bjøntegaard, Erik J. Sellevold, Comparison of tensile and compressive creep of fly ash concretes in the hardening phase, Cement and Concrete Research 95 (2017) pp. 188-194.

SynerCrete'18 International Conference on Interdisciplinary Approaches
for Cement-based Materials and Structural Concrete
24-26 October 2018, Funchal, Madeira Island, Portugal

MECHANICAL PROPERTIES OF CEMENT BASED MATERIALS – EXTENDED ROUND ROBIN TEST OF COST ACTION TU 1404

Violeta Bokan Bosiljkov [(1)], Marjeta Kramar Fijavž [(1)], Marijana Serdar [(2)]

(1) University of Ljubljana, Faculty of Civil and Geodetic Engineering, Slovenia
(2) University of Zagreb, Faculty of Civil Engineering, Croatia

Abstract
The Extended Round Robin Testing program (RRT+) of COST ACTION TU1404 is the main activity within Working Group 1 (WG 1): Testing of cement-based materials (CBMs). In its Main Experimental Phase the RRT+ program is divided into six group priorities, among which group priority 1d (GP1d) deals with mechanical properties and creep of CBMs across several scales: hardened cement paste, mortar and concrete. One of the aims of the RRT+ as a whole is to extensively characterize a set of predefined CBMs and support the development and validation of material models in WG2 - modelling and benchmarking. At the end of the Main Experimental Phase of RRT+, results of 15 laboratories were available for analyses in the scope of GP1d. This paper focuses on statistical analysis of reported test results. The analysis was carried out for properties at 7 and 28 days, where the number of reported test results was high enough. For the compressive strength, observations of the mortar and concrete scale are given. For the tensile strength and unloading E-modulus, only the results at concrete scale are presented and discussed.

1. Introduction

The Extended Round Robin Testing program (RRT+) of COST ACTION TU1404 European project is the main activity within Working Group 1 (WG 1): Testing of cement-based materials (CBMs) [1]. The Main Experimental Phase of the RRT+ started in November 2016, after detailed guidelines for the test protocols [2] had been made available on the Action web site [1]. Test protocols under group priority 1d (GP1d) of WG1 can be broadly divided into two stages. The first stage includes the determination of the basic mechanical properties of hardened cement paste, mortar and concrete, which are compressive strength, splitting tensile strength and unloading E-modulus from compression (with Poisson's ratio) and dynamic

characterization of isotropic elasticity by ultrasound test [3]. The foreseen testing ages of specimens are 24, 30, 36, 48 and 72 hours, and 7 and 28 days. It is aimed at providing input testing parameters for the second stage of the tests. The second stage includes tests of creep behaviour of CBMs and advanced test methods.
A total of 25 laboratories expressed interest to participate in the testing of CBMs' properties in the framework of GP1d [3]. At the end of the Main Experimental Phase results of 15 laboratories were available for analyses in the scope of the first stage tests. The number of tests and the extent of testing campaign (scale of testing, testing age, shape of specimen, etc.) vary considerably between different laboratories. The majority of 15 laboratories reported only the results of compressive strength measured on the OC and MOC concrete at 7 and 28 days.

This paper focuses on statistical analysis of the reported test results. In case of compressive strength at least 3 laboratories reported results for the mortar and concrete scale, at 7 and 28 days. Therefore, the determination of correlation between concrete and the corresponding mortar compressive strength is possible for the two ages. For the tensile strength and the unloading E-modulus only the results for concrete compositions, at 7 and 28 days, were reported by a significant number of laboratories, which allows us to carry out statistical analysis of the test results.

2. Materials and test methods

Compositions of the CBMs under consideration, ordinary mortar (OM), modified ordinary mortar (MOM), ordinary concrete (OC) and modified ordinary concrete (MOC), are given in [2]. OM and MOM present "identical" mixtures on the mortar scale, in relation to the concrete compositions: OC and MOC, respectively. The main difference between the concrete compositions is the w/c ratio, which is 0.52 for the OC (and for the associated OM) and 0.42 for the MOC (and for the associated MOM). Reduction in the w/c for the modified compositions was obtained by increasing cement content of the mixture (considerably), its water content (slightly) and by increasing the content of active component of superplasticizer (amount of the SP – water) from 0.09% to 0.17% in relation to the cement mass.

Protocols described in [2] were followed for the mixture preparation and determination of compressive strength (f_c), splitting tensile strength (f_{st}) and unloading E-modulus from compression (E_s). These are standard tests that are performed routinely in most of the participating laboratories. Although prismatic (preferably 100 mm x 100 mm x 200 mm) or cylindrical (preferably 150 mm x 300 mm) shapes of the specimens were proposed for the compressive tests, beside cubic one (150 mm cube), in order to obtain relevant data for the creep tests in the second stage of the GP1d program, the majority of laboratories decided to carry out compressive tests on the cubic specimens only. As a rule, 3 replicates were used to determine a particular property of the CBMs, for compressive strength. However, 6 replicates were used by a limited number of laboratories. All reported results were considered in the statistical analyses. Since the majority of 15 laboratories reported concrete compressive strengths for the 150 mm cube, conversion factor 1.25 was used to estimate the 150 mm cube strength for the laboratories that measured compressive strength on standard cylinder (150

mm x 300 mm or 100 mm x 200 mm) or 100 mm x 100 mm x 200 mm prism. For the tensile strength results, the shape of the specimen was not considered as influencing parameter. Moreover, results of direct tensile strength reported by one laboratory were added to the analysed results.

For the statistical analysis of the reported test results Wolfram Mathematica computing system [5] was used. The normality of the data was tested graphically (ProbabilityPlot) as well as by performing a goodness-of-fit test (DistributionFitTest). In reality, however, we do not have enough samples for any test to be appropriate; therefore we will not address this issue. In order to show particularity of individual laboratory results, they are presented using a boxplot, also called a box and whisker plot, in order to show the spread and centres of each data set. Measures of spread include the interquartile range, with minimum and maximum value of the considered property. Measures of centre include the mean value (i.e., the average), presented by a black line, and the median (the middle of a data set), presented by a white line. The general mean of the whole group is reported only for the results of compressive strength. The analysis of variance tests (ANOVA) were carried out to compare mean values of different laboratories (labs). Mandel's h and k statistics were calculated to track the possible outliers, following the standard ISO 5725-2 [6].

3. Results and discussion

3.1 Compressive strength

Compressive strength is one of the most important performance indicators to assess the similarity of concrete mixtures. In Fig. 1 the results for the OC an MOC concretes are given for 7 (OC7, MOC7) and 28 days (OC28, MOC28). 11 labs reported results for the OC concrete. General mean for the compressive strength of the group is 37 MPa and 50 MPa for 7 and 28 days, respectively. Values are lower than reported in the Initial Experimental Phase of the RRT^{+}, where general mean at 7 days was 40 MPa (30 labs) and 52 MPa at 28 days (26 labs) [4]. This is a consequence of higher spread of the reported results in the Main Experimental Phase, due to low compressive strengths reported by labs 3 and 4. However, despite these low compressive strengths, all the reported values for OC28 are higher than 37 MPa, which means that all OC mixtures prepared in different laboratories comply with the same concrete class of C30/37. Two labs reported 6 results for the OC composition (lab 10 and 15) at 7 and 28 days, and lab 10 reported 6 results also for the MOC composition at both ages. However, these two labs used 150 x 300 mm cylinder to determine compressive strength. Thus, correction factor of 1.25 was used to estimate the 150 mm cube compressive strength. Comparison of results between the OC and the MOC for the particular laboratory that reported both results reveal, as a rule, considerably higher spread of test results for the MOC composition. We can also see (Fig. 1) that for the MOC composition only lab 7 and lab 8 reported compressive strength results at 7 and 28 days. General mean of the group regarding MOC compressive strength is 51 MPa at 7 days and 67 MPa at 28 days. All MOC mixtures prepared in different laboratories comply with the concrete class of C45/55.

We calculated Mandel' s h and k coefficients for the OC7, OC28, MOC7, and MOC28 results of compressive strength and compared them to the critical values of these statistics (presented

by red dashed lines in Fig. 1) for the significance level 0.05 according to ISO 5725-2 [6]. The tests show that the results obtained by different laboratories are consistent. No outliers were identified (Fig. 1).

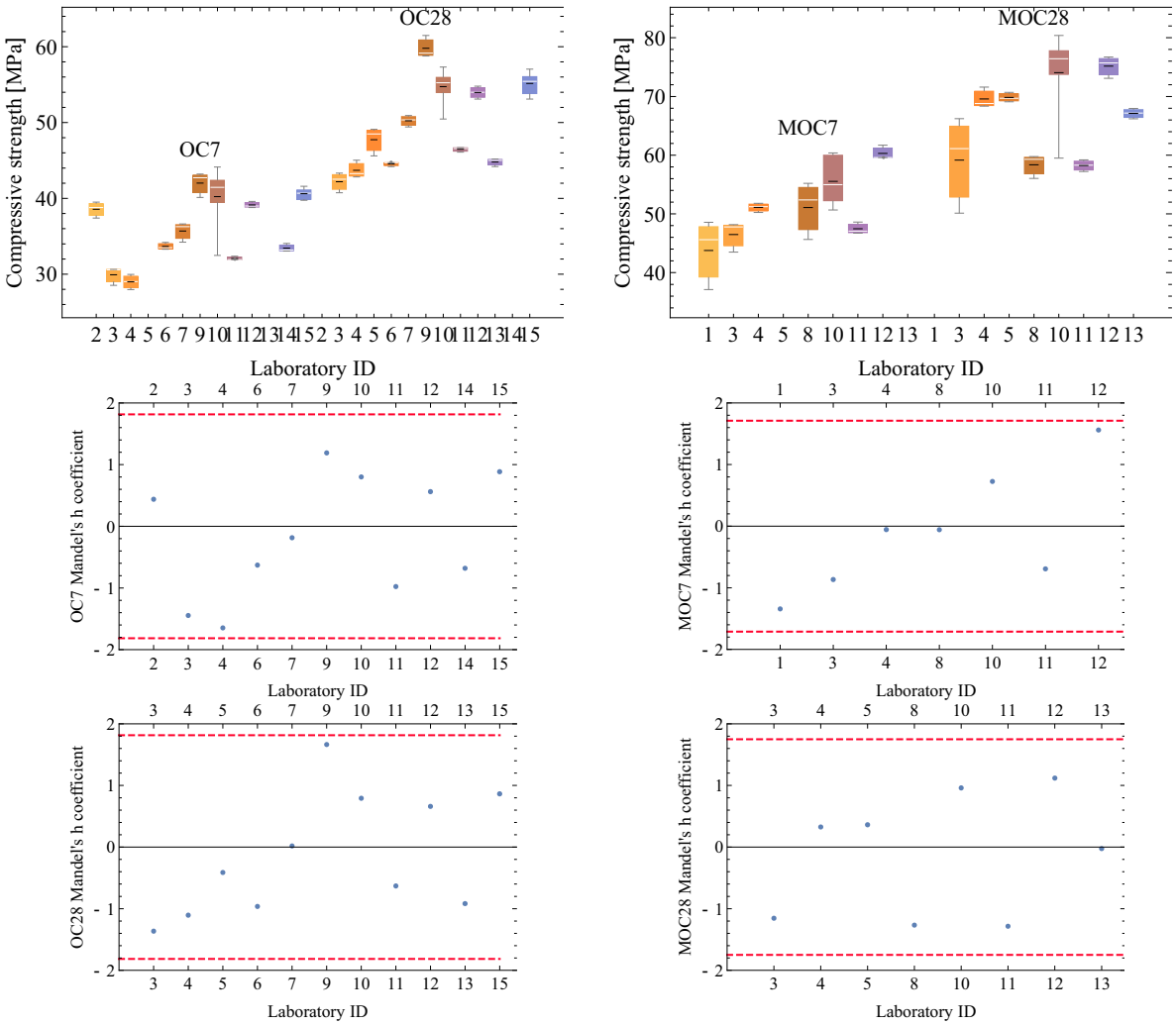

Figure 1: Concrete compressive strength boxplots of individual laboratory measured on the 150 mm cube for the OC and MOC, and Mandel's h coefficient

Only 3 labs reported results on the mortar scale, for the MOM7, OM7 and OM28. For the MOM composition, lab 1 reported the highest spread of test results, using 6 replicates to determine its compressive strength, and lab 2 reported the lowest spread of test results (on 3 replicates). Mean compressive strengths of the two labs, on the other hand, do not differ significantly (62 MPa for the lab 1 and 64.5 MPa for the lab 2). Mean compressive strength of lab 3 is 35.5 MPa, which is not a realistic value. Since this strength is lower than that of the OM7 reported by the same lab, where w/c ratio is considerably higher, it is highly likely that mistakes were made during the processing of the test results, or possible formation of micro cracks, due to autogenous shrinkage [7], reduced the OM7 compressive strength considerably. General mean of the group regarding OM compressive strength is 43 MPa and 59 MPa for 7

and 28 days, respectively. In relation to the OC compressive strengths, the obtained values are higher, which was expected.

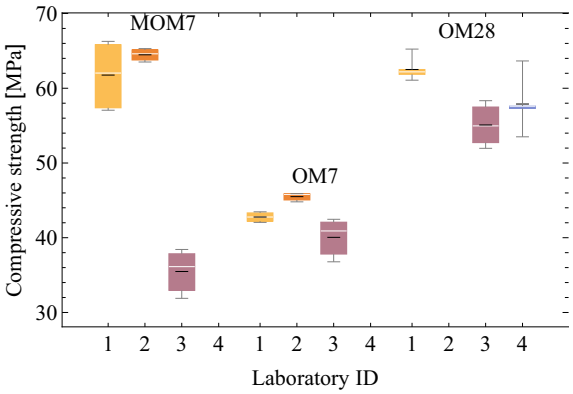

Figure 2: Mortars compressive strength boxplots of individual laboratory measured on 40 mm cube (half of 40 mm x 40 mm x160 mm prism)

According to Pearson's correlation test with significance level 0.05 all the tested pairs of OM-OC and MOM-MOC samples are linearly independent. The test was carried out only for laboratories that reported measurements for identical compositions on mortar and concrete scale, with the same number of test results (3). The analysis of variance tests for every mixture (OM, MOM, OC and MOC) and age of specimens (7 and 28 days) with significance level 0.01 show that, with the only exception of OM7, the means of the compressive strengths between different laboratories all differ significantly.

3.2 Tensile strength

By the analysis of variance tests with significance level 0.01 all the means differ significantly for the concrete tensile strength. Therefore, the reported results were compared to the interval of the tensile strengths calculated from the mean compressive strength for individual laboratory by using modified MC2010 expressions [8]:

lower bound value: $f_{st,min} = 0.7 \cdot 0.3 \cdot (f_{cm})^{2/3}$,

upper bound value: $f_{st,max} = 1.3 \cdot 0.3 \cdot (f_{cm})^{2/3}$,

where f_{cm} stands for the mean compressive strength measured on cylinder 150 mm x 300 mm. Wherever individual lab reported 150 mm cube compressive strengths, conversion factor 0.8 was used to determine the f_{cm}.

From the results in Fig. 3 it is evident that lab 10 stands out with high values of the mean tensile strength for all compositions and ages, and with high spread of the test results for the OC composition at 28 days. At the same time, all reported tensile strength data are much higher than the calculated upper bound value of lab 10, for the OC and MOC composition. Therefore, results of lab 10 will be excluded from the discussion. At the OC composition the lowest values were reported by lab 4 (mean values of 2.11 MPa and 3.24 MPa for 7 and 28 days, respectively), where 80/300 mm cylinder was used to determine the splitting tensile strength of concrete. However, all the data of lab 4 are inside its calculated interval of tensile strengths. The highest mean tensile strength at 7 days was reported by lab 15 (3.63 MPa on 100/100/200 mm prism), and at 28 days by lab 6 (4.47 MPa on 150/300 mm cylinder), while

lab 15 reported the mean value of 4.21 MPa. All the data of lab 15 are inside its calculated intervals of tensile strengths. Lab 6, on the other hand, measured higher tensile strengths than estimated by the calculated interval, which is true also for lab 5. For the rest of the labs that reported results for the OC composition, all data are inside the calculated intervals. We calculated lower and upper bound value of the OC tensile strength interval also from the general mean compressive strength of the group, for 7 days ($f_{st,min}$ 2 MPa, $f_{st,max}$ 2.7 MPa) and 28 days ($f_{st,min}$ 2.5 MPa, $f_{st,max}$ 4.6 MPa). With the exception of lab 10, mean tensile strengths of all labs lie inside the appropriate calculated intervals.

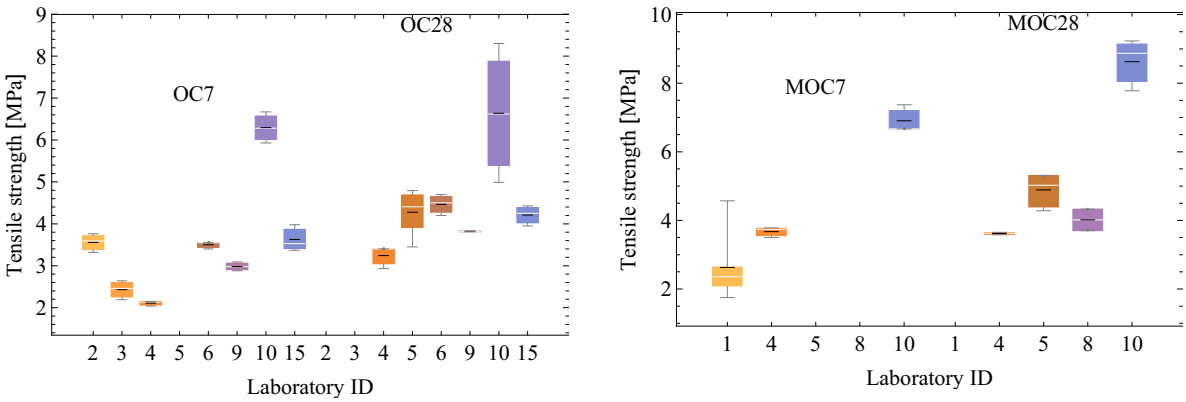

Figure 3: Concrete tensile strength boxplots of individual laboratory for the OC and MOC

For the MOC composition only a few labs reported results as presented in Fig. 3. The data reported by labs 4, 5 and 8 are all inside the calculated intervals for the particular lab. They are also inside the tensile strength intervals calculated from the general mean compressive strength of the group, for 7 days ($f_{st,min}$ 2.5 MPa, $f_{st,max}$ 4.6 MPa) and 28 days ($f_{st,min}$ 3 MPa, $f_{st,max}$ 5.5 MPa). For lab 1, on the other hand, only 3 out of 6 results lie inside the calculated interval of the lab, while the lowest two (1.75 MPa and 2.09 MPa) and the highest (4.17 MPa) value are outside.

3.3 Unloading modulus of elasticity

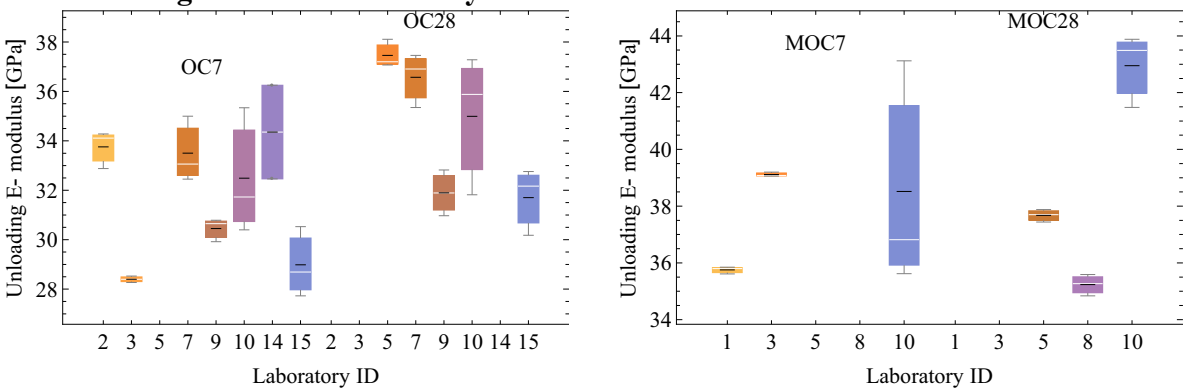

Figure 4: Unloading modulus of elasticity boxplots of individual laboratory for the OC and MOC

By the analysis of variance tests with significance level 0.01, only the means of MOC at 7 days do not differ significantly. Therefore, the reported results were compared to the interval

of the E-modulus calculated from the mean compressive strength for individual lab by using MC2010 expressions [8]:
lower bound value: $E_{s,min} = 21.5 \cdot 10^3 \cdot 0.9 \cdot (f_{cm}/10)^{1/3}$,
upper bound value: $E_{s,max} = 21.5 \cdot 10^3 \cdot 1 \cdot (f_{cm}/10)^{1/3}$,
where f_{cm} stands for the mean compressive strength measured on cylinder 150 mm x 300 mm. Wherever individual lab reported 150 mm cube compressive strengths, conversion factor 0.8 was used to determine the f_{cm}. The lower limit belongs to limestone aggregates and the upper one to quartzite aggregates. The actual aggregate used for the OC and MOC compositions contains silicates and limestone [2], which justifies the selection of the interval limits for E-modulus.

Results for the unloading E-modulus are presented in Fig. 4. By comparing experimental OC7 results of individual laboratory to its calculated E_s interval we can conclude that only for labs 3 and 9 all the reported data lie inside the interval, and for lab 15 the mean value lies inside the interval. The rest of the labs reported higher values of the E-modulus, with mean values between 3 % and 15 % higher than appropriate upper bound value of the calculated E_s. At the OC28, the mean values of lab 10 and lab 15 lie inside the interval, the mean E-modulus of lab 9 is 2.4 % lower and that of lab 5 and lab 7 is 15 % and 7 % higher, respectively, compared to the appropriate bound value of the calculated E_s interval.

By comparing the experimental MOC7 results of individual laboratory to its calculated E_s interval, we can conclude that the measured values are all considerably higher than the upper bound value of the appropriate interval, by 10 %, 17 % and 9 % for labs 1, 3 and 10, respectively. When the same comparison is carried out for the MOC28, all results are considerably higher than the upper bound value of the appropriate E_s interval only for lab 10 (11 % higher mean value). Data of labs 5 and 8, which did not report the MOC7 results, lie all inside the calculated E_s interval of the particular lab.

4. Conclusions

This paper presents and discusses results of statistical analyses performed on the data of CBMs mechanical properties, gathered during the Main Experimental Phase of the RRT$^+$, in the framework of group priority 1d. At the end of the Main Experimental Phase results of 15 laboratories were available for analyses. The number of experimental tests and the extent of testing campaign (scale of testing, testing age, shape of specimen, etc.) vary considerably between different laboratories. Therefore, statistical analyses were carried out only for compressive strength (mortar and concrete scale), tensile strength (concrete scale) and unloading E-modulus (concrete scale), measured at 7 and 28 days, where significant number of laboratories reported the obtained results. The main conclusions are as follows:

- Comparison of the results of compressive strengths between the OC and the MOC, as well as between the OM and the MOM, for the particular laboratory that reported both results, reveal considerably higher spread of test results for the modified compositions.
- Results of the OC compressive strengths reported by different laboratories indicate the same reproducibility of experimental results as in the Initial Phase of the RRT+.

- For laboratories that reported compressive strengths for identical compositions on mortar and concrete scale, with the same number of test results, the tested pairs of OM-OC and MOM-MOC samples are linearly independent.
- The analysis of variance tests for every mixture (OM, MOM, OC and MOC) and age of specimens (7 and 28 days) shows that the means of the compressive strengths, tensile strengths and unloading E-modulus from compression between different laboratories all differ significantly. The only exceptions are compressive strength of the OM and E-modulus of the MOC at 7 days.
- With the exception of one laboratory, tensile strengths reported by different laboratories are inside the limits calculated using the MC2010 expressions.
- Unloading E-moduli reported by different laboratories indicate high scatter of results for this property and, especially for measurements at 7 days, the reported results are higher than estimated by relevant MC2010 expressions.

Acknowledgements
The authors would like to acknowledge networking and dissemination support by the COST Action TU1404 (http://www.tu1404.eu/). The research performed within the RRT+ program of the COST Action is on volunteering basis, since there is no budget foreseen for research activities. Therefore, the authors would like to express their sincere gratitude to all participating laboratories for their dedicated work within this experimental campaign. The authors also acknowledge financial support of EDF, France, CEVA Logistics, Austria and Germany, OeBB Infra, Austria, Staten Vegvesen, Norway and Schleibinger Gerate, Germany. This work was partially supported by Slovenian Research Agency through Programme P2-0185 and Research Project J2-8194.

References
[1] COST Action TU 1404, http://www.tu1404.eu/ (accessed in June 2018)
[2] Staquet, S. et al., RRT+ Main phase of the Extended Round Robin Testing programme for TU1404, Testing protocols, Ver. 22th November 2016, (2016), 57p.
[3] Bokan-Bosiljkov, V. et al., Progress on Testing of Mechanical Properties of Cement Based Materials - Extended Round Robin Test of Cost Action TU 1404, RILEM Proceedings PRO 118 from International Conference on Advances in Construction Materials and Systems, India (2017), 171-178.
[4] Serdar M., Staquet S., Schlicke D., Rozière E., Trtnik G., Nanukuttan S., Azenha M., "Extended Round Robin test RRT+ Initial Phase – Results and lessons learned", presentation at the COST TU1404 Zagreb meeting, March 2016, 34p
[5] Wolfram Research, Inc., Mathematica, Version 11.1, Champaign, IL (2017).
[6] Wilrich, P., Critical values of Mandel's h and k, the Grubbs and the Cochran test statistic, AStA Advances in Statistical Analysis. 97 (2013), 1-10.
[7] Klun, M., Strmšek, L., Bokan-Bosiljkov, V., Strength and elastic properties of cement based materials – contribution of University of Ljubljana to the RRT+ of COST Action TU 1404, Proceedings of the SynerCrete'18 International Conference (2018), 6p.
[8] Model Code 2010, Final draft, Volume 1, FIB Bulletin 65, March 2012.

SynerCrete'18 International Conference on Interdisciplinary Approaches
for Cement-based Materials and Structural Concrete
24-26 October 2018, Funchal, Madeira Island, Portugal

STRENGTH AND ELASTIC PROPERTIES OF CEMENT BASED MATERIALS – CONTRIBUTION OF UNIVERSITY OF LJUBLJANA TO THE RRT+ OF COST ACTION TU 1404

Martin Klun [(1)], Lucija Strmšek [(2)], Violeta Bokan Bosiljkov [(1)]

(1) University of Ljubljana, Faculty of Civil and Geodetic Engineering, Slovenia
(2) STRABAG, Slovenia

Abstract
Research group at the University of Ljubljana carried out extensive test campaign in the framework of the Extended Round Robin Testing program (RRT+) of COST ACTION TU1404. In this paper the first phase test results are given and discussed. The tests were carried out on modified cement paste, ordinary mortar and modified ordinary mortar, at the ages of 24, 30, 36, 48, 72 hours and 7 and 28 days. Hardened properties were evaluated by destructive standard tests and by measurements of compressive and shear ultrasonic waves. The obtained results show big influence of high content of SP with retarding effect on the properties of the modified cement paste and modified ordinary mortar. The age of samples of 2 days was estimated as the time when the retarding effect of the SP stops to act. Formation of micro cracks, due to autogenous shrinkage of the cement paste in the modified compositions, was seen as the source of tensile strength decrease observed at specimens' age of 7 days.

1. Introduction

The Extended Round Robin Testing program (RRT+) of COST ACTION TU1404 European project is the main activity within Working Group 1 (WG 1): Testing of cement-based materials (CBMs) [1]. The RRT+ program is divided into six group priorities, among which group priority 1d (GP1d) deals with mechanical properties and creep of CBMs across several scales – hardened cement paste, mortar and concrete [2].
Research group at the University of Ljubljana (UL FGG) carried out extensive test campaign in the framework of the RRT+, by focusing mainly on the hardened properties of CBMs in within GP1d. The tests of hardened properties were divided in two phases. In the first phase tests were carried out on modified cement paste (MCP), ordinary mortar (OM) and modified

ordinary mortar (MOM) aged 24, 30, 36, 48, 72 hours and 7 and 28 days. Due to unexpected test results showing drop of the CBMs flexural and tensile strength at certain ages of the specimens, the tests were repeated (second phase tests) on the MCP and MOM, and additional tests were carried out on modified ordinary concrete (MOC). In this way mechanical and elastic properties of CBMs across several scales were determined in the same laboratory.
In this paper only results of the first test phase are presented and discussed.

2. Materials

Compositions of the MCP, MOM and OM are given in [3]. They present "identical" mixtures on the mortar and paste scale, in relation to two reference concrete compositions: ordinary concrete (OC) and modified ordinary concrete (MOC) [3]. The main difference between the concrete compositions is the w/c ratio, which is 0.52 for the OC (and for the associated OM) and 0.42 for the MOC (and for the associated MOM and MCP). Reduction in the w/c for the modified compositions was obtained by increasing cement content of the mixture (considerably), its water content (slightly) and by increasing the SP content by factor around 2.5. Ordinary cement paste with the w/c ratio of 0.52 is not stable enough at the fresh state (bleeding) and is thus problematic for the accurate assessment of the mechanical properties on the paste scale. That is why only the MCP was kept in the main experimental phase of the RRT+.

3. Test methods and testing

Protocols described in [3] were followed for the mixture preparation, with some deviations. For the MCP mixing the EN 163-1 standard blade was used, because special blade required in the Testing protocol [3] is not available in the UL FGG laboratory. At the same time, temperature in the laboratory in which specimens were prepared and tested differed from the required temperature of (20 ± 2)°C.

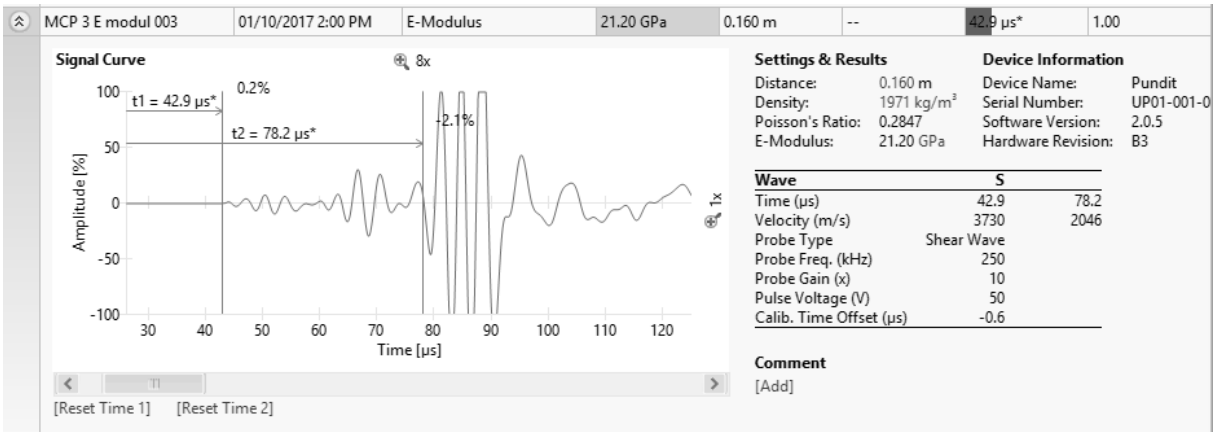

Figure 1: Determination of the dynamic elastic properties using the Pundit device.

Protocols of the GP1d [3] were followed when hardened properties of the CBMs, compressive strength (f_c), splitting tensile strength (f_{st}) and unloading elastic modulus from compression (E_s) were determined. Additionally, flexural strength (f_{ft}) and static Poisson's ratio from compression (ν_s), and ultrasonic pulse velocity (UPV) measurements were carried out. The Pundit PL-200 equipment was used in order to determine dynamic elastic parameters of CBMs, such as dynamic elastic modulus (E_d), dynamic shear modulus (G_d) and dynamic Poisson's ratio (ν_d) (Fig. 1). For the measurements of compressive and shear waves, P-wave and S-wave transducers of 150 kHz and 250 kHz were applied, respectively.
The tests were carried out on specimens aged 24, 30, 36, 48 and 72 hours and 7 and 28 days.

4. Test results and discussion

4.1 Fresh properties

In December 2016, CBMs mixtures were prepared to cast 40 mm x 40 mm x 160 mm prisms in order to determine dynamic elastic properties and compressive, flexural and splitting tensile strengths of MCP, MOM and OM. In January 2017 additional mixtures were prepared to cast 40 mm x 40 mm x 80 mm prisms in order to determine the static elastic modulus and Poisson's ratio of MCP, MOM and OM. Due to lower temperature of the laboratory in December 2016, initial temperature of particular mixture was much lower than required [3], although all materials were stored at (20±1) °C for at least 7 days prior the mixing. Properties of the MCP, MOM and OM in fresh state are given in Tab. 1. The MCP was stable and without evidence of bleeding.

Table 1: Fresh properties of tested CBMs

	December 2016			January 2017		
	T [°C]	**Flow value [mm]**	**Density [kg/m^3]**	**T [°C]**	**Flow value [mm]**	**Density [kg/m^3]**
MCP	14.7	267	1919	18.1	283	1926
MOM	15.1	220	2262	17.8	219	2262
OM	15.2	226	2214	18.3	203	2186

The results in Tab. 1 lead to the conclusion that the difference in the fresh mixture temperature, due to low temperature of the air in the laboratory during mixing, did not have any important influence on the fresh properties of the MCP and MOM, that is on the CBMs with very high content of SP.

4.2 Hardened properties

Fig. 2 presents the results of CBMs' compressive tests. Logarithmic scale was used to distinguish between values at ages up to 2 days. The results show that, despite much lower w/c ratio at the MOM (0.4), its compressive strength up to 30 hours is the same as for the OM (w/c 0.52). Observed behaviour is most probably due to much higher content of SP in the MOM and its retarding effect, which was observed also at demoulding of the MOM and MCP specimens after 24 hours. Both specimens looked as if their final setting time was close to 24 hours. For the MCP this observation is supported by the results of the setting time test (EN

196-3) reported by the TU Graz [4], where initial and final setting time was equal to 23.5 and 26.6 hours, respectively. However, at the TU Graz, laboratory mixing blade and laboratory environment were according to set requirements [3]. Similar influence of SP with retarding effect to the mechanical properties of SCC mixtures was observed at the UL FGG earlier [5].
For the CBMs under consideration the age of 2 days seems to represent the time when retarding effect of SP stops to act. Retarding effect is much lower for the OM, due to considerably lower dosage of SP than in case of the MCP and MOM. Compressive strength of the MCP is lower than at the MOM from 1.5 days on. Higher number of micro cracks inside the MCP specimens, due to autogenous shrinkage, is most probable reason for the observed behaviour.

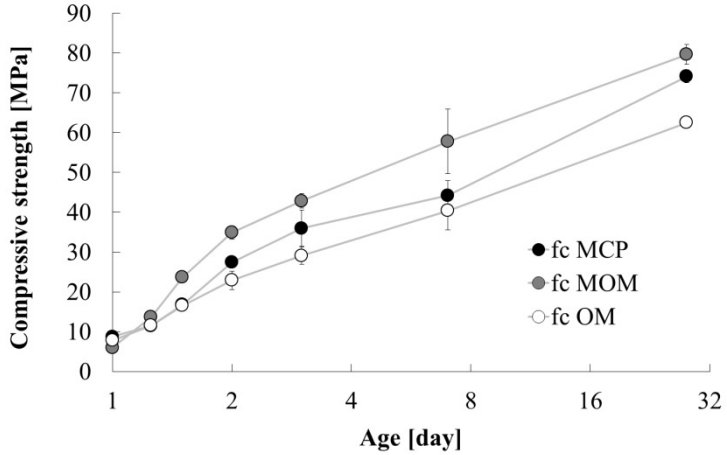

Figure 2: Compressive strength development with specimen's age.

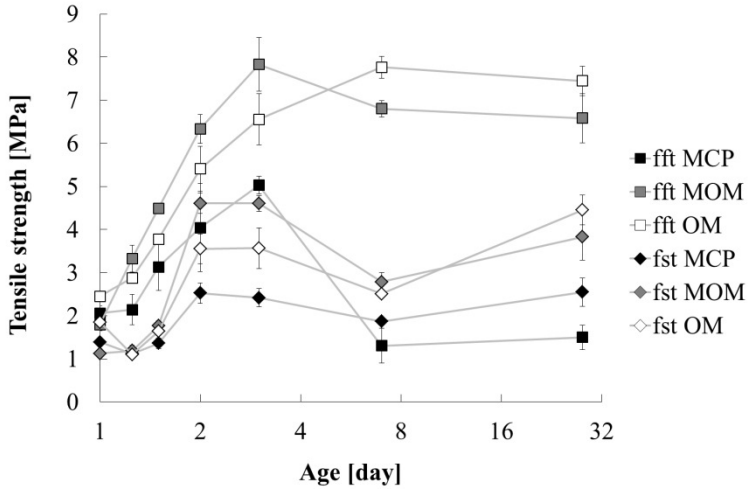

Figure 3: Flexural and splitting tensile strength development with specimen's age.

Fig. 3 shows results of CBMs flexural (f_{ft}) and splitting (f_{st}) tensile strength. When calculating tensile strength, validity of elastic theory was adopted. However, at the ages of 24, 30 and 36 hours impress of loading pieces and loading rollers into specimens was observed at splitting and flexural test, respectively, for the MCP and MOM specimens. Therefore, the results in Fig. 3 may not present realistic values of tensile strength at very early age. We can see (Fig. 3) that f_{ft} of the MCP and MOM is increasing with age up to 3 days, and at the age of

7 days drop in f_{ft} was obtained. Decrease of f_{ft} was extreme for the MCP and much lower for the MOM. This is in agreement with the compressive strength at 7 days (Fig. 2), where the average value obtained for the MCP is much lower than expected. At 28 days f_{ft} of the MCP and MOM is the same as at 7 days. Because also in the second phase test similar behaviour of MCP and MOM was observed, we can conclude that the presence of micro cracks inside the specimens is responsible for the observed behaviour. Autogenous shrinkage of the cement paste can be responsible for the micro crack formation. Results of splitting tensile test do not follow the pattern observed for the flexural strengths, since f_{st} increases only up to 2 days, stays the same until 3 days and after that drop in the strength was obtained at 7 days. However, the decrease in f_{st} for the MCP is much lower, compared to the decrease of f_{ft}. On the other hand, the MOM shows much higher relative drop of f_{st}, compared to f_{ft}. At the age of 28 days all specimens show higher f_{st} than at 7 days.

Fig. 4 shows the results of unloading elastic modulus in compression (E_s), measured on prisms 40 mm x 40 mm x 80 mm, and dynamic modulus of elasticity (E_d), determined by the UPV measurement. We can see that also these results confirm retarding action of SP up to 2 days, since E_s is higher than or equal to E_d at age lower than 2 days. From 2 days on elastic moduli increase with the specimen's age and the ratio between E_d and E_s stays constant and equal to 1.21, 1.26 and 1.11 for the MCP, MOM and OM, respectively.

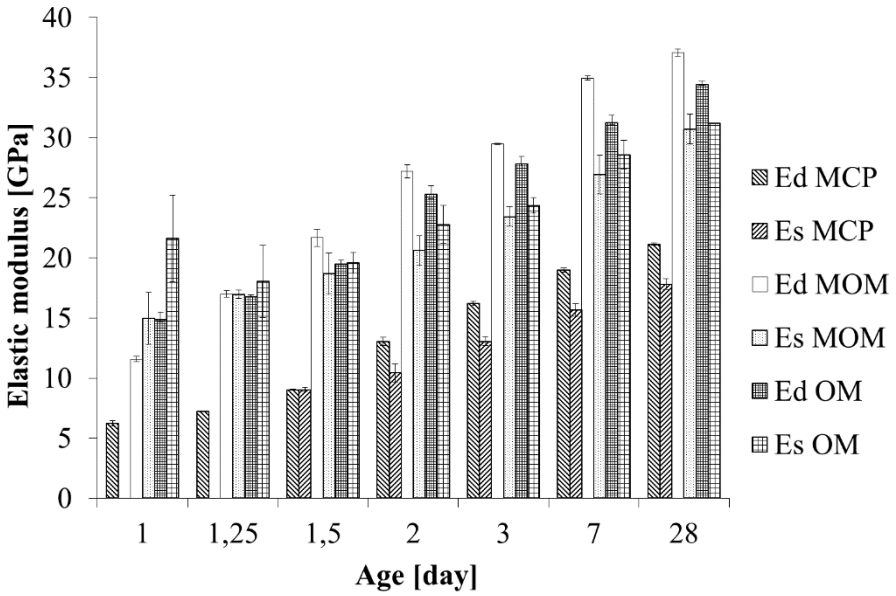

Figure 4: Static and dynamic elastic modulus of CBMs.

Based only on the results of dynamic shear modulus (Fig. 5), retarding effect of SP is clearly evident only up to the age of 30 hours, where the values of G_d are the same for the MOM an OM, despite much lower w/c ratio at the MOM. Only correlation between the shear moduli of the MCP and MOM reveals that the behaviour is also for this elastic property different for ages lower than 2 days, compared to that at the age of 2 days or higher.

For the MCP the values of Poisson's ratios ν_d and ν_s are around 0.3 and 0.25, respectively, and for the MOM around 0.27 and 0.19, respectively. In case of the OM, ν_d and ν_s are around 0.27 and 0.20, respectively. For the modified compositions, the ν_d values show decreasing tendency as the function of the specimen's age, and the ν_s values show increasing tendency.

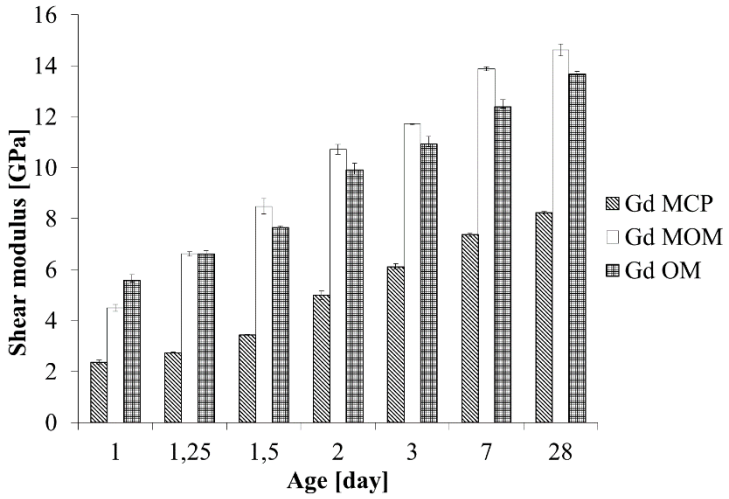

Figure 5: Dynamic shear modulus of CBMs.

5. Conclusions

Test results presented in the paper show that by using combination of destructive standard tests and non-destructive UPV measurements, when evaluating properties of hardened CBMs, realistic explanation of the test results that do not confirm "common knowledge" in the area of the CBMs is possible. However, additional microstructural analyses are needed to finally confirm our observation.

Acknowledgements
This work was financially supported by the Slovenian Research Agency through Programme Group P2-0185, Research Project J2-8194 and PhD project of Martin Klun. The authors acknowledge networking support by the COST Action TU1404.

References

[1] Serdar, M. et al., COST Action TU1404 : recent advances of the Extended Round Robin Test RRT+, RILEM Proceedings PRO 120 from 2nd International RILEM/COST Conference on Early Age Cracking and Serviceability in Cement-based Materials and Structures, Belgium (2017), 63-70
[2] Bokan-Bosiljkov, V. et al., Progress on Testing of Mechanical Properties of Cement Based Materials - Extended Round Robin Test of Cost Action TU 1404, RILEM Proceedings PRO 118 from International Conference on Advances in Construction Materials and Systems, India (2017), 171-178.
[3] Staquet, S. et al., RRT+ Main phase of the Extended Round Robin Testing programme for TU1404, Testing protocols, Ver. 22th November 2016, (2016) 57p
[4] Bregar, R. et al., Main experimental phase RRT+ COST TU 1404 – Supplementary report of the TU Graz to Excel data sheets, Austria (2017), 25p
[5] Bokan-Bosiljkov, V. et al., New type of superplasticizer for SCC mixtures with increased robustness, RILEM PRO 90 from International Conference on Rheology and Processing of Construction Materials, France (2013), 6p.

SynerCrete'18 International Conference on Interdisciplinary Approaches
for Cement-based Materials and Structural Concrete
24-26 October 2018, Funchal, Madeira Island, Portugal

VOLUME STABILITY OF CEMENT-BASED MATERIALS: ROUND-ROBIN TESTING WITHIN COST ACTION TU1404

Emmanuel Roziere[(1)], Marijana Serdar[(2)], Stéphanie Staquet[(3)], Dirk Schlicke[(4)], Miguel Azenha[(5)], Ahmed Zakarya Bendimerad[(1)], Brice Delsaute[(3)], Vinciane Dieryck[(6)], Jacek Golaszewski[(7)], José Granja[(5)], Terje Kanstad[(8)], Anja Klausen[(8)], Zhenming Li[(9)], Elica Marušić[(10)], Martina Pezer[(2)], Antonio Ribeiro[(11)], Sofia Ribeiro[(11)], Aljoša Šajna[(13)], François Toutlemonde[(12)], Guang Ye[(9)], Behzad Zahabizadeh[(5)]

(1) GeM, Ecole Centrale de Nantes, Nantes, France
(2) Faculty of Civil Engineering, University of Zagreb, Zagreb, Croatia
(3) BATir, Université Libre de Bruxelles ULB, Brussels, Belgium
(4) Graz University of Technology, Institute of Structural Concrete
(5) Department of Civil Engineering, University of Minho (ISISE), Guimarães, Portugal
(6) Belgian Building Research Institute, Limelette, Belgium
(7) Silesian University of Technology, Gliwice, Poland
(8) Norwegian University of Science and Technology (NTNU), Trondheim, Norway
(9) Faculty of Civil Engineering and Geosciences, TU Delft, Netherlands
(10) Institut IGH, Split, Croatia
(11) LNEC, Lisboa, Portugal
(12) IFSTTAR, France
(13) Slovenian National Building and Civil Engineering Institute, Slovenia

Abstract
Advanced experimental techniques and modelling are necessary to predict the evolution of existing structures and design more sustainable materials and structural systems. An Extended Round Robin Testing program (RRT+) has been designed within COST Action TU 1404 "Towards the next generation of standards for service life of cement-based materials and structures". The RRT+ program provides a platform to compare non-standardized techniques. The results presented in this paper are related to "Volume stability" with a focus on autogenous deformation. 11 laboratories were actually involved in the testing program. They used different measuring techniques but the preliminary results showed good overall agreement. A deeper analysis requires data related to hydration and hardening kinetics. The tested concrete mixtures showed relatively low shrinkage magnitudes. The evolution of autogenous deformations is discussed taking into account their stress-inducing potential.

1. Introduction

COST Action TU1404 is entitled "Towards the next generation of standards for service life of cement-based materials and structures", as it gives a special attention to the issue of analysing serviceability under the combined effect of imposed deformations (namely, due to thermal and hygral effects) together with applied loads, with due account for viscoelasticity and cracking effects [1]. Such analysis requires advanced models and measuring techniques to take into account the main phenomena and determine the input parameters. Among the three main working groups (WG) of the Action, the WG1 designed an Extended Round Robin Testing program (RRT+) with two stages: the Initial Phase and the Main Phase. The objective of the Initial Phase was to define procedures for preconditioning, mixing and curing of concrete well enough so that laboratories could prepare a comparable concrete. The Main phase provided a platform to compare non-standardized or advanced testing procedures [2]. Since a vast range of properties were targeted, the experimental work and analysis was divided into Group Priorities (GP) focusing on different groups of properties. This paper presents some of the methods and results of GP1e on "Volume stability" [3]. This gathers advanced tests to characterize the causes (hygral and thermal changes) and consequences (shrinkage-induced cracking) of volumes changes, from fresh state to long-term behaviour. Preliminary results shown in this paper are mainly related to autogenous deformations.

2. Materials and methodology

2.1 Reference mixtures

The "Ordinary" concrete mixture (OC) and "Modified" concrete mixture (MOC) were designed by working group 1 (WG1) of COST Action TU1404 [4] and their compositions are given in RRT+ documents [5]. The mix-design of OC is based on Vercors Project [6], which aims at reproducing nuclear reactor containment building at the scale of one third. Note that OC differs from Vercors concrete in terms of cement type and plasticizer content. Namely, in RRT+ CEM I 52.5 N-SR3 CE PM-CP2 NF HRC cement was used, instead of CEM I 52.5 N CE CP2 NF with a higher C_3A amount used in the Vercors project.

Table 1: Concrete mixtures, amounts [kg/m^3].

	OC	**MOC**
Cement, CEM I 52,5 N-SR3 Gaurain	320	439
Dry sand, 0-4 mm, REC GSM LGP1	830	772
Fully saturated gravel,		
4-11mm, R GSM LGP1	449	525
8-16 mm, R Balloy	564	424
Admixtures, Plasticizer SIKAPLAST Techno 80	1.44	3.73
Added water	180.7	178.4
W_{eff}/C	0.52	0.40

The MOC mixture is derived from the OC mixture. The modifications are namely a decreased W/C ratio as well as the corresponding necessary changes in regard to the plasticizer and paste volume to achieve different properties of fresh and hardened material when compared to OC. In terms of volume stability (GP1e), MOC is expected to show higher thermal and autogenous deformations. Cement paste (MCP) and mortar mixtures (OM, MOM) were derived from OC and MOC mixtures [2]. The paste and mortar mixtures were designed to allow multiscale modelling performed in the WG2. Some measuring techniques are actually based on smaller specimens but these volumes should remain representative of the tested materials.

2.2 Methodology

15 COST Action members initially committed to participate in the part of RRT+ program dedicated to Volume stability. 11 Laboratories were actually involved in testing activities; the corresponding laboratory numbers are given in Table 2. The research within the COST Action is performed on volunteering basis, since there is no budget foreseen for research activities. The experimental program was relatively wide, from early-age to long-term behaviour, with and without restraint.

Table 2: COST Action members involved in experimental program.

	OC	**MOC**
Chemical shrinkage	9 (OCP, OM)	
Early age (0-24h) autogenous shrinkage	1, 2, 3, 6, 8, 11, 12, (OCP, OM), 9 (OM)	1, 2, 5, 9 (MCP)
Early age (0-24h) plastic shrinkage	1, 7	
Restrained shrinkage, TSTM	8	8
Drying shrinkage, weight loss	1, 6, 10, 11 (OM), 9	1, 6, 9
Restrained shrinkage, ring test	1, 5, 9, 13	1
Thermal dilation	3, 5, 8	

RRT+ provides a platform to compare the different methods and to discuss the degree to which the experimental procedure or the data analysis should be standardized to obtain consistent results. This is the case for free shrinkage measurements for instance, as these data are used as input data of models. The measurement of autogenous shrinkage has been a major concern for the last decades but there is still no consensus on the geometry of the specimens [7] and the time when deformations should be initialized [8]. Laboratories #1, 2, 6, 8 performed horizontal measurements with rigid prismatic moulds (from 70x70 to 100x100 mm² cross-section), Laboratories #9 and 11 used the corrugated tubes method, and Laboratories #3 and 12 used BTJADE system with vertical corrugated mould [7].
Some experimental techniques are not meant to be standardized; they were used in connection with WG2 activities such as benchmarks and validation of models before upscaling. Temperature Stress Testing Machine (TSTM) allows the measurement of deformations from

the casting of concrete specimen, in controlled temperature conditions [9]. The specimen can move freely until a deformation threshold is reached. An additional load is then applied to cancel the deformation. As a consequence a TSTM system can provide restraint by applying loads, in tension or compression. The determination of stresses and strains at each increase of load allows the assessment of elastic modulus. The comparison between cumulated stresses and tensile strength provides the evolution of the risk of cracking. The TSTM system allows investigating free and restrained shrinkage, mechanical properties, and creep in compression and tension [10-11] from early age.

3. Preliminary results

3.1 Autogenous deformation

Autogenous deformation was measured in quasi isothermal controlled conditions. 8 laboratories participated in this part of the RRT+. They provided the evolution of deformations from fresh to hardened state. During the first hours, several phenomena take place in fresh concrete such as thermal dilation/contraction, settlement, etc. The induced volume changes are not of interest as they do not have stress-inducing potential until the material starts to harden. The monitoring of other properties is necessary to determine "time-zero" and provide the relevant shrinkage curve. As such information was not systematically provided by the participating laboratories, the first derivative (with respect to time) was used to analyse the deformation data. For all the laboratories its values were relatively low from the ages of 16 and 18 hours for OC and MOC respectively. These times were chosen to initialize the curves, except for Lab#9. They monitored the setting of OM and MCP using Vicat needle and obtained final setting times of 14.5 and 25.5 hours respectively. Their curves were initialized at these times (Figs. 1 and 2).

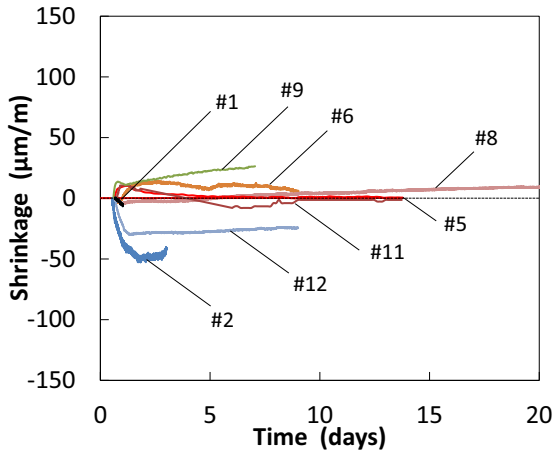

Fig. 1: OC shrinkage from fresh state

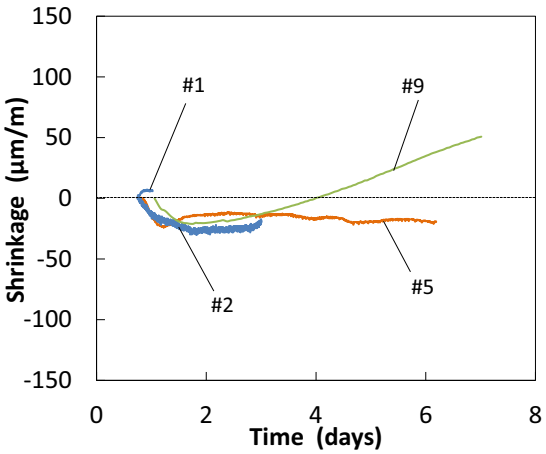

Fig. 2: MOC shrinkage from fresh state

Figure 1 shows discrepancies between the 8 data series, but the magnitudes are consistent with the relatively high water-to-cement ratio of ordinary concrete (0.52). For a given experimental absolute uncertainty, the relative uncertainty increases with a decrease in shrinkage magnitude. High performance concrete generally show autogenous deformations of

hundreds of µm/m [7], whereas normal strength concrete such as OC studied here show significantly lower shrinkage magnitudes in sealed conditions. Another cause of discrepancies is the determination of "time-zero". Additional information is needed to assess this time and a common methodology should be used to analyse the results; however the participating have different procedures to determine setting time or time-zero and some do not have any equipment.
The four shrinkage curves of MOC specimens are plotted on Figure 2. Most of evolutions show swelling between 16 and 36 hours. This behaviour has already been reported in previous studies of autogenous deformations [12]. In spite of significantly lower water-to-cement ratio of 0.40, MOC show slightly higher shrinkage magnitude (Fig. 2).

3.2 Restrained shrinkage – TSTM

TSTM test was performed on OC in quasi-isothermal conditions for a significant time period (Fig. 3). The control started at 6.7 hours and the deformation threshold triggering load increment was 6 µm/m. Between two subsequent load increments, the stress was kept constant through load control. The strain curve represents the cumulated strain assessed by adding the strains between two load increments. During the first days a moderate swelling was observed thus compressive stresses developed, then concrete progressively shrank. This result confirms the behaviour observed by several laboratories in dilation rigs (Fig. 1). The first load increment occurred at 22.3 hours and reached 0.15 MPa in compression. This time can be compared to the initialization time chosen for the analysis of free autogenous deformation (3.1). After more than 60 days, the stress remained relatively low. The upcoming TSTM tests will be performed with realistic temperature histories as the studied concrete mixtures showed significant hydration heat.

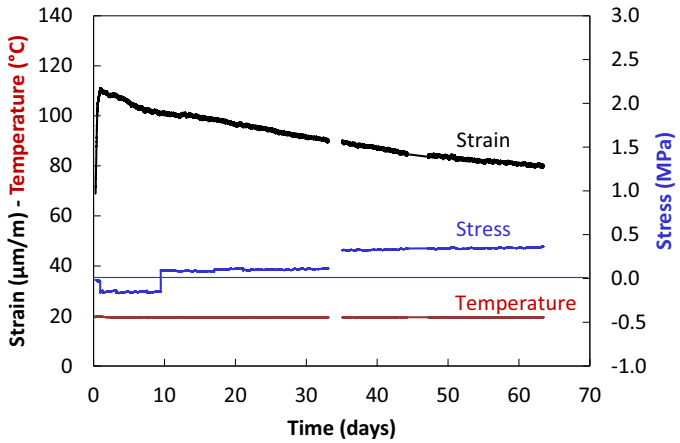

Fig. 3: TSTM test at NTNU on OC under controlled 20°C temperature.

4. Conclusion

Eleven European laboratories were involved in volume stability testing, mainly free and restrained shrinkage. The experimental program targeted early-age as well as long-term behaviour, in sealed and drying conditions. The tests were performed on concrete, mortar, or paste, depending on the available test rigs. In the framework of COST Action TU1404, the

same raw materials have been sent to all the participants and a very detailed mixing procedure has been defined in Extended Round-Robin Testing (RRT+) to limit the scatter of results due to materials and their preconditioning. Autogenous deformations showed discrepancies, which are related to two main issues. First both studied concrete mixtures were characterized by relatively high water-to-cement ratios, thus low shrinkage magnitudes, which emphasizes the influence of experimental uncertainties. Second the determination of time-zero was not satisfying and further analyses are required. This paper only presents a part of available results. Experimental campaign yielded satisfactory results, as several laboratories provided consistent data even if the measuring procedures were not standardized. The evolution of other properties is often needed to perform deeper analysis of volume changes. The obtained data are also being used to design benchmarks and update models, thus they actually contribute in reaching the goals of COST Action TU1404.

References

[1] COST Action TU 1404, http://www.tu1404.eu/
[2] Serdar M., Staquet S., Gabrijel I., Cizer O., Nanukuttan S., Bokan-Bosiljkov V., Rozière E., Šajna A., Schlicke D., Azenha M., COST Action TU1404: recent advances of the Extended Round Robin Test RRT^{+}, 2nd International RILEM/COST Conference on Early Age Cracking and Serviceability in Cement-based Materials and Structures - EAC2, 12–14 September 2017, ULB-VUB, Brussels, Belgium, 10 p.
[3] Bjøntegaard, Ø., Martius-Hammer, T.A., Krauss, M., Budelmann, H. Recommendation for Test Methods for AD and TD of Early Age Concrete Round Robin Documentation Report: Program, Test Results and Statistical Evaluation, RILEM, 2015
[4] Staquet S., Serdar M., Delsaute B., Rozière E., Schlicke D., Nanukuttan S., Azenha M., Further works on concrete at early age coordinated within COST TU1404 European project, JCI-RILEM International Workshop CONCRACK5, 10 p.
[5] RRT+, Main phase of the Extended Round Robin Testing programme for TU1404, http://www.tu1404.eu/rrt/current-status-of-rrt-and-deadlines/
[6] http://fr.amiando.com/EDF-vercors-project.html
[7] Roziere E., Delsaute B., Loukili A., and Staquet S., Experimental Assessment of Autogenous Shrinkage, CONCREEP10, 2015, Vienna, Austria, 983-992
[8] Huang, H., Ye, G. Examining the "time-zero" of autogenous shrinkage in high/ultra-high performance cement pastes, Cement and Concrete Research, Volume 97, 2017, 107–114
[9] Staquet S., Delsaute B., Darquennes A., Espion B., Design of revisited TSTM system for testing concrete since setting time under free and restraint conditions. Proceedings of the RILEM-JCI International Workshop CONCRACK 3, 15-16 March 2012, Paris, France
[10] Estensen Klausen, A., Kanstad, T., Bjøntegaard, Ø. Sellevold, E. Comparison of tensile and compressive creep of fly ash concretes in the hardening phase, Cement and Concrete Research, Volume 95, 2017, 188-194
[11] B. Delsaute, C. Boulay, S. Staquet, Creep testing of concrete since setting time by means of permanent and repeated minute-long loadings, Cem. Concr. Compos., 73 (2016), pp. 75-88
[12] Lura P. Autogenous deformation and internal curing of concrete, DTU, The Netherlands, PhD thesis; 2003. 180p.

SynerCrete'18 International Conference on Interdisciplinary Approaches
for Cement-based Materials and Structural Concrete
24-26 October 2018, Funchal, Madeira Island, Portugal

BENCHMARK NUMERICAL SIMULATION IN MICRO-LEVEL WITHIN THE COST ACTION 1404

Peng Gao [1,2], Hua Dong [1], Jiayi Chen [1], Guang Ye [1]

(1) Delft University of Technology, Delft, The Netherlands
(2) South China University of Technology, Guangzhou, China

Abstract
This paper aims to present an example of the benchmark numerical simulation for cement-based materials in Micro-level within COST Action 1404 by using numerical tools developed at Delft University of Technology. In the benchmark, the Portland cement paste with water-to-cement ratio 0.4 at temperature 20 ºC was used. The input parameters included the chemical and mineral composition, the density, the specific surface and the particle size distribution of Portland cement. The hydration process and microstructure development of Portland cement paste were simulated with HYMOSTRUC3D model. The water permeability and chloride diffusivity of Portland cement paste were simulated with Lattice Boltzmann method based on simulated microstructure. The mechanical properties of Portland cement paste, including load-displacement curve, elastic modulus, tensile strength and cracking pattern were simulated with a 3D lattice finite element fracture model.

1. Introduction

The benchmark numerical simulation in Micro-level of cementitious materials was launched within the COST Action 1404. Delft University of Technology, as one of the participants, has joint the benchmark numerical simulation. Fig. 1 shows the outline of the simulation performed by Delft University of Technology. The mineral composition, particle size distribution and density of PC, and the water to cement (w/c) of cement paste, etc., were taken as input parameters. HYMOSTRUC3D model [1-3] was used to simulate the hydration process and microstructure development of cement paste. With HYMOSTRUC3D model, the overall degree of hydration of PC, degree of hydration of minerals of PC, heat release, capillary porosity, pore size distribution, chemical shrinkage and compressive strength of PC paste were simulated. Using the Lattice Boltzmann method [4] the water permeability and

chloride diffusivity of cement paste were simulated, in which the microstructure of PC paste simulated by HYMOSTRUC3D model was taken as input. The mechanical properties including load-displacement curve, elastic modulus, tensile strength and cracking pattern of cement paste were simulated with the lattice finite element fracture analysis method [5], in which the microstructure of cement paste simulated with HYMOSTRUC3D model was also taken as input.

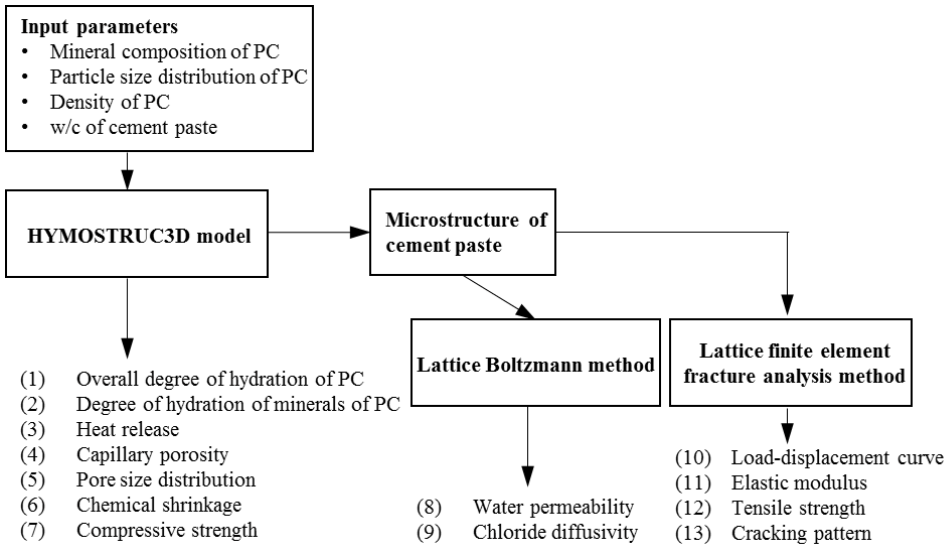

Figure 1: Outline of the simulation performed by using numerical tools developed by Delft University of Technology

2. The properties of raw materials

The mineral composition of PC measured with Quantitative X-Ray Diffraction method (Q-XRD) is: 58.3% C_3S, 20.7% C_2S, 3.6% C_3A, 7.3% C_4AF and 2.4% gypsum. The density of PC is 3.20 g/cm^3. Figure 2 shows the particle size distribution of PC measured with laser diffraction particle size analyser. The measured particle size distribution of PC follows the Rosin Rammler Bennett (RRB) distribution, viz.: $G(x) = 1 - exp\,(-bx^n)$. $G(x)$ is the cumulative weight, x is the particle diameter, n and b are fitting parameters. The water-to-cement ratio (w/c) of the PC paste is 0.4.

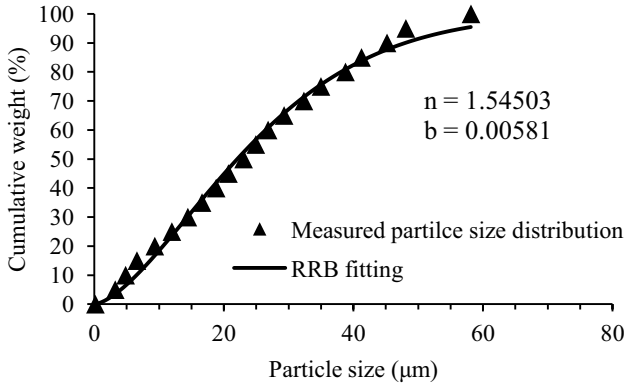

Figure 2: Measured and fitted particle size distribution of PC

3. Modelling approach

3.1 Simulation with HYMOSTRUC3D model

K_0 and δ_{tr} are two important modelling parameters of HYMOSTRUC3D model. K_0 is the initial penetration rate of the reaction front of hydrating PC-components, viz., C_3S, C_2S, C_3A, C_4AF. δ_{tr} is the transition thickness when the hydration mechanism of C_3S, C_2S, C_3A, C_4AF change from *phase boundary reaction* to *diffusion-controlled reaction.* Both the values of K_0 and δ_{tr} are calculated according to [6]. The calculated values of K_0 of the reaction fronts of C_3S, C_2S, C_3A and C_4AF are 0.111, 0.007, 0.055 and 0.027 [μm/h], respectively, and the values of δ_{tr} for the reaction fronts of C_3S, C_2S, C_3A and C_4AF are 4.339, 3.904, 4.365 and 1.441 [μm], respectively. Based on the modelling parameters, the hydration process and microstructure of PC paste were simulated with HYMOSTRUC3D. The microstructure of hydrating cement paste consists of inner and outer hydration products, calcium hydroxide, unhydrated cement and capillary pores. To simulate the transport and mechanical properties the microstructure of PC paste was digitized to a dimension of 100×100×100 μm^3 (resolution = 1 $\mu m/voxel$).

3.2 Simulation with Lattice Boltzmann method

a. Modelling parameters for the simulation of water permeability

With the method described in [4] (D3Q19 model was used), the water permeability of PC paste was simulated.

b. Modelling parameters for the simulation of chloride diffusivity

To simulate the chloride diffusivity of cement paste, specific diffusion coefficients of chloride were assigned to water (2.032E-9 m^2/s), inner product (1.0E-12 m^2/s) and outer product (9.0E-12 m^2/s). Then extra 3 liquid layers were added to two ends at direction of simulation. The concentration at the start layer was set at constant and the concentration gradient between the last two layers was set at zero. The boundary condition was set as bounce-back at the surface of unhydrated cement particle and calcium hydroxide. D3Q19 model was also used.

3.3 Simulation with lattice finite element fracture analysis method

The bulk elastic modulus of the cement paste was simulated with the lattice finite element fracture analysis method as reported by Qian et al. [5]: The bottom voxels of PC paste are fixed. An incremental tensile displacement was given at each top voxel of PC paste. Correspondingly, the response stress at the top surface nodes was simulated with the lattice finite element fracture analysis method. The bulk elastic modulus of PC paste was calculate from the tensile displacement and the response stress.

4. Simulation results

The simulated properties of PC paste, like the capillary porosity, compressive strength and water permeability of PC paste at specific ages, viz., 1, 3, 7 and 28 days are given in Table 1. This will be convenience for the validation with experiments. However, to present the simulation results, like the degree of hydration of different minerals of PC, the pore size

distribution of PC paste, the water flow in PC paste, etc., more directly, these simulation results are plotted in figures.

Table 1: Simulated properties of PC and PC paste at different ages

Simulated properties	Unit	1day	3days	7days	28days
Overall degree of hydration	[α]	0.36	0.58	0.68	0.79
Heat release of PC	[J/g]	171.2	277.8	326.6	370.4
Capillary porosity		0.38	0.28	0.24	0.18
Chemical shrinkage	[mL/100g]	2.10	3.87	4.60	5.37
Compressive strength	[MPa]	2.9	14.1	20.4	28.5
Water permeability	[m-2]	1.29E-13	4.06E-14	2.62E-14	1.08E-14
Chloride diffusion coefficients	[m2/s]	4.63E-11	2.25E-11	1.67E-11	9.36E-12
Elastic modulus	[GPa]	2.12	6.16	8.25	13.12
Tensile strength	[MPa]	4.13	10.63	15.38	29.45

Figure 3 shows the degree of hydration of different minerals of PC simulated with HYMOSTRUC3D in comparison with the experimental results. The experimental results were provided by COST Action. Figure 3 shows that the simulation results of C_3S and C_2S phases are in good agreement with experiments but C_3A and C_4AF shows discrepancy. The pore size distribution of PC paste simulated with HYMOSTRUC3D is shown in Figure 4.

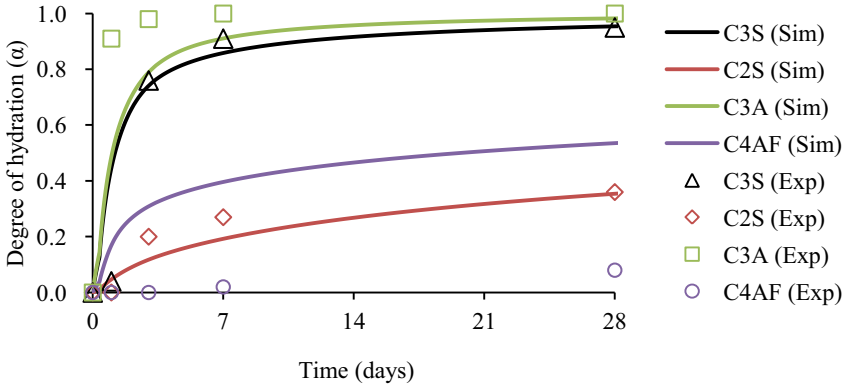

Figure 3: Simulated and measured degree of hydration of different minerals of PC

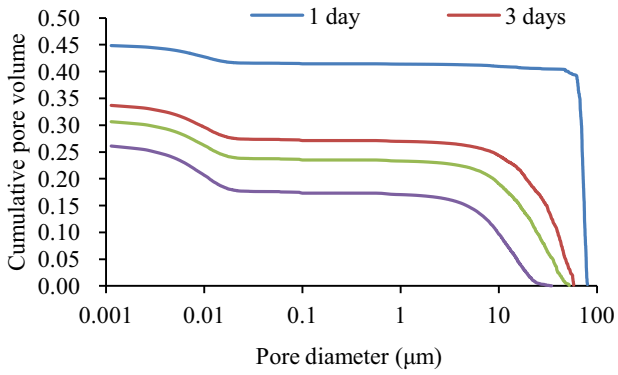

Figure 4: Simulated pore size distribution of cement paste

Figure 5 illustrates the streamline of water flow through the PC paste at hydration age of 1 day and Figure 6 shows the simulated concentration filed of chloride in PC paste at curing age of 7 days.

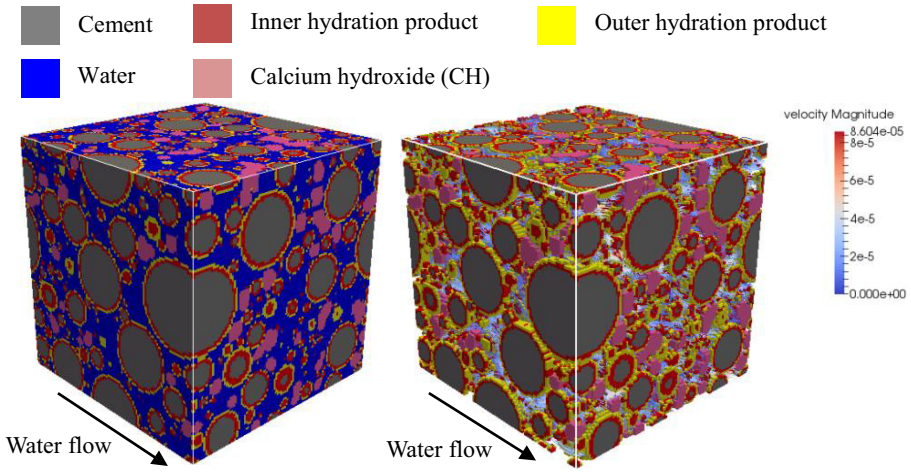

(a) Simulated microstructure at 1 day (b) Streamline of water flow

Figure 5: Simulated water flow in a 1 day-old PC paste (w/c = 0.4)

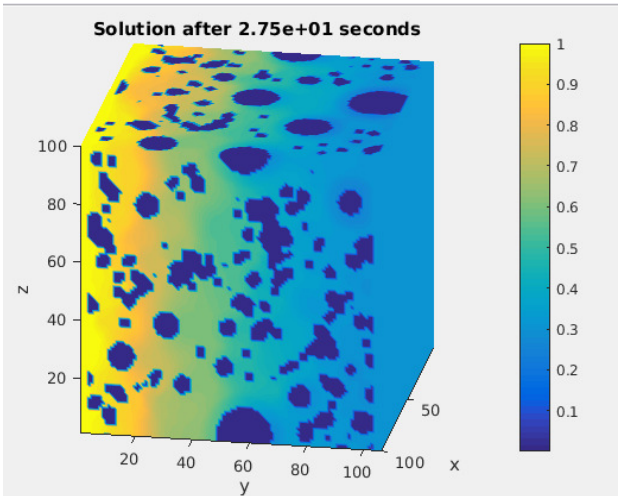

Figure 6: Simulated concentration filed of chloride in PC paste (time = 7 days)

Figure 7 presents the simulated load-displacement curve of PC paste at different ages. The maximum stress from 15 MPa increases to 29 MPa when curing age change from 7 days to 28 days. In Figure 8 the simulated cracking pattern of PC paste at curing age of 7 days and 28 ages are illustrated.

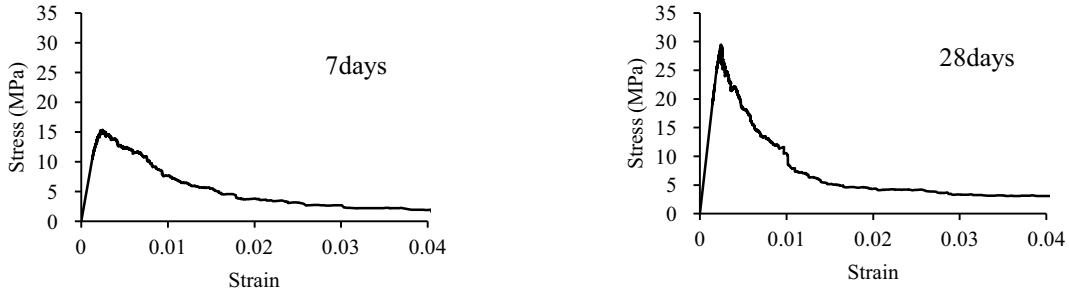

(c) time = 7 days (c) time = 28 days

Figure 7: Simulated load-displacement curve of cement paste at different ages

(a) time = 7 days (b) time = 28 days

Figure 8: Simulated cracking pattern of PC paste at different ages

5. Conclusions

This study presents the benchmark numerical simulation results for cement-based materials in Micro-level performed by using numerical tools developed at Delft University of Technology. In further study, the simulated properties of PC and PC paste will be used to compare the experimental data, and compare the simulation results from different research groups.

References

[1] Van Breugel, K, Simulation of hydration and formation of structure in hardening cement-based materials, PhD Thesis, Delft University of Technology (1991)
[2] Koenders, E. A. B., Simulation of volume changes in hardening cement-based materials, PhD Thesis, Delft University of Technology (1997)
[3] Ye, G., Experimental Study and Numerical Simulation of the Development of the microstructure and permeability of cementitious materials, PhD Thesis, Delft University of Technology (2003)
[4] Zhang, M., Multiscale lattice Boltzmann-finite element modelling of transport properties in cement-based materials, PhD Thesis, Delft University of Technology (2013)
[5] Qian, Z. W., Schlangen, E., Ye, G. et al. Prediction of mechanical properties of cement paste at microscale. Materiales de Construccion 60 (2010) 7-18
[6] Nguyen V.T. Rice husk ash as a mineral admixture for ultra high performance concrete PhD Thesis, Delft University of Technology (2011)

SynerCrete'18 International Conference on Interdisciplinary Approaches
for Cement-based Materials and Structural Concrete
24-26 October 2018, Funchal, Madeira Island, Portugal

COMPARISON BETWEEN THE EXPERIMENTAL MEASUREMENT RESULTS AND THE MICROMECHANICAL MODELLING ON THE AGEING BASIC CREEP OF VERCORS CONCRETE

Shun Huang [(1)(2)(3)], Julien Sanahuja [(1)], Luc Dormieux [(2)], Benoit Bary [(3)], Eric Lemarchand [(2)], Laurent Charpin [(1)] and Romain Thion [(1)]

(1) EDF lab, Site des Renardieres, Route de Sens, Ecuelles, 77250 Moret sur Loing, France
(2) École Nationale des Ponts et Chaussées, 77455 Marne-la-Vallée, France
(3) CEA, DEN, DPC, SECR, Laboratoire d'Etude du Comportement des Bétons et des Argiles, F-91191 Gif-sur-Yvette, France

Abstract
The concrete creep is critical for the prestressed containment building of nuclear power plants, since creep yields prestress relaxation. To develop a model of material behaviour incorporating the ageing creep, given the multi-scale and multi-physics nature of concrete, the creep experiments and the micro-mechanical modelling approach are attractive on the study of the VeRCoRs concrete, which is a typical formulation for the construction of the containment building.
The experimental campaign is carried out to characterize the ageing basic creep at different scales and at different ages of loading with the formulation of the VeRCoRs concrete. The purpose of the experiments is to describe the basic creep behaviour on cement paste, mortar and concrete. The ageing viscoelastic part (the basic creep) of the experimental results are concerned in the comparison. Moreover, for each specimen loaded, a complete unloading is performed to highlight the effect of creep recovery. The basic creep strain rate decreases with the increase of the age of loading (corresponds to an increase of the hydration degree).
A direct confrontation between the experimental results and the modelling results is also performed. The ageing basic creep behaviour is compared with the application of mean-field homogenisation schemes.

1. Experimental study of the creep of cement paste, mortar and concrete with the formulations derived from the materials for the VeRCoRs mock-up

The purpose of the experiments is to describe the characterization experiments of autogenous shrinkage, and basic creep under uni-axial compression at 20 °C and 50% RH at the different

ages of loading (1 day, 2 days, 3 days, 7 days, 28 days, 3 months and potentially 1 year in 2018) on cylindrical samples of cement paste, mortar and concrete, to validate the aging viscoelastic model. The mix design of cement paste, mortar and concrete was derived from the materials of the VeRCoRs mock-up in EDF for the construction of the containment building (at the scale of the corresponding mortar, the cement paste is the matrix; at the scale of the VeRCoRs concrete, the corresponding mortar is the matrix).These characterization experiments were carried out on two geometries: small cylindrical specimens with the diameter of 3.6 cm and the height of 18 cm for cement paste and mortar, and big cylindrical specimens with the diameter of 8 cm and the height of 29 cm for concrete. The non-drying shrinkage and creep experiments are carried out at different times. For this reason, it was decided to use 3 layers of self-adhesive aluminium tape on the shaft and the ends of the sample to perform the seal. This requires the preparation of different pieces of tape for each sample. There has been assessment of the effectiveness of the adhesive aluminium tape. For example, the mass loss of the specimens during 370 days has been 0.37g, so that the relative mass loss is only 0.051% of the mass of the sample. This assessment confirms the feasibility of claiming sealed conditions

For each loading time, the constant load is calculated to be lower than 1/3 of the compressive strength, and controlled, to keep the creep behaviour in the linear regime.

Until now, the creep experiments at the scale of cement paste, of mortar and of the VeRCoRs concrete have been carried out with the ages of loading at 1 day, 2 days, 3 days, 7 days, 28 days and 3 months. The creep experiments at the scale of cement paste and of mortar with the age of loading at 1 year is ongoing. In addition, the experiments at the scale of cement paste are performed at 2 different water–cement ratio (w/c=0.525 and w/c=0.400).

2 samples from the same batch are tested for each loading time. The axial displacement sensors are placed at 120° vertically. The loading is performed by imposing a constant stress.

The temperature evolution in the lab is controlled around 20°C. But the continuous monitoring of the sample temperature, done during the measurements in order to take into account the effect of temperature on the hydration process, reveals that several abrupt temperature changes was caused by the air conditioning unit issues. For example, the temperature in the lab has rose from 20°C to 34°C during 1 day on 08/28/2017 and the abrupt temperature changes larger than 1°C have happened 6 times until now, which make it more feasible and necessary to adopt a method to take into account the accelerating effect of a given temperature history to experiments.

An equivalent time t_{eq} is thus computed with the Eq (1) proposed by Freiesleben Hansen and Pedersen in [1].

$$t_{eq}(t,T) = \sum_{0}^{t} \exp\left(-\frac{E_a}{R}\left(\frac{1}{273+T} - \frac{1}{273+T_{ref}}\right)\right) \Delta t \quad (1)$$

Where:

- T is the temperature, in °C
- T_{ref} is the reference temperature, generally 20°C
- R is the universal gas constant, 8.314J/mol/K
- E_a is the apparent activation energy, in J/mol

This equation models the accelerating effect of a given temperature history T in comparison with a reference temperature T_{ref} (when $T > T_{ref}$). The apparent activation energy E_a is determined from the curve fitting of the experimental data with respect to the compliance model for basic creep described as follows:
In the light of recent developments, the compliance data can be fitted using a creep law reworked by Torrenti [2] based on ideas arising from an analysis of experimental tests. Indeed, this law showed that the derivative of the compliance dJ/dt tends to $1/Ct$ when t was large. Based on the compliance data from the experiments on VeRCoRs materials, the value of C for a given material depends on the age of loading t_0. But this compliance function underestimate the compliance value in the range of $10^{-2} - 10^{0}$ days. So a Kelvin unit with the retardation time $\tau_{Kelvin} = 10^{-2}$ day is added in the compliance function to correct the error value in the range of $10^{-2} - 10^{0}$ days.
The ageing compliance model for basic creep is thus the following:

$$J(t,t_0) = \frac{1}{E(t_0)} + \frac{1}{C(t_0)} Log\left(1 + \frac{t-t_0}{\tau(t_0)}\right) + \frac{1}{E_{Kelvin}(t_0)}\left(1 - e^{-\frac{t-t_0}{\tau_{Kelvin}}}\right) \quad (2)$$

Where:

- $E(t_0)$ is the Young's modulus at the age of loading, in GPa
- $C(t_0)$ is a variable depending on mix design and the age of loading, describing the long term creep, in GPa
- $\tau(t_0)$ is a kinetic constant depending on the age of loading, in day.

The Eq (2) describes only the compliance reaction to a step of load, but the loading period (about 20 seconds) is ignored. To consider the loading period, the Eq (2) is improved to the Eq (3) with the application of the Laplace-Carson transform [3]:

$$J(t,t_0) = \left(\frac{t_{load} - (t-t_0)}{E(t_0)t_{load}} - \frac{\frac{(t-t_0+\tau(t_0))\ln\left(\frac{t-t_0+\tau(t_0)}{\tau(t_0)}\right)}{C(t_0)t_{load}} + \frac{t_{load}-t}{C(t_0)t_{load}}}{\ln(10)} \right) Heaviside(t - t_{load}) + \frac{t}{E(t_0)t_{load}} + \frac{\frac{(t+\tau(t_0))\ln\left(\frac{t+\tau(t_0)}{\tau(t_0)}\right)}{C(t_0)t_{load}} - \frac{t}{C(t_0)t_{load}}}{\ln(10)} + \frac{1}{E_{Kelvin}(t_0)}\left(1 - e^{-\frac{t-t_0}{\tau_{Kelvin}}}\right) \quad (3)$$

Where t_{load} is the loading period in day.
With the nonlinear least squares optimization between the Eq (3) and the experimental results, the value of $E(t_0)$, $C(t_0)$, $\tau(t_0)$ and E_a can be identified for each experiment with a given age of loading and a given material.
The experimental evolution of the strain/stress ratio of basic creep strain is presented in Fig. 1 (autogenous strains have been subtracted). For each sample loaded, a complete unloading is performed to highlight the effect of creep recovery. As expected, from the scale of cement paste to that of mortar, then to that of concrete, the compliance of basic creep is lower and lower. Moreover, the basic creep strain rate decreases with the increase of the age of loading (which corresponds to an increase of the hydration degree). The curves are used to compare with the modelling behaviour results.

2. Micromechanical model (Example dedicated to mortar scale)

With the parameters identified from the experiments, micromechanical model can be developed to perform the multi-scale homogenization model.

2.1 Identification of parameters

There are three steps to finish the processes of the identification of parameters.
Firstly, the Eq (1) and the Eq (3) are applied in the nonlinear optimization to calculate the correct apparent activation energy $E_a(t_0)$ considering the effect of temperature on the hydration process, with which the equivalent time $t_{\mathrm{eq}}(t_0)$ can be calculated for each experiment. The correct $E_{Kelvin}(t_0)$ is optimized in this step, too.
Secondly, the compliance results during the loading period (about 20 seconds) in the equivalent time t_{eq} are used the nonlinear optimization with the Eq (3) to define the correct Young's modulus at the age of loading $E(t_0)$.
Thirdly, with the correct $E(t_0)$, a least squares polynomial fit process is performed with the end of the compliance results. The derivative of the compliance dJ/dt tends to $1/C(t_0)$ when t was large, which aides to calculate $C(t_0)$.
Fourthly, with the correct $E(t_0)$ and the least squares polynomial fit line, $\tau(t_0)$ iscalculated.
With this method, the analytical solution of the compliance for each material and each age of loading is calculated with the form of the Eq (3). An example is presented in the Fig. 2.

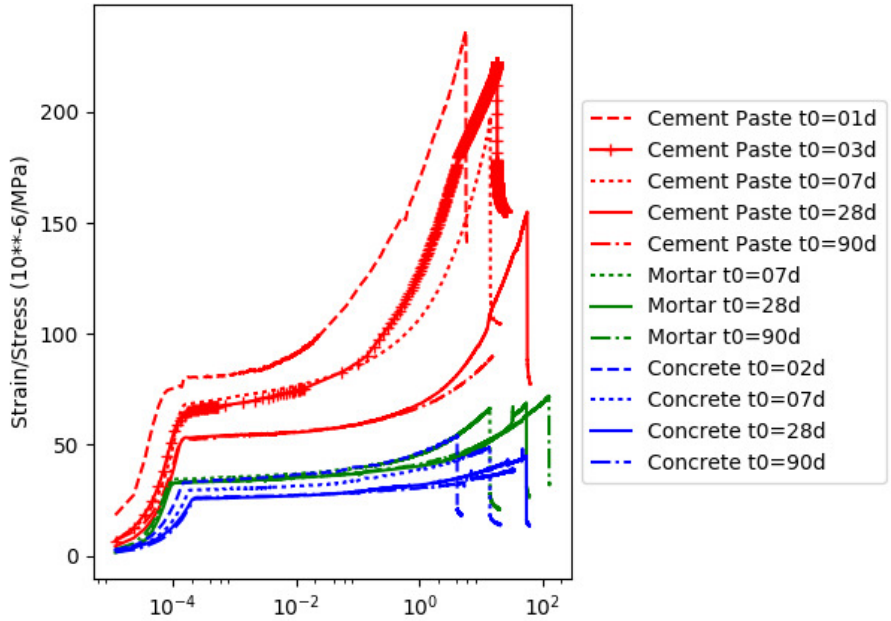

Figure 1: ε/σ evolution: loading age effect (t0 = age of end of loading).

$E(t_0), C(t_0), \tau(t_0), E_a(t_0), E_{Kelvin}(t_0)$ and $t_{\mathrm{eq}}(t_0)$ for each age of loading can be calculated with this method. And $E(t_0), C(t_0), \tau(t_0)$ and $E_{Kelvin}(t_0)$ can be described as follows:

$$f(t_0) = A + B(1 - e^{-\frac{t_0}{D}}) \tag{4}$$

The method of optimization is applied with the Eq (4) to calculate the proper parameter A, B and D for $E(t_0), C(t_0), \tau(t_0)$ and $E_{Kelvin}(t_0)$ for t_0 varies from 1 day to 1 year.

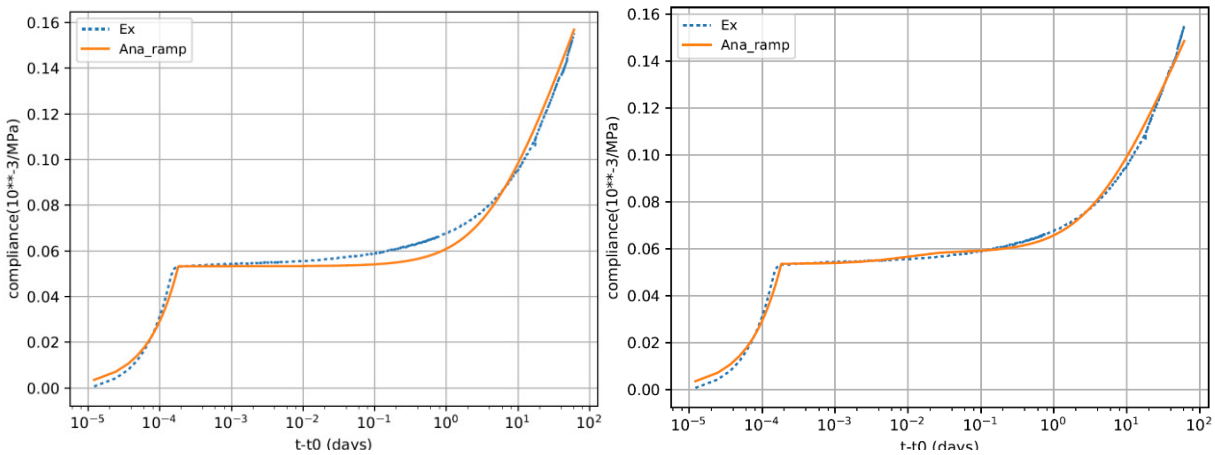

Figure 2: Example: evolution of strain/stress of specimen. Left: logarithmic function result (solid line), Right: model result (solid line), cement paste with age of loading = 28 days).

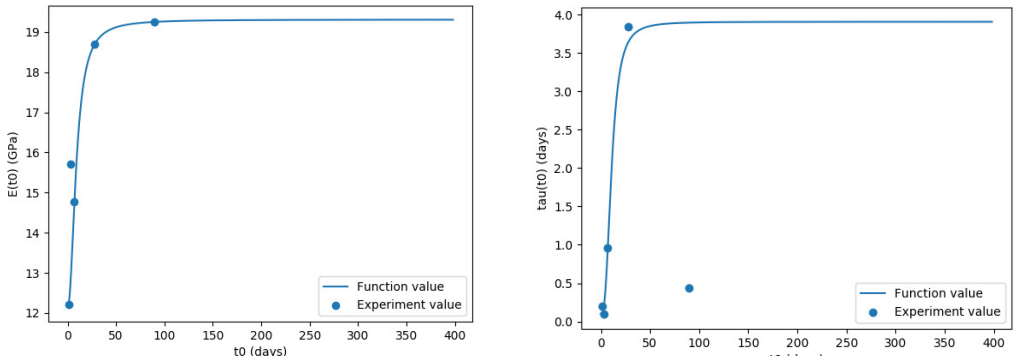

Figure 3: Experimental value (dots) and model (plain line) of $E(t_0)$ (left) and $\tau(t_0)$ (right).

2.2 Upscaling using homogenization

This part proposes a semianalytical approach to estimate the effective aging viscoelastic behaviour characterized by the compliance tensors as functions of two time variables (t, t_0) [3]. The Mori–Tanaka homogenization scheme and the self-consistent homogenization schemes is then applied to upscale the ageing viscoelastic behaviour from the scale of cement paste to the scale of mortar (with cement paste as the ageing viscoelastic matrix and sand as the inclusion), and from the scale of mortar to the scale of concrete (with mortar as the ageing viscoelastic matrix and coarse aggregate as the inclusion). The mechanical behaviour of sand and coarse aggregate are supposed to be elastic.

For the upscaling from the scale of cement paste to that of mortar, the volume fraction of sand is obtained by the mix design of the mortar samples: $f_{sand} = 0.54$. With the same principle, for the upscaling from the scale of mortar to that of concrete, the volume fraction of the phase of coarse aggregate is obtained by the mix design of the concrete samples: $f_{aggregate} = 0.39$.

In the VeRCoRs concrete, the mechanical properties of aggregates are as in the Table 1.

The effective aging uniaxial compliance function is plotted in Fig. 4 as continuous lines with the method mentioned in [4].

3. Conclusion and prospects

Homogenization modelling results underestimate the compliance and this underestimation is more evident at the early age. However, the model shows the tendency to underestimate the experimental results. It thus opens to us new ways for improving the quality of the model by: 1. Taking into account the cement paste/aggregate interface (ITZ); 2. Developing the microcracking of the VER during hydration; 3. The Poisson's Ratio of the matrix can also be regarded as a variable of time $\vartheta(t_0)$ to improve the model.

Table 1: Mechanical properties of materials of different scales for the VeRCoRs concrete.

	Sand	Coarse aggregate	Cement paste	Mortar
Young's Modulus (GPa)	50	55		
Poisson's ratio	0.27	0.27	0.23	0.24

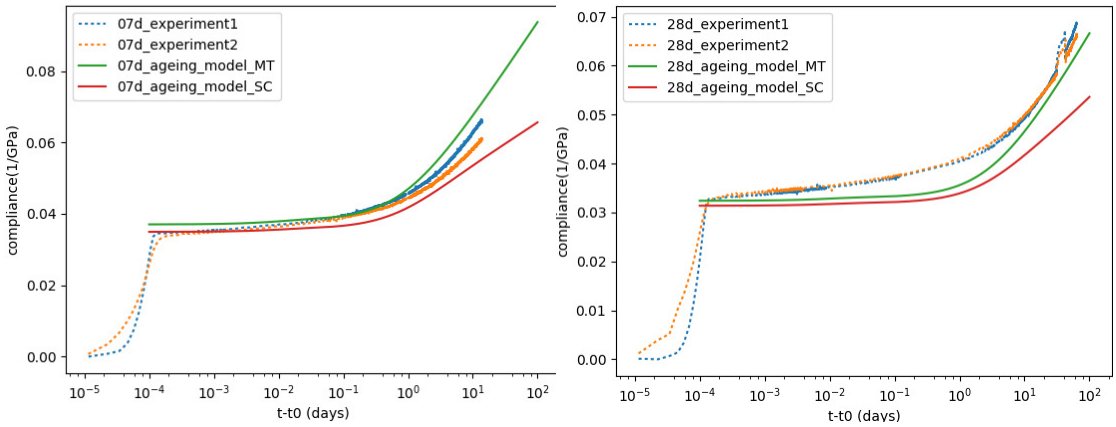

Figure 4: Effective uniaxial compliance [5] functions of mortar (w/c=0.525), plotted for various ages of loading $t_0 = 7\ days, 28\ days$. Comparison between the experimental results (2 dotted lines) and the upscaling using Mori–Tanaka and the self-consistent homogenization scheme from the scale of cement paste to the scale of mortar (continuous line).

References

[1] Freiesleben Hansen, Pedersen EJ (1977) "Maturity Analysis by Computer for Controlled Curing and Hardening of Concrete," Nord Betong, no. 1, pp. 21-25.
[2] Torrenti JM, Le Roy R (2015) Analysing and modelling basic creep. In Concreep-10 conference, Vienna
[3] Sanahuja, J (2014). "Homogenization of solidifying random porous media: Application to ageing creep of cementitious materials." RILEM Symp. on Concrete Modelling, Beijing.
[4] Sanahuja J, Huang S (2017) Mean-Field Homogenization of Time-Evolving Microstructures with Viscoelastic Phases: Application to a Simplified Micromechanical Model of Hydrating Cement Paste. Journal of Nanomechanics and Micromechanics.7:4016011.
[5] Salençon J., Salencon J., & SpringerLink (Online service). (2001). Handbook of continuum mechanics: General concepts thermoelasticity. Berlin/Heidelberg: Springer Berlin Heidelberg. doi:10.1007/978-3-642-56542-7

SynerCrete'18 International Conference on Interdisciplinary Approaches
for Cement-based Materials and Structural Concrete
24-26 October 2018, Funchal, Madeira Island, Portugal

MACROSCOPIC HYGRO-MECHANICAL MODELING OF RESTRAINED RING TEST - RESULTS FROM COST TU1404 BENCHMARK

Vít Šmilauer [(1)], Tobias Gasch [(2)], Arnaud Delaplace [(3)], David Bouhjiti [(4)], Fragkoulis Kanavaris [(5)], Miguel Azenha [(6)], Laurie Lacarrière [(7)]

(1) Czech Technical University in Prague, Czech Republic
(2) KTH Royal Institute of Technology, Stockholm, Sweden
(3) LafargeHolcim Research Center, Isle d'Abeau, France
(4) Chair PERENITI – 3SR, Laboratory, University of Grenoble Alpes, France
(5) Previously in University of Minho, currently in Arup, London, UK
(6) ISISE, University of Minho, Portugal
(7) INSA, Toulouse, France

Abstract
The restrained ring test under constant temperature is used for estimating cracking tendency of pastes, mortar or concrete. This test induces hygro-mechanical interactions, with intricate interplay of several phenomena such as autogenous shrinkage, drying shrinkage, basic and drying creep, as well as evolution of tensile strength and fracture energy. The benchmark described in this paper relies on extensive experimental data sets obtained through the extended Round Robin Testing programme (RRT+) of COST Action TU1404. Five teams took part with their simulation models. A series of outputs were produced, starting from mass loss of a prism through its axial deformation up to stress/strain evolution in the ring. Three teams quantified also damage due to drying and stress concentration around a ring's notch. All models showed excellent performance on mass loss while strain validation showed higher scatter and influence of several other factors. The benchmark demonstrated high capability of used models and emphasized strong role of calibration with regards to available experimental data.

1. Introduction

The restraint ring shrinkage test is a well-established method for testing cementitious binders for crack resistance during early ages, adopted further in e.g. ASTM C1581 or AASHTO T334. R. Carlson used the test already in 1942 [1] and a strong correlation with concrete surface cracking after 53 years was found. Several papers were published afterwards for optimizing binders and models using the ring, as shown in the review of reference [2].

COST Action TU1404 "Towards the next generation of standards for service life of cement-based materials and structures" has set up this benchmark to simulate experimental results on a reference concrete (labelled as 'OC') and to test different modelling approaches. Interested participants received input experimental data and they knew experimental results in advance in order to calibrate further their models if needed. The participants were free to use their modelling approaches and models, however, several intermediate steps were required to validate their partial data. Five participants took part in the benchmark:

1. Arup+University of Minho, (ARUP+UMinho)
2. CTU in Prague (CTU)
3. KTH Royal Institute of Technology, Stockholm (KTH)
4. LafargeHolcim Research Center, Isle d'Abeau (LafargeHolcim)
5. Chair Pereniti-3SR Lab, Grenoble (Pereniti)

Experimental methods were defined in the documentation of the Extended Round Robin testing programme (RRT+) of COST TU1404 [3], including the restrained ring shrinkage test. Since deformation of the ring is driven dominantly by drying, the benchmark had two consecutive stages: hygro-mechanical simulation of drying prims 100×100×400 mm and hygro-mechanical simulation of the ring. Fig. 1 shows ring geometry, whereas Table 1 presents the composition of OC concrete mix used in the experiment.

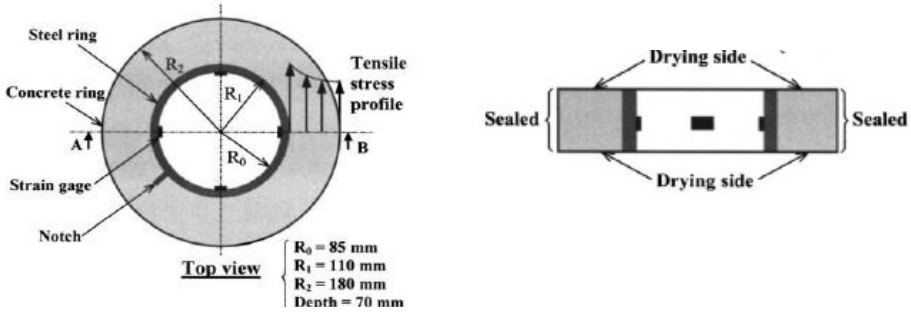

Figure 1: Geometry of the ring test

Table 1: Composition of OC concrete mix [3].

Basic Material	Type of the material	Amount [kg/m^3]
Cement	CEM I 52.5 N-SR3 CE PM-CP2 NF HRC Gaurain	320
Dry sand	0-4 mm, REC GSM LGP1 (13 % of CaO and 72 % of SiO2)	830
Fully saturated gravel	4-11mm, R GSM LGP1 (rounded, containing silicate and limestone)	449
	8-16 mm, R Balloy (rounded, containing silicate and limestone)	564
Admixtures	Plasticizer SIKAPLAST Techno 80	1.44
Added water	Water that needs to be added to the mixer	172.4
w_{eff}/c		0.52

2. Description of models used by participants

Participants used different governing equations and constitutive models for hygro-mechanical coupled simulations, as shown in Table 2. Four models for moisture transport were based on

single-phase balance equations with humidity or moisture field as the unknowns. The KTH model used mass balance of a gas-phase and a liquid-phase based on the thermodynamically constrained averaging theory. All moisture models used non-constant diffusivity, decreasing with lowering relative humidity. Some participants took advantage of desorption isotherm which was known from a similar mature Vercors concrete [4] with calibrated saturation from TU1404 data. Total water content at the full saturation of mature concrete was found as 165.3 kg/m^3. Only KTH model considered water consumption during hydration and its effect on decreasing evaporable water content during hydration.
All participants used small strain decomposition and incremental stress-strain relationship to account for creep. The most advanced models used the following incremental constitutive law

$$\Delta\varepsilon = E''\left(\Delta\varepsilon - \Delta\varepsilon'' - \Delta\varepsilon_{as} - \Delta\varepsilon_{ds} - \Delta\varepsilon_f\right) \quad (1)$$

where ε_{as} is the autogenous shrinkage strain, ε_{ds} is the drying shrinkage strain and ε_f stands for fracturing strain. Except KTH, the participants assumed linear relation between drying shrinkage strain rate and relative humidity/moisture rate using a shrinkage factor. Four participants used fracture material model for crack initiation and propagation, usually in the framework of isotropic damage model.

Table 2: Summary of used equations, material models, software and computation times.

	Arup+UMinho	**CTU**	**KTH**	**LafargeHolcim**	**Pereniti**
Equation for moisture transport	Humidity balance, h	Humidity balance, h	Gas-phase and liquid-phase, water, dry air	Water balance, w	Water balance, w
Material model for creep	Double-power law	Calibrated B3/B4	Calibrated B3 with MPS theory	Two ageing Kelvin units	Burger model
Material model for fracture	Multidirectional fixed crack model	Isotropic damage model	Isotropic damage model	-	Stochastic isotropic damage model
Software	iDiana, Diana, Matlab	OOFEM	COMSOL	Aster	Aster
Computation time - prism	20 min	8 min	3.5 min	2 min	3.5 min
Computation time - ring	20 min	20 min	10 min	5 min	21 min

3. Results and discussion

3.1 Prism

The first part considered simulation of a prism 100×100×400 mm which started drying at 50 % RH after 1 day of sealed hydration. For this test, the mass loss in Fig. 2 and the total strain in Fig. 4 were measured in RRT+. Total strain is used for the identification of the parameter managing the moisture transport (through the measurement of mass loss) and for the shrinkage coefficient in models using linear relation between the moisture rate and the drying strain.
Drying shrinkage tests were held for 22 days and the asymptotic value at very long time was deduced from tests performed on smaller 70×70×280 mm specimens for which the hydric

equilibrium is reached faster (-450 με and 89.2 kg/m^3 of water loss for drying shrinkage at 50%RH and –50 με for autogenous shrinkage) [3].

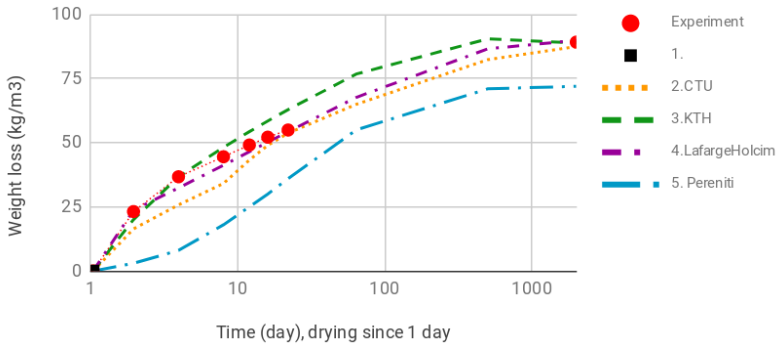

Figure 2: Weight loss of a prism 100×100×400 mm.

Fig. 3 shows models calibration to E-modulus and basic creep at t'=1 day. It is noted that the team of Arup+UMinho have used data for E-modulus from a distinct source within the RRT (data from EMM-ARM method measured at UMinho on the same concrete). Fig. 4 then provides the simulated total shrinkage (autogenous and drying) on the axis of the prism. It can be seen that the identification of the shrinkage models allows a good reproduction of the results. Criteria for fracture initiation used splitting tensile strength 1.4 MPa at 2 days, 3.5 MPa at 7 days and 4.5 MPa at 28 days.

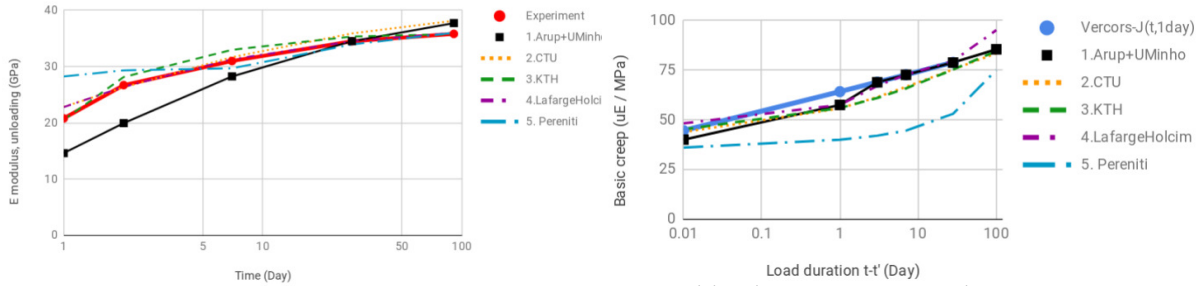

Figure 3: Calibration for E modulus and basic creep at t'=1 day.

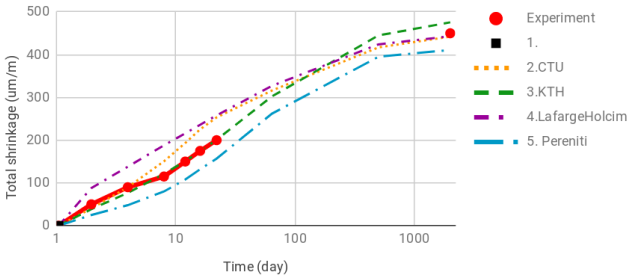

Figure 4: Total shrinkage on prism's axis.

3.2 Ring

Once the drying kinetics were validated on the prism, simulation of ring test took place using the same constitutive laws for moisture transport. All participants used a 3D model except LafargeHolcim who used axisymmetric model without any damage. Fig. 5 shows meshes in hygro-mechanical models.

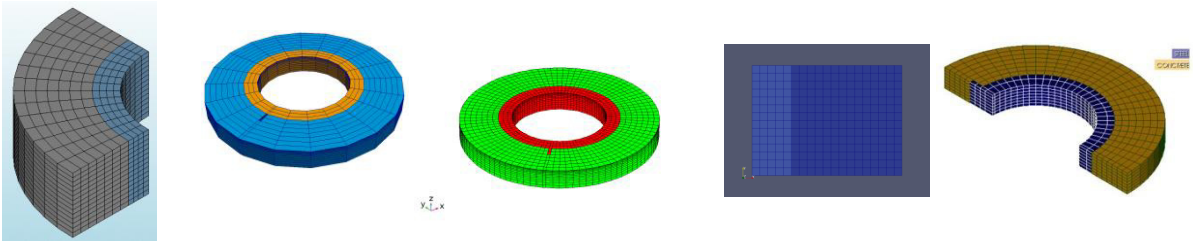

Figure 5: Meshes used in hygro-mechanical simulations of the ring.

First, the models validated steel strain, as shown Fig. 6. Except for the results from Pereniti, where strain localization occurs earlier than observed in the selected reference ring test, the participants have all simulated the experimentally measured strain rather well up to the maximum strain. Damage occurs immediately after the drying on dried horizontal surfaces up to a few mm, further damage occurs after approximately 10 days around steel, breaking up standard linear creep law. This is probably the main cause of slow strain decrease after the strain peak at 70 με at 50 days.

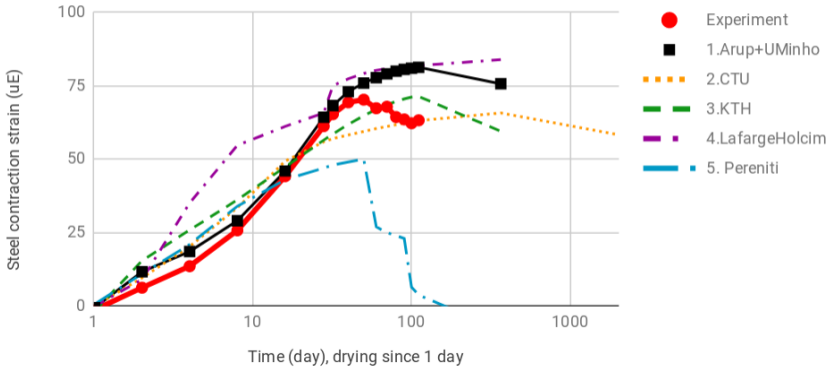

Figure 6: Validation of hoop steel strain.

Two material points are interesting for stress evolution; proximal point close to steel ring and distal point close to vertical exterior. Hoop stresses testify non-constant stress distribution across the ring as known even from analytical elastic solution [2]. Models provided blind prediction which is summarized in Fig. 7. The notch in the ring created small stress concentration but, due to stress gradient, it did not propagate to a visible crack even after experimental 111 days (except in the case of Pereniti team where visible cracks are obtained within 51 days). Fig. 8 shows non-validated and blind weight loss predictions of the ring.

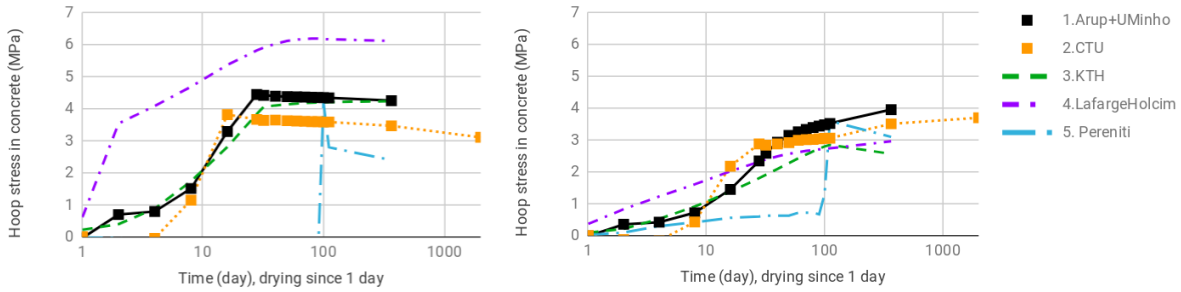

Figure 7: Proximal and distal hoop stress in concrete, blind prediction.

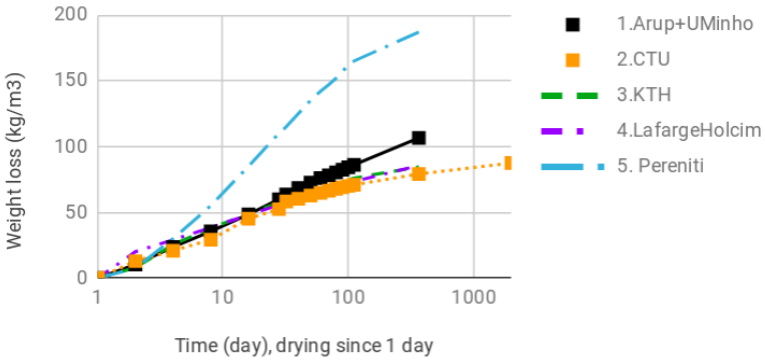

Figure 8: Blind prediction of ring's weight loss.

4. Conclusions

This benchmark extensively used available experimental data generated in the RRT+ programme of COST Action TU1404. Selection of feasible and reasonable data was a prerequisite for successful macroscopic validation of the ring test. The results from five participants showed:

- Drying shrinkage presents the main driving strain and mass loss needs validation. Data on prisms 100×100×400 mm with asymptotic values served for this purpose.
- Ageing creep with correct evolution of E-modulus represents sensitive constitutive law for stress evolution, damage and potential macro-crack formation.
- Hygro-mechanical models performed generally well. Nonlinear creep occurring close to tensile strength would likely improve strain evolution after its maximum. The variability of results is both due to calibration on limited data sets and models' limitations.

Acknowledgements
The authors would like to acknowledge networking support by the COST Action TU1404 (www.tu1404.eu). Czech Technical University acknowledges support of Technology Agency of the Czech Republic in the project TH03020404. The team of UMinho acknowledges the support of FCT/FEDER(COMPETE2020) through the research project IntegraCrete PTDC/ECM-EST/1056/2014 (POCI-01-0145-FEDER-016841).

References

[1] Burrows, R. W., The visible and invisible cracking of concrete, ACI monograph, 1998
[2] Turcry, P., Loukili, A., Haidar, K, Pijaudier-Cabot, G., Belarbi, A., Cracking Tendency of Self-Compacting Concrete Subjected to Restrained Shrinkage: Experimental Study and Modeling, Journal of Materials in Civil Engineering (2006), 46-54
[3] COST TU1404, RRT+ Main phase of the extended round robin testing programme for TU1404, testing protocols, (2016).
[4] EDF. Projet VeRCoRs. (2015-2021). https://www.conference-service.com/EDF-VeRCoRs-Benchmark-2018/welcome.cgi

SynerCrete'18 International Conference on Interdisciplinary Approaches
for Cement-based Materials and Structural Concrete
24-26 October 2018, Funchal, Madeira Island, Portugal

BACKGROUND FOR A NEW EUROCODE 2-ANNEX: EVALUATION OF EARLY-AGE AND LONG-TERM CRACKING DUE TO RESTRAINED DEFORMATIONS

Terje Kanstad [(1)], Anja Estensen Klausen [(1)]

(1) Norwegian University of Science and Technology (NTNU), Trondheim, Norway

Abstract
It is agreed within the relevant CEN-committees that Eurocode 2 should give regulations that clearly describe how imposed deformations including early age effects can be accounted for in structural serviceability limit state design. This paper aims to give background for some of the proposed methods and text in a new annex including literature references, verifications and explanations of the applied methods and parameters. A new equation for development of mechanical properties is included as basis for stress calculation. It is accounting particularly for the time right after setting, and can also be applied for general reference ages between 28 and 91 days. A simplified approach based on the age adjusted effective E-modulus, which has been proven to work well also at early ages is included. It applies an effective E-modulus accounting both for aging and creep. The most recent draft of the annex considers the largest tensile stress for two particular stages, at temperature equilibrium at early ages, and at the design life. The crack strain is described, while the crack spacing is found in the main SLS-chapter as for ordinary loads, and thus the surface crack width may be calculated.

1. Introduction

Cracking may impair the performance of concrete structures due to aesthetics, durability, and tightness. The consequences are related to economy and sustainability, and it is important that Eurocode 2 gives regulations that clearly describe how and when cracking shall be accounted for in the structural design. The new proposed Annex D is entitled "Evaluation of early-age and long-term cracking due to restraint [1], and considers the effects of temperature changes due to the concrete's hardening process and basic shrinkage in combination with imposed deformations accurring at later ages. The main objective of the proposed methods is to evaluate the cracking risk, and provide guidance on crack calculations if cracking is expected to occur. The major focus is on through-cracks, which may span over the whole thickness of

the concrete member, and occur in the cooling phase of the hardening process, typically between 2 and 30 days after casting depending mainly on the dimension of the structural member and the binder type. Possible measures to reduce the amount of through-cracking are to use concretes with low heat production, concretes with low coefficient of thermal expansion, cooling pipes in the hardening concrete, heating cables in the restraining concrete, reduced fresh concrete temperature, or to reduce the degree of restraint for the hardening concrete member. The measures may be expensive, and as the significance of early age cracking is case-dependent, it is important that the measures are reflecting the criticality of cracking. The typical temperature and stress histories at early ages are illustrated in Figure 1, where T_{ci} is the fresh concrete temperature, $T_{c,max}$ the maximum concrete temperature due to hydration heat, T_0 the temperature of the restraining structure, while ΔT_{min} is an additional temperature drop which might be due to daily or seasonal temperature variations. The most unfavourable moment in time for early-age cracking is denoted t_{crit}, corresponding to the moment when temperature equilibrium with the restraining structure is achieved (within 2ºC). It might be relevant to consider crack-control in the following three states: (1) At temperature-equilibrium between the recently cast concrete structural member and the restraining structure. (2) At commissioning of the structure. (3) During the design service life. In the two latter cases, the temperature reduction ΔT_{min} and drying shrinkage must be added to the early age effects. In the present draft of the annex the formulations are particularly directed towards (1) and (3). If particular demands are related to tightness, durability or appearance, the cumulative impact of early age effects, load effects and later imposed deformations must be considered in the crack control. Otherwise, the crack control of these states can be verified separately. To restrict cracking either crack prevention or crack limitation may be used. The latter may be achieved either by minimum reinforcement for crack limitation as explained in section 9 of the Eurocode [1], or by calculations.

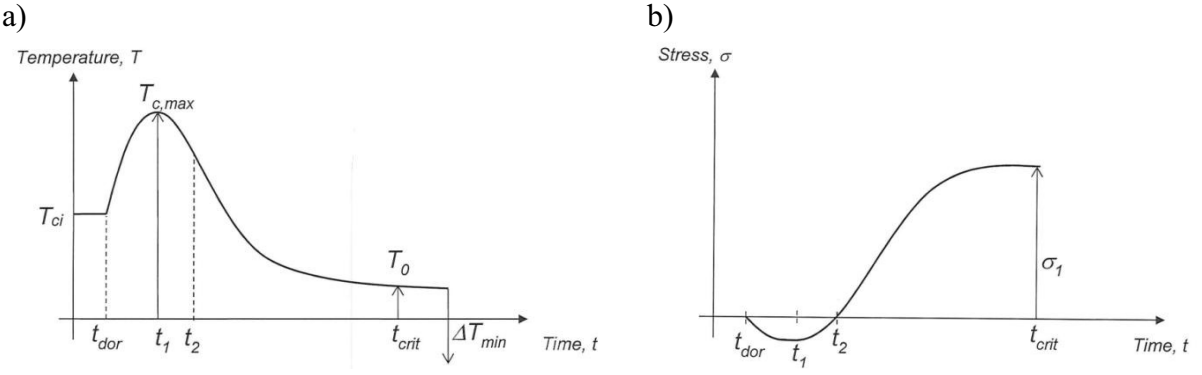

Figure 1: Typical temperature (a) and stress (b) histories due to early age effects [1]

2. Time-development of mechanical properties

The time-development of the compressive strength, for t<91 days, is described as:

$$f_c(t_{eq}) = ß \cdot f_{c28} \qquad ß = exp\left\{s\left(1 - \sqrt{\frac{t_{ref} - t_{dor}}{t_{eq} - t_{dor}}}\right)\sqrt{\frac{28 - t_{dor}}{t_{ref} - t_{dor}}}\right\} \qquad (1)$$

Default values for the material parameters are presented in Table 1 reflecting two novel points: Introduction of the parameter t_{dor} (Figure 1, "end of the dormant phase") that defines when stiffness and strength start to be significant. This is a decisive parameter to include thermal dilation and basic shrinkage in a consistent way because both effects may develop very fast at early ages, and typically, it varies between 8 and 13 maturity hours. The parameter may be strongly affected by admixtures, and it is important that the choice of the parameter is consistent with basic shrinkage and temperature development. The modification of the equation with the last square root-sign term including the term $t_{ref,}$, which can vary between 28 and 91 days, makes it possible to utilize the strength increase after 28 days which may be significant for low heat and more environmentally friendly concretes. Default values for s and t_{dor} are given in Table 1 below, which is based on experimental results in [2,3,4,5].

Table 1: Parameters for strength development

Cement	High early strength [R]		Ordinary strength (N)		Low early strength (S)	
Strength	s	t_{dor}(d)	s	t_{dor}(d)	s	t_{dor}(d)
<C35	0,3	0,35	0.35	0,45	0.4	0,5
C40-C55	0.2	0,3	0.25	0,4	0.35	0,45
>C60	0.1	0,3	0.17	0,35	0,3	0,4

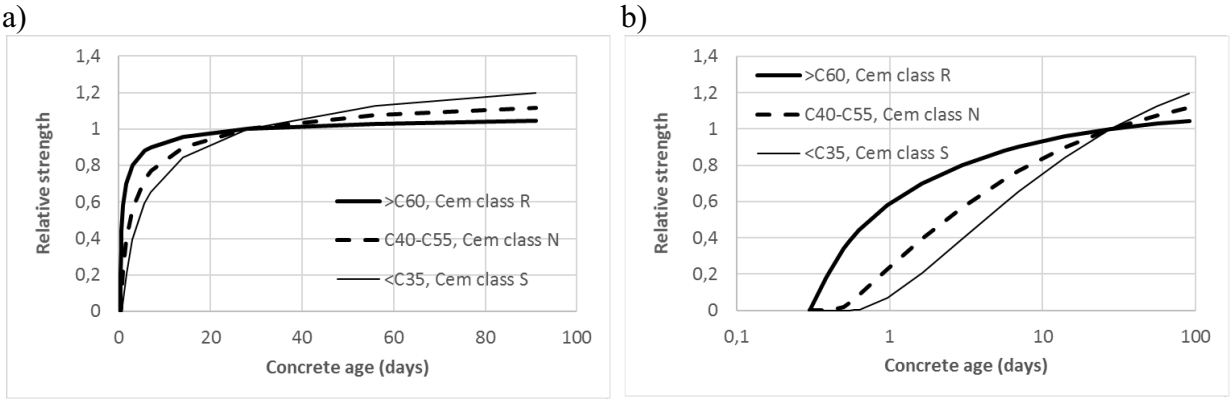

Figure 2 – Time development of compressive strength

3. Stress calculation

This section is mainly meant for verification of if cracking will occur or not. Obviously nonlinear finite element analysis are often used for such stress calculations, but still it is found useful to include a simplified method based on the effective E-modulus method. Such method can give the solution for a specified position in a structural member at a specific time. The simplified approach is based on the well-known age adjusted effective E-modulus method (Trost–Bazant), which has been proven to work well also at early ages [6,7] as illustrated in Figure 3. The method is based on uncracked concrete cross sections and applies an effective

E-modulus accounting for aging and creep. Using parameters described in Table 1 and Figure 1, the tensile stress in a predefined position, including cumulative impacts, can be determined.

$$\sigma_1(t) = (\Delta\varepsilon_T(t-t_2) + \varepsilon_{cbs}(t-t_2))E_1 \cdot R_1 + \alpha_T \cdot \Delta T_{min} \cdot E_2 \cdot R_2 + \varepsilon_{cds}(t-t_2) \cdot E_3 \cdot R_3 \quad (2)$$

Where t_2 is the time when the stress changes sign. For early age problems the time t should be set equal to t_{crit} as defined in Figure 1, while if cumulative impacts are included t is the relevant design service life. $\Delta\varepsilon_T(t-t_2)=k_1(T_{max}-T_o)\alpha_T$ represents the part of the temperature causing tensile stresses and $\varepsilon_{cbs}(t-t_2)$ is the part of the basic shrinkage occurring in the cooling phase and ε_{cds} is the drying shrinkage strain. $E_1 = E_c(t_{2eq})/(1+k_2*\varphi(t,t_{2eq}))$ is the effective E-modulus representing the cooling phase. Default values based on Scandinavian practice [6,7] are $k_1=0,9$ and $k_2=0,8$. The parameters E_2 and E_3 are corresponding longterm E-modules representative for the additional effects. Three different values for the degree of restraint are used in expression (2). This is because this parameter will vary with the concrete age and the time period considered, and because the structural system may change with time.

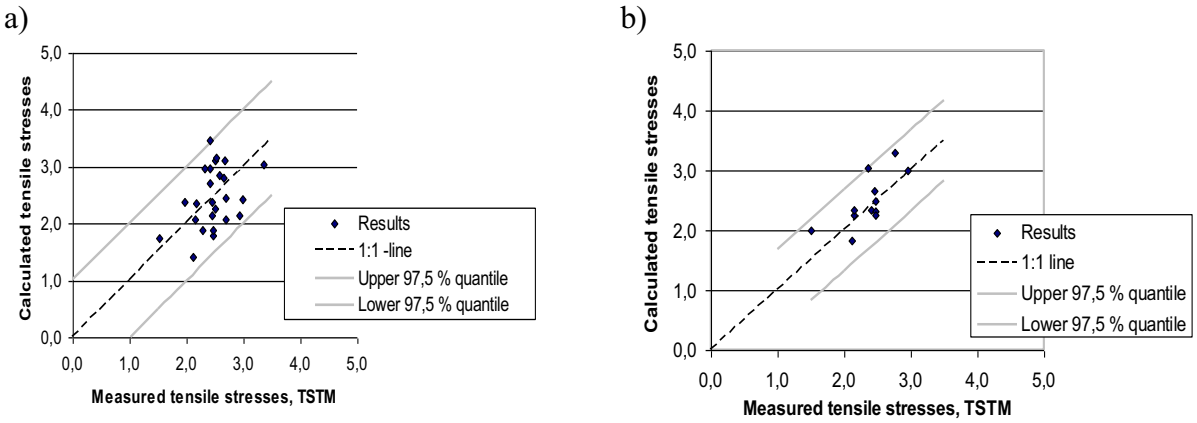

Figure 3: Verification of stress calculation methods, (a) Age adjusted effective E-modulus method, (b) Linear viscoelasticity for aging materials [6].

The most recent draft of Eurocode 2 [1] modifies equation (2) for two particular stages, but a verification corresponding to [6,7] still remains. At temperature equilibrium (t_{crit}), and for longterm analysis at the design life (t), the expressions are:

$$\sigma_1(t_{crit}) = R_1 \frac{E_c(t_{crit})}{1+\chi\varphi_{st}}\left(k_1\alpha_T\left(T_{c,max} - T_0\right) + \varepsilon_{cbs}(t_{crit})\right) \quad (3)$$

$$\sigma_1 = R_1 \frac{E_{c28}}{1+\chi\varphi(t,t_{crit})}\left(k_1\alpha_T\left(T_{c,max} - T_0\right) + \varepsilon_{cbs}(t)\right) + R_2 E_{c28}\,\alpha_T \Delta T_{min} + R_3 \frac{E_{c28}}{1+\chi\varphi(t,t_s)}\,\varepsilon_{cds} \quad (4)$$

R_1, R_2 and R_3 are representative restraint factors as described previously. $\chi\varphi_{st}$ accounts for short term creep, and its value may be estimated as 0.55. χ is the aging coefficient (corresponding to k_2 in equation (2)) which may be taken as 0.8. $E_{c,28}$ is the tangent modulus of elasticity of concrete at an age of 28 days.

4. Crack width calculation

The annex [1] describes the crack strain, while the crack spacing is found in the main SLS-chapter as for ordinary loads, and thus crack width at the concrete surface may be calculated as:

$$w_{calc} = S_{r,max} \cdot (\varepsilon_{sm} - \varepsilon_{cm} + \eta_r \varepsilon_{cs}) \tag{5}$$

where w_{calc} is the surface crack width, $S_{r,max}$ the maximum crack spacing, ε_{sm} and ε_{cm} are the mean strains in the reinforcement and the concrete, respectively. The parameter η_r is 0 for short-term loading and long-term loading in the crack formation stage and equal to 1.0 in other cases while ε_{cs} is the shrinkage strain
For elements subjected to restrained imposed strains and which are restrained at the edges (typically walls on foundations), (ε_{sm} - ε_{cm} + $\eta_r\varepsilon_{cs}$) in Equation (5) may be calculated as:

$$\varepsilon_{sm} - \varepsilon_{cm} + \eta_r \varepsilon_{cs} = R\varepsilon_{free} - k_t \cdot \frac{f_{ct,ef}}{E_{cm}} \tag{6}$$

where R is the restraint factor, ε_{free} is the imposed strain, k_t is a coefficient dependent on the nature and duration of the load, $f_{ct,ef}$ is the mean value of the tensile strength of the concrete at the time when the cracks are expected to occur while E_{cm} is the modulus of elasticity.
For elements restrained at the edges, the annex [1] states that ($R\varepsilon_{free}$) in Equation (6) can be taken as ε_r:

$$\varepsilon_r = R_1[k_1\alpha_T(T_{\max} - T_0) + \varepsilon_{cbs}(t_{crit} - t_2)] + R_2\alpha_T\Delta T_{\min} + R_3\varepsilon_{cds} \tag{7}$$

where the parameter k_1 = 0.9 takes into account that the tensile stress development starts slightly after the maximum temperature (due to the initial thermal expansion), α_T is the coefficient of thermal expansion, ε_{cbs} is basic shrinkage, ε_{cds} drying shrinkage, while t_{crit}, t_2, ΔT_{min} and R_1, R_2 R_3 are parameters described previously in this paper.

5. Concluding remarks

This paper presents parts of the background for the new Eurocode 2 Annex D entitled "Evaluation of early-age and long-term cracking due to restraint". The Annex has been elaborated for some years by the technical group CENTC250/SC2/WG1/TG7, where the authors did the main part of the writing. However, it is now published by CEN/TC 250/SC 2/WG1/PT1 as a final draft [1]. However, the work on this Annex will continue, and it might therefore be changed before the final version of the next Eurocode 2 is published. Presently this is scheduled for 2023.

References

[1] CEN/TC 250/SC 2/WG 1 PT1prEN 1992-1-1: Eurocode 2: Design of concrete structures – Part 1-1: General rules, rules for buildings, bridges and civil engineering structures, Annex D pp 234-239. Report N 1358, June 2018.

[2] Kanstad, T.; Hammer, T.A.; Bjøntegaard, Ø.; Sellevold, E. J. Mechanical Properties of Young Concrete: Part I - Experimental Results related to Test Methods and Temperature Effects. Materials and Structures 2003 ;Volume 36. p. 218-225
[3] Klausen, A.; Early age crack assessment of concrete structures: experimental investigation of decisive parameters. Trondheim: NTNU,2016 (ISBN 978-82-326-1850-7) PhD-thesis.
[4] Neville, A.M.; Properties of concrete, Pitman, London, 1975.
[5] Graf, O., et al; Die eigenschaften des betons. Springer Verlag, Berlin, 1960.
[6] Kanstad, T. Verification of three different calculation methods for early age concrete. In: Crack Risk Assessment of Hardening Concrete Structures. The Nordic Concrete Federation 2006 ISBN 82-91341-97-4. p. 101-110
[7] Larson, M.; Estimation of crack risk in early age concrete, simplified methods for practical use, Licentiate thesis, Luleå technical university, Sweden 2000:10, ISSN 1402-1757.

CONCRETE TECHNOLOGY

AND

ADVANCED MATERIAL TESTING

SynerCrete'18 International Conference on Interdisciplinary Approaches
for Cement-based Materials and Structural Concrete
24-26 October 2018, Funchal, Madeira Island, Portugal

A CONCRETE HOME FOR MARINE MICRO INHABITANTS

Atteyeh S. Natanzi [(1)], Ciaran McNally [(1)]

(1) School of Civil Engineering - University College Dublin (UCD), Dublin, Ireland

Abstract
In the last decades, the prevalence of artificial marine structures along natural shorelines has increased significantly. In some parts of the world, more than half of the available natural shoreline has been covered by these structures. Epibiotic diversity has been shown to decrease significantly on submerged artificial structures due to the reduced environmental heterogeneity of artificial environments. Natural rocky shores provide microhabitats through their rough surfaces, pits, rock pools and crevices. In contrast, modern building materials typically fail to provide many of these features. The ecological value of artificial coastal infrastructure could be increased through careful design of pre–fabricated ecological engineering units. Material selection is a crucial parameter in the design of these units. Reinforced concrete plays an important role in the design process due to its ease of production, relatively low cost and its suitability for mass construction.
To maximise the potential of concrete to support biodiversity and natural capital, binder composition, aggregate type, and texture are considered to be important parameters. To investigate these parameters, an experimental programme has been developed which is focusing on a number of different concrete designs. Key engineering parameters, such as strength, chloride diffusion coefficient, and their ecological colonisation performance are evaluated.

1. Introduction

In the last 40 years, the number of urban dwelling people has nearly doubled, with urbanized areas quadrupling in size [1]. Almost two thirds of the world's population is now estimated to live in coastal areas [2]. As the population has increased in coastal areas, more pressure has been put on coastal ecosystems through habitat conversion, increased pollution and more demand for marine resources [3]. These types of marine developments are always associated with fragmentation and loss of natural habitats, damaged seascapes and reduced biodiversity [4]. This irreversible alteration, often from natural to urban infrastructure development, is

considered to be one of the main threats to coastal ecosystem and sustainability [5]. Natural habitats provide microhabitats through their rough surfaces, pits, rock pools and crevices. In contrast, modern building materials typically fail to provide many of these features, with a notable impact on the organisms that would seek to colonise these surfaces. Artificial marine structures could support more invasive non-indigenous species and less diverse communities than natural habitats [5, 6]. The ecological value of artificial coastal infrastructure could be increased through careful design of pre–fabricated ecological engineering units. Material selection is a crucial parameter in the design of these units. Reinforced concrete plays an important role in the design process due to its ease of production, relatively low cost and its suitability for mass construction. Concrete composition plays a significant role in biodiversity enhancement of marine structures [7]. More than half of marine infrastructures are made using Portland cement concrete, and this has been shown to provide a good support for colonising organisms as calcareous skeletons deposit calcium carbonate onto the surface in the biogenic build-up process [8]. Concrete, however, has a high surface alkalinity (pH 12-13 compared to 8 for seawater), and this could reduce settlement of marine organisms and result in communities dominated by a few alkotolerant taxa such as barnacles [9]. The addition of pozzolanic materials such as GGBS to the concrete mix could reduce the alkalinity of the concrete and create more suitable surfaces for colonisation by marine species [10]. As chloride ingress in reinforced concrete structures in marine environments is one of the most challenging forms of degradation, replacement of Portland cement by pozzolanic materials such as GGBS could improve concrete durability and delay the reinforcement corrosion [11]. Chloride ions exist in seawater and can destroy the passive layer at the rebar surface when the chloride concentration at the cover depth is greater than the critical chloride concentration (C_{cr}). Previous research [12,13] has shown that as the GGBS content increases, the possibility of steel corrosion decreases. Other factors such as surface texture, holes, crack pits and pools have been also investigated and are found to have a significant and direct effect on increasing biodiversity on artificial marine infrastructures [14].
Although some research has been conducted to use concrete as a new habitat for marine micro habitants, they rarely consider the engineering side and focus mainly on ecological issues. Here, the alternative possibility of using coastal infrastructures as a habitat for epibiota is exploring. The service life that may be expected from these different mix designs is also examined and show how they are being assessed in the field.

2. Materials and Methods

A number of concrete mixes were designed with a view to assessing their engineering performance, as well as their ability to support marine life. A number of specimens were cast for each mix, including:

- 8 reinforced concrete tiles of dimension 200 x 200 x 40 mm which would be installed in a marine environment;
- 3 concrete cylinders of diameter 100mm and height 200mm for assessing resistance to chloride ingress;
- 6 concrete cubes of dimension 100mm to confirm concrete strength at 7 and 28 days.

As the concrete tiles would be subject to corrosion arising from sea-borne chlorides, the exposure class was considered to be XS3. This also corresponds to the tidal zone, as the

samples will not be fully submerged, and subjected to spray and inter-tidal conditions. For this particular exposure class, the Irish National Annex to EN206 requires a minimum cement content of 360 kg/m^3, a maximum water/binder ratio of 0.5 and a minimum strength class of C35/45.Nine different concrete compositions were designed in this study, and parameters of interest were binder type, aggregate type and influence of plasticiser. Two binder compositions were used: 100% CEM I, and a 50% blend of CEM I and GGBS. This was selected as it was considered that it would provide a higher chloride resistance, as well as a significant change in concrete alkalinity that could influence marine colonisation. Plasticiser was also added as a variable and the selected dosage was 0.8% of cement content. It is not expected to have any major influence on the engineering performance, but its influence on colonisation behaviour is completely unknown. Finally, the coarse aggregates chosen were limestone and granite. Limestone is the dominant aggregate type in Ireland and significant quantities of concrete are manufactured using this. Granite was also chosen, as anecdotal experience has shown that marine organisms are often attracted to materials with the reddish colour of coralline algae. As such, the granite colouring is of interest to us and will be used as a variable for the field testing. A final mix (mix 9) was added to the testing programme as an initial assessment of the influence of concrete texture, whereby a rough surface was obtained by removing the concrete surface as the material was setting. A full list of the selected mixes is described in Tab. 1.

Table 1: Concrete mix design compositions.

Mix	Binder	Aggregate	Reinforcement	Plasticiser
1	CEM I	Limestone	Steel mesh	No
2	CEM I	Limestone	Steel mesh	Yes
3	CEM I + GGBS	Limestone	Steel mesh	No
4	CEM I + GGBS	Limestone	Steel mesh	Yes
5	CEM I	Granite	Steel mesh	No
6	CEM I	Granite	Steel mesh	Yes
7	CEM I + GGBS	Granite	Steel mesh	No
8	CEM I + GGBS	Granite	Steel mesh	Yes
9	CEM I	Limestone	Steel mesh	Yes

2.1 Concrete Characterisation

Compressive strength of the concrete cubes was obtained by testing according to EN 12390-3 [15]. The chloride resistance was determined by use of a chloride migration test, and the particular method used was the non-steady state migration test according to NordTest NT BUILD 492 [16]. The test involves driving chloride ions through a concrete section of 100mm diameter and 50mm thickness under the action of the electric field. The catholyte solution is 10% NaCl by mass in tap water and anolyte solution is 0.3M NaOH in distilled water. A voltage, typically of the order of 30 V is applied for 24 hours, after which the concrete sample is removed and split. The depth of chloride penetration is visually determined by spraying 0.1 M silver nitrate solution on the freshly split concrete section. To determine the chloride concentration at the depth, X, for a service life of t=50 years, Cranks solution to Ficks Law was used:

$$C(x,t) = C_{sn}\left[1 - \text{erf}\left(\frac{X}{2\sqrt{D_m t}}\right)\right] \quad (1)$$

where C_{sn} is surface chloride concentration and D_m is the mean chloride diffusion coefficient for the exposure time t and calculated from Eq. (2) and (3).

$$D_m(t) = \frac{1}{t}\int_0^t D(\tau).d\tau \quad (2)$$

$$D(\tau) = D_R(\frac{t_R}{t})^m \quad (3)$$

For this study, the surface chloride concentration was taken as 0.8% by mass of binder. This is based on research by Poulsen and Sørensen [17] who assessed 34 year old concrete bridges in a marine environment. It is recognised that this is a time and material dependent parameter, but the use of a fixed value is considered appropriate for comparative purposes. The parameter *m* is an age factor, and based on the work of Attari et al. [18] is taken as 0.17 for 100% OPC binders and 0.3 for binders containing 50% GGBS, t_R is reference time (in this case 81 days). Determination of effective diffusion coefficients from migration testing is as described by Tang and Nilsson [19].

3. Results and Discussion

3.1 Compression test

The results of the compression testing are presented in Tab. 2. It can be seen that the use of a 50% GGBS replacement level resulted in almost no change to the strength. The most significant change was in the early strength of the concrete samples manufactured using granite aggregate, but this appears to be reduced at 28 days. All samples comfortable achieve the minimum strength of exposure class XS3 (C35/45).

Table 2: Concrete compressive strength results.

Mix	Average 7 days compressive strength (MPa)	Average 28 days compressive strength (MPa)
1	41.30	50.24
2	40.78	45.13
3	35.79	50.12
4	31.72	49.94
5	34.78	47.46
6	32.93	41.92
7	26.32	47.42
8	26.40	45.74

3.2 Chloride Migration

Results of the chloride migration testing are shown in Tab. 3. The required service life was 50 years, and as such the data was manipulated using equations 1, 2 and 3 so as to produce the time dependent diffusion coefficient for this period. This is then used to determine the

chloride content at a selected concrete cover depth of 50mm. Corrosion is typically accepted to be initiated when the chloride concentration reaches a critical value of 0.4% by mass of binder.
In all cases it can be seen that the critical variable is the use of GGBS; without this, the required service life of 50 years cannot be achieved. This is supported by other research in this area [20]. The influence of the other parameters (plasticiser, aggregate) is found to be much lower, and these can be utilised without compromising performance of the concrete.

Table 3: Results of chloride resistance tests.

Mix	D_{nssm} ($x10^{-12}$ m^2/s)	D_R ($x10^{-12} m^2/s$)	D_m ($x10^{-12} m^2/s$)	C(5,50)
1	17.08	13.00	3.66	0.51
2	21.46	16.61	4.67	0.54
3	3.52	2.39	0.44	0.14
4	3.34	2.25	0.41	0.13
5	17.40	13.26	3.73	0.52
6	18.05	13.75	3.87	0.52
7	3.00	1.96	0.36	0.11
8	3.13	2.06	0.38	0.12

The next strand in this work is the ecological assessment of the concrete mixes, and the 200mm concrete tiles were deployed on a breakwater on Ireland's east coast in April 2018 (Fig.1). Samples are attached to the exposed and sheltered surfaces on this rocky breakwater and are fully submerged during high tide. They will remain in this intertidal environment for 12 months to evaluate the influence of concrete mix design on colonisation behaviour. Quadrat sampling will determine if different concrete mixes can lead to improved substrates for marine life. This strand of the work will be reported at a later stage.

Figure 1: Concrete tiles installation and deployment.

4. Conclusions

Corrosion of reinforced concrete is the main threat to marine structures. The results of our service life prediction showed that the addition of GGBS plays a significant role in achieving

the required service life and that if this is included then other parameters can be included without issue. Concrete mixes with limestone aggregate were also shown to be slightly stronger than mixes with granite aggregate. The connection between these engineering parameters and the marine colonisation behaviour will be monitored with interest over the next 12 months.

References

[1] Seto, K.C. et al, A meta-analysis of global urban land expansion, PloS one 6(8) (2011), e23777
[2] Creel L. Ripple effects: population and coastal regions, Washington, DC: Population Reference Bureau, (2003)
[3] Airoldi L. and Beck MW., Loss, status and trends for coastal marine habitats of Europe, In Oceanography and marine biology, CRC Press, (2007), 357-417
[4] Dugan, J.E. et al, 8.02-Estuarine and coastal structures: environmental effects, a focus on shore and nearshore structures, Treatise on estuarine and coastal science 8 (2011), 17-41
[5] Glasby, T. and Connell, S., Urban structures as marine habitats, Ambio 28 (1999), 595-598
[6] Mineur, F. et al, Changing coasts: marine aliens and artificial structures, Oceanography And Marine Biology: An Annual Review 50 (2012), 1027-1051
[7] Dennis, H.D. et al, Reefcrete: Reducing the environmental footprint of concretes for eco-engineering marine structures, Ecological Engineering (2017)
[8] Risinger, J.D., Biologically dominated engineered coastal breakwaters, PhD Thesis, Louisiana State University and Agricultural and Mechanical College (2012)
[9] Guilbeau, B.P. et al, Algae attachment on carbonated cements in fresh and brackish waters—preliminary results, Ecological Engineering 20(4) (2003), 309-319
[10] Bertos, M.F. et al,A review of accelerated carbonation technology in the treatment of cement-based materials and sequestration of CO_2, Journal of Hazardous Materials 112(3) (2004), 193-205
[11] Pacheco-Torgal, F. and Jalali, S., Cementitious building materials reinforced with vegetable fibres: A review, Construction and Building Materials 25(2) (2011), 575-581
[12] Pack, S.W. et al, Prediction of time dependent chloride transport in concrete structures exposed to a marine environment, Cement and Concrete Research 40(2) (2010), 302-312
[13] Cheewaket, T. et al, Long term performance of chloride binding capacity in fly ash concrete in a marine environment, Construction and Building Materials 24(8) (2010), 1352-1357
[14] Evans, A.J. et al, Drill-cored rock pools: an effective method of ecological enhancement on artificial structures, Marine and Freshwater Research, 67(1) (2016), 123-130
[15] National Standards Authority of Ireland, EN 12390-3: Testing hardened concrete: compressive strength of test specimens, (2012)
[16] NordTest, NTBuild 492. Method for chloride migration coefficient from non-steady state migration experiments in concrete, mortar, and cement-based repair materials (1999)
[17] Poulsen, S.L. and Sørensen, H.E., Chloride ingress in old Danish bridges. In Proceedings 2nd International Congress on Durability of Concrete (ICDC), New Delhi, India(2014)
[18] Attari, A., McNally, C. and Richardson, M.G., A probabilistic assessment of the influence of age factor on the service life of concretes with limestone cement/GGBS binders, Construction and Building Materials 111(2016), 488-494
[19] Luping, T. and Nilsson, L.O., Rapid determination of the chloride diffusivity in concrete by applying an electric field, Materials Journal 89(1) (1993), 49-53
[20] McNally, C. and Sheils, E., Probability-based assessment of the durability characteristics of concretes manufactured using CEM II and GGBS binders, Construction and Building Materials 30 (2012), 22-29

SynerCrete'18 International Conference on Interdisciplinary Approaches
for Cement-based Materials and Structural Concrete
24-26 October 2018, Funchal, Madeira Island, Portugal

AMINO-ALCOHOLS AS CORROSION INHIBITORS AGAINST SULPHATE-INDUCED CORROSION OF MILD STEEL REINFORCEMENT IN FRESH CALCIUM SULPHOALUMINATE BASED CEMENTITIOUS MATERIALS: PRELIMINARY STUDIES

Yegor Morozov [(1)], Simone Pellegrini [(2)], Sergio Lorenzi [(3)], Fátima Montemor [(1)]

(1) Centro de Química Estructural, Instituto Superior Técnico, Universidade de Lisboa, Lisbon, Portugal
(2) Security Building Service S.R.L., Via Santi Filippo e Giacomo, Covo (Bergamo), Italy
(3) Department of Engineering, University of Bergamo, Bergamo, Italy

Abstract

Calcium sulphoaluminate cements (CSA) are unique in properties and application. However, despite numerous advantages, the corrosion of mild steel reinforcement in fresh CSA mortars and concretes at early stages of binder hydration, caused by the combination of low pH and high concentration of dissolved sulphates, is their greatest limitation. Thus, the elimination of rebar corrosion is the indispensable requirement for wide market acceptance and successful application of CSA in construction practice. In this regard, the use of corrosion inhibitors seems to be the most promising solution, considering cumulatively the ease of their introduction into existing construction practice, expected corrosion prevention efficiency, and costs, supported by the fact that they would be required only for short periods.

The performance of corrosion inhibitors of amino-alcohol family was briefly assessed by electrochemical impedance spectroscopy in simulating alkaline solutions containing sulphates. In this paper 2-aminoethanol (MHEA), diethanolamine (DHEA) and triethanolamine (THEA) as well as commercial corrosion inhibitor blends – Sika® FerroGard®901 (SF901) and Sika® FerroGard®903 (SF903) were tested as preventive repair measure. Highly preliminary results suggested that MHEA and SF903 eliminated sulphate-induced depassivation of steel, providing long-lasting protection of reinforcement, thus they should be addressed in the future for detailed and versatile studies.

1. Introduction

Calcium sulphoaluminate cements are unique. They are in focus as an alternative hydraulic binder with low environmental impact, one tonne of which is accompanied by the release of just 340 kg of CO_2. CSA are perfect for pre-cast construction due to high early strength and rapid hardening [1], which together with high frost resistance of fresh binders make them attractive for cold weather construction. CSA mortars and concretes evidence limited shrinkage in shrinkage-compensating formulations, or could be used to make self-stressing concrete [1-3]. However, the principal difference with respect to ordinary Portland cement (OPC) is the intrinsic immunity of CSA-based materials against sulphate attack [4], which together with lower porosity [5], can result in improved durability and higher performance. In addition, CSA binders are less alkaline compared to OPC, being suitable for glass-fibre cement composites [1]. However, CSA concretes could be more susceptible to carbonation with an adverse effect on the passivation of steel reinforcement, as it has been proven for blended cements . Long-term durability of CSA in terms of steel reinforcement corrosion is not well documented yet [1]. Therefore in our previous work, the behaviour of mild steel was studied in simulating solutions of wide pH-sulphate combinations to obtain sulphate – pH corrosion diagram, over which reported ranges of pore solution composition for pure CSA and OPC binders estimated after 30 minutes and 85 days after initiation of hydration [2, 6-8] were superimposed.

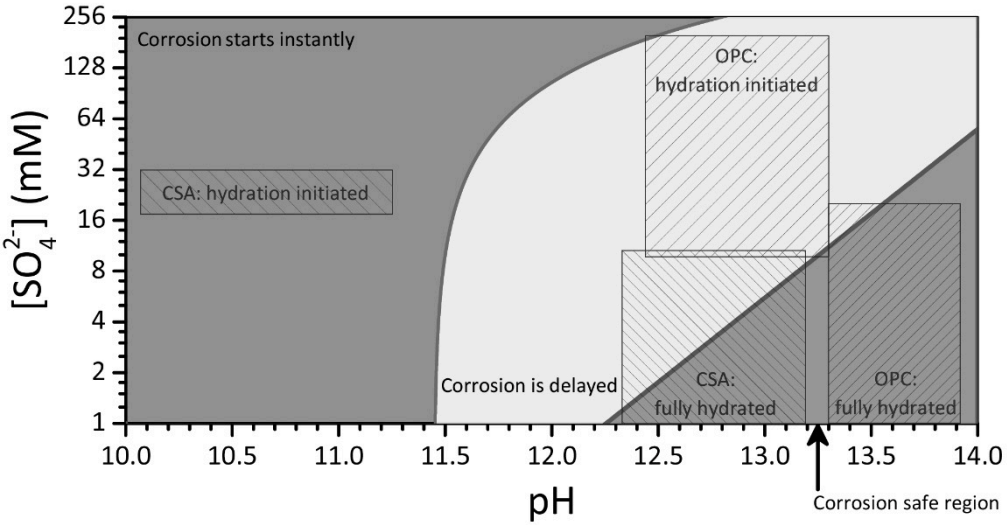

Figure 1: Schematic sulphate - pH corrosion diagram of mild steel

Previous preliminary findings suggest that the sulphate-induced corrosion of common mild steel reinforcement is very likely to happen and will start instantly in pure CSA binder at early stages of hydration (Fig. 1), though the conditions found in fully hydrated state are favourable for steel passivation, unlike to OPC-based mortars and concretes. In addition, it has been proven that once initiated, the corrosion of steel reinforcement proceeded further, and repassivation could not be observed even after favourable conditions were met.

Therefore, despite numerous advantages, the corrosion of mild steel reinforcement in fresh CSA mortars and concretes, caused by the combination of low pH and high concentration of dissolved sulphates, is their greatest limitation. Therefore, preventive or corrective solutions are of the greatest demand, since the elimination steel reinforcement corrosion in CSA-based

cementitious materials during binder hydration is the indispensable requirement for wide market acceptance, and successful application of CSA in construction practice.
Among various preventive repair approaches to diminish the risk of concrete cracking and extend the service life of CSA-based reinforced structures, the use of corrosion inhibitors to stop sulphate-induced corrosion of plain low carbon steel seems to be a promising solution, considering cumulatively the costs, the ease of their introduction into existing construction practice, expected corrosion prevention efficiency. Supported by the fact that inhibitors would be required just for short periods of initial binder hydration, they could be used in smaller quantities. Previously amino-alcohols were reported to be effective corrosion inhibitors against chloride-induced corrosion of steel reinforcement, as they create protective adsorption layer on steel surface, thereby competing with chloride ions that cause passive oxide film thinning and disruption followed by pitting corrosion propagation [9-13]. Thus, we aim to study several amino-alcohols (Fig. 2), such as 2-aminoethanol (MHEA), diethanolamine (DHEA) and triethanolamine (THEA), as well as commercial blends Sika® FerroGard®901 (SF901) and Sika® FerroGard®903 (SF903), as corrosion inhibitors against sulphate-induced corrosion in alkaline solutions, that simulate liquid phase of CSA binder at early hydration stage.

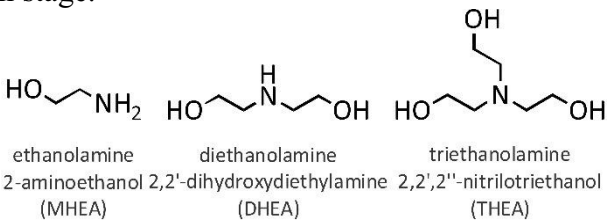

Figure 2: Chemical structures of corrosion inhibitors

2. Materials and experimental procedures

Low carbon steel CK45K reinforcement rebar (in wt.%: C 0.4, Mn 0.7, Si 0.2, S max. 0.05, P max. 0.05, balance – Fe) of 1.2 cm in diameter was cut perpendicularly to the axis with a water-cooled circular sand saw. Copper wire was attached to the inner side of steel piece with a silver paint, and the pieces were embedded into epoxy resin. Samples were polished under water using SiC papers up to 1000 grit at 500 rpm, rinsed with deionized water and ethanol, dried with compressed air. Finally, 3M™ Scotchrap™ 50 tape was applied over polished surface, defining the exposed area of 0.24 cm^2. At least three identical samples were prepared for all the tests and conditions.
Corrosion tests were performed in 0.316 mM NaOH solution, containing 10.0 mM of K_2SO_4 and corrosion inhibitors – MHEA, DHEA or THEA of 50 mM; or 12 kg/m^3 of SF901 or SF903. MHEA, DHEA, and THEA were purchased from Sigma-Aldrich, while SF901 and SF903 were kindly provided by Sika Portugal. All reagents were used without further modification.
The corrosion behaviour of steel samples in the presence of inhibitors was studied mainly by electrochemical impedance spectroscopy (EIS) [10, 13-15]. EIS tests were performed in three-electrode arrangement (Pt wire as a counter electrode, saturated calomel electrode as a reference electrode, and steel sample as a working electrode) using Autolab PGSTAT302N by applying single sinusoidal potential perturbations of 10 mV (rms) versus open circuit potential within frequency range 50 kHz to 5 mHz. The EIS data were fitted by ZView 3.5a software.

3. Results and discussion

As expected from our previous findings, the corrosion of mild steel started instantly when it was placed into sulphate-rich media, as evidenced by low impedance values. Both $|Z|_{5mHz}$, proportional to polarization resistance, R_P, and $|Z|_{1\text{-}10Hz}$, proportional to passive film resistance, R_{PF}, decreased with time, and bode phase angle plot suggested the depression of capacitive response of the passive film. On the other hand, in the presence of 50 mM MHEA (Fig. 3), initial (1 h) $|Z|_{5mHz}$ was 182 kOhm·cm^2 compared to 3.7 kOhm·cm^2 for the reference sample. They values increased with immersion time, after 50 hours reaching MOhm·cm^2 – a level normally observed for mild steel in passive state, and stabilizing at 1.5-1.6 MOhm·cm^2 after 15 days of immersion. Middle frequency impedance values also increased with time, reaching 4.3 kOhm·cm^2 (3.15 Hz) on 23rd day. Thus, progressive development of the passive film and its capacitive behaviour, evidenced from phase angle Bode plot (Fig. 3), was clearly observed. However, pH of the solution was higher (11.32), when compared to the reference sample (pH 10.44), and this had to be considered in evaluation of corrosion inhibition efficiency [18]. Therefore, steel exposed to 3.16 mM NaOH (pH 11.46) solution containing 10.0 mM of K_2SO_4 was tested. It was found that rebars were subjected to severe corrosion, and EIS spectra were close to 0.316 mM NaOH, suggesting that in the case of MHEA a specific metal-inhibitor interaction is responsible for corrosion protection.

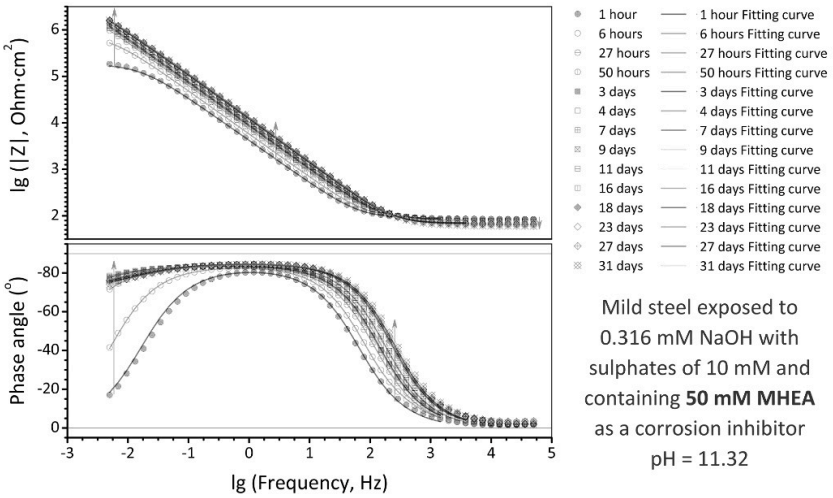

Figure 3: EIS spectra of mild steel exposed to sulphates in the presence of 50 mM MHEA

Like MHEA, DHEA showed similar behaviour in the beginning, evidenced by high $|Z|_{5mHz}$ values – 240 and 646 kOhm·cm^2 after 1 and 6 hours, but after 7 hours values decreased abruptly till 2.3 kOhm·cm^2, suggesting corrosion onset, as passive film disrupted, indicated by $|Z|_{1\text{-}10Hz}$. Since depassivation occured earlier than 3 days of immersion, as it is required for favourable conditions to reach naturally during hydration, DHEA coud not be used. The addition of THEA, on the other hand, did not show any improvement at all. In particular, observed $|Z|_{5mHz}$ were 1.77, 1.45 and 1.15 kOhm·cm^2, when compared to 2.87, 1.29 and 1.26 kOhm·cm^2 for blank sample after 6 hours, 1 and 2 days. Same behaviour was observed in middle frequency range.

Sika® FerroGard®901 and Sika® FerroGard®903 are commercial products initially designed to prevent chloride-induced corrosion of steel reinforcement. SF901 is a concrete admixture, i.e.

added during fresh concrete preparation (12 kg/m^3), being therefore more suitable for the intended application under consideration. SF903, on the other hand, is an impregnating solution, which is applied over concrete surface (0.5 kg/m^2), thus the dosage to be tested was unclear, but 12 kg/m^3 was fixed for both.

Regardless of high expectations, SF901 was not able to provide neither short- nor long-term protection of steel reinforcement against sulphate-induced corrosion even at relatively high dosage. $|Z|_{5mHz}$ values were close to ones observed for the reference sample, being 1.60, 1.71 and 1.36 kOhm·cm^2 after 6, 23 and 46 hours of immersion. SF903, on the other hand, showed perfect protection against sulphate-induced corrosion (Fig. 4), similarly to MHEA (Fig. 3). Both $|Z|_{5mHz}$ and $|Z|_{3.15Hz}$ increased with time, reaching stable values after ca. 11 - 16 days. In particular, observed $|Z|_{5mHz}$ (Fig. 4) values were 0.182, 0.758, 0.99, 1.43 and 1.51 MOhm·cm^2 after 1 hour, 1, 2, 12 and 31 days, indicating no corrosion of steel, highly capacitive response pointed out the existence and development of intact passive film. Such high corrosion protection performance, despite pH of 9.69 (Fig. 4), lower than that for the reference sample tested in the absence of corrosion inhibitor, confirming specific metal-inhibitor interaction.

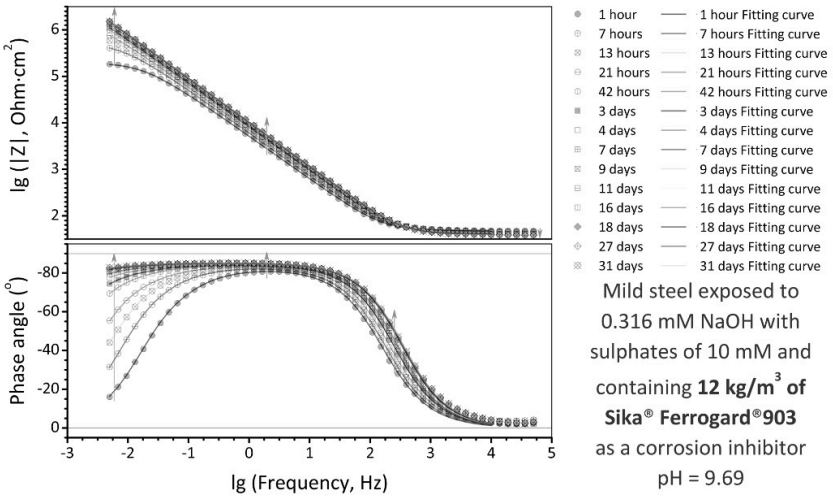

Figure 4: EIS spectra of mild steel exposed to sulphates in the presence of SF903

4. Conclusions and Future work

In the current paper, the use of corrosion inhibitors to mitigate corrosion of plain carbon steel reinforcement in fresh calcium sulphoaluminate based materials, and consequently reduce the risk of the formation of concrete cracks was studied as a preventive method. Various amino-alcohols were assessed as corrosion inhibitors against the destructive action of sulphate ions in alkaline media, simulating a liquid phase of calcium sulphoaluminate binders at early stage of cement hydration. Among tested, 2-aminoethanol and Sika® FerroGard®903 have proven their high corrosion inhibition performance both in short- and long-term, providing cheap, robust, and elegant technological solution for the intrinsic incompatibility of carbon steel reinforcement with calcium sulphoaluminate binders. Nevertheless, these agents have to be comprehensively studied in the future to elucidate their optimum dosage with respect to the dissolved sulphate content, and to confirm their compatibility with binders to ensure that none of strength and service characteristics of calcium sulphoaluminate based mortars and concrete

were affected by their addition into the fresh mix. On top of that, other compounds will be evaluated in the future studies as corrosion inhibitors for the intended application.

Acknowledgements
The authors acknowledge Fundação para a Ciência e Tecnologia for funding Centro de Química Estructural (UID/QUI/00100/2013) and PhD grant SFRH/BD/88016/2012. In addition, the authors also acknowledge the CA15202 for financial support, and Sika Portugal - Produtos Construção e Indústria, SA. for materials provided.

References

[1] P.C. Aïtcin, Binders for Durable and Sustainable Concrete, Taylor & Francis, 2007.
[2] F. Winnefeld, B. Lothenbach, Hydration of calcium sulfoaluminate cements - Experimental findings and thermodynamic modelling, Cem. Concr. Res., 40 (2010) 1239-1247.
[3] L. Zhang, F.P. Glasser, Hydration of calcium sulfoaluminate cement at less than 24 h, Adv Cem Res, 14 (2002) 141-155.
[4] S. Ioannou, et al., Performance characteristics of concrete based on a ternary calcium sulfoaluminate-anhydrite-fly ash cement, Cem. Concr. Compos., 55 (2015) 196-204.
[5] G. Bernardo, et al., A porosimetric study of calcium sulfoaluminate cement pastes cured at early ages, Cem. Concr. Res., 36 (2006) 1042-1047.
[6] M. Andac, F.P. Glasser, Pore solution composition of calcium sulfoaluminate cement, Adv Cem Res, 11 (1999) 23-26.
[7] L. Pelletier-Chaignat, et al., Influence of the calcium sulphate source on the hydration mechanism of Portland cement–calcium sulphoaluminate clinker–calcium sulphate binders, Cem. Concr. Compos., 33 (2011) 551-561.
[8] P. Chaunsali, Early-age hydration and volume change of calcium sulfoaluminate cement-based binders, Doctor of Philosophy in Civil Engineering Dissertation, University of Illinois, 2015
[9] B. Elsener, et al., Migrating Corrosion Inhibitor Blend for Reinforced Concrete: Part 1 — Prevention of Corrosion, Corrosion, 55 (1999) 1155-1163.
[10] H.E. Jamil, et al., An electrochemical and analytical approach to the inhibition mechanism of an amino-alcohol-based corrosion inhibitor for reinforced concrete, Electrochim. Acta, 48 (2003) 3509-3518.
[11] P. Marcus, et al., Localized corrosion (pitting): A model of passivity breakdown including the role of the oxide layer nanostructure, Corros. Sci., 50 (2008) 2698-2704.
[12] M. Ormellese, et al., A study of organic substances as inhibitors for chloride-induced corrosion in concrete, Corros. Sci., 51 (2009) 2959-2968.
[13] Y. Morozov, et al., Alkanolamines as corrosion inhibitors against chloride-induced corrosion of mild steel in basic media, The European corrosion congress EUROCORR 2015, Graz, Austria, 2015.
[14] K. Hladky, et al., Corrosion Rates from Impedance Measurements - an Introduction, Br. Corros. J., 15 (1980) 20-25.
[15] P. Marcus, F.B. Mansfeld, Analytical Methods In Corrosion Science and Engineering, CRC Press, 2005.

SynerCrete'18 International Conference on Interdisciplinary Approaches
for Cement-based Materials and Structural Concrete
24-26 October 2018, Funchal, Madeira Island, Portugal

ASPECTS OF ACTIVATED FLY ASH: A COMPARATIVE STUDY OF DIFFERENT MECHANICAL TREATMENTS

Alexander Mezhov [(1)], Ursula Pott [(2)], Dietmar Stephan [(2)], Konstantin Kovler [(1)]

(1) National Building Research Institute, Technion – Israel Institute of Technology, Haifa, Israel
(2) Technische Universität Berlin, Berlin, Germany

Abstract
The paper presents a new type of blended binder consisting of Ordinary Portland Cement and mechanochemically activated Fly Ash. The activation was performed by means of three different types of mill: vibratory ball mill, vibratory disc mill and planetary ball mill, in presence of anionic surfactant and without it. Activation was performed until the same surface area was achieved for all the samples regardless of the mill type. The structure of fly ash was characterized by X-ray diffraction and scanning electron microscopy. The properties of blended binder were examined by rheological measurements. It was found that introduction of surfactant in the mill allows to decrease yield stress and viscosity of blended binder up to 45% and 40%, respectively, in comparison to conventional introduction of surfactant. Hydration of blended binder was characterized by ultrasonic measurement and shows predictable retardation effect, that is commonly known for anionic surfactants. Blended binder prepared with fly ash interground with surfactant show higher strength than fly ash activated apart of surfactant.

1. Introduction

Fly ash is a well-known and useful by-product that is being used in concrete technology for many years. When added to ordinary Portland cement (OPC) to create a blended binder, the amorphous silica in FA reacts with $Ca(OH)_2$ and forms C-S-H gel. The usage of FA as supplementary cementitious material (SCM) is limited since it accounts for retarded hydration, delayed setting times and reduced early strength [1]. To increase the benefits of FA usage, several types of activation are used nowadays: chemical activation (mostly by means

of alkaline activators); mechanical activation by its milling; thermal treatment and combined methods.
Mechanical activation of FA has several aspects: decrease in particle size – positively influencing the strength properties [2] due to higher reactivity, and therefore speed up the reaction with $Ca(OH)_2$; increasing the amount of amorphous phase [3].
Various types of mills are commonly used for mechanical activation: vibratory ball mills [4]; planetary ball mills [3], [5] vibratory disk mills [6], etc. In order to improve the efficiency of milling special additives can be used. In the cement production industry these additives are known as grinding aids, and they have been used at the stage of clinker grinding since the 1930s [7]. It has been suggested that in some cases the beneficial action of these modifiers is governed by mechano-chemical activation (MCA) [8]. This technology has already been in use for many years [9] and was also applied for FA activation [10],[11]. For MCA the type of additive plays a critical role. In this project, Polynaphthalene Sulfonate (PNS) was chosen as a surfactant. This choice is based on the past research related to obtaining so-called "Low water demand binders" [12] by milling the cement jointly with an anionic surfactant; in this case PNS.
This research is focused on the mechanical activation of FA by means of three types of milling, using vibratory disc mill (DM), vibratory ball mill (BM) and planetary ball mill (PBM). FA is activated jointly with the surfactant and without it in order to examine mechano-chemical theory as a method for FA activation.

2. Experimental

2.1 Materials

The fly ash is a low calcium fly ash class F, collected from "Orot Rabin" power station (Ashdod, Israel). Mineral compositions are presented in Table 1.

Table 1. Mineral composition of fly ash (by X-ray diffraction).

Phase	Quartz	Hematite	Mullite	Periclase	Lime
Weight, %	15.6	7.3	73.2	2.8	1.1

Cement is CEM I 52,5 R. Commercially available Polynaphthalene Sulfonate was used as a surfactant. Sand is standard according to DIN EN 196-1.

2.2 Methods

2.2.1 Milling protocols are presented below:

- Vibratory disk mill. Grinding media is two disks. Milling time: 1, 5, 15, 30 and 60 min. Milling regime: 5 min milling, 5 min break.
- Vibratory ball mill. Grinding media is stainless cylpebs. Milling time: 15, 30, 60 and 120 min.
- Planetary ball mill (PBM). Fritsch Pulverisette 5 classic line. Milling time: 15, 30, 60 and 120 min. Milling time regime: 5 min milling, 5 min break. The milling speed is 200 rpm.

2.2.2 Specific surface area is measurement according to DIN 1164 by Blaine.

2.2.3 Particle Size Distribution is measured by Malvern Mastersizer 2000.

2.2.4 Casting and curing is performed according to EN 196-1:2016 (E). Water to binder ratio is 0.5. Binder to sand ratio is 1:3. FA substitutes 10% wt. of cement in blended binder. Compressive strength was tested after 28 days of curing.

2.2.5 Rheological measurements are implemented without sand. Water to binder ratio was 0.5. Rheometer: Anton Paar Rotational Rheometer Rheolab QC incorporating a crossed-blade impeller stirrer. The samples for rheological measurements were equilibrated in three intervals: (1) A continuously increasing shear rate of 0 to 50 s^{-1} at an acceleration of 1 s^{-2}. (2) A constant shear rate of 50 s^{-1} for 50 s. (3) The rheology measurement was performed with the shear rate being increased from 0 to 100 s^{-1} at a rate of 1 s^{-2}.

2.2.6 Ultrasonic measurements are performed by Ultrasonic Measuring Test System IP-8, UltraTest GmbH. The US frequency of 25 kHz of the transmitter was performed by the piezoelectric effect with an excitation voltage of 600 V. During the measurements, the development of the P-wave velocity was recorded over a period of 48 h each 60 s.

3. Results and Discussion

3.1 Milling

FA is activated in three types of mill with subsequent measurement of specific surface area and finesses. Milling was performed until all the powders achieved the same specific surface by Blaine, around 770±10 m^2/kg, while the initial specific surface area of FA was 360 m^2/kg. The particle size and milling time are presented at Table 2. The samples were milled jointly with PNS (# 3; 5; 7) and a part of it (# 2; 4; 6).

Table 2. Median particle size and milling time of activated fly ash.

#	Samples	Median Particle Size, μm	Milling time, min
1	Fly Ash	31.1	0
2	DM FA	8.8	5
3	DM (FA+PNS)	7.6	5
4	BM FA	8.3	60
5	BM (FA+PNS)	7.2	60
6	PBM FA	8.4	120
7	PBM (FA+PNS)	6.9	120

The morphology of activated FA is presented in Fig. 1. It can be seen that morphology of FA is independent from presence of PNS during the activation.

3.2 Rheology

Rheological curves of blended binders are presented in Fig. 2. Partial replacement of cement to non-activated FA leads to decreasing of viscosity.

All the curves were calculated by means of the standard Bingham model. The values of yield stress and viscosity are given in Tab.3. Interestingly, yield stress and viscosity are strongly related with type on introduction of PNS. The samples 4, 7 and 10 were prepared with

chemically introduced PNS (dissolved in water), while the samples 5, 8 and 11 - with mechano-chemically introduced PNS. The contrast between chemical and mechano-chemical introduction of PNS is clearly seen: yield stress and viscosity of the pastes dosed with mechano-chemical introduction of PNS decreased up to 45% and 40%, respectively.
It was also found that mechano-chemical introduction had a positive influence on strength (Tab. 3). FA activated in BM and PBM jointly with PNS had 10% higher strength (the samples 8 and 11), than the samples dosed with chemically introduced PNS. Nevertheless, all the samples regardless the way of PNS introduction had lower strength, than activated FA. This fact is related to retardation effect of PNS.

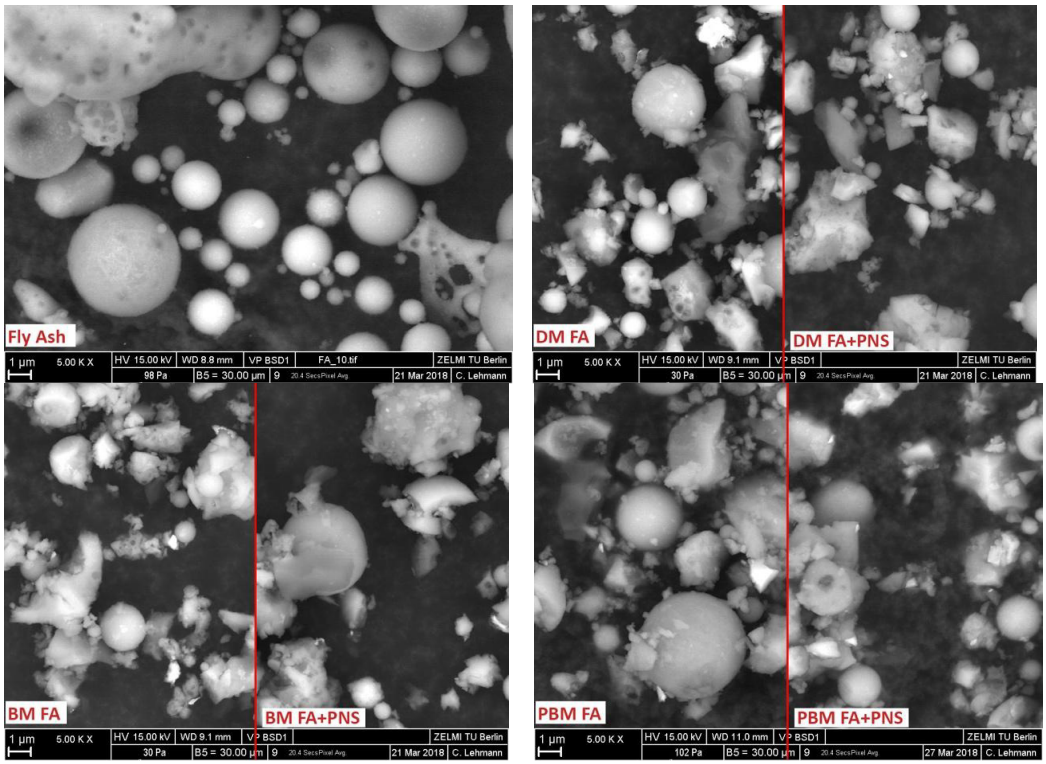

Figure 1: morphology of fly ash activated in different types of mills.

Table 3: Yield stress, viscosity and compressive strength of blended binders.

#	Samples	Yield Stress, Pa	Viscosity, mPa·s	Compressive Strength (28 days), MPa
1	Cement	430	2678	69.3
2	C + FA	400	2000	63.3
3	C + DM FA	475	2239	59.0
4	C + DM FA+PNS	191	1850	62.3
5	C + DM (FA+PNS)	98	1056	61.7
6	C + BM FA	466	2840	66.7
7	C + BM FA+PNS	261	1346	62.7
8	C + BM (FA+PNS)	145	1029	66.0
9	C + PBM FA	452	2477	67.3
10	C + PBM FA+PNS	159	1372	60.3
11	C + PBM (FA+PNS)	100	1031	63.7

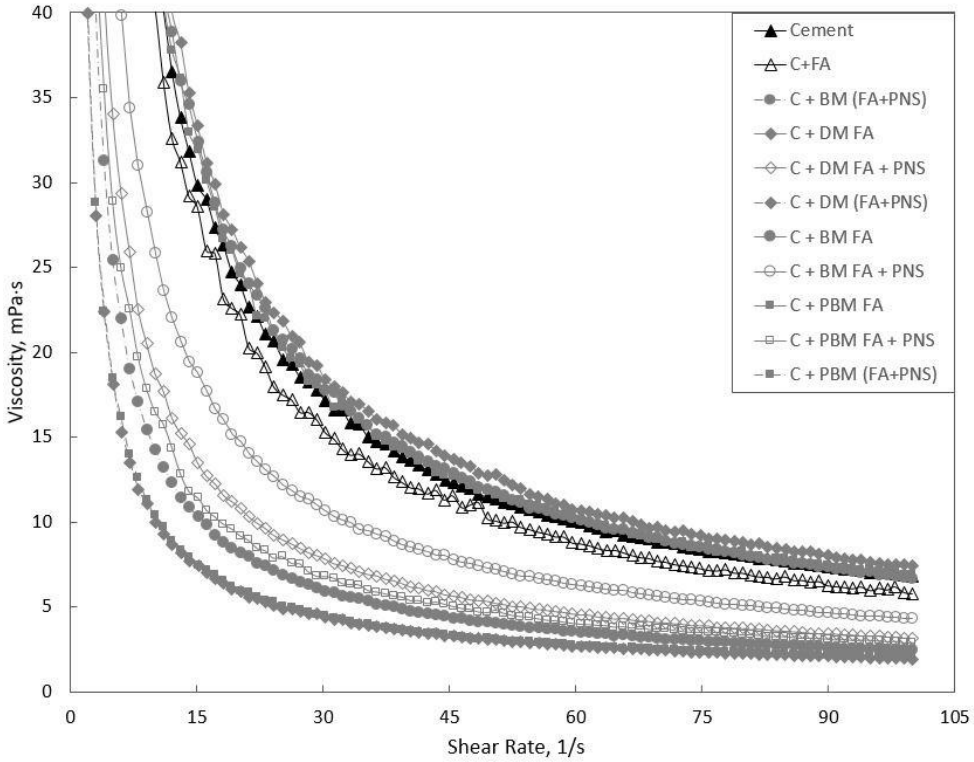

Figure 2: Viscosity of fly ash activated in different types of mills.

3.3 Ultrasonic measurements

Hydration of blended binders is characterised by ultrasonic velocity that is presented in Fig. 3. Cement without any surfactant and FA has the highest rate of hydration. Substitution of cement to FA has a retardation effect due to the pozzolanic reaction. Once the PNS is introduced in the blended binder, it exhibits the slowest hydration rate regardless the type of the mill and the method of PNS introduction. Apparently, this phenomenon occurs due to overlapping of the two retardation effects: one from the FA and another one from the PNS itself.

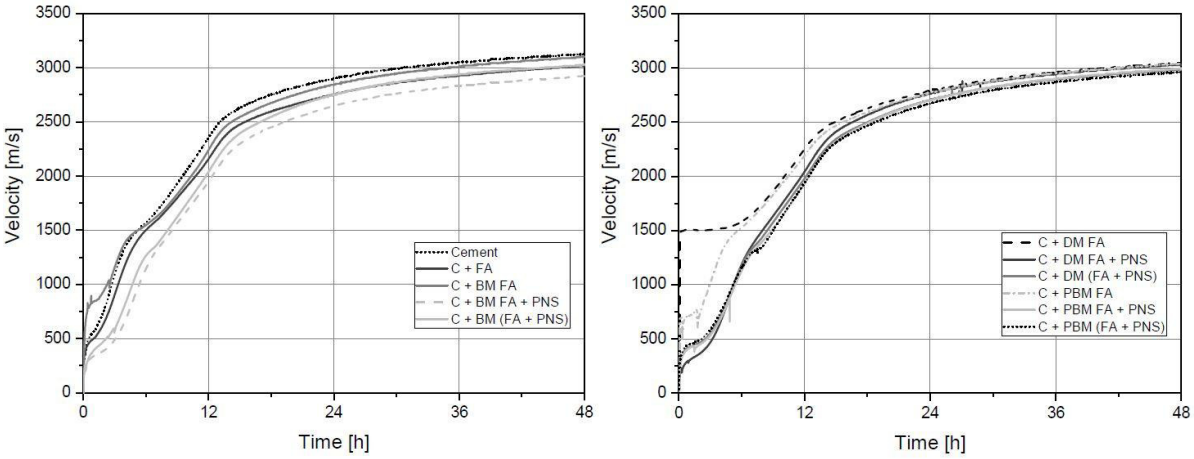

Figure 3: Ultrasonic velocity of blended binders.

4. Conclusions

1. Changing of specific surface area is related with mill type and independent from the presence of PNS into the mill.
2. Introduction of PNS in the mill allows to decrease yield stress and viscosity of blended binder up to 45% and 40%, respectively, in comparison to conventional introduction of surfactant.
3. Blended binder prepared with fly ash interground with surfactant show higher strength than fly ash activated apart of surfactant.
4. Regardless of the type of introduction, presence of PNS diareses the strength, due to retardation effect.

Acknowledgments
This research was accomplished in the framework of Short Term Scientific Mission sponsored by COST Action TU 1404 "Towards the next generation of standards for service life of cement-based materials and structures".

References

[1] D. P. Bentz and C. F. Ferraris, "Rheology and setting of high volume fly ash mixtures," Cem. Concr. Compos., vol. 32, no. 4, pp. 265–270, 2010.
[2] G. Li and X. Wu, "Influence of fly ash and its mean particle size on certain engineering properties of cement composite mortars," Cem. Concr. Res., vol. 35, no. 6, pp. 1128–1134, 2005.
[3] D. K. Rajak, A. Raj, C. Guria, and A. K. Pathak, "Grinding of Class-F fly ash using planetary ball mill: A simulation study to determine the breakage kinetics by direct- and back-calculation method," South African J. Chem. Eng., vol. 24, pp. 135–147, 2017.
[4] S. Kumar and R. Kumar, "Mechanical activation of fly ash: Effect on reaction, structure and properties of resulting geopolymer," Ceram. Int., vol. 37, no. 2, pp. 533–541, 2011.
[5] A. G. Patil and S. Anandhan, "Influence of planetary ball milling parameters on the mechano-chemical activation of fly ash," Powder Technol., vol. 281, pp. 151–158, 2015.
[6] A. Terzić, N. Obradović, L. Andrić, J. Stojanović, and V. Pavlović, "Investigation of thermally induced processes in corundum refractory concretes with addition of fly ash," J. Therm. Anal. Calorim., vol. 119, no. 2, pp. 1339–1352, 2015.
[7] Z. Sun et al., "Preparation of polycarboxylate-based grinding aid and its influence on cement properties under laboratory condition," Constr. Build. Mater., vol. 127, pp. 363–368, 2016.
[8] K. Sobolev, "Mechano-chemical modification of cement with high volumes of blast furnace slag," Cem. Concr. Compos., vol. 27, no. 7–8, pp. 848–853, 2005.
[9] P. Balaz, Mechanochemistry in Nanoscience and Minerals Engineering. Springer-Verlag, Berlin-Heidelberg, 2008.
[10] G. Intini, L. Liberti, M. Notarnicola, and F. D. I. Canio, Mechanochemical Activation of Coal Fly Ash for Production of High Strength Cement Conglomerates, vol. 17, pp. 557–561, 2009.
[11] M. Sadique, H. Al-Nageim, W. Atherton, L. Seton, and N. Dempster, "Mechano-chemical activation of high-Ca fly ash by cement free blending and gypsum aided grinding," Constr. Build. Mater., vol. 43, pp. 480–489, 2013.
[12] V. R. Falikman, V.R., Bashlykov, "Law water demand binder technology for environmental friendly cements with low clinker content," 2011, pp. 633–642.

SynerCrete'18 International Conference on Interdisciplinary Approaches
for Cement-based Materials and Structural Concrete
24-26 October 2018, Funchal, Madeira Island, Portugal

ASSESSMENT OF INTERNAL RELATIVE HUMIDITY AND TEMPERATURE OF CEMENT-BASED MATERIALS – PARALLEL STUDY USING TWO SENSOR SYSTEMS

Martin Klun [(1)], Violeta Bokan Bosiljkov [(1)], Samo Beguš [(2)], Slaven Ranogajec [(2)], Zvonko Jagličić [(1), (3)]

(1) University of Ljubljana, Faculty of Civil and Geodetic Engineering, Ljubljana, Slovenia
(2) University of Ljubljana, Faculty of Electrical Engineering, Ljubljana, Slovenia
(3) Institute of Mathematics, Physics and Mechanics, Ljubljana, Slovenia.

Abstract
A custom made sensor system for measuring the temperature and relative humidity inside the cement-based materials (CBMs) was prepared and its functionality compared with a commercially available ConSensor 2.0 system. The obtained results show adequate functioning of the custom made sensor when measuring temperature inside the CBMs. Measurements of relative humidity were not yet compared to reference sensor measurements. However, continuous decrease of relative humidity at accelerated drying of CBM confirmed adequate protection of the sensor and thus its resistance to highly alkaline environment. Additionally, ConSensor 2.0 system was able to follow the cement hydration process through measurements of the CBMs' electrical conductivity (C) in a similar way as the ultrasonic P-waves. Based on the obtained C(t) and dC/dt(t) profiles we were able to estimate initial and final setting times and the time of the most intensive development of the hydration products.

1. Introduction

The sensor system for measuring the temperature and humidity within the cement-based materials currently in the process of development at the University of Ljubljana (UL) consists of a temperature and moisture sensor, the system for acquiring and processing signals, the power supply and the system for wireless data transfer. Since we would like to mix the sensor system into fresh cement-based material, before casting of the material into formwork, the system has to be wireless, of suitable dimension (size range of a few cm), with long-term

operation and resistance to environmental effects (water, alkaline environment). Denotation CM sensor system will be used for this product, where CM stands for "custom made".

The first version of the CM sensor system is available for testing. We decided to carry out parallel tests using the CM sensor system and commercially accessible ConSensor 2.0 system [1], which measures temperature and conductivity of the cement-based materials (CBMs). Compositions of CBMs used for the testing are the same as those in the RRT+ programme of the COST TU1404 Action [2].

The paper presents and discusses results of obtained measurements. Temperature profile T(t) inside the CBMs, measured by using the CM sensor, is compared to the T(t) profile of the ConSensor 2.0 system. Relative humidity profile RH(t) of the CBMs is presented as measured by the CM sensor. It has not yet been compared to reference sensor measurements. Moreover, the development of electrical conductivity of the tested CBMs measured by the ConSensor 2.0 system is presented and analysed, in order to determine characteristic phases during setting and hardening of the CBMs.

2. Experimental Setup

Two different CBM mixtures, namely, a modified ordinary mortar (MOM) and modified cement paste (MCP), were used to monitor the process of hydration.

2.1 Custom made sensors

The multichannel measuring system was composed of eight combined temperature and relative humidity sensors and a main data logging unit (Raspberry Pi3). The sensing probes were capacitive sensors with digital I2C interface (SHT25 by Sensirion) enclosed in a filter cap for protection against dust, water immersion and against contamination by cement-based material, providing IP67 protection according to the European standard EN 62262 [3]. The built system had an operating range of 0 % to 100 % relative humidity (RH). In order to ensure the least possible structural intrusiveness, the sensor probes were assembled to be physically as small as possible (6 mm × 6 mm × 2 mm). The prototype sensor probes were connected to the main data logging unit by means of extremely thin wired connection leads (4 × 0.1 mm in diameter) to avoid any unwanted thermodynamic effects (air bubble lock, minimised heat flux, capillary action, etc.) from the surface of the material to the sensors.

Prior to immersion of the sensor into cement-based mixtures, the built system was calibrated by comparison in an accredited temperature laboratory at relative air humidity from 10 % to 95 %, while the temperatures were controlled at 20 °C and 40 °C. Maximal measuring errors of the sensors were below 2.5 % RH and standard uncertainties better than 2.2 % RH.

2.2 Specimens

Table 1: Shortcut for the combinations of the two mixtures and two sensors in each mixture.

ConSensor (CS) (temperature, conductivity)	Custom made sensor (CM) (temperature, RH)
MOM1-CS	MOM1-CM
MOM2-CS	MOM2-CM
MCP1-CS	MCP1-CM
MCP2-CS	MCP2-CM

Fig. 1 shows the position of sensors in a mould made of extruded polystyrene. Each specimen is of size 10 cm × 5 cm × 15 cm. For each mixture (MOM and MCP) two identical specimens were prepared, each with an inbuilt CS sensor and a CM sensor. Altogether four specimens were prepared. The short names assigned to each combination of particular mixture and sensor are collected in Tab. 1.

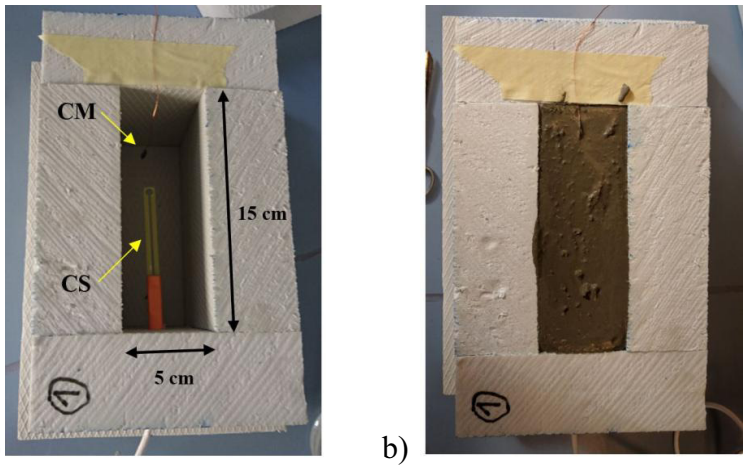

a) b)

Figure 1: Positions of sensors in a specimen with a height of 10 cm (a), and an image after casting the mixture (MOM or MCP) (b).

3. Results and discussion

The time dependent temperatures of two MOM and two MCP specimens are shown in Fig. 2. Time t = 0 is the time when casting of particular specimen was finished. The temperature profiles are almost identical for all four sensors in each CBM mixture, confirming correct functioning of the new CM sensors. The maximal temperature is higher when measured with the CM sensors, by about 5°C (7%) and up to 1°C (2.5%) for the MCP and MOM compositions, respectively. It results from the competition between the heat generated by the cement hydration and the heat transfer between the specimen and the environment. For the "massive" CS sensor the heat transfer to the environment is increased compared to the CM sensor, which results in a lower maximal temperature measured by the CS sensor. The CM sensors are connected to the main data logging unit with four tiny copper wires that provide only negligible heat flux.

The time dependent conductivity $C(t)$, measured by the CS sensor, and its time derivative $dC/dt(t)$ are shown in Fig. 3 a), b), and c), for the MOM and MCP mixtures. Also temperature-time ($T(t)$) profiles are presented, together with the $dC/dt(t)$ diagrams. From the results given in Fig. 3 we can see excellent correlation between the $dC/dt(t)$ and $T(t)$ profiles.

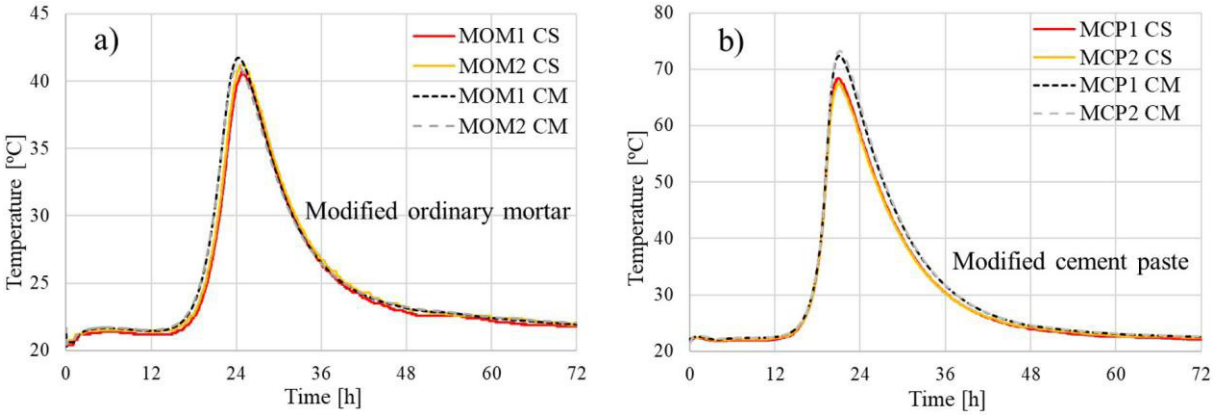

Figure 2: Temperatures of two MOM specimens (a) and two MCP specimens (b).

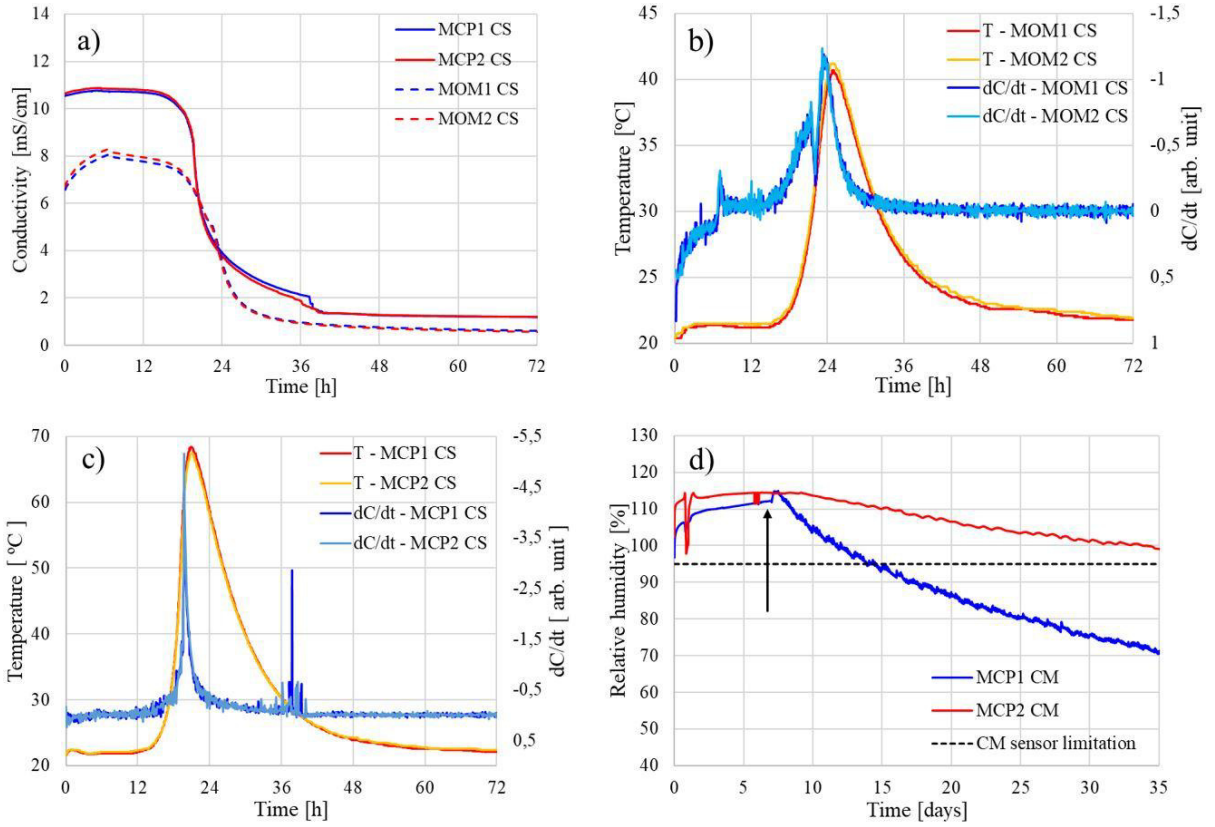

Figure 3: Time dependent conductivity (a), time dependent temperature (the same data as in Fig. 2 for CS sensors) and time derivative dC/dt for MOM specimens (b) and MCP specimens (c). Relative humidity of MCP specimens in a long term scale (d). The arrow denotes the time when the MCP1specimen was put on the electric heater.

Vogrič et al. [4] show that five characteristic time periods of the cement hydration process, defined by different characteristic points (initial and final setting time, percolation of solid phases, de-percolation of water saturated pores, and the time of the most intensive solidification process) that appear on typical v_P(t) profile, where v_P presents velocity of US P-waves, also appear on the $C(t)$ profile. By considering the correlation between these two profiles given in [4], we can estimate initial setting time (t_I), final setting time (t_F) and the most intensive development of the hydration products (CP4), from the $C(t)$ and $dC/dt(t)$ profiles in Fig. 3 b) and c). The CP4 time corresponds to the time at the minimum value of the $dC/dt(t)$ profile. The obtained values are given in Tab. 2.

Table 2: Initial (t_I) and final (t_F) setting times and the time of the most intensive development of the hydration products (CP4).

	MCP	**MOM**
t_I [hours]	12 - 13	15.5
t_F [hours]	15 - 16	17.5
CP4 [hours]	19.5 – 20.5	23.2 – 24.4

Initial and final setting times of the MOM reported by Staquet and Serdar [5] are 13.15 and 14.82 hours, respectively. We can see that in our case the cement hydration process was slower, which can be due to two years older cement sample used for the tests by the UL. Moreover, the most intensive development of the hydration products was close to 20 and 24 hours for the MCP and MOM mixture, respectively.

Finally, long term functioning and stability of the CM sensors were examined by the measurements of relative humidity (Fig. 3 d). In all but one specimen the relative humidity was above 95 % during the first month of the measurements. Here we wish to point out again that the CM sensors were calibrated up to 95 % RH, at 20 °C and 40 °C. The reported values above 100 % RH in Fig. 3 d) are meaningless and mean only that the sensors were saturated. On day 7, after the casting (marked with an arrow in Fig. 3 d), specimen MCP2 was demolded and put on an electric heater that maintained temperature of the specimen, measured by the CM sensor, at 35±1 °C. This is the reason for accelerated drying of this specimen which was detected by the CM sensor. At time t = 14 days the measured RH drops below 95 % and an exponential-like decrease of measured RH can be observed in Fig. 3 d). With this approach we were able to confirm the appropriate protection of the CM sensors against alkali environment in fresh mortar and cement paste. Moreover, obtained RH profiles in Fig. 3 d) are very similar to the internal RH development in cement paste specimens at 20 °C reported in [6]. However, further tests and comparison with the reference RH sensor are needed in order to confirm correct working of the CM sensor when measuring relative humidity inside the CBMs.

5. Conclusion

Test results presented in the paper show that custom made CM sensors were able to measure the development of the temperature inside particular CBM mixture correctly, since the temperature profiles measured by the CM sensors are almost identical to the same profiles measured by the commercial CS sensors. Moreover, by adopting accelerated drying of the selected MCP specimen we were able to follow also continuous decrease of the relative humidity with time inside the MCP specimen. In this way we confirmed that the used protection system of the CM sensor is adequate, since the sensor is resistant to high alkaline environment.

ConSensor 2.0 system was able to follow the early age evolution of the CBMs properties through measurements of the CBMs' electrical conductivity as function of time. The obtained results are in very good correlation with the measurements of P-wave propagation through the CBMs. Based on this correlation we were able to determine initial and final setting time and the time of the most intensive development of the hydration products, for MCP and MOM mixtures.

Acknowledgements

This work was financially supported by the Slovenian Research Agency through Research Project J2-8194, Programme Group P2-0185, and PhD project of Martin Klun.

References

[1] Van Breek, A., Dielectric properties of young concrete, Non-destructive dielectric sensor for monitoring the strength development of young concrete, PhD thesis, Delft University (2000)

[2] Staquet, S. et al., RRT+ Main phase of the Extended Round Robin Testing programme for TU1404, Testing protocols, Ver. 22th November 2016, (2016) 57p

[3] EN 62262, Degrees of protection provided by enclosures for electrical equipment against external machanical impacts (IK code), CEN, EU (2002)

[4] Vogrič, N. et al., Experimental monitoring of early formation of cement paste structure, Gradbeni vestnik 66 (2017), 307-313 (in Slovenian language)

[5] Staquet, S. and Serdar, M., Extended Round Robin Test RRT+ Main Phase, PPT presentation, COST TU 1404 Zagreb meeting, Croatia (2016)

[6] Chen, H. et al., Prediction of self-desiccation in low water-to-cement ratio pastes based on pore structure evolution, Cem Concr Res 49 (2013), 38-47

SynerCrete'18 International Conference on Interdisciplinary Approaches
for Cement-based Materials and Structural Concrete
24-26 October 2018, Funchal, Madeira Island, Portugal

CARBONATION RESISTANCE OF HIGH-VOLUME FLY ASH (HVFA) MORTAR: EFFECT OF APPLIED CO_2 CONCENTRATION

Philip Van den Heede [(1)], Didier Snoeck [(1)], Tim Van Mullem [(1)], Nele De Belie [(1)]

(1) Magnel Laboratory for Concrete Research, Ghent University, Belgium

Abstract
To save time, the carbonation resistance of cementitious materials is usually assessed in an accelerated manner by exposing the material to CO_2 levels that highly exceed the atmospheric CO_2 concentration. However, a too high acceleration of the carbonation reaction could induce chemical, microstructural and mineralogical changes and excess production of the water reactant that are unrealistic. In this paper, it was evaluated whether the outcome of colorimetric carbonation experiments at 10% CO_2 for High-Volume Fly Ash (HVFA) mortar could still be used for calculating natural carbonation rates and to do an adequate service life assessment. This seems not true. The effect of full carbonation at 10% CO_2 on the capillary water uptake was also assessed gravimetrically and visually on neutron radiographs. This water uptake was found to be significantly lower than after full carbonation at only 1% CO_2.

1. Introduction

The carbonation resistance of cementitious materials is usually determined through accelerated laboratory experiments. Samples of a composition of interest are exposed to CO_2 levels that significantly exceed the around 0.04% CO_2 present in ambient air, at a given relative humidity (usually 60% RH) and temperature (usually 20°C). At regular time intervals, a number of samples is split and phenolphthalein is sprayed onto the fractured surfaces to visualize the front of the carbonation-induced pH drop. Depending on the test protocol, the applied CO_2 concentration can vary from 1 % up to 50 % CO_2 [1]. Today, there is more and more concern that exposure to CO_2 concentrations above 3 % CO_2 may modify the whole carbonation process too much [2]. Subsequent conversion of the result to a realistic natural carbonation rate using the often used calculation approach of Sisomphon and Franke [3] could highly underestimate the actual carbonation rate and the related service life in environments where carbonation-induced steel corrosion is a dominant mechanism, and this due to (i)

chemical, microstructural and mineralogical changes affecting the permeability, and (ii) excess water production during carbonation causing pore blocking [1, 4-7]. For now, it remains unclear which of these mechanisms is more dominant for potentially 'green' binder systems in which large cement portions are replaced by fly ash to lower cement related CO_2 emissions [1]. In this paper, it has been evaluated for High-Volume Fly Ash (HVFA) mortar to what extent natural carbonation rates estimated from experiments conducted at 10% CO_2 underestimate those estimated from tests conducted at 1% CO_2 and the atmospheric CO_2 concentration and how probabilistic service life predictions for carbonation-induced steel depassivation are affected by it. Moreover, 2 h neutron radiography monitored capillary sorption experiments cf. Snoeck et al. [8] were performed to study carbonation-induced changes in capillary water transport properties.

2. Materials and methods

2.1 Mortar mixtures

All tests were performed on HVFA mortar with a low carbonation resistance. The proportioning of the sand and binder for one batch of mortar was the same as for the standard mortar specified in NBN EN 196-1, and amounted to 1350 g and 450 g, respectively. The binder portion consisted for 50% of CEM I 52.5 N and for 50% of class F fly ash. The applied water-to-binder (W/B) ratio equalled 0.55, which is higher than the 0.50 value which is normally prescribed for a standard mortar. A high cement replacement level was used to make sure there was less carbonatable material, i.e. portlandite, available. This ensures a lower buffer capacity for the penetrating CO_2 and thus a faster inward movement of the carbonation front. Increasing the W/B ratio facilitated a higher porosity, and thus also a faster ingress of CO_2.

2.2 Sample preconditioning and carbonation testing

For the colorimetric carbonation tests, a series of mortar cubes (side: 100 mm) were made. After 24 hours in a wet curing chamber at 20°C and 95% RH the cubes were demoulded, whereupon the cubes were stored again in the wet curing chamber until they reached 7 days of age. Then, they were dried in an oven at 40°C for 4 days to ensure a uniform moisture distribution in the cubes. Subsequently, the cubes were carefully wrapped in aluminium tape on all sides except for one exposure side. In this condition, they remained in a climate room at 20°C and 60% RH for 3 days. The next days, the cubes were equally divided among that same climate chamber, the carbonation chamber at 1% CO_2, 20°C, 60% RH, and the carbonation chamber at 10% CO_2, 20°C, 60% RH. At regular time intervals, three cubes were taken out of each chamber for colorimetric carbonation depth assessment using phenolphthalein. The neutron radiography monitored capillary sorption tests were performed on a series of 160×20×40 mm³ prismatic mortar prisms. To make sure these experiments could be performed during an already scheduled measuring campaign at the Paul Scherrer Institute (PSI) in Switzerland, the preconditioning of those samples was somewhat different. Upon demoulding after 24 hours, the samples were immediately exposed to either 1% CO_2 (8 samples) or 10% CO_2 (8 samples) in the carbonation chambers that were mentioned before, and this for 21 days. During this period, CO_2 was able to penetrate the prisms from all sides. Given the fact that the prisms were quite thin, 21 days of exposure to 10% and also 1% CO_2 should normally be sufficient to have fully carbonated samples. Before taking the samples to PSI for testing, the samples were oven dried at 40°C for 4 days. After drying, 3 samples per

test series were split and sprayed with phenolphthalein to verify whether they were indeed fully carbonated. This was the case. The remaining 5 samples per test series were subjected to the neutron radiography monitored capillary sorption tests.

2.3 Probabilistic service life prediction

The time to carbonation-induced steel depassivation was estimated using a very basic limit state function representing the well-known square-root-time relation for carbonation (Eq. (1)).

$$g\left(d, x_c(t)\right) = d - A \cdot \sqrt{t} \tag{1}$$

with d, the concrete cover (lognormal, 35±8 mm), $x_c(t)$, the carbonation depth at time t (years), and A, the carbonation coefficient corresponding with the atmospheric CO_2 concentration (normal, standard deviation (stdv): ±1 mm/√years). Three different values for this carbonation coefficient were to be considered, i.e. the value obtained directly from a natural non-accelerated carbonation test at around 0.04% CO_2, 20°C and 60% RH (A_{atm}), and two estimates as calculated from accelerated carbonation experiments at 1% ($A_{atm\ est\_1\%}$) and 10% CO_2 ($A_{atm\ est\_10\%}$) using Eq. (2)) cf. [3].

$$A_{atm\ est} = A_{acc} \frac{\sqrt{c_{atm}}}{\sqrt{c_{acc}}} \tag{2}$$

with $A_{atm\ est}$, the estimated natural carbonation coefficient representing exposure to the atmospheric CO_2 %, as estimated from accelerated carbonation tests at the same temperature and RH, yet at an elevated CO_2 level (mm/√years), A_{acc}, the carbonation coefficient measured during these accelerated carbonation experiments at elevated CO_2 levels (mm/√years), c_{atm}, the atmospheric CO_2 concentration (around 0.04% CO_2), and c_{acc}, the CO_2 concentrations applied during the accelerated carbonation tests (1% or 10% CO_2). Probabilities of failure (P_f) as a function of time were calculated using the First Order Reliability Method (FORM) available in the probabilistic Comrel software. In accordance with *fib* Bulletin 34 [9], P_f for steel depassivation cannot exceed 0.10. As soon as it does, the end of service life has been reached.

2.4 Neutron radiography monitored capillary sorption tests after carbonation

As mentioned in Section 2.2, two times 5 prisms carbonated at 1% and 10% CO_2, respectively, were subjected to the neutron radiography monitored capillary sorption tests at the PSI. This experiment comprised gravimetric recordings of the water uptake and a visualization of the water penetration front. Just before the start of the test, the sides of the prisms were sealed with aluminium tape, to ensure unidirectional water uptake via the bottom surface. The bottom surface was partially taped so that water could only penetrate via the 100 × 20 mm² central area of that surface. The top 160 × 20 mm² surface of the prisms was not covered with aluminium tape. The initial mass of the prisms was recorded on a Sartorius 238 BP 3100 S balance (0.01 g accuracy). Next, the specimens were put on rods in small water basins. The water immersion depth amounted to ±3 mm. After 2 hours, the prisms were removed from the water basins and their end mass was determined. To combine the gravimetric information with a visualization of the water penetration front during capillary water uptake, the sorption experiments were performed at the thermal neutron imaging facility NEUTRA. This facility is part of the spallation neutron source SINQ of the Paul

Scherrer Institute (PSI) in Switzerland. For more technical details on the beam line and the procedures followed for correction and post-processing of the raw neutron radiographs, we refer to Snoeck et al. [8].

3. Results and discussion

3.1 Colorimetric carbonation assessment

Logically, exposing the studied HVFA mortar to CO_2 levels (10% and 1% CO_2) that highly exceed the atmospheric CO_2 concentration of around 0.04%, results in significantly higher carbonation depths as a function of the square-root-of-time (Figure 1a). The corresponding carbonation coefficients amounted to 15.01 mm/√weeks ($A_{10\%}$), 7.79 mm/√weeks ($A_{1\%}$) and 2.21 mm/√weeks (A_{atm}), respectively. The carbonation coefficient obtained for a CO_2 level of 1%, was estimated using Eq. (2) in which $A_{acc\ and}\ c_{acc}$ equalled $A_{10\%}$ and 10%, and $A_{atm\ est}$ and c_{atm} were replaced with $A_{1\%\ est}$ and 1%, respectively. This gives an estimated carbonation coefficient of 4.75 mm/√weeks (Figure 1b), which is only 61% of the value that was actually measured at 1% CO_2 (7.79 mm/√weeks). This is a first indication that Eq. (2) is not valid for CO_2 concentrations as high as 10%. Furthermore, both $A_{1\%}$ and $A_{10\%}$ were used once as input for the conversion formula (A_{acc}, Eq. (2)). As such, two estimated carbonation coefficients for the atmospheric CO_2 concentration were obtained which could be compared with the actually measured one (Figure 1a: 2.21 mm/√weeks) during the non-accelerated carbonation experiment, i.e. 2.46 mm/√weeks and 0.95 mm/√weeks (Figure 1b). While the former estimated value is quite well in range with the actually measured natural carbonation coefficient of 2.21 mm/√weeks, the latter seems to be substantially lower. Clearly, conducting a carbonation experiment at 10% CO_2 and using Eq. (2) to obtain an estimate for the atmospheric carbonation rate, strongly underestimates the natural carbonation rate for the studied HVFA binder system.

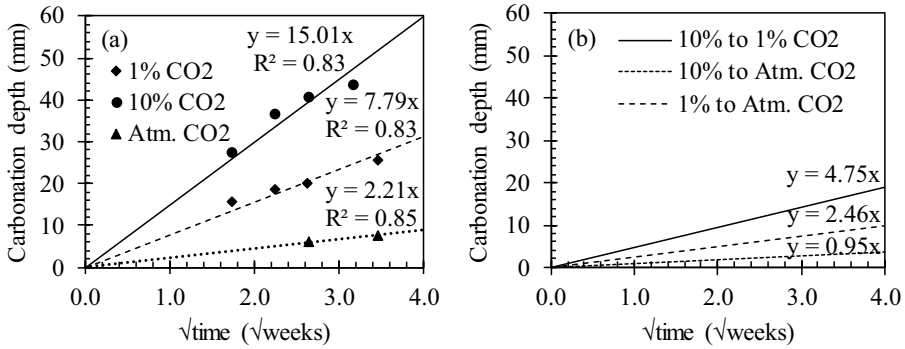

Figure 1: Measured (a) and estimated (b) carbonation coefficients for 1% and 10% CO_2 and the atmospheric CO_2 concentration.

3.2 Service life assessment for carbonation-induced steel depassivation

When using the actually measured carbonation coefficient for the atmospheric CO_2 concentration in the prediction model (Eq. (1)), it would only take around 2.5 years before the carbonation front in the studied HVFA mortar reaches the location of the reinforcing steel at a typical cover depth of 35 mm. A very similar prediction outcome (2 years) was obtained with the estimated $A_{atm\ est\ 1\%}$ value. For conversion of a carbonation coefficient obtained at 1% to a corresponding one for the atmospheric CO_2 concentration, Eq. (2) seems certainly valid. It

gives a reliable service life prediction. This can totally not be done for a carbonation coefficient measured at a CO_2 concentration of 10%. Estimated atmospheric carbonation coefficients calculated from this value underestimate the actual carbonation rate and thus overestimate the potential service life of the HVFA binder system. One would wrongfully assume that it would take about 12.5 years before the carbonation front reaches the reinforcing steel. Subsequent corrosion-induced damage prediction and adequate planning of future repair will for sure be compromised by adopting the latter approach.

3.3 Neutron radiography monitored capillary water uptake after carbonation

The total mass decrease (Δm ↓) of the mortar prisms during the 4-day drying period at 40°C after carbonation was recorded. The same was done for the mass increase (Δm ↑) during the subsequent capillary sorption experiment. The values obtained are presented in Table 1.

Table 1: Gravimetric measurements during pre-drying at 40°C and the 2h capillary sorption test

# Sample	Δm ↓ pre-drying	Δm ↑ capillary sorption	# Sample	Δm ↓ pre-drying	Δm ↑ capillary sorption
a_1%	1.48 g	13.07 g	a_10%	3.68 g	9.64 g
b_1%	1.56 g	12.73 g	b_10%	3.64 g	9.16 g
c_1%	1.57 g	12.77 g	c_10%	3.74 g	9.54 g
d_1%	1.61 g	13.82 g	d_10%	3.64 g	11.20 g
e_1%	1.62 g	14.60 g	e_10%	3.71 g	10.40 g
avg± stdv	1.57±0.06 g	13.40±0.80 g	avg±stdv	3.66±0.06 g	9.99±0.81 g

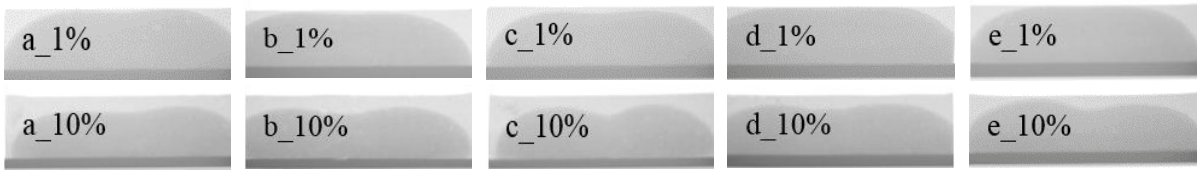

Figure 2: Neutron radiographs of HVFA mortar prisms after full carbonation at 1% or 10% CO_2 and a 2 h capillary sorption experiment.

For both Δm ↓ and Δm ↑, a clear difference could be observed between the prisms that were carbonated at 1% and 10% CO_2. Apparently, 4 days of drying at 40°C after full carbonation at 10% CO_2 results in a significantly higher mass loss (10% CO_2: 3.66 ± 0.06 g versus 1% CO_2: 1.57 ± 0.06 g). The reason for this behaviour remains unclear at the moment. Possibly, this is related to more abundant production of water – a key reactant of the carbonation process besides calcium carbonate – at higher CO_2 levels cf. [6,7]. This excess water should then also be removed during the subsequent drying step. However, this theory needs to be confirmed. Carbonation tests on samples with embedded humidity sensors are ongoing to monitor the excess water production. Another striking observation with regard to the gravimetric measurements relates to the clear difference in mass increase during the 2 h capillary sorption test between samples carbonated at 1% and 10% CO_2. The substantially lower mass increase after full carbonation at 10% CO_2 (9.99 ± 0.81 g versus 13.40 ± 0.80 g at 1% CO_2) implies less water uptake. The corresponding neutron radiographs showing the water penetration fronts not extending over the full height of the specimens further confirm this (Figure 2). From these results, it seems that a more dense and less permeable HVFA mortar is obtained

by carbonating them at 10% CO_2. This finding was not immediately expected, since binder systems with high cement replacement levels, have less portlandite (CH) available which makes them more prone to carbonation of calcium–silicate–hydrates (C–S–H), causing a coarsening of the pore structure and not a densification [4]. Mercury intrusion porosimetry has been planned to see what has happened to the overall porosity and pore size distribution of these samples.

4. Conclusions

- Atmospheric carbonation coefficients estimated from accelerated carbonation experiments at 10% CO_2 highly underestimate the actual values for HVFA binder systems and thus seriously overestimate the service life in environments where carbonation-induced corrosion is at risk. This was clearly observed from colorimetric carbonation experiments.
- HVFA mortar fully carbonated at 10% CO_2 is characterized by a significantly lower capillary water uptake than HVFA mortar fully carbonated at 1% CO_2. Both gravimetric measurements and visual assessment of neutron radiographs confirmed this.

Acknowledgements
Philip Van den Heede is postdoctoral fellow of Research Foundation—Flanders (FWO) (project No. 3E013917) and acknowledges its support. The authors also would like to thank the PSI for granting beam time at the NEUTRA SINQ facility (proposal ID No. 20170327). They are also grateful to Mr. Hovind of PSI and Mr. Hillewaere of the Magnel laboratory for their help.

References

[1] Van den Heede, P., Durability and sustainability of concrete with high volumes of fly ash, PhD thesis, Ghent University (2014)
[2] Castellote, M. et al, Chemical changes and phase analysis of OPC pastes carbonated at different CO_2 concentrations, Mater Struct 42 (2009), 515-525
[3] Sisomphon, K. and Franke, L., Carbonation rates of concretes containing high volume of pozzolanic materials. Cem Concr Res 37 (2007), 1647-1653
[4] Borges, P.H.R. et al, Carbonation of CH and C–S–H in composite cement pastes containing high amounts of BFS, Cem Concr Res 40 (2010), 284-292
[5] Thiéry, M., et al, Investigation of the carbonation front shape on cementitious materials: Effects of the chemical kinetics, Cem Concr Res 37 (2006), 1047-1058
[6] da Silva, F.G. et al, Sources of variations when comparing concrete carbonation results, J Mater Civ Eng 21 (2009), 333-342
[7] Saetta, A.V. and Vitaliani, R.V., Experimental Investigation and numerical modeling of carbonation process in reinforced concrete structures, Part I: Theoretical formulation, Cem Concr Res 34 (2004), 571-579.
[8] Snoeck, D. et al, Water penetration through cracks in self-healing cementitious materials with superabsorbent polymers studied by neutron radiography, CemConcrRes (2018), und. review
[9] *fib* Bulletin 34, Model code for service life design, fib, Switzerland (2006)

SynerCrete'18 International Conference on Interdisciplinary Approaches
for Cement-based Materials and Structural Concrete
24-26 October 2018, Funchal, Madeira Island, Portugal

CHARACTERISATION OF CONCRETE PUMPING BEHAVIOUR

Egor Secrieru [(1)], Viktor Mechtcherine [(1)]

(1) Technische Universität Dresden, Institute of Construction Materials

Abstract

Pumping is a widely and effectively used transportation and placing method for fresh cement-based materials. Despite the immense progress in the field of concrete technology in the last decades, including the application of additive manufacturing, so far there are still no official regulations to be used for the assessment and accurate prediction of concrete pumping behaviour. The design of a concrete pumping process becomes especially challenging when high performance concretes including highly viscous high-strength or self-compacting suspensions are involved.

In the present research, the pumping behaviour of concrete is characterised using state of the art rheological and numerical tools. The concrete mixtures under investigation exhibit various principal flow types which are already defined at low flow rates: partial bulk shear in a conventional vibrated concrete and pronounced bulk shear in the case of a self-compacting concrete (SCC). The obtained results are validated in full-scale pumping experiments. The pressure-flow rate curves serve as a reliable pumpability indicator for comparison between predicted results from experimental methods with tribometer/viscometer and Sliper devices, simulations with computational fluid dynamics (CFD) and actual results from full-scale tests.

1. General

Pumping of concrete plays a tremendous role in the contemporary construction industry. According to the European Ready Mixed Concrete Organisation, the amount of ready-mix concrete conveyed by pumping amounts 32 % and shows a rising trend worldwide [1].

In the context of concrete technology pumpability is a characteristic of the mixture describing its ability to be pumped easily and trouble-free through a conveying line. The flow behaviour of fresh concrete in a pipeline is related to the composition of the concrete and its ability to generate sufficient lubricating material to reduce the friction at the pipe wall-concrete interface [2].

The nature of concrete in its fresh and hardened states is perpetually evolving. The modern generation of concretes, e.g., high-performance concretes possess usually elevated viscosity in comparison to conventional vibrated concretes (CVC). The result is an increase in the effective pumping pressure needed to achieve a particular flow rate [3].
A series of practical guidelines for determination of pumping parameters in a concrete pumping operation has been used since the fifties of the last century [4] but are limited to CVC assuming the formation and full contribution of the lubricating layer to the concrete flow: The fresh material properties are accounted for slump or flow table test results, that by chance can be attributed to concrete yield stress parameter. Even so, such approaches fail in predicting pumpability of highly flowable or self-compacting concretes (SCC), for which the viscosity plays a crucial role during pumping [5]. Certainly, preliminary full-scale pumping tests are performed exclusively for large construction projects to ensure the suitability of the fresh material properties. With this respect, reliable tests to provide rapid means of concrete pumpability assessment are necessary [6].

2. Experimental investigation

2.1 Mixture and design parameters

The compositions of the two representative mixtures CVC and SCC are summarised in Tab. 1.

Table 1: Matrix composition of concrete mixtures under investigation.

Material	**Density [kg/m^3]**	**Unit mass [kg/m^3]**	
		CVC	SCC
CEM III/A 42.5 N	3075	360	360
Fly ash	2200	-	220
Sand 0/2	2650	781	667
Sand/gravel 2/8	2650	508	434
Gravel 8/16	2650	526	450
Water	1000	180	180
PCE HRWRA	1040	2.88	5.51
Water-to binder ratio [-]	-	0.50	0.31
Vol. aggregates [-]	-	0.69	0.59
Design strength [-]	-	C45/55	C55/67
Flow table[1], slump flow[2] [mm]	-	530[1]	673[2]
Air content [%]	-	1.40	2.00
Density [kg/m^3]	-	2370	2270

The concrete mixtures were prepared at ready-mix station. The rheological tests were performed inside a warehouse on fresh concrete taken dfrom the truck. The experimental circuit used for full-scale pumping experiments amounted ca. 154 m in length, cf. Fig. 1a. The entire circuit included three 180°, cf. Fig. 1b. The pipeline comprised two sections with

distinct diameters, Ø 125 and 100 mm, eight pressure sensors and a flow meter, cf. Figs. 1c and 1d.

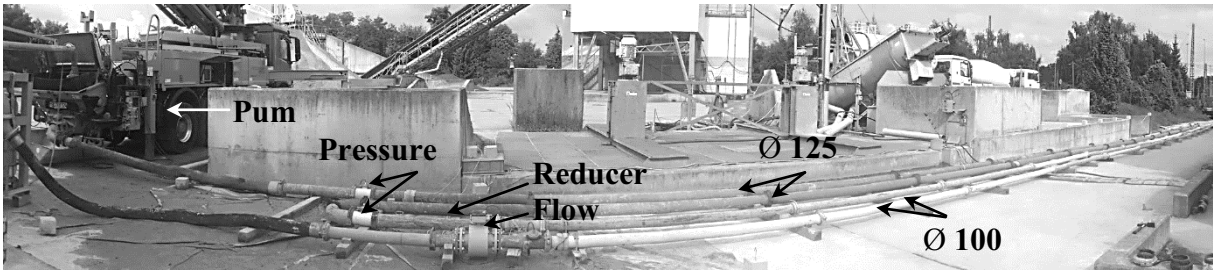

a)

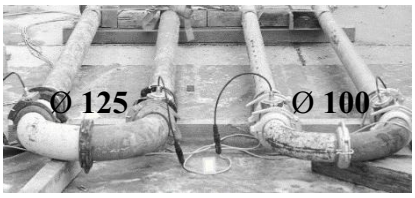

b)

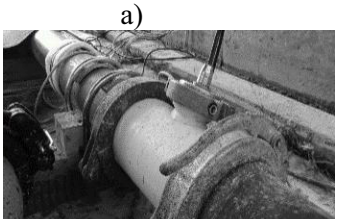

c)

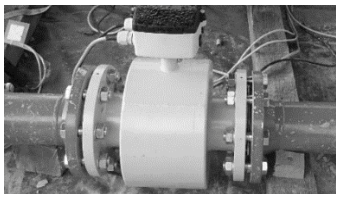

d)

Figure. 1: a) Overview of the full-scale setup, b) 180° bends of two diameters, c) pressure sensor and d) flow meter.

2.2 Characterisation of concrete flow in pipeline

The pumping behaviour of fresh concrete can be well characterised applying the rheological and tribological properties of concrete bulk and the forming lubricating layer (LL). Based on Kaplan's approach [2] the pressure-flow rate relationship (*P–Q*) is analytically estimated with Eq. (1), for concretes showing pure plug flow, and Eq. (2) in case of shear flow behaviour:

$$P = \frac{2L}{R}\left[\tau_{0i} + \frac{Q \cdot \mu_i}{\pi \cdot R^2}\right] \quad (1), \qquad P = \frac{2L}{R}\left[\tau_{0i} + \frac{\frac{Q}{\pi \cdot R^2} - \frac{R}{4 \cdot \mu}\tau_{0i} + \frac{R}{3 \cdot \mu} \cdot \tau_0}{1 + \frac{R}{4 \cdot \mu} \cdot \mu_i} \cdot \mu_i\right] \quad (2)$$

where τ_{0i} is the yield stress [Pa] and μ_i the viscosity parameter [Pa·s/m] of the lubricating layer measured by tribometer; τ_0 is the yield stress [Pa] and μ plastic viscosity [Pa·s] of the bulk concrete measured by viscometer, cf. Figs. 2a and 2b; R is the radius [m] and L the pipe length [m]. A further employed device was Sliper [7], that represents a novel approach to directly estimate the pumping pressure for a specific flow rate and pipe geometry, cf. Fig. 2c.

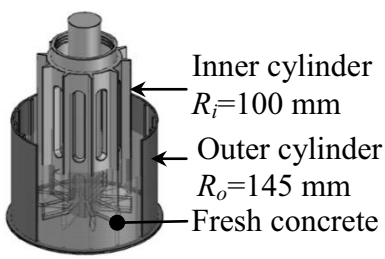

a)

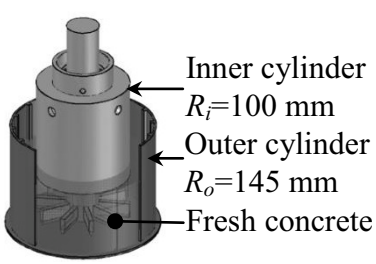

b)

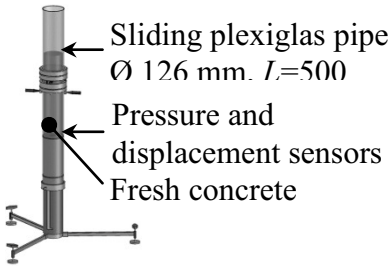

c)

Figure 2: a) Viscometer and b) tribometer geometries, c) Sliper device.

The measured rheological parameters are shown in Tab. 2 and refer to the results obtained at the time of inserting the concrete into the pipeline. Further details are available in [8].

Table 2: Rheological parameters of concretes used in full-scale pumping tests [8].

Device	**Parameter**	**CVC**		**SCC**	
		Concrete bulk	LL	Concrete bulk	LL
Viscometer	Plastic viscosity μ [Pa·s]	30	-	36	-
	Yield stress τ_0 [Pa]	112	-	18	-
Tribometer	Viscosity μ_i [Pa·s/m]	-	944	-	2349
	Yield stress τ_{0i} [Pa]	-	48	-	11
Sliper	Viscosity b [Pa·s/m]	587	-	935	-
	Yield stress a [Pa]	141	-	21	-

2.3 Numerical model

The numerical simulations were performed using computational fluid dynamics (CFD) in combination with the available commercial software ANSYS Fluent®. The single fluid approach was applied to model the flow of concrete in the pipeline following the approach presented in [9]. In addition to the no-slip condition at the concrete-pipe wall interface [10], the following assumptions were made:

- Concrete flow behaviour is approximated to that of a Bingham fluid and is considered continuous, laminar (Re < 1) and time-independent;
- The model consists of lubricating layer (LL) and concrete bulk regions. The properties of each region are assigned in the form of parameters as obtained from rheological experiments, cf. Tab. 2;
- The thickness and rheological properties of LL are constant along the pipeline.

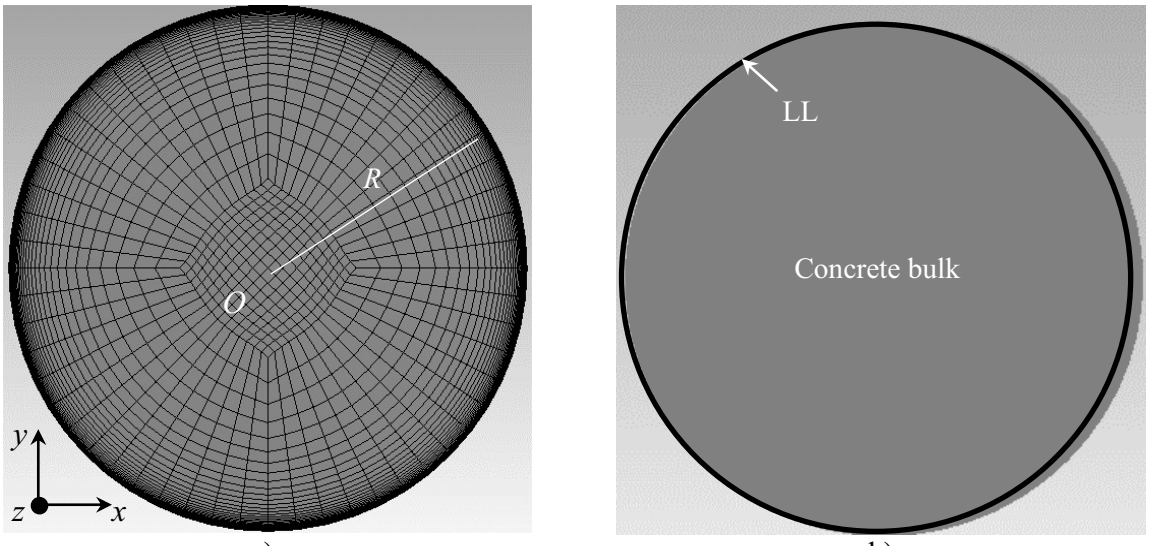

a) b)

Figure 3: a) Generated mesh of pipe cross-section;
b) boundaries between lubricating layer (LL) and concrete bulk.

3. Results and discussion

The experimental tools applied in this research to characterise the pumping behaviour and predict the necessary pumping pressure for the investigated concretes were successfully verified based on real results from full-scale pumping in terms of *P*–*Q* relationship, cf. Figs. 4a and 4b.

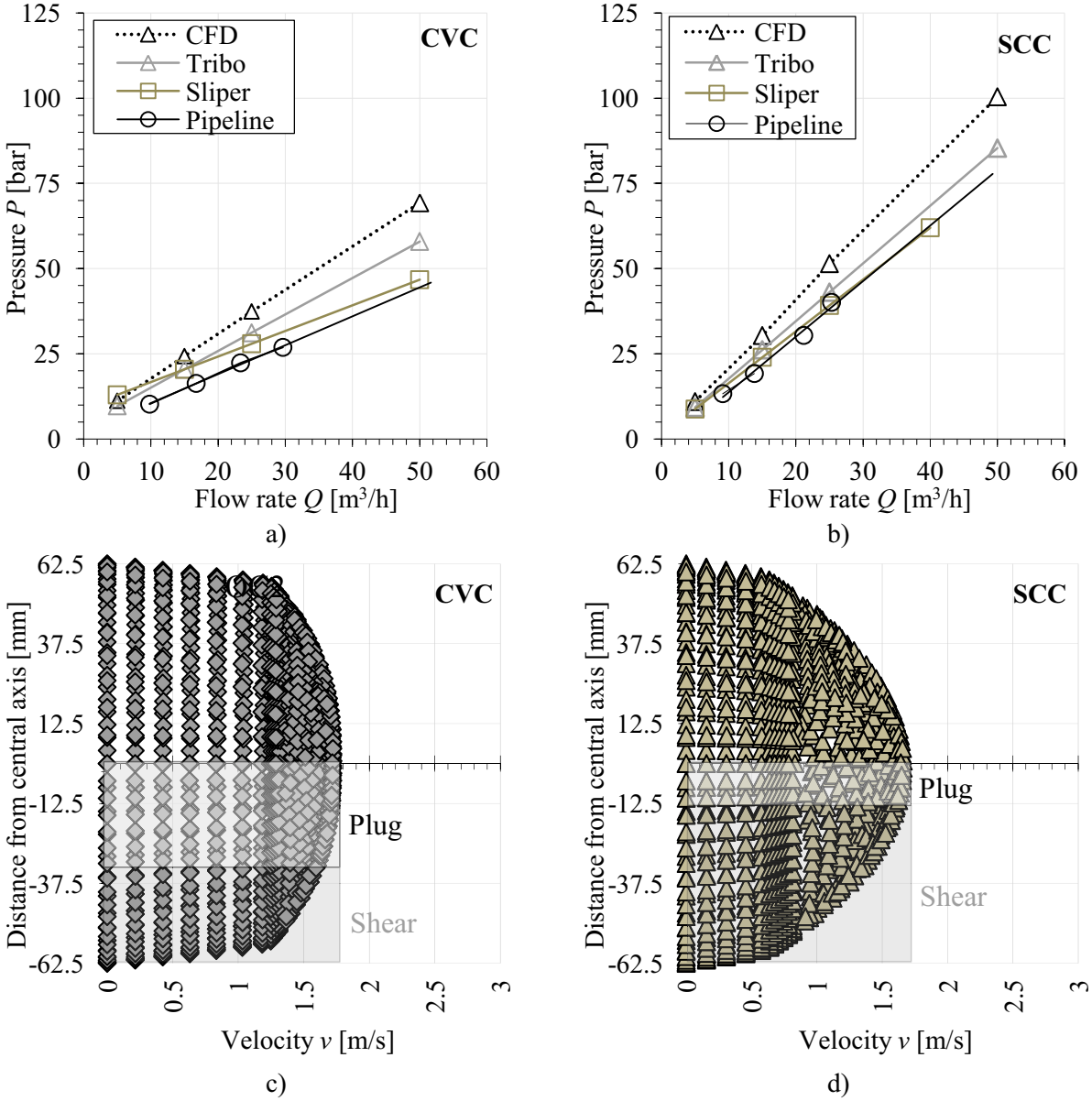

Figure 4: Comparison of *P*–*Q* determined by experimental tools and full-scale pumping for the investigated concrete mixtures a) CVC and b) SCC; resulting velocity profiles in the pipeline cross-section for c) CVC and d) SCC obtained from CFD simulations for pipe diameter Ø 125.

The used methods, i.e. viscometer/tribometer and Sliper slightly overestimate the pumping pressure. It seems that concrete undergoes structural breakdown corresponding to the elevated

shear rates in the pipes implying a lower needed pumping pressure than predicted based on tests at lower shear rates. Further, CVC mixture shows a shallower slope of the *P–Q* curve corresponding to "higher pumpability" in comparison to viscous SCC mixture.
The calculated velocity profiles are depicted in Figs. 4c and 4d; they correspond to a flow rate of $Q = 30$ m^3/h. It can be seen that for all the mixtures the flow type is a combination of plug and shear. The regions of flow types, plug or shear, are represented schematically in order to illustrate and emphasise the considerable impact of pipe geometry on the material flow behaviour and high shear deformations at the pipe wall-concrete interface.

4. Conclusions

The paper proposes easy-to-use methods for a reliable characterisation of concrete pumping behaviour. The methods discussed herein, i.e., viscometer/tribometer, Sliper and numerical simulations, were verified in full-scale pumping experiments on concretes showing different flow behaviour: predominantly plug for ordinary concrete CVC and shear type for SCC. The CFD model represents a powerful instrument to investigate the velocity profiles and pressure fields of the pumped concretes in the pipeline and can be applied for the prediction of material behaviour during pumping. The entire research study included an extended palette of concrete mixtures and it allows the authors to recommend the adoption and use of the methods under consideration of their limitations discussed in [8].

Acknowledgements
The present project was financially supported by the Federal Ministry for Economic Affairs and Energy and German Federation of Industrial Research Associations, grant number 18361 BR/1 „Zielsichere betontechnische Gestaltung des Pumpens von Frischbeton".

References

[1] ERMCO, Ready-Mixed Concrete Industry Statistics 2016, 2017.
[2] D. Kaplan, F. de Larrard, T. Sedran, Design of concrete pumping circuit, ACI Mater. J. 102 (2005) 110–117.
[3] D. Feys, G. De Schutter, R. Verhoeven, Parameters influencing pressure during pumping of self-compacting concrete, Mater. Struct. 46 (2013) 533–555.
[4] Placing concrete by pumping methods, ACI 304.2R-96 (reapproved 2008), 1996.
[5] D. Feys, G. De Schutter, K.H. Khayat, R. Verhoeven, Changes in rheology of self-consolidating concrete induced by pumping, Mater. Struct. 49 (2016) 4657–4677.
[6] G. De Schutter, D. Feys, Pumping of fresh concrete: Insights and challenges, RILEM Tech. Lett. (2016) 76–80.
[7] K. Kasten, Gleitrohr – Rheometer, Ein Verfahren zur Bestimmung der Fließeigenschaften von Dickstoffen in Rohrleitungen, PhD thesis, TU Dresden, 2010.
[8] E. Secrieru, Pumping behaviour of modern concretes - Characterisation and prediction, PhD thesis, TU Dresden, 2018.
[9] M. Choi, N. Roussel, Y. Kim, J. Kim, Lubrication layer properties during concrete pumping, Cem. Concr. Res. 45 (2013) 69–78.
[10] L.N. Thrane, Form Filling with Self-Compacting Concrete, PhD thesis, Technical University of Denmark, 2007.

SynerCrete'18 International Conference on Interdisciplinary Approaches
for Cement-based Materials and Structural Concrete
24-26 October 2018, Funchal, Madeira Island, Portugal

CHLORIDE DIFFUSION RESISTANCE OF LIMESTONE CALCINED CLAY CEMENT (LC3) CONCRETE

Quang Dieu Nguyen [(1)], M.S.H Khan [(1)], Arnaud Castel [(1)]

(1) Centre for Infrastructure Engineering and Safety, School of Civil and Environmental Engineering, The University of New South Wales, Sydney, Australia

Abstract
This paper aims to evaluate the chloride diffusion resistance of limestone calcined clay cement (LC3) concrete by accelerated chloride migration and bulk chloride diffusion techniques. Three concrete mixes have been utilized: one mix using only General Purpose (GP) cement and two LC3 concretes with 15% and 20% GP cement replaced by a constant ratio 2:1 by mass of calcined clay and limestone. The mechanical and transport properties of three concretes were investigated. LC3 concrete with 15% substitution presented the higher compressive strength than reference concrete. Moreover, LC3 concretes showed the better performance in surface resistivity comparing with plain GP concrete. Rapid chloride penetration test (RCPT), chloride migration test and bulk diffusion tests were conducted. LC3 concretes containing 15% or 20% substitution of calcined clay and limestone increased significantly the chloride diffusion resistance comparing with the reference concrete in all diffusion tests.

1. Introduction

Recently, limestone calcined clay cement (LC3) has received increasing worldwide attention due to its synergic advantage of calcined clay and limestone in ternary blended cement. Mechanical properties, crystalline analysis, rheological properties, carbonation and sulphate resistance of LC3 blends were reported in numerous studies [1-7]. Specifically, Shi et al. [4, 5] investigated the chloride binding capacity of LC3 mortars and revealed that cement-metakaolin-limestone blends produced higher Friedel's salt formation, which presents the higher binding capacity of LC3 mortars.
Tuutti [8] proposed a service life model of chloride-induced corrosion including two stages: the initiation stage and propagation stage. In the first stage, chloride ingress penetrates into

steel bars inside concrete and triggers the reinforcement corrosion. Critical chloride content known as the sufficient amount of chloride to promote active corrosion is a decisive input parameter in service life model of reinforced concrete structures [9]. Therefore, corrosion resistance against chloride diffusion into concrete is critical importance for the durability of reinforced concrete in chloride bearing-environment. Due to the current literature, this work aims to evaluate the impact of calcined clay and limestone in LC3 concrete on the chloride resistance, which facilitates the utilization of LC3 concrete in practical purpose.

2. Experimental program

2.1 Materials

The limestone calcined clay cement concrete used in the study is a ternary blend of General Purpose (GP) cement, calcined clay and limestone. The GP cement complies with the Australia Standard AS 3792-2010 and is similar to ASTM Type I cement (ASTM C150/C150M). The limestone branded as Stone Dust was supplied by Boral Construction Materials Limited in New South Wales, Australia. The calcined clay used was made using a flash calcination process and supplied by Argeco, France. Table 1 shows the chemical composition of all cementitious materials determined by X-ray fluorescence (XRF).
Fine aggregate is Sydney sand with specific gravity of 2.65 and water absorption of 3.5%. Crushed basalt supplied from Dunmore quarry in New South Wales, Australia was utilized as coarse aggregate. Its characteristics comprised specific gravity of 2.8, maximal nominal size of 10mm and water absorption of 1.6%.

Table 1: Chemical composition of cementitious materials.

Chemical composition	GP cement (wt. %)	Calcined clay (wt. %)	Limestone (wt. %)
SiO_2	19.74	70.42	0.39
Al_2O_3	4.70	22.34	0.11
Fe_2O_3	2.98	2.34	0.1
CaO	64.62	0.49	57.51
MgO	1.48	0.16	0.29
Na_2O	0.21	0.1	-
K_2O	0.64	0.19	-
TiO_2	0.31	1.1	-
SO_3	2.24	0.02	-

2.2 Concrete mix design

Three concrete mixes were fabricated to investigate the properties of concrete with the high replacement of cement by calcined clay and limestone with the ratio 2:1 by mass in this study. The details of the mix designs are shown in the Table 2. After mixing, concrete was poured into cylinders with 100mm diameter and 200mm height in two layers and a vibrating table

was utilized to compact and remove entrapped air in concrete. After surface finishing, all moulds were covered by using lids to prevent the surface from moisture loss. All concrete specimens were removed from cylinder moulds after one day. All concretes were placed into a lime-saturated water bath continuously for 7 days. After immersion in lime water, the specimens were stored in the controlled room at a fixed temperature of 23±2^{o}C and relative humidity of 50% until the testing dates.

Table 2: Mix design details of concretes.

Materials (kg/m^3)	**LC3-0**	**LC3-15**	**LC3-20**
Coarse aggregate	1221	1221	1221
Fine aggregate	620.8	620.8	620.8
Total binder	388	388	388
GP cement	388	329.8	310.4
Calcined clay	0	38.8	50.4
Limestone	0	19.4	27.2
Water/binder ratio	0.45	0.45	0.45
Water	174.5	174.5	174.5

2.3 Mechanical and transport concrete properties tests:

The compressive strength, indirect tensile strength and surface resistivity were measured at 28 days in accordance with ASTM C39, ASTM C496 and AASHTO TP95, respectively.

2.4 Chloride diffusion tests:

At 28 days of curing, 100×200mm cylinders were cut into discs with 50mm of height and 100mm of diameter with 25mm sections from the top and bottom of the cylinders being removed. The 50mm discs were utilized to conduct RCPT (ASTM C1202) and rapid migration test (NT Build 492).

The bulk diffusion test was carried out following ASTM C1556 protocol by using 75mm height discs cut from standard cylinders. The discs were immersed in 16.5% NaCl solution for 35 days. After the exposure duration, concrete powders were taken every 1mm from the exposure surface to 25mm using the Germanm Profile Grinder PF-1100. The apparent chloride diffusion coefficients (D_a) of three types of concrete were calculated by using total chloride content profile measured by Metrohm 855 Robatic Titrosampler (a potentiometric titration machine).

3. Results and discussion

3.1 Mechanical and transport properties

Table 3 presented compressive strength, indirect tensile strength and surface resistivity of three different types of concrete at 28 days. LC3-15 concrete obtained the highest compressive strength, followed by LC3-0 and LC3-20 concrete. The average compressive strength of LC3-20 concrete was approximately 94% of LC3 concrete, which indicates 20% replacement rate of calcined clay and limestone in binder was only marginally decreased the

compressive strength. The highest indirect tensile strength was 4.6MPa achieved by LC3-0 concrete whilst LC3-20 concrete reported the lowest indirect tensile strength of 4.4MPa. The substitution of calcined clay and limestone in LC3 concrete increased significantly in surface resistivity comparing with plain OPC concrete. LC3-0 concrete showed the lowest surface resistivity at 19.4kΩ-cm while LC3-15 obtained the highest value at 27.3 kΩ-cm.

Table 3: Mechanical and transport properties of LC3 concretes at 28 days.

Concrete type	Compressive strength (MPa)	Indirect tensile strength (MPa)	Surface resistivity (kΩ-cm)
LC3-0	52.3	4.6	19.4
LC3-15	58.0	4.3	27.3
LC3-20	49.3	4.4	23.3

3.2 Chloride diffusion tests

The results of RCPT, chloride migration test and bulk diffusion test were shown in Table 4. Fig. 1 illustrates the total chloride profiles after 35 days immersion in 16.5% NaCl solution. In all tests, LC3-15 and LC3-20 concretes outperformed significantly in comparison with LC3-0 reference concrete. Over 4500 Coulombs passed through the LC3-0 concrete in RCPT, which classifies plain OPC concrete as high chloride ion penetrability following ASTM C1202 recommendation. By contrast, LC3-15 and LC3-20 concretes reduced remarkably the total charge passed to over 50% comparing with LC3-0 concrete. Regarding rapid migration test, LC3-0 obtained the highest magnitude of non-steady-state migration coefficient at 21.7×10^{-12} m^2/s whilst 15% and 20% combination of calcined clay and limestone in binder reduced the amplitude to 12.9×10^{-12} m^2/s and 11.9×10^{-12} m^2/s, respectively. Similarly, after 35 days of exposing in 16.5% NaCl solution, LC3-0 presented the highest amplitude of apparent chloride diffusion coefficient at 34.4×10^{-12} m^2/s within three concretes while calcined clay and limestone reduced significantly the coefficient in LC3-15 and LC3-20 with the values of 7.7×10^{-12} m^2/s and 8.2×10^{-12} m^2/s. From figure 1, LC3-15 and LC3-20 concretes obtained the higher total chloride content to 8mm from the exposed surface than that of plain concrete. However, the total chloride content of LC3-15 and LC3-20 decrease significantly and the magnitude was lower total chloride content of LC3-0 concrete after 8mm of depth. Moreover, LC3-0 concrete manifested a continuous decrease until 25mm whilst both LC3-15 and LC3-20 concretes exhibited stable chloride content after 15mm of the exposure depth.

Table 4: Results of RCPT, rapid migration test and bulk diffusion test.

Concrete type	Charge passed (Coulombs) ASTM C1202	Non-steady-state migration coefficient (10^{-12} m^2/s) NT Build 492	Apparent chloride diffusion coefficient (10^{-12} m^2/s) ASTM C1556
LC3-0	4545	21.7	34.4
LC3-15	2104	12.9	7.7
LC3-20	2263	11.9	8.2

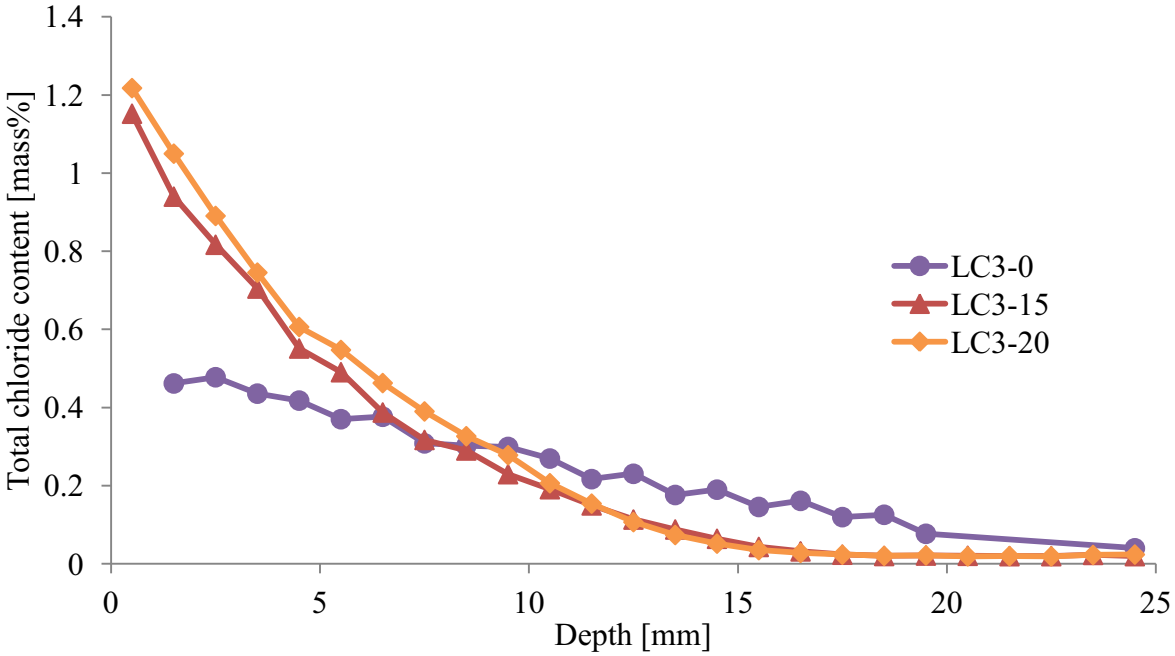

Figure 1: Total chloride content profile of LC3 concrete.

4. Conclusion

The mechanical properties including compressive strength and indirect tensile strength of concrete containing calcined clay and limestone were compatible with plain concrete while the utilization of calcined clay and limestone increased the surface resistivity. Overall, three different test protocols including RCPT, chloride migration test and bulk diffusion test provided the similar results for the resistance of LC3 concretes against chloride ingress. The combination of calcined clay and limestone in binder increased significantly the chloride diffusion resistance in comparison with plain OPC concrete.

References

[1] Antoni, M. et al, Cement substitution by a combination of metakaolin and limestone, Cement and Concrete Research, 42 (2012) 1579-1589
[2] Tironi, A. et al, Blended Cements with Limestone Filler and Kaolinitic Calcined Clay: Filler and Pozzolanic Effects, Journal of Materials in Civil Engineering, 29 (2017) 1-8
[3] Kunther, W. et al, Thermodynamic modeling of hydrated white Portland cement–metakaolin–limestone blends utilizing hydration kinetics from 29 Si MAS NMR spectroscopy, Cement and Concrete Research, 86 (2016) 29-41
[4] Shi, Z.G. et al, Role of calcium on chloride binding in hydrated Portland cement–metakaolin–limestone blends, Cement and Concrete Research, 95 (2017) 205-216
[5] Shi, Z.G. et al, Friedel's salt profiles from thermogravimetric analysis and thermodynamic modelling of Portland cement-based mortars exposed to sodium chloride solution, Cement Concrete Comp, 78 (2017) 73-83

[6] Vance, K. et al, Hydration and strength development in ternary portland cement blends containing limestone and fly ash or metakaolin, Cement and Concrete Composites 39 (2013) 93-103
[7] Vance, K. et al, The rheological properties of ternary binders containing Portland cement, limestone, and metakaolin or fly ash, Cement and Concrete Research 52 (2013) 196-207
[8] Tuutti, K. , Corrosion of steel in concrete, Swedish Cement and Concrete Research Institute, Stockholm, Sweden (1982)
[9] Angst, U.M., Elsener, B., The size effect in corrosion greatly influences the predicted life span of concrete infrastructures, Sci Adv 3 (2017) 1-8

SynerCrete'18 International Conference on Interdisciplinary Approaches
for Cement-based Materials and Structural Concrete
24-26 October 2018, Funchal, Madeira Island, Portugal

COMPARISON OF STANDARD CONCRETE AND ECO-CONCRETE IN RESPECT TO FUNCTIONAL, ENVIRONMENTAL AND DURABILITY PERFORMANCE

Joachim Juhart [(1)], Rok Bregar [(1)], Gheorghe Alexandru David [(1)], Markus Krüger [(1)]

(1) Graz University of Technology, Graz, Austria

Abstract
In this study eco-concrete and in particular its paste is designed by a combined filler concept with the aim of optimizing its performance in respect to functionality, environmental impact and durability. Cement (PC) content is below the limits of traditional standards while w/c-ratio exceed such limits. The paste-mix development is based on a combination of particle packing optimization techniques, the reduction of water demand for certain flowability and designing an optimal mix of PC with properly selected, eco-friendly micro-fillers and "eco-fillers". Subsequently the performance of the developed eco-concrete (ECO) in terms of workability, strength and durability indicators is evaluated versus a standard concrete (REF corresponding to normal concrete of RRT+ test of COST action 1404). While the functional performance of ECO in terms of workability (i.e. spread at flow-table) and strength is at least equivalent to REF, the eco-friendliness is substantially improved (global warming potential -36% and embodied energy -19%). Durability indicators, such as open porosity, water penetration depth and air permeability, show nearly equivalent performance of ECO and REF.

1. Introduction

In times of climate change it is a desirable goal to reduce greenhouse gas emissions (CO_2-equivalent, global warming potential, GWP) and embodied energy (primary energy demand, PE) of the worldwide most used construction material – normal concrete. Cement clinker, which represents 95% of Ordinary Portland cements (PC) and is also the main constituent of Portland composite cements, is mainly responsible for GWP and PE of normal concrete [1]. Thus enhancing the clinker-efficiency or cement efficiency in normal concrete is required to reduce GWP and PE while keeping a required performance.

Principles of "green concrete" or ecological concrete were pointed out by [1], [2], [3]. The general approach of this study is illustrated in Fig. 1. The key to success is to optimize the mix composition in terms of packing density and water demand especially of the powders that represent the paste (i.e. all granular materials with a maximum grain size < 125 µm) taking into account their environmental impact. In an optimized paste PC with its high GWP and PE is partly substituted by properly selected very fine micro-fillers (MF, mean particle diameter d_{50} < 5 µm) and coarser eco-fillers (EF, 5 µm ≤ d_{50} < 30 µm) that have low water demand and environmental impact. In this study the fillers are properly selected limestone powders, but furthermore other stone-powders (dolomite, quartz, residuals etc.) or secondary cementitious materials, especially secondary raw materials (ground granulated blast furnace slag, fly ashes etc.) can be utilized according to the presented method if regional available. An optimized mix of PC/EF/MF requires less water for certain workability than the original granular mix (mainly PC). This is (i) due to packing optimization which corresponds to a physical filler effect of MFs placed into voids instead of interstitial water, and/or an optimized grain size distribution of all granular materials; (ii) due to a significant amount of EF which have a high sensitivity to water addition and therefore lower the water demand for certain flowability of a mix and (iii) water can be reduced by the addition of superplasticizers (SP). SP have to be used sparingly due to their high environmental impact, see Fig. 2. With such an optimized mix it would be possible to lower the w/c-ratio (water/cement) and achieve higher strength to design (ultra) high performance concrete. In our case of eco-concrete the paste-mix is ecologically optimized by substituting cement with eco-friendly fillers. Such eco-pastes typically have the same or an even higher w/c-ratio as pure PC-pastes, but have a decreased w/p-ratio (water/powder-ratio, "powder" = PC/EF/MF) at equal flowability.

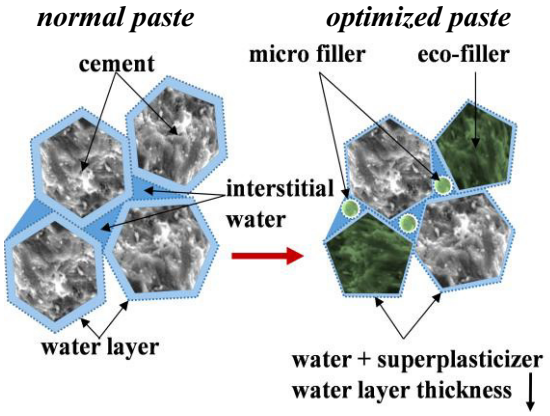

Figure 1: Optimizing paste by combined fillers.

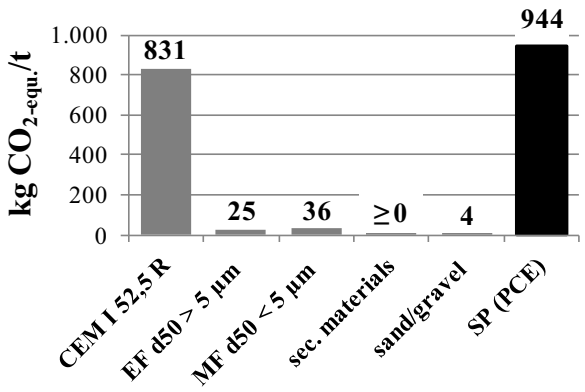

Figure 2: GWP of concrete constituents.

Traditional descriptive concepts of actual standards (e.g. EN 206-1:2014 and its national applications, e.g. ÖNORM B 4710-1:2018) prescribe a minimum cement content and maximum w/c of concrete, whereas innovative "eco-concretes" exaggerate these limits. Fortunately new, performance oriented approaches such as the "equivalent concrete performance concept" (ECPC) exist in the mentioned standards. It is shown in the outlined paper how to prove equivalent performance of a newly developed concrete (ECO) with reduced environmental impact to the reference concrete (REF) according to ECPC.

2. Materials and Mix Design

2.1 Materials and Design of the Paste

For the selection of the materials and mix-optimization of the paste the combined filler concept according to [4], [5] was applied to (i) experimentally characterize fine powders in terms of their packing density and water demand for certain flowability and (ii) to systematically optimize mix-ratios of PC, MF and EF of eco-pastes. Tab. 1 shows properties of source materials considered and of the eco-paste with a finally found mix ratio of OPC/EF/MF of 50/25/25 V.-%. Their significant properties are ρ (true density), d_{50}, V_{ws}/V_p (water demand at the saturation point,), ϕ_{exp} (wet packing density) and $V_{wf,100}/V_p$ (i.e. water demand at the onset of flow) as well as E_p (sensitivity of an individual material or mix to water addition). The parameters and the optimum mix-ratio were determined by a new combination of methods described in detail in [4], [5]. V_{ws}/V_p is defined as water saturation point that is determined by the maximum power consumption of a mixer and indicative for the maximum reachable wet packing density ϕ_{exp}. The flowability of mixes is tested subsequently by performing spread flow tests with increased V_w/V_p-ratios (volumetric w/p-ratios) with a Hägermann cone on a dry glas plate according to [6]. $V_{wf,100}/V_p$ represents the water demand at the onset of flow (where the spread flow f_{100} is identical to the base diameter of the lifted cone, i.e. 100 mm) and E_p is the sensitivity of the mix to water addition. By E_p different powders can be compared with respect to flowability. The lower E_p, the easier a material flows by adding a certain increment of water. Subsequently the strength of hardened pastes with different mixes of PC/EF/MF at constant spread flow is determined by compressive test according to EN 196-6. This additional information can be used for selecting a suitable mix-ratio of an eco-paste with equal strength to a pure OPC reference paste.
The data for the environmental indicators GWP and PE are shown in Tab. 2 and Fig. 2. They were taken from equivalent materials published in [4], [5] calculated by the method of Life Cycle Assessment (LCA) according to ISO EN 14044:2006 using SimaPro software (v. 7.3) and the ecoinvent database [7]. Fig. 2 shows that PC exceeds the environmental impact of finely milled stones, aggregates and secondary raw materials (GGBS, FA) by far. Superplasticizers possess very high GWP and PE due to the energy demand of the production according to [8].

Table 1: Properties of granular source materials of the paste and its optimum mix.

Type	ρ (g/cm³)	d_{50} (µm)	V_{ws}/V_p (-)	ϕ_{exp} (-)	$V_{wf,100}/V_p$ (-)	E_p (-)
CEM I 52.5 N SR3	3.17	10.5	0.75	0.57	0.99	0.102
EF (limestone)	2.70	6.9	0.68	0.60	0.79	0.047
MF (limestone)	2.73	2.2	0.61	0.62	0.63	0.013
Paste Mix (PC/EF/MF=50/25/25)	2.94	7.5	0.61	0.62	0.61	0.011

2.2 Concrete Mix Design

Concrete mixes REF and ECO were designed with the same volume of paste, same sieve line of aggregates as well as maximum grain size of 16 mm with mix-ratios according to Tab. 2. Equal SP-type and low SP-content was used for ECO and REF to minimize SP environmental impact. However, ECO had a significantly lower PC content and w/p-ratio but higher packing density than REF. Despite a significantly higher w/c-ratio of ECO than REF, flowability and

strength were nearly the same. REF corresponds to the concrete used in the extended round robin test program of COST action 1404 "Towards the next generation of standards for service life of cement based materials and structures". The aggregates used had a not neglectable water adsorption (WA_{24}-coefficient of sand 0/4 is 0.77 wt.%, of gravel 4/11 is 2.61 wt.%, of gravel 8/16 is 2.25 wt.%) which had to be considered as follows. The gravel was added fully water-saturated to the mix, but the sand was added in dry state. Effective water was assumed to correspond to the added water minus adsorbed water of the sand plus water content of SP, which leads to an effective w/c of 0.52 for REF and 0.58 for ECO.

Table 2: GWP, PE of concrete constituents as well as concrete mix-composition.

type	**GWP (kg CO_2-equ./t)**	**PE (MJ/t)**	**REF (kg/m^3)**	**ECO (kg/m^3)**
CEM I 52.5 N SR3	831	4030	320.0	208.3
EF limestone	25	717	-	104.2
MF limestone	35	1005	-	104.2
sand 0/4 mm, dry	4	58	830.0	827.1
gravel 4/11 mm, fully saturated	4	58	449.0	447.4
gravel 8/16 mm, fully saturated	4	58	564.0	562.0
SP (80% water content)	944	29150	1.4	1.4
added water	0	0	172.4	126.4
effective water	0	0	167.1	121.2
w_{eff}/c	-	-	0.52	0.58

3. Testing and Evaluation Methods

The performance of the produced concrete mixes was tested in terms of workability, strength and durability indicators and of environmental impact was evaluated. The flow-table spread (i.e. spread diameter on the flow-table after defined compaction according to EN 12350-5: 2009) of the mix 10 min after water addition (spread_10) was tested as well as the value 30 min after water addition (spread_30). The compressive strength was tested on concrete cubes (150 mm, n = 3) according to EN 12390-3:2009 - stored under water until testing - at an age of 1 day ($f_{cm,\,1d}$) and 28 days ($f_{cm,\,28d}$). Open porosity was determined in accordance to EN 1936:2007 (water uptake of cubes ~50 mm after complete drying under partial vacuum related to the volume of specimen). The depth of water-penetration was tested according to EN 12390-8:2009 with specifications according to ONR 23303:2010 on water cured concrete prisms (200*200*120 mm^3) at the age of 28d. Pressured water was applied to one surface in 2 steps of 1.75 and 7.0 bar up to 3 and 14 days, respectively. Afterwards each specimen was split, and the water penetration depth was measured. Air permeability was tested with two different testing procedures. First testing procedure was carried out in accordance to Swiss Standard SIA 262/1:2013 "air permeability on site" with a "PermeaTORR" device [9] on concrete cubes (150 mm). Specimen were stored under water to an age of 28d, then dried at 50°C for 8d, then stored at 65% r.h. and 20°C until testing at an age of 62 d. The rate of increase of pressure in the inner chamber due to unidirectional air-flow through the cover concrete was measured and directly linked to the calculated coefficient of air-permeability

K_{SIA} [9]. For the second procedure a "Testing" bubble counter [11] was used and air permeability was tested in principle according to a RILEM specification [10]. Cylindrical specimen were casted (d=150 mm, cut to h=50 mm, n=2), stored under water to an age of 28d, then dried at 50°C until 56d, then stored at 65% r.h. and 20°C until testing at an age of 91 d. Specimen were sealed on their sides. An overpressure was applied on the bottom of the specimen, so that a certain volume of inert gas (in our case air was used) migrated through the whole concrete disk. It was measured by the rate of ascent of a soap bubble at different pressure steps (2.5, 3.0, 3.5 bars). Corresponding coefficient of permeability K_{RIL} was calculated as the mean coefficient of the three pressure steps [10], [11]. The ecological impact of 1 m³ fresh concrete was calculated according to the values for GWP and PE of the source materials and their content in fresh concrete to compare REF and ECO.

4. Results and Discussion

Tab. 3 shows tested fresh- and hardened concrete properties as well as durability indicators. The aim of improving ecological performance while keeping workability and strength at the level of the reference concrete was reached. GWP of ECO was reduced up to 36% and PE up to 19% compared to REF. Very soft consistency of the fresh concrete just after mixing was achieved (spread_10 equal to 52±2 cm). However ECO loses its consistency faster than REF, as it can be read from the values spread_30 in relation to spread_10 of both mixes. The reason may be the lower w/p-ratio and the selected SP-type. Changing it from a highly liquefying type to a more consistency-keeping type could compensate the effect. The 1d-strength of ECO is significantly higher than that of REF, whereas the 28d-strength is equal, which means low w/p and a high content of MF accelerate strength development. This can be seen as an advantage, for example for precast applications, but may be disadvantageous for applications to massive construction elements regarding temperature rise and early shrinkage.

Table 3: Tested concrete properties with their standard deviation and calculated GWP and PE.

	unit	**REF**	**ECO**
flow-table spread_10	cm	54.3±0.3	50.5±1.3
flow-table spread_30	cm	43.5±0.5	37.0±0.0
1-day strength $f_{cm,\ 1d}$	N/mm²	11.3±1.1	17.5±0.4
28-day strength $f_{cm,\ 28d}$	N/mm²	55.4±2.2	56.2±3.5
open porosity	%	13.4±0.5	11.5±0.5
water penetration depth	mm	15.0±1.67	17.8±0.3
air permeability coefficient K_{RIL}	10^{-16} m²	1.03±0.19	0.26±0.01
air permeability coefficient K_{SIA}	10^{-16} m²	0.02±0.01	0.03±0.00
GWP	kg/m³	282	180
PE	MJ/t	1715	1400

Regarding durability performance, a differentiated view is necessary. ECO´s open porosity and gas permeability coefficient K_{RIL} is lower than REF´s. It is the other way round regarding air permeability coefficient K_{SIA} and water penetration depth. However, water penetration depth of REF and ECO are below limits of the Austrian Standard ÖNORM B 4710-1:2018

(class XW1 limits 50 mm, XW2 25 mm). Regarding air permeability, Torrent [9] classifies REF and ECO to "low permeability" (K_{SIA} 0.1-1.0 E-6 m^2). Further durability measures as carbonation depth (not tested explicitly) only correlate to limited extent to tested permeability indicators, as additional aspects (as for example the $Ca(OH_2)$ puffer capacity) have to be considered.

5. Conclusions and Outlook

In this study eco-concrete and in particular its paste is designed by a combined filler concept with the aim of optimizing its performance in respect to functionality, environmental impact and durability. PC content is below the limits of traditional descriptive standards while w/c-ratio exaggerates such limits. The performance of the developed eco-concrete (ECO) in terms of workability, strength and durability indicators is evaluated versus a standard reference concrete (REF). While the functional performance of ECO in terms of workability (i.e. spread at flow-table) and strength (i.e. early age and 28d strength) is at least equivalent to REF, the eco-friendliness is substantially improved (GWP -36% and PE -19%). Durability indicators – open porosity, water penetration depth and air permeability – overall show nearly equivalent performance. In detail, water penetration and air permeability tested according to RILEM are lower of ECO than of REF while for water penetration and air permeability according to SIA it is the opposite. Further investigations on a larger number of specimen, mix variations as well as durability aspects are pending to derive clear relationships between mix-parameters and durability indicators and to clarify the significance of indicators and their testing methods.

References

[1] Glavind, M. et al, Guidelines for green concrete structures, International Federation for Structural Concrete (2012)
[2] Fennis-Huijben, S.A.A.M., Design of ecological concrete by particle packing optimization" PhD thesis, Delft University of Technology (2010)
[3] Proske, T et al, Eco-friendly concretes with reduced water and cement contents — Mix design principles and laboratory tests, Cem Concr Res 51 (2013), 38–46
[4] Juhart J et al, Durable Eco-Crete in Austria: Materials and Mix Design Methods, Proc. International Symposium - Environmental Friendly Concrete - Eco-Crete (2014), 311–8
[5] Juhart, J et al, A new combined filler concept for eco-concrete, Proc. of 14th International Congress on the Chemistry of Cement (ICCC 2015) (2015)
[6] Okamura, H. and Ozawa, K., Mix design for self-compacting concrete, Concrete library of JSCE (1995)
[7] EcoinventCenter, ecoinvent database v2.2: Swiss Center for LCA (2010)
[8] Schiessl, P. and Stengel T., Nachhaltige Kreislaufführung mineralischer Baustoffe (2006), in: Haist, M. et al, „Entwicklungsprinzipien und technische Grenzen der Herstellung zementarmer Betone", Beton- und Stahlbetonbau 3 (2014), 202–215
[9] Materials Advanced Services Ltd, Torrent, R., User manual PermeaTORR, http://www.m-a-s.com.ar, 22.05.2018
[10] RILEM TC 116-PCD, Permeability of Concrete as a Criterion of its Durability. Materials and Structures 32 (1999)
[11] TESTING Bluhm & Feuerherdt GmbH, Betriebsanleitung Prüfeinrichtung zur Messung der Luftpermeabilität, https://testing.de/de/2.0331, 22.05.2018

SynerCrete'18 International Conference on Interdisciplinary Approaches
for Cement-based Materials and Structural Concrete
24-26 October 2018, Funchal, Madeira Island, Portugal

COMPRESSIVE STRENGTH DEVELOPMENT OF FLY ASH CONCRETES CURED UNDER DIFFERENT CONDITIONS

T. Altuğ Söylev [(1)], Turan Özturan [(2)]

(1) Gebze Technical University, Kocaeli, Turkey
(2) Boğaziçi University, Istanbul, Turkey

Abstract
The use of fly ash as a cement replacement material brings economic, environmental advantages to concrete technology as well as some improvements in the properties of concrete. However, fly ash concrete may not reach specified strength values because of slower pozzolanic reaction and consequently its use in concrete is limited. Effective curing can lead to higher use of fly ash in concrete, by enabling higher strength at earlier ages. In the present study, the effect of three different curing regimes on the compressive strength (3, 7, 28, 56 and 91 days) of concretes with 0, 15, 30 and 45% fly ash replacement ratios. The ratios represent fly ash percentages with respect to the total binder content. The curing regimes were 1) air curing; 2) one week 30°C water curing + air curing; 3) one week 20°C water curing + air curing. Specimens with hot water curing (no 2) yielded higher results until 28 days when compared to those with mild water curing (no 3). The air curing caused lowest results with significant differences compared to water curing regimes. Water curing was effective in closing the gap between concretes with and without fly ash. However, beyond 15% cement replacement ratio, fly ash concretes had lower strength, even at 91 days.

1. Introduction

The use of fly ash as a cement replacement material provides important advantages in many applications, beside the economic and environmental effect, by reducing the heat evolution, by improving durability etc. However, cement replacement ratio by fly ash has limitations due to the slower strength development of fly ash compared to Portland cement, which causes lower strength, particularly at early-ages. This effect was shown in the study of Gopalan et al. with the concretes containing up to 80% fly ash [1]. The prediction of compressive strength at different ages can be successfully made by using the maturity method. However, the

parameters used in this method are well applied to the Portland cement concrete exposed to water curing of different temperatures. For different binders under different curing conditions, the method may not be so straightforward. Xu et al. [2] who used the activation energy and equivalent time for maturity calculation, indicate that for high volume fly ash concrete they should be modified. Maturity approach worked better after applying different constants for different mineral additions in the study of Boubekeur et al [3]. Eren [4] calculated the parameters of the maturity method for concretes with 30% and 50% cement replacement by fly ash cured at five different curing temperatures and tested at five different ages. The results show that the parameters are different in each mix and condition, therefore they may be considered as material properties. The present study presents the effect of different curing conditions on the compressive strength development of concretes with and without fly ash and a detailed combination of temperature-age. The results trends were analyzed by interpreting the principles of the maturity method.

2. Experimental study

Three cubes of 150 mm were used to test the compressive strength of four different concrete mixes (Table 1) (0, 15, 30, 45% fly ash by mass of total binder) at three different curing conditions (Twelve concretes in total). Curing Condition 1 was air curing in hot and very humid laboratory conditions. Curing 2 and Curing 3 consist of 7-days water curing (30°C and 20°C respectively) and air curing until testing. CEM I 52.5 Portland cement and Class C fly, 5mm river sand, 10mm and 20mm basaltic crushed stones, naphthalene sulphonate based superplasticizer were the materials of concrete. The target slump of 22 cm was obtained by slightly adjusting the superlasticizer content. Compressive strength was tested at 3, 7, 28, 56 and 91 days after casting. The letters and the first digits in Table 1 indicate the replacement ratio by mass of total binder content and the third digit in Table 2 shows the curing condition.

Table 1: Concrete mixes.

kg/m^3	**FA00**	**FA15**	**FA30**	**FA45**
Cement	430	365	300	235
Fly ash	0	65	130	195
Water	215	215	215	215
C agg (20mm)	564	557	550	540
C agg (10mm)	562	553	548	539
Sand	669	658	652	640
Superplasticizer	2.15	2.17	2.11	2.12

3. Results and Discussion

As expected, water cured specimens had significantly higher strength development and strength decreased with the increase of fly ash content (Figs. 1-4). The 7-days strength was equalized in 3 days and the 28-days strength was equalized in 7 days when hot water curing was applied instead of air curing in concretes with and without fly ash. The strength of FA451

was only 41% of the highest strength at 28 days (FA002). There was partial strength recovery at 91 days and the ratio of the strength recovery was a function of fly ash content in concrete.

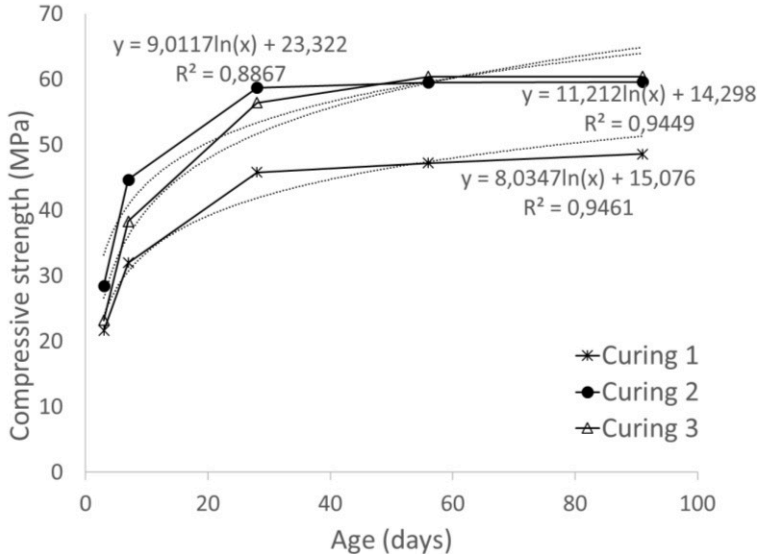

Figure 1: Strength development of FA00 at different curing conditions.

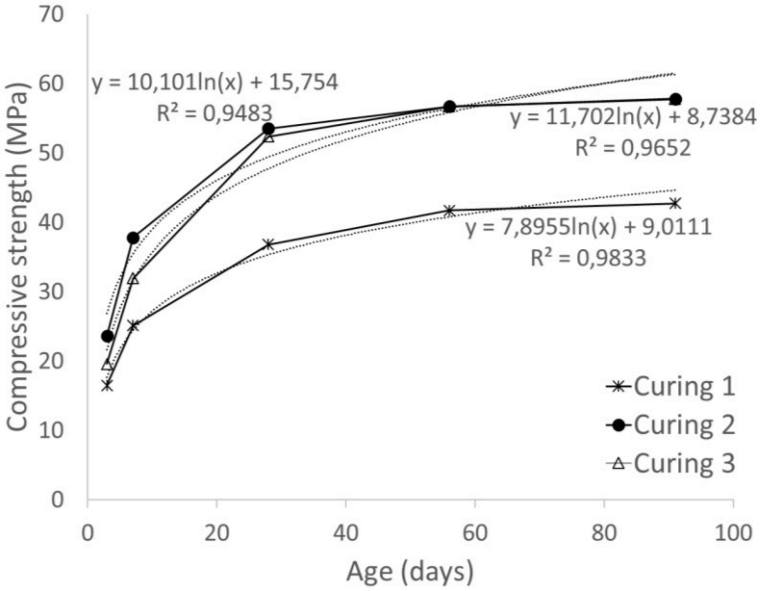

Figure 2: Strength development of FA15 at different curing conditions.

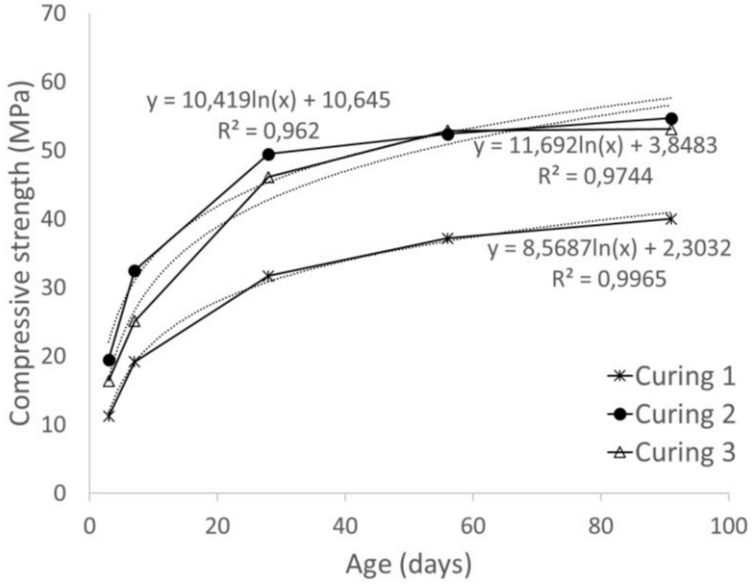

Figure 3: Strength development of FA30 at different curing conditions.

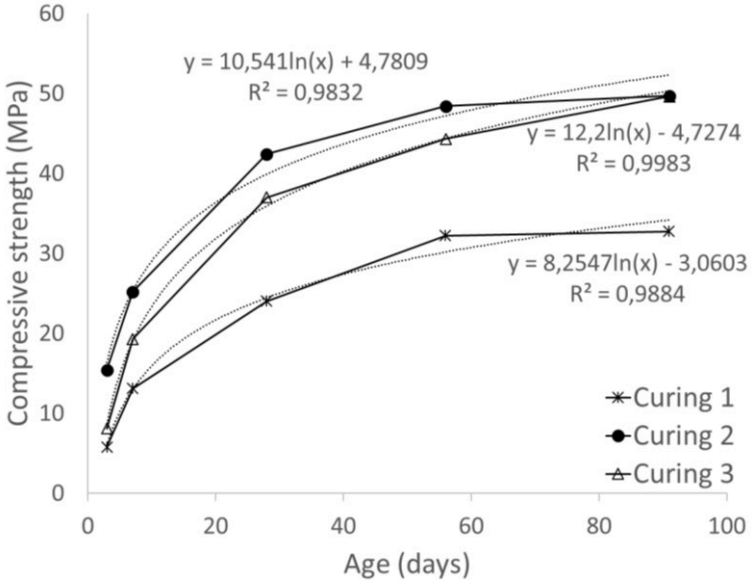

Figure 4: Strength development of FA45 at different curing conditions.

Control concretes exposed to Curing 3 had lower strength at early ages but they crossed over the strength of control concretes exposed to Curing 2, towards 56 days (Fig. 1). This behavior supports the well-known crossover effect for concretes cured at lower temperature at early ages. However, the crossover effect decreased (Fig. 2) and then disappeared (Figs. 3 and 4) with the increase of fly ash content, which emphasizes the importance of hot water curing for fly ash concrete.

Water curing leaded to higher rate of strength gain up to 28 days for fly ash concretes with and without fly ash (Figs. 1-4). However, the rate of strength gain up to 28 days decreased with increasing fly ash content (Figs. 2-4). In order to quantify this behavior, logarithmic trend lines with equation and R-square value were added to the strength development curves. For concretes without fly ash, the increase up to 28 days is sharp but very low after 28 days and the strength is almost constant until 91. Therefore, the strength development graph appears like the combination of two separate lines with different slopes rather than a continuous curve (Fig. 1). As a result of this, the strength development of concretes without fly ash does not fit well the logarithmic curve as indicated by the low R-square values. With an increase in fly ash content, the strength development becomes more continuous up to 91 days and it starts to fit better to the logarithmic curve (Figs. 2-4). On the other hand, the difference in R-square values between different curing conditions is insignificant at higher cement replacement ratios as the strength development becomes more and more slower even in Curing 2 and 3 (Figs. 3-4).
The ratio of the strength to 91-days strength as a percentage, S/S_{91}, for concretes without fly ash is given in Table 2. It is interesting to note that the rates of strength gain of concretes exposed to Curing 1 and Curing 3 are very close at almost all ages. The strength at Curing 3 was higher due to the higher availability of water which can react with a higher amount of Portland cement. On the other hand, as the mechanism of hydration is the same, the increase of S/S_{91} with age was similar despite the difference in the amount of hydrated cement. However, in fly ash concretes the mechanism of hydration is different. As pozzolanic reaction depends on the availability of $Ca(OH)_2$, when more Portland cement is reacted, the rate of the pozzolanic reaction will be higher. Consequently, the rate of strength gain at Curing 3 is higher than that at Curing 1.
This behavior can be explained with the principles of the maturity method. The maturity function, which is simply the product of temperature and age, is given by the following equation (Eq. 1) for the isothermal conditions:

$$S = S_{\infty} \frac{k_T (t - t_0)}{1 + k_T (t - t_0)} \qquad (1)$$

where S is strength at any age, S_{∞} is the limiting strength at infinite age, k_T is the rate constant, t is time and t_0 is the initial time below which there is no strength development. The rate constant increases with increasing curing temperature. The maturity method is based on the calculation of a relative strength rather than strength, which is given by the ratio S/S_{∞}.

The limiting strength can be assumed to be theoretically independent of the curing temperature. However, this generalization cannot be directly applied in the present study for two reasons. First, concretes cured in air curing can practically never reach the same strength as that of water cured specimens. It is well known that the water/cement ratio does not affect the rate constant significantly. The air cured specimens can be considered as different concrete mixes compared to the water cured specimens since the cement available for hydration is lower as in the case of a concrete with low water/cement ratio. Consequently, the rate constant can be similar for Curing 1 and 3 but the limiting strength is different. Second, high volume fly ash concretes need hot water curing to complete their hydrations so fly ash

concretes cured in mild and hot water can also be considered as different mixes in the evaluation of maturity. As the mechanism of hydration and the effect of curing are different, the rate constants and the limiting strengths are different for concretes with and without fly ash. Therefore, the approach used to evaluate the rate of strength gain by taking the ratio S/S_{91} for each concrete mix individually at different ages looks appropriate for evaluating the rate of strength gain (Table 2 and Figs. 1-4).

Table 2: S/S_{91} (%) at different ages for concretes exposed to different curing conditions.

Age (days)	**3**	**7**	**28**	**56**	**91**
FA001	44	66	94	97	100
FA002	48	75	98	100	100
FA003	38	63	93	100	100

4. Conclusion

The rate of strength gain with respect to 91 days strength was similar in the concrete mixes without fly ash at Curing 1 and Curing 3. In hot water curing (Curing 3), the rate was higher. Similar trend was observed for fly ash concretes, but water cured specimens had higher rate. The lower rate of strength gain was reflected to the shape of the logarithmic trendline and the more continuous strength development before and after 28 days resulted in better fitting to the trendline. The strength of specimens cured in mild water crossed over the strength of the specimens cured in hot water after 28 days. For fly ash concretes, the crossover effect was not observed. Hot water curing looks necessary to compensate low strength development of fly ash concretes. The rate of strength gain was related to the curing type, curing temperature and fly ash content. The findings can be useful in the application the maturity method, particularly for high volume concretes exposed to different curing conditions.

References

[1] Gopalan, M. K. and Haque, M. N., Strength development of fly ash concretes, Mater Struc 19 (1986), 33-37
[2] Xu, G., Tian, Q., Miao, J., Liu, J., Early-age hydration and mechanical properties of high volume slag and fly ash concrete at differen curing temperatures Constr Build Mater 149 (2017) 367-377
[3] Boubekeur, T., Ezziane, K., Kadri, E.H., Estimation of mortars compressive strength at different curing temperature by the maturity method, Constr Build Mater 71 (2014) 299-307
[4] Eren, Ö., Strength development of concretes with ordinary Portland cement, slag or fly ash cured at different temperature, Mater Struc 35 (2002) 536-540.

SynerCrete'18 International Conference on Interdisciplinary Approaches
for Cement-based Materials and Structural Concrete
24-26 October 2018, Funchal, Madeira Island, Portugal

DEVELOPMENT OF A HEATING MORTAR BLOCK SYSTEM FOR SNOW MELTING THROUGH QUASI MICROWAVES

Yosuke Ito [(1)], Shinji Kawabe [(1)]

(1) Nagoya Institute of Technology, Aichi, Japan

Abstract
Snow shoveling requires effort in regions of snowfall. There are various types of snow removal systems that do not depend on manpower; however, they exhibit some problems.
We can solve these problems by developing a snow melting system containing heating mortar blocks that convert electromagnetic waves into thermal energy. This system utilizes the electric arc furnace oxidizing slag, which is aggregated as an electromagnetic absorption material. Thus, this system can be expected to reduce the environmental load. Moreover, this system can melt snow more quickly as compared to that observed using the conventional methods. This study exhibits the snow melting performance of the heating mortar block system.

1. Introduction

Snow shoveling requires considerable effort in regions of snowfall. Some elderly people living in such areas cannot remove snow on their own. There are various types of snow removal systems that do not depend on manpower; however, they exhibit some problems. A snow melting system with electric heating cables requires its heat source cables to be buried deep inside the ground to avoid being cut by the load. Therefore, it requires a longer time to melt the snow and makes the running cost high. A snow melting system by groundwater sprinkling pollutes the road with contained minerals in the groundwater. The system also causes ground subsidence by overusing the groundwater. The snow-melting agent contained chloride that causes the rusting of iron structures. Therefore, a new system is expected to be invented that can cause the snow to melt more quickly as compared to that observed in the other existing systems.
We are able to solve these problems by developing a snow melting system containing heating mortar blocks that convert electromagnetic waves into thermal energy. Fig. 1 depicts the

overview of the heating mortar block system to melt snow. This system utilizes a microwave of a frequency of 2.45 GHz. Oscillators with 2.45-GHz frequency are extensively available at a reasonable price because they are produced in bulk as components of microwave ovens in Japan. Moreover, as compared to the conventional methods, this system can melt snow more quickly. This system obtains the heat that is required to melt snow in the following three steps. (1) The oscillator generates the electromagnetic waves of 2.45-GHz frequency. (2) The electromagnetic waves are leaked from the slot on the leaky waveguide. (3) This microwave is irradiated by heating the mortar blocks.

Fig. 2 exhibits the structure of the heating mortar block, which comprises the following three layers: (1) a base layer (without electromagnetic absorption ability) using sand as an aggregate, (2) an electromagnetic absorption material layer using electric arc furnace oxidizing slag as an aggregate, and (3) an electromagnetic shielding material layer using the arranged steel fibers. The electromagnetic waves are transmitted through the base layer and are absorbed by the electromagnetic absorption material layer and are further converted into heat. The electromagnetic waves that are not absorbed are reflected by the electromagnetic shielding material layer and are prevented from leaking outside.

The proposed system melts snow using the heating mortar blocks that generates heat from electromagnetic absorption. In contrast, the conventional snow melting system melts snow using the heat generated from the electric heating cables. The electric heating cables that are used as heat sources are buried deep inside the ground to avoid disconnection. However, electromagnetic absorption materials, used as heat sources, and leaky waveguides, which transmit electromagnetic waves, exhibit only a minor risk of disconnection. Therefore, because the heat source of a heating mortar block can be placed near to the ground surface, the proposed system can cause the snow to efficiently melt in a short time.

As depicted in Fig. 2, (1) the base layer is mortar with sand as an aggregate, which exhibits almost no electromagnetic absorption ability. Hereinafter, "mortar with sand as an aggregate" is referred to as "the sand mortar." (2) The electromagnetic absorption material layer exhibits an ability to absorb electromagnetic waves due to the presence of electric arc furnace oxidizing slag as an aggregate. Hereinafter "mortar with electric arc furnace oxidizing slag as an aggregate" is referred to as "the slag mortar." (3) The electromagnetic shielding material layer is a mortar that contains steel fibers that are arranged to exhibit an electromagnetic shielding ability. This study exhibits the snow melting performance of the heating mortar block system.

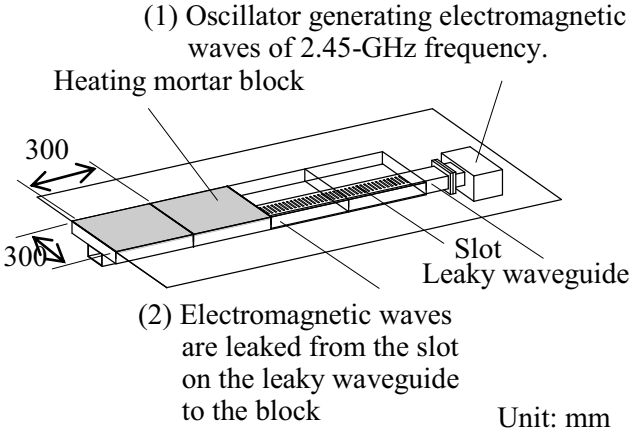

Figure 1: The heating mortar block system

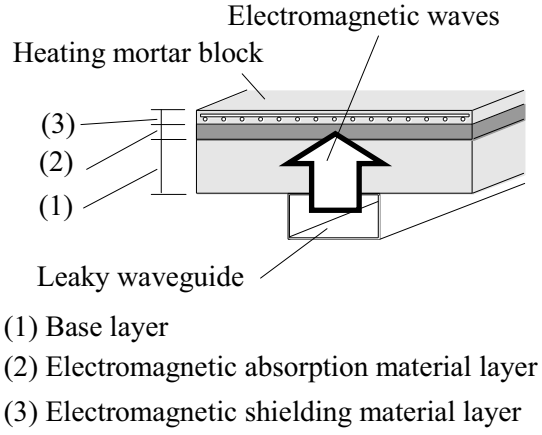

Figure 2: Heating mortar block

2. Design theory

If the absorbed power coefficient by the sample is S_0, the input power is P (W), irradiating time is t (s), and heating value is Q (J:W・s), Eq. (1).

$$Q = |S_0|^2 P \cdot t \tag{1}$$

Eq. (1) depicts the relation between the absorbed power coefficient and the heating value, and it can be observed that the heating value, Q, increases when the absorbed power coefficient increases. Therefore, an electromagnetic wave absorber can be utilized as a heating material.

3. Sample

3.1 Heating mortar block

Slag mortar contains electric furnace oxidizing slag as an aggregate. The electric furnace oxidizing slag is an industrial by-product that is generated when the recycled iron is produced. Hereinafter, "electric furnace oxidizing slag" is referred to as "slag." The composition of the slag is presented in Tab. 1. Because the slag exhibits a crystal structure containing iron oxide, it depicts a characteristic of magnetic loss (absorption) of the electromagnetic waves [1].
Slag and sand mortar are manufactured using the optimum mix proportion and thickness [2] to enhance the electromagnetic absorption ability. The mix proportion of the slag and sand mortar is presented in Tab. 2. The cement that has been used is the ordinary Portland cement. The thickness of the slag mortar is 8 mm, and the thickness of the sand mortar is 29 mm, considering that the mortar contains water. A waterproofing agent is added to the cement to prevent frost damage and change in the electromagnetic absorption ability due to the large amount of water absorption. The composition of the waterproofing agent is presented in Tab. 3. The cut wire netting [3] for shielding the electromagnetic waves is installed on the slag mortar, and a mortar having a thickness of 8 mm is coated on the cut wire netting to form a shielding material layer. The sample is dried for 1 day in air and is cured underwater for more than 5 days. Further, the sample is dried until it reaches an absolute dry state in a thermo-hygrostat at 100 °C. The heating mortar block is a square having a side of 300 mm.

3.2 Leaky waveguide

The leaky waveguide [4] is depicted in Fig. 1. There are slots on the top surface of the leaky waveguide. The width of the slot is 1.6 mm, and the length is 30 mm; the interval is 10 mm.

3.3 The Snow melting system using the heat generated from the electric heating cables

The concrete to bury the electric heating cables exhibits a width of 300 mm, a length of 2400 mm, and a thickness of 150 mm. Four electric heating cables were buried at intervals of 70 mm in the length direction at a depth of 50 mm from the upper surface of the concrete. The mix proportion of the concrete is presented in Tab. 4.

4. Measurement

The snow melting performance is clarified by performing the melting snow measurement. This experiment is performed using both the heating mortar block system (Fig. 1) and the electric heating cable system to melt the snow. The experimental setup is depicted in Fig. 3. To prevent the heating mortar block from affecting the electromagnetic wave leakage performance of the slot, as depicted in Fig. 4, the heating mortar blocks are installed upward at approximately 60 mm from the leaky waveguide using the U-shaped groove.
Each area that is capable of snow melting is approximately 0.3 × 2.4 m. Eight heating mortar blocks are installed one row above the leaky waveguide.
The snow melting performance is evaluated by the area at which the snow was melted and the amount of melted snow. To confirm the area at which the snow was melted, photographs of the snow melting condition were captured at an interval of 30 minutes, as depicted in Fig. 5, and were binarized; further, the area of the road surface that was exposed by melting the snow is detected. The amount of melted snow is calculated based on the amount of remaining snow. As depicted in Fig. 6, in the cross section and a direction perpendicular to the leaky waveguide, the heating mortar block and concrete with electric heating cable are divided into six, and the amount of snowfall at the division boundary is measured at an interval of every 30 minutes. We calculate the sum of decreases of the snow cover at the boundary of each division and assume this to be the "snow melt amount."
The electric power consumed in each area that capable of snow melting by the heating mortar block system and the electric heating cable system is 200 W. The measurement time is 330 minutes. The conditions to perform the snow melting measurement are presented in Tab. 5.

5. Results and consideration of measurement

Fig. 7 depicts the relation between the ratio of the snow melting area and the measurement time. Snow melts quickly due to stirring effect caused by walking on snow. Therefore, the measurement time until walking becomes possible is compared. A person can walk easily if the width of the road surface is about 150 mm or more. Thus, comparing the time required to melt the snow accumulated on 50% of the total area can help us to judge the superiority and

Table 1: Chemical components of the slag (Weight %)

CaO	SiO_2	MnO	MgO	FeO	Fe_2O_3	Al_2O_3	Cr_2O_3	TiO_2	P_2O_5	Total
19.53	12.92	5.66	4.57	19.67	24.13	8.40	1.97	0.42	0.332	97.60

Table 2: Mix proportion of mortar (Weight ratio)

	Cement	Slag	Sand	Water	Waterproof agent
Slag mortar	100	150	-	45	0.3
Sand mortar	100	-	300	45	0.3

Table 3: Mix proportion of waterproof agent (Weight ratio)

Mixture such as higher fatty acid salt	Poly(oxyethylene) nonylphenyl ether	Water
30–35	< 2.0	64–69

Table 4: Mix proportion of concrete (Weight ratio)

Cement	Sand	Gravel	Water	air-entraining and water-reducing admixture	air-entraining admixture
100	163	108	54	1.0	0.5

inferiority of the snow melting performance. In the heating mortar block system, the road surface is exposed in 90 minutes, and the snow melting area is observed to become more than 50% of the total area in approximately 170 minutes. However, the electric heating cable system requires approximately 205 minutes because the snow melting area exceeds 50% of the total area. Because the power consumption is proportional to the measurement duration, the heating mortar block system can reduce the electric energy by approximately 17% as compared with that observed in the electric heating cable system.
Fig. 8 depicts the relation between the snow melting amount and the measurement duration. Throughout the measurement, the heating mortar block system exhibits more snow melting and better snow melting performance than those exhibited by the electric heating cable system.
Fig. 9 depicts the photograph that was captured 150 minutes after initiating the measurement,

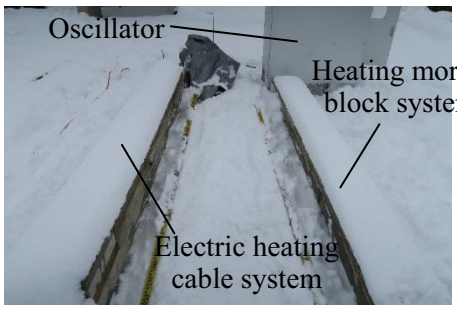

Figure 3: Snow melting experiment equipment

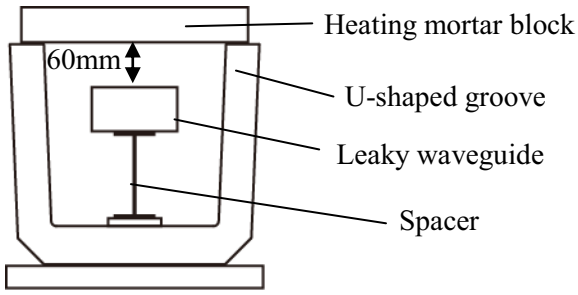

Figure 4: Cross sectional view of the heating mortar block system for melting snow

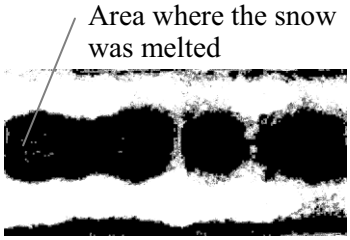

Figure 5: Binarized photograph

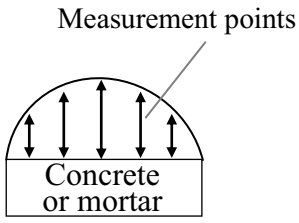

Figure 6: Measurement points

Table 5: The conditions of snow melting measurement

Place	Fukui Prefecture in Japan
Measuring date	Jan. 16, 2018
Temperature	0 °C
Snow depth	100 mm

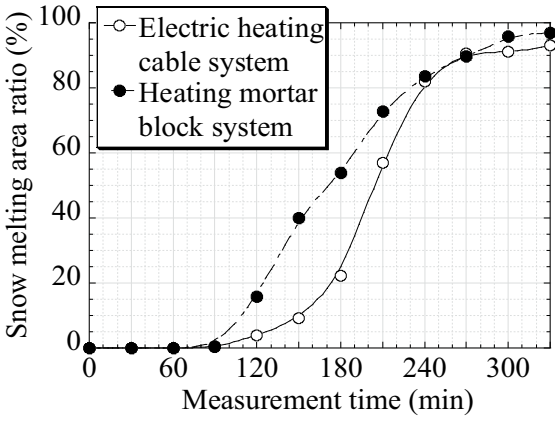

Figure 7: Relation between the ratio of snow melting area and measurement duration

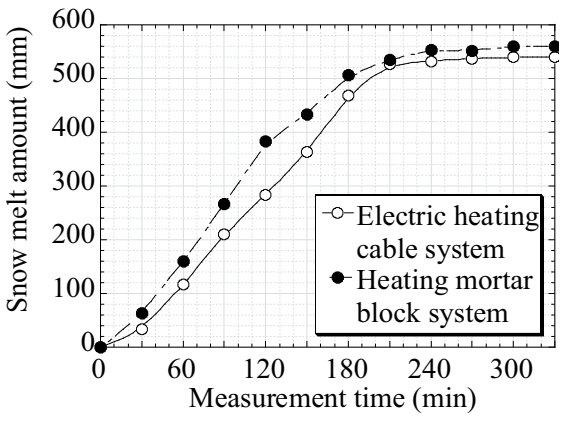

Figure 8: Relation between the snow melting amount and measurement duration

Figure 9: After 150 minutes

Figure 10: After 330 minutes

whereas Fig. 10 depicts the photograph that was captured after 330 minutes. The melting snow conditions of the heating mortar block system and the electric heating cable system exhibit the maximum difference after 150 minutes of initiating the measurement. After 330 minutes from the start of the measurement, there was no snow left in both the systems.

6. Conclusion

By conducting the experiment, the following points were clarified.

(1) The heating mortar block system can reduce the electric energy by approximately 17% as compared to that observed in the electric heating cable system.
(2) Throughout the measurement, the heating mortar block system exhibits more snow melting and improved snow melting performance as compared to those exhibited by the electric heating cable system.

Acknowledgments

This work was partially supported by the JSPS KAKENHI Grant Number JP16K18183 and JP16K06569. Some suggestions were provided by the Honorary Professor of the Nagoya Institute of Technology, Tetsuo Ikeda, and Ten corporation. The experiment was conducted with the help of Haruki Taguchi and Hideyuki Yasui, who are both students of Nagoya Institute of Technology. We gratefully acknowledge their supports and contributions to the research that has been reported in this study.

References

[1] Kawabe, S., Ikeda. T., Ito. Y., Development of the Heating Mortar Block to Melt Snow by the Quasi Microwave, Journal of Structural and Construction Engineering 69 (586), Japan (2004), 1-5
[2] Ito, Y., Ohba, S., Kawabe, S., Effects of thickness of the base layer on electromagnetic absorption in heating mortar blocks for snow melting through quasi microwave, Journal of Advanced Concrete Technology 16, Japan (2018), 170-178
[3] Ito, Y., Kawabe, S. and Ohba, S., Study of Electromagnetic shielding material on heating mortar blocks for melting snow through quasi microwaves, Journal of Structural and Construction Engineering 82 (731), Japan (2017), 1-10
[4] Ito, Y., Kawabe, S. Ohba, S. and ANZAI, H., Study of A Leaky Waveguide on Heating Mortar Blocks for Melting Snow through Quasi Microwaves, Journal of Structural and Construction Engineering 82 (737), Japan (2017), 969-978

SynerCrete'18 International Conference on Interdisciplinary Approaches
for Cement-based Materials and Structural Concrete
24-26 October 2018, Funchal, Madeira Island, Portugal

DURABILITY PROPERTIES OF AUTOCLAVED AERATED AND HIGH PERFORMANCE FOAMED CONCRETE

Genadijs Sahmenko [(1)], Aleksandrs Korjakins [(1)], Eva Namsone [(1)]

(1) Riga Technical University, Riga, Latvia

Abstract
Autoclaved Aerated Concrete (AAC) and Foam Concrete (FC) are sustainable lightweight intelligent materials for the modern building industry. FC is a more universal material and it may be applied both for monolithic and prefabricated constructive elements. Flexible technology of FC allows achieving a wide range of properties (density 200 – 1800 kg/m3 and compressive strength 0.2 – 40 MPa). The range of properties of a typical AAC includes density 250 – 800 kg/m3 and compressive strength 0.5 – 10 MPa, but normal weight ready-mixed concrete is characterized by density > 2000 kg/m3 and compressive strength 30 – 50 MPa.
In comparison with ACC, FC is more durable, at the same time, FC has lower strength at the same density, comparing to the aerated autoclaved concrete. The aim of this study is to elaborate high performance foam concrete, characterized by high durability properties and competitive compressive strength.
In the framework of this study, foam concrete compositions were elaborated, using intensive mixing technology and micro admixtures in order to improve their physical and mechanical properties. Properties of the elaborated compositions, such as density, compressive strength, capillary water absorption and frost resistance, were compared with the properties of commercially used AAC. The obtained FC compositions are characterized by low water absorption, high frost resistance and strength – density relation comparable with AAC.

1. Introduction

Autoclaved Aerated Concrete (AAC) and Foam Concrete (FC) are two types of cellular concrete that are traditionally used in modern civil engineering. Its positive properties include simple technology, utilisation of local raw materials and by-products, as well as low embedded energy and carbon dioxide emission and economic benefits to transport [1].

Ecological benefits of cellular concrete are determined by its composition, because air cells take up to 80% from the total volume of the material. AAC technology provides chemical aeration of lime-silicate mix and thermal treatment in special steam pressure chamber, which saves a lot of energy. AAC technology allows producing only prefabricated elements. Production technology of FC provides mechanical aeration of cement mortar using foaming agents [2]. Therefore, FC is a more universal material and it may be applied both for monolithic and prefabricated constructive elements. Controlling the ratios of components and technological parameters, a wide range of FC properties may be achieved: density 200 – 1800 kg/m3 and compressive strength 0.2 – 40 MPa. The range of properties of a typical AAC includes density 250 – 800 kg/m3 and compressive strength 0.5 – 10 MPa, but normal weight ready-mixed concrete is characterized by density > 2000 kg/m3 and compressive strength 30 – 50 MPa. Both FC and AAC have advantages and disadvantages. [1] High specific strength (strength – density ratio) is an advantage of AAC, at the same time, AAC is characterized by high water uptake and hygroscopicity. Lower strength at the same density is a disadvantage of FC compared to the aerated autoclaved concrete. Drying and carbonation shrinkage also increases the risk of cracking and loss of durability. Both materials are intended for use on wall constructions, there is a risk of material water saturation during construction process. In the conditions of wet and cold climate, negative effect of moisture is aggravated by freezing-thawing cycles. Thus, the following factors of FC durability should be taken into account: mechanical strength, water absorption, frost resistance, carbonation, and shrinkage.

Two FC preparation methods may be mentioned; the method of pre-foaming consists in mixing together of specially generated foam and prepared cement mortar. The other one, mixed-foaming method, implies mixing and foam generation in one mixing tank.

Previous investigations [3] demonstrated that highly intensive mixing has a lot of advantages: it provides homogenous mix, promotes accelerated hydration and effective use of cement, and keeps together fine aggregate and the agglomerated cement. Intensity of mixing depends on speed of mixing elements. Traditional low speed mixers are characterized by speed about 2 m/s, turbulence 2 – 10 m/s, and effect of cavitation may be achieved at the speed >15 m/s. FC compositions prepared in a turbulence mixer with the effect of cavitation have been evaluated in this study.

The aim of this study is to elaborate high performance foam concrete, characterized by high durability properties and competitive compressive strength. In the framework of this research, foam concrete compositions were elaborated using intensive mixing technology. Micro admixtures, porous aggregates and superplasticizers were applied in order to improve their physical and mechanical properties.

2. Materials and methods

Basic components of FC mixes are normal type Portland cement CEM I 42.5 N and natural washed sand (fraction size 0/0.5 mm), it was used as a filling component. A synthetic foaming agent (PB-Lux) was mixed with water and added during the mixing.

Lightweight filling materials (foamed glass grains and microspheres, or cenospheres) were used as filling, density reducing and internal curing component. Silica-alumina microspheres is a by-product from the combustion of coal in the thermal power plants [4]. Micro spheres

have a very hard shell, but they have density in the range of 600 to 900 kg/m^3 due to their hollow structure [5].
Pulverized silica fume and metakaolin were added as supplementary cementitious materials and an effective pozzolanic admixture [6]. These also decrease a potential risk of alkali – silica reactions in case of using foamed glass aggregate [7].
Eight experimental FC mixes were elaborated and produced using mixed-foaming technology. Composition I may be considered a reference mix. Compositions II, IIP, III and IIIP contain cenospheres, but Compositions III and IIIP are produced with superplasticizer, which allows decreasing water cement ratio. Compositions IP, IIP and IIIP contain lightweight filler – foamed glass granules, 4/8 mm.
First six mixes were produced in the laboratory mixed-foaming turbulence mixer providing mixing intensity up to 1,000 min^{-1}. Mixes SF and SF/C were produced in Warmhouse Ltd. industrial turbulence mixer with the cavitation effect. Mix compositions (in mass proportions) are presented in Table 1.
The samples, 100x100x100mm cubes, were prepared and cured in normal hardening conditions (20+2^{o}C, RH>90%). The samples of commercially available AAC with the same dimensions were used as reference AAC samples (GB400 with density 400 kg/m^3 and GB550 with density 550 kg/m^3).
Compressive strength and density were determined in accordance with EN 772-1.
Capillary water absorption of the exposed concrete surface was determined immersing one side of the samples in water according to LVS EN 772 – 11. The values of the capillary surface water absorption (g/dm^2) were evaluated as mass difference of the saturated and dry sample (g) related to the exposed surface area (gm^2). After capillary water absorption test, the same specimens were subjected to frost resistance test by freezing to -20^{o}C and thawing at +20^{o}C (according to LVS CEN/TS 12390-9). After being exposed to freeze-thaw cycles, the specimens were visually inspected and the quantity of the crumbled particles (g/m^2) was determined.

Table 1: Mix compositions.

	I (REF)	**IP**	**II**	**IIP**	**III**	**IIIP**	**SF**	**CF/C**
Portland cement CEM I 42.5 N	1.00	1.00	1.00	1.00	1.00	1.00	1.00	1.00
Sand	0.63	0.63	–	–	–	–	0.57	0.57
Water	0.61	0.61	0.75	0.75	0.63	0.63	0.80	0.80
Foaming agent	0.006	0.006	0.004	0.004	0.006	0.006	0.002	0.002
Cenospheres	–	–	0.50	0.50	0.50	0.50	–	–
Metakaolin	0.05	0.05	0.05	0.05	0.15	0.15	–	–
Silica Fume	0.04	0.04	0.04	0.04	0.04	0.04	0.03	0.03
Foamed glass granules, 4/8 mm	–	0.70	–	0.80	–	0.60	–	–
Plastic fibres	0.002	0.002	0.002	0.002	0.002	0.002	0.001	0.001
Carbon fibres	–	–	–	–	–	–	–	0.001
Superplasticizer	–	–	–	–	0.01	0.01	–	–

3. Results and discussion

Testing results of FC and AAC compositions are summarized in Table 2. Very low frost resistance of commercially produced AAC concrete may be recognized: after 10 – 16 cycles, the samples were almost totally destroyed (see Fig. 1). Comparing a FC sample (IP) and the same density AAC sample (GB550), at least twice lower strength of the FC sample was observed. The use of light weight fillers allows decreasing the density of FC samples (Compositions IP, IIP and IIIP). Combining cenospheres with foamed glass provides a more effective mix composition: FC sample IIP has the same strength as AAC sample GB550 with the same density. The best result was achieved by complex use of foamed glass, cenospheres and superplasticizer, which provides lower water cement ratio: strength of sample IIIP exceeds the strength of AAR sample GB550 of the same density 1.5 times. FC compositions with cenospheres and foamed glass showed much less surface scaling after freeze-thaw cycles (<60 g/m^2) compared to AAC samples (>1500 g/m^2).
The highest compressive strength, density and frost resistance were achieved for high density FC samples (SF and SF/C) produced in the industrial mixer with cavitation effect. No damages were observed after 76 (see Fig. 1) and 100 cycles and moderate surface scaling <100 g/m^2 after 130 cycles, thereby frost resistance can be evaluated as F100, which is comparable with normal concrete. Strength values of these compositions (13 – 18 MPa) also are comparable with the strength of normal weight concrete.

Table 2: Results summary.

Designation	Density (kg/m3)	28 d. compressive strength (MPa)	Freeze-thaw cycles	Weight loss (g/m^2)	Capillary water absorption 1 h (g/dm^2)
I (REF)	736	2.5	14	5	43.9
IP	565	1.4	14	60	17.6
II	769	6.3	14	130	28.3
IIP	445	2.5	14	50	14.0
III	952	14.4	14	110	7.9
IIIP	589	5.7	14	30	4.8
SF	1210	13.7	100	<100	12.2
SF/C	1360	18.2	100	<100	10.0
GB400	400	2.4	10	>1500	46.0
GB550	550	3.6	10	>1500	63.0

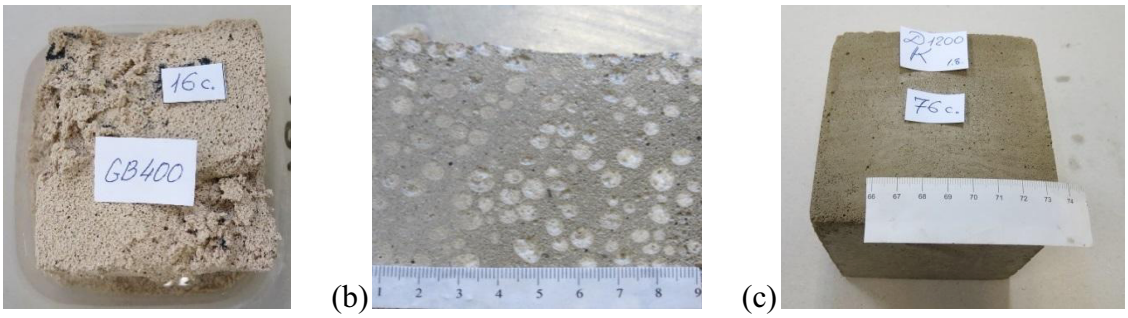

(a) (b) (c)

Figure 1: (a) AAC (GB400) after 16 cycles: material is destroyed; (b) IIIP after 14 cycles: scaling 30 g/m^2; (c) SF/C (D1200) after 76 cycles: scaling <100 g/m^2.

The hihest values of capillary water absorption (>40 g/dm^2) were demonstrated by the samples ofg AAC (GB400 and GB600) and FC without light weight fillers and superplasticizer (Composition I). Adding foamed glass grains twice decreases water absorption (comparing Compositions I and IP, II and IIP, III and IIIP). Complex use of foamed glass, cenospheres and superplasticizer makes it possible to decrease water uptake up to nine times compared to the reference mix I. Previous studies [8] proved that the use of light weight fillers allows decreasing drying shrinkage up to six times.

Correlation diagram between strength and density is built for different FC compositions produced in the industry and in the laboratory (see Fig. 2). The relation close to parabolic is obtained. The authors suggest considering compositions situated above the averaged curves as effective, and compositions situated below the averaged curves as non-effective. Consequently, mix compositions SF, SF/C, IIP, IIIP may be considered effective (high performance), but composition above the curve – non-effective.

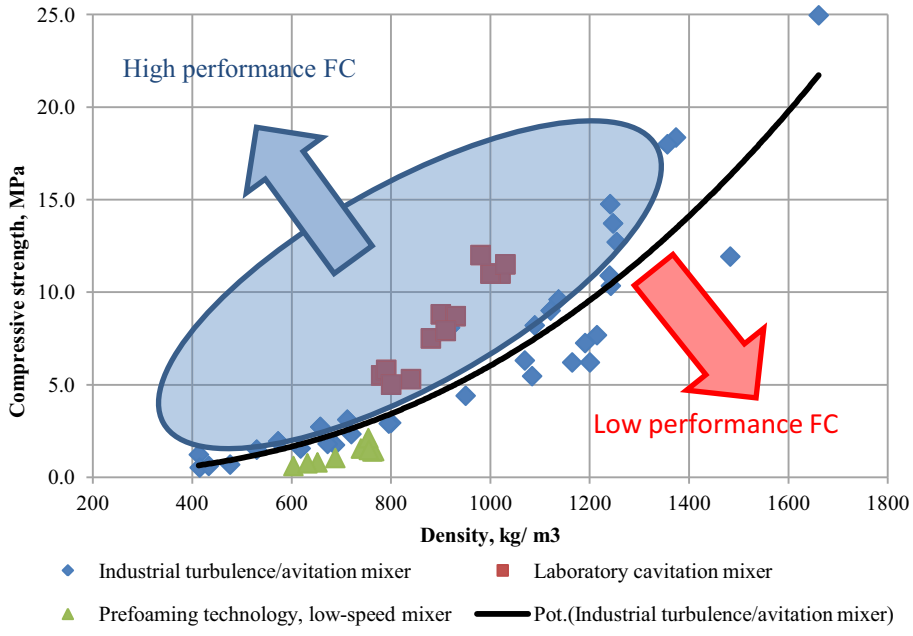

Figure 2: Correlation density – compressive strength.

4. Conclusions

- Compared to the traditional autoclaved aerated concrete (AAC), foam concrete (FC) allows obtaining a more durable material in terms of improved water resistance, frost resistance and durability.
- Traditional autoclaved aerated concrete (AAC) has higher strength comparing to traditional foam concrete in the range of densities 400 – 600 kg/m3. The use of turbulence and cavitation mixing technologies combined with lightweight fillers and modifying admixtures is a way to obtain high performance foam concrete with higher strength compared to the traditional pre-foaming foam concrete and AAC.
- Complex use of foamed glass, cenospheres and superplasticizer allows reducing capillary water absorption up to eight times and reducing drying shrinkage up to six times due to the effects of self-curing and formation of the skeletal material.

Acknowledgement
The financial support of the European Regional Development Fund project Nr.1.1.1.1/16/A/007 "A New Concept for Sustainable and Nearly Zero-Energy Buildings" is acknowledged.

References

[1] M. Kavita and C. Tarjani, "Comparison on Auto Aerated Concrete to Normal Concrete," no. March, pp. 90–94, 2016.
[2] K. Ramamurthy, E. K. Kunhanandan Nambiar, and G. Indu Siva Ranjani, "A classification of studies on properties of foam concrete," Cem. Concr. Compos., vol. 31, no. 6, pp. 388–396, 2009.
[3] G. Sahmenko, A. Korjakins, and E. Namsone, "High Performance Foam Concrete Produced in Turbulence Mixers," in SBE 16 Malta Europe and the Mediterranean Towards a Sustainable Built Environment, 2016, pp. 71–78.
[4] N. Ranjbar and C. Kuenzel, "Cenospheres : A review," Fuel, vol. 207, pp. 1–12, 2017.
[5] K. S. Chia, M. H. Zhang, and J. Y. R. Liew, "High-strength high-performance lightweight concrete : a review," 9th Int. Symp. high Perform. Concr. Verif. Util., no. August, pp. 9–11, 2011.
[6] O. Poznyak and A. Melnyk, "Non-autoclaved aerated concrete made of modified binding composition containing supplementary cementitious materials," Bud. i Archit., vol. 13, no. 2, pp. 127–134, 2014.
[7] E. Namsone, G. Sahmenko, E. Namsone, and A. Korjakins, "Reduction of the capillary water absorption of foamed concrete by using the porous aggregate," IOP Conf. Ser. Mater. Sci. Eng., vol. 251, no. 1, 2017.
[8] E. Namsone, G. Šahmenko, A. Korjakins, and E. Namsone, "Influence of Porous Aggregate on the Properties of Foamed Concrete," Constr. Sci., vol. 19, no. 1, pp. 13–20, 2016.

SynerCrete'18 International Conference on Interdisciplinary Approaches
for Cement-based Materials and Structural Concrete
24-26 October 2018, Funchal, Madeira Island, Portugal

EFFECT OF INITIAL CURING ON CORROSION BEHEAVIOR OF STEEL BARS IN FA CONCRETE UNDER DRY AND WET ACTIONS

Wakako Sugino [(1)], Keiyuu Kawaai [(1)], Isao Ujike [(1)]

(1) Ehime University, Ehime, Japan

Abstract
This study reports on the effect of initial curing on the corrosion behavior in Fly ash (FA) concrete, which was examined through chloride-induced corrosion tests induced by dry and wet cycles. After 182 days of the corrosion tests, corrosion properties in the specimens cured under dry or wet conditions including (sealed moist curing and water curing) were examined based on cathodic polarization properties, half-cell potential, and microcell and macrocell corrosion current density. In particular, detailed analysis was carried out on the resistance against ingress of corrosive substances such as moisture and dissolved oxygen via cathodic polarization measurements in determining the rate of oxygen permeability on embedded steel bars. It is noted that segmented steel bars comprising two steel elements (steel element-I closer to the exposed surface; steel element-II far from the exposed surface) was embedded in the specimens. Based on the results obtained in this study, the results suggest that the macrocell corrosion observed in water cured specimens could be triggered by oxygen concentration cell actions.

1. Introduction

When corrosion of steel bars occurs in concrete, anodic reactions in which iron ionizes and cathodic reactions in which oxygen is reduced progress on the surface of the steel bar. And a corrosion cell between the electro-chemical reactions is formed. It is reported that oxygen permeability is one of the significant factors that greatly affect the corrosion processes of steel bars in concrete [1]. In addition, corrosion of steel bars in concrete is classified into microcell corrosion and macrocell corrosion [2]. Generally, when anodic and cathodic reactions occur at the same or extremely close positions, they are referred to as microcell corrosion. On the other hand, macrocell corrosion occurs at positions where anodic reactions and cathodic reactions are separated from each other and the corrosion progresses locally. Factors

contributing to the macrocell corrosion formation include heterogeneity in the concrete, uneven distribution of chloride content, ambient environment, and, variations in dissolved oxygen concentrations. In addition, especially in Fly ash (FA) concrete, initial curing is a significant factor affecting durability and corrosion. This study examines the effect of initial curing on the corrosion behavior in fly ash (FA) concrete subjected to dry and wet actions.

2. Experimental program

2.1 Materials and mix proportion

In this study, water to binder ratio (W/B) was selected as 50% for both OPC and FA mixtures. FA (JIS A 6201 type-II) was used as partial replacement of cement with a replacement ratio of 30%. Fig. 1 shows the schematic of the reinforced concrete specimens. The specimens are of cross section, 100×150 mm and 200 mm long. And segmented steel bars comprising round steel bar (ϕ22) and length of 100 mm, were embedded at the depth of 20 mm from the exposed surface. The steel bars were divided into two elements in the perpendicular direction of the section which was connected by epoxy resin with a thickness of 1 mm. It is noted that the segmented steel bars comprising two steel elements (steel element-I closer to the exposed surface; steel element-II far from the exposed surface) was embedded in the specimens. Tab. 1 shows the mix proportions of concrete mixtures and Tab. 2 shows the materials properties of the aggregate used in this study. The specimens were demolded and cured under different conditions as summarized in Tab. 3. After cured, 5 surfaces except for the exposed surface were covered with epoxy resin.

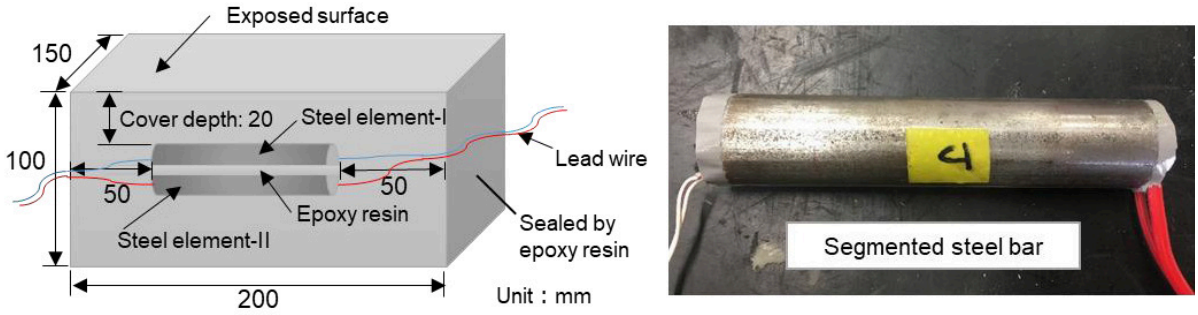

Figure 1: Schematic of the reinforced concrete specimens.

Table 1: Mix proportion

Mixtures	W/B (%)	Unit weight (kg/m^3)					(g/m^3)	
		W	C	FA	S	G	AEA-WRA	AEA
OPC	50	175	350	-	845	922	5597	1400
FA	50	175	245	105	829	905	2099	700

Table 2: Properties of aggregate

Fine aggregate (S) Coarse aggregate (G)	Types	Specific gravity (SSD)	Absorption capacity	Fineness modulus
S	Crushed sand obtained from sandstone	2.61	0.88	2.87
G	Crushed sandstone G_{max}: 20 mm	2.63	1.15	-

Table 3: Cases of initial curing condition

Mixtures	Age of demolding	Curing	CASE
OPC	1 day	Water (28 days)	A
	3 days	Air (28 days)	B
FA	1 day	Water (28 days)	D
	1 day	Sealed moist (7 days)	E
	1 day	Sealed moist (14 days)	G
	3 days	Air (28 days)	J

2.2 Electro-chemical measurements

Chloride-induced corrosion tests using salt wate at a concentration of 10% NaCl was carried out through dry and wet cycles. The specimens were left under room conditions controlled at 20^{o}C (4 days for the dry conditions and 3 days for the wet conditions). Half-cell potential (ASTM C876), and cathodic and anodic polarization curves were measured at the end of each wet period. In addition, the macrocell corrosion current density was measured using a zero-resistance ammeter connected between each steel element [2]. The rate of oxygen permeability was estimated based on the result of the cathodic polarization curve in which limiting current density is assumed according to past research [3].

3. Results and discussion

3.1 Half-cell potential

Fig. 2 shows the half-cell potentials of steel elements-I and II measured in the OPC and FA specimens up to 22 cycles of the dry and wet exposure tests. Fig. 3 shows differences in the half-cell potentials measured between the steel elements-I and II up to 22 cycles. It is noted that the positive value indicates the potential on the steel element-I is more negative. As can be seen in Fig. 2, the half-cell potential for both steel elements-I and II was the most positive in the case of the water cured FA specimens (D) until the age of 28 days. And, the results show that initiation time of the corrosion was dependent on the initial curing conditions. As shown in Fig. 3, in the cases of sealed moist cured FA specimens until the age of 7 days and 14 days and air cured FA specimens until the age of 28 days, the half-cell potential on the steel element-I close to the exposed surface is more negative and the steel element-II is relatively positive compared to those of the steel element-I. In contrast to the results, in the case of water cured FA specimens until the age of 28 days, the half-cell potential observed between the steel element-I and II draws a distinction in that the potential on the steel element-II was likely to be more negative. Thus, clear differences in the corrosion properties taking place on the steel elements were observed especially in the water cured FA specimens.

Based on the observations made in the potentials, it is assumed that the potential differences observed between the steel element-I and II could contribute to macrocell corrosion formation, which is discussed in Section 3.2.

3.2 Macrocell corrosion current density

Fig. 4 shows the results of the macrocell corrosion current density measured using a zero-resistance ammeter in each specimen for 1 week from the age of 175 days to 182 days. From these figures, in the cases of water cured OPC and FA specimens until the age of 28 days, element-I is observed to form cathodic region in the corrosion cell. On the other hand, the steel element-II in the other FA specimens is like to form cathodic region. Thus, the anodic and cathodic regions specified based on the current flows via macrocell corrosion are observed to be varied depending on the initial curing conditions. The results obtained in the macrocell corrosion current density are consistent with the electromotive force caused by the potential differences observed in Section 3.1. Generally, the steel element-I closer to the exposed surface could form anodic region owing to increased concentration of chloride ions through the dry and wet cycles. However, such corrosion behavior was not observed in the case of water cured specimens of OPC and FA until the age of 28 days.

As mentioned in introduction, apart from the electromotive force caused by the potential

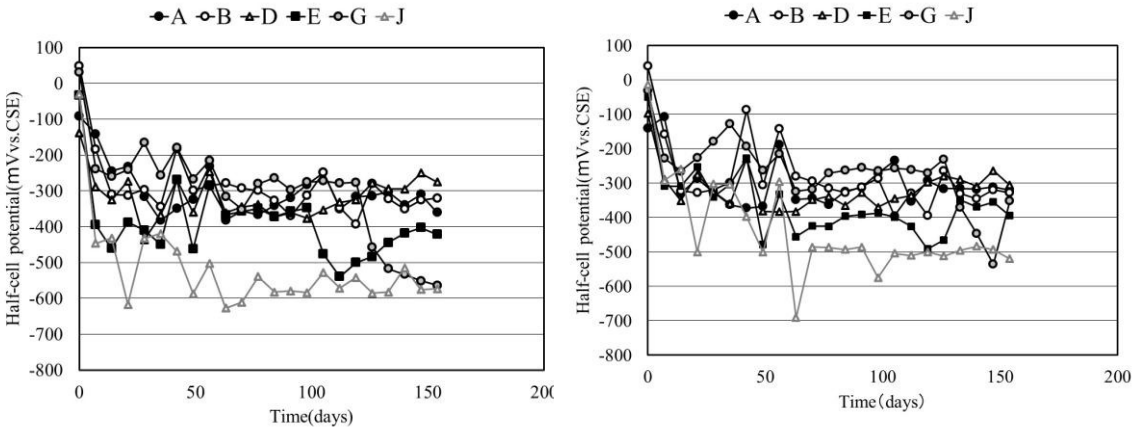

Figure 2: Half-cell potential (left: element-I, right: element-II).

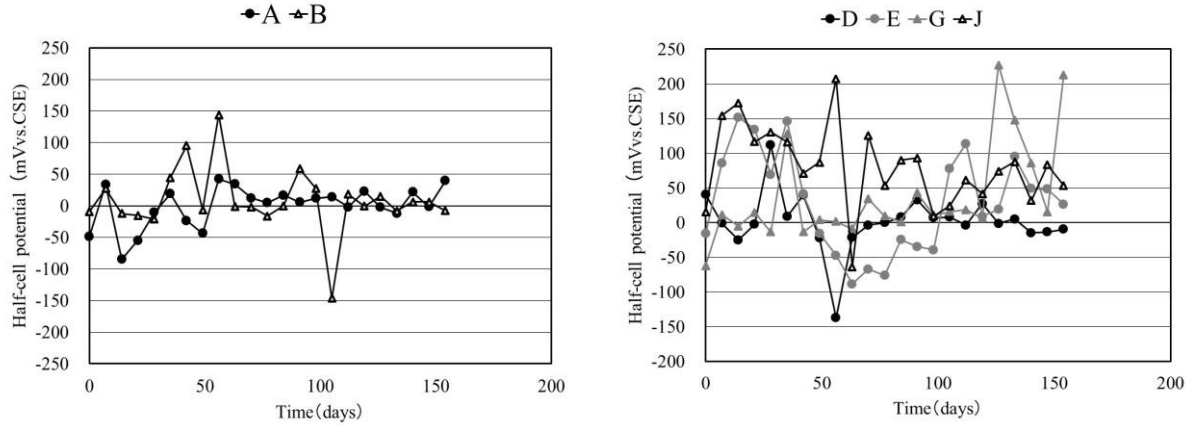

Figure 3: Differences in the half-cell potential measured on the steel element-I and II (left: OPC, right: FA).

difference, the oxygen concentration cell could be a significant factor contributing to the macrocell action on the steel bar in concrete. The regions on steel bars with lowered dissolved oxygen concentration tend to become the anode, and the regions on steel bars with relatively higher concentrations serve as the cathode, thus forming the concentration cell in promoting the corrosion in the anodic region. It has been pointed out that it plays a major role in corrosion of steel bars in concrete [4].

In the case of air cured specimens, the permeation front could penetrate up to the deeper zones of the cover concrete, and the steel element-II could be exposed to the water containing dissolved oxygen for longer periods compared to the water cured specimen [5]. However, the permeation front gradually becomes shallower for both cases, and then it was found to be slightly deeper in the case of water cured specimen. This is expected to reach the steel element-I. In addition, in the case of water cured specimen, the difference in the dissolved oxygen concentration could be possibly larger owing to the denser pore structure formed which has higher resistance against the water ingress. Based on the results obtained in this experiment, there is a good possibility that the steel element-II of the steel bar with lower dissolved oxygen concentration became the anode, and the steel element-I of the steel bar served as the cathode, thus forming the concentration cell. The results are consistent with the potential difference observed between the steel element-I and II. The rate of oxygen permeability on the steel elements is further discussed in Section 3.3.

3.3 Oxygen Permeability (Cathodic Polarization)

Fig. 5 shows the rate of oxygen permeability measured on the steel element-I and II at the age of 28 days. As can be seen in the cases of water cured OPC and FA specimens, the results show that the rate of oxygen permeability is clearly higher in the steel element-I of the segmented steel bar compared to those observed in the steel element-II. This led to the largest differences in rate of oxygen permeability measured between element-I and element-II. The rate of oxygen permeability is relatively lower in the steel element-II of the segmented steel bars and the oxygen permeability is found to be higher in the steel element-I in the case of water cured until the age of 28 days. In the FA specimens, the rate of oxygen permeability is gradually expected to change due to the pozzolanic reactions and the dry and wet cycles from the age of 28 days to 91 days. However, in the case of water cured specimens, the permeation front could reach deeper zones of cover concrete i.e. embedded steel bar element- I when steady state is assumed to reach. The results suggest that in the case of water cured specimens until the age of 28 days, the oxygen concentration cell action could be triggered via difference

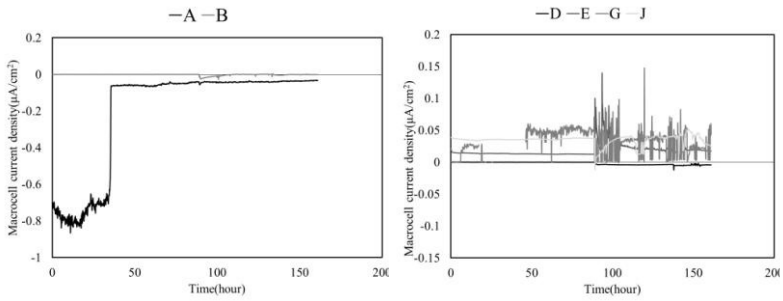

Figure 4: Macrocell corrosion current density (left: OPC, right: FA).

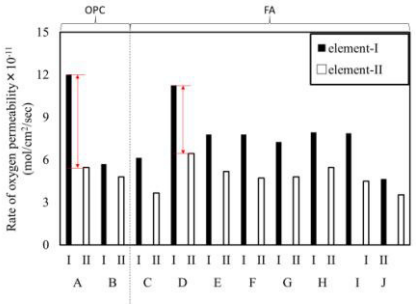

Figure 5: Rate of oxygen permeability.

of the rate of oxygen permeability observed in the steel bar located closer to and far away from the exposed surface. This agrees with the results of the anodic and the cathodic region specified based on the current flows of the macrocell corrosion formed in th segmented steel bars.

4. Conclusion

Especially in FA concrete, initial curing is a significant factor contributing to the corrosion resistance. This study examined the effect of initial curing on the corrosion behavior and properties in FA concrete, which was conducted via chloride-induced corrosion tests. In particular, this study aimed at examining the effect of initial curing on the macrocell corrosion formation under dry and wet actions.

In the cases of water cured OPC and FA specimens until the age of 28 days, the difference in the rate of oxygen permeability between steel element-I (closer to the exposed surface) and II (far away from the exposed surface) at age of 28 days was found to be the largest compared to those observed in the specimens with other curing conditions. The results indicate that the difference in the macrocell corrosion properties observed up to the age of 182 days can be adequately explained by the differences observed in the rate of oxygen permeability between the element-I and II of the segmented steel bars, which was measured at the age of 28 days immediately after the initial curing was carried out. Based on the results obtained in this study, it is suggested that the macrocell corrosion observed in water cured specimens could be triggered by oxygen concentration cell actions.

References

[1] Mohanned, T.U., Otsuki, N. and Hamada, H., Oxygen permeability in cracked concrete reinforced with plain and deformed bars, Cem Concr Res, 31 (2001), 829-834.
[2] Miyazato, S. & Otsuki, N., The estimation of macrocell corrosion rate of rebar in existing concrete using non-destructive tests, Concr Res Tech, 12 (2001), 93-103. (in Japanese)
[3] Nagataki. S. Otsuki. N. Moriwake, A. & Miyazato. S. 1996. The experimental study on Corrosion Mechanism of Reinforced Concrete at Local Repair Part. Journal of Materials, Concrete Structures and Pavements, JSCE, 544(32), 109-119. (in Japanese)
[4] Gouda, V.K. & Mourad, H.M., Corrosion Science, 14 (1974) p. 681.
[5] Kawaai, K. & Ujike, I., Effect of Initial Curing on Ingress of Corrosive Substances and Corrosion Resistance in Fly Ash Concrete, Journal of the Society of Materials Science, 66 (2017), 608-614. (in Japanese)

EFFECT OF MARBLE POWDER WASTE ON THE PROPERTIES OF SELF COMPACTING CONCRETE

Ali M. Mansor [(1)], Asaad A. Elshab [(1)], Ruben P. Borg [(2)], Ahmed M. M. Hamed [(2)]

(1) Department of Civil Engineering, University of Tripoli, Libya
(2) Faculty of the Built Environment, University of Malta, Malta

Abstract

The marble production industry generates a considerable amount of waste materials in Libya. Waste is generated in the mining, processing and polishing stages. The processing wastes are dumped, with a negative impact on the environment. However there is potential in the reuse of marble waste, particularly in the manufacture of concrete products. This study was conducted to investigate the influence of marble powder (MP), as a partial cement replacement in self-compacting concrete (SCC). Several SCC mixes were prepared with varying replacement of cement with MP. The properties of fresh SCC were determined through the slump flow, + T50 time, V-funnel, J-ring and L-box tests. In addition, hardened concrete properties including compressive strength, density, Young's modulus, stress-strain curve and Poison's ratio after 28 and 90-days were assessed. Results show that the fresh properties of SCC with MP cement replacement of up to 50% were in good agreement with specifications. As expected the compressive strength decreases with an increase in MP. The study confirmed that waste generated in marble manufacture has a great potential in SCC.

1. Introduction

Waste materials can be exploited in the production of Self-Compacting Concrete (SCC). SCC is characterized by an increased powder content when compared to conventional vibrated concrete. The recycling of waste from different industrial sectors leads to environmental and economic benefits. Significant quantities of waste marble powder are generated in the processing of marble with negative impacts on the environment. Marble powder (MP) is increasingly seen as a valuable resource if transformed into an engineering material for the construction industry. Several studies have been conducted on SCC produced with marble powder. İlker Bekir Topçu et al. [1] reported that the workability of fresh SCC is not affected

with a marble dust content of up to 200 kg/m^3, while the mechanical properties decreased. Valeria Corinaldes et al. [2] concluded that 10% substitution of sand with marble powder resulted in maximum compressive strength at about the same workability. Amit Kumar Tomar, et al. [3] reported that waste MP can be utilized in concrete as a filler contributing to a reduction in the total void content while affecting strength. Anuj et al. [4] compared MP in SCC to SCC mixes based on fly ash and sand. Ulubeylia et al [5] concluded that the use of waste marble in conventional concrete as a fine/coarse aggregate improved hardened concrete properties. The increase in waste marble replacement ratios in self-compacting concrete, resulted in a decrease in the mechanical properties of concrete.
The objective of this research was to invesitgate the fresh and hardened properties of SCC, produced using waste MP, as a partially cement replacement (0% to 50%) by weight of cement. The investigation included the assessment of the rheologial and hardened properties.

2. Experimental methodology

2.1 Materials

The marble powder used for this work was collected from marble production plants in Tripoli, Libya, for a consistent marble type. The waste was crushed and ground to a fineness of 125μm. Ordinary Portland cement (OPC) type 42.5N conforming to the Libyan standards 340-2009 was used as the binder. Two different sizes of coarse aggregate were used, 10 mm and 14 mm, together with two types of fine aggregate; local natural sand and ground sand. Clean tap water was used as the mixing water and Sika Viscocrete Tempo 12 was used as a water reducer and superplasticizer. SCC mixes with MP replacement levels by weight of cement, ranging from, 0% to 50%, were prepared. The mixes are presented in Table 1.

Table 1: Details of constituents of the SCC mixes.

Mix No.	Total Powder kg/m^3	Cement kg/m^3	MP kg/m^3	MP %	Water lt	w/p	w/c	Total CA (10+14mm) kg/m^3	Total FA kg/m^3	Viscocrete liter
1	500	500	0	0	179.2	0.36	0.36	911.6	808.4	7.5
2	500	475	25	5	179.2	0.36	0.38	911.6	808.4	7.5
3	500	450	50	10	179.2	0.36	0.40	911.6	808.4	7.5
4	500	425	75	15	179.2	0.36	0.42	911.6	808.4	7.5
5	500	400	100	20	179.2	0.36	0.45	911.6	808.4	7.5
6	500	375	125	25	179.2	0.36	0.48	911.6	808.4	7.5
7	500	350	150	30	179.2	0.36	0.51	911.6	808.4	7.5
8	500	325	175	35	179.2	0.36	0.55	911.6	808.4	7.5
9	500	300	200	40	179.2	0.36	0.60	911.6	808.4	7.5
10	500	275	225	45	179.2	0.36	0.65	911.6	808.4	7.5
11	500	250	250	50	179.2	0.36	0.72	911.6	808.4	7.5

2.2 Mix design and concrete testing

Several trial mixes were produced intended to optimize the mix in view of rheological requirements. Ingredients were first mixed in dry conditions in the mixer for one minute. The water was added gradually to the dry mix and the material was mixed for another minute. The chemical admixture was added to the mix and the concrete was mixed for a further three minutes. After the mixing procedure was completed, the fresh concrete properties were determined through the measurement of slump flow time and diameter, J-Ring, L-Box and V-

funnel flow time tests. Minor adjustments to the mix water were considered for mixes with MP in view of the water absorption of the MP. The tests were carried out according to the EFNARC guidelines. Specimens were cured in a laboratory environment until the time of testing for hardened properties at 28 and 90 days.

3. Results and discussion

3.1 Fresh properties

Fresh SCC is required to be flowable, stable and segregation resistant. Results show that SCC with MP had a satisfactory performance with regards to workability and homogeneity requirements. Slump-flow, V-funnel and L-box test results were, in general, in a good agrement with the limits presented in the European Guidelines for Self-Compacting Concrete (EFNARC). As shown in table 1, the content of the superplasticizer was kept constant with a constant water / powder (w/p) ratio and varying water / cement (w/c) ratio. Details of the fresh properties of SCC mixes are given in Table 2.

Table 2: Fresh Properties of SCC mixes.

Mix No	MP Content (kg)	w/p ratio	w/c ratio	Slump flow (mm)	T50 (sec)	J-Ring (mm)	L-Box (H2/H1)	V-funnel (sec)
1	0	0.36	0.36	800	2	10	0.88	8
2	25	0.36	0.38	715	4.3	7	0.824	10.3
3	50	0.36	0.40	720	3.1	15	0.875	9.1
4	75	0.36	0.42	680	4.5	20	0.83	10.5
5	100	0.36	0.45	740	2.8	10	0.85	8.8
6	125	0.36	0.48	760	3	10	0.878	9
7	150	0.36	0.51	800	2	12	0.918	8
8	175	0.36	0.55	800	2	2	0.87	8
9	200	0.36	0.60	730	4	2.5	0.81	10
10	225	0.36	0.65	710	2.8	3	0.78	8.8
11	250	0.36	0.72	730	2.6	5	0.877	8.6
EFNARC Spec.	---	---	---	650 - 800	2 – 5s	0 - 10	0.8 – 1.0	6 – 12s

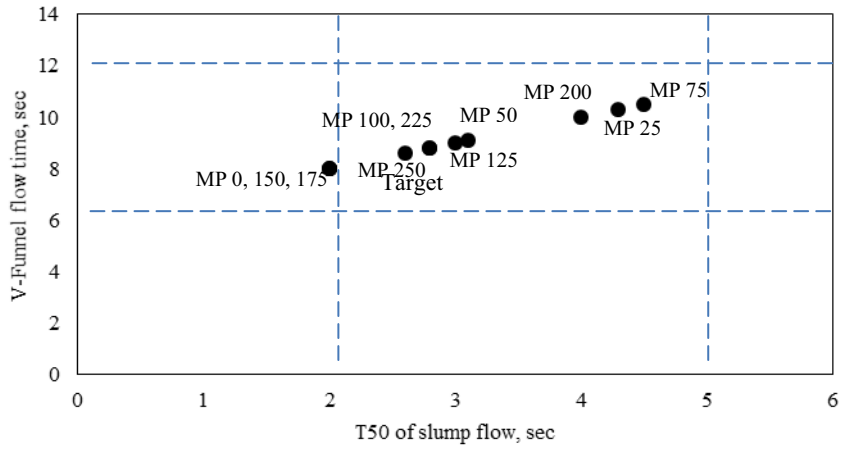

Figure 1: Relationship between V-Funnel time and T50 slump flow.

The relationship between the required time to reach 500 mm slump-flow and time of flow through the V-funnel, to determine the segregation resistance is shown in Fig. 1. The results are withen the targeted limits and no segregation was observed.

3.2 Hardened concrete properties

The 28-day and 90-day compressive strength results are presented in table 3 and figure 2. It is clear that the compressive strength of SCC samples with MP as cement replacement is less than the strength of the control mix. This behavior was expected since MP is considered to act as an inert filler material rather than a reactive material. While the water / powder ratio was maintained constant for the mixes, the water / cement ratio increased resulting in a reduction in strength.

Table 3: Compressive strength of SCC mixes.

Sample	1	2	3	4	5	6	7	8	9	10	11
28 d Comp. Strength (MPa)	54.9	46.9	43.4	43.4	39.2	36.7	34.3	32.4	29.9	25.3	20.1
90 d Comp. Strength (MPa)	57.3	48.4	44.6	49.9	47.6	39.6	35.5	33.5	36.9	29.6	22.1

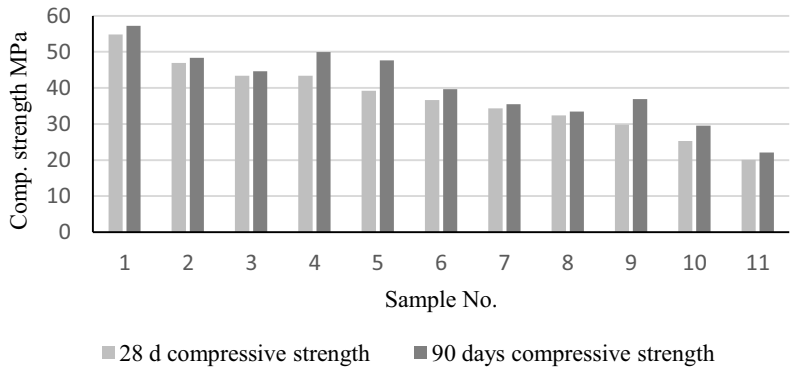

Figure 2: Compressive strength for different MP percentages.

The results reported in table 4 for hardened SCC indicate that the density is not significantly affected with the introduction of MP. The MP acted as a fine aggregate filling the voids in the concrete matrix.

Table 4: Density of SCC.

Sample	1	2	3	4	5	6	7	8	9	10	11
Density (kg/m^3)	2400	2405	2402	2367	2385	2364	2349	2357	2365	2347	2331

The stress - strain relationships for SCC with MP are presented in Figures 3 to 8. Large strains are registered for higher replacement levels of MP, associated with a decrease in the compressive strength. This may be attributed to the micro-cracks generated at the paste - MP interface. Still the strain at the ultimate stress is around 0.003.

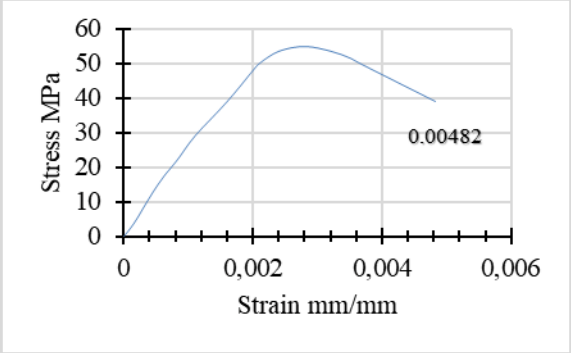

Figure 3: Stress-strain curve, Mix 1 at 28d

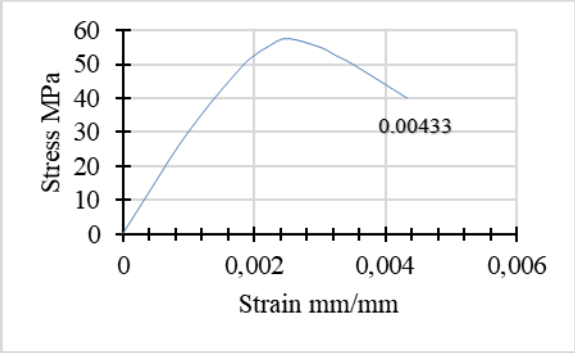

Figure 4: Stress-strain curve, Mix 1 at 90d.

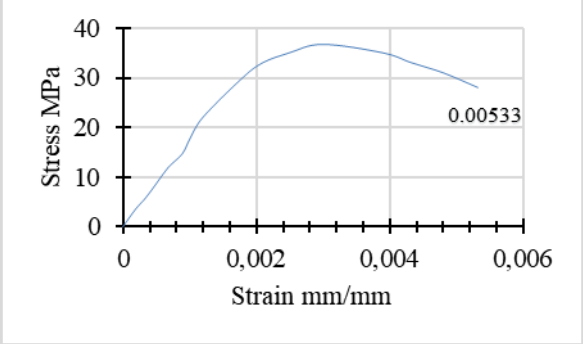

Figure 5: Stress-strain curve, Mix 6 at 28d.

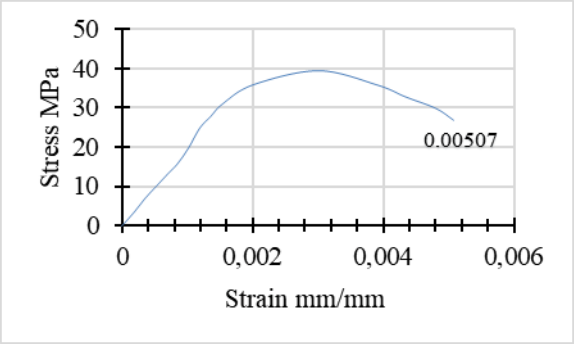

Figure 6: Stress-strain curve, Mix 6 at 90d.

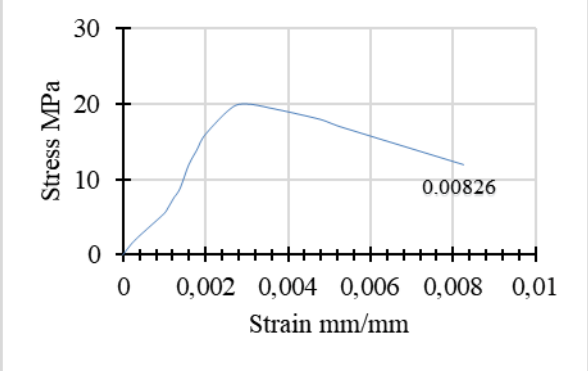

Figure 7: Stress-strain curve, Mix 11 at 28d.

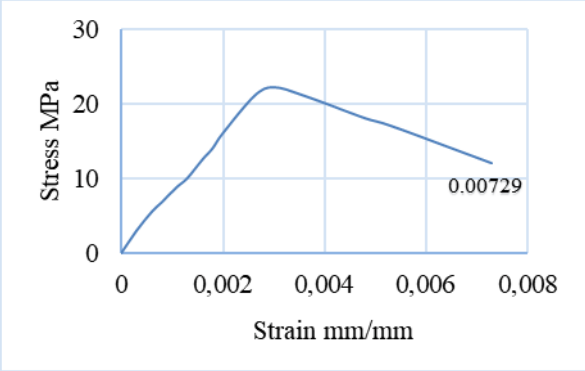

Figure 8: Stress-strain curve, Mix 11 at 90d.

The results presented in table 5 indicate that the efficiency of the cement (strength achieved for a certain amont of cement content, in MPa/kg) was about 0.1 MPa/ kg of cement. This has not been significantly affected by the different percentage replacement levels of cement with MP and can be interpreted as the MP not contributing in the hydration process. Figures 9, 10 present the modulus of elasticity at 28 days and 90 days respectively.

Table 5: Efficiency of cement (MPa/kg).

Sample	1	2	3	4	5	6	7	8	9	10	11
28d Effici.	0.11	0.10	0.10	0.10	0.10	0.10	0.10	0.10	0.10	0.09	0.08
90d Effici.	0.11	0.10	0.10	0.12	0.12	0.11	0.10	0.10	0.12	0.11	0.09

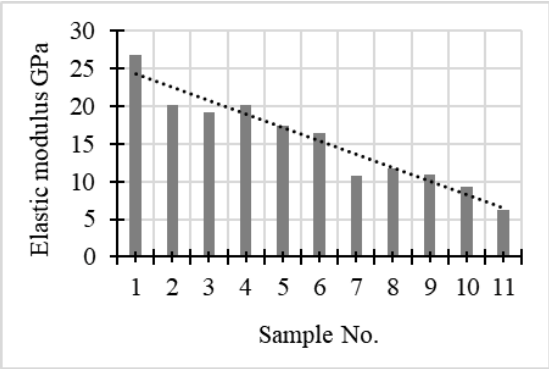

Figure 9: Modulus of elasticity at 28d.

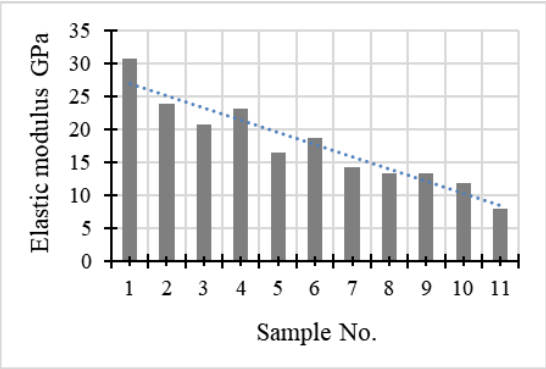

Figure 10: Modulus of elasticity at 90d.

5. Conclusion

On the basis of the experimental investigation conducted on the application of marble powder in self compacting concrete, the following conclusions can be drawn:

1. Marble powder MP can be recycled and used in the production of SCC as a partial replacement of cement.
2. The MP in the mixes affected the fresh properties of the SCC when compared to the control mix. However in general, the different fresh properties of SCC for the different mixes with MP were within the EFNARC limits.
3. MP did not present any improvement in the mechanical properties of SCC at 28 and 90 days. High replacement levels of cement result in significant reductions in compressive strength, at equal water / powder ratios.
4. The density of SCC was not significantly affected with varying MP in the mixes.
5. The efficiency of the cement has not been significantly affected by the different percentage replacement levels of cement with MP.
6. The disposal of waste MP from the intensive marble production industry in some regions has a negative impact on the environment. However MP has the potential to be used in Self compacting concrete, reducing its environmental impact.

References

[1] Topçu, İ.B. et al, Effect of waste marble dust content as filler on properties of self-compacting concrete, Construction and Building Materials 23(5) (2009), 1947-1953
[2] Corinaldes, V. et al, Characterization of marble powder for its use in mortar and concrete, Construction and Building Materials 24(1) (2009), 113-117
[3] Tomar, A.K. et al, Review on utilization of waste marble powder in self-compacting concrete, Intern. Journal of Engineering Trends and Technology 37(2) (2016), 122-124
[4] Anuj, et al, Rheology of Self Compacting concrete with Marble Powder mixes in comparison to Fly ash and Sand Based Mixes, (2016)
[5] Ulubeylia, G.C. and Artirb, R., Properties of Hardened Concrete Produced by Waste Marble Powder, World Conference on Technology, Innovation and Entrepreneurship, Procedia Social and Behavioral Sciences 195 (2015), 2181-90
[6] Standard Test Methods for unit weight and voids in aggregates – American Society for Testing and Materials, ASTM C29/M129 (2007)

SynerCrete'18 International Conference on Interdisciplinary Approaches
for Cement-based Materials and Structural Concrete
24-26 October 2018, Funchal, Madeira Island, Portugal

ESTIMATING THE STRESS DEVELOPMENT IN EARLY AGE CONCRETE WITH MINERAL ADDITIONS FROM COUPLED MEASUREMENTS

Jérôme Carette [(1)], Brice Delsaute [(1)], Stéphanie Staquet [(1)]

(1) BATir department, Université libre de Bruxelles (ULB), Brussels, Belgium

Abstract
In order to evaluate the efficiency of a given supplementary cementitious material, its mechanical behaviour has to be thoroughly investigated. In particular, early-age micro-cracking might occur at a time when all concrete properties evolve, while the rate of evolution of autogenous and thermal deformations is still very high. If these deformations are restrained, stresses are induced as the concrete hardens. These stresses are both homogenously distributed and localized, depending on the scale considered, and may lead to localized cracking if the stress overpasses the strength of the material. The aim of this study is twofold. First, prediction models are presented. These models are specifically designed for the very early age description of in terms of strength, elastic properties, autogenous deformation as well as creep development of concrete with high content of mineral additions. Secondly, newly developed modelling strategies are confronted to experimental measurement of the stress development in restrained deformation conditions with a TSTM device. This study highlights the limits of the viscoelastic modelling approach using the superposition principle for modelling the early age behaviour of concrete with mineral additions.

1. Introduction

Most supplementary cementitious materials (SCM) have a large impact on the chemical processes at the origin of the mechanical properties of concrete. In order to evaluate the efficiency of a SCM, its mechanical behaviour thus has to be thoroughly investigated. In particular, the early age behaviour of concrete is at the origin of an initial stress state, which might induce the development of micro-cracking. Indeed, early-age cracking occurs at a time when all concrete properties evolve, while the rate of evolution of autogenous and thermal deformations is still very high. If these deformations are restrained, stresses are induced as the

concrete hardens. These stresses may lead to localized cracking if the stress overpasses the strength of the material. The parameters that should be considered for crack prediction in restrained deformations are : the amplitude of the deformation, the viscoelastic behavior of the concrete, the strength of the material, and in particular its tensile strength, and the amount of restraint applied to these deformations. In previous studies, experimental assessment of the early age evolution of these above properties were presented. In parallel, models were successfully proposed, allowing proper consideration both of the early age behaviour and of the presence of SCM. The properties that were assessed from the setting time [1] include elastic properties as well as compressive and tensile strength [2], the autogenous deformation [3] and the creep behaviour [4]. These models as well as their corresponding empirical models are presented in this paper. They are used for computing the stress development in the case of fully restrained autogenous deformations from the setting time. The autogenous deformation includes the early age swelling deformation (supposedly originating from ettringite formation [3]) and the self-desiccation deformation. The results of this empirically-optimized model are confronted to experiments of the stress development in fully restrained conditions. As a result, situations in which the superposition principle cannot be easily applied are identified.

2. Materials and method

2.1 Concrete mix designs

Two binder types are studied (Tab. 1). They contain various combinations of CEM I 52.5 N, blast-furnace slag (BFS) and gypsum. The latter is added in order to keep the sulfate content constant between compositions. The water/binder ratio (w/b) is 0.4 for all compositions. Additional information related to the chemical composition of each binder component as well as the mechanical behavior of these compositions are available in [1-3].

Table 1. General composition of the tested concretes

[kg/m³]	**C1**	**C2**
Aggregate 10/14	873	873
Aggregate 6/10	210	210
Sand 0/4	853	853
CEM I 52.5	432	104
Blast furnace slag	-	291
Gypsum	-	22
Water	173	167

2.2 Test setup

The stress development in fully restrained deformations conditions is measured for two tested compositions C1 and C2. This is performed through a dedicated Temperature Stress Testing Machine (TSTM) [5-8]. This test is used to cancel step-wise the deformations in a horizontal concrete sample. In order to do so, compensation cycles are applied with a jack attached to the mobile head of the mould. These cycles consist in applying a force to the concrete sample

every time the measured displacements exceeds a given threshold. Once this threshold (corresponding to 6 μm/m deformation) is overpassed, the sample is loaded until the displacements come back to zero. Once this is achieved, the tensile (or compressive) stress is kept constant up to the next threshold is exceeded. These cycles continue until a major cracking occurs. The compensation cycles are started as soon as concrete reaches its final setting t_0, determined based on the combined measurement of ultrasonic compression and shear wave transmission velocity [1]. Tensile strength is obtained from t_0 based on tensile splitting strength test [2]. The elastic modulus is also measured from t_0 through a cyclic methodology using the TSTM device [2,9]. Finally, the autogenous deformation is measured with the BTJADE device [10]. This continuous measurement ensures fully isothermal and sealed conditions from the mixing to several weeks. Therefore, the autogenous deformation (including the early age swelling deformation) is determined from as soon as t_0 [3].

3. Modelling of the early age properties

The models that are presented in this section are not necessarily obtained from standard codes. They are carefully chosen, for each considered property, based on three main criteria:

- Its ability to represent correctly the property evolution from the setting time
- Its number of material parameters to be determined experimentally
- Its ability to be applied to any of the tested materials, with and without SCM

The following equations Eq. (1-3) result from these considerations. All materials parameters for the expressions of compressive strength f_c, tensile strength f_t and elastic modulus E are identified from experiments.

$$f_c(t) = f_{c,28} \,.\, e^{-\frac{s_c}{t}} \tag{1}$$

$$f_t(t) = f_{t,28} \,.\, e^{-\frac{s_t}{t}} \tag{2}$$

$$E(t) = E_{28} \,.\, e^{-\left(\frac{s_E}{t}\right)^r} \tag{3}$$

A new model was previously developed for representing the autogenous deformation ε_{au} of concrete with and without SCM at early age [3]. This model explicitly considers the contribution of the self-desiccation phenomenon ε_{sd} (Eq. (5)) but also the early age swelling deformation ε_{sw} (6). This expansion is assumed to be resulting from the ettringite formation, especially in presence of blast furnace slag [3]. The overall equation that is used is shown in Eq. (6-7), where α is the degree of hydration, α_0 is the degree of hydration at final setting, A_{sd} and A_{sw} are amplitude parameters for the self-desiccation and swelling deformations respectively. The swelling deformation increases with a kinetic factor which includes two parameters a_{sw} and b_{sw}, which depend mostly on the cement type.

$$\varepsilon_{au} = \varepsilon_{sw} + \varepsilon_{sd} \tag{4}$$

$$\varepsilon_{sd}(t) = A_{sd} \,.\, \tilde{\alpha}(t) \tag{5}$$

$$\varepsilon_{sw}(t) = A_{sw} \,.\, \left(1 - \mathrm{e}^{-a_{sw}\,\tilde{\alpha}(t)^{b_{sw}}}\right) \tag{6}$$

$$\tilde{\alpha}(t) = \frac{\alpha(t) - \alpha_0}{1 - \alpha_0} \tag{7}$$

The creep behaviour is modelled according to a modified version of the model code 2010 expression [11]. This expression is shown in Eq. (8). The parameter τ is computed in Eq. (9) as a function of the time derivative of the elastic modulus. The material parameters p and q depend on the tested composition. The relaxation is deduced analytically from the creep coefficient according to the effective modulus method (Eq. (10)), which provides acceptable results in comparison with a more accurate numerical computation [12].

$$\varphi_c(t,t') = \frac{E(t')}{C} + ln\left(1 + \frac{t-t'}{\tau(t')}\right) \tag{8}$$

$$\tau(t') = mininmum\begin{cases} q\left(\frac{dE(t')}{dt}\right)^p \\ .088\left(\frac{dE(t')}{dt}\right)^{-1} \end{cases} \tag{9}$$

$$\varphi_r(t,t') = \frac{1}{1+\varphi_c(t,t')} \tag{10}$$

From all the above equations, the following equation must be verified in order to avoid cracking:

$$-f_c < \sum_{t'=t_0}^{t} \Delta(\varepsilon_{au} + \varepsilon_{th})\,.\,E(t')\,.\,\varphi_r(t,t') < f_t \tag{11}$$

4. Results and discussion

The results of the TSTM experiments performed at 20°C as well as the modelled stress build up in fully restrained conditions are shown in Fig. 2. The grey zones in these figures represent zones where stress is higher than the compressive / tensile strength. The C2 composition presents a significant amount of computed compressive stress due to the large amplitude of the swelling deformation in the presence of blast-furnace slag. The composition C1 presents significant tensile stress development in the first days after mixing, ultimately leading to its cracking at 48h, as shown by the sudden drop in the experimental stress value. The C2 composition did not show this cracking tendency, even after more than 2 weeks of testing.

The modelling strategy is based on the visco-elastic stress computation, considering the effect of creep, and by applying the superposition principle. The values of elastic modulus, autogenous deformation and creep are deduced from experimental measurements. However, there are very large differences between the predicted and experimental values. Two main issues can be observed. First, in the presence of Portland cement only, the model is very accurate until the tensile behaviour is reached. After this point, the model progressively underestimates the stress in the material. At the time of cracking of the sample, the computed stress is only 50% of what is obtained experimentally. Secondly, the early age expansion of C2 is not observed to generate compressive stress in the experiment, while the model

estimates up to 2.5 MPa of compressive stress after 48h. In this same experiment, the rate of tensile stress increase seems to be accurately predicted with the model, while the actual values are not correct.

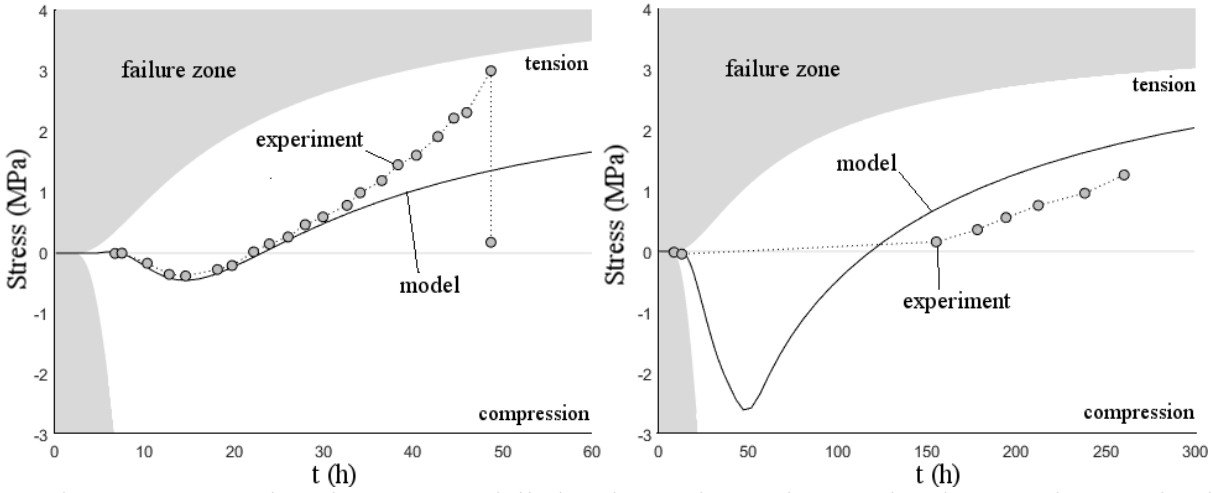

Figure 2. Comparison between modelled and experimental stress development in restrained autogenous deformations conditions (left) for concrete C1 and (right) for concrete C2.

These observations are expected to be the result of the combination of the following mechanisms, which are not included in the model:

- the creep function is deduced from experiments in compression. However, short term creep in tension is actually much lower than creep in compression [5]. The longer term creep is similar in tension and in compression. This explains why the C2 estimation of the rate of stress increase in tension is acceptable, since the loading in that latter case occur in a much longer amount of time than C1 (approximately 7 times slower),
- the principle of superposition can hardly be applied for stresses higher than 50% of the strength [9]. This explains why there is so large differences at high tensile stresses in the C1 mix,
- the linear principle of superposition is not verified in the case of strain reversals [9], which are observed in this study, especially in the case of C2. This explains why the absolute value of the modelled stresses in C2 is far from the experiment after 150h even if the rate of increase is plausible,
- the large swelling observed in the free autogenous deformation of C2 does not generate significant stress in the experiments in contrast with the predicted values. This cannot be explained by any of the above considerations. A possible mechanism for this observation is related to the ettringite formation. Indeed, if the swelling is caused by this ettringite production, it is possible that under confined compressive conditions, the ettringite does not form as an expansive hydrate (either by smaller sized needles or by lower production rate). In this case, the lack of compressive stress in the experiments would be due not to an issue regarding the estimation of creep, but rather to the feedback effect of stress on the formation of expansive hydration products such as ettringite.

4. Conclusions

To conclude, it can be expected that the build-up of stress inside concrete samples under restrained deformations can be very difficult to predict, even in simple uniform 1-D situations. In addition to the well-known limits of applying the superposition principle (such as for high stress/strength ratio on when strain reversals are considered), coupled with the difficulty to assess the early age tensile creep, these computations are challenged by possible feedback mechanisms between the microstructural build-up and the stress state of the material. This issue might be particularly relevant in the case of early ettringite expansion.

References

[1] Carette J & Staquet S., Monitoring the setting process of eco-binders by ultrasonic P-wave and S-wave transmission velocity measurement: Mortar vs concrete, Construction and Building Materials, 2016, 110, 32-41
[2] Carette J. & Staquet S., Monitoring and modelling the early age and hardening behaviour of eco-concrete through continuous non-destructive measurements: Part II. Mechanical behaviour, Cement and Concrete Composites, 73, pp. 1-9, 2016
[3] Carette, J., Joseph S., Cizer Ö, Staquet S., Decoupling the autogenous swelling from the self-desiccation deformation in early age concrete with mineral additions: micro-macro observations and unified modelling, Cement and Concrete Composites, 85, pp. 122-132, 2018
[4] Brice Delsaute, Jean-Michel Torrenti, Stéphanie Staquet, Is the Model Code 2010 able to reproduce the basic creep of concrete with high substitution of Portland cement by mineral additions?, Under review in Structural Concrete, 2018.
[5] B. Delsaute, New approach for monitoring and modelling for the creep and shrinkage behaviour of cement pastes, mortars and concretes since setting time, PhD thesis, Université libre de Bruxelles (ULB), 2016.
[6] A. Klausen, T. Kanstad, Ø. Bjøntegaard, E. Sellevold, Comparison of tensile and compressive creep of fly ash concretes in the hardening phase, Cement and Concrete Research, 95, 2017, pp. 188-194
[7] P. Lura, K. van Breugel, I. Maruyama, Effect of curing temperature and type of cement on early-age shrinkage of high-performance concrete, Cement and Concrete Research, 31, 2001, pp. 1867-1872
[8] G. M. Ji, T. Kanstad, and Ø. Bjøntegaard, Calibration of Material Models against TSTM Test for Crack Risk Assessment of Early-Age Concrete Containing Fly Ash, Advances in Materials Science and Engineering, 2018
[9] Delsaute B, Boulay C, Granja J, Carette J, Azenha M, Dumoulin C, Karaiskos G, Deraemaeker A, Staquet S., Testing Concrete E- modulus at Very Early Ages Through Several Techniques: An Inter- laboratory Comparison, Strain, 2016
[10] Boulay, C., 2012. Test rig for early age measurements of the autogenous shrinkage of a concrete, Concrack 3, RILEM Publications, 111-122.
[11] B.Delsaute, J.-M.Torrenti, S.Staquet, Modeling basic creep of concrete since setting time, Cement and Concrete Composites, 83, pp. 239-250, 2017
[12] Z. P. Bažant, Numerical determination of long-range stress history from strain history in concrete, Matériaux et Construction, 5 (3), pp 135–141, 1972

SynerCrete'18 International Conference on Interdisciplinary Approaches
for Cement-based Materials and Structural Concrete
24-26 October 2018, Funchal, Madeira Island, Portugal

EVALUATION OF STRENGTH OF REINFORCED CONCRETE SLABS OPERATING UNDER THE CHANGING WATER LEVEL

Raimondas Šadzevičius [(1)], Rosita Norvaišienė [(1)] Edita Smetonaitė [(2)]

(1) Kaunas University of Applied Engineering Sciences, Kaunas, Lithuania
(2) Kaunas University of Technology, Kaunas, Lithuania

Abstract
Reinforced concrete slabs for ponds slope protection are under the impacts of various loads (ice, swimming solids or sediments, etc.) and aggressive environment; therefore they deteriorate and lose their durability especially in the zone of changing water level. The compressive strength of functioning concrete structures of hydraulic structures can be evaluated by testing the samples cut out from the investigated structures or by non-destructive methods (using rebound hammer).
During the investigation it was noticed, that all the investigated surfaces of reinforced concrete slabs for strengthening slopes of ponds in the zone of changeable water level are more or less deteriorated in form of pitting. Schmidt hammer rebound number and compressive strength of irregular samples taken from the reinforced concrete slabs were used for evaluation of whole upstream slope of pond. It is known, that the rebound hammer test shows only the state of the surface of concrete, therefore the result of compressive strength obtained by examining the core samples is more reliable, as it shows the strength of concrete in deeper layers. The irregular samples were taken from more deteriorated slabs, made from weaker concrete, compared with less deteriorated slabs tested by Schmidt hammer.

1. Introduction

The surface protective layer of concrete and the joints of the slabs are damaged due to the processes of degradation (corrosion of concrete and reinforcement, erosion, biological decomposition) and due to the environment (cold cycles, ice, shock waves, mosses, grasses, shrubbery, periodic impregnation, etc.). The most destructive processes violates the protective layer of low-quality concrete (low strength and frost resistance), which crumbles when is influenced by cold cycles, its physical-mechanical properties are changing, the damage-

pittings- are formed. The pittings form and develop for a number of reasons [1, 2], among which, as one of the most important, are mentioned the destructive effects of cold cycles. The surface of concrete layer is broken in the following order: the expanding ice front displaces water from cementitious stone capillaries and pores under pressure, which exceeds the limit of tensile concrete strength; the surface of concrete layer degrades. Also, the structure degradation is caused by the accumulation of technological errors (inadequate composition of concrete, poor workmanship, concrete delamination), and specific service conditions [3].
The pond of Graužė III with the earth dam (hereinafter –ED), built in 1973 was chosen for the research which is a typical example of Lithuanian small ponds (whose area is < 5 ha). The upper pool slope is covered with reinforced concrete slabs (175 × 100 cm), which are arranged in four rows with 138. Under water there are two rows of slabs, the third row of slabs is at the level of the changeable water level, the fourth is above the normal water level (NWL). These rows of slabs are divided into zones [4] (Fig.1).

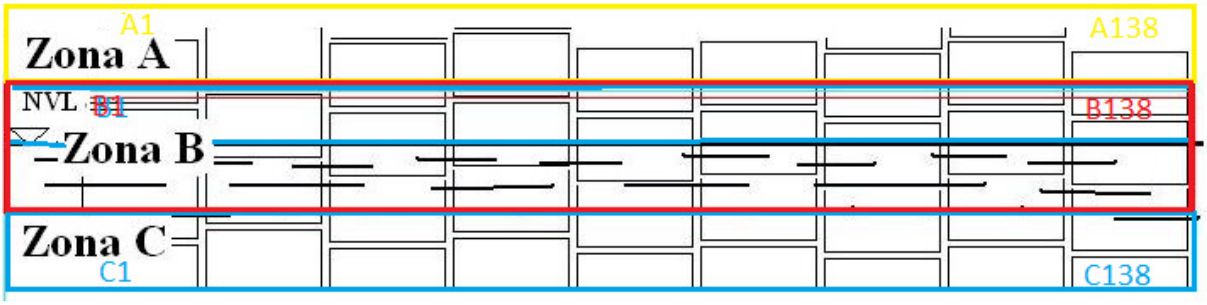

Figure 1: Zoning of slabs (in vertical direction): zone A – above the changeable water level; zone B – at changeable water level (above or below NWL); zone C – zone under water (below NWL).

The slabs of the dams A and B are horizontally divided into 12 sectors every 10 meters. The test area Zone A (in the vertical direction) is chosen 1.10 m above the NWL, and in the Zone B (in the vertical direction) it is selected 0.10 m above the NWL. The concrete strength of each section is determined.

2. Methodology

The actual compressive strength of reinforced concrete slabs for the earth dam slope protection (hereinafter SDP) was determined by the non-destructive method using E. Schmidt system device according to standard methods [1, 5; 6] and destructive methods according to the non-standard [7, 8] methodology. The macrostructure of the outer (hereinafter - protective) layer of SDP concrete, as well as of any other building materials of mineral origin, is not homogeneous, therefore the dispersion of its physical-mechanical properties is estimated by variance, coefficient of variation, average square deviation, and other statistical indicators.
Using the non-destructive method with a rebound hammer of concrete Cat.58−CO181/N (Schmidt's system), an actual compressive strength of concrete was measured. The non-destructive testing of compression strength was performed in accordance with the Standard EN 12504-2:2012, using the Schmidt Hammer. Before and after every examination, the

device was calibrated using the standard anvil. Research results were statistically evaluated: the average compressive strength of concrete f_c, the variation coefficient v and the root-mean-square deviation σ were calculated using "Microsoft Excel" macros.
The compressive strength of concrete was determined by destructive methods when testing non-dangerous places of the structures when taking out irregularly shaped concrete pieces on non-aligned surfaces. This method is more suitable for the determination of the compressive strength of weaker concrete (up to 10 MPa), which is especially relevant for determining the strength of SDP of ponds. The reliability of the method has been demonstrated by comparing the results obtained when testing samples of the same strength according to the standard methodology. Concrete pieces for testing were taken out from reinforced concrete structures by cutting.

Figure 1: Destructed slabs for ponds slope protection in zone B.

The concrete pieces were placed in sealed polyethylene bags. Samples were measured with a slider, with an accuracy of 1.0 mm. Before the test, concrete pieces were carefully inspected. Cracked, layered and hallow samples were rejected.
The specimens, whose diameter corresponded to the diameter of the standard specimens, and samples with a smaller diameter than the standard, were compressed with available stamps. Dimensions of concave stamps are indicated in Table 1. The pit of the stamp is 10 mm.

Table 1: Dimensions of the stamps.

n	**Diameter d, mm**	**Area A_n, mm^2**
1	35.7	1000
2	50.5	2000
3	71.4	4000
4	100.0	7850

Remark: *n* – number of stamps.

The size of most of the concrete pieces was appropriate to test with stamps of maximum diameter (d = 100 mm). Before the test, the pits of the selected stamps were filled with a levelling mortar with a compressive strength close to that of the concrete to be tested. The specimens were prepared in accordance with the requirements of standard [8] with hydraulic press MC–1000 (Fig. 2). The compression load was evenly increased to (0.6 ± 0.4) (N/mm^2)/s intensity. During the test, large concrete pieces, tested with stamps of 100 mm diameter, broke into smaller parts. The pieces of the broken concrete piece, if they were not damaged, were tested with a stamp of a smaller diameter by using compression machine – hydraulic press. After the test, the character of the destruction of the samples was evaluated, measured the largest particle size of the concrete filling.

Figure 2: The sample in hydraulic press MC–1000

3. Discussion

The compressive strength of SDP was determined by E. Schmidt device in April of 2012. In the same year, SDP concrete investigations were carried out using destructive methods according to the research methodology for the evaluation of the compressive strength of concrete in an attempt to test irregularly shaped specimens. The tests using destructive methods were repeated in October of 2014. The results of the tests are presented in Table 2. Mostly, the concrete is damaged in the area of ice and waves (changeable water level - zone B - see Figure 1), pittings are developing most in this area. In the case of improperly installed protective reinforcement concrete layer and its damage favourable conditions for reinforcement corrosion are created.

As it can be seen from the results of Table 2, the values of the average compressive strength of concrete used in the level of the changeable water level (zone B - see Figure 1) –f_{ck}=7,11 MPa are smaller than in zone A above the water (Fig. 1) –f_{ck}=7,20 MPa. The highest destructive effect of frost is expected in Zone B.

The destructive effect of cold is increasing with increasing humidity and negative temperatures (freezing water expands, its volume increases by about 9% and destroys concrete). Maximum moisture and the lowest temperature during cold cycles are foreseen in Zone B. In Zone C, the construction is heated by the water, and in the Zone A the water absorbability of the concrete decreases. In the case study, it was observed that slabs of Zone B are more affected by environmental factors and pittings are often formed in this area.

Table 2: Data of reinforced concrete slabs tests of Graužė III ED.

Research area	**2012 (zone A)**		***2012 (zone B)***		***2012 (zone B) (non-destructive)***			**2014 (zone B)**	
Sectors	f_{ck}, **MPa**	***S*, MPa**	f_{ck}, **MPa**	***S*, MPa**	f_{ck}, **MPa**	***S*, MPa**	***v*, %**	f_{ck}, **MPa**	***S*, MPa**
0-10m	8.19	2.98	7.3	1.28	13.9	2.13	15	6.48	0.93
10-20m	5.78	0.64	7.19	1.48	13.4	1.96	14	8.28	1.91
20-30m	6.57	1.07	6.48	1.34	17.8	3.85	22	7.22	2.86
30-40m	6.51	1.52	6.22	1.01	22.4	6.54	28	6.53	1.29
40-50m	6.17	1.15	8.07	6.11	16.9	2.33	13	6.13	0.82
50-60m	5.29	0.59	5.34	0.57	11.3	1.42	13	5.69	0.5
60-70m	9.73	5.3	6.44	1.14	14.2	3.11	22	5.69	1.25
70-80m	6.44	0.82	10.5	4.47	26.8	4.98	18	9.33	4.55
80-90m	6.75	0 .93	6.42	1.51	17.6	2.5	14	6.09	1.16
90-100m	9.51	4.56	5.82	1.16	22.9	2.85	12	7.69	4.63
100-110m	9.14	2.39	8.14	2.08	20.4	2.27	11	6.64	1.53
110-120m	6.26	1.36	7.41	0.68	29.1	1.79	6	7.06	1.8
Whole slope	**7.20**	2.03	**7.11**	1.90	**18.9**	2.98	15.67	**6.90**	1.94

Remark. Markings in the table: average compressive strength of concrete f_{ck}, MPa; average square deviation *S*, MPa; coefficient of variation *v*, %.

Analysing the results of 2012 presented in Table 2, it was found that the strength of the SDP without damage to structures, determined by E. Schmidt system device, was bigger than the strength determined by the destructive method. This is explained by the fact that undisturbed (non-destroyed slabs) were tested by a non-destructive method, while irregularly shaped specimens, the samples taken out from reinforced concrete structures (from the reinforced concrete slabs of the ED) were tested using the destructive test methods according to the evaluation of the compressive concrete strength. It is also known that using a non-destructive method, with E. Schmidt system device, results higher values due to the environmental impact of the carbonisation of the surface protective concrete layer [9].

4. Conclusions

The selected examples of hydraulic structures were presented and the durability problems occurring in concrete structures were revealed. In most cases, concrete is damaged in the impact zones of ice and waves - pittings is most evident in this area.

As it can be seen from the results, using non-destructive method (E. Schmidt system) the values of compressive concrete strength were 2-4 times higher than using the destructive method. These differences are possible due to the aforementioned reasons – non-destroyed slabs were tested using the non-destructive method and due to carbonization, the surface strength of the slabs is higher.
The compressive strength of concrete was determined by destructive methods when testing non-dangerous places of the structures when taking out irregularly shaped concrete pieces on non-aligned surfaces. The reliability of the method has been demonstrated by comparing the results obtained when testing samples of the same strength according to the standard methodology. The rebound hammer test shows only the state of the surface of concrete, therefore the result of compressive strength obtained by examining the drilled cores is more reliable, because tested concrete is not effected by carbonization, but in some cases, it is necessary to use the non-destructive methods, when it is impossible to drill the cores due to weak concrete or thin structures as slabs.

References

[1] ACI Manual of Concrete Practice Part3–2001, Strength Evaluation of Existing Concrete Buildings. American Concrete institute, Farmington hills (2001), 24
[2] Venckevičius V. and Žilinskas R., Reconstruction and repair of buildings (in Lithuanian). Kaunas (2000)
[3] Berkowskia, P. and Kosior-Kazberukb, M., Material and structural destruction of concrete elements in the industrial environment. Modern Building Materials, Structures and Techniques, MBMST 2016. Procedia Engineering 172 (2017), 96 – 103
[4] Webber, D. et al, Design of Small Dams. Manual US Department of the Interior Bureau of Reclamation. Washington: A Water Resources Technical Publication, (1987)
[5] EN 12504-2:2012 Testing concrete in structures - Part 2: Non-destructive testing - Determination of rebound number
[6] Hannachim, S. and Guetteche, M. N., Review of the Rebound Hammer Method Estimating Concrete Compressive Strength on Site. Proceedings of International Conference on Architecture And Civil Engineering (ICAACE'14) (2014), 118-127
[7] Vaišvila, K. A. and Lindišas, L., The research of the compression strength of concrete on reinforced concrete structures of functioning water engineering constructions. The 7th International Conference „Modern building materials. Structures and techniques" (2001)
[8] EN 12504-1:2009 Testing concrete in structures - Part 1: Cored specimens - Taking, examining and testing in compression
[9] Šadzevičius, R. et al, Comparison of concrete compressive strength values obtained using rebound hammer and drilled core specimens // Rural Development 2015: Towards the Transfer of Knowledge, Innovations and Social Progress: Proceedings of the 7th International Scientific Conference (2015)

SynerCrete'18 International Conference on Interdisciplinary Approaches
for Cement-based Materials and Structural Concrete
24-26 October 2018, Funchal, Madeira Island, Portugal

EXPERIMENTAL INVESTIGATION OF ACCELERATORS IN FLOOR CONCRETE MIXTURE UNDER COLD CLIMATIC CONDITIONS

Themistoklis Tsalkatidis [(1)], Even Solbraa [(1)]

(1) Norwegian University of Life Sciences, Ås, Norway

Abstract
Cold climatic conditions are challenging when casting concrete since they significantly increase both the setting and the finishing time of concrete. The use of accelerators is known to counteract this retardation but it has mostly been examined under laboratory-controlled environment. This paper investigates the effect of admixtures, used in a typical concrete floor mixture, during cold weather exposure conditions, with temperatures ranging from +3 to -5^{0}C, by performing three tests. The concrete mixture is first tested without the presence of additives and then with hardening, setting and combinations of hardening and setting accelerators. A total number of eleven case studies are examined. In each test, five specimens of slabs with dimensions of 1 by 1 by 0.1 m are constructed. The setting and finishing times of concrete are evaluated empirically. The compressive strengths of the concrete mixtures after 18, 24 and 30 hours are defined by testing cubic specimens. The experimental results verify that the presence of hardening and setting additives in concrete reduce the time for the finishing phase of a floor under cold climatic conditions. This reduction is close to 50% whilst at the same time the early strength of the concrete increases up to eleven times.

1. Introduction

Concrete is a construction material that is affected by environmental conditions. Under cold climatic conditions, the hydration of cement becomes slower thus increasing the transition period from the initial plastic to the final rigid concrete state. In order to control the setting and finishing time of concrete, the use of admixtures such as set accelerators is highly recommended [1-4]. This paper examines the behaviour of a typical concrete floor mixture, with and without additives, during winter conditions in southern Norway [5]. An experimental analysis consisting of three tests is performed. Different additives are added to the reference

mixture resulting in eleven case studies. The workability and the development of early strength of concrete mixture are also considered.

2. Experimental program

2.1 Concrete

The reference floor mixture is concrete B30M60 standard FA without accelerating additives, a typical mixture used in Norwegian structures [5]. This is equivalent to C30/37.

2.2 Admixtures

Mapefast hardening accelerator (HA), Mapefast set accelerator (SA), Mapetard retarder (R), Mapefast Ultra N (HA) and Master X-Seed 100 (HA) are used as admixtures. Hardening, set accelerators and retarders are added in order to examine different case studies [5].

2.3 Methodology

The experimental procedure consists of three tests performed in temperatures ranging from +3 to -5^{0}C [6-8].The specimens used in the tests are concrete slabs with dimensions of 1 by 1 by 0.1 m. Five slabs for each test and eight cubes from each slab are constructed, resulting in a total number of 15 slabs and 120 cubes. The overview of the concrete mixtures is presented in Tab.1.

Table 1: Concrete mixtures examined.

Test Number	Mixture 1	Mixture 2	Mixture 3	Mixture 4	Mixture 5
Test 1	Reference	Reference+2% Mapefast HA+1% Mapefast SA	Reference+2% Mapefast HA+ 0.2% Mapetard R+1% Mapefast SA	Reference+1.5% Mapefast SA	Reference+ 3% Mapefast HA
Test 2	Reference	Reference+2% Mapefast Ultra N +1% Mapefast SA	Reference+2% Mapefast Ultra N+ 0.2% Mapetard R +1% Mapefast SA	Reference+1.5% Mapefast SA	Reference+ 3% Mapefast Ultra N
Test 3	Reference	Reference+2% Master X-Seed +1% Mapefast SA	Reference+2% BASF X-Seed + 0.2% Mapetard R +1% Mapefast SA	Reference+1.5% Mapefast SA	Reference+ 3% Master X-Seed

The main aims of the tests are to determine the setting and finishing times of concrete floor mixtures with or without the presence of admixtures. For the measurement of the setting time a cube of each concrete mixture is temperature logged. The setting time of the mixture is determined when the temperature of the cube has an increase of 2°C [9]. Finishing time is determined by the penetration length of a M10 bolt in the specimen. When the penetration is measured below 1cm then the specimen is ready to be brushed. The concrete has been cured using a curing membrane.
The workability and the strength of the concrete are also measured. For the determination of the compressive strength of the concrete at early stages, cubic specimens are tested after 18, 24 and 30 hours. Half of the cubes tested are placed indoor whereas the other half is placed outdoor. Regarding the workability of concrete, slump measurements are taken from the time of the addition of admixtures until the slump is measured below 200 mm. The flow is also measured and it has been found above the 340 mm limit for 200 mm of slump [10].The used methods are presented in Tab. 2.

Table 2: Methods used.

Measurement	**Method used**
Setting time	Temperature logging
Finishing time	Bolt penetration
Strength	Compressive testing of cubes
Workability	Slump and flow calculations

3. Results and discussion

3.1 Setting time

The setting time is defined when the temperature of the cube has increased 2°C [9]. The setting times of the mixtures are presented in Tab. 3.

Table 3: Setting times of tests 1 and 3.

Mixture	**Setting time (hours):**
Test 1	
Reference	29.5
HA+SA	21.5
HA+R+SA	30
SA	23
HA	26
Test 3	
Reference	>30
X-Seed+SA	Undetermined
X-Seed+R+SA	28.5
SA	24.5
X-Seed	17.5

In test 2, as shown in Fig. 1, the temperature development in the logged concrete cubes was not satisfactory, therefore only tests 1 and 3 are taken into consideration.

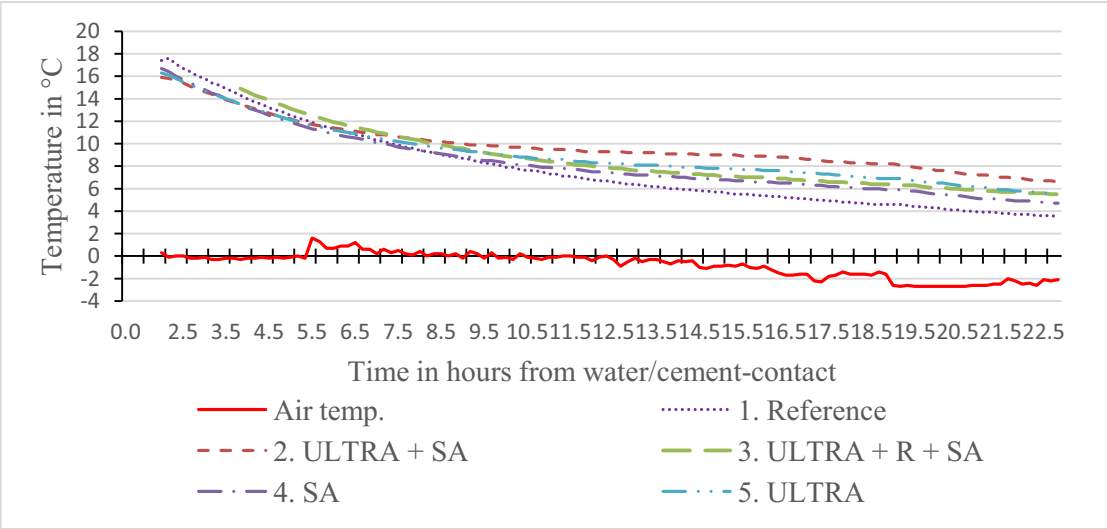

Figure 1: Temperature development in test 2.

3.2 Finishing time

The finishing time is achieved when the M10 bolt has a penetration equal to 10 mm. The following Fig. 2 depicts the finishing times for all tests. Mixtures 2 and 4 proved to be the most efficient. The difference in setting time between the reference mixtures of the tests must be related to a different water-to-cement ratio, concrete production temperature and weather conditions in each test.

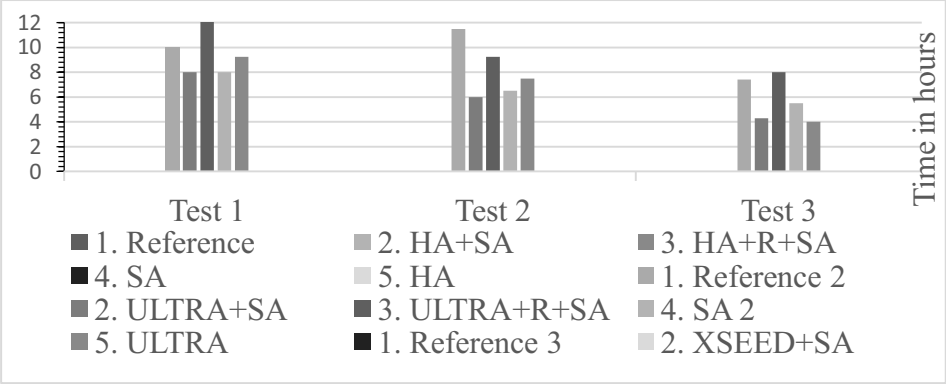

Figure 2: Finishing times.

3.3 Strength and workability

In Fig. 3 the compressive strength of the cubes measured after 18 hours is shown. The use of additives is proven to boost the early strength increase significantly, in all time measurements. Regarding workability, the use of both the hardening accelerators and the retarder has enhanced the workability of the reference mixture, as shown in Fig. 4. The average flow measurement is 342.5 mm, above the limit of 340 mm [10], when the slump is 200 mm.

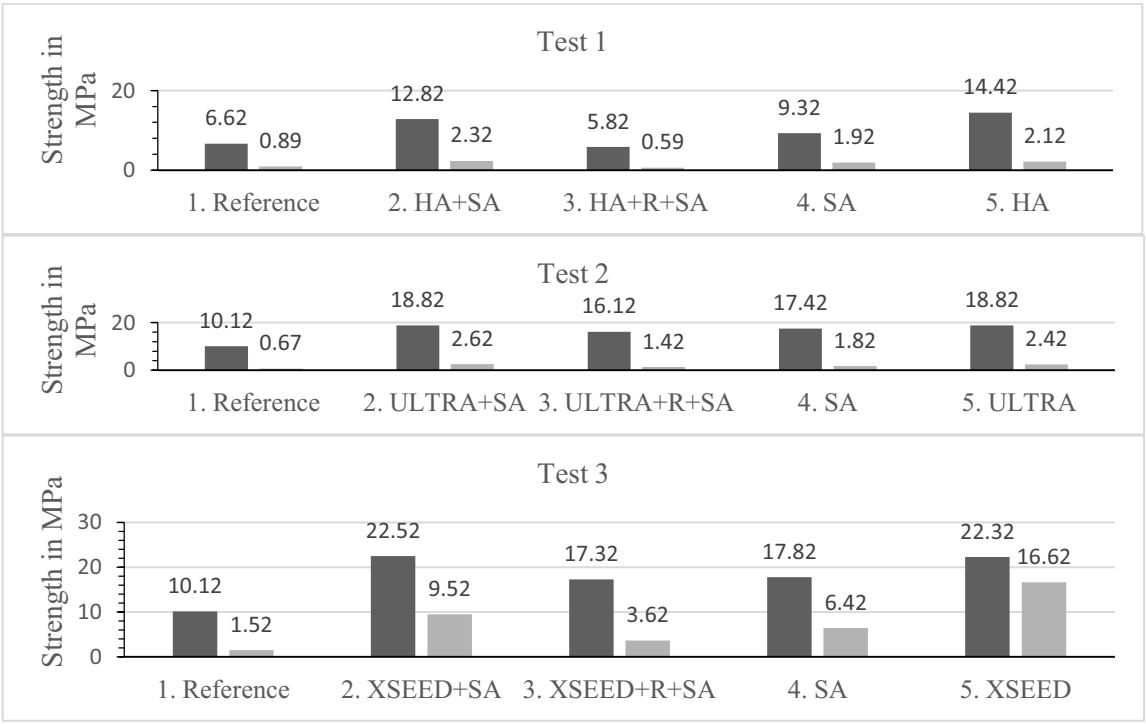

Figure 3: Compressive strengths of cubes after 18 hours inside (left) and outside (right).

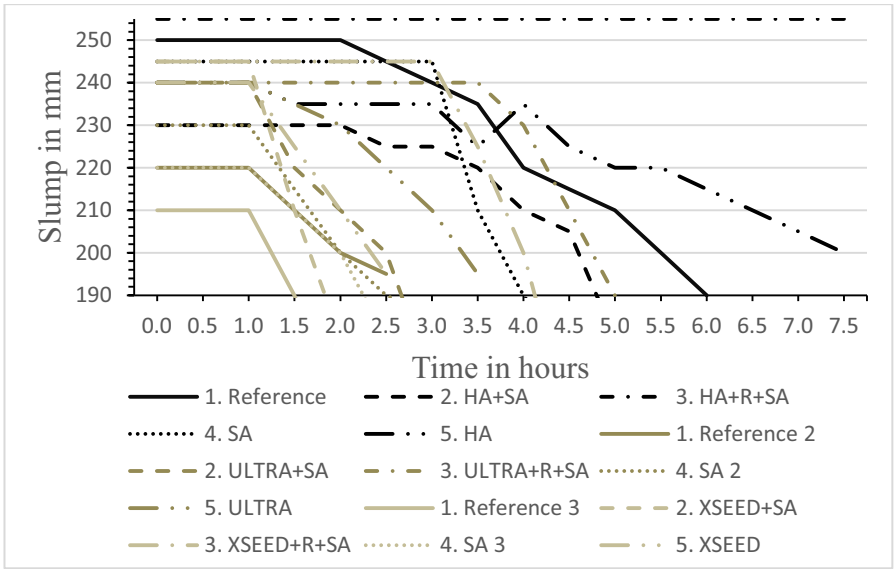

Figure 4: Slump measurements.

4. Conclusions

The main conclusions of the experimental investigation are the following:

- The use of admixtures in a typical floor concrete under cold climatic conditions mixture significantly accelerates the setting and finishing times. The setting time can be decreased by up to 42% and the finishing time by up to 48% compared to the reference concrete

mixture where no additives are used. This is particularly important for countries that experience long winters such as Norway.

- The early compressive strength accumulation rate increases by adding a combination of hardening and setting accelerators in the reference mixture. The use of a single hardening accelerator can in some cases produce the same results, depending of the characteristics of the additive.
- The workability of concrete is best controlled when a combination of hardening accelerator and retarder is added to the reference mixture. Hardening accelerators are proven to enhance the workability of concrete.
- The combinations of Mapefast Ultra N or Master X-Seed 100 with Mapefast R have found to be the most effective in order to control the consistency of concrete.
- The use of single or combinations of admixtures is recommended provided that it is done in a monitored manner. A misuse of additives can result in unwanted effects.
- The temperature development of concrete in test 2 was very small, probably due to the lower temperature of concrete of 24.1^0C from production in comparison to tests 1 (26.1^0C) and 3 (26.7^0C). Nevertheless, setting is still present in test 2 specimens.

References

[1] Bost, P. et al, Comparison of the accelerating effect of various additions on the early hydration of Portland cement, Con and Build Mat 113 (2016), 290-296
[2] Fatma, K. et al, Behavior of fresh and hardened concretes with antifreeze admixtures in deep-freeze low temperatures and exterior winter conditions, Con and Build Mat 76 (2015), 388-395
[3] Riza, P., The effect of antifreeze additives on fresh concrete subjected to freezing and thawing cycles, Cold Reg Sc and Tech 127 (2016), 10-17
[4] Ryou, J.-S. and Lee, Y.-S., Properties of early-stage concrete with setting-accelerating tablet in cold weather, Mat Sc and Eng A 532 (2012), 84-90
[5] Solbraa, E., Eksperimentell undersøkelse av akseleratorer i gulvbetong under kaldt klima, MSc thesis, Norwegian University of Life Sciences (2018) (In Norwegian)
[6] NS-EN12350-2:2009, Testing fresh concrete- Part 2: Slump-test, Standard Norge, Norway (2009)
[7] NS-EN12390-2:2009, Testing hardened concrete- Part 2: Making and curing specimens for strength tests, Standard Norge, Norway (2009)
[8] NS-EN13670-2:2009+NA:2010, Execution of concrete structures, Standard Norge, Norway (2010)
[9] Road standards, section 14.623 Avbinding, The Norwegian Public Roads Administration, Norway (1997) (In Norwegian)
[10] Publication nr15, Betonggulv- gulv på grunn og påstøp, Norwegian Concrete Association, Norway (2017) (In Norwegian)

SynerCrete'18 International Conference on Interdisciplinary Approaches
for Cement-based Materials and Structural Concrete
24-26 October 2018, Funchal, Madeira Island, Portugal

EXPERIMENTAL INVESTIGATION OF NEW CEMENT COMPOSITES LONG-TERM PROPERTIES

Andina Sprince [(1)], Leonids Pakrastins [(1)], Liga Radina [(1)]

(1) Riga Technical University, Latvia

Abstract
The purpose of this research is to experimentally determine the long-term properties of several new cement composites with unconventional additives - borosilicate lamp glass filler, montmorillonite mineral additive, and polyvinyl alcohol (PVA) fibres. Test specimens were prepared and subjected to constant compression load in a permanent temperature and level of moisture. The investigated laboratory determined properties included the compressive strength values, shrinkage strain, uniaxial compressive creep strain values and then the following parameters were calculated – creep coefficient, specific creep, creep modulus. The obtained experimental results showed that for the various mixes of new cement composites the creep coefficient was the same as for normal strength cement composite, ranging from 0.2 to 3; specific creep values were 10-85 microstrain /MPa; creep modulus was 15-105 GPa. The experimental study proves that new elaborated mixes can be successfully used in the production of concrete, thus potentially decreasing the use of cement, which would lead to a reduction of carbon dioxide released into the atmosphere.

1. Introduction

Nowadays the construction material industry is developing rapidly, with an ever-increasing tendency towards the use of new materials. Since the beginning of the 20th century, scientists and cement composite technologists are working on developing new, various types of structural multi-component cement composites, the solutions ranging from mixtures with a reduced quantity of cement and smaller aggregate dimensions, to fibers being used as disperse reinforcement, introduction of various chemical additives and a lowered cement-water ratio, as well as substituting some of the cement with recycled materials, etc. [1, 2, 3, 4]. The newly developed cement composite matrixes, in general, have improved physical properties, e.g., their microstructure — cement paste accounts for a larger part of the volume, and the porosity

is reduced, leading to cement composites with smaller water absorption and better frost resistance properties [5, 6, 7]. Although the effect on these properties has been conscious, there are still several obstacles that prevent a more widespread use of these newly developed cement composites in construction. One of the main problems is insufficient information about the long-term properties, which are essential in ensuring safe and prolonged exploitation of structures.

2. Materials and Methods

One of the goals of the experiments was to find out whether the new cement composites can be competitive and whether their long-term properties are equivalent to those of normal strength cement composite (the compressive strength of normal concrete has a value ranging between 20 and 40 MPa and the high strength concrete will have strength above 40 MPa). During the research following cement composites were made and tested (graphs show designation and transcription of various cement composites):

- 20% S; 40% S; Ref S – high strength cement composite that has 20%; 40% borosilicate lamp glass micro size part powder obtained from reused lamp glass and used as an additive replacing a part of cement amount and reference composition for cement composite with borosilicate lamp glass additive. Cubic compressive strength at 28-day age appropriately ~60MPa; ~55MPa; ~63 MPa. Long-term test specimen dimensions 40×40×160 mm; at the beginning of experimental tests the age of cement composite specimen 51 days; loading level in long-term load tests 40% of ultimate stresses; in the long-term properties' tests the specimens were placed under constant static (permanent) load for 90 days; air-dry.
- ECC PVA – engineered cement composites with PVA (2%) fibres. Cubic compressive strength at 28-day age 47 MPa. Long-term test specimen dimensions Ø40×160 mm; at the beginning of experimental tests the age of cement composite specimen 28 days; loading level in long-term load tests 25% of ultimate stresses; in the long-term properties' tests the specimens were placed under constant static load for 100 days; air-dry;
- PS M – high strength cement composite with 1% montmorillonite mineral nano-size particles that in their essence is a powder of very fine, especially processed clay particles as an additive replacing a part of cement amount and Ref M – high strength cement composite (reference composition for cement composite with montmorillonite mineral nano additive). Cubic compressive strength at 28-day age appropriately ~55 MPa; ~78 MPa. Long-term test specimen dimensions 40×40×160 mm; at the beginning of experimental tests the age of cement composite specimen 57 days; loading level in long-term load tests 40% of ultimate stresses; in the long-term properties' tests the specimens were placed under constant static load for 90 days; air-dry;

The cement composite mixtures were prepared using a double shaft laboratory mixer (BHS, 3 kW, 20–100 rpm). The compressive strength of the specimens was determined in the compression machine "Controls", model No. C56G2, with an accuracy of ± 1% and a measurement range of 0-3 kN; the loading speed was 0.8 MPa/s.

All the creep specimens were loaded with a constant static load, regularly performing strain readings. The specimen does not encounter bending. For determination of the correct creep amount, shrinkage strains determined in parallel to geometry specimens and in equivalent

environmental conditions, only without the load, were subtracted from the total strains (because of the paper's limited pages amount, there have not be shown the detailed creep and shrinkage result graphs). The basic and drying creep components haven't been determined separately. It has been assumed that the difference of specimen's age - 28, 51, 57 days, does not significantly influence the test results (because typically, it is expected that a concrete mix will reach 100% of its design strength in 28 day). During the tests all specimens were kept in a dry atmosphere of controlled conditions: temperature 23±1ºC and relative humidity 35±3% [8, 9].

For all the creep specimens before placing into creep lever test stand, strain gauges were attached to the side surfaces. The strains were measured using Aistov electrical strain gauges with a scale interval of 1 μm and maximum range of ± 5 mm. Creep lever test stand (see Fig.1) allows using specimens (≤ 70 mm) more characteristic to the dimensions of high and ultra-high strength cement composite structures. With these stands, it is possible to apply constant loading on the specimens and to keep it uniform over a long period of time. In addition, it is not necessary to adjust the stress level during the experiments, the calibration curves are linear, no energy resources are consumed, and it is possible to test cement composites with the maximum aggregate dimension ≤ 5 mm, simultaneously ensuring economic use of materials. The lever arm ratio of the creep testing stand was 1:40. The accuracy of the counterweights was 1/100 kg or 0.01%. Therefore, the accuracy of creep levers is 0.01×40 = ± 0.4 kg.

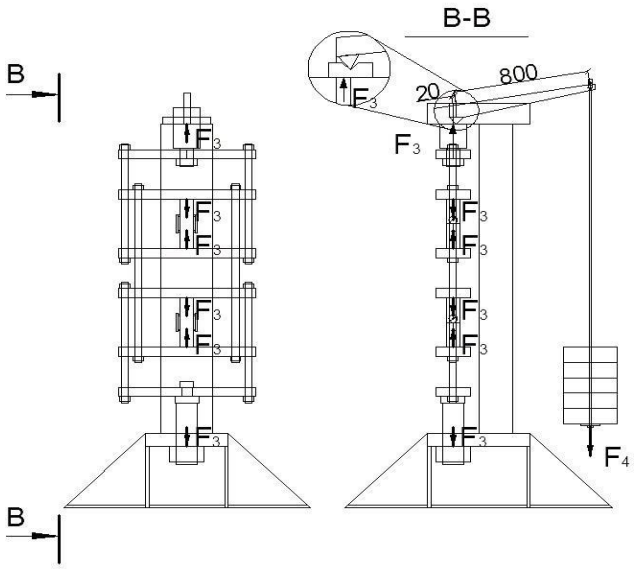

Figure 1: Creep lever test stand for determination of uniaxial compression creep strains (F3 = F4 × lever arm).

3. Results and Discussion

During the experiments, the values of strength, deformability and long-term properties of various new cement composites were found and parameters for designing of safe structures were determined, which have not been found out up until now.

Figure 2. shows the cubic compressive strength of various cement composites and values were from 32 to 60 MPa at the beginning of the tests and from 48 to 80 MPa at the end of tests. The largest cubic compressive strength was determined for cement composite without unconventional additives.

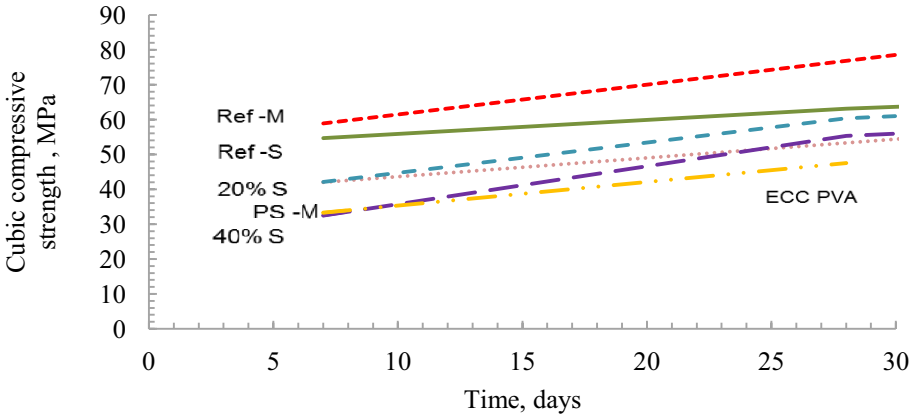

Fig. 2. Cubic compression strength of different kind of new cement composites

Creep coefficient shows the proportion of creep strain and elastic strain. Experimental data for the various mixes of cement composites show that for cement composite creep coefficient were the same as for normal strength cement composite and were within margins of 0.2 to 3 (see Fig.3), which does not comply with data of literary sources which predict a significant decrease of this coefficient [10]. The obtained results show that the proportion of elastic and creep strain for normal and high strength cement composites maintain similar proportions.

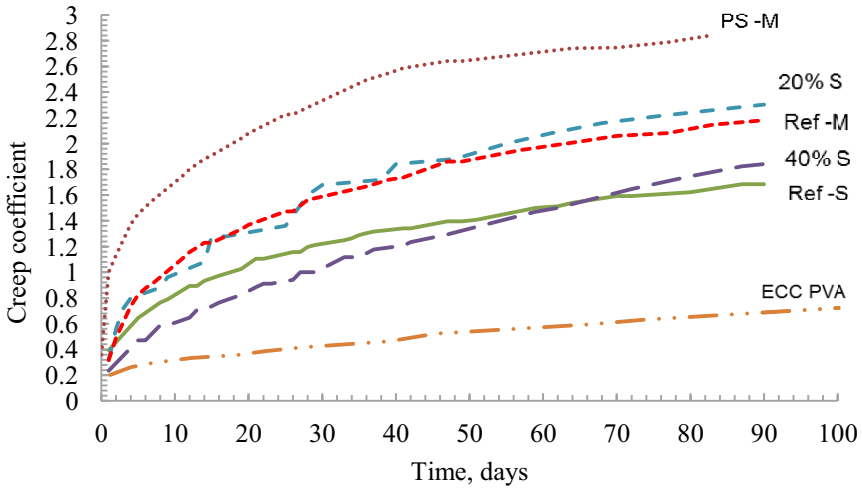

Figure 3: Creep coefficient in compression of different kind of new cement composites.

Specific creep is the most objective parameter of long-term loading as it excludes stress effect on long-term strains. Figure 4. shows specific creep of various cement composites and values

were from 10 to 85 microstrain /MPa. The largest specific creep was determined for cement composite with montmorillonite additive.

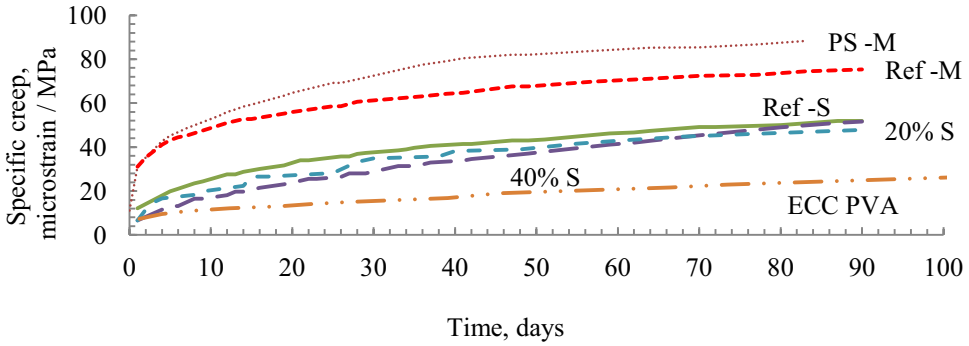

Figure 4: Specific creep in compression of different kind of new cement composites.

Creep modulus is the proportion of applied stress and creeps strain. This long-term parameter can be used for determining the displacement of long-term loaded structures after a long time period. Figure 5. shows the creep modulus of various new cement composites. As it can be seen, creep modulus has the tendency to decrease in time which can be explained by the increase of creep strain and total strain. The lower the creep modulus is, the less is creep in the material. Displacement amount rapidly increases in the first week, then the displacement speed in time decreases and approximately after 60 days significant changes in displacement cannot be observed anymore.

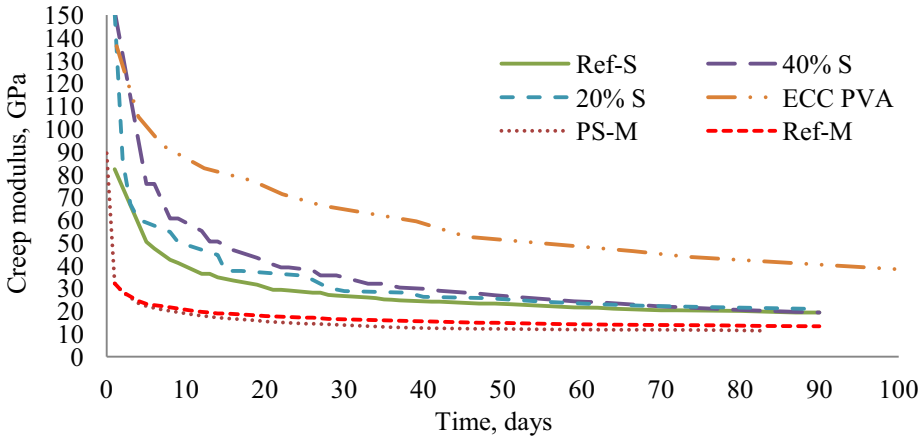

Figure 5: Creep modulus in compression of different kind of new cement composites.

It was experimentally determined that montmorillonite and borosilicate lamp glass added to cement composites neither significantly improves nor decreases the mechanical and deformability properties. The difference of the provided results reaches up to 20% to the reference cement composite results; therefore, it must be concluded that the use of such new cement composite made with alternative, more ecologic, nature-friendly mineral additive of recycled material in construction is permissible.

Similarly, it can be seen from the experimental results that PVA fibres improve long-term and durability properties of normal strength cement composites.

4. Conclusions

Experimentally obtained results for various cement composite tests confirm the hypothesis raised by various leading researchers (Neville, Brooks, Bazant, Gardner, Lockman, Fanourakis, Gilbert, Ranzi, Wittmann, Rusch and others) - the higher is the density of cement composite, the stronger it is and strain is lesser. Similarly, it has been experimentally proved that cement composite final strength increases with cement composite age and it is not substantially affected by its subjection to loading.

The obtained experimental results showed that for the various new cement composites the creep coefficient was the same as for normal strength cement composite. After approximately 90 days of loading creep coefficients values of new cement composites were 0.2-3; specific creep values were 10-85 microstrain /MPa; creep modulus was 15-105 GPa.

The use of new additives will also give an indirect positive effect on the global environment, as, by increasing the use of new unconventional cement compositions and by reducing the dimensions of the cross-sections of structures, the total amount of cement consumption will decrease and, by substituting part of the cement with recycled mineral fillers, the use of non-renewable resources and non-biodegradable waste will also be reduced.

References

[1] Fathifazl G., Razaqpur A.G., Isgor B., Abbas A., Foumier B., Somon F. Creep and drying shrinkage characteristic of concrete produced with coarse recycled concrete aggregate. Cement and Concrete Composites vol. 74 (2011), 1026-1037
[2] Fehling E., Schmidt M., Walraven J., Leutbecher T., Frolich S. Ultra-High Performance Concrete UHPC. Ernst&Sohn, Berlin (2014)
[3] Naaman A. E., Reinhardt H. W. High Performance Fiber Reinforced Cement Composites. RILEM Publications S.A.R.L., Proceedings PRO6, France (2003)
[4] Prisco M., Plizzari G., Vandewalle L. Fibre reinforced concrete: new design perspectives. Materials and Structures Vol. 42 (2009), 1261-1281
[5] Gilbert R. I., Ranzi G. Time-Dependent Behaviour of Concrete Structures. London and New York: Spon Press (2011) 3, 5, 9-11, 25-30, 26, 27, 33
[6] Neville A. M., Creep of Concrete and Behaviour of Structures. Concrete International No.5 (2002)
[7] Lu J., Poon C.S., Improvement of early age properties for glass-cement mortar by adding nanosilica. Cement and Concrete Composites Vol. 89 (2018), 18-30
[8] Rilem TC 107 - CSP: Creep and Shrinkage Prediction Models: Principles of Their Formation. Measurement of Time-Dependent Strains of Concrete, Materials and Structure, Vol. 31 France (1998)
[9] ACI 209.2R-08. Guide for Modeling and Calculating Shrinkage and Creep in Hardened Concrete, ACI Committee 209, USA (2008)
[10] BS EN 1992-1-1:2004. Eurocode 2: Design of concrete structures - Part 1-1: General rules and rules for buildings, CEN (2004)

SynerCrete'18 International Conference on Interdisciplinary Approaches
for Cement-based Materials and Structural Concrete
24-26 October 2018, Funchal, Madeira Island, Portugal

EXPERIMENTAL PROCEDURES FOR DETERMINING THE LEVEL OF SEGREGATION OF LIGHTWEIGHT AGGREGATE CONCRETES

Afonso Miguel Solak [1,2], Antonio José Tenza-Abril [1], Francisco Baeza-Brotons [1]
Victoria Eugenia García-Vera [3], Marcos Lanzón [3]

(1) Department of Civil Engineering, University of Alicante, Alicante, Spain
(2) CYPE Ingenieros S.A., Alicante, Spain
(3) Department of Architecture and Building Technology, Technical University of Cartagena, Cartagena, Spain

Abstract
In this work, four different segregation indexes were applied to evaluate the segregation phenomenon in lightweight aggregate concretes (LWAC). LWAC permits greater design flexibilities, positively impact the energy consumption of the buildings and may mean a substantial cost saving. However, LWACs are susceptible to present aggregate segregation during mixing, transport, placement and dormant periods, due to density differences between components. Segregation causes a non-uniform distribution of aggregates in the mixture and may strongly affect the strength and durability of the material. These facts justify the use of indexes to properly quantify this phenomenon. Just a few segregation indexes that permit an evaluation of hardened concrete samples were found in the bibliography. The non-destructive ultrasonic pulse velocity method has been widely applied to the investigation of concrete materials and its results can be easily related to the physical properties of the materials, such as the concrete density. In this study, four experimental segregation indexes were tested applying two different types of experimental data: classic methods of density measurement and through ultrasonic velocities. The results prove the effectiveness and precision of the methods proposed and compare their advantages and disadvantages within another method found in the literature.

1. Introduction

Vibration is an industrial practice to compact fresh concrete in a formwork and around reinforcement. During this process, the yield stress of concrete is reduced or cancelled so the

concrete flows by its weight [1] for releasing air bubbles and producing concrete with higher density, strength and durability [2]. During the mixing of lightweight aggregate concrete (LWAC), due to the low density of the aggregates and the longer mixing times LWAC is susceptible to segregation of the aggregates as a result of the differences between the densities of their components [3]. Segregation, the tendency for coarse aggregate to separate from mortar, remains one of the major problems in fresh concrete [4]. In LWAC the tendency to the floatation of the lightweight aggregate (LWA) grows with the increase of the vibration energy and therefore the concrete must present an adequate cohesion to avoid the phenomenon of segregation [5]. The consequences of segregation are numerous and may affect the strength and durability of structures [4]. Visual inspection is insufficient to evaluate the degree of concrete segregation [6] and just a few segregation indexes that permit an evaluation of hardened concrete samples were found in the bibliography. Ke [7] estimated a segregation index (SI_{Ke}) dividing the specimens into four equal sections and using the densities obtained from the upper (ρ_{top}) and lower (ρ_{botton}) slices of a cylinder. A possible segregation tends to reduce the density in the upper section because the lightweight aggregates tend to float in the mortar matrix. The index is calculated according to the Eq (1). If SI_{Ke}=1, it can be considered that the sample shows perfect uniformity. An index of less than 0.95 indicates a start of segregation [7].

$$SI_{\mathrm{Ke}} = \frac{\rho_{top}}{\rho_{botton}} \tag{1}$$

The non-destructive ultrasonic pulse velocity (UPV) method has been widely applied to the investigation of concrete. These measurements are able to predict different properties of the materials. Solak [5] found empirical correlations between p-wave UPVs and densities of LWAC sections. The main objective of this study is to test four experimental segregation indexes applying classical density measurement methods and UPV measurements methods.

2. Experimental program

2.1 Materials

Four different concretes were manufactured considering different types of LWA, different modes of vibration (one or two layers) and different theoretical densities. The experimental campaign involved the production of a concrete made with LWAs using the Fanjul method [8], in order to produce LWAC with a target density of 1700 kg/m^3 and 1900 kg/m^3. Tab. 1 presents the manufacturing characteristics of these concrete and includes their mix proportions. All samples were manufactured with the same water to cement ratio of 0.6, resulting in 350 kg/m^3 of cement and 210 kg/m^3 of water to produce 1 m^3 of concrete. CEM I 52.5 R cement with an absolute density of 3176 kg/m^3 was used for all the concretes; 2 types of expanded clay were used as lightweight aggregate; its physical properties are described in Tab. 2. The bulk density of the LWAs was obtained according to the procedure described in the standard UNE EN 1097-3. In addition, the density of the particles in the dry state was determined by the methodology proposed by Fernández-Fanjul et al [9], the absorption of water at 24 hours according to the UNE EN 1097-6 (pre-dried particles soaked in distilled water). The methods/standards used for testing are also presented in Tab. 2. Before mixing,

and to avoid the loss of water from kneading by absorption, the LWAs were presaturated. During the mixing, the water content of the LWA and the surface water content were determined, to make the appropriate corrections and maintain a constant effective water to cement ratio of 0.6.

Table 1: Manufacturing characteristics and mix proportions to produce 1 m^3 of concrete.

Concrete	Samples	Theoretical Densities	Vibration	Type of LWA	Fine Coarse (kg/m³)	LWA (kg/m³)
LWAC1	20 uds	1700 kg/m³	two layers	Arlita Leca HS	723.9	416.2
LWAC2	20 uds	1900 kg/m³	two layers	Arlita Leca HS	1046.0	294.0
LWAC3	20 uds	1700 kg/m³	one layer	Arlita Leca M	991.1	148.9
LWAC4	20 uds	1900 kg/m³	one layer	Arlita Leca M	1234.8	105.2

Table 2: Characteristics of aggregates and the methods/standards used for testing

Property	Method	Arlita Leca M	Arlita Leca HS	Fine Aggregate
Dry particle density (kg/ m³)	According to [9]	482	1019	2688
Bulk density (kg/ m³)	UNE EN 1097-3	269	610	1610
24 h Water absorption (%)	UNE EN 1097-6	36.6	12.2	0.12

2.2 Experimental procedures

In the present study, four experimental segregation indexes were tested applying two different types of experimental data: the first type, using classic methods of density measurements and the second, through UPV measurements. The experimental procedures are presented in Fig.1.

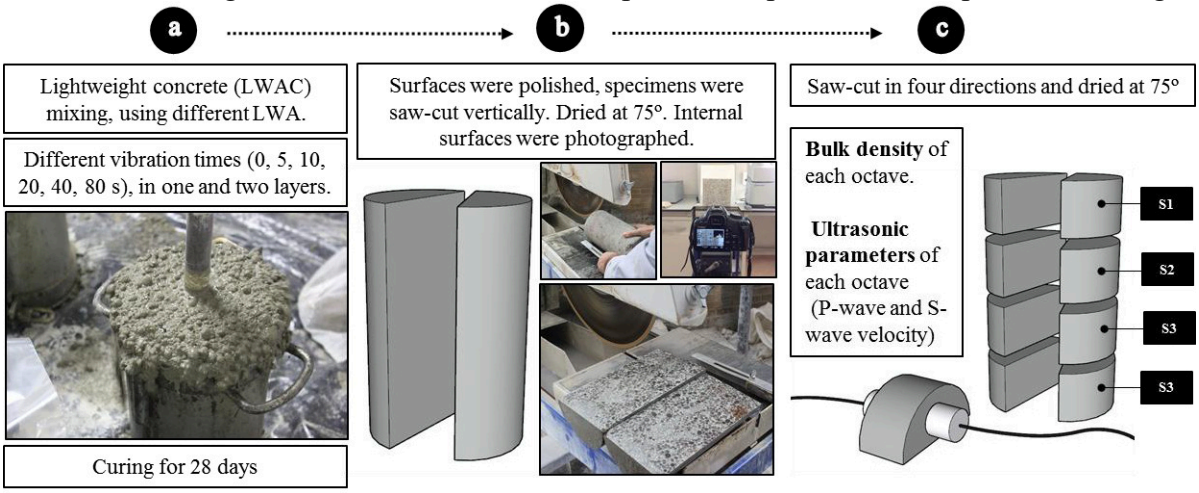

Figure 1: Flowchart of the methodology used in this study.

Cylindrical samples (Ø150mm and 300mm height) were compacted using an electric Ø25mm needle vibrator of 18000 rpm/min. Specimens were vibrated during 6 different times (0-5-10-20-40-80 seconds), in one and two layers (Tab. 1) in order to stimulate different behaviors and create different scenarios. These procedures were repeated 4 times, considering different times between mixing and molding of 15, 30, 60 and 90 min). After being made and cured in water at a temperature of 20 ± 1°C for 28 days, the specimens were saw-cut through

longitudinal axis and their sections were photographed for visual analyses. Subsequently the specimen halves were then saw-cut into four equal parts, resulting in octaves, which had their bulk densities determined. Ultrasonic pulse velocity tests were further applied for each octave. Compressional (p-wave) and shear (s-wave) wave velocities were obtained using the direct transmission configuration using polarized Panametric transducers (250 KHz). Visco-elastic couplants were used to achieve good contact between the transducer and the samples.

2.3 Segregation indexes

In this work three new experimental segregations indexes were tested and compared with the methodology proposed by Ke [7] as a validation criteria. The first index (SI_A), based on density measures, estimate a quantification for the segregation phenomenon considering the densities of the upper section of the sample (ρ_{top}) and the average between the densities of the four sections ($\rho_{average}$). Similarly to $SI_{Ke,}$ a possible segregation tends to reduce the density in the upper section because the lightweight aggregates tend to float in the mortar matrix. The more intense is the phenomenon, the higher is the difference between ρ_{top} and $\rho_{average}$. If SI_A=1, it can be considered that the sample shows perfect uniformity. The index is calculated according to the Eq. (2).

$$SI_A = \frac{\rho_{top}}{\rho_{average}} \tag{2}$$

The second and the third indexes tested in this work, SI_B and SI_C respectively, are based on UPV measurements. These measurements are a non-destructive technique and when the ultrasonic pulse is applied to concrete it enables to predict different properties of the material. Solak [5] found empirical correlations between p-wave UPVs and densities of LWAC sections. SI_B estimates the segregation considering the UPVs obtained from the upper (UPV_{top}) and lower (UPV_{botton}) slices of the samples. In LWAC a possible segregation tends to reduce the density in the upper section and as consequence, a reduction of the UPVs. The index is calculated according to the Eq. (3) and as described to the other indexes, if SI_B=1, it can be considered that the sample shows perfect uniformity.

$$SI_B = \frac{UPV_{top}}{UPV_{botton}} \tag{3}$$

The third index, $SI_{C,}$ estimates the segregation phenomenon considering the UPVs of the upper section of the sample (UPV_{top}) and the average between the UPVs of the four sections of the sample ($UPV_{average}$). The index is calculated according to the Eq. (4) and SI_c=1, it can be also considered that the sample shows perfect uniformity.

$$SI_C = \frac{UPV_{top}}{UPV_{average}} \tag{4}$$

3. Results and Discussion

Scatter diagrams were plotted to identify the possible correlation between SI_{Ke} and the new segregation indexes. SI_{Ke} and SI_A (Fig. 2a) presented the higher coefficient of determination

(R^2), reaching 0,9463. The same behavior was observed comparing the graphs of Fig. 3a and Fig 3b. Correlations between SI_{Ke} and SI_B (Fig. 2b) and SI_{Ke} and SI_C (Fig. 2c) are not as high as the first method tested, but the curves maintain the same ascendant slope tendency, presenting more dispersion on SIs near 1 (homogeneity).

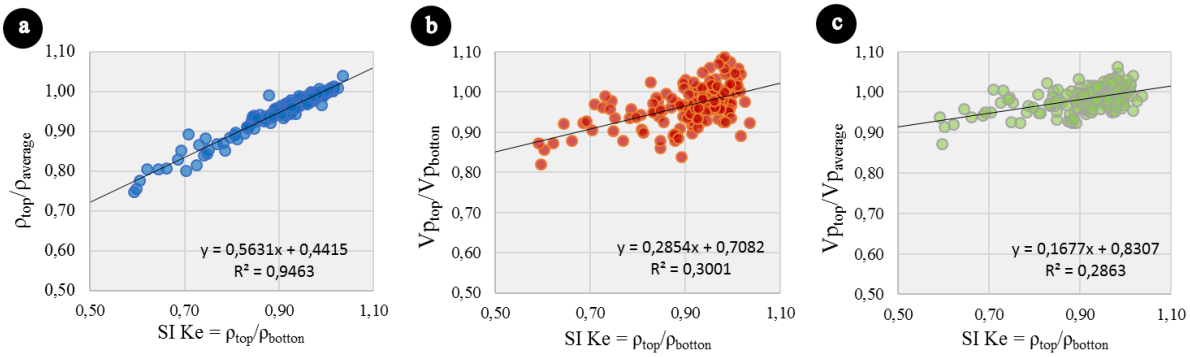

Figure 2: Scatter diagrams: SI_{Ke} vs SI_A (a), SI_{Ke} vs SI_B (b) and SI_{Ke} vs SI_C (c).

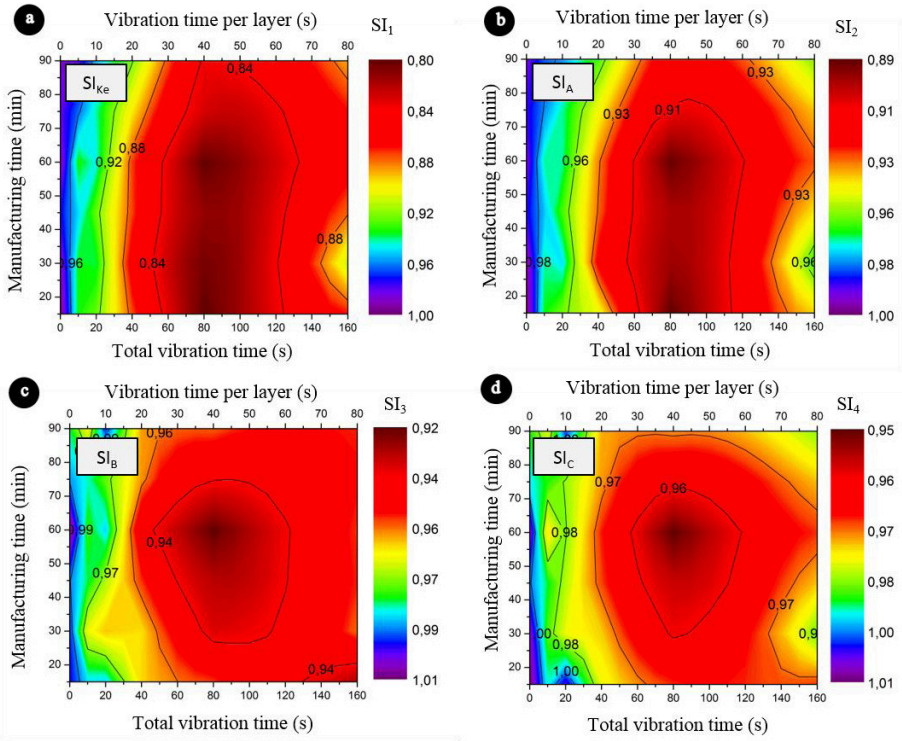

Figure 3: Segregation indexes for the concretes studied in this work

All SIs presented similar behaviors for the concretes studied (Fig. 3). However, some differences between SIs based on density and SIs based on UPVs were identified for manufacturing times of less than 30 minutes and more than 80 minutes. These differences can be identified comparting the central dark area of Fig. 3a and Fig. 3b, which have a shape of a "horseshoe" and the central dark area of Fig. 3c and Fig. 3d, which have "circular" shape. The scales of each index are also different. SI_{Ke} presented the highest difference between its minimum and maximum values (0.80 to 1.00) while SI_C presented the lowest variation (0.95 to 1.01).

4. Conclusion

This study presents an experimental study on segregation in lightweight aggregate concretes (LWAC) presenting different ways to quantify this phenomenon. From the results presented in this study the following conclusions are drawn:

- A new segregation index applying density measurements was presented in this study.
- Based on the clear relation between ultrasonic waves and concrete densities, ultrasonic waves measurements could be used to evaluate the concrete segregation in hardened samples. Two new non-destructive methods to obtain a segregation index based on UPV measurements were presented.
- Although UPV methods are less accurate and may not detect certain heterogeneities, they are non-destructive and easy to apply methods.

Acknowledgements
This research was funded by the University of Alicante (GRE13-03) and (VIGROB-256). The authors wish to express their gratitude to Phd program in Materials, Structures and Soil Engineering of the University of Alicante.

References

[1] Tattersall G, Baker P. The effect of vibration on the rheological properties of fresh concrete. Mag Concr Res 1988;40:79–89. doi:10.1680/macr.1988.40.143.79.
[2] Banfill PFG, Teixeira MAOM, Craik RJM. Rheology and vibration of fresh concrete: Predicting the radius of action of poker vibrators from wave propagation. Cem Concr Res 2011;41:932–41. doi:10.1016/j.cemconres.2011.04.011.
[3] Yu QL, Spiesz P, Brouwers HJH. Ultra-lightweight concrete: Conceptual design and performance evaluation. Cem Concr Compos 2015;61:18–28. doi:10.1016/j.cemconcomp.2015.04.012.
[4] ACI Committee 238. Report on Measurements of Workability and Rheology of Fresh Concrete. Farmington Hills: 2008.
[5] Solak AM. El fenómeno de la segregación en hormigones ligeros. Análisis mediante procesamiento de imágenes y estudio ultrasónico. Universidad de Alicante, 2017. doi:10.13140/RG.2.2.23798.29763.
[6] ACI Committee 213. Guide for Structural Lightweight-Aggregate Concrete. Reported by ACI Committee 213; 2003.
[7] Ke Y. Caractérisation du Comportement mécanique des bétons de granulats légers : expérience et modélisation. Université de Cergy-Pontoise, 2008.
[8] Fernández-Fanjul A, Tenza-Abril AJ. Méthode FANJUL: Dosage pondéral des bétons légers et lourds. Ann Du BâTiment Des Trav Publics 2012;5:32–50.
[9] Fernández-Fanjul A, Tenza-Abril AJ, Baeza-Brotons F. A new methodology for determining particle density and absorption of lightweight, normal-weight and heavy weight aggregates in aqueous medium. Constr Build Mater 2017;146:630–43. doi:10.1016/j.conbuildmat.2017.04.052.

SynerCrete'18 International Conference on Interdisciplinary Approaches
for Cement-based Materials and Structural Concrete
24-26 October 2018, Funchal, Madeira Island, Portugal

EXPOSITION TO ACID ATTACK OF MORTARS WITH NANOSILICA, ZINC STEARATE AND ETHYL SILICATE COATING

Victoria Eugenia García-Vera[(1)], Antonio José Tenza-Abril [(2)], Marcos Lanzón[(1)], Afonso Miguel Solak [(2)(3)]

(1) Department of Architecture and Building Technology, Technical University of Cartagena, Murcia, Spain
(2) Department of Civil Engineering, University of Alicante, Alicante, Spain
(3) CYPE Ingenieros S.A., Alicante, Spain

Abstract
The demand for durable cementitious materials for applications where they are subjected to aggressive chemical environments is growing. As an example, some infrastructures can be affected by acid attacks, such as sanitation networks, foundations, infrastructures in contact with groundwater or in agricultural and farm facilities. Acid attacks are one of the most severe mechanisms in the deterioration of cementitious materials. The main objective of this study is to compare the physical and mechanical changes of four different mortars subjected to an acid attack (3% w/w of H_2SO_4 solution). The mortars produced were: i) control mortar; ii) mortar with nanosilica; iii) mortar with zinc stearate; and iv) mortar with an ethyl silicate coating. After 28 days of hardening, the samples were exposed to an acid attack by immersing the specimens in a H_2SO_4 solution. Physical changes (mass loss, ultrasonic impulse velocity and water absorption) and mechanical changes (compressive strength) were determined after the acid attack exposure. The results show that the lowest mass loss after 90 days of acid attack was observed in the zinc stearate mortar. Moreover, the zinc stearate mortar was also the one that had a lower percentage of strength loss after the acid attack.

1. Introduction

External sources of sulfates have a detrimental impact on cementitious materials, such as concretes and mortars. External sulfate attack is a slow process originated from the outside and it can take years to manifest itself causing internal changes of the microstructure. These changes are manifested in physical and mechanical alterations such as strength loss, mass

variation, cracking, softening, decohesion, etc. [1-2]. There are two types of sulfate attacks, which can be classified as either chemical or physical. Chemical attacks are common in buried concretes exposed to sulfate waters existing in groundwater, where the sulfates react with aluminate hydrates to produce ettringite and gypsum. When a concrete is submerged in sulfate water a physical attack can occur due to the crystallisation of sulfate salts inside the pores of the concrete when it dries, this attack mechanism is usual in tidal zones where there are cycles of wetting and drying [3].

To obtain durable mortars and concretes against sulfate attacks is important to control the materials used during the manufacturing process, low w/c ratio (w/c ratio lower than 0.45 is considered safe), curing conditions, etc. [1]. In addition, it is possible to use additions (e.g. fly ash) or additives to extend the durability of cementitious materials. Mortars containing nanosilica have been studied in acid environments and its effectiveness has been proven in reducing the loss of both mass and compressive strength after an acid attack. This is because the nanosilica refines the pore structure creating a more compact microstructure, which reduces porosity and absorptivity [4]. Zinc stearate is one of the most frequently used materials to achieve hydrophobic mixtures [5]. It is used with different types of binders, such as cements, clays and limes. Lanzón et al. [6] proved its effectiveness on adobe materials exposed to an acid-rain attack. However, this material has not been extensively studied in cementitious mixtures exposed to acid attacks. Ethyl silicate is a liquid solution that is applied in the form of a coating and its use has been widely utilized for the stone consolidation. The ethyl silicate reacts with the substrate where is applied on, and after curing, it has a pozzolanic effect. Moreover, ethyl silicate decreases the capillary suction [7]. However, this material, like zinc stearate, has not been widely studied on cementitious materials exposed to chemical attacks.

The aim of this study is to analyze the behavior of four different mortars exposed to acid attack: an untreated mortar, a mortar with nanosilica, a mortar with zinc stearate and a mortar with an ethyl silicate coating.

2. Materials

Four types of mortars were studied: i) control mortar; ii) mortar with nanosilica; iii) mortar with zinc stearate; and iv) mortar with an ethyl silicate coating. The dosage used for the mortars was one part cement (CEM I / 52.5R), 0.45 parts water and three parts of fine limestone aggregate. For adequate workability of the mortars, 1.5 % w/w on the amount of cement of superplasticizer (Sika ViscoCrete-5980) was added to the mixtures. The nanosilica mortar was manufactured adding 2% w/w of nanosilica (MasterRoc MS 685) on the cement amount. The zinc stearate mortar was made adding 2% w/w of zinc stearate (Alfa Aesar, 33238 ZnO) on the cement quantity. Finally, the ethyl silicate coating was carefully sprayed at a controlled distance (10 cm) using a small airbrush (Fig. 1, left).

3. Methods

3.1 Manufacturing and curing process of the mortars and acid attack simulation

Six prismatic specimens (40 x 40 x 160 mm) per each type of mortar were manufactured following the procedure of the standard EN 196-1 [8]. All the specimens were cured in a

humidity chamber for 28 days. The ethyl silicate coating was applied in the midst of the curing process, that is, after two weeks the specimens were taken out from the humidity chamber the time necessary to apply the coating. After applying the coating, the specimens were returned into the humidity chamber. After 28 days of curing, all the specimens were taken out from the humidity chamber. Half of the 24 specimens were exposed to an acid attack and the other half were used as a reference. The reference specimens were maintained in standard laboratory conditions, and the acid attack was performed by immersing the specimens into a H_2SO_4 solution (3% w/w) (Fig. 1, centre). The H_2SO_4 solution was changed weekly so that the concentration of acid sulphuric did not have an excessive variation. The change of the solution was made as follows: i) the specimens were extracted from the solution, and were gently brushed under a weak flow of tap water to eliminate rests of material weakly adhered to the surface; ii) the acid solution used was changed by a new solution; and iii) the specimens were reintroduced into the new solution.

Figure 1. Left: airbrush used to spray the specimens. Centre: specimens submerged in the sulphuric solution (C = control; E = ethyl silicate coating; Z = zinc stearate; NS = nanosilica). Right: specimens before being broken in the testing machine at $t_{118(90)}$. The white specimens are those subjected to the acid attack, and the grey specimens are the reference ones.

3.2 Study of the physical and mechanical properties of the mortars

To study the mass variation, the specimens were weighed six times: 28 days after the manufacture and before starting the simulation (0 days of acid exposure) [$t_{28(0)}$]; at 7 days [$t_{35(7)}$]; 14 days [$t_{42(14)}$]; 21 days [$t_{49(21)}$]; 28 days [$t_{56(28)}$] and 90 days [$t_{118(90)}$] of acid attack exposure. The percentage of mass loss were calculated taken into account the initial weights [$t_{28(0)}$].

The ultrasonic pulse velocity test was performed following the EN 12504-4 standard [9]. The test consisted in measuring the propagation time of the ultrasonic waves along the longest dimension of the specimen (160 mm). Contact transducers emitting ultrasonic pulses at 54 kHz were coupled to the end sides of the specimens. Three determinations were made per sample, the wave velocity was computed as quotient of the specimen length divided by the propagation time. The test was performed for all the specimens, both for the specimens that had been subjected to the acid attack simulation and for those that did not. The ultrasonic test was carried out at 28 days [$t_{56(28)}$] of the acid attack simulation.

The compressive strength test was conducted according to the EN 196-1 standard [10]. A conventional mortars/bricks testing machine was utilized, at speed of 2.4 kN/s until failure

with a strain gauge load cell of 20 T capacity. For all the specimens, the test was carried out at 28 [$t_{56(28)}$] and 90 [$t_{118(90)}$] days of acid attack exposure (56 and 118 days from their manufacture).
The capillary water absorption test was performed at 90 days [$t_{118(90)}$] of exposure to the acid attack following the standard EN-1015-18 [11]. According to the standard, the water absorption coefficient is the line slope that joins the points corresponding to 10 minutes and 90 minutes in the curve that represents the mass variation of water absorbed per unit area as a function of the square root of time, i.e. the coefficient was computed using the formula:
$C = (M_2 - M_1) / (A \cdot (t_2^{0.5} - t_1^{0.5}))$
where:
C = capillary water absorption coefficient, $k/(m^2 \cdot min^{0,5})$
M_1 = specimen mass after the immersion for 10 minutes, k
M_2 = specimen mass after the immersion for 90 minutes, k
A = surface of the specimen face submerged in the water, m^2
t_2 = 90 minutes
t_1 = 10 minutes

4. Results

4.1 Compressive strength

All the specimens no subjected to the acid attack increased their strength at $t_{118(90)}$ in comparison with that at $t_{56(28)}$ (Fig. 2, left), this strength increase is common in mortars curing under standard conditions. The specimens with the ethyl silicate coating had the highest strength for $t_{56(28)}$ and $t_{118(90)}$, and the zinc stearate specimens had the lowest strength, having lower strength at $t_{56(28)}$ than the control specimens, although at $t_{118(90)}$ they slightly exceed them. In the time interval from $t_{56(28)}$ to $t_{118(90)}$ all the specimens treated increased their strength more than the control ones. The zinc stearate specimens increased approximately twice (8.5%) than the other two (4% - 4.6%) (Fig. 3, left).

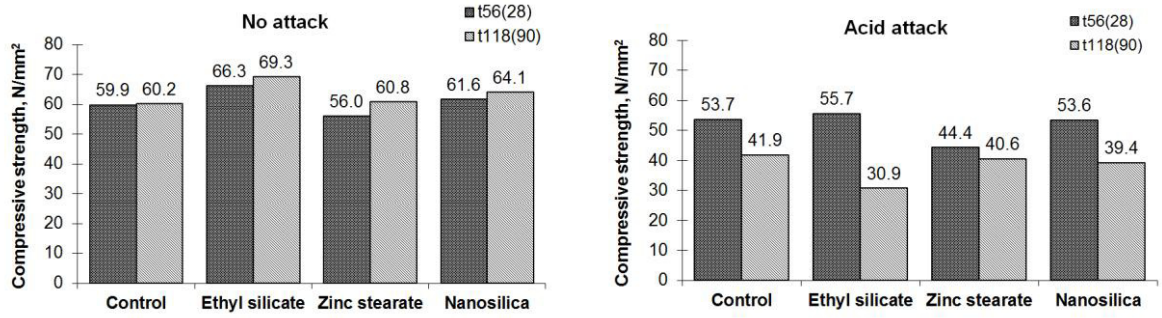

Figure 2. Compressive strength evolution, without acid attack (left) and with acid attack (right) at $t_{56(28)}$ and $t_{118(90)}$.

The compressive strength for the mortars exposed to the acid attack was lower than the compressive strength of the non-attacked mortars, this strength decrease occurred at $t_{56(28)}$ and $t_{118(90)}$ (Fig. 2, left vs right). For all the attacked mortars, the strength at $t_{56(28)}$ was lower than

the strength at $t_{118(90)}$ (Fig. 2, right). The zinc stearate mortar had the lowest compressive strength decrease (8.4 %) compared to the rest of mortars (22% - 44.6%) (Fig. 3, left).

4.2 Mass loss

The analysis of the mass loss as a function of the exposure time to the acid attack (Fig. 3, right) showed that the resistance to the attack of the nanosilica mortar and the mortar treated with an ethyl silicate coating was similar to the control mortar. However, the zinc stearate mortar was the one that best resisted the attack, its mass loss (22.9%) at $t_{118(90)}$ was lower than for the other mortars (37.3% for the nanosilica mortar, and 39.2% for the mortar treated with ethyl silicate).

4.3 Ultrasonic impulse velocity

The ultrasonic propagation velocity obtained for all the mortars studied was similar except for the zinc stearate mortar that was the lowest. As occurred with the compressive strength, when the mortars were exposed to acid attack, the ultrasonic pulse velocity was reduced (Fig. 4, left). The results demonstrate that the ultrasonic technique reflects the deterioration caused by acid attack in the mortars studied.

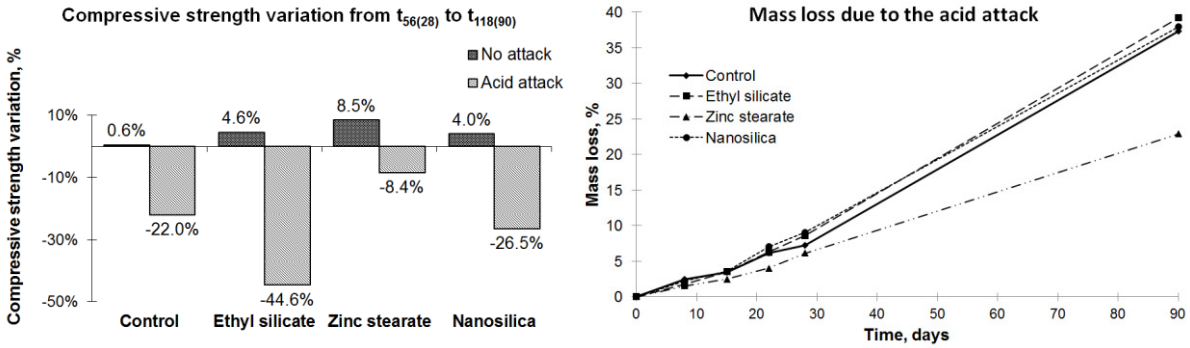

Figure 3. Left: variation percentage of the compressive strength from $t_{56(28)}$ to $t_{118(90)}$. Right: mass loss as a function of the exposure time to the acid attack.

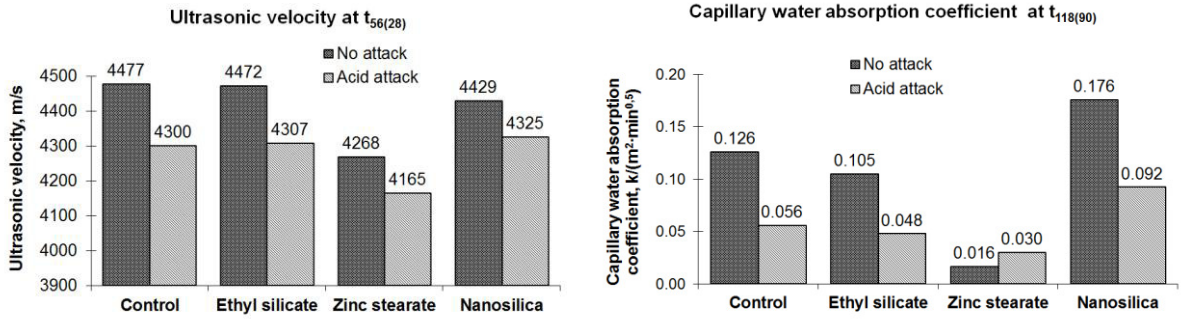

Figure 4. Left, ultrasonic velocity at $t_{56(28)}$. Right, coefficient water absorption at $t_{118(90)}$.

4.4 Capillarity water absorption

The study of capillarity water absorption (Fig. 4, right) showed that the absorption coefficient of the mortars decreased when they were exposed to the acid attack, except the zinc stearate mortar that increased it coefficient from 0.016 before to 0.030 after the acid attack. This

finding may be due to the effect of the gypsum layer created on the surface of the mortar (Fig. 1, right) during the acid attack. In the mortars with zinc stearate, the layer of gypsum absorbs more water than the interior of the specimen in which the gypsum layer does not exist. Notwithstanding, mortars with zinc stearate have demonstrated its hydrophobic effect.

5. Conclusions

In this work, the effects of acid attack on physical and mechanical properties of four different mortars were analyzed (control mortar, nanosilica mortar, zinc stearate mortar and a mortar with an ethyl silicate coating). From the results presented in this study the following conclusions are drawn:

- After the acid attack, all the mortars presented a reduction of their mass and lower compressive strength. Greater impact in the reduction with longer periods of acid attack.
- Mortars with zinc stearate in the dosage exhibited the lowest mass loss and lowest reduction in compressive strength after 90 days of acid attack exposure.
- Mortars with zinc stearate have demonstrated its hydrophobic effect with the lowest coefficient of capillary water absorption (attacked and non-attacked by acid).

References

[1] Monteiro, P.J. and Kurtis, K.E., Time to failure for concrete exposed to severe sulfate attack, Cem and Concr Res 33(7) (2003), 987–993
[2] Zhihong, Z. W. and Xiaomeng, X. S., Deterioration of fracture toughness of concrete under acid rain environment, Eng Fail Anal, 77 (2017), 76-84
[3] Whittaker, M. and Black, L., Current knowledge of external sulfate attack. Advances in Cement Research. ICE Publishing, (2015), 1-14
[4] Deb, P., Sarker, P. K. and Barbhuiya, S., Sorptivity and acid resistance of ambient-cured geopolymer mortars containing nano-silica, Cem & Conc Comp, 72 (2016), 235-245
[5] Falchi, L., Zendri, E., Müller, U. and Fontana, P., The influence of water-repellent admixture on the behavior and the effectiveness of Portland limestone cement mortars, Cem & Conc Comp, 59 (2015), 107-118
[6] Lanzón, M. Martínez, E., Mestre, M. and Madrid, J.A, Use of zinc stearate to produce highly-hydrophobic adobe materials with extended durability to water and acid-rain, Cons & Buil Mat, 139 (2017), 114-122
[7] Pigino, B, Leemann, A. and Lura, P., Ethyl silicate for surface treatment of concrete – Part II: characteristics and performance, Cem & Conc Com, 34 (2012), 313-321
[8] EN 196-1:2005, Methods of testing cement - Part 1: Determination of strength, CEN, (2005)
[9] EN 12504-4:2006, Testing concrete - Part 4: Determination of ultrasonic pulse velocity, CEN, (2006)
[10] EN 196-1:2005, Methods of testing cement - Part 1: Determination of strength, CEN, (2005)
[11] EN-1015-18, Methods of test for mortar for masonry - Part 18: Determination of water absorption coefficient due to capillary action of hardened mortar (2002)

SynerCrete'18 International Conference on Interdisciplinary Approaches
for Cement-based Materials and Structural Concrete
24-26 October 2018, Funchal, Madeira Island, Portugal

GAS DIFFUSION IN CEMENTITIOUS MATERIALS: TEST METHODS REVIEW

Fabien Gendron [(1)], Mouna Boumaaza [(2)], Philippe Turcry [(1)], Bruno Huet [(2)], Abdelkarim Aït-Mokhtar [(1)]

(1) University of La Rochelle, LaSIE UMR CNRS 7356, La Rochelle, France
(2) LafargeHolcim Research Center, Saint Quentin Fallavier, France

Abstract
The durability of reinforced concrete structures is strongly related to phenomena controlled by gas or liquid diffusion. Thus, gas diffusivity of concrete is a relevant durability indicator especially for carbonation induced corrosion. However, there is so far no standard procedure for the determination of this property. In the present paper, the main existing procedures for gas diffusion are first described. Two newly developed test methods are then presented. These procedures, which involve either CO_2 or O_2, consist in assessing the gas diffusivity from an unsteady state diffusion. These diffusion tests are compared through results from a campaign carried out on oven-dried cement pastes made with OPC and a mix of blast furnace slag and OPC. All the so-determined diffusivities are finally compared to data from literature. The main challenge of such a comparison is to find diffusivity values obtained for the same type of materials at equal hydric state. It is concluded that round robin tests would be of great interest for the future development of gas diffusion tests.

1. Introduction

The durability of reinforced concrete structures is strongly related to reactive transport phenomena such as carbonation. The latter involves the diffusion of atmospheric carbon dioxide within the material porous network. The corrosion rate of reinforcing bars itself is partly controlled by the diffusion of gaseous dioxygen in concrete. Therefore, gas diffusivity of concrete is undoubtedly an appropriate indicator for long term durability issues. Such an indicator could be used in performance based approaches of concrete structures design, for instance through the equivalent performance concept. Moreover, gas diffusivity is a key-property in the modelling of transport phenomena for the prediction of the structure service life. If ongoing efforts are invested in the design of testing procedures, there is so far no

standard procedure for the determination of gas diffusivity. The existing procedures that can be found in literature are based on quite different principles [1]. Furthermore, in performance based approach, other material properties (e.g. porosity, gas permeability, chloride diffusivity) or performance tests (e.g. accelerated carbonation test) are still preferred to gas diffusivity. It should be noted that there are relatively few studies on gas diffusion in concrete, compared to investigations on other transport phenomena such as permeation or ion diffusion.
In the present paper, the main existing techniques for gas diffusion tests are firstly described. Two newly developed tests are then presented. These experimental procedures, which involve diffusion of carbon dioxide and oxygen, respectively, consist in assessing the gas diffusivity from a non-steady state. In both procedures, the time-evolution of the gas concentration in a downstream chamber due to the diffusion through the tested sample is measured by means of local gas probes. Results of two testing laboratories using these diffusion tests are compared through an experimental campaign carried out on oven-dried cement pastes specimens. The tested pastes were made with an ordinary Portland cement (OPC) and a mix of OPC and blast furnace slag. Finally, all the so-determined diffusivities are compared to data from literature.

2. Principles of gas diffusion tests from literature

Figure 1 illustrates the principles of the main gas diffusion tests found in literature. In the procedure type 1, the specimen, placed between two chambers, is exposed to two pure gases or gas mixes. The time-evolution of gas 1 concentration in the lower chamber is measured, while its concentration is kept constant in the upper one. From this data, Fick's laws are used to calculate the effective diffusion coefficient. This kind of procedure is performed either in the transient state or in the steady state. In the latter case, the concentration gradient of gas 1 is kept almost constant by renewing the gas in the lower chamber after each measurement. Since the gas 1 concentration remains low, a very accurate gas analyzer has to be used [3].

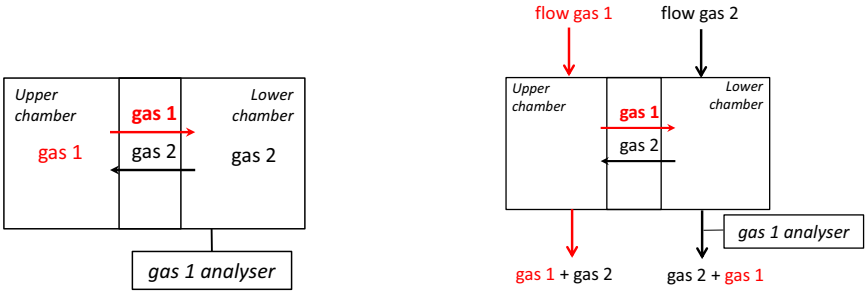

Figure 1: Classical procedures for gas diffusion: type 1 (left) and type 2 (right) [1].

Previously developed by Lawrence [2], the procedure type 2 consists in exposing both opposite faces of the specimen to streams of gas 1 and gas 2. While these gases flows are maintained constant, the increasing concentration of gas 1 in the outing gas from the lower chamber is determined by an analyzer. When the steady state is reached, gas 1 concentration becomes constant and its value can be used to calculate the diffusion coefficient knowing the gas flow rate using Fick's first law of diffusion.
Diffusion tests are currently done with pure gases, such as hydrogen or oxygen, which are somewhat inert for cementitious matrices [3-7]. Some authors presented also results from CO_2 diffusion tests [1, 8-10].

3. New proposed diffusion tests

3.1 Experimental set-ups

Two diffusion tests were recently proposed, one for CO_2 diffusion [8] and the second one for atmospheric O_2 diffusion [6]. They are based on the procedure type 1 described previously taking into account the transient state. Fig. 2 gives an overview of the set-ups (chambers, specimen and seals). In both procedures, the concentration of the considered gas, CO_2 or O_2, is measured continuously by means of a gas sensor located in the downstream chamber. Apart from the gas nature, the main difference between the two tests lies in the upstream system. In the CO_2 diffusion set-up, the upstream chamber is connected to a CO_2 bottle and is filled by a mix of air and CO_2 with a controlled CO_2 concentration (for instance 10% by volume). In the O_2 diffusion setup, there is no upstream chamber: one face of the specimen is in contact with the ambient air, i.e. at a O_2 concentration of around 20% by volume. The absence of O_2 bottle makes the great relevance of this setup from a practical point of view. At the beginning of O_2 diffusion test, the downstream chamber is flushed with nitrogen during maximum 20s to reach an O_2 concentration lower than 0.3%. Before CO_2 diffusion test, such a flushing of the downstream chamber is not required: the CO_2 concentration is assumed to be negligible. For both tests, tested specimens are discs of cement paste or mortar (40 to 70mm in diameter, 5 to 30mm in thickness for CO_2; 40mm in diameter and 2 to 15mm in thickness for O_2). Note that a second version of the O_2 diffusion test was also developed for concrete.

Figure 2: Overview of CO_2 (left) and O_2 (right) diffusion set-ups.

The result of both tests is an accumulation curve of the considered gas in the downstream chamber. The effective diffusion coefficient is computed by minimizing the difference between experimental data and concentration time-evolution calculated with the Fick's second law.

3.2 Round robin tests

The previously described tests were compared through a round-robin testing campaign carried out on seven specimens of hardened cement pastes. The latter contained either an OPC or a mix of OPC and blast furnace slag (BFS) [6]. The pastes were made with two volumetric water/binder ratios, namely 1.6 and 1.9 (i.e. w/b mass ratios of around 0.5 and 0.6 respectively). The tested specimens were discs with a diameter of 40 mm and a thickness between 3 and 4mm. Before testing, all specimens were cured during 6 months, water-saturated under vacuum in order to determine porosity and then dried at 80°C until constant mass. After oven-drying, O_2 diffusion tests were carried out first. The specimens were then

sent by post to the second laboratory. Before CO_2 diffusion tests, the specimens were re-dried at 80°C to obtain as much as possible the same hydric state than before O_2 diffusion. Tab.1 gives composition, porosity and effective diffusion coefficient of each specimen.

Table 1: Composition, porosity and diffusivities of the tested specimens.

Binder (% in mass)	w/b in vol. (-)	Porosity (-)	D_{O2} (10^{-8} m²/s)	D_{CO2} (10^{-8} m²/s)
OPC (100%)	1.6	0.43	9.1	16.8
OPC (100%)	1.9	0.48	10.6	26.0
OPC (100%)	1.9	0.48	15.5	28.0
OPC+BFS (50%+50%)	1.6	0.46	3.8	8.0
OPC+BFS (50%+50%)	1.6	0.46	4.0	6.6
OPC+BFS (50%+50%)	1.9	0.51	8.5	15.2
OPC+BFS (50%+50%)	1.9	0.51	4.7	13.0

For a given binder type, the effective diffusion coefficient increases with porosity, whatever the considered gas. At equal w/b volume ratio, OPC specimens are more diffusive than BFS specimens although the latter are more porous. This is usually explained by the finer pore structure of pastes containing BFS [6].

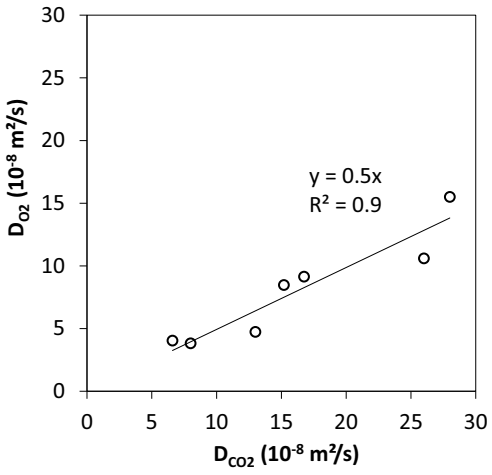

Figure 3: O_2 effective diffusion coefficient versus CO_2 effective diffusion coefficient.

Figure 3 compares O_2 diffusivities (D_{O2}) and CO_2 diffusivities (D_{CO2}). A rather good correlation is observed. However, the obtained ratio D_{O2}/D_{CO2} (=0.5) is not expected. By assuming that Knudsen diffusion is the dominant phenomenon, this ratio should be equal to 1.17, i.e. the squared ratio of molar masses $(M_{CO2}/M_{O2})^{1/2}$ [11]. Apart from differences due to the setups, an explanation of the difference between theoretical ratio and experimental one is a possible damage of the specimens due to the re-drying at 80°C before the second diffusion tests series with CO_2. At least, this emphasizes the care which has to be taken in the handling of specimens used for round-robin tests.

4. Comparison with literature data

The main characteristics of the rare data on gas diffusion through dried hardened cement pastes used for comparison are the followings.

- Diffusivities from [3-5] were determined with the same setup using the procedure type 1 with H_2. The tested pastes were made with CEMI (OPC) or CEMV type cements with w/c mass ratios from 0.3 to 0.5 and were dried at 3% RH and 20°C before testing.
- Diffusivities from [7] were determined using the procedure type 2 with O_2. The paste contained CEMI type cement with w/c mass ratios from 0.3 to 0.5, oven-dried at 105°C.
- Diffusivity from [9] were determined using procedure type 2 with CO_2 diffusion carried out on OPC paste with w/c mass ratio of 0.5 dried at 10% RH and 20°C.
- Diffusivities from [1] were determined with procedure type 1 with CO_2. The pastes were made of CEMI cement or a mix of CEMI and BFS (25-75% in mass) with w/b mass ratios from 0.3 to 0.5. Before diffusion, the specimens were oven-dried at 105°C.
- Diffusivities from [10] were extrapolated from a function fit by the authors on results of CO_2 diffusion tests carried out on OPC carbonated pastes with w/c from 0.4 to 0.8 conserved at different RH between 40 and 90%.

According to Graham's law, an "equivalent" CO_2 diffusivity was calculated by multiplying the diffusivity of the gas used for diffusion test by the ratio $(M_g/M_{CO2})^{1/2}$ where M_g is the molar mass of the diffusing gas species. In Fig. 5, the so-obtained coefficients were plotted versus porosity for ease of comparison. In addition, values calculated from the model in [12] giving the diffusivity as a function of the porosity were also plotted.

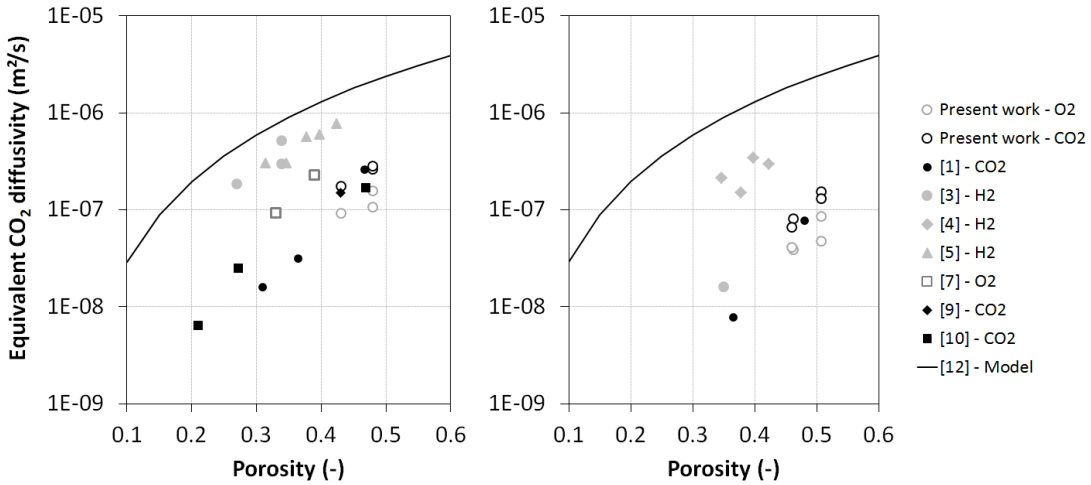

Figure 4: CO_2 effective diffusion coefficient deduced from literature data compared to data from the present round-robin tests, for OPC pastes (left) and pastes containing BFS (right).

Whatever the used test, diffusivity of OPC pastes is higher than diffusivity of pastes containing BFS, at equal porosity. Diffusivity depends on other characteristics of the porous network such as tortuosity. Thus, the proposed model [12] could not assess the gas diffusivity for blended cement pastes. Moreover, the plotted values in Fig. 4 are clearly scattered. Especially, a high difference is observed between diffusivities deduced from [3-5] and diffusivities from the setups presented here and from other literature data [1, 7-10]. This could

question the assumption of Knudsen diffusion mechanism. Above all, these results highlight the need of a broad round robin testing campaign.

5. Conclusion

Gas diffusivity of concrete is undoubtedly a relevant durability indicator of reinforced concrete structures. Effort has to be done to develop simple and reliable diffusion tests. In the present paper, newly developed tests were presented and compared with literature data. The main challenge of such a comparison is to find diffusivities determined for the same type of material (w/b ratio, binder type, porosity, curing age, etc.) at equal hydric state. Round robin tests carried out with various setups and procedures would be of great interest for the future development of gas diffusion tests. Mortars could be suitable materials for such a campaign since literature data on mortars are more numerous than data on cement pastes.

References

[1] Namoulniara, K. et al, Measurement of CO_2 effective diffusion coefficient of cementitious materials, EJECE 20 (2016), 1183-1196
[2] Lawrence, C.D., Transport of oxygen through concrete, Br Ceram Proc 35 (1984), 277-293
[3] Sercombe, J. et al, Experimental study of gas diffusion in cement paste, Cem Concr Res 37 (2007), 579-588
[4] Boher, C. et al, Influence of the pore network on hydrogen diffusion through blended cement pastes, Cem Concr Comp 37 (2013), 30-36
[5] Vu, T.H., Caractérisation de la phase solide et transferts de gaz dans les milieux poreux insaturés. Etude expérimentale et modélisation appliquées à la diffusion de l'hydrogène dans les matériaux cimentaires, PhD Thesis, Université de Toulouse (2009)
[6] Boumaaza, M. et al, A new test method to determine the gaseous oxygen diffusion coefficient of cement pastes as a function of hydration duration, microstructure, and relative humidity, Mater Struct 51 (2018)
[7] Wong, H.S. et al, Influence of the interfacial transition zone and microcracking on the diffusivity, permeability and sorptivity of cement-based aterials after drying, Mag Concr Res 61 (2009), 571-589
[8] Turcry, Ph. Et al, CO_2 diffusion in cementitious materials: experimental investigation, 2nd International RILEM/COST Conference on Early Age Cracking and Serviceability in Cement-based Materials and Structures, Belgium (2017)
[9] Jung, S.H. et al, Measurement device and characteristics of diffusion coefficient of carbon dioxide in concrete, ACI Mat Journal 108 (2011), 589-595
[10] Houst, Y.F, and Wittmann, F.H., Influence of porosity and water content on the diffusivity of CO_2 and O_2 through hydrated cement pastes, Cem Concr Res 24 (1994), 1165-1176
[11] Leemann, A. etal, Steady-state O2 and CO2 diffusion in carbonated mortars produced with blended cements, Mat Struct (2017)
[12] Thiéry, M. et al, Investigation of the carbonation front shape on cementitious materials: Effects of the chemical kinetics. Cem Concr Res 37 (2007), 1047-1058

SynerCrete'18 International Conference on Interdisciplinary Approaches
for Cement-based Materials and Structural Concrete
24-26 October 2018, Funchal, Madeira Island, Portugal

HEAT OF HYDRATION OF TERNARY-, QUATERNARY- BLENDED CEMENTS

Arnaud Delaplace [(1)], Denis Garcia [(1)], Marie Bayle [(1)], Quentin Favre-Victoire [(1)]

(1) LCR LafargeHolcim, Saint-Quentin-Fallavier, France

Abstract
The heat release of seven different binders (Portland cement+two or three cementitious materials) during hydration process are evaluated. Two experimental protocols are compared: the first one is a standard quasi-adiabatic test performed at two different temperatures, the second one is an industrial test performed at a single temperature. The use of cementitious materials allows as expected to reduce the heat release during hydration process. The heat release normalized by the binder content is given for the different blended binders.

1. Introduction

Predicting temperature evolution into massive structures is mandatory in many projects in order to be sure that the maximum temperature and the gradient temperature will not exceed a prescribed value specified in the project specifications. This prediction can be achieved starting from an experimental characterization of the binder (using for example a calorimeter), then using a numerical solver that takes into account the relevant boundary conditions of the structure.
Limiting heat of hydration of cement can be done by using cementitious materials. These mineral additions can also be used to improve mechanical performance of the concrete. It leads to blended cements, with one, two or even three additional components. Chemical hydration reactions of the different species are strongly coupled and change the heat release of the binder.
We propose in this study to characterize heat of hydration of high performance concretes based on a Portland cement blended with silica fume and/or fly ash and/or slag. Two apparatus are used, an industrial non-calibrated calorimeter and a calibrated one. We focus the analysis on comparing the heat of hydration of the different binders. The mechanical

performance of the concretes will be also evaluated in order to get the optimized strength/heat release ratio for the blended binders.

2. Experimental characterization of the binder thermal fingerprint

The following analysis is based on the assumption that the hydration rate of the binder can be represented by the Arrhenius law:

$$\frac{\partial \xi(T)}{\partial t} = A(\xi) exp\left(\frac{-E_a}{RT}\right) \quad (1)$$

in which T is the temperature, ξ is the hydration degree ranging between 0 to 1, A is the affinity function [s^{-1}], E_a is the activation energy [J/mol], R is the ideal gas constant [8,314 J/mol/K].

2.1 Experimental apparatus

Two apparatus are used in this study:

- The first apparatus (QAB test) is a quasi-adiabatic test realized in a calibrated calorimeter on 16×32cm-concrete cylinders at two different temperatures (Fig. 1-left). One test lasts around 7 days and allows evaluating both the heat release and the activation energy [1].
- The second test (MeTooHeat test) is performed on small 7×12cm cylinders into a non-calibrated calorimeter (Fig.1-right). The test lasts around 48h [2]. Due to the small size of the specimen, this test is usually performed on mortar samples, with a mixdesign corresponding to the concrete one without the coarse aggregates [3]. It leads to a high proportion of binder, allowing a more accurate determination of the heat release. In this study and because the binder content is important, we use the same concrete mixdesign tested in the QAB box in order to evaluate the capability of the MeTooHeat device to determine the heat release directly on the target concrete mixdesign.

Figure 1: the QAB calibrated calorimeter used on concrete (left) and the non-calibrated calorimeter used on small sample (right).

2.2 Binders description

Seven binders are studied, based on four raw materials: a Portland cement (CEM I 52.5N), a silica fume, a fly ash and a slag. The weight percentages of oxides of the raw materials are given in Tab 1.

Table 1: weight percentage of oxides for the binder components

	SiO_2	Al_2O_3	Fe_2O_3	CaO	MgO	K_2O	Na_2O	SO_3
Cement	20,46	4,91	2,79	64,38	0,97	0,85	0,16	3,13
Fly Ash	57,51	24,74	6,4	2,41	1,46	2,2	1,77	0,26
Slag	37,95	10,19	0,38	42,93	6,63	0,35	0,23	1,61
Silica fume	>95							

The proportion of the binder and the free water used in the concrete mixdesigns are given in Tab 2. The type of these concretes corresponds to high performance concretes.

Table 2: binders proportion

	C1	C2	C3	C4	C5	C6	C7
Cement [kg/m^3]	365	272	336	240	256	328	199
FA [kg/m^3]	0	204	201	204	224	131	0
Slag [kg/m^3]	225	140	67	145	140	131	378
SF [kg/m^3]	65	66	67	60	60	65	65
Total [kg/m^3]	**655**	**682**	**671**	**649**	**680**	**655**	**642**
Free Water [kg/m^3]	197	182	179	195	190	196	184
Water/binder	0,30	0,27	0,27	0,30	0,28	0,30	0,29

3. Results and on-going work

- QAB calibrated calorimeter

The analysis of the test is based on the evaluation of the heat released by the binder, q, considering the heat loss parameters a and b of the calorimeter:

$$q(t) = C_{tot}\big(\theta(t) - \theta(0)\big) + \int_0^t \big(a + b\theta(u)\big)\theta(u)du \quad (2)$$

in which θ is the temperature difference between the hydrating sample and a reference temperature (usually measured in a reference concrete sample), C_{tot} is the total heat capacity

of the concrete sample and of the calorimeter. The hydration degree is assumed to be proportional to the heat release. For each concrete, the first test has been performed with a reference temperature of 10°C (lab temperature and initial concrete temperature), the second one at 20°C. Then, the activation energy can be identified from the two temperature evolution curves, using the so-called "superposition method" [4]. The main assumption of this method is that a single constant activation energy is considered for the global binder (cement+cementitious materials). The evolutions of temperature corrected by the heat loss are plotted in Fig. 2 for the 7 binders.

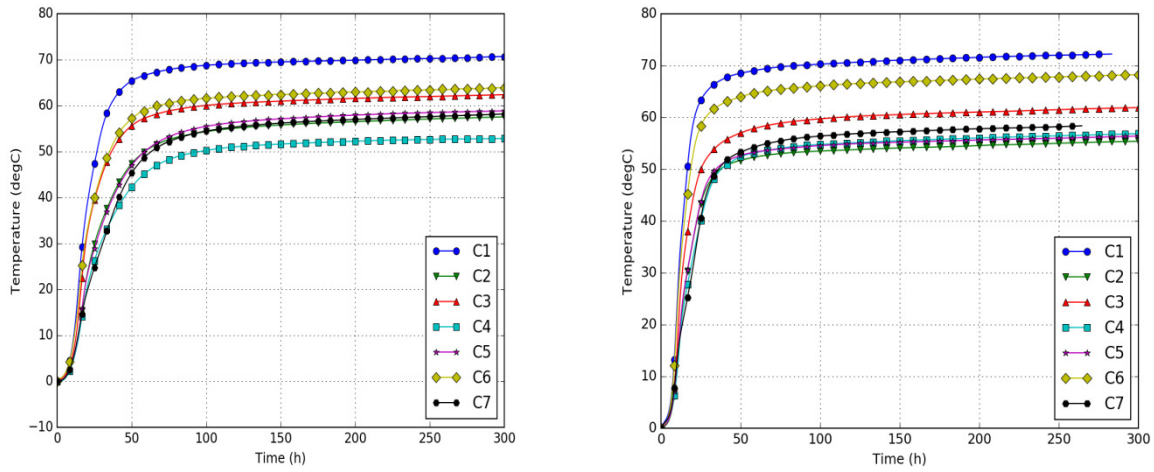

Figure 2: evolution of the temperature difference ($T(t)$-$T(0)$) corrected by the heat loss of the calorimeter: -left-: reference temperature of 10°C, -right-: reference temperature of 20°C

- Industrial non calibrated calorimeter

This test is performed at a single temperature. An activation energy E_a=45000 J/mol is assumed for the identification. Fig. 3 shows the results for the seven concretes. As mentioned above, the use of the concrete mix design is not optimal, and the increase of temperature (lower than 5°C for concretes 5 and 7) is not enough to have a fine evaluation of the heat release.

From these temperature evolutions, the heat release per gram of binder are computed for both tests (Tabs. 3 and 4), and the activation energy is computed for the QAB tests (Tab. 3). The activation energy ranges between 40000 and 48500 J/mol, except for concrete 3. There is no specific reason to have a different value for this concrete and the experiment should be repeated to verify the value. Although the assumption of having a single constant value of activation energy for these coupling hydration reactions is strong, the identified values are in agreement with values provided in literature [5, 6].
Fig. 4 gives the comparison of the heat release computed for the different binders. The MeTooHeat measurements on the small concrete samples are not satisfactory: a mortar must be used in this apparatus to limit result variability and to increase temperature range during the test. The low values of heat release can be explained by the low water/cement ratio for the considered high-performance concrete mix designs.

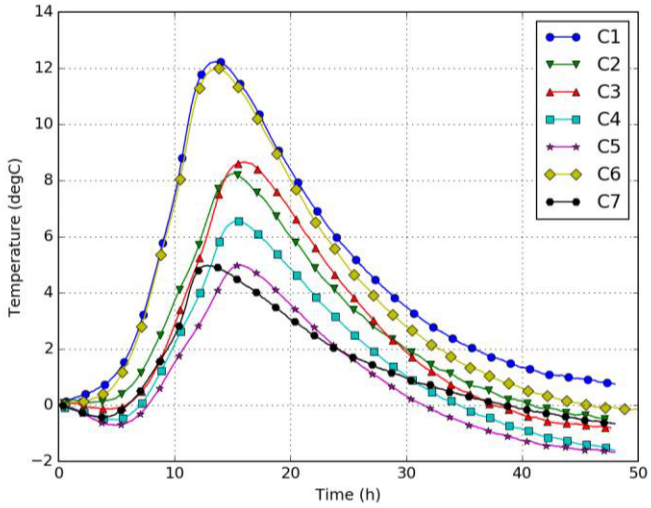

Figure 3: evolution of temperature difference ($T(t)$-$T(0)$) for the industrial apparatus

Table 3: Results of QAB analysis

	C1	C2	C3	C4	C5	C6	C7
Q [J/g binder]	254	192	209	203	191	240	208
Ea [J/mol]	48452	40702	32716	45053	42702	45580	47823

Table 4: Results of MeTooHeat analysis

	C1	C2	C3	C4	C5	C6	C7
Q [J/g binder]	314	226	277	219	194	282	206

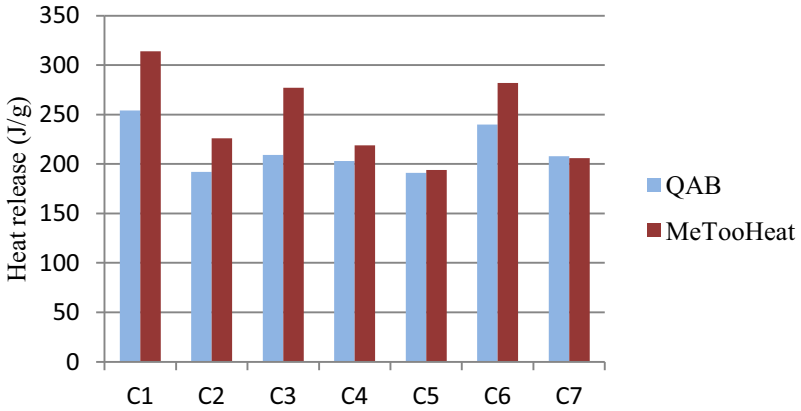

Figure 4: Comparison of the heat release for the different binders identified with the calibrated calorimeter (QAB) and with the industrial apparatus (MeTooHeat).

Additionally to these thermal tests, the compressive strength of the concretes will be characterized in order to evaluate the best strength/heat release ratio of the blended binders. Although the tests are still under progress, the first results show that the better ratios are obtained for the binders with a limited amount of Portland cements. The final results will be provided during the conference.

References

[1] Boulay, C., Torrenti, J.M., Andre, J.L., Saintilan, R.: Quasi-adiabatic calorimetry for concretes: Influential factors, Bulletin des laboratoires des ponts et chaussées 278 (2010), 19-36
[2] Šmilauer, V., Baquerizo, L., Matschei, T., Havlásek, P., Ricardo Leal da Silva, W. Hájková, K.: Contemp - a virtual thermo-mechanical simulator for hydrating reinforced concrete blocks with extension to service life. Proceedings of the International RILEM Conference Materials, Systems and Structures in Civil Engineering Segment on Service Life of Cement-Based Materials and Structures (2016)
[3] Lacarrière, L., Delaplace, A., Benhamouda, A.: Influence of the experimental apparatus on the prediction of temperature evolution in massive structure. Proceedings of the 2nd International RILEM/COST Conference on Early Age Cracking and Serviceability in Cement-based Materials and Structures - EAC2 (2017)
[4] National Project CALIBE, 'Operation of Civil Engineering Plan', Recommandations. Résistance du béton dans l'ouvrage : la maturométrie (2001)
[5] D'Aloïa, L., Chanvillard, G. Determining the ''apparent'' activation energy of concrete Ea–numerical simulations of the heat of hydration of cement. Cem Concr Res 32 (2002), 1277-1289.
[6] Broda. M, Wirquin. E, Duthoit. B. Conception of an isothermal calorimeter for concrete – determination of the apparent activation energy. Mater Struct 35 (2002), 389-94.

SynerCrete'18 International Conference on Interdisciplinary Approaches
for Cement-based Materials and Structural Concrete
24-26 October 2018, Funchal, Madeira Island, Portugal

HYDRATION PROCESS OF NATURAL HYDRAULIC LIME BLENDED CEMENT MORTARS

Reda Jaafri [(1)], Emmanuel Rozière [(1)], Syed-Yasir Alam [(1)], Ahmed Loukili [(1)]

(1) Ecole Centrale de Nantes, Institut de Recherche en Génie Civil et Mécanique (GeM), Nantes, France

Abstract
This paper presents the influence of natural hydraulic lime (NHL) on setting and early-age hydration of cement-based materials. A reference mortar was designed with a water-to-cement ratio of 0.6. At a constant paste volume, cement was replaced with increasing mass proportions of 12.5%, 25% and 50% of NHL. The freshly mixed mortars were tested for hydration process and setting properties. Thermogravimetry and differential scanning calorimetry measurements were also carried out. The undertaken experimental approach shows that the nucleation on NHL particles leads to an acceleration of early-age hydration and a reduction of initial setting time. Thermal analyses also show faster production of portlandite and ettringite during the acceleration period of hydration. This rapid formation of hydration products at early age could provide a considerable benefit in shrinkage mitigation.

1. Introduction

The mix-design of a self-leveling mortar is a compromise between the fluidity and the stability required to avoid phase separation problems. The stability of self-compacting mortar can be improved through the use of mineral additions with water retention properties, such as lime. In addition to their beneficial effect on mortars' stability, mineral additions allow decreasing the cement content, which leads to a significant decrease in the cost of production, in the ecologic impact and in other negative effects (increased thermal constraints and shrinkage). In the past few years, lime has been increasingly used in the production of self-leveling screeds thanks to its stabilizing power and the workability provided to mixtures [1].
Two types of lime exist: aerial lime and natural hydraulic lime. They differ in their properties and in their hardening process. Natural hydraulic lime (NHL) is preferred to aerial lime for screeds' production since it hardens in water following a chemical reaction between the active particles of calcium silicate C_2S and water. It provides additional strengths, higher

permeability and deformability, and better resistance to moisture, frost and salt attack. However, there are very few publications to date on blended mortars of cement and NHL.
Cement-based structures with large exchange surfaces are subjected to significant drying effects, particularly to plastic and drying shrinkage. It should be noted that if the shrinkage takes place while the material has begun to harden, strong internal restraint stresses develop and thus increase the risk of cracking. In addition, the initial setting time is also important as it should allow the transport and the placement of the mortar without affecting its workability. Setting time and shrinkage are therefore properties that are of major interest for mortars.
This study focuses on the effect of cement substitution by natural hydraulic lime (NHL) on the setting and the hydration of cement-based materials. In addition to these two properties, thermal analyzes are performed to understand the effect of lime on the production rate of ettringite and portlandite.

2. Experimental investigation

2.1 Mortars mix-design

The aim of this study is to determine the influence of NHL on setting and hydration of fresh mortars. Preliminary tests allowed to set the reference mortar mix-design with a water-to-cement ratio of 0.6. It is composed of Portland cement (CEM I 52.5 N), siliceous sand 0/4mm, and water. The chemical and physical properties of cement and NHL are summarized in Tab.1. The amount of cement in the reference mortar was then substituted by mass, but at a constant paste volume, with 12.5%, 25% and 50% of NHL (Tab. 2).

Table 1 : Cement and NHL properties

	Cement	**NHL**
C_3S (%)	68	-
C_2S (%)	11	35
C_3A (%)	8	0.5
C_4AF (%)	7	0.5
$CaCO_3$ Unburnt (%)	-	25
Free $Ca(OH)_2$ (%)	-	26.2
BET (m^2/g)	0.77	3.6
d50 (µm)	15	10.5
Density (g/cm^3)	3.12	2.68

Table 2 : Compositions of studied mortars

	Ref.	**12.5% NHL**	**25% NHL**	**50% NHL**	**100% NHL**
Cement (kg/m^3)	467	401	337	216	0
NHL (kg/m^3)	0	57	112	216	401
Sand (kg/m^3)	1389	1389	1389	1389	1389
Water (kg/m^3)	280	280	280	280	280
Initial setting time (h)	5.6	4.4	4.1	3.6	-
S_{tot} (m^2/g)	0	0.51	1.2	3.8	-

2.2 Methods

According to the European standard EN 196-3, the Vicat test was used to monitor initial setting times for all the mixtures. The test was conducted on samples stored in water at 20 °C in order to avoid the drying of the upper surfaces.

A TamAir isothermal calorimeter was used to determine the heat flow of mortar samples during hydration Tests were conducted at a temperature of 20 °C. The samples were 100 g in mass and cement was replaced with sand for the reference ampoule.

Thermal analyses were also conducted in order to determine the chemical activity of NHL and its effect on the nature and evolution of the hydration products. The evolution of portlandite and ettringite was monitored using different techniques: differential thermal analysis (DTA), thermogravimetric analysis (TGA), and differential scanning calorimetry (DSC). The tests were performed on the paste fractions of the reference and the 50% NHL mortars (Tab. 2) at 3, 8 and 12 hours. About 150 mg of finely ground samples were heated from 20 °C to 1100 °C under nitrogen atmosphere, with a heating rate of 10 °C/ min.

3. Experimental results and discussion

Setting time is an engineering property that is of major interest for cementitious materials. Initial setting time must allow for easier transport and placement of the mortar without its workability being impacted. The effect of NHL on setting was studied by measuring the initial setting time for mortars with increasing NHL content. Tab. 2 shows for each of the studied mortars the initial setting time and the total surface of contact defined as the total specific surface area available per mass of cement S_{tot} (calculated by Eq. (1)). It shows that, compared to the reference mixture, the replacement of cement by NHL leads to a significant acceleration of initial setting.

$$S_{tot} = \frac{S_{LF}.m_{LF} + S_{NHL}.m_{NHL}}{m_C} \quad (1)$$

Where S_{LF} and S_{NHL} are the specific surface areas from BET analyses respectively of LF and NHL, and m_{LF}, m_{NHL} and m_C are the masses of LF, NHL and cement respectively in the mixtures.

On initial consideration, the amount of clinker in the mixture decreases with increasing cement substitution rate, resulting in a delay in setting. Nevertheless, the greater specific surface area generated by the NHL grains contributes to the creation of new CSH seeds [2], which accelerates hydration and setting. The accelerating effect of the specific surface area provided by the NHL is substantial until an optimal surface is reached. Beyond this surface, the incorporation of the powder no longer has an accelerating effect; percolation - which is defined here as the formation of a continuous solid skeleton, requires in fact more time to reach [3].

To understand the effect of NHL on the hydration of cementitious materials, the heat flow during hydration was monitored for the studied mortars. With the exception of the first exothermic peak, no significant heat flow was measured for the 100% NHL mortar. It can therefore be considered that the hydration of NHL had no influence on calorimetry

measurements from 1h. Thus, for all the studied mortars, the heat flow is normalized by the amount of cement in the sample (Fig. 1).

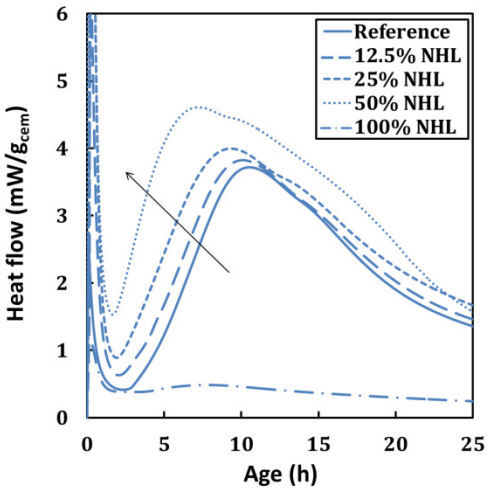

Figure 1: Heat flow curves for mortars with increasing NHL proportions

The curves represent the four characteristic periods of cement hydration, namely the initial reactions, the dormant, the acceleration and the deceleration periods. The last two periods correspond mainly to the hydration of alite (C_3S) which is the main phase of cement clinker. Another peak corresponding to the "sulfate depletion peak" may appear as a shoulder on the decreasing part of the main peak [4]. This aluminate peak corresponds to an acceleration of C_3A dissolution as soon as the sulphate carrier is completely dissolved. The aluminates actually react with the sulphate to form ettringite. However, it has been reported that a significant quantity of ettringite is produced before this aluminate peak.

The progressive leftward shifts and the earlier apparition of the hydration peak as well as the induced shorter induction periods (Fig. 1) indicate the acceleration of the mortars' hydration when cement is substituted by NHL. Since, apart from the first exothermal peak, no significant hydration reaction of NHL is observed during the first hours, the NHL accelerating effect can be considered similar to that of aerial lime which has been reported in the literature [5]. The acceleration could be attributed to nucleation on lime particle surfaces or to homogeneous nucleation within pores rather than to a supersaturation of pore solution. Indeed, the influence of the amount of NHL is observed while the concentration of the pore solution is supposed to be the same for all samples after the first dissolution peak [5].

It appears from Fig. 1 that the sulfate depletion peak becomes visible on the isothermal calorimetry curves after 9 hours for the 50% NHL paste and after 13 hours for the reference paste. This suggests a faster formation of ettringite in NHL mortars.

The evolution of ettringite in the system was monitored using DSC by measuring the consumption of the setting regulator (gypsum for example) by the mineral phases of clinker C_3A and C_4AF to produce ettringite. Indeed, the evolution of the endothermic peak located between 120 and 160 °C is inversely correlated with the production of ettringite [6]. This peak disappears after 12h and 8h respectively for the reference and the 50% NHL pastes (Fig. 2), suggesting that ettringite is more rapidly produced in NHL mixtures. This confirms the earlier apparition of the sulfate depletion peak observed in Fig. 1.

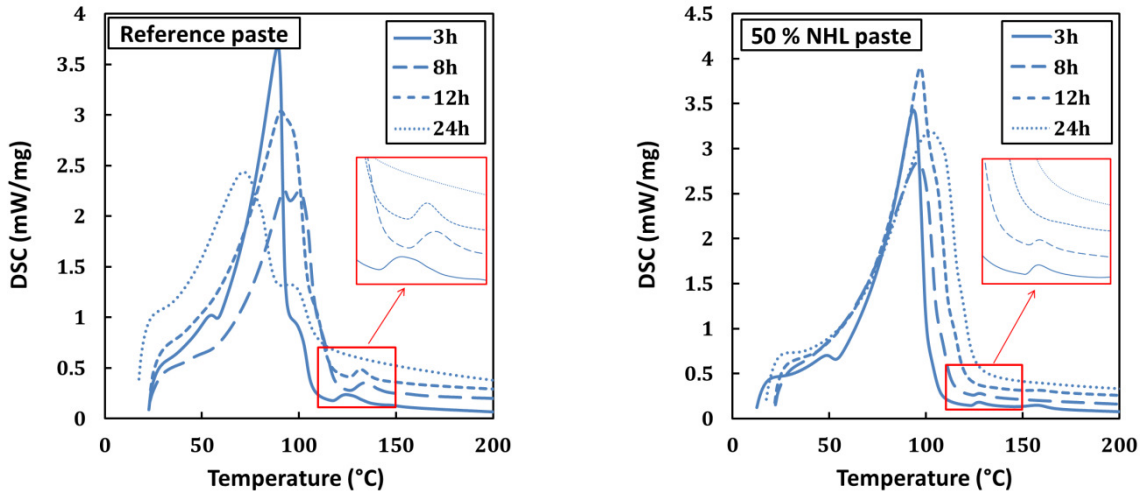

Figure 2: DSC for reference and 50% NHL pastes

TGA measurements were also performed on the reference and the 50% NHL pastes in order to examine the influence of NHL on the production rate of portlandite. It is well known that portlandite crystals decompose between 400 and 500 °C. The measured mass loss due to the evaporation of water is used to calculate the amount of portlandite in the mixture.

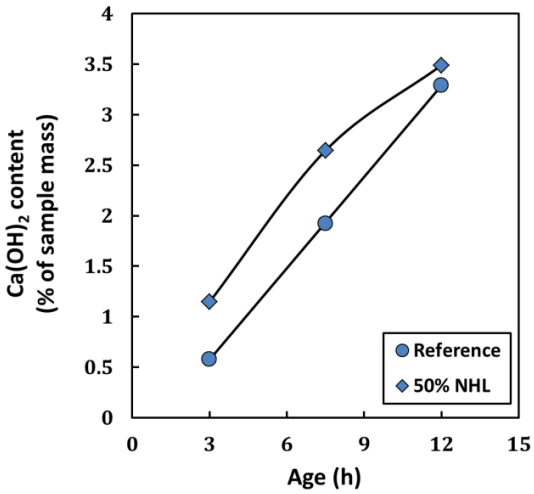

Figure 3: Evolution of the portlandite content for reference and 50% NHL pastes

The evolution over time in $Ca(OH)_2$ content in the two pastes are shown in Fig. 3. Note that the values shown for the 50% NHL paste are corrected by removing the proportion of $Ca(OH)_2$ initially brought by NHL powder. This fraction of portlandite was determined through TGA measurements conducted on NHL dry powder. This ensures that only the portlandite produced following the hydration of cement is considered.

It can be observed that during the acceleration period, the production rate of $Ca(OH)_2$ is higher for the 50% NHL paste. This confirms that NHL does indeed have an influence on the dissolution-precipitation processes related to the hydration of C_3S.

If this rapide formation of hydration products (particularly ettringite and portlandite) take place while the stiffness of the material is relatively low, it can result in an expansion period at early age. Compressive stresses are thus induced in the system and could provide a considerable benefit in plastic shrinkage mitigation.

4. Conclusions

In the present paper the effect of natural hydraulic lime/cement substitution on the setting and early hydration of cement-based mortars was investigated. The substitution of cement by natural hydraulic lime was observed to have the folowing effects:

- An acceleration of the early-age hydration and a reduction of initial setting times. This accelerating effect is due to nucleation on the lime particle surfaces rather than to a supersaturation of the interstitial solution.
- The accelerating effect of the surface area provided by the NHL is substantial until an optimal surface is reached. Beyond this surface, the incorporation of the NHL no longer has an accelerating effect since percolation requires more time to reach.
- Thermal analyzes show that the acceleration of hydration is accompanied by a higher production rate of ettringite and portlandite, which can cause crystaline pressures that could compensate for plastic shrinkage strain at a early-age.

References

[1] H. Güllü, "On the viscous behavior of cement mixtures with clay, sand, lime and bottom ash for jet grouting," *Constr. Build. Mater.*, vol. 93, pp. 891–910, 2015.
[2] E. Berodier and K. Scrivener, "Understanding the Filler Effect on the Nucleation and Growth of C-S-H," *J. Am. Ceram. Soc.*, vol. 97, no. 12, pp. 3764–3773, Dec. 2014.
[3] L. Stefan, F. Benboudjema, J. M. Torrenti, and B. Bissonnette, "Prediction of elastic properties of cement pastes at early ages," *Comput. Mater. Sci.*, vol. 47, no. 3, pp. 775–784, 2010.
[4] W. Lerch, "The influence of gypsum on the hydration and properties of Portland cement pastes," *Am. Soc. Test. Mater.*, vol. 46, pp. 1252–1297, 1946.
[5] M. Fourmentin *et al.*, "Porous structure and mechanical strength of cement-lime pastes during setting," *Cem. Concr. Res.*, vol. 77, pp. 1–8, 2015.
[6] A. Darquennes, S. Staquet, M.-P. Delplancke-Ogletree, and B. Espion, "Effect of autogenous deformation on the cracking risk of slag cement concretes," *Cem. Concr. Compos.*, vol. 33, no. 3, pp. 368–379, Mar. 2011.

SynerCrete'18 International Conference on Interdisciplinary Approaches
for Cement-based Materials and Structural Concrete
24-26 October 2018, Funchal, Madeira Island, Portugal

IMPROVEMENT OF THE MICROWAVE ABSORPTION CHARACTERISTICS BY SINTERING SLAG AS AGGREGATE

Haruki Taguchi [(1)], Yosuke Ito [(1)], Shinji Kawabe [(1)]

(1) Nagoya Institute of Technology (NIT), Aichi, Japan

Abstract
In regions of heavy snowfall, removing snow requires considerable effort. The heating mortar block system that uses an oscillator with a frequency of 2.45 GHz has been investigated for melting snow. Using this system, snow can be quickly and easily melted. The electric arc furnace oxidizing slag (hereinafter referred to as "slag") can convert the electromagnetic (EM) waves into heat. Utilizing this property, an EM absorption material used in the heating mortar is mortar mixed with slag as an aggregate (hereinafter referred to as "slag mortar"). The components of the slag vary based on the plant that is being produced. It has been clarified by previous studies that both components and particle sizes of slag affect the EM wave absorption ability of the slag mortar. Therefore, this study attempts to improve the EM wave absorption ability of slag mortar by sintering slag.

1. Introduction

In regions of heavy snowfall, removing snow requires considerable effort. It is particularly difficult for the elderly to go out. As depicted in Fig. 1, the snow on the public roads are removed using snow removal vehicles; however, snow removal, especially from the entrance of house to the front road, is often manually performed.
The heating mortar block system that uses an oscillator with a frequency of 2.45 GHz has been studied to melt snow [1], [2]. Conventional systems with electric heating cables exhibit a disadvantage that it requires time to warm up because the heating cables are buried deep inside the ground to avoid being cut. Using the heating mortar block system ensures that the snow will melt in a quicker and easier manner as compared to that observed in the systems using electric heating cables. As depicted in Fig. 2, the heating mortar block comprises the following three layers: (1) a base layer, (2) an electromagnetic (EM) absorption material layer, and (3) an EM shielding material layer. The electric arc furnace oxidizing slag can convert the

EM waves into heat. Hereinafter, "the electric arc furnace oxidizing slag" will be referred to as "slag." Utilizing this property, an EM absorption material is used and is mortar mixed with slag as an aggregate. Hereinafter, "mortar mixed with slag as an aggregate" will be referred to as "slag mortar." An EM absorption material layer is placed near the surface to ensure that the heating mortar block can melt snow efficiently.

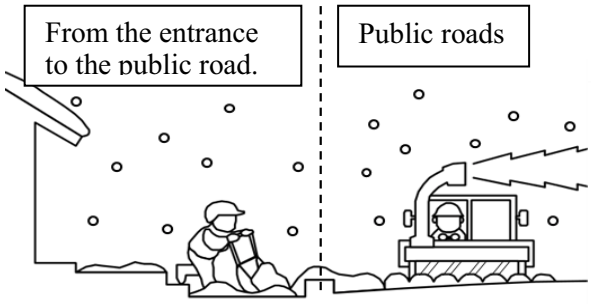

Figure 1: The state of the snowfall regions.

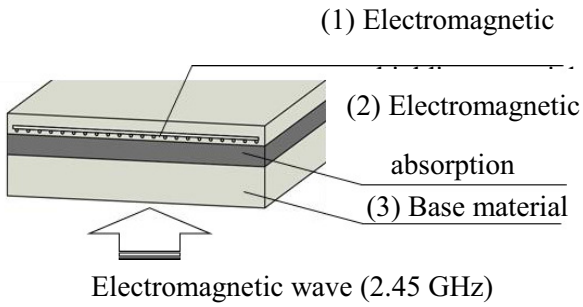

Figure 2: The heating mortar block.

The components of slag vary based on the plant that is being produced. It has been clarified by previous studies [3] that both components and particle sizes of slag affect the EM wave absorption ability of the slag mortar. This study attempts to improve the EM wave absorption ability of slag mortar by sintering slag, which exhibits low EM wave absorption ability, and by changing the crystal structure of slag.

2. The complex permittivity and permeability

The EM wave absorption ability is evaluated by return loss (RL). RL is calculated using the complex permittivity and permeability. Because the slag contains a magnetic oxide that depicts ferrimagnetism, it is classified as a magnetic loss material. The permittivity and permeability of the magnetic loss material are represented by complex numbers, and the complex permittivity, $\dot{\varepsilon}$, and permeability, $\dot{\mu}$, are defined in Eqs. (1) and (2), respectively.

$$\dot{\varepsilon} = \varepsilon' - j\varepsilon'' \quad (1)$$

$$\dot{\mu} = \mu' - j\mu'' \quad (2)$$

where ε' and ε'', μ' and μ'' are the real and imaginary parts of complex permittivity and permeability, respectively, and *j* is an imaginary number.

3. Materials

3.1 Electric arc furnace oxidizing slag

Two types of slags, slags A and B, which are industrial by-products generated while producing recycled iron using an electric furnace, are used. The slags A and B differ in components, production process, and grain shape. The mass ratio of the components of slags A and B obtained by the qualitative analysis of inorganic elements using X-ray fluorescence

are presented in Tab. 1 in terms of oxides. The particle size of slags A and B is 0.3–0.6 mm, and the absolute dry densities of slags A and B are 3.59 and 3.73 g/cm^3, respectively.

Table 1: Chemical components of the slag (Weight %).

Components	CaO	SiO_2	MnO	MgO	FeO	Fe_2O_3	Al_2O_3	Cr_2O_3	TiO_2	P_2O_5	Total
Slag A	22.93	18.09	9.84	5.20	29.20	6.24	15.57	3.53	1.71	0.17	99.23
Slag B	20.69	13.63	7.97	3.34	30.79	5.67	10.32	3.55	0.47	0.43	96.86

3.2 Slag mortar

The mix proportion of the slag mortar is presented in Tab. 2. The cement used in the slag mortar is an ordinary Portland cement. The specimen is manufactured by filling the waveguide with slag mortar. The specimen is exposed to air for 1 day and is cured underwater for 5 days. Further, the specimen is dried until it reaches an absolute dry state.

Table 2: Mix proportion of the slag mortar (Weight ratio).

Cement	Slag	Water	Waterproofing agent
100	150	45.0	0.30

4. Measuring method

4.1 The complex permittivity and permeability

The complex permittivity and permeability of slag mortar are measured using the S parameter measurement method and the Nicolson–Ross method. The measuring equipment is depicted in Fig. 3. The EM waves are transmitted from Port 1 of a vector network analyzer and are irradiated to the specimens of slag mortar via a coaxial cable and a coaxial waveguide converter. The EM waves are reflected, transmitted, or absorbed by slag mortar. The reflected EM waves are received again at Port 1, and the reflection coefficient is calculated. The transmitted EM waves are received at Port 2, and the transmission coefficient is calculated. The complex permittivity and permeability of slag mortar are calculated using the reflection coefficient and transmission coefficient that were obtained by the Nicolson–Ross method.

4.2 Sintering method

Slag is sintered by an electric muffle furnace depicted in Fig. 4. Insert the slag into a heat-resistant container, as depicted in Fig. 5; further, place it in an electric muffle furnace, and sinter it at different temperatures as will be specified in section 5.1.

5. Measurement of the complex permittivity and permeability of slag mortar

5.1 Measurement conditions

This section intends to clarify the changing condition of the EM wave absorption ability by confirming the effect that was caused by the change in the sintering temperature on the

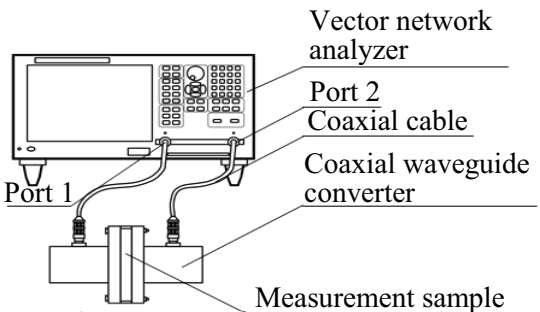

Figure 3: S parameter measuring device.


Figure 4: Electric muffle furnace.

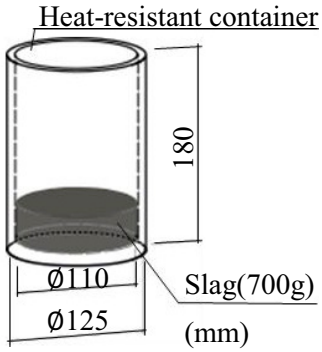

Figure 5: Condition of the sintering slag test.

complex permittivity and permeability of slag mortar. The sintering temperature of the slag is set to 200℃, 400℃, 600℃, 800℃, and 1,000℃, and the sintering time is 8 hours each. When the slags A and B are sintered at 1,100℃ and 900℃, respectively, a part of the minerals that are contained in the slag melts and solidifies, and the slag cannot be treated as an aggregate. Therefore, by considering practicality, sintering is performed at 1,000℃ and 800℃ in case of slags A and B, respectively.

5.2 The complex permittivity and permeability as a function of frequency

For the slag mortar that uses slag A as an aggregate, the real part, ε′, and the imaginary part, ε″, of complex permittivity along with the imaginary part, μ″, of complex permeability as a function of frequency are depicted in Figs. 6 to 8, respectively. Similarly, for the slag mortar that uses slag B as an aggregate are depicted in Figs. 9 to 11, respectively. Because the real part, μ′, of complex permeability is approximately 1 within the measurement range, the data exhibiting the relation between μ′ and frequency are omitted. The complex permittivity and permeability of the slag mortar was altered by sintering the slag. The changing range of ε′ is extensive for slag A than for slag B throughout the frequency, and ε″ decreases when slag A is sintered at 1,000℃. In case of μ″, the value becomes larger when slags A and B are sintered at 1,000℃ and 800℃, respectively.

5.3 The complex permittivity and permeability of slag mortar at 2.45 GHz

The relation between ε′ at 2.45 GHz of the slag mortar using slags A and B and the sintering temperature is depicted in Fig. 12. The relation between μ″ and the sintering temperature is presented in Fig. 13. ε′ changes several times in slag A that was sintered at 800 ℃ or more, whereas slag B exhibits relatively few changes. This is because the chemical components are different and because the mineral structure produced by sintering is different in slags A and B. μ″ increases at 800℃ or more in case of both slags A and B, and it is expected that the EM wave absorption ability of the slag mortar will be altered by sintering the slag.

6. Calculated return loss of slag mortar

Using the measurement results of the complex permittivity and permeability of slag mortar that were obtained in chapter 5, RL is calculated at a frequency of 2.45 GHz and the EM wave

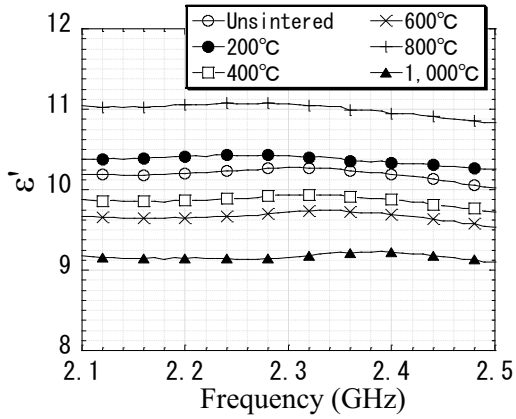

Figure 6: Real part of complex permittivity (slagA aggregate).

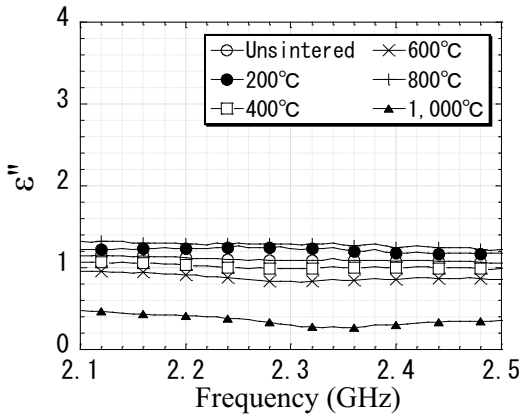

Figure 7: Imaginary part of complex permittivity (slagA aggregate).

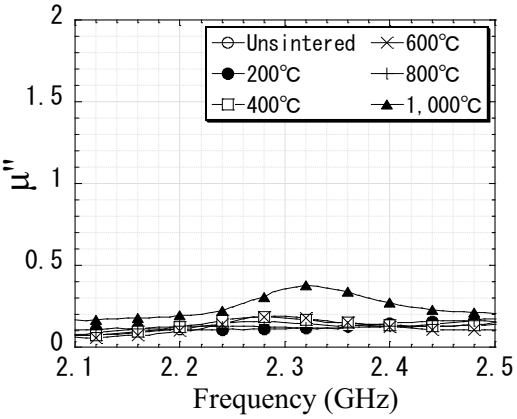

Figure 8: Imaginary part of complex permeability (slagA aggregate).

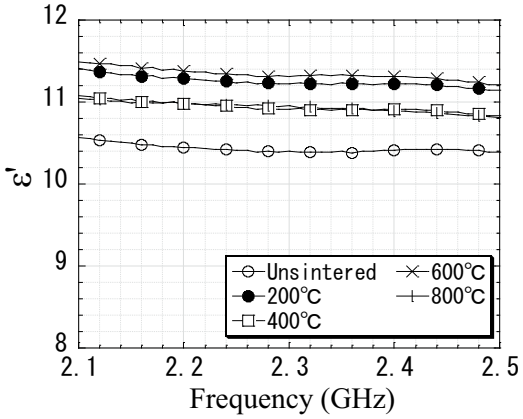

Figure 9: Real part of complex permittivity (slagB aggregate).

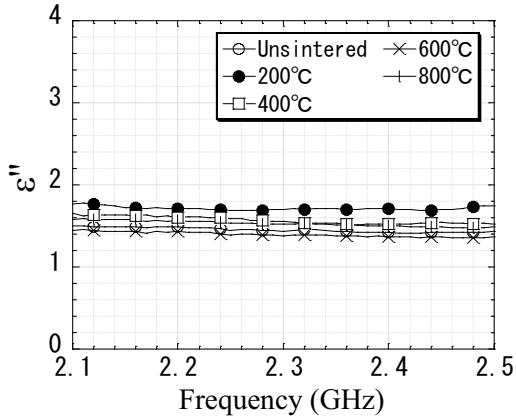

Figure 10: Imaginary part of complex permittivity (slagB aggregate).

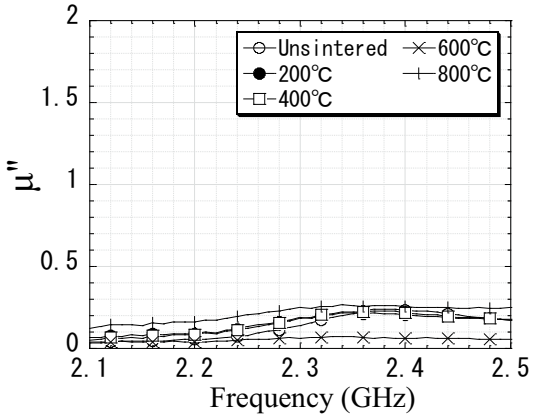

Figure 11: Imaginary part of complex permeability (slagB aggregate).

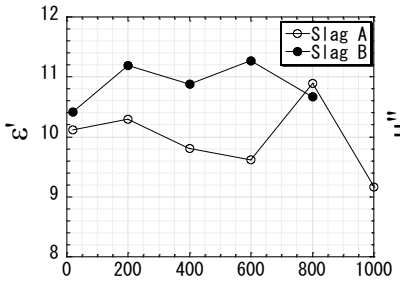

Figure 12: ε' and sintering temperature.

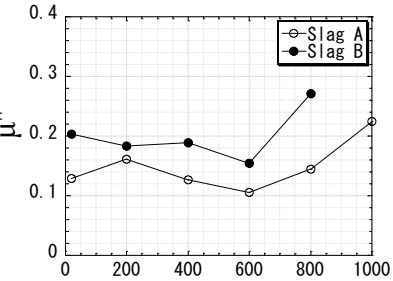

Figure 13: μ'' and sintering temperature.

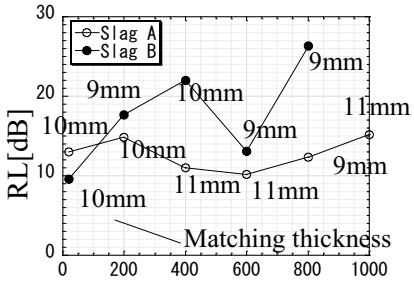

Figure 14: RL and sintering temperature.

absorption ability of the slag mortar is evaluated. The relation between RL of the slag mortar and the sintering temperature of the slag at a matching thickness is depicted in Fig. 14. RL of the slag mortar using unsintered slag A is 13.0 dB at a matching thickness of 10 mm, whereas that of the slag mortar using slag A that was sintered at 1,000 ℃ is 15.2 dB at a matching thickness of 11 mm. On the other hand, RL of the slag mortar using unsintered slag B is 9.6 dB at a matching thickness of 10 mm, whereas that of the slag mortar using slag B that was sintered at 800 ℃ is 26.3 dB at a matching thickness of 9 mm. Therefore, it is expected that the EM wave absorption ability of the slag mortar will be improved by sintering the slag. This makes it possible to produce slag mortar that depicts the EM wave absorption ability at a desired level, regardless of the type of slag.

7. Conclusions

(1) The complex permittivity and permeability of the slag mortar was altered by sintering the slag.
(2) It was assumed that the EM wave absorption ability of the slag mortar will be improved by sintering the slag.

Acknowledgments
This research was partially supported by the Matching Planner Program from Japan Science and Technology Agency (JST) and the JSPS KAKENHI Grant Number JP16K18183 and JP16K06569. Some suggestions were provided by the Honorary Professor of the Nagoya Institute of Technology, Ikeda Tetsuo, and Ten corporation. We gratefully acknowledge their supports and contributions to the research reported in this study.

References
[1] Kawabe, S., et al, Development of the heating mortar block to melt snow by the quasi microwave, Journal of Structural and Construction Engineering 69(586) (2004), 1-5
[2] Ito, Y. et al, Effects of thickness of the base layer on electromagnetic absorption in heating mortar blocks for snow melting through quasi microwave, Journal of Advanced Concrete Technology 16 (2018), 170-178

SynerCrete'18 International Conference on Interdisciplinary Approaches
for Cement-based Materials and Structural Concrete
24-26 October 2018, Funchal, Madeira Island, Portugal

INFLUENCE OF RECYCLED AGGREGATE AND RECYCLED SAND ON THE DEVELOPMENT OF THE EARLY AGE PROPERTIES OF CONCRETE SINCE SETTING

Brice Delsaute [(1)], Stéphanie Staquet [(1)]

(1) Université Libre de Bruxelles, Brussel, Belgium

Abstract
This paper aims at identifying the effect of the substitution of natural coarse aggregate and sand by recycled aggregate and sand on the early age development of the free deformation and the mechanical properties since setting. For this purpose, a new experimental testing protocol for the characterization of cementitious materials at early age is used. This new approach is based on the repeated application of thermal variation and loading using a newly developed testing device. The high porosity and absorption of the recycled aggregate and sand induces a strong reduction of the autogenous deformations, the modulus of elasticity and the strength during the hardening process. An elastic calculation of the restraint of the free deformations shows that the use of recycled aggregate and sand decreases the risk of cracking.

1. Introduction

Aggregates, which are the backbone of concrete, are inequitably distributed resources and far from inexhaustible. Their transport is very energy intensive and it is therefore necessary to use local resources to reduce the environmental impact of the very huge production of concrete in the world. One solution to this problem is the use of recycled aggregate instead of natural aggregate. For structural applications, the use of these "green" materials requires a complete characterization of the evolution of the physical and mechanical properties which are quite different from those of standard concretes. At early age, the autogenous strain and the coefficient of thermal expansion (CTE) are two of the most important concrete properties that are responsible of volume changes of cement based materials. The restraint of the autogenous and thermal strain can induce early age cracking in concrete structures (especially for massive structures). To determine the risk of cracking, it is also necessary to define other concrete properties such as the heat release by the cement, the strength and the elastic

modulus. This paper aims to identify the effect of the substitution of natural aggregate and sand by recycled aggregate and sand on the development of concrete properties at early age and to estimate their impact on the risk of cracking induced by the restrained of the free deformation in sealed conditions.

2. Materials and methods

2.1 Concrete compositions

The substitution of natural aggregate by recycled one is studied on four concretes for which mix proportions are given in Table 1. Each composition was defined in the frame of the French National project RECYBETON. For each composition, the effective water to equivalent binder ratio (0.65) and the volume fraction of aggregate and sand are the same. The content of cement, limestone filler and superplasticizer is slightly adapted to obtain the same workability. Concrete are referred by 'X'RS'Y'RA where 'X' and 'Y' are the percentage of replacement of natural sand and natural aggregate by recycled sand (RS) and recycled aggregate (RA) in volume respectively. The first composition, called 0RS0RA, is a reference concrete without recycled aggregate and sand. For the second and third composition, 30 and 100% of the natural aggregate are replaced by recycled aggregate in volume. For the last composition 30RS0RA, 30% of the natural sand is replaced by recycled sand in volume. An ordinary Portland cement of type CEMII/A-L 42.5 N was used. Gravels and sand were used in saturated-surface-dry conditions.

Table 1: Mixture proportions in kg/m³ and materials properties [1].

	0RS0RA	**0RS30RA**	**0RS100RA**	**30RS0RA**
Natural gravel 6,3/20	820	462	-	829
Recycled gravel 10/20	-	296	701	-
Natural gravel 4/10	267	228	-	190
Recycled gravel 4/10	-	-	163	-
Natural sand 0/4	780	813	806	549
Recycled sand 0/4	-	-	-	235
CEM II/A-L 42.5, C	270	276	282	276
Limestone filler, L	45	31	31	31
Superplasticizer, SP	0.747	0.861	0.798	0.798

For consideration of the ageing and the main temperature effects, concrete properties are expressed in function of the equivalent time t_{eq} (Eq. 1) which is based on the Arrhenius law and is function of the age of the material t, the evolution of the temperature T (°C), a reference temperature T_r (here 20°C), the universal gas constant R (=8.314 J/mol/K) and the apparent activation energy E_a (J/mol). The apparent activation energy was determined according to isothermal calorimetry results obtained in [2] and is equal to 35.15 kJ/mol.

$$t_{eq}(t,T) = \int_0^t \exp\left(\frac{E_a}{R}\cdot\left(\frac{1}{273+T(s)}-\frac{1}{273+T_r}\right)\right)\cdot ds \quad (1)$$

2.2 Methods

Assessment of the temperature in quasi-adiabatic conditions

Quasi-adiabatic calorimetry (QAB) allows a continuous measurement of the temperature in quasi-adiabatic conditions which is similar to the evolution of the temperature in case of massive concrete structures. The testing device so-called QAB box was developed at the LCPC laboratory (now IFSTTAR) for the monitoring of the heat release [3]. During the test, the temperature inside the concrete sample is recorded as well as the temperature of the room. Tests were performed on ± 15.5 kg concrete samples.

Assessment of the elastic properties

For the monitoring of the elastic properties, cylindrical specimens with a diameter of 97 mm and a height of 550 mm are produced. A dummy specimen with exactly the same dimensions is also produced. Samples are surrounded by 2 self-adhesive aluminum sheets in order to keep the sample in sealed conditions. An electromechanical testing setup with an extensometer in Invar© designed at ULB is used for the monitoring of the E-modulus by means of repeated loadings. The equipment is located in an air-conditioned room with a control system of the temperature and the relative humidity. The longitudinal displacement is measured with an extensometer composed by two rings spaced of 350 mm and three rods on which the 3 displacement sensors placed at 120° are pressed. Three anchorages with elastic blades are used for each ring to assure a good link between the concrete displacement and the sensor.

Assessment of the autogenous strain and the coefficient of thermal expansion

The free strain of the studied concretes is measured from casting using the BTJADE device. The test rig is composed of a vertical flexible corrugated PVC mould to monitor the free strain and fixed metallic parts. The whole frame is placed in a temperature controlled bath. In addition, repeated thermal variations are applied during the test in order to define the evolution of the CTE. Complete details about the device and the test protocol are given in [4].

3. Experimental results

3.1 Temperature evolution in quasi-adiabatic conditions

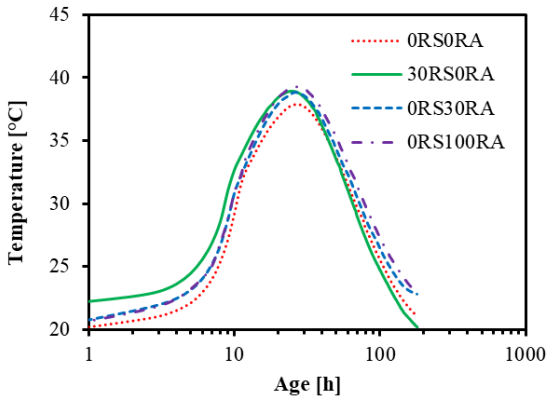

Figure 1 : Evolution of the temperature inside the cylindrical concrete sample.

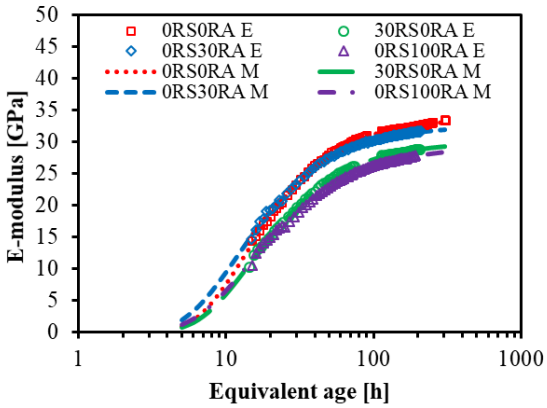

Figure 2 : Evolution of the E-modulus (E – Experimental data and M – Model) since 4 hours after setting

Each minute, the temperature of the sample and the one of the testing room is recorded. Measurements start around 30 minutes after the first contact between water and cement till a concrete age of 180 hours. In Figure 1, the recording of the concrete temperature is presented. For each composition, the temperature of the sample increases significantly between an age of 5 and 11 hours. The temperature peak is reached between an age of 23 and 26 hours and has a magnitude between 38 and 40°C. The evolution of the temperature is very similar between each composition.

3.2 Elastic modulus

Measurements on the samples have started 4 hours after setting. The whole test duration is 1 week. The temperature of the sample is set to 20°C and is recorded since the casting. For each repeated loading, the E-modulus is calculated from the set of recordings (load and displacement in the central section) between 30% and 80% of loading [5,6]. Results are given according to the equivalent time in Figure 2. The substitution of 30% of natural aggregate by recycled one does not change significantly the evolution of the E-modulus while a rate of substitution of 100% induce a decrease of the E-modulus by 5 GPa at an age of 1 week. The substitution of 30% of natural sand by recycled sand induces a decrease of the E-modulus by 4 GPa at an age of 1 week. The modeling of the E-modulus is carried out with Eq. 2 [7] where t_{eq} is expressed in hour, p_E and r_E are material parameters which are related to the kinetic evolution of the elastic modulus, $E(t_{eq} = \infty)$ is expressed in GPa and corresponds to the value of the elastic modulus at an infinite time. Values of all parameters are given in Table 2.

$$E(t_{eq}) = E(t_{eq} = \infty).\exp\left(-\left(\frac{p_E}{t_{eq}}\right)^{r_E}\right) \quad (2)$$

Table 2 - E-modulus coefficient for Equation 2

Composition	$E(t_{eq} = \infty)$ [GPa]	p_E [h]	r_E [/]
0RS0RA	33.6	13.6	1.28
30RS0RA	29.9	14.7	1.22
0RS30RA	32.6	11.9	1.21
0RS100RA	29.3	14.4	1.11

3.3 Autogenous strain and coefficient of thermal expansion (CTE)

Autogenous strains are set to zero at the final setting time. The measurements of the autogenous strain are shown in Figure 3. A similar evolution is observed after the final setting (between 10 and 12 hours according to the composition) and goes on till an equivalent age of 24 hours. During this period, shrinkage is observed and evolves very similarly for each composition and is associated to the self-desiccation of the cement paste. Then a divergence takes place between the evolutions of the different compositions. The high porosity of the recycled aggregate and sand is at the origin of these differences between the three compositions. When self-desiccation occurs, relative humidity decreases inside the cement paste. In such case, recycled aggregate plays the role of water storage agent that refills capillarity pores during the hardening process and avoids or reduces the self-desiccation mechanism with the continuous release of water. Results of the CTE are given in Figure 4. During setting, a strong and quasi instantaneous decrease of the CTE takes place during the

same limited time slot for each composition (between an equivalent age of 6 and 8 hours). Then a low decrease or increase of the CTE is observed for each composition till and equivalent age of 24 hours. Then, the CTE does not evolve significantly anymore. For the composition with the highest rate of substitution of natural aggregate by recycled one, the value of the CTE is globally higher and a limited increase of the CTE is observed after several days of age (because of the internal curing effect induced by the high porosity of the recycled aggregate).

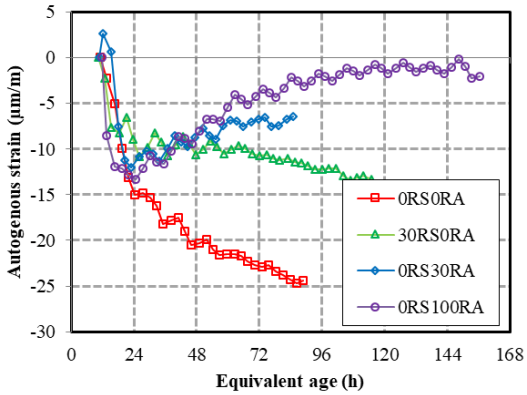

Figure 3 : Evolution of the autogenous strain

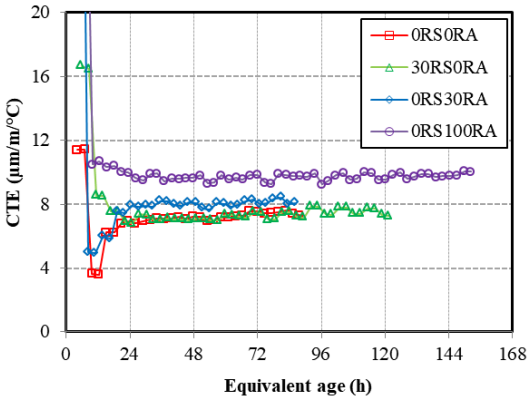

Figure 4 : Evolution of the coefficient of thermal expansion

4. Evaluation of the stress under restrained condition

In order to evaluate the influence of recycled aggregate and sand on the risk of cracking, an elastic calculation of the full restraint of the free deformations is performed according to Eq. 3 where ε_r is the restrained strain. Basic creep was not considered for the calculation.

$$\sigma = -\sum_{t'=t_0}^{t} \Delta\varepsilon_r \cdot E(t') \tag{3}$$

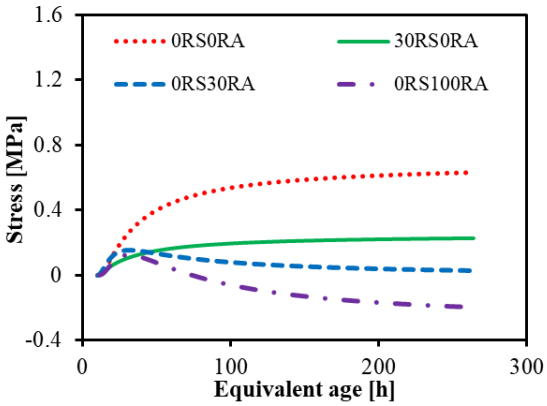

Figure 5 : Stress development in case of full restrained of the autogenous strain

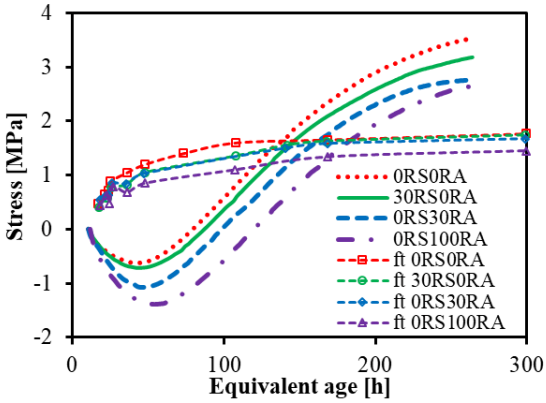

Figure 6 : Stress development in case of full restrained of the autogenous and thermal strain

Two scenarios were investigated. First, only the full restrained situation of the autogenous strain was considered (Figure 5). In this scenario, the decrease of the E-modulus and the autogenous shrinkage induced by the presence of recycled aggregate/sand leads to a significant decrease of the stress. At an equivalent age of 260 hours, the elastic stresses computed for the composition without recycled aggregate are equal to 0.6 MPa while compressive stresses of -0.2 MPa were computed for the composition 0RS100RA. Secondly, both autogenous and thermal strain were fully restrained (Figure 6). The thermal strain were computed by considering the evolution of the CTE and the evolution of the temperature recorded in the QAB. As in the first scenario, the substitution of natural aggregate/sand by recycled aggregate/sand leads to a decrease of the stress induced by the restraint strain. This is explained by the lower E-modulus and the lower increase of the CTE in the composition with recycled aggregate/sand. In addition, the evolution of the stress are compared to the evolution of the tensile strength obtained in [1].

5. Conclusion

A new experimental methodology based on repeated testing method is presented for the characterization of the early age behavior of concrete composed of recycled aggregate and sand in sealed conditions. The presence of recycled aggregates and sand induces a strong reduction of the autogenous shrinkage, the modulus of elasticity and the strength during the hardening process. An elastic calculation of the restraint of the free deformations shows that the use of recycled aggregate and sand decreases the risk of cracking of concrete structure (especially with recycled aggregate) which highlights the interest of the use of recycled aggregate for mass concrete. For further study, the internal curing effect of recycled aggregate could be studied on cement based materials with lower effective water-to-binder ratio (composition for which the self-desiccation phenomenon is very significant).

References

[1] A.Z. Bendimerad, E. Rozière, A. Loukili, Plastic shrinkage and cracking risk of recycled aggregates concrete, Constr. Build. Mater. 121 (2016) 733–745.
[2] H. Kada-Benameur, E. Wirquin, B. Duthoit, Determination of apparent activation energy of concrete by isothermal calorimetry, Cem. Concr. Res. 30 (2000) 301–305.
[3] C. Boulay, J.M. Torrenti, J. Andre, R. Saintilan, Quasi-adiabatic calorimetry for concretes : Influential factors, Bull. Des Lab. Des Ponts Chauss Ees. (2010) 19–36.
[4] B. Delsaute, S. Staquet, Decoupling Thermal and Autogenous Strain of Concretes with different water/cement ratios during the hardening process, Adv. Civ. Eng. Mater. 6 (2017) 22.
[5] B. Delsaute, C. Boulay, J. Granja, J. Carette, M. Azenha, C. Dumoulin, G. Karaiskos, A. Deraemaeker, S. Staquet, Testing Concrete E-modulus at Very Early Ages Through Several Techniques: An Inter-laboratory Comparison, Strain. 52 (2016) 91–109.
[6] B. Delsaute, C. Boulay, S. Staquet, Creep testing of concrete since setting time by means of permanent and repeated minute-long loadings, Cem. Concr. Compos. 73 (2016) 75–88.
[7] B. Delsaute, J.-M. Torrenti, S. Staquet, Monitoring and modeling of the early age properties of the Vercors Concrete, in: TINCE 2016, Paris, 2016: p. 12.

SynerCrete'18 International Conference on Interdisciplinary Approaches
for Cement-based Materials and Structural Concrete

24-26 October 2018, Funchal, Madeira Island, Portugal

INFLUENCE OF SELECTED FACTORS ON UNCERTAINTY OF RHEOLOGICAL MEASUREMENT OF FRESH MORTARS

Jacek Gołaszewski [(1)], Grzegorz Cygan [(1)], Małgorzata Gołaszewska [(1)]

(1) Silesian University of Technology, Gliwice, Poland

Abstract

The paper presents the results of research carried out to determine the uncertainty, repeatability and reproducibility of rheological measurements of mortars in variable conditions. Obtained results allow to assess the repeatability of rheological measurements as good and show the good resistance of the rheometer and test procedure used to the time and operator's influence. It was confirmed that variations in mortar constituents may significantly affect the repeatability and reproducibility of the measurements.

1. Introduction

The measurement uncertainty of set of measurements is usually expressed as the standard deviation or confidence level. Attributes of the measurement method related to uncertainty are: accuracy, precision, repeatability and reproducibility. Accuracy is the closeness of the mean of a set of measurement results to the true value of measuring quantity. Precision is the degree of closeness between results of repeated measurements of the same quantity. Repeatability and reproducibility are the degree of compliance of successive measurement results of the same measured quantity, carried out under the same measurement conditions or in changed measurement conditions respectively. In general, the available literature lacks the information on the attributes of rheometer made measurements of mortars and concretes. This makes it difficult the analysis of results of research into rheological properties of mortars or concretes, including the aspect of the significance of the influence of various material and technological factors. The paper presents the results of research on uncertainty, repeatability and reproducibility of rheological measurements of mortars performed using Viskomat NT rheometer. Although the research refers to the specific rheometer and procedure, it may be useful in the analysis of rheological measurements and its uncertainty in general.

2. Experimental

The influence of following factors on uncertainty and precision (repeatability and reproducibility) of measurements of rheological parameters of mortars was investigated:

- Time of testing intervals - 6 series of tests - the first 3 series were made during first week, and next 3 after respectively 1, 2 and 3 months;
- Operator - measurements of rheological parameters were made under the same conditions by four operators with different experience during one week;
- Variations in mortar constituents:
  (1) type of sand - standard sand acc. [4] or ordinary sand were used for mortars, ordinary sand portion was prepared without or by quartering;
  (2) batch of cement - batches of cement delivered over a period of 2 months from one cement plant (on average 1 per week, 7 batches were tested);
  (3) batch of superplasticizer SP- batches of the SP of the same trade name delivered over period of 3 months (on average 1 per month, 3 batches were tested). Cements CEM I different in C_3A content (C1 - 2%, C2 - 7%, C3 - 12%) were used in this part of research.

Uncertainty and precision of the measurements of rheological parameters was expressed using the coefficient of variation V, given in percent. It is calculated as quotient of the absolute measure of the variability of a given characteristics during the measurements (defined as a standard deviation σ) and the average value of this characteristic. For study the effects of factors ANOVA was also used. Analysis was performed in the Statistica 13.1 program.

Rheological properties of fresh mortars and concretes are characterized by the Bingham model parameters: yield stress τ_o [Pa] and plastic viscosity η_{pl} [Pas]. The yield stress τ_o determines the stress above which the material becomes a fluid. The plastic viscosity η_{pl} is a measure of how easily the material will flow, once the yield stress is overcome. The principles of rheology and rheological measurements are presented in existing literature i.e. [1,2]. Rotational Viskomat NT rheometer was used, its construction and operating principles are presented in [3]. For this rheometer the Binhgam equation is used in conventional form:

$$M = g + h\,N \tag{1}$$

Measurement of rheological parameters of the mortar consists of determination of torque M [Nmm] on stationary probe mounted concentrically in a rotating with different speeds N [1/s] cylindrical container with sample. On this basis it is possible to determine, using the method of least squares, an equation of M – N curve, and thus the rheological parameters g [Nmm] and h lNmms] of the mortar corresponding to yield value τ_o plastic viscosity η_{pl} respectively.

The composition of the mortars was based on the composition of standard mortars according to [4] (cement - 450g, sand 1350g). Mortars with w/c = 0.55 or 0.45 (mortars without or with SP respectively) of fluidity adequate for measuring range of Viskomat NT were used. Different cements CEM I were used in the individual parts of the research. Cements were stored in plastic bags during the research period. Standard sand according to [4] was used and

ordinary sand was used in the part where the influence of the sand type and the method of preparation of ordinary sand were investigated. Mortars with ordinary sand were too stiff to be measured and 0.3% of plasticizer was used for obtain its adequate flowability. All mortars were prepared according to [4] procedure. Mortars were prepared and measurements were performed in an air-conditioned room at temperature 20°C ± 1°C, mortars temperature during measurement was maintained 20°C ± 1°C using thermostatic device. The measurements was carried out after 5 and 60 minutes from the end of mixing.

3. Test results and discussion.

3.1. General remarks

Tested mortars were characterized by yield value g values in the range from 11 to 61 Nmm and plastic viscosity h in the range from 6 to 21 Nmms. Mortars were stable and showed no tendency to segregation and sedimentation. The average R^2 for individual rheological measurements which is a statistical measure of how well the regression line approximates the real data points and provides information about the goodness of a Bingham model for characterize rheological properties of mortars, was 0.990 (with $R^2_{min} = 0.982$). This confirms a very good fit of the Bingham model as a model characterizing the rheological properties of the tested mortars. Taking into account all series of measurements of mortars with standard sand, the average coefficients of variation are for the yield value g is $V_g = 4.3\%$ and for plastic viscosity h $V_h = 4.1\%$. The coefficients of variation V_g and V_h for a series carried out under the same measurement conditions are always less than 10%, which makes it possible to consider the repeatability of measurements using Viskomat NT to be good.

3.2. Influence of time of testing intervals

As shown in Tab. 1 the coefficient of variation for average rheological parameters on particular days is less than 2 %. This indicates no impact of the time of testing intervals on the results of rheological parameters measurement. This is confirmed by the ANOVA (Fig. 1), which shows that differences in rheological parameters of mortars measured in different time are statistically insignificant.

Table 1: Average yield stress g [Nmm], plastic viscosity h [Nmms], coefficients of variation V_g i V_h [%] of mortars measured in different time days

Time/number of repetitions	after 10 min				after 60 min			
	g	h	V_g	Vh	g	h	V_g	Vh
Time 1 (day 1, week 1)/3	34	12.2	3.6	3.2	39	8.8	4.5	3.2
Time 2 (day 2, week 1)/4	34	12.4	4.5	2.6	38	8.7	2.3	1.8
Time 3 (day 3, week 1)/4	33	12.1	5.2	6.5	37	8.7	5.7	1.7
Time 4 (day 4, month 1)/4	33	11.9	4.6	5.0	38	8.9	5.5	4.8
Time 5 (day 5, month 2)/3	34	12.5	2.9	2.4	38	9.0	5.5	3.5
Time 6 (day 6, month 3)/3	33	12.4	4.9	8.1	38	8.9	6.5	3.7
Average	34	12.3	4.3	4.6	38	8.8	5.0	3.1
Coef. of variation V of average [%]	1.4	1.9			1.5	1.5		

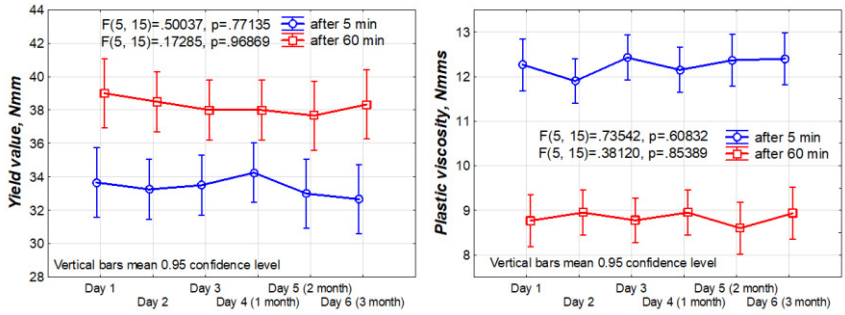

Figure 1: ANOVA of the influence of time (day) on rheological parameters of mortars.

3.3. Influence of operator

As Tab. 2 indicates, the coefficient of variation V of average rheological parameters measured by individual operators does not exceed 2.1%. It means the lack of influence of the operator on the measurements of rheological parameters. This is confirmed by the ANOVA (Fig. 2), which shows that influence of operator is statistically insignificant.

Table 2: Average yield stress g [Nmm], plastic viscosity h [Nmms], coefficients of variation V_g and V_h [%] of mortars measured by different operators

Operator /number of repetitions	after 10 min				after 60 min			
	g	h	Vg	Vh	g	h	Vg	Vh
Operator 1/5	24.3	12.6	5.5	3.7	41.3	9.5	4.4	4.8
Operator 2/5	25.0	12.4	3.4	4.3	42.1	9.8	3.6	2.0
Operator 3/5	24.8	12.1	4.5	6.1	41.9	10.0	5.2	7.2
Operator 4/6	24.8	12.4	4.7	3.4	41.6	9.6	6.5	4.4
Average	24.7	12.4	4.5	4.4	41.7	9.7	4.9	4.6
Coef. of variation V of average [%]	1.2	1.6			0.8	2.1		

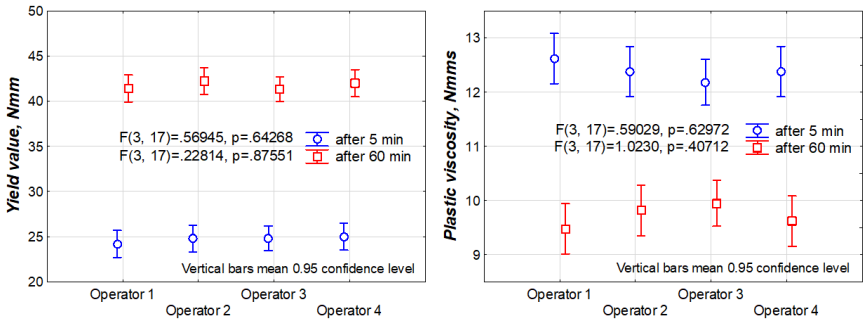

Figure 2: ANOVA of the influence of operator on rheological parameters of mortars.

3.4. The influence of variations in mortar constituents

3.4.1. Influence of cement and SP batch. As Fig. 3 - 4 and Tab. 3 indicate, that the change of cement or SP batch may significantly influence the rheological properties of mortars. It is worth to notice that tested mortars with different CEM I batches differ from each other in particular by the effect of the workability loss (Fig. 3) and effect of SP batch is the greater the higher the amount of C_3A in the cement.

Table 3. Average yield stress g [Nmm], plastic viscosity h [Nmms], coefficients of variation V_g and V_h [%] of mortars made of cement CEM I from different batches

Batch/number of repetitions	after 10 min				after 60 min			
	g	Vg	h	Vh	g	Vg	h	Vh
Batch 1/3	24	4.0	10.3	4.2	53	4.4	7.5	6.7
Batch 2/3	28	4.1	8.5	4.3	42	4.7	6.7	6.1
Batch 3/3	25	4.2	8.9	3.3	35	4.6	6.5	6.1
Batch 4/3	25	3.9	11.5	3.7	37	4.3	8.4	6.1
Batch 5/3	23	4.5	9.6	1.1	41	5.5	7.6	3.0
Batch 6/3	22	3.5	12.4	2.3	37	4.2	9.8	4.0
Batch 7/3	25	4.2	12.6	4.5	46	3.5	9.6	1.5
Average	24	4.0	10.5	3.3	42	4.4	8.0	4.8
Coef. of variation V of average [%]	7.7		15.7		15.1			16.3

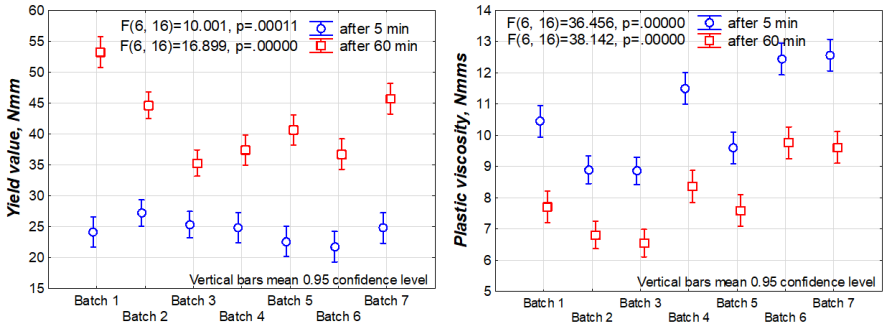

Figure 3: ANOVA of the influence of a CEM I batch on rheological parameters of mortars.

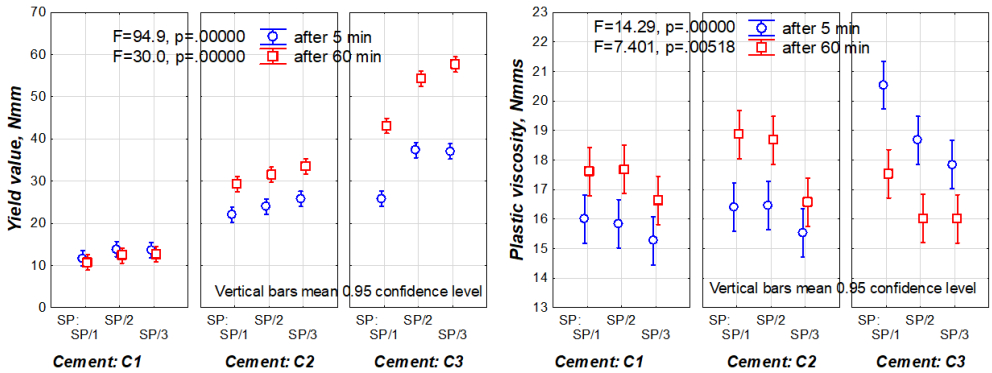

Figure 4: ANOVA of the influence of a SP batch on rheological parameters of mortars.

Table 4: Average yield stress g [Nmm], plastic viscosity h [Nmms], coefficients of variation V_g and V_h [%] of mortars made of different sand and in a different way prepared

Sand type/ number of repetitions	after 10 min				after 60 min			
	g	Vg	h	Vh	g	Vg	h	Vh
Standard sand/10	24	4.2	11.5	3.3	38	4.3	11.2	4.3
Ordinary sand quartered/10	26	6.8	17.0	5.5	25	6.2	16.0	5.8
Ordinary sand non quartered/10	26	10.6	16.9	6.8	26	11.3	15.8	8.1

3.4.2. The influence of the type and method of sand sample preparation. As Tab. 4 indicates, coefficients of variability of measurements of rheological parameters of standard sand mortar do not differ from the coefficients obtained in other stages of research. The coefficients of variation of rheological parameters for mortars with ordinary sand are much higher than in the case of mortars with standard sand. A particularly large coefficient of variations was obtained for mortar with non-quartered ordinary sand, in case of the yield value g they are over 10%. Quartering of the ordinary sand reduces the dispersion of results, however, it is still higher than in the case of mortars with standard sand. It is also worth to note, that in the case of mortars with ordinary sand prepared by quartering or without quartering the same mean rheological parameters were obtained. This means that applying quartering improves precision without affecting accuracy of rheological measurements.

4. Conclusions

The Bingham model describes well the rheological properties of the tested mortars. The coefficients of variation for all individual series of rheological measurements performed under the same conditions were always clearly smaller than 10%. It allows to assess the repeatability of performed rheometer measurements as good. Taking the number of measurements as significant and assuming the repeatability r as 2.8 V, it can be calculated that the limits of repeatability for rheometer measurement performed using Visomat NT under conditions presented in p. 2 are for the yield value is r_g = 13% g, and similarly for plastic viscosity r_h = 13% h.

Under given conditions, the results of the measurement of the rheological parameters and their variability coefficient are not affected by the long intervals in mortar testing time (up to 3 months) and the operator. This indicates good reproducibility of measurements performed on different dates and by different operators.

In general, lack of control of the batch of cement or superplasticizer may significantly affects the repeatability and reproducibility of the test results. It is recommended to plan the research in order to perform it with the same batch of materials. The sand type and the method of its preparation significantly affect the repeatability and reproducibility of test results for mortars. It is beneficial to use standard sand, because its grading is strictly defined and controlled during production.

References

[1] Tattarsall, G H, Banfill, P F G., The Rheology of Fresh Concrete, Pitman Books Limited, Boston, USA, (1983)
[2] N. Roussel, Understanding the Rheology of Concrete, Woodhead Publishing Ltd, (2012)
[3] http://www.schleibinger.com/cmsimple/en/?Rheometers:Viskomat_NT_Rheometer_f._Mortar_and_Paste, 30.06.2018
[4] PN EN 196-1: Methods of testing cement - Part 1: Determination of strength (2006)

SynerCrete'18 International Conference on Interdisciplinary Approaches
for Cement-based Materials and Structural Concrete
24-26 October 2018, Funchal, Madeira Island, Portugal

INFLUENCE OF THE MIXTURE COMPOSITION OF CEMENTITIOUS PASTES WITH OPTIMIZED PACKING DENSITY ON SETTING AND HARDENING STUDIED BY ULTRASOUND INVESTIGATION

Markus Krüger [(1)], Rok Bregar [(1)], Gheorghe Alexandru David [(1)], Joachim Juhart [(1)]

(1) Graz University of Technology, Graz, Austria

Abstract
Ultrasonic methods have been developed in the past to study properties of cement based materials in the fresh and hardening period. Especially by combined shear and compressional wave measurements, several possibilities exist for better describing the changing properties of cementitious materials at very early age. Within the paper test results (Vicat and Ultrasound) from different cementitious pastes with optimized packing density (use of inert micro and eco fillers as replacement of Portland cement clinker) are presented and discussed. Dynamic elastic properties at early age like the dynamic shear modulus and the dynamic elastic modulus are calculated from the ultrasound investigations and correlated with standard test methods. Based on the experimental investigations it is discussed that the setting and hardening of cementitious mixes can by strongly influenced by just optimizing packing density. The concept of optimizing packing density results in a decreased water demand and thus reduced water film thickness between the particles that can be calculated analytically. It is shown that the calculated water film thickness is a good indicator not only for initial and final setting, but also for workability and strength development.

1. Introduction

The properties of cement based materials in the fresh and hardening period are currently measured with rather conventional methods. Ultrasonic methods have been developed in the past using through-transmission techniques and analysing the whole waveform. Today ultrasound is accepted as a very useful tool to continuously investigate the setting and hardening process of cementitious materials [1-4]. Although many different concepts for the mix design of concrete with optimized performance are developed already, design still

strongly relies on trial mixing and testing. The reason for this is the complexity of the hydration of cementitious materials and the evolvement of the microstructure.
With respect to new concrete mixture concepts that especially focus on the optimization of the binder composition by using a well-defined amount of supplementary cementitious materials, many traditional concrete mix design methods to predict workability, setting and hardening as well as strength development fail. This is especially true for mixes, at which clinker is partly substituted by a filler [5]. In the current study, properly selected limestone powders of different size are selected as fillers in order to reduce the water demand while keeping the workability constant. However, it is also the setting and hardening behaviour as well as the strength development, which is strongly influenced.

2. Materials and Mix Design

Powder materials referred to in this study are classified into a group of micro-filler (MF) and eco-filler (EF) according to their mean particle diameter d_{50}.
The used micro-filler has a $d_{50} < 3$ µm that is significantly smaller than that of OPC. The eco-filler shows slightly smaller mean particle size but similar Blaine value like the cement. Details on the particle size distribution of the materials and the corresponding mixes determined by laser diffraction (HELOS) are presented in [5].

Table 1: Characteristic properties of the used materials.

Type	**ρ** (g/cm³)	**d_{50}** (µm)	**Blaine** (cm²/g)	**$V_{w,s}/V_p$** (-)	**ϕ_{exp}** (-)	**$V_{w,170}/V_p$** (-)
CEM I 52.5 N SR3	3.17	10.5	3744	0.75	0.57	1.13
EF (limestone)	2.70	6.9	4032	0.68	0.60	0.68
MF (limestone)	2.73	2.2	9314	0.61	0.62	0.65

Table 2: Composition and selected properties of the investigated mixtures.

		REF A1	**ECO B1**	**ECO C1**	**REF A2**	**ECO B2**	**ECO C2**	**REF A3**	**ECO B3**	**ECO C3**
flowability		standard consistency EN 196-3			ø = 190 mm			ø = 275 mm		
Cem I 52,5 N		100	40	50	100	40	50	100	40	50
$LIME_{ECO}$ (EF)	[V.-%]	0	60	25	0	60	25	0	60	25
$LIME_{MICRO}$ (MF)		0	0	25	0	0	25	0	0	25
w/c		0.28	0.59	0.38	0.40	0.85	0.42	0.48	1.03	0.43
V_w/V_p	[-]	0.90	0.74	0.61	1.27	1.09	0.66	1.53	1.31	0.68
V_w/V_c		0.90	1.86	1.21	1.27	2.72	1.32	1.53	3.27	1.35
$V_{w,s}/V_{p\ (MEM-ST)}$		0.72	0.69	0.61	0.72	0.69	0.61	0.72	0.72	0.61
$f_{cm,1d}$		47.9	19.5	42.8	30	7.7	42.7	19.7	4	37.1
$f_{cm,7d}$	[N/mm²]	91.3	46.1	80.5	57.3	21.9	74.6	37.5	12.7	73.8
$f_{cm,28d}$		107	58.1	100.1	82.9	29.1	84.8	53.2	19.7	82.3
density	[kg/m³]	2114	2023	2111	1949	1916	2136	1860	1841	2110

As the amount of water to achieve a certain workability of a water/powder-mix plays a major role, Table 1 show also the values for water demand $V_{w,s}/V_p$, which is the volume of water at saturation point and $V_{w,fi}/V_p$, which is the volume of water for a certain flowability (spread flow fi=170 mm) and V_p which is the volume of powder in the mix. These values were determined by a method (MEM-ST) presented by Juhart et al. [5].

3. Experimental setup and laboratory tests

For the ultrasound measurements the FreshCon-system was used. The test setup of the FresCo-system is similar to that proposed by a RILEM recommendation worked out by RILEM TC 218-SFC [3]. However, besides the usage of a container equipped with p-wave transducers with a center frequency of 500 kHz an additional container with two broadband s-wave transducers with a center frequency of 250 kHz are used. To study the setting and hardening time at very early age in the following a test time of 24 hours was considered with a test interval of 5 minutes. In a post processing procedure the measurements were analysed and dynamic elastic parameters were calculated according to Krueger et al. [4]. Additionally Vicat needle test was conducted to determine initial setting time and final setting time of each given mixture.

4. Test results and evaluation of the mixes

Figure 1 shows the evolution of the dynamic shear modulus calculated from the ultrasound measurements for the first 24 h of hydration of the reference mix *REF A* and the packing density optimized mix *ECO C* for different workability resp. water content.

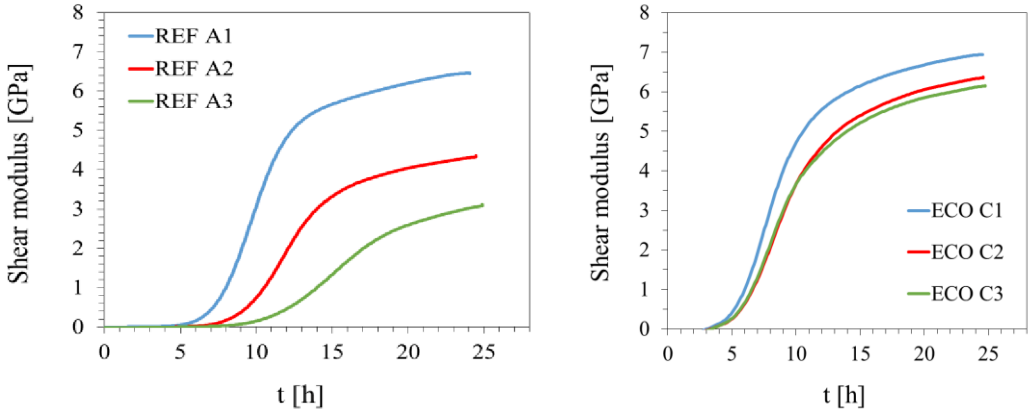

Figure 1: Evolution of dynamic shear modulus calculated from US testing.

Table 3 lists the results from the Vicat tests and also a certain time for which a specific dyn. elastic modulus (@ 0.1 GPa) resp. a specific shear modulus (@ 0.1 GPa and 0.2 GPa) was determined by the ultrasound testing. In addition to that, a water film thickness (WFT) was calculated. For the calculation one can use, among others, a relatively simple model like that of Krell, which is a mass-related method [6]. For the following calculation a modified equation (1), which is based on volumetric data as presented by Teichmann, is used [7]. With this model, an average water film thickness (WFT) can be calculated around each particle.

Here it is assumed that in the cementitious paste each particle is surrounded by a water film of the same thickness and where all cavities are filled with water and all particles are dispersed in the system. The water film thickness is determined as a function of the experimental packing density ϕ_{exp}, the powder content V_P, the water demand or the pore volume at saturation point $V_{w,s}$, the resulting specific surface area s_{vf} (Blaine value of the total mix, neglecting uncertainty for Blaine > 5000 cm²/g) and the total water content $V_{w,fi}$. Although the WFT is obviously directly related to the V_w/V_p ratio, the influence of the specific surface is dominating factor.

$$\mathrm{WFT} = \frac{V_{w,fi} - V_{w,s} \cdot \dfrac{1-\phi_{exp}}{\phi_{exp}}}{s_{vf} \cdot V_P} \tag{1}$$

Table 3: Water film thickness and dynamic elastic properties of the investigated mixtures.

		REF A1	ECO B1	ECO C1	REF A2	ECO B2	ECO C2	REF A3	ECO B3	ECO C3
flowability		standard consistency acc. EN 196-3			ø = 190 mm			ø = 275 mm		
Water film thickness (WFT)	(µm)	0.15	0.04	0.00	0.47	0.35	0.03	0.69	0.54	0.05
t (E_{dyn}= 0,1 GPa)	[h]	5.00	3.92	3.50	6.78	5.50	4.00	8.28	5.83	3.90
t (G_{dyn}= 0,1 GPa)	[h]	5.90	4.66	4.22	7.78	6.93	4.58	9.60	7.75	4.50
G_{dyn} (initial Vicat)	[GPa]	0.05	0.02	0.01	0.13	0.07	0.016	0.16	0.2	0.03
Vicat initial set	[h]	5.35	3.68	3.05	7.97	6.43	3.47	10.25	9.32	3.90
Vicat final set	[h]	6.87	4.50	4.22	8.97	8.06	4.42	10.92	10.28	5.53

5. Discussion

From Tab. 3 and Fig. 1 one can see that the initial setting determined by the Vicat test strongly correlates with the increase of G_{dyn} calculated from the ultrasound testing. If the Vicat initial setting time is compared to G_{dyn} at the time of initial setting according to Vicat (see Fig. 2, left), G_{dyn} is higher for mixes that show later setting time. Taking into account that the Vicat needle test is a kind of a shear test one may postulate that values for Vicat initial setting should be obtained at a constant G_{dyn}. As this is not the case for the tested mixtures and if we neglect the influence of different air content, the main reason for that can be found in the WFT. From Fig. 2 (right) it can be seen that the WFT is the governing factor influencing the initial setting of the mixtures and not the composition of the cementitious matrix or the w/c ratio. However, the dominant role of the WFT at the very early stage decrease with increasing hydration time, although a general trend to higher strength at lower WFT can be observed.

Similar results have already been published by Berodier and Scrivener [8]. It was shown that independent from the nature of the particles the WFT resp. a smaller particle distance lead to an accelerated hydration rate. Several interpretations of the relation of WFT and early age hydration have been proposed by different researchers, among which are chemical effects, mechanical effects (esp. increased shearing during mixing [8, 9]) or just the geometrical effects, i.e. smaller particle distance allows the hydration products to earlier bridge the opposite particles. However, these effects do not explain why the replacement of cement

clinker with an inert material like limestone power accelerates the hydration rate, if the calculated particle distance is considered as constant. One reason can be found in the fact that nucleation of the C-S-H is increased by increased particle surface. But it was also shown that nucleation of C-S-H preferably can be – if compared with other supplementary materials like quartz powder etc. – observed on limestone surface [8, 9]. Thus, surface area and type of surface resp. material are important factors driving the early age hydration.

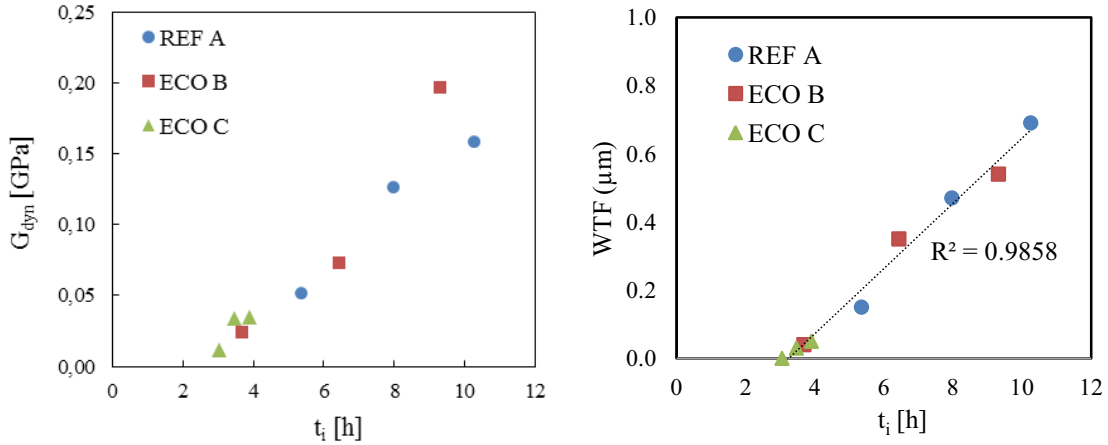

Figure 2: Dyn. shear modulus (left) and water film thickness (right) versus setting time according to Vicat needle test.

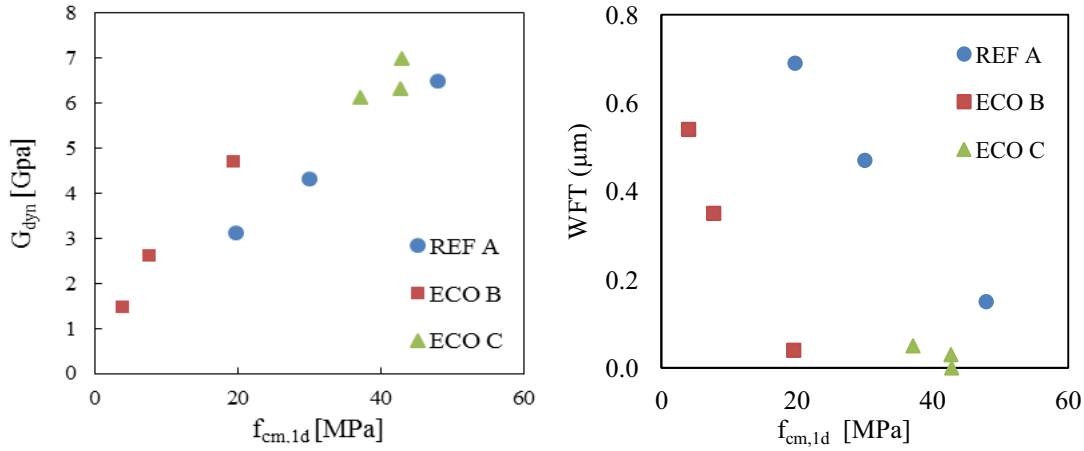

Figure 3: Dyn. shear modulus (left) and water film thickness (right) versus one day strength.

From the tests on workability it can also be confirmed that the particle interaction (esp. electrical double layer) is not negligible, either with respect to the workability but also to early age hydration and strength development [10, 11]. In this context it has to be noted that also the assumption that each particle is surrounded by a water film of the same thickness will not correspond with the reality.

Figure 3 shows the early age strength at one day vs. dyn. shear modulus after 24 h and vs. WFT. As expected dyn. shear modulus (and also dyn. elastic modulus, which is not shown here) correlates quite well with the strength for all the mixes. However, if WFT is plotted versus one day compressive strength a mix independent correlation between these two values

cannot be found. Although a clear trend of increasing strength with decreasing WFT is visible, the different mixture proportions and here the packing density and the W/C ratio have a strong influence on the early age strength, as it is known from traditional mix design experience.

6. Conclusions

From the test series and the results presented in this paper some conclusions can be drawn:

- The dynamic elastic properties derived from the US testing show good correlation with the strength development independently from the mixture composition.
- The initial setting time of a cementitious material can be estimated from WFT as well as from dyn. shear modulus calculated from ultrasound testing; If initial setting should be determined by an absolute value of dyn. shear modulus, the aspect of WFT has to be considered, i.e. lower WFT results in lower dyn. shear modulus at initial setting.
- From the conducted experiments it can be postulated that there is a linear relationship between WFT and initial setting, which is independent from the matrix composition. Thus, initial setting can be adjusted by the WFT quite easily. However, this aspect has to be further investigated if it holds true for different mixtures.

References

[1] Robeyst, N. et al, Monitoring the setting of concrete containing blast-furnace slag by measuring the ultrasonic p-wave velocity. Cem. Concr. Res. 38(10) (2008), 1169-1176
[2] Carette, J., Staquet, S., Monitoring the setting process of eco-binders by ultrasonic P-wave and S-wave transmission velocity measurement: Mortar vs. concrete, Constr. Build. Mater. 110 (2016), 32-41
[3] Reinhardt, H.-W. et al, Recommendation of RILEM TC 218-SFC: Sonic methods for quality control of fresh cementitious materials. Testing of fresh concrete by ultrasound transmission. RILEM TC 218-SFC, Materials and Structures 44 (2011), 1047-1062
[4] Krüger, M. et al, Non-destructive evaluation of eco-friendly cementitious materials by ultrasound. International RILEM Conference on Materials, Systems and Structures in Civil Engineering, Denmark (2016), Vol. 2 503-512
[5] Juhart, J. et al, A new combined filler concept for eco-concrete, Proc. of 14th International Congress on the Chemistry of Cement (ICCC 2015), Beijing (2015)
[6] Krell, J., Die Konsistenz von Zementleim, Mörtel und Beton und ihre zeitliche Veränderung (in German), PhD thesis, RWTH Aachen (1985)
[7] Teichmann, T., Einfluss der Granulometrie und des Wassergehaltes auf die Festigkeit und Gefügedichtigkeit von Zementstein (in German), PhD thesis, University of Kassel (2007)
[8] Berodier, E., Scrivener, K., Understanding the filler effect on the nucleation and growth of C–S–H. J Am Ceram Soc 97(12) (2014), 3764-3773
[9] Berodier, E., Impact of the supplementary cementitious materials on the kinetics and microstructural development of cement hydration, PhD thesis, Switzerland (2015)
[10] Kwan, A.K.H., Li, L.G., Combined effects of water film thickness and paste film thickness on rheology of mortar, Mater Struct 45(9) (2012), 1359-1374
[11] Kwan, A.K.H., Wong, H.H.C., Effects of packing density, excess water and solid surface area on flowability of cement paste, Advances in Cement research, 20(1) (2008), 1-11

SynerCrete'18 International Conference on Interdisciplinary Approaches
for Cement-based Materials and Structural Concrete
24-26 October 2018, Funchal, Madeira Island, Portugal

INFLUENCE OF UGANDAN VOLCANIC SCORIA AS AGGREGATES IN CONCRETE

Stephen O. Ekolu [(1)], Kgashane T. Moila [(1)], Mikaash Bhagwager [(1)], Harry Quainoo [(1)]

(1) Department of Civil Engineering Science, University of Johannesburg, South Africa

Abstract
This paper presents an investigation conducted on potential use of volcanic scoria as fine and coarse aggregates in concrete. In some developing countries, volcanic scoria is a widely available natural pozzolan which is presently not fully exploited for construction applications. In the present study, mortar mixtures of 3.0 aggregate/cement ratio and 0.5 water/cement ratio (w/c) or concretes of 0.6 w/c were used. Mortar samples of 50 mm cubes and 25 x 25 x 285 mm prisms containing 100% volcanic scoria aggregate (VAG) were prepared then used to determine compressive strength and drying shrinkage. In addition, concretes of 0.6 w/c containing 0, 50 or 100% VAG were used to prepare 70 dia x 140 mm height cylinders for measurement of elastic modulus. It was found that VAG mixtures gave slightly higher drying shrinkage than the control, while compressive strength and elastic modulus decreased significantly as the proportion of VAG aggregate content increased.

1. Introduction

Both scoria and pumice are vesicular igneous rocks typically emanating from volcanic eruptions, but their characteristics are quite different. Pumice is generally white or grey in colour, highly vesicular and exhibits a froth-like appearance. It forms from pyroclastic flow of hot gases and lava that was generally fluid during the process of effusion. Scoria, however, forms from iron-rich hot lava. It is typically darker and more dense than pumice [1]. A study was conducted by [2] in which the normal weight coarse aggregates in concrete were replaced with pumice aggregates in different proportions ranging from 0 to 100% pumice. Mixtures of 1:2:3 and 1:2:4 cement to fine aggregate to coarse aggregate were used to prepare samples at a water/cement (w/c) ratio of 0.45. The pumice aggregates had an oven-dry density of 763 kg/m^3 and a high water absorption of 37%, which were quite different compared to 2470 kg/m^3 and 2.86% for normal aggregate, respectively. It was reported that the 28-day

compressive strength, tensile strength, and Young's modulus, all decreased whereas the drying shrinkage and water absorption significantly increased, owing to the use of pumice in concrete. The 100% pumice aggregate mixture gave a 28-day tensile and compressive strength of 2.6 MPa and 22 MPa respectively, relative to 3.7 MPa and 35 MPa of the control. The oven-dry density for 100% pumice mixture was 1852 kg/m^3 compared to 2415 kg/m^3 for the control mix. Investigation by [3] found that water absorption was as high as 32.1% for pumice concrete compared to 1.6% for normal aggregate concrete. This result was attributed to the characteristically high porosity of pumice. They reported up to 50% increase in drying shrinkage for the pumice concretes. Saturating the pumice aggregate before batching was suggested to be capable of minimizing the effects of high water absorption by pumice.
In an earlier investigation by [4], Ugandan volcanic scoria was studied for potential use as a pozzolanic material and found to be of Class N pozzolan. The present study focussed on potential use of the scoria as aggregates in concrete. The mixtures with or without scoria aggregates were tested for compressive strength, drying shrinkage and modulus of elasticity.

2. Experimental work

2.1 Volcanic scoria aggregate

The volcanic scoria used in this investigation was obtained from the Rwenzori mountain range at the Western branch of the East African rift valley located at the border between Uganda and the Democratic Republic of Congo. Volcanic scoria is abundantly found in the region and could provide a cost-effective source as a cementitious material [4,5] which could be employed for low cost housing, among other uses. The scoria is a characteristically dark vesicular rock, easily broken into large chunks. Figure 1 shows samples of the crushed coarse and fine volcanic scoria aggregates (VAG). Samples of the scoria were finely ground into a powder finer than 45 μm size, and used for chemical analysis which was conducted using X-ray fluorescence (XRF). Table 1 gives the chemical compositions of scoria and of CEM 52.5 N cement used in this study. Microanalysis using X-ray diffraction (XRD) was also done to determine the mineralogical composition of scoria.

Table 1: Chemical compositions of cement and volcanic scoria ash.

Sample	SiO_2	Al_2O_3	Fe_2O_3	CaO	MgO	SO_3	K_2O	Na_2O
CEM1 52.5N (%)	17.8	3.45	3.86	68.5	1.37	3.41	0.27	0.24
Scoria (%)	42.8	14.6	13.5	10.4	6.95	0.22	3.21	3.3

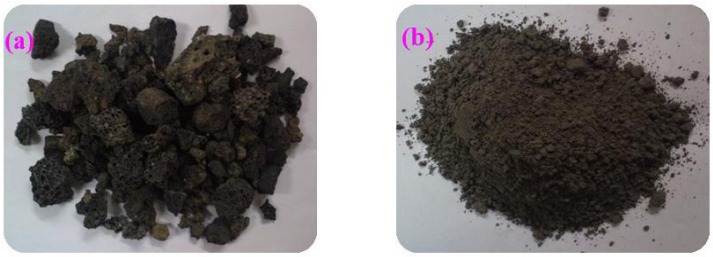

Figure 1: Volcanic scoria aggregate (a) 19 mm coarse aggregate, (b) fine aggregate.

2.2 Mixtures

Portland cement CEM I 52.5 N supplied by Pretoria Portland Cement (pty) Ltd was used to prepare mortar and concrete mixtures, shown in Table 2. Crushed granite (fine and coarse) aggregates were used as control. Mortars of 3.0 aggregate/cement ratio and 0.55 or 0.60 water/cement (w/c) were prepared, in which standard silica sand was replaced by 100% volcanic scoria as fine aggregate. Mortar cubes of size 50 mm were prepared for compressive strength testing. Also, mortar prisms of size 25 x 25 x 285 mm were made for drying shrinkage measurement. Mortar compressive strengths were tested at 3, 7, 14, 28 days while drying shrinkage was monitored under a laboratory environment of 23^{o}C and 40 to 55%RH. Concrete mixtures of 0.60 w/c were prepared incorporating 0, 50, 100% coarse VAG and used to cast cylindrical samples of size 70 dia x 140 mm height. Electrical strain gauges were attached at curved sides of the cylinders and used to monitor changes in strain during monotonic loading. These results were used to determine the modulus of elasticity and compressive strength of the VAG concretes.

Table 2: Mortar and concrete mixtures used in the experiments.

Ingredients	**Mortar**				**Concrete**		
Samples	**50 mm cubes**		**25 x 25 x 285 mm prisms**		**70 dia x 140 mm cylinders**		
VAG*(%)	**0**	**100**	**0**	**100**	**0**	**50**	**100**
CEM I 52.5N (g)	1172	1172	586	586	1800	1500	1500
Granite sand (g)	3316		1320		4400	1800	
Granite stone (g)					4400	1800	
Scoria sand (g)		3316		1320		1800	3600
Scoria stone (g)						1800	3600
Water (g)	646	636	360	360	1100	900	900

*VAG – volcanic scoria aggregates

3. Results and discussion

3.1 Fineness, density, and the pozzolan classification

Scoria was ground to a fine powder of Blaine fineness 372.8 m^2/kg which was at a similar level as that of CEM 52.5 N whose fineness was 378 m^2/kg. The scoria powder had a density of 2930 kg/m^3 which is lower than 3150 kg/m^3 of CEM I 52.5 N. From the chemical composition given in Table 1, the natural pozzolan had a low CaO but rich in SiO_2 as expected. Its combined SiO_2+Al_2O_3+Fe_2O_3 is 70.9%, which meets the minimum requirement of 70% stipulated in ASTM C 618-03 [5]. The SO_3 content and moisture content were determined to be 0.22% and 1.0%, which are also lower than the maximum requirements of 4.0% and 3.0%, respectively. These results affirm the findings of an earlier study [3] in which a full range of the classification parameters for the natural pozzolan were determined in accordance with ASTM C 618-03 [5]. Recent researches indicate that the volcanic scoria pozzolans may also be suitable for producing geopolymer cementitious systems [7,8].

3.2 Water absorption and drying shrinkage

The water absorption of VAG aggregates was determined to be 13.9% and 19.2% for coarse and fine aggregates, which are much higher than the corresponding 1.66% and 4.3% for the control (granite) aggregates. Figure 2 gives results of mortar shrinkage containing 100% VAG fine aggregate. The VAG mortars show higher drying shrinkage over the control, which is consistent with reports in the literature [2,9]. It can be seen that use of the VAG led to an increase of up to 6% in drying shrinkage. This increase in drying shrinkage may be partly attributed to the higher water absorption and vesicular structure of scoria, whose mixtures tend to exhibit a more porous matrix that allows greater loss of water during evaporation. In addition, the relatively lower elastic modulus of VAG (Section 3.3), provides less restraint on the movement of paste due to shrinkage, in turn giving higher shrinkage behaviour for VAG relative to control.

3.3 Compressive strength and modulus of elasticity

The strength effect of using VAG was investigated using both mortars and concrete mixtures. Mortars were prepared using 100% VAG fine aggregate as replacement for the control. Figure 3(a) shows the change in compressive strength results for ages of up to 28 days. It can be seen that use of 100% VAG sand led to a reduction in compressive strength at all the ages. At later ages, however, there was progressive gain in strength of VAG mortars over the strength of control. At ages of 3 to 7 days, the strength of VAG mortars was 30 to 40% lower than that of control. At later ages of 14 to 28 days, the strength loss had decreased to about 21%, as seen in Figure 3(b). The higher strength gain at later ages is indicative of the pozzolanic reaction of VAG that must have occurred. In a pozzolanic reaction, the $Ca(OH)_2$ produced from hydraulic reaction of Portland cement with water, reacts with the amorphous silica of the pozzolan, leading to secondary formation of calcium silicate hydrate (CSH) product which is responsible for strength gain. Accordingly, the effects of a pozzolanic reaction in cementitious systems occur at later ages. It is interesting that pozzolanic behaviour occurs even in VAG aggregates that are much coarser than the fine powder which typically gives more pronounced pozzolanic effects [4]. The density of VAG mortar was 2211 to 2216 kg/m^3, which is 5 to 8% lower than 2339 to 2395 kg/m^3 for control.

The effects of scoria on compressive strength and elastic modulus were also determined using concrete mixtures of 0.6 w/c containing 0, 50, 100% VAG coarse aggregates. Figure 4 gives the stress-strain behaviour of VAG concrete obtained using 70 dia x 140 mm cylinders. It is clear in Figure 4(a) that there was a significant decrease in stress resistance as the proportion of VAG in the mixture increased. The strength (in MPa) and elastic modulus (in GPa) of control granite concrete were of similar levels. However, VAG concrete showed a distinct difference between the two properties, with its elastic modulus being always significantly lower than the corresponding strength, as seen in Figure 4(b). Indeed, the elastic modulus of VAG concrete in GPa was 55 to 65% of concrete strength in MPa. A replacement of 50% coarse granite aggregates using VAG gave a 27.5% and 55.5% decrease in strength and elastic modulus, relative to control. The 100% VAG concrete showed over 70 to 80% decrease in strength or elastic modulus.

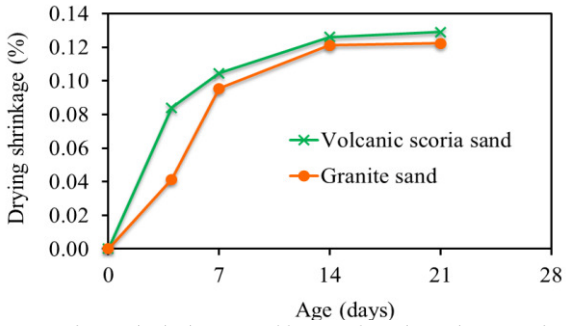

Figure 2: Drying shrinkage effect of volcanic scoria mortar.

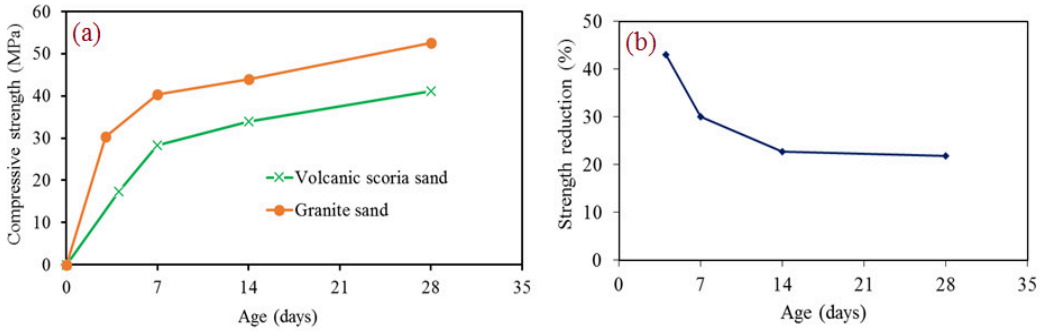

Figure 3: Effect of scoria aggregates on compressive strength of mortars (a) strength development, (b) strength gain at later ages due to pozzolanic reaction.

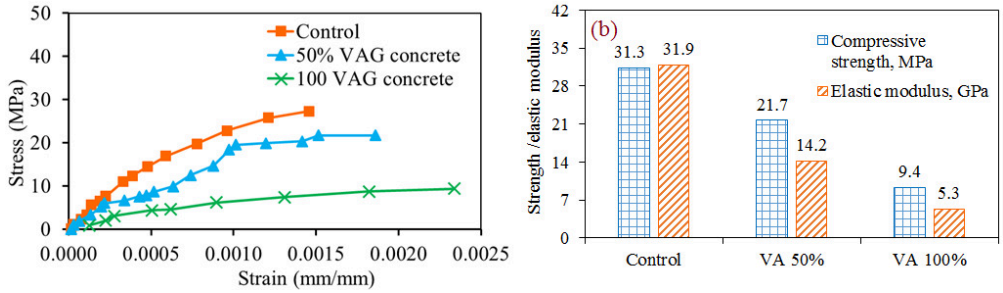

Figure 4: Volcanic scoria concrete (a) stress-strain behaviour, (b) strength and elastic modulus.

3.4 Mineralogy

Figure 5 gives XRD results showing the mineralogical composition of volcanic scoria ash passing 45 µm. It can be seen that the main minerals of the scoria comprised mullite (aluminosilicate), quartz (SiO_2) and haematite (Fe_2O_3). These observations are consistent with the XRF results (Table 1) which show these oxides to be the main constituents of the volcanic scoria. It should, however, be noted that while XRF gives the total amount of constituents that are both amorphous and crystalline, XRD only detects the crystalline minerals present. Pozzolanic behaviour depends on amorphous silica which is usually not detectable by XRD.

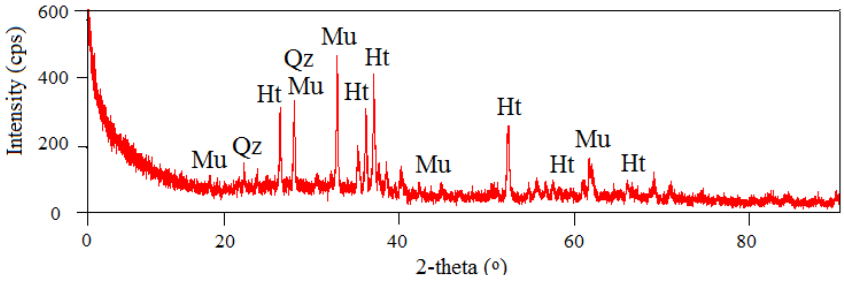

Figure 5: X-ray diffraction pattern of volcanic scoria, Mu – mullite, Ht – haematite, Qz – quartz.

4. Conclusions

Upon evaluation of the volcanic scoria for potential use as aggregate in concrete, it was found that the scoria fine aggregate exhibits a pozzolanic reaction leading to increase in late strength development relative to that of control. The scoria consisted mainly of mullite, and phases of haematite and quartz. When used as aggregate, the volcanic scoria aggregate gave higher water absorption and higher shrinkage than the normal crushed aggregates. There is a decrease in compressive strength and elastic modulus in proportion with the amount of scoria aggregate incorporated into concrete.

Acknowledgements

This research was financially supported by the National Research Foundation (NRF) of South Africa, IPRR Grant No. 96800. The authors are grateful for the support given by NRF.

References

[1] Evans, E.J, Inglethorpe, S.J.D, and Wetton, P.D, Evaluation of pumice and scoria samples from East Africa as lightweight aggregates, Mineralogy and Petrology, Technical Report, WG/99/15, NERC (1999), British Geological Survey, Keyworth, Nottingham, UK
[2] Hossain, K.M.A., Properties of volcanic pumice based cement and lightweight concrete, Cem Concr Res 34 (2004), 283–291
[3] Hossain, K.M.A., and Lachemi M., Mixture design, strength, durability, and fire resistance of lightweight pumice concrete, ACI Mater J, 104(5), 2007, 449-457
[4] Ekolu, S.O., Thomas, M.D.A., and Hooton, R.D., Studies on Ugandan volcanic ash and tuff, Proc. 1st Intl. Conf. on Adv. in Eng. and Tech., Entebbe, Uganda, July 2006, 75-83
[5] Day, R.L., Pozzolans for use in low-cost housing, A state-of-the-art report, International Development Research Centre, Ottawa, Canada, September 1990
[6] ASTM C 618-03, Standard specification for coal fly ash and raw or calcined natural pozzolan for use in concrete, ASTM Intl, West Conshohocken, PA, 2003, www.astm.org
[7] Naghizadeh, A., and Ekolu, S.O., Pozzolanic materials and waste products for formulation of geopolymer cements in developing countries: a Review, Concrete Beton, Jour Concr Soc S Africa, 151 (2017), 22-31
[8] Tchadjie, L.N., and Ekolu, S.O., Enhancing the reactivity of aluminosilicate materials toward geopolymer synthesis, Jour Mat Sci 53 (2018), 4709–4733
[9] Neville, A.M., Properties of concrete, 4th Edition, 1996, New York, John Wiley and Sons Inc

SynerCrete'18 International Conference on Interdisciplinary Approaches
for Cement-based Materials and Structural Concrete
24-26 October 2018, Funchal, Madeira Island, Portugal

INVESTIGATION, ASSESSMENT AND REALTIME READJUSTMENT OF THE RHEOLOGICAL PROPERTIES OF SELF COMPACTING CONCRETE

Ivan Parić [(1)], Wolfgang Kusterle [(1)]

OTH Regensburg, Regensburg, Germany

Abstract

This paper discusses a new fresh concrete control system with the following structure: a rheometer measures the fresh concrete directly after the mixing process, during a short break. The viscosity and the dynamic yield point are determined by a ball rheometer. The rheological parameters viscosity and dynamic yield point describe the consistency and thus the pouring ability and consequently the quality of Self Compacting Concrete (SCC). Data collected from the measurement are the basis for an expert system which will help to readjust mixes with deviating rheology.

Firstly, investigations were carried out during the development of different SCC mixtures in the COST TU 1404 Action. Secondly, investigations were done in two precast plants. A ball rheometer was installed in the respective mixers. The SCC for premium precast products was tested then during ongoing production. In addition, several test series were carried out in the laboratory of the OTH with the respective constitutive materials.

During the test series, the mix designs of the well working SCC's were modified by using a deviating water content. Subsequently, using the rheological data, water, superplasticizer or stabilizing agents were added to the mix, trying to reach proper workability again. The graphs for the changing rheological properties as a function of the respective amount of start water content and additional water dosage or admixture dosage were generated and analyzed for the mixes of the two precast plants. With this information and experience, an expert system for the mix readjustment is currently under development.

1. Introduction

Fresh concrete testing, including workability testing, is one of the important quality tests for concrete structures. Maintaining the workability within given numbers for a defined time is essential for a fast and effective casting process.
Concrete workability is a complex phenomenon, which is difficult to define with a few parameters or by a single testing procedure [1]. Rheological tests of SCC may be performed using one-point tests, as given in EN 12350-9, which will not give exact rheological numbers, or by using costly stationary concrete rheometers.
Rheological measurements will give more reliable data regarding workability than one-point tests [1]. The following figure 1 shows a way, how the physically data from rheological measurements can be used to reach an ongoing proper workability of SCC.

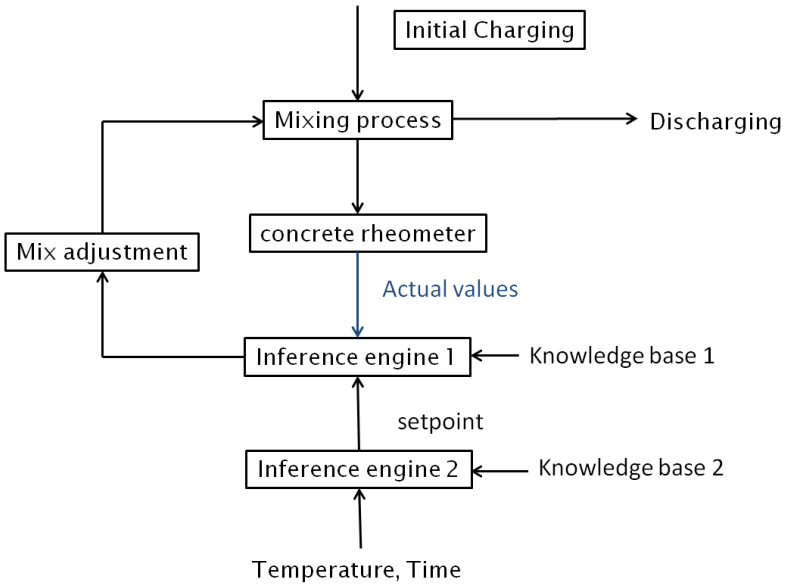

Figure 1: Principle of an expert system for SCC production [2].

2. COST TU 1404 Development procedure of some SCC recipes [3]

2.1 Tests

Based on the reference concrete mix of the initial experimental phase given by COST TU 1404, the development of Self Compacting Concrete (SCC) mix-design was realized with both of the cements available in the TU 1404.
Tested cements which are produced by Ciments Calcia in Gaurain-Ramecroix, Belgium:

- CEM I 52.5 N CP 2
- CEM I 52.5 N – SR 3 PM-CP2

Hard coal pulverised fly ash (PFA) according to EN 450 used:

- Rofament from Rohrdorfer Zement, Germany

The aim was a robust SCC mix-design. The development, according to the approach of Okamura, was divided into investigations on cement paste, mortar and in a final step the testing of the concrete with a ball rheometer.
For demonstrating the robustness of the developed SCC with a cement-fly ash-ratio of 65/35 the water content was raised stepwise by 7.82 l/m³. This equals a stepwise water/cement ratio increase of 0.02.

Table 1: Concrete mix-design for both cements

	Gravel 4/11	Gravel8/16	Sand 0/4	CEM	PFA	Water	SP	Unit
Initial weight 1 m³	357	436	794	392	156	144	7.825	kg

Rheological measurements were performed using a Ball rheometer and profiles described in [4]. The rising water amount in the mixture changes the rheological properties as shown in table 2, figures 2 and 3. The Dynamic yield stress, Bingham yield stress, viscosity and V-funnel time are decreasing while the slump flow is increasing.

Table 2: Rheological properties versus increasing water amount.

Water [l/m³]	Dynamic yield stress g_D [N mm]	Bingham yield stress g_B [N mm]	Slump flow[mm]	V-funnel time [s]	Viscosity [-]
183	212.17	88.58	597.5	16.6	85.78
192	134.72	49.35	675.0	9.13	52.53
200	66.71	19.68	762.5	7.46	36.31
207	51.24	12.72	-	3.43	25.91

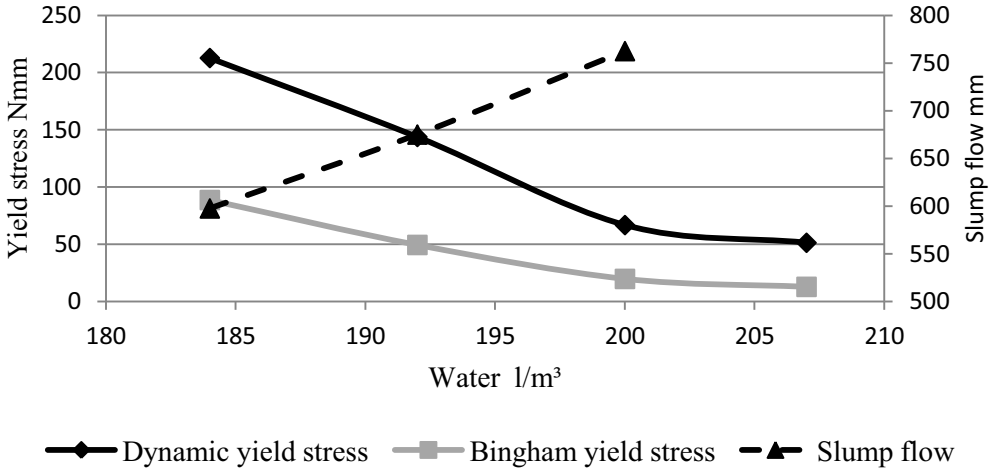

Figure 2: Yield stress and slump flow versus water content.

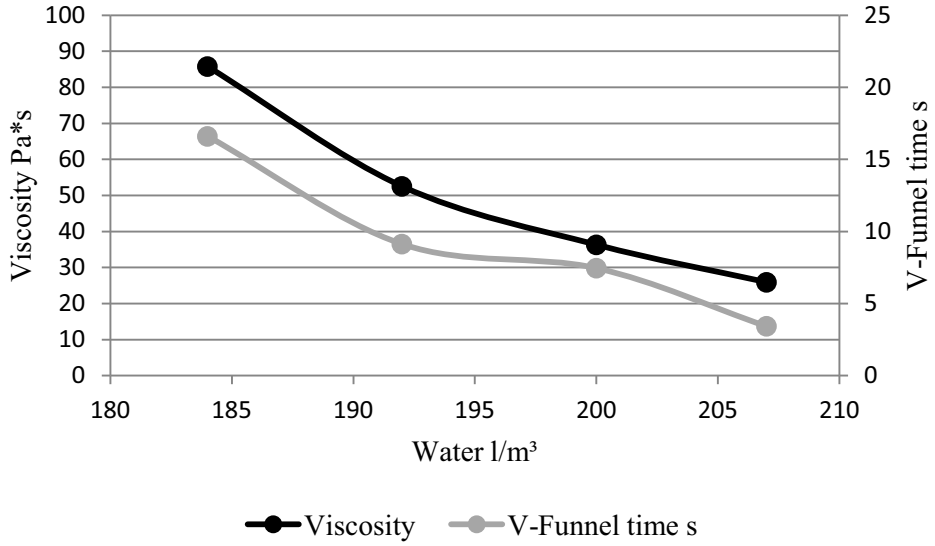

Figure 3: Viscosity and V-funnel time versus water content.

The tested mix designs showed both a well-fitting slump flow and V-funnel time over a range of mixing water, which indicates that these mixtures form a solid basis for a robust SCC mix-design. Furthermore the rheological results are in line with results from classic one point tests. The experience gained during the investigations in the COST Action TU 1404 were an important fundament for further developments regarding an expert system.

3. Self-compacting concrete with real-time readjustment of the mix-design in the concrete mixer

The results presented in this section were investigated during a Bavarian research project. The aim of the presented investigations was to predict which quantity of water should be added to obtain a correct rheology. Investigations were done in two precast plants and in parallel with the two different SCC mixes in the laboratory of the OTH Regensburg. This was the way to build up the knowledge base 1 (shown in figure 1) for both mixes. Thereby it was possible to define different areas of workability. The knowledge base was tested in some manual readjustment tests. An example for the data obtained for the knowledge base 1, is given for one specific mix in figure 4. It demonstrates the changes in consistency with a rising water amount in one single test. Other investigations were done with superplasticizer and different stabilizer. These values are also part of the data for the knowledge base 1. The configuration of the measuring system is different to the tests in the COST action. The speed of rotation is chosen lower, the ball is smaller. This leads to lower absolute values in the respective results. An optimum of workability for the here presented mix and test set-up is given by the value 20 for the dynamic yield stress and the viscosity.
In this test the water content was raised stepwise by 5.2 l/m^3. This equals a w/c ratio of 0.01 [5].

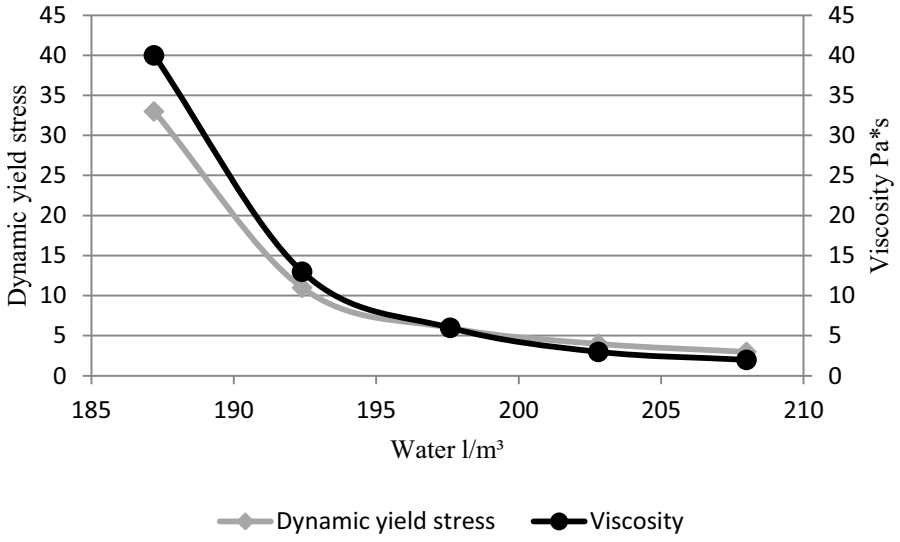

Figure 4: Viscosity and dynamic yield stress versus rising amount of water.

3.1 Tests for readjustments

The test results in figure 5 show the manual use of the knowledgebase 1 for this blend. This mixture was produced too stiff, with a lack of water. In this case 182 l/m³ of water (equivalent to a w/c of 0.35) was the starting point. With the information from the expert system a readjustment with a defined amount of water in one step and within short time was possible [4]. The data of the knowledge base was still used without Inference engine. The amount of water was calculated manually.

Similar readjustments have been done with superplasticizer and stabilizer. In the last test series, a new programmed Inference (app) engine was tested. First automated readjustments using an app show promising results.

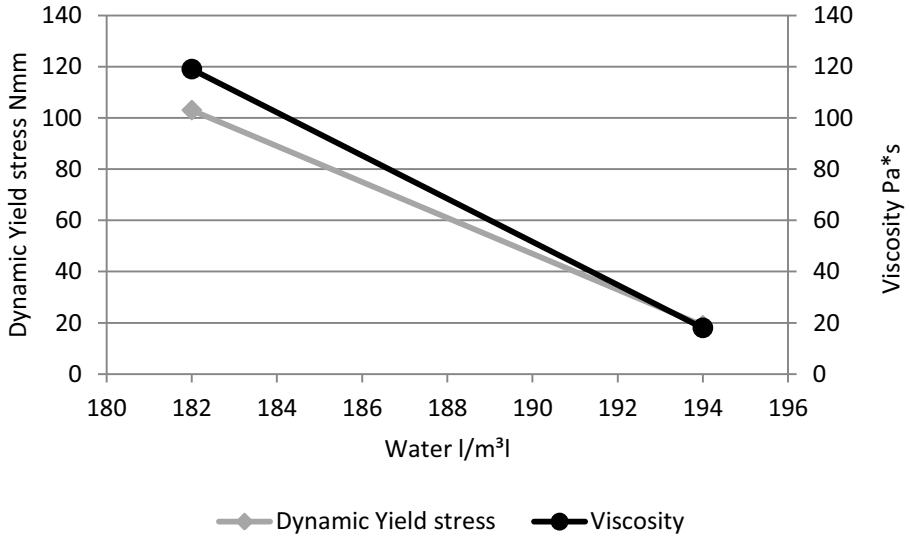

Figure 5:Readjustment with water in one step.

4. Conclusions and outlook

During tests with varying water content, it was clearly demonstrated that results of the one-point tests coincided with rheology. When the slump flow increased, the V-funnel time and the yield stress decreased. This is an important finding for the future, because time-consuming one-point tests, such as slump flow and V-funnel time, can be replaced by inserting a rheometer into the concrete mixer for a fast test. In our tests, a ball rheometer delivered accurate and comparable data within a short time.

Ball rheometers with low shear rate are very effective in assessing rheological properties of SCC. The necessary short testing time allows the measurement as a final part of the mixing process.

Tests with different mixtures, distinguished only in small quantities of water content, show accurate and reliable results. With the help of stabilizers, it is possible to readjust a mix which is too soft and tends to segregation. With superplasticizer or, if possible with small amount of water, too stiff mixes may be adjusted. The development of an automated process using the detected data for a mix adaption is the topic of an ongoing research program.

Acknowledgement

We want to thank the Bavarian Research Foundation for funding these investigations.

References

[1] Khrapko, M., Aufrechterhaltung der erforderlichen Verarbeitbarkeit von SVB, (Maintaining the required workability of SCC) BetonWerk international, Vol. 2, Nr. 2/2012 (2012).

[2] Paric, I. and Kusterle, W., Selbstverdichtender Beton mit zeitnaher Aussteuerung der Mischungszusammensetzung im Betonmischer. (Self-compacting concrete with real-time control of the mix composition in a concrete mixer), research proposal, OTH Regensburg, Regensburg (2015).

[3] Glashauser, J. and Feuerer, F., Entwicklung einer robusten SVB-Rezeptur nach Okamura fuer den Ringversuch "COST TU 1404 Action" und rheologischer Untersuchungen, (Development of a robust SCC-mix design according to Okamura for the Round Robin test "COST TU 1404 Action" and additional rheological tests), Bachelor thesis: OTH Regensburg (2016).

[4] Paric, I. and Kusterle, W., The realtime assessment of the rheological parameters of SCC. In: Thrane, L.N., Proc. Of the international RILEM conference Materials, Systems and Structures in Civil Engineering 2016, Segment on Fresh Concrete. Proceedings PRO 115, ISBN 978-2-35158-184-1 Paris (2016).

[5] Reuter, C., Stepper, H., Zeitnahe Aussteuerung der rheologischen Frischbeton-eigenschaften von selbstverdichtendem Beton durch Betonzusatzmittel und Wasser, (Realtime modulation of the rheological fresh concrete properties of self-compacting concrete by concrete admixtures and water) Bachelor thesis: OTH Regensburg (2017).

SynerCrete'18 International Conference on Interdisciplinary Approaches
for Cement-based Materials and Structural Concrete
24-26 October 2018, Funchal, Madeira Island, Portugal

MACRO- AND MICRO-STRUCTURE EVALUATIONS OF RECYCLED POST-CONSUMER GLASS CEMENTITIOUS MATERIAL FOR CONCRETE

Marija Krstic [(1)], Julio F. Davalos [(1)]

(1) Department of Civil Engineering, The City College of New York, New York, USA

Abstract
Concrete is the most used material in the world, second only to water. The production of cement is energy intensive and has raised significant environmental concerns since one ton of cement produces an equal ton of CO_2. In the USA, about 90 million tons of cement are used annually, with three million tons used in New York. The concrete industry is facing critical challenges with availability of essential Supplementary Cementitious Materials (SCMs), which are commonly used to partially replace cement for the production of concrete mixes. Recently and particularly in the Northeastern USA, there is a scarcity of fly-ash —as most widely used SCM in concrete . Recycled mixed-color post-consumer glass has a good potential to become one of the leading SCMs for concrete. With the goal of contributing to the implementation of sustainable concrete, this paper focuses on the development and characterization of mix designs with different percentages of cement replacement by a new SCM from recycled post-consumer glass, known commercially as Pozzotive. Concrete formulations with Pozzotive were evaluated at macro- and micro-level, showcasing significant strength and durability performances. This research has been successfully applied in field projects for sidewalk and high-rise building constructions and is contributing to the development of ASTM standard specifications for Glass-SCM.

1. Introduction

The recycling operations of glass are problematic, costly, and often subsidized due to lack of profitable value-added product markets, particularly for color glass. At the same time, the concrete industry is facing a critical scarcity of essential cementitious materials which are commonly used to partially replace cement for the production of concrete mixes in construction. SCMs are fine powders of micro particles that when combined with cement produce high-performance concrete mixes with enhanced strength and durability properties.

Due to these benefits, SCMs, or pozzolans, are used in nearly all concrete mix designs for major buildings, sidewalks, roadways, bridges, and other infrastructure applications. In particular, fly-ash is the most widely used SCM produced as a byproduct from the residue of coal-burning plants [1]. But due to environmental concerns and costs a significant percentage of coal power plants is shutting down or converting to cheaper natural gas, resulting in shortage and price increase of fly-ash particularly in the North Eastern region of the USA. These two challenges, the lack of a major market for recycled glass and dwindling supply of fly-ash, present a unique and transformative opportunity for benefiting both the glass recycling industry and concrete production industry, through the development and implementation of glass SCM for concrete.

Challenges for Glass Recycling: In the USA, about 12.5 million tons of post-consumer glass (or 80 lbs per person) is generated annually, with only about 23% being recycled. In NY City, 140,000 tons are generated and about 50% is recycled. Worldwide, glass represents 6% of about 2 billion tons per year of solid waste. The recycling of glass in the USA has increased more than 4 times in the last 20 years. But most recyclers faced significant challenges and economic hardships processing glass, particularly color glass which has no real market and is generally used as low-cost granulated filler material. Glass is heavy (about 20% of total solid-waste weight), harsh on processing equipment, and costly to recycle. The research described in this paper offers the potential for post-consumer recycled glass to become a highly sought after material for producing cementitious pozzolan for concrete.

Challenges for the Concrete Industry with Decreased Availability of SCMs: The production of **c**ement is energy intensive (~ 5% of total global energy) and results in one ton of CO_2 per one ton of cement [2]**.** In the USA about 90 million tons of cement are used annually (CO_2 emissions equivalent to 300 million cars) [2]. To produce *green* high-performance concretes, SCMs such as fly-ash and slag are used to partially replace cement content [3]**.** Fly-ash has been the most popular pozzolan, but recently its availability has decreased due to 25% of coal-fired power plants shutting down or converting to cleaner natural gas [4]**,** [5]**.** Compounding this problem, granulated blast-furnace slag, is produced mainly outside the USA (Canada 35%, Japan 32%, Spain 12%, Italy, Brazil and others [6]). Thus, there is a pressing need for an alternate SCM to fly-ash, and post-consumer glass can be effectively and economically transformed into value-added pozzolanic material for concrete [7], [8], [9].

In 2013, a research was performed to study the effect waste glass powder in concrete. The workability, compressive strength, and density of concrete with used waste glass powder were evaluated in the lab. They concluded that using waste glass powder increased the workability and compressive strength of concrete, while reducing the density in comparison to standard mixture of concrete [8]. Another study in 2017 proposed the use of high volume glass powder as cement replacement in concrete. The microstructures, mechanical and durability properties of such concretes in the long term were investigated. Their results showed better mechanical behaviors, and higher durability performance [10].

2. Research Significance and Contributions

With the goal of contributing significantly to the implementation of sustainable High Performance Concrete, this study focuses on the development, evaluations, and field

implementations of mix designs with different percentages of cement replacement by a new SCM from recycled post-consumer glass, known commercially as Pozzotive. In addition to conventional macroscale tests, micro-level experiments were performed in the laboratory to study the microstructural interactions. This research also included full-scale field applications for sidewalks and high-rise building in New York City. This is the first large scale high-rise building application of Glass-SCM in the USA. The results of this study are being used on collaborative efforts to develop ASTM specifications for post-consumer Glass-SCM, which can benefit both the concrete and the solid waste management industries worldwide.

2.1 Macro-Scale Evaluations

Materials: The cementitious materials used for this study included Portland cement type I; post-consumer Glass-SCM Pozzotive, with an average particle size of 13 μm; Class F fly ash, and slag. The aggregates conformed to standard specification ASTM C33. The coarse aggregate was Nova Scotia crushed granite with a maximum nominal size of 3/4" (19 mm), specific gravity of 2.69, and absorption of 0.7. The fine aggregate was Roanoke sand with specific gravity of 2.63, and absorption of 0.4. The chemical admixtures as per ASTM C494 were surfactants for water reduction and air entraining. Six concrete mix designs were produced according to ASTM C192 and C511. For the six mix designs described next, the testing was performed for fresh and hardened concrete as per ASTM standard specifications. For compressive strength as per ASTM C39, the cylinders were tested at ages of 7, 28, 56 and 90 days. For flexural strength as per ASTM C78, the beams were tested at ages of 14, 28 and 56 days. For durability evaluations, rapid chloride permeability (RCP) test was performed on cylindrical disks as per ASTM C1202.

Mix Designs and Methods: The evaluations were based on ASTM standard specifications, and they were divided into two categories, strength/stiffness and durability. Only some of the most important evaluations are presented in this paper. The mix designs developed in the lab were based on specifications for sidewalk construction by the NY City Department of Design and Construction (NYC-DDT). Based on literature review and experience, six mix designs were selected: One with a 100% Portland cement as a control; three with percent replacements of cement by 20, 30 and 40% with glass SCM; and for correlation purposes with glass-SCM, one mix with 30% fly ash, and one with 40% slag. The last two mix designs were included because concrete mixes with fly ash and slag are the most commonly used; hence, concretes with Glass-SCM can be directly compared with them. The testing methods for strength/stiffness evaluations included compression, split tensile, flexure, static modulus, and dynamic modulus. In addition, free-shrinkage was also evaluated. The early compressive strength of concrete with slag is expected to be higher than with fly ash, because slag is a more cementitious material and hydration reactions occur early. Compressive strengths of concrete with Glass-SCM are expected to achieve or exceed the values obtained for the other mixes. In general, results for flexural strength are expected to be higher than for split tensile (both are indirect measures of tensile strength). As is generally the case, the dynamic modulus of elasticity is expected to be higher than the static modulus of elasticity. Concretes with SCMs are expected to have less shrinkage than straight cement concrete. The durability methods selected included RCP, and freeze-thaw cycling. For RCP results, the concretes with SCMs are expected to have lower permeability values than the mix with straight cement. This is primarily a diffusivity test used as an indirect method to evaluate the permeability of concrete when exposed to chloride ions from deicing salts during wintry

season or from exposure to ocean water. The freeze-thaw cycling test is design to simulate seasonal weather changes causing distress in concrete, for up to 400 accelerated cycles in a programmable environmental chamber. Once again, the mixes with SCM are typically known to outperform concretes with straight cement.

Compressive Strength: We evaluated compressive strength at different ages to monitor the strength development with time. The compressive strength test results for up to 90 days enabled to compare the relative strength developments of the six mix designs. It is generally accepted that the early high strength is due to the hydration reactions while the strength at later stages is driven by the pozzolanic reactions [11]. When using SCM materials in concrete the strength continues to increase in later ages because of pozzolanic activity [12], [13]. The compressive strength results are shown in Figure 1 for the six mix designs. At 7 days, the highest value was for the concrete with 100% cement (CM) and the lowest for 40% glass (G-40). This is due to the dominant cementitious hydraulic nature of cement. Consequently, the higher content of SCM for G-40 possibly slowed the early rate of hydration. At the age of 28 days, the concrete with 40% slag (S-40) showed the highest strength, because after cement, slag has the most cementitious content [14]. At 56 days, the tests for the mix designs with Glass-SCM showed significant increases in strength, with G-40 and S-40 at about the same level. At the age of 90 days, G-40 still showed increase in strength above the other mixes. Among all the mixes, G-40 had the overall highest strength gain of 105 % between 7 and 90 days.

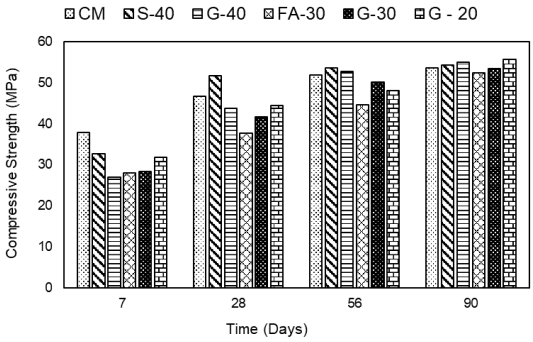

Figure 1: Comp. strength of 6 mix designs.

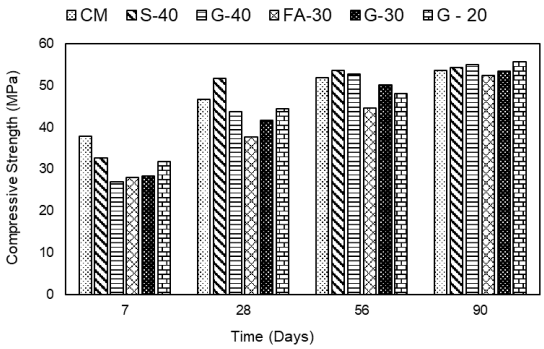

Figure 2: Flex. strength of 6 mix designs.

Flexural strength: This test induces primarily flexural stress, but can serve to evaluate tensile strength, since the test specimen is unreinforced and collapses due to critical tensile stresses at the bottom of the beam specimen. Most studies showed that flexural strength is higher (within ~10%) than the indirect Split-Tensile strength, due to differences in specimen geometry, loading, and state of internal stresses in the test samples. Three specimens per mix design were tested at 14, 28 and 56 days [15]. The results in Figure 2 show that all three Glass-SCM mixes outperformed the Slag and fly-ash counterparts.

Permeability: The resistance of concrete to chloride penetration is one of the most important concerns regarding the durability of concrete structures. The Rapid Chloride Permeability (RCP) test method consists of relating the electric charge through the specimen to the resistance to chloride ion penetration. In general, most concretes become progressively less permeable with time. In general, the addition of pozzolanic SCM materials improves the resistance to chloride penetration and reduces the chloride-induced corrosion initiation of steel reinforcement [16]. In Figure 3 the lowest permeability values were obtained for Glass-SCM

mixes. The notable improvement in resistance to chloride infiltration is the result of partial blocking of pores in hydrated cement paste with the products of pozzolanic reactions provided by Glass-SCM [17]. At 90 days, the slag samples tested at about 1100 Coulombs, which is considered low, while the G-40 specimens showed outstanding results with less than 300 Coulombs, which is an exceptional low value.

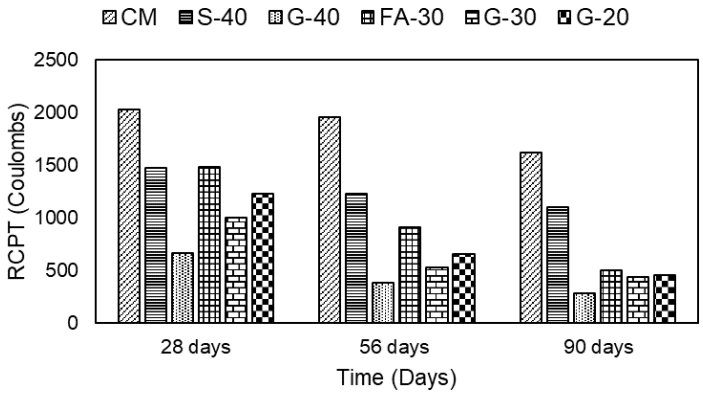

Figure 3: Rapid Chloride Permeability

2.2 Micro-scale Evaluations

Overview of research in progress: The research in progress includes microstructure evaluations of cement pastes focused on chemical and physical characterizations. Pastes will follow the same percentages of cement replacements as the six mix designs described above, to establish correlations between Micro- and Macro-levels. The results will be used to better understand and explain the macroscopic behavior of Glass-SCM concretes and recommend their effective implementations in practice. Methods have been selected to show how Glass-SCM influences the formation of binding compounds due to hydration reactions when water is added to the mix, such as Calcium-Silicate-Hydroxide (C-S-H gel), which for cement forms as 50-60% of total hydration products and beneficially influences the strength and durability characteristics. The glass pozzolan is very rich in silica dioxide SiO_2 (about 70%) and its addition as SCM to concrete generates secondary or pozzolanic reactions. These pozzolanic reactions are slower than hydraulic reactions; however, they contribute to additional formation of C-S-H gel that leads to higher strength and lower permeability. The particle size distribution will be determined by laser diffraction method. The scanning electron microscopy (SEM) with Energy Dispersive X-ray Spectroscopy (EDX) will be used to determine the morphology and chemical composition of the non-hydrated cementitious materials and hydrated pastes and their hydration products, either combined with the X-ray Diffraction method (XRD) or with gas adsorption method (BET) for identifying the specific surface area (SSA). These characterization methods will provide valuable insights into the chemical interactions of the SCMs, cement and the natural aggregates, to better explain macroscopic results.

2.3 Field Applications

This project has contributed to field application projects for sidewalks and high-rise building construction. The first sidewalk project was completed in South Jamaica, Queens, New York, in May 2016. Three different mix designs were used: 20% and 40 % Glass and a typical

sidewalk concrete with 30% fly ash Class F. The in-situ and lab test results for glass mixes showed close correlations, and the field performance of these concrete mixes had been evaluated for over a year under exposure to traffic and weather conditions, with no visible signs of distress. More recently (April, June, and September 2017), two higher strength mixes were implemented in components of a 23-story building in Hallets Point, Queens, NY. The mixes for this application were produced with 30% Glass as self-consolidating concretes. Two mix designs were used: One with 55 MPa (8,000 psi) for a slab and several columns on the 5th floor, and the other with 70 MPa (10,000 psi) for a parapet wall on the 8th floor and also for the bulkhead roof. The test results so far indicate that the target strengths and performances were successfully achieved and actually surpassed significantly. Glass-SCM has also been used on sidewalk projects elsewhere: (1) in Montreal, Canada as 10% replacement, and this province has made a commitment to use glass pozzolan in all future sidewalk construction [18]; (2) in Mountain View, California using a mix with 50% cement, 30% slag, and 20% Glass-SCM. Their mix design followed the guidelines and glass material described in this paper, and they obtained very good results.

References

[1] Wilson, M. L. and Kosmatka, S. H., Design and Control of Concrete Mixtures, 15th ed., Portland Cement Association (2014)
[2] "Concrete." http://minerals.usgs.gov/minerals/pubs/commodity/cement/
[3] Davalos, J. F. et al, Advanced materials program – High performance concrete mixes for cast-in-place bridge decks in West Virginia; WVDOT/DOH Res. Proj. No. T699-AMP-1.00 (2006)
[4] http://www.bloomberg.com/graphics/2015-coal-plants/
[5] http://www.eia.gov/todayinenergy/detail.cfm?id=21232
[6] http://atlas.media.mit.edu/en/visualize/tree_map/hs92/import/show/all/2618/2013/
[7] Kamali, M. and Ghahremaninezhad, A., Effect of glass powders on the mechanical and durability properties of cementitious materials, Constr Build Mater 98 (2015), 407-416
[8] Vasudevan, G. and Pillay, S.G.K., Performance of using waste glass powder in concrete as replacement of cement, Am J Eng Res 2(12) (2013) 157-181
[9] Shi, C. et al, Characteristics and pozzolanic reactivity of glass powders, Cem Concr Res 35(5) (2005), 987-993
[10] Du, H., and Tan, K.H., Properties of high volume glass powder concrete, Cement and Concrete Composites 75 (2017), 22-29
[11] Mehta, P. K. and Monteiro, P. J. M., Concrete, Microstructure, Properties, and Materials, 4th ed., Mc Graw Hill Education (2014)
[12] Omran, A. and Tagnit-hamou, A., Performance of glass-powder concrete in field applications, Constr Build Mater 109 (2016), 84-95
[13] Shao, Y. et al, Studies on concrete containing ground waste glass, Cem Concr Res 30(1) (2000), 91-100
[14] Khatib, J. M. and Hibbert, J. J., Selected engineering properties of concrete incorporating slag and metakaolin, Constr Build Mater 19 (2005), 460-472
[15] Siddique, R., Performance characteristics of high-volume class F fly ash concrete, Cem Concr Res 34 (2003), 487-493
[16] Chindaprasirt, P., Resistance to chloride penetration of blended Portland cement mortar containing palm oil fuel ash, rice husk ash and fly ash, Constr Build Mater 22 (2008), 932-938
[17] Nassar, R. and Soroushian, P., Field investigation of concrete incorporating milled waste glass, Journal of Solid Waste Technology and Management 37(4) (2011), 307-319
[18] https://healthymaterialslab.org/news/glass-in-concrete

SynerCrete'18 International Conference on Interdisciplinary Approaches
for Cement-based Materials and Structural Concrete
24-26 October 2018, Funchal, Madeira Island, Portugal

MONITORING FRESH CEMENTITIOUS MATERIAL BY DIGITAL IMAGE CORRELATION (DIC)

Evin Dildar Dzaye [(1), (2)], Geert De Schutter [(2)], Dimitrios Aggelis [(1)]

(1) Vrije Universiteit Brussel, Brussels, Belgium
(2) Ghent University, Magnel Laboratory for Concrete Research, Ghent, Belgium

Abstract
Concrete undergoes strong displacements due to different processes at very early state, like shrinkage. This early state of concrete affects the long-term concrete performance. The concrete deformation cannot be directly attributed to a single process, due to the complexity of different processes such as, evaporation, water migration, settlement, formation of hydrates, shrinkage, early age cracking. Monitoring concrete properties at a very fresh state is essential to understand the different ongoing processes. Digital image correlation (DIC) has proven very useful as an optical and contactless method for surface monitoring of several materials. In the present paper the displacement distribution of fresh cementitious material from plastic state up to hardened state is studied by means of DIC. Moreover, an innovative technique of speckle pattern creation is presented, since creation of a pattern on fresh (and hence viscous) cementitious materials is not straightforward. The specimen surface is covered with a speckle pattern that deforms together with the specimen. The principle of DIC realizes a 3D continuous monitoring by recording the images at different time steps and comparing it to the reference or undeformed image. The experimental results confirmed the effectiveness and correctness of the new technique giving a global overview much more representative than point measurements with traditional displacement meters.

1. Introduction

After casting, concrete stiffens with age that leads to concrete volume reduction (shrinkage). Properties of concrete are affected by its volume reduction caused by the loss of moisture due to evaporation process. Furthermore, there are several factors leading to concrete displacement such as the hydration reaction [1] between water and cement, drying process due to changes of pore water and thermal properties. The displacement of concrete has

detrimental effect on concrete quality. For this reason, it is essential to understand the evolution of concrete displacement. Recently several studies on concrete displacement are performed by means of DIC. The technique of DIC was very useful as an optical and contactless method for surface monitoring of several materials. Maurouc et al. [2] applied DIC to study cracking of coating mortar due to drying and DIC proved the ability to show the pattern and width of cracks. In another study, strain and crack distribution in concrete due to drying process was monitored by means of DIC [3]. Lagier et al. [4] evaluated cracking due to drying process by 2D-DIC. Yang et. al. [5] applied 3D-DIC to study the effect of aggregate size and volume on the drying process of concrete and mortar. The non-uniform strain distribution increased with increased drying time of concrete.
This study focuses on the vertical deformation (settlement) of fresh mortar in fresh stage (few minutes after casting) to understand concrete drying process. The experimental results will be compared to classical point measurement methods. DIC mapping can evaluate the settlement distribution on the surface that decrease the final material properties. Consequently, concrete drying process can be adjusted to reduce shrinkage formation, similar to the work of Slowik et al. [6].

2. Overview of DIC principle

Digital image correlation (DIC) is a non-contact optical- numerical technique that offers the possibility to measure complex displacement and deformation of different materials. This system consists of a pair of high resolution cameras that build a stereoscopic vision to measure the surface deformation. The cameras are synchronized to record simultaneously images of the sample at a constant time interval. The sample surface is covered with randomly distributed white and black speckles. DIC software identifies the white and black speckles then measures the grey intensity of local zones. Displacement in space translated to movement of the speckle pattern is perceived as change on the grey intensity level compared to a reference stage [7]. The correlation between a reference and a 'deformed' image is built on the degree of grey level similarity [8]. The accuracy of DIC measurement depends on the speckle pattern quality. There are several techniques to create black-white speckle patterns. Researchers performed different ways to create patterns, such as marked pen [8], spray paint and airbrush guns [9].The pattern should have clear contrast between black and white colour. Pixels are grouped and analysed in subset areas. Subset should be optimally chosen to keep measuring even in the case of great size movements. The creation of the speckles on fresh cementitious material is challengeable since speckles move or get absorbed on wet surface. In the present study, an innovative method of speckle pattern is analysed that allows understanding the drying process of fresh concrete. The specimen surface is covered by a powder speckle pattern (Aluminium oxide and carbon) immediately after casting the mortar into the mold.

3. Materials and experimental setup

3.1 Material

Cement mortar specimen were performed with ordinary portland cement (cement CEM I 52.5N and water). The mix design was prepared with 1 part of cement, 2 parts of sand, see

Tab. 1. The cement mortar was mixed in a laboratory concrete mixer for 3 min at low speed. Afterwards, the material was poured into metallic mold of size 150x150x150 mm (internal dimensions).

Table 1: Cement mortar mix design.

Cement [g]	Sand [g]	Water [g]	Water to binder ratio
2618.3	5236.6	1178.2	0.45

3.2 Experimental setup

Above the sample surface a pair of digital cameras (AVT Stingray) were installed, see Fig.1(a). The resolution of the cameras are 2504 by 2056 pixels. White light was installed above the sample surface to provide lighting to the monitoring area during the measurement. On the specimen surface white-black speckle pattern was created as shown in Fig.1(b). Firstly, a layer of white aluminium oxide powder covered the half sample surface. Later, well-distributed black dots of carbon powder are applied on the surface. Only the half of the sample surface is covered with speckle pattern since in the other half the vertical LVDT is placed. Consequently, DIC can visualize an area at which the left, right and bottom sides as shown in Fig.1(b) are attached to the metallic mold and the top side stands in the middle area of the sample. The boundary conditions are not identical for all four sides of the analysis area. The total area observed by DIC is equal to 135x63 mm^2. DIC analysis were performed with 61x61 subsets with a step size of 10 between subset centres.

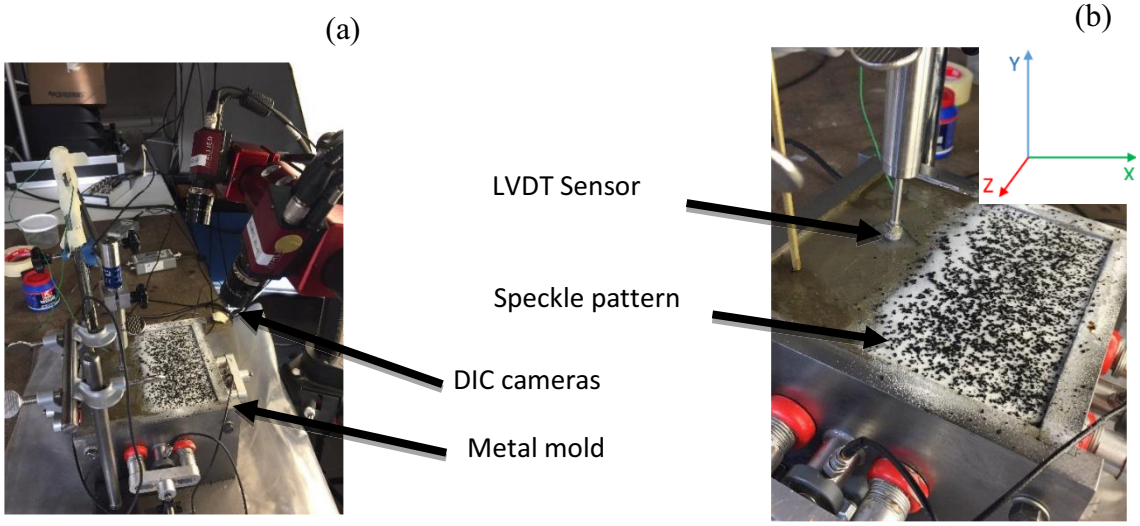

Figure 1: (a) overview of experimental setup including DIC; (b) sample surface covered with speckle pattern including LVDT sensor and DIC coordinate.

The measurement and the post-processing analysis was conducted using VIC-Snap and VIC-3D software respectively. The analysis is done considering an axis system shown in Fig.1(b). The displacement vectors U, V, W in mm are calculated at X, Y, Z directions respectively. DIC monitoring started up to 20 min after_casting. Reference starting point (Time 0) is considered the time of casting and the duration of the experiment was approximately 3 days. Furthermore, one Linear Variable Differential Transformer (LVDT) was installed vertically

on the sample surface to measure the settlement. The vertically arranged LVDT tip touched a 20×20 mm metallic wire lattice that was applied on the specimen top surface Fig. 1(b). Consequently, the sensor tip was prevented from penetration as well as floating on the surface.

4. Results and discussions

In the fresh state, water accumulate on mortar top surface (known as 'bleed water'). The accumulated water evaporates with time that causes mortar shrinkage in the early periods. This way, volume loss and displacement triggers plastic shrinkage.

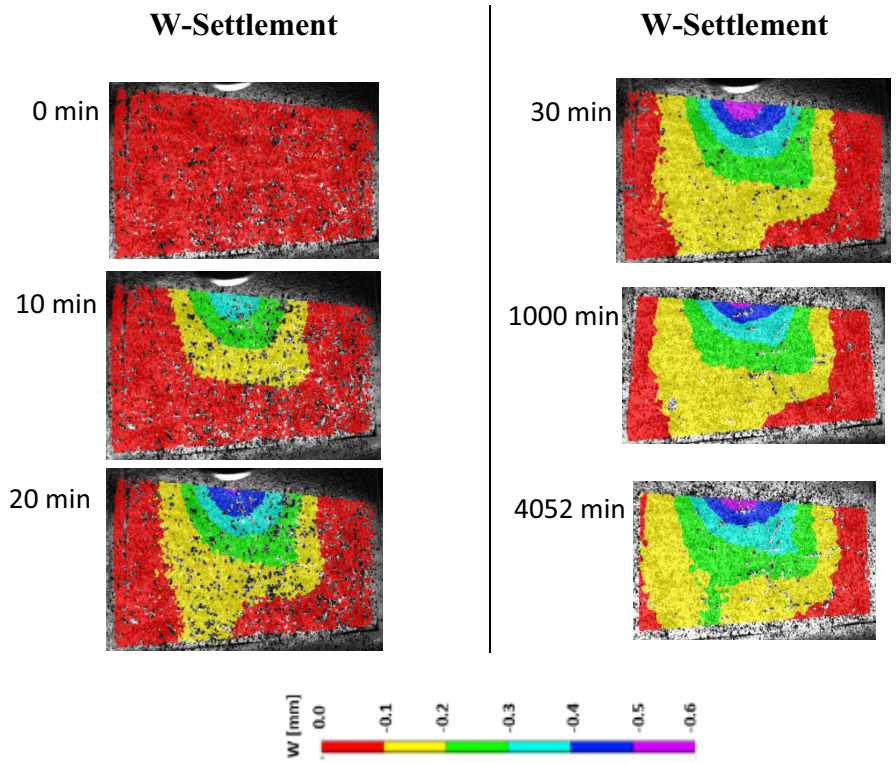

Figure 2: DIC surface settlement at discrete monitoring stages.

DIC allows monitoring settlement (vertical displacement) at different curing stages as shown in Fig. 2. The images visualize the evolution of settlement (W) at different monitoring stages. Time 0 stands for the start of monitoring and in this period mortar is in plastic state. The speckle pattern was fast applied after casting, therefore DIC monitoring starts as soon as 20 minutes after casting. An increased displacement in z direction at the surface takes place 10 minutes after monitoring. W displacement standing for surface settlement exhibits its highest value in the specimen top centre standing for specimen centre. At fresh state (representatively in 10, 20 and 30 minutes), settlement effect extends further. The pink regions exhibit the highest settlement evolution at the centre of the surface. It is visible that displacement is not uniformly distributed on the surface. The evolution of the settlement starts from the centre to the edges. It is possible that bleed water movement controls the settlement evolution. The

hardening process of the particle structure decreases the settlement rate at later stages. At hardening state (1000 and 4052 minutes) the evolution of the settlement rate decreases. DIC compared to traditional contact sensors, measures the settlement in contactless mode, therefore the sensor cannot affect the measurement process. Based on the observed DIC maps, it is evident that a point measurement of settlement is not sufficient to describe settlement. Settlement of a point at the surface is influenced by its elevation compared to the surrounding areas.

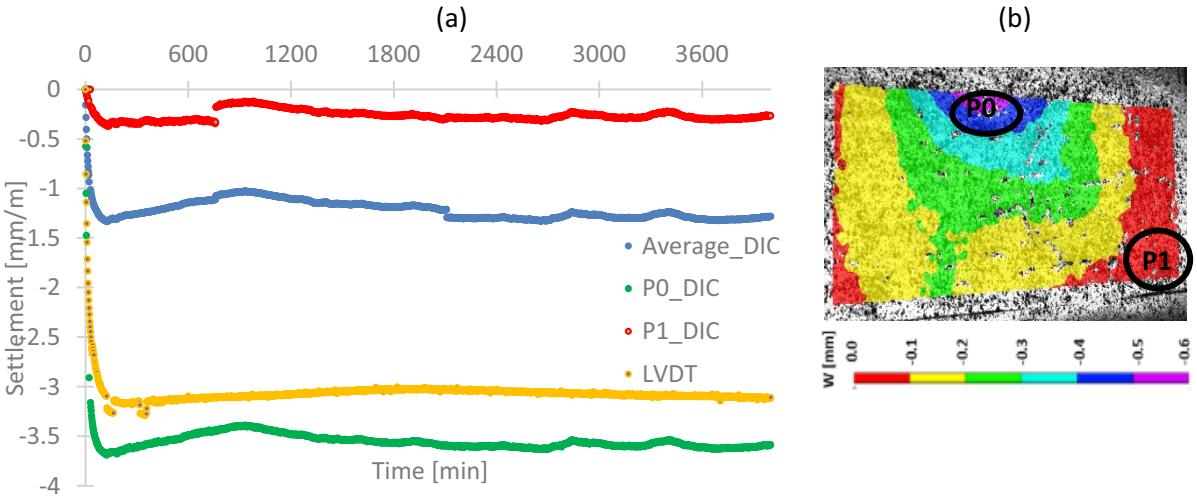

Figure 3: (a) DIC settlement and LVDT at different locations; (b) representative for the points (P0, P1 and total average area) of DIC measurement.

Settlement monitored by DIC the points with the highest settlement (P0), the lowest settlement (P1) and total average area are compared to classical LVDT point measurement as shown in Fig. 3(a). The locations of the points (P0, P1) and the total average area measured by DIC is presented in Fig. 3(b). The settlement reaches its maximum value 140 minutes after monitoring in all four curves. Beyond this time, the range is significantly wide between point P0 (-3.6 mm/m) and P1 (-0.3 mm/m). While the point measurement of LVDT presents a settlement of -3.1 mm/m and the average DIC measurement presents a settlement -1.3 mm/m after 140 min, see Fig. 3(a).

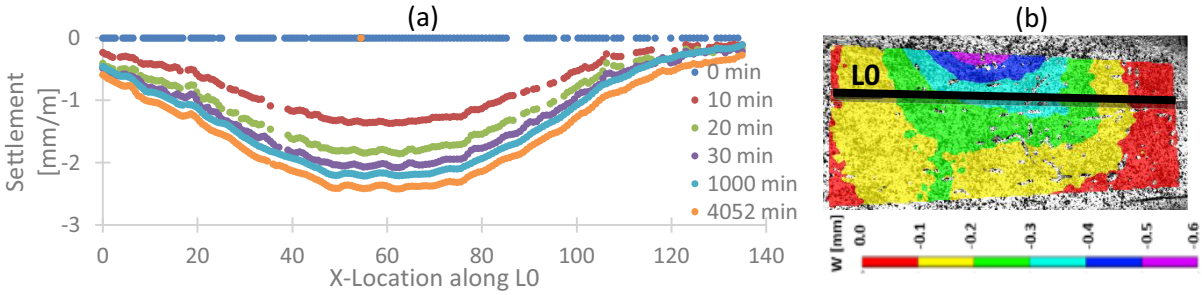

Figure 4: (a) Settlement distribution for mortar at discrete curing stages along Line L0; (b) the location of line L0 on the sample surface.

The difference in settlement between LVDT and DIC measurement in the absolute value is related to the circumstance that DIC considers the total surface area and LVDT monitors the

settlement at a point of the surface. It is clear that no robust conclusion can be attained when considering only point analysis. This is an evident for the significant drawback of the point analysis. In Fig. 4(a-b), the Settlement of points standing along line (L0) crossing the sample is presented at discrete stages of curing. It is revealed that as soon as 10 minutes after casting, the settlement progresses differently at different positions exhibiting the highest value of settlement close to the centre of the specimen and confirms the relatively "axisymmetric" profile.

5. Conclusions

This paper focuses on an effective technique of DIC to evaluate the displacement distribution of mortar in fresh state (few minutes after casting). DIC allows monitoring the non-uniform displacement distribution at different locations on sample surface. This approach realizes a deeper understanding of concrete hardening process and offering data for the whole surface that is not possible with the classical LVDT point measurement. Further study should be done regarding the accuracy of the speckle pattern that is affected by the bleed water in the first hours after casting.

References

[1] Wieslaw, K., Cement and Concrete Chemistry, Springer (2014)
[2] Mauroux, T. et al, Study of cracking due to drying in coating mortars by digital image correlation, Cement and Concrete Research 42(7) (2012), 1014-1023
[3] Maruyama, I. and Sasano, H., Strain and crack distribution in concrete during drying, Materials and Structures 47(3) (2014), 517-532
[4] Lagier, F. et al, Numerical strategies for prediction of drying cracks in heterogeneous materials: Comparison upon experimental results, Engineering Structures 33 (2011), 920-931
[5] Chen, Y. et al, Application of 3D-DIC to characterize the effect of aggregate size and volume on non-uniform shrinkage strain distribution in concrete, Cement and Concrete Composites 86 (2018), 178-189
[6] Slowik, V. et al, Capillary pressure in fresh cement-based materials and identification of the air entry value, Cement and Concrete Composites 30(7) (2008), 557-565
[7] Lecompte, D. et al, Quality assessment of speckle patterns for digital image correlation, Optics and Lasers in Engineering 44 (2006), 1132-1145
[8] Sutton, M.A. et al, Image Correlation for Shape, Motion and Deformation Measurements, Basic Concepts, Theory and Applications, Springer, New York, USA (2009)
[9] Barranger, Y. et al, Digital Image Correlation accuracy : influence of kind of speckle and recording setup, EPJ Web of Conferences 6, 31002 (2010)

SynerCrete'18 International Conference on Interdisciplinary Approaches
for Cement-based Materials and Structural Concrete
24-26 October 2018, Funchal, Madeira Island, Portugal

NEW INSIGHTS ON THE SEGREGATION DUE TO MANUFACTURE CONDITIONS OF LIGHTWEIGHT AGGREGATE CONCRETES

Afonso Miguel Solak [1,2], Antonio José Tenza-Abril [1], Francisco Baeza-Brotons [1], Victoria Eugenia García-Vera[3], Marcos Lanzón[3]

(1) Department of Civil Engineering, University of Alicante, Alicante, Spain
(2) CYPE Ingenieros S.A., Alicante, Spain
(3) Department of Architecture and Building Technology, Technical University of Cartagena, Cartagena, Spain

Abstract
Lightweight aggregate concrete (LWAC) is susceptible to segregation because of the differences between the densities of lightweight aggregates and mortar, influencing the strength and durability of concrete. Besides that, due to high workability and low viscosity, LWAC is susceptive to segregation during mixing process, transporting, placement and dormant period. In the present study, three variables related to the manufacturing process of LWAC samples were studied. Six different LWACs were manufactured considering different times of vibration, in one and two layers. To verify the influence of the initial hydration of Portland cement and consequently loss of workability in the segregation, the same LWACs were manufactured considering different times between mixing and molding. A statistical analysis was applied for establishing the structure of the variable dependence in segregated concretes. The results contribute to a better understanding of the segregation in lightweight concrete concluding that the vibration time per layer and the type of vibration of LWAC have a significant influence on the segregation of the samples.

1. Introduction

In recent years, more attention has been paid to the development of lightweight aggregate concrete (LWAC) [1]. LWAC substantially reduces building cost, eases construction, allows greater design flexibility and in some cases it may be considered a relatively 'green' building material, as the reduction in the concrete density results in superior thermal, acoustic and fire resistance and leads to a positive impact on the energy consumption of a building [1]. LWAC

compaction remains one of the major problems in fresh concrete because excess vibration time can easily produce the segregation phenomenon [2]. When lightweight aggregate (LWA) is used with a considerable lower density compared to that of the paste, an upward segregation of the coarse aggregate might be experienced [3]. The ability of fresh concrete to remain homogeneous during consolidation is a critical issue in the mixture design [2]. A homogeneous randomly-oriented-aggregate distribution improves the mechanical properties, durability, stability and impermeability of concrete [4]. In lightweight aggregate concrete, the constituent LWAs may have a lower strength and elastic modulus than the mortar matrix [1] and a region presenting high aggregates concentration may also lead to local concrete pathologies when a long time period is considered [5]. Besides that, due to high workability, commonly found in LWACs, this material is susceptive to segregation during mixing, transporting, placement and dormant periods. In the present study, three variables related to the manufacturing conditions of LWACs samples were analyzed focusing on their influence on the segregation phenomenon. Therefore, several authors have proposed different methodologies to quantify the phenomenon of segregation proposing segregation indexes involving the volumetric fraction of aggregates at different heights of a concrete specimen [2]; image-processing-based techniques [6] and the densities of different sections of a concrete specimen [7]. The last one, selected for the present work and proposed by Ke [7], estimate a segregation index (SI_{Ke}) dividing the specimens into four equal sections and using the densities obtained from the upper (ρ_{top}) and lower (ρ_{botton}) slices of a cylinder. A possible segregation tends to reduce the density in the upper section because the lightweight aggregates tend to float in the mortar matrix [7].

2. Experimental program

2.1 Materials

The experimental campaign involved the production of a concrete made with LWAs using the Fanjul method [8], in order to produce LWAC with a target density of 1700 kg/m^3 and 1900 kg/m^3. Six different concretes were manufactured considering different types of LWA, different modes of vibration (one or two layers) and different theoretical densities. Table 1 presents the manufacturing characteristics of these concrete and includes their mix proportions. All samples were manufactured with the same water/cement ratio (w/c) of 0.6, resulting in 350 kg/m^3 of cement and 210 kg/m^3 of water to produce 1 m^3 of concrete. CEM I 52.5 R cement with an absolute density of 3176 kg/m3 was used for all the concretes; 2 types of expanded clay were used as lightweight aggregate; its physical properties are described in the Table 2. The bulk density of the LWAs was obtained according to the procedure described in the standard UNE EN 1097-3. In addition, the density of the particles in the dry state was determined by the methodology proposed by Fernández-Fanjul et al [9], the absorption of water at 24 hours according to the UNE EN 1097-6 (pre-dried particles and in distilled water). The methods/standards used for testing are also presented in the Table 2. Before mixing, and to avoid the loss of water from kneading by absorption, the LWAs were presaturated. During the mixing, the water content of the LWA and the surface water content were determined, to make the appropriate corrections and maintain a constant effective a/c ratio of 0.6.

Table 1: Manufacturing characteristics and mix proportions to produce 1 m^3 of concrete.

Concrete	Samples	Theoretical Densities	Vibration	Type of LWA	Fine Aggregate (kg/m³)	LWA (kg/m³)
LWAC1	20 uds	1700 kg/m³	two layers	Arlita Leca HS	723.9	416.2
LWAC2	20 uds	1900 kg/m³	two layers	Arlita Leca HS	1046.0	294.0
LWAC3	20 uds	1700 kg/m³	one layer	Arlita Leca M	991.1	148.9
LWAC4	20 uds	1900 kg/m³	one layer	Arlita Leca M	1234.8	105.2
LWAC5	5 uds	1700 kg/m³	one layer	Arlita Leca M	991.1	148.9
LWAC6	5 uds	1700 kg/m³	one layer	Arlita Leca HS	723.9	416.2

Table 2: Characteristics of aggregates and the methods/standards used for testing

Property	Method	Arlita Leca M	Arlita Leca HS	Fine Aggregate
Dry particle density (kg/ m³)	According to [9]	482	1019	2688
Bulk density (kg/ m³)	UNE EN 1097-3	269	610	1610
24 h Water absorption (%)	UNE EN 1097-6	36.6	12.2	0.12

2.2 Experimental Procedures

In the present study, three variables related to the manufacturing process of LWAC samples were studied. The cylindrical samples (Ø150mm and 300mm height) were compacted using an electric needle vibrator of 18000 rpm/min and a Ø25mm needle. The specimens were vibrated with 6 different times (0-5-10-20-40-80 seconds), in one and two layers (Table 1) to evaluate the variables "vibration time per layer (VTL)" and "manufacturing type (MTy), respectively. These procedures were repeated 4 times, considering different times between mixing and molding (variable "manufacturing time (MTi)" of 15, 30, 60 and 90 min), to verify differences on the consistency of the concretes. The flowchart of the Fig 1 represents these procedures.

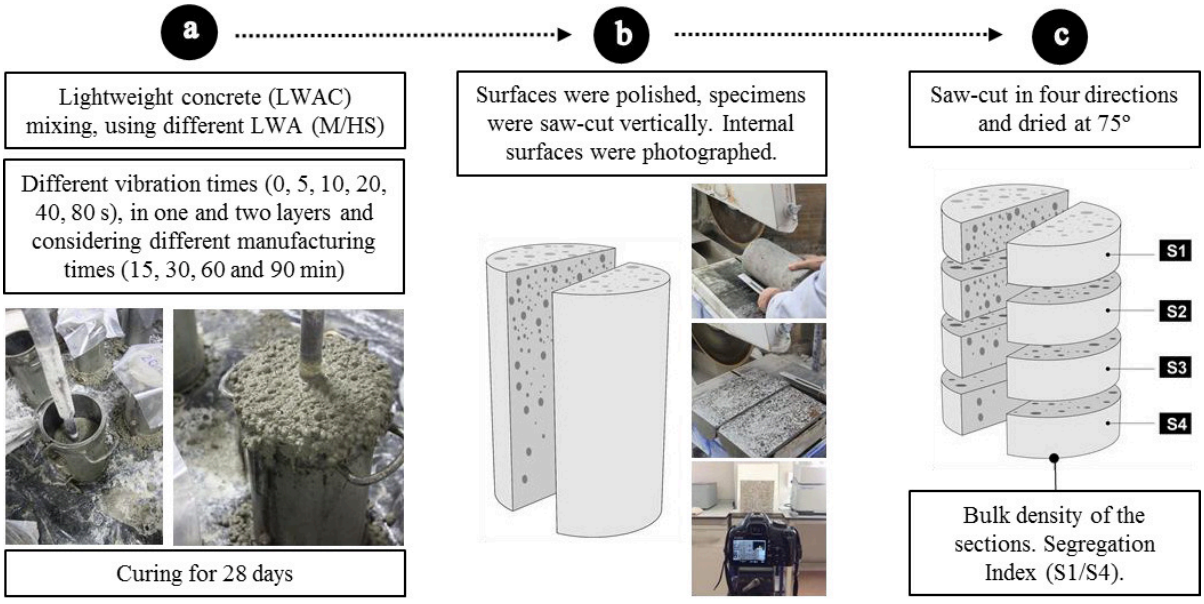

Figure 1: Flowchart of the methodology used in this study.

After being made and cured in the water at a temperature of 20 ± 1°C for 28 days, the specimens were saw-cut through its longitudinal axis and their sections were photographed for visual analyses. Subsequently the specimen's halves were then saw-cut into four equal parts, resulting in octaves, which had their bulk densities determined. Using the density values of the upper and lower sections, the segregation index was obtained according to the methodology indicated by Ke (SI_{Ke}) [7].

2.3 Statistical data analysis

A statistical analysis was applied for establishing the structure of the variable dependence and their interrelationship using XLSTAT® by Addinsoft®. First, a Shapiro-Wilk test was performed to verify the normality of the data. Second, scatter diagrams and Pearson's correlation coefficients were performed to identify existing patterns and quantify the linear association between two variables. Third, the analysis of variance (ANOVA) established the effect of each factor on the studied parameters and the possible interaction between the factors. Moreover, the statistically different groups were determined using Tukey's HSD test ($P < 95\%$).

3. Results and discussion

The results of the Shapiro-Wilk test confirmed the normal distribution of the analyzed data. The scatter diagrams confirmed the linear correlation between VTL and SI_{Ke} (Figure 2a). In the LWAC production with strong vibration stages in which LWA tends to float, Fig 2 displays that longer vibration time causes more pronounced displacement of the LWA to the upper part of the concrete specimen due to prolonged yield stress reduction. Given the p-value of the F statistic computed in the ANOVA, and given the significance level of 5%, the information brought by the explanatory variable (VTL) is significantly better than what a basic mean would bring. According to the Tukey's HSD test a 95 % level of confidence, the variable VTL should be classified in different groups or subsets: Group A for VTL≤10s; Group B for 10s<VTL≤20s; Group C for 20s<VTL≤40s and Group D for VTL>40s.

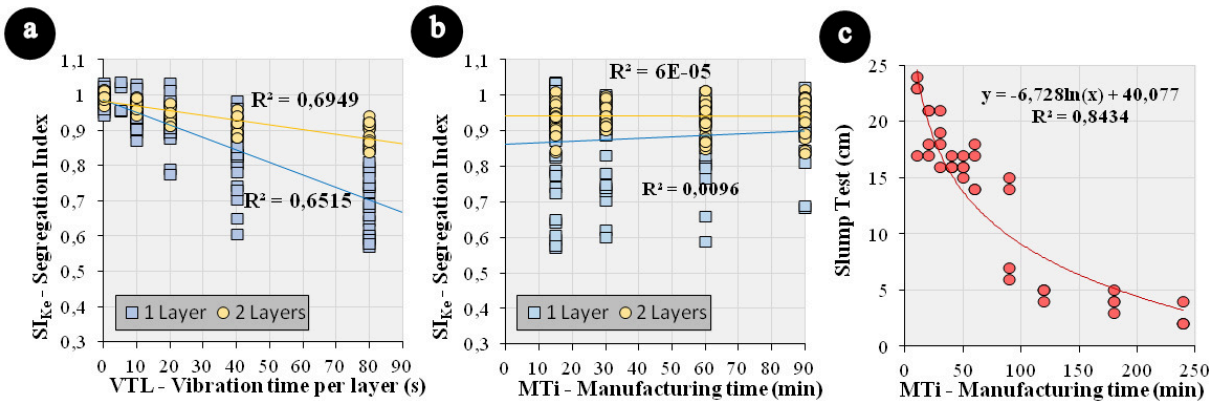

Figure 2: Scatter diagrams: SI_{Ke} vs VTL (a), SI_{Ke} vs MTi (b) and Slump Test vs MTi (c).

Focusing on the "manufacturing type" (MTy), the values presented important differences between the vibration in one or two layers. Fig. 2a shows that for the same vibration time per

layer, concretes vibrated in one layer presented more segregation. The same results are visible comparing Fig. 3a (1 layer) and Fig. 3b (2 layers), were de red areas indicate higher levels of segregation. As described by Ke [7], if SI_{Ke}=1, it can be considered that the sample shows perfect uniformity, and an index of less than 0.95 indicates a start of segregation. Manufacturing the samples in two layers resulted in more homogenized concretes and samples more resistant to the segregation phenomenon. The start of segregation for samples manufactured in one layer was observed in earlier periods than in samples manufactured in two layers. For those vibrated in one layer, the segregation starts between 10 and 20 seconds of total vibration (Fig 3a) and for those vibrated in two layers between 40 and 60 seconds of total vibration (Fig 3b). Given the p-value of the F statistic computed in the ANOVA, and given the significance level of 5%, the information brought by the explanatory variable (MTy) is significantly better than what a basic mean would bring. According to the Tukey's HSD test a 95 % level of confidence, the variable "manufacturing type" should be classified in two different groups: Group A for one layer and Group B for two layers.

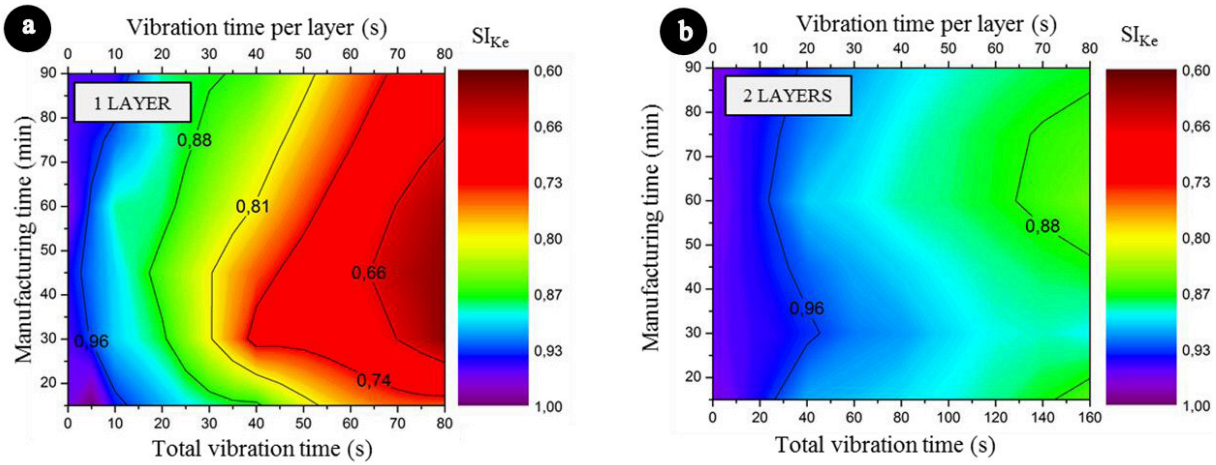

Figure 3: Behavior of the samples considering the variables evaluated in this study: manufacturing type (MTy), manufacturing time (MTi) and vibration time per layer (VTL).

However, the consistency of fresh concrete, directly related to the manufacturing time (Fig. 2c) does not present a clear correlation with SI_{Ke}, and the scatter diagrams of Fig 2b confirmed that there are no linear correlations between the variables MTi and SI_{Ke}. In this case, given the p-value of the F statistic computed in the ANOVA, and given the significance level of 5%, the information brought by the explanatory variable (MTi) is not significantly better than what a basic mean would bring. The fact that this variable does not bring significant information to the model may be interpreted in two different ways: either the variable does not contribute to the model, or some covariates that would help explaining the variability are missing and must be included in the study. According to the Tukey's HSD test a 95 % level of confidence, the variable "manufacturing time" should be classified in just one group of analysis.

4. Conclusions

This study presents an experimental study on segregation in lightweight aggregate concretes (LWAC) considering different variables related to the manufacturing process of LWAC samples. From the results presented in this study the following conclusions are drawn:

- The statistical analysis revealed that the manufacturing type (vibration in one or two layers) and the vibration time per layer are parameters that affect the segregation of concrete. However, regarding consistency of fresh concrete and manufacturing time, for the concretes studied in this research the results of the statistical analysis do not allow an obvious conclusion.
- Concretes vibrated in two layers presented lower segregation than concretes vibrated in one layer, indicating the importance of this parameter during the manufacturing of lightweight aggregate concrete samples. Different sample sizes and different vibration frequencies should be analyzed for more accurate results on this behavior.

Acknowledgements
This research was funded by the University of Alicante (GRE13-03) and (VIGROB-256). The authors wish to express their gratitude to Phd program in Materials, Structures and Soil Engineering of the University of Alicante.

References

[1] Cui HZ, Lo TY, Memon SA, Xing F, Shi X. Analytical model for compressive strength, elastic modulus and peak strain of structural lightweight aggregate concrete. Constr Build Mater 2012;36:1036–43. doi:10.1016/J.CONBUILDMAT.2012.06.034.
[2] Navarrete I, Lopez M. Estimating the segregation of concrete based on mixture design and vibratory energy. Constr Build Mater 2016;122:384–90. doi:10.1016/j.conbuildmat.2016.06.066.
[3] European Union – Brite EuRam III. EuroLightCon 1998, LWAC Material Prperties - State of the Art. 1998.
[4] Han J, Wang K, Wang X, Monteiro PJM. 2D image analysis method for evaluating coarse aggregate characteristic and distribution in concrete. Constr Build Mater 2016;127:30–42. doi:10.1016/j.conbuildmat.2016.09.120.
[5] Ke Y, Ortola S, Beaucour A, Cabrillac R, Dumontet H. Influence of aggregates on mechanical behavior of lightweight aggregate concrete: experimental characterization and modeling. First Euro-Mediterranean Adv. geomaterials Struct., Hammamet: 2006.
[6] Barbosa FS, Beaucour AL, Farage MCR, Ortola S. Image processing applied to the analysis of segregation in lightweight aggregate concretes. Constr Build Mater 2011;25:3375–81. doi:10.1016/j.conbuildmat.2011.03.028.
[7] Ke Y. Caractérisation du Comportement mécanique des bétons de granulats légers : expérience et modélisation. Université de Cergy-Pontoise, 2008.
[8] Fernández-Fanjul A, Tenza-Abril AJ. Méthode FANJUL: Dosage pondéral des bétons légers et lourds. Ann Du BâTiment Des Trav Publics 2012;5:32–50.
[9] Fernández-Fanjul A, Tenza-Abril AJ, Baeza-Brotons F. A new methodology for determining particle density and absorption of lightweight, normal-weight and heavy weight aggregates in aqueous medium. Constr Build Mater 2017;146:630–43. doi:10.1016/j.conbuildmat.2017.04.052.

SynerCrete'18 International Conference on Interdisciplinary Approaches
for Cement-based Materials and Structural Concrete
24-26 October 2018, Funchal, Madeira Island, Portugal

PARTICLE-MATRIX PROPORTIONING OF HIGH STRENGTH LIGHTWEIGHT AGGREGATE CONCRETE

Elisabeth Leite Skare [(1),(2),(3)], Jelena Zivkovic [(1)], Stefan Jacobsen [(1)], Jan Arve Øverli [(1)]

(1) Department of Structural Engineering, Norwegian University of Science and Technology (NTNU), NO-7491 Trondheim, Norway
(2) NorBetong AS (HeidelbergCementGroup), Heggstadmyra 6, NO-7080 Heimdal, Norway
(3) Department of Mechanical Engineering, Technical University of Denmark, 2800 Lyngby, Denmark

Abstract
Production of lightweight aggregate concretes (LWAC) requires specific knowledge and processes in order to achieve good workability of paste and concrete. A particularly demanding case is high strength lightweight aggregate concrete, i.e. having 28-day characteristic compressive strength in the range 60-80 N/mm^2 with oven dry density equal or less than 2000 kg/m^3. Coarse manufactured lightweight aggregates themselves often lack particles smaller than 2 mm, which together with open aggregate porosity causes a certain loss of workability during the first minutes after mixing. An efficient way of improving this is by particle-matrix proportioning. The desired concrete workability can be obtained by combining the filler modified paste with a suitable amount of coarse aggregate particles. In order to investigate this, several different LWAC mixes have been tested with the lightweight aggregate Stalite, an argillite slate from the US. We found that the particle-matrix proportioning approach can give desired workability of the LWAC mixes. This methodology is economical since no increase in cement and admixtures dosage is needed.

1. Introduction

The material properties of lightweight aggregate concrete (LWAC) are mainly depending on the properties of the used lightweight aggregate (LWA). LWA has different water absorption properties, geometry, surface, shape, rigidity, porosity and density compared to normal density aggregate, which all together have impact on LWAC [1]. One of the main challenges in preparation of LWAC is to achieve good workability and stability of the mix. Two main

challenges encountered when making the LWAC are different density of the LWA and the paste that may cause LWA segregation by floating, and estimation of mix water absorption of LWA that can cause very unstable concrete and lack of control of effective mass ratio. Most of the lightweight aggregates are split to several fractions. Coarser fractions of the lightweight aggregates are often very precisely fractioned and do not contain fines. One more challenge is to provide good packing of aggregate and paste, which might be difficult when using just one specific fraction of prefabricated LWA. Porosity of the LWA is in the range from 2 till 30% of volume, which in a mix, if not presaturated, absorbs a large amount of mix water from the fresh paste [2,3]. The most demanding case is preparation of high strength lightweight aggregate concrete. In order to achieve desired strength of LWAC, larger sizes of LWA, ≥ 8mm, are required, which often are in lack of particles smaller than 2 mm. Together with open porosity and high absorption, this causes a certain loss of workability during the first minutes after mixing. A previous investigation has found that when pre-wetted LWA is used, the workability is influenced little by the LWA type [5]. The aggregate used in this investigation was Stalite, fraction 1/2″. The dry aggregate density is 805 kg/m^3 and the saturated surface dry density is 833 kg/m^3. This paper investigates how the desired concrete workability can be obtained by combining lightweight coarse aggregate particles with a suitable amount of crushed fines, by using the method of particle-matrix proportioning. Several different mixes have been prepared where the amount of the fines were varied, and the workability has been measured according to the well-known slump procedure [4]. In addition, the total amount of water in the mixes have been controlled by measuring the moisture of the aggregate itself.

2. Methodology and results

The workability of the fresh concrete was measured, as well as visual inspection of the stability, in a series of LWAC mixes. The main idea when designing the LWAC mixes was using the particle-matrix proportioning method to obtain necessary workability (slump and stability against LWA floating) in high-strength LWAC mixes, by using a suitable paste. The 1/2 ″ fraction Stalite, an argillite slate-based LWA, was used in all the mixes, see sieve curves in Fig. 2. The experimental program was made up of four different batches of LWA. For determination of workability the slump test method was used [4], see Fig.1. The stability has been controled by visual inspection.

Figure 1: Slump method

2.1 Grading

Structural-grade Stalite LWA is made from various raw materials, including suitable slates, fly ashes, or blast furnace slags. The Stalite used in this investigation is first mined from naturally deposits of argillite slate and later pyroprocessed in a rotary kiln process. After manufacturing the material is divided into proper sizes (3/4", 1/2" and 3/8" with respectively maximum aggregate sizes 18, 12.5 and 9.5 mm, and then their moisture contents is adjusted to a predetermined level. The fraction 1/2 ″ is used in this investigation. Figure 2 shows particle size distributions from 4 different batches used in this study showing good agreement with each other, even though the batches were purchased and transported from different localizations and at different times. Fig 2 also shows that the Stalite has a low content of fines.

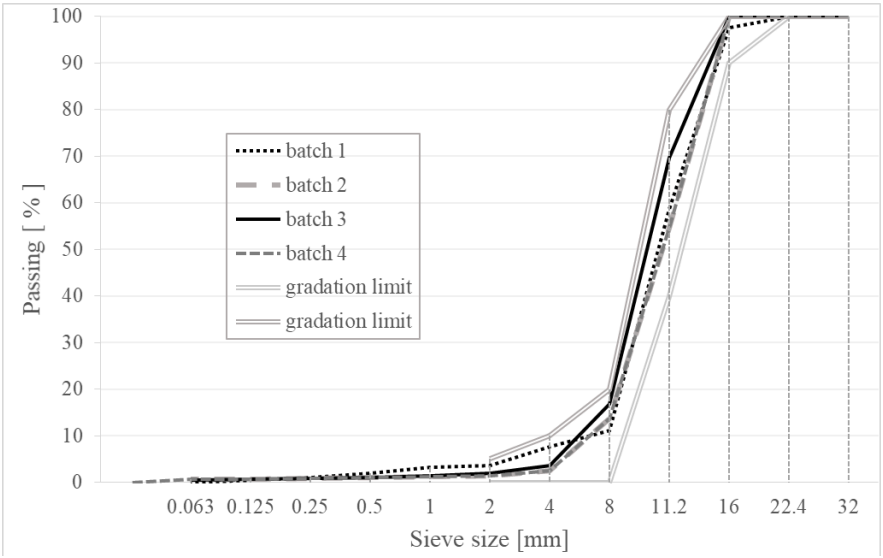

Figure 2: Sieve curves for aggregate Stalite fraction 1/2 ″, batches 1-4,

2.2 Particle-matrix proportioning

Particle-matrix proportioning is a model that is dividing concrete into two phases: a matrix phase and a particle phase. The matrix phase consists of all solid particles less than 125 microns, as well as water and additives. The particle phase consists of all solid particles larger than 125 microns. In the particle-matrix model, the matrix phase fills all voids between the aggregate particles. Workability and consistency of the LWAC follow from the ratio between the phases [4]. This tool, particle-matrix proportioning, is making concrete production more sustainable and economical, optimizing concrete properties by controlling the composition of the particles and the matrix. By adjusting the amount and grading of the fines in the paste and varying volume fraction of the paste, the concrete workability can be controlled and improved substantially [6]. In addition, when using particle-matrix proportioning the stability of LWAC mixes can be improved. When increasing the amount of fines, the internal cohesion increases and that prevents bleeding, paste separation and segregation of LWAC [4]. In this investigation, LWA Stalite is used in all the mixes. Due to the splitting process, the Stalite is in lack of fine particles. A 0-2 mm sand was added to some of the mixes, in order to avoiding gap-graded aggregate and hence reduce the volume fraction of paste needed to obtain workable concrete.

Table 1: Proportioned concrete mix compositions (kg/m3)

Mix No.	Cement Norcem Anlegg FA [kg]	Microsilica Elkem [kg]	Free Water [kg]	Batch No.	Aggregate Stalite 1/2″ [kg]	Sand Årdal 0-8 mm [kg]	Sand Ramlo 0-2 mm [kg]	Absorbed water Stalite +sand	Superplas. Mapei Dyn. SR-N [m.% of cem.]
M1	399.5	19.8	167.7	1	571.9	720.3		40.1	0.64
M2	420.7	21.9	193.5	2	537.1	543.0	232.4	49.2	1.23
M3	420.8	22.2	195.7	2	521.8	543.6	232.9	48.0	1.21
M4	431.8	20.4	176.4	2	566.9	730.1		51.0	1.33
M5	424.4	22.3	174.2	2	575.6	507.6	190.4	41.3	1.06
M6	423.8	22.3	174.0	2	585.1	516.0	193.5	52.5	1.19
M7	427.7	22.5	200.4	2	564.6	560.1	124.5	50.6	1.13
M8	431.8	20.3	176.5	2	581.4	705.0		52.1	1.25
M9	427.5	22.5	203.7	4	514.0	535.5	229.4	47.2	0.73
M10	442.2	23.3	146.0	4	515.4	536.8	230.0	6.1	0.75
M11	440.3	23.2	180.8	3	517.5	539.0	231.0	38.8	0.89

Table 2: Fresh concrete mix parameters

Mix No.	Matrix volume [l/m^3]	w/b	w/p	$\rho_{theoretical}/\rho_{measured}$	Slump test [mm]	Stalite Moisture [% of dry aggregate]	Stability: Floating of LWA*	Stability: Bleeding/ Halo*
M1	350	0.40	0.33	1920 / 1993	140	8.2	Yes	Yes
M2	375	0.44	0.39	1967 / 2013	230	11.43	No	No
M3	375	0.44	0.39	1967 / -	240	11.43	No	No
M4	365	0.39	0.33	1968 / -	210	8.5	Yes	Yes
M5	360	0.39	0.33	1943 / -	200	6.2	No	Yes
M6	360	0.39	0.33	1921 / -	250	8.5	No	Yes
M7	376	0.44	0.40	1930 / -	230	11.43	No	No
M8	365	0.39	0.33	1922 / -	210	8.5	Yes	Yes
M9	378	0.45	0.41	1967 / 1927	250	12.5	No	No
M10	326	0.31	0.28	1929 / 1989	170	0.1	Yes	No
M11	360	0.39	0.35	1967 / 2015	190	6.3	No	No

* Visual qualitative assessment

2.3 Experimental program and results

The experimental program consists of eleven different LWAC mixes, see Tab. 1 and Tab. 2. Tab. 1 shows nominal, uncorrected proportions. In Tab. 2 are given properties of fresh concrete.

The main parameters varied in the mixes were the amount of fines, incorporated in the sand Ramlo 0-2mm, SP-dosage, as well as the moisture content of the LWA Stalite. Pre-wetted LWA Stalite was used in all the mixes, except in mix M10, where Stalite was very dry with a moisture content of 0.1%, see Tab. 2. Aggregate absorbed water was not considered as free water. Measured workability was in the range from 140 mm to 250 mm. This workability experiment has been done in combination with a casting experiment, and mixers with different capacities have been used, depending on the necessary concrete amount. Mix M1 has been mixed in an 800 litres capacity mixer, while mixes M9-M11 has been produced in a 250 litres capacity mixer, both with vertical pedals. The mortar in mix M3 has been produced at a concrete plant, and mixed together with the Stalite in the concrete truck mixer. The remaining mixes are trial mixes, performed in a mixer with a capacity of 10 litres with vertical pedals.

In addition, stability of LWAC was controlled, by visual qualitative assessment. In the mixes M1, M4, M8 and M10 it was noted coarse aggregate separation, when LWA particles float on the paste [4]. In the mixes M1, M4, M5, M6 and M8 it was observed slight bleeding as a sheen on the concrete mass and presence of the Mortar Halo [7], see Tab. 2.

3. Discussion

The particle-matrix proportioning method resulted in good workability in terms of stability and slump of the LWACs, by increased matrix volume and content of fines. From Tab.1 and Tab. 2 we see that matrix volumes and admixture dosages seem to explain the observed slump values, since the proportioned w/b- and w/p- ratios not are varying to a large extent among the mixes, as respectively from 0.31-0.45 and 0.28-0.41. The low slump of M1 relates to its low matrix volume and SP dosage. The higher slump of M4 and M8 correspond to high matrix volume and SP dosages. Finally, for M2, M3, M7 and M9 a higher slump is measured due to higher matrix volumes. For M5, M6 and M11 the matrix volumes are all the same but for the mix with lower slump, M11, the SP dosage were lower than for M5 and M6. Mix M10 has the lowest matrix volume due to lower water content in the LWA, i.e absorption of mix water.

For the mixes without fine sand from 0-2 mm, mixes M1, M4 and M8 floating of the LWA and slight bleeding as a water sheen at the edges of the concrete mass and poor paste viscosity were observed. Floating of the LWA was also observed for mix M10 where the Stalite was dry. Floating of the LWA on the paste might be caused by the density differences between the paste and the aggregate. From tab. 2 it is obvious the difference between the theoretical and measured density and they are often offset by 40-50 kg/m3. This huge difference is due to the releasing of water from aggregate during the drying process.

From all mentioned above it is obvious that by using the particle-matrix method, workability and stability may be improved significantly. When controlling the amount of fine sand in the mix it is possible to achieve desired workability, without increasing amount of cement and silica, and particle-matrix proportioning is hence more economical and practice.

4. Conclusions

Desired workability and stability was achieved in almost all LWAC mixes, expect for the mixes without any fine sand. The mix with the dry aggregate obtained desired workability as a result of additional fines. By adding fines, it is possible to reduce the amount of water in the mix significantly, and still maintain good workability. Mixes without fine sand from 0-2 mm did not achieve enough stability, it is observed floating of the LWA and slight bleeding as a water sheen at the edges of the concrete mass. In general, particle-matrix proportioning by increasing the matrix volume by addition of sand is an economical and practical method, since sand is a more widespread and cheaper ingredient than cement and silica. In addition, methodology is not fully developed and future research have to be carried out.

Acknowledgements
The work presented in this paper is part of an ongoing PhD studies in the DACS project (Durable Advanced Concrete Solutions) and in the MiKS project (Microproportioning with Crushed Sand). The DACS partners are Kværner AS (project owner), Norwegian Research Council, Axion AS (Stalite), AF Gruppen Norge AS, Concrete Structures AS, Mapei AS, Multiconsult AS, NorBetong AS, Norcem AS, NPRA (Statens Vegvesen), Norwegian University of Science and Technology (NTNU), SINTEF Byggforsk, Skanska Norge AS, Unicon AS and Veidekke Entreprenør AS. The MiKS partners are Norcem AS, Norstone AS, Norbetong AS, Feiring Bruk AS, Skanska, SINTEF, National Institute of Standards and Technology (NIST), Norwegian University of Science and Technology (NTNU) and Technical University of Denmark (DTU).

References

[1] ACI Committee 213, 2003, "Guide for Structural Lightweight-Aggregate Concrete (ACI 213R-03)", American Concrete Institute, Farmington Hills, MI, United States.
[2] Punkki J. and Gjørv O.E., Effect of water absorption by aggregate on properties of high-strength lightweight concrete, Proceedings from the International Symposium on Structural Lightweight Aggregate Concrete, Sandefjord, Norway (1995), 604-616.
[3] ACI 211.2-98, 1998, (Reapproved 2004) "Standard Practice for Selecting Proportions for Structural Lightweight", ACI Manual of concrete practice, Part1, PP. 211.2-1-17.
[4] S. Jacobsen et al, Concrete Technology 1. TKT 4215. Kompendium. Norwegian University of Science and Technology (2016), Chap. 3, 3-6 and 13-14; and Chap. 4, 12-22.
[5] Hammer T.A. and Smeplass S., The influence of the lightweight aggregate properties on material properties of the concrete, Proceedings from the International Symposium on Structural Lightweight Aggregate Concrete, Sandefjord, Norway (1995), 517-532.
[6] R.Cepuritis, Development of crushed sand for concrete production with microproportioning, PhD thesis, Norwegian University of Science and Technology (2016)
[7] A. El hassan et al, The Impacts of Visual Stability Index on Flowability and Segregation 1 Properties of Self – Consolidating Concrete, Proceedings from the Transportation Research Board 94th Annual Meeting , Washington DC, United States (2015).

SynerCrete'18 International Conference on Interdisciplinary Approaches
for Cement-based Materials and Structural Concrete
24-26 October 2018, Funchal, Madeira Island, Portugal

PHOTOCATALYTIC NOVEL CONCRETE MATERIAL APPLICATION AND ITS LIFE TIME STANDARD TESTING

František Peterka (1)

(1) Nanotec System, Praha, Institute of Nanomaterials of TUL, Liberec, Czech Republic

Abstract
Photocatalytic cementitious building materials, mainly with incorporation of TiO_2 are being advertised as the promising technique to keep surface clean just thanks to illumination by light. This light-induced phenomenon can be applied for self-cleaning and disinfecting surfaces as building façades, decorative mortars, culture monuments etc. In addition, concentration of air pollutants such as NO_x and VOC's, frequently encountered in trafficked areas and the urban environment can also be reduced. However, there are still doubts and questions about the durability of the photocatalytic activities. To answer the logic question about the photocatalytic products service life, standardized testing methods have to be set up to give more reliable answers to the potential end users. First attempts have been made by Czech Republic and Belgian research groups within the European normalization efforts of CEN/TC386 "Photocatalysis". The testing method based on several years' studies incl. photocatalytic concrete manufactures was proposed for vertical as well as horizontal surfaces.
This presentation presents examples of results of these investigations as the first step towards the evaluation of the life time of these photo-active air purifying products.

1. Photoactive coating systems for environmental cleaning - new solutions

Photocatalytic technologies offer new ecological technical solutions. The so-called solar self-cleaning allows the destruction of microorganisms on the façades of houses and the surfaces of other objects, including historical monuments. In the Czech Republic there are tens of thousands of insulated panel houses affected by the growth of algae and mold.

Figure 1: Light cleaning effect of BALCLEAN after 1 year of application on different cement containing surfaces.

Historical buildings are subjected to destruction in the polluted environment of large cities. The newly developed transparent nanocomposite system BALCLEAN with solar photocatalytic self-cleaning and disinfecting function is used to prevent the growth of algae on insulated objects and historical buildings.
The origin of the BALCLEAN coating system and its introduction to the market preceded many years of development and testing of photocatalytic applications, with several research teams from the Institutes of the Academy of Sciences of the Czech Republic and the Technical University of Liberec. NANOTEC SYSTEM was founded for the rapid application of photoactive nanomaterials, with the participation of leading Czech scientists in the field. At present, this company has the know-how for the following applications:

- Prevention of growth of microorganisms on façades of apartment buildings
- Protection of concrete constructions and structures
- Protection of historical objects

The BALCLEAN painting system is produced by the leading Czech manufacturer of coatings Barvy a Laky Teluria a.s., which concluded an exclusive agreement for its application to apartment buildings with the Pragotherm sevis fasád, s.r.o..

2. Application the BALCLEAN on shaded houses - Pragotherm sevis fasád, s.r.o.

Pragotherm sevis fasád, s.r.o. focuses on the treatment of insulated buildings, including façades affected by algal and mold growth. The traditional use of long-term inefficient biocidal chemicals is replaced by a new photocatalytic technology that demonstrated beneficial effects on the environment (removing harmful micro-organisms and removing gaseous pollutants). New ecological technology has a long-term activity against the growth of all microorganisms on façades. Pragotherm sevis fasád, s.r.o. performs a two-year nationwide monitoring of algae-covered objects in all towns and municipalities in the Czech Republic. In the 23 000 apartment buildings, the algae and mold will be removed during the next two to three years, and then a protective photocatalytic coating will be applied to the refurbished façades. In 2017, 40,000 square meters were treated, in 2018 expected to grow to 100,000 square meters.

3. Understanding the type of biological pollution to assess the limits of photocatalysis

Pragotherm servis fasád, s.r.o. in cooperation with the Technical University of Liberec is doing microbiological sampling on façades covered with algae. In addition to the results of

microbiological analyzes, it collects other relevant data on the state of the insulated façades. Home owners get information about the types of micro-organisms growing on façades, what causes their growth, how the algae and molds affect the insulation system, and also the possible health risks for the residents of the house. Protocols also include a proposal for a technical solution, including recommendations for gardening of surrounding bio zone. For the period 2016 to 2017, Pragotherm sevis fasád, s.r.o. processed a total of 267 microbiological protocols of residential houses affected by algae. We expect that by the end of 2019, a total of 2,000 objects will be monitored and processed.. This project is unique in its scope and focus in Europe. The aim of this research is to find out the causes and consequences of the massive presence of microorganisms in most of the insulated objects in Central Europe.

4. Application to Sights - Gallery of the Capital City of Prague

The Gallery of the City of Prague has a number of monuments under management, which need to be quickly repaired and then protected. Deteriorating the environment has prompted the need to develop new technologies for their protection, and photoactive paint systems appear to be very promising.
Czech experts on the application of modern technologies to monuments developed the MONDIS (Monument Damage Information System), designed to preserve and transfer knowledge about the state, the causes of damage, and the course and results of repairs of immovable monuments. The MONDIS system provides a basis for mapping and cataloging historical objects suitable for treatment with a photoactive nanocomposite system. In cooperation with the Prague City Gallery, a test room of the first 10 plasters suitable for new technology treatment was selected, starting in the spring of 2018. This pilot experiment was preceded by a number of laboratory tests and applications on identical materials used in listed buildings. As well as fulfilling the necessary legislation was the rule. That is why it can be assumed that the evaluation of the results of this pilot experiment with the new technology will be successful and will be followed by applications to hundreds of other monumental objects that need to be repaired and protected in the capital city of Prague and worldwide.

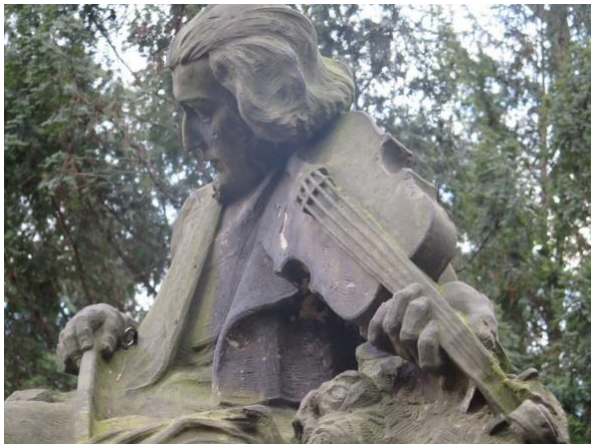

Figure 1: Example of a statute suitable for protection using modified BALCLEAN system

5. Photocatalytic products service life time

Standardized method to evaluate material ageing giving answer to photocatalytic surface life time is still missing. Czech Republic already proposed the photocatalytic life time evaluation as the possible new CEN standard within CEN/TC 386. The basic idea is to specify the accelerated aging conditions for a variety of photocatalytic materials like cement-based materials, paints, thin films, etc. for different applications (e.g. horizontally on a road surface or vertically on a building façade), based on already existing durability tests in the field of application and with a possibility to define different photocatalytic durability classes.
Research teams at the Institute for Nanomaterials, Advanced Technologies and Innovations of Technical University Liberec (TUL)together with Italcementi co. as well as from the Belgian Road Research Centre prepared the concept of the evaluation of the reduction in photocatalytic performance caused by different degradation processes encountered in practice such as abrasion or weathering of the photocatalytic surface (Figure 2).

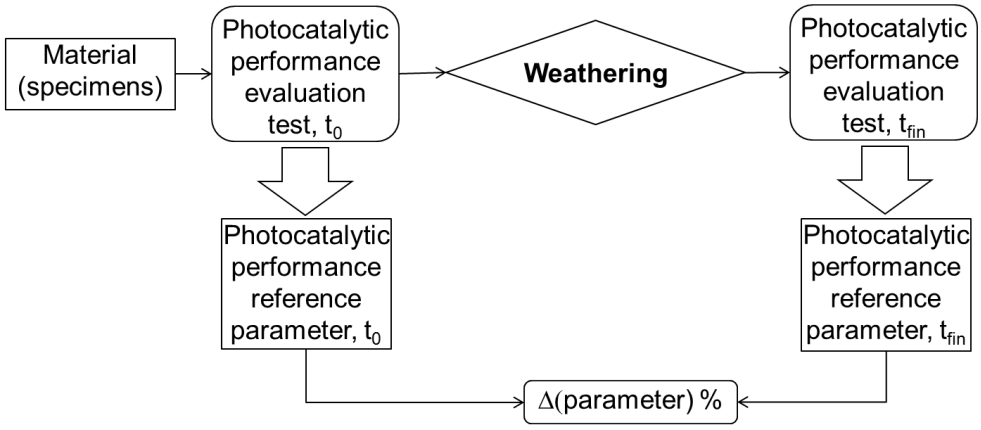

Figure 2: Concept of evaluation of photocatalytic performance reduction due to weathering.

Weathering for instance, is the adverse response of a material or product to the environmental conditions it is exposed to, often causing unwanted and premature product failures, where the main contributing factors are sunlight, temperature, moisture, and possible contamination by intermediate products formed during the photocatalytic process. In the case of photocatalytic materials, sunlight is needed to initiate the degradation process and drives it forward, but also leads to transformation of reaction products that can poison the TiO_2 catalyst embedded in the building material. In addition, temperature and humidity (RH) together with UV ageing can also change the catalyst texture and/or the matrix material, and cause adverse effects as well [1, 2].
The objective of artificial weathering or the ageing test in general, is thus to reproduce the degradation processes and resulting damage that occurs naturally, in a laboratory under accelerated and reproducible conditions. Furthermore, the photocatalytic performance should be evaluated according to standard methods already accepted or to draft methods which are under development on international (ISO) and/or European (CEN) level, see e.g. [3].
The Institute of Nanomaterials at TUL and researchers from Czech academic Institutes were involved in development of novel nano composite photoactive coatings to be applied for self-

cleaning activity of building façades or industrial cementitious materials commercially named BALCLEAN and recently being also working on photocatalytic materials applied in the bulk or at the surface where abrasion might also play a significant role.

6. Photoactive materials and testing methods

NANOTEC SYSTEM with research teams from TUL, Czech Academy of Sciences and closely collaborating with industrial partners on the application of BALCLEAN are testing service life based on the standard tests for self-cleaning, antimicrobial properties and air purification effect. The air purification effect of the coated surface area is in this case considered to be a beneficial side effect.

Photocatalytic activity testing
First of all, the photocatalytic self-cleaning activity of the coatings was determined on the one hand according to the ISO 10678:2010 standard method based on methylene blue decomposition [4]. Methylene blue (MB) is degraded upon contact with the photoactive surface under UV illumination. An aqueous solution of MB is used for these tests.
On the other hand, BALCLEAN was also applied on the outer concrete facade of a building (Fig. 3). The effect of the photocatalytic coating on the wall was followed by visual change surface analysis. For the analysis the Flip-Pal plus mobile scanner and the DoSa software application were used to describe the colour intensity changes of the surface. This analysis was performed more than one year after the coating application.

Figure 3: Photos of the entrance of Institute for Nanomaterials at TUL consisting of concrete panels which were protected by the BALCLEAN coating. To observe the self-cleaning function, only each second stream was coated, as illustrated in the picture on the right.

Weathering test applied to coated cementitious samples
As an example, a combined weathering cycle used for testing of coating systems for exterior use according to the standard method CSN – EN 927-6 was applied:

- 24 h condensation of water at T = 45°C
- 2,5 h UV-A irradiation at 1 W/m^2 and T = 60°C, followed by 0.5 h water spraying at 6-7 l/min.

The BALCLEAN coating was applied on mortar samples of 5x5 cm with an upper layer of acrylate, silicate or silicone paint. In addition, the BALCLEAN coating was prepared with different amounts of photoactive nanomaterial (3% and 5%). Measurements of the photocatalytic activity were made on these samples before and after applying the artificial weathering test described above by all available ISO and CEN standard methods.The corresponding changes in photocatalytic material performance were evaluated.

7. Discussion and conclusion

The reduction in photocatalytic air purifying activity of coated and painted cement based materials is significant, but regarding self-cleaning performance the material can still keep its expected function after more than one year of outdoor exposure .However to approve the final version of CEN standard proposal for durability, accelerated weathering must be modified accordingly. In addition, the correlation between the conditions of the artificial weathering test and the expected life time (5, 10 years or even less) of the photocatalytic activity needs to be further investigated.
To guarantee the life time of advertised photocatalytic function to potential investors is important. To design broadly accepted CEN standard concerning accelerated ageing of photocatalytic cement based building materials the expertize of more experts from different fields is needed.

Acknowledgements
These topical activities of the Institute for Nanomaterials of Technical University Liberec (TUL) were supported by the Czech Ministry of Education, Youth and Sports in the framework of COST program and by Technological Agency

References
[1] Fujishima, A., Zhang, X. & Tryk, D.A., TiO2 photocatalysis and related surface phenomena, Surf Sci Rep 63 (2008), 515–582.
[2] Peterka, F, Cleaning by photoactive nanosurfaces. Public Service Review: European Science & Technology, Issue 11, pp. 68-69 (2011)
[3] CEN Technical Committee 386 "Photocatalysis" Business Plan—(internet) Draft BUSINESS PLAN CEN/TC386 PHOTOCATALYSIS. Available online: https://standards.cen.eu/BP/653744.pdf (accessed on 16th of June 2016).
[4] ISO 10678:2010, Fine ceramics (advanced ceramics, advanced technical ceramics) - Determination of photocatalytic activity of surfaces in an aqueous medium by degradation of methylene blue, International Standards Organization, (2010).

SynerCrete'18 International Conference on Interdisciplinary Approaches
for Cement-based Materials and Structural Concrete
24-26 October 2018, Funchal, Madeira Island, Portugal

PHYSICAL EVOLUTION OF THE INTERFACE OF FRESH CONCRETE/FORMWORK FROM PLACEMENT TO SETTING TIME

Typhanie Craipeau [(1) (2)], Arnaud Perrot [(1)], Fabrice Toussaint [(2)], Thibaut Lecompte [(1)]

(1) Institut de Recherche Dupuy De Lôme, Centre de recherche Christian Huygens, Lorient, France
(2) LafargeHolcim Research Center, Lyon, France

Abstract

Cement hydration induces water consumption which induces a reduction of the capillary pressure in the concrete. The equilibrium of pressure implies an increase of the granular stress which is able to transmit shear stress to any support. Slipforming process is characterized by a continuous moving of the formwork, which creates adhesion phenomena and potential damages which have to be assessed and ideally reduced.
Experimental devices have been designed in order to evaluate the friction at this interface during the first hydration period. The role of pore water pressure is investigated and controlled in order to separate the influence of pore water pressure and hydrates formation.

1. Introduction

Concrete is a very versatile material whose rheological properties have to be adjusted, depending on the application and the process. The interface between the concrete and its support may also be critical at different states of its maturity.
The present study aims to characterize the evolution of the concrete interface with a support as a function of its level of hydration at very early age.
For example, in a slipforming process, concrete is continuously poured and the formwork is very frequently raised in order for the concrete to stand by itself at the bottom, after a few hours of hydration. This technique [1], see **Figure 1**, is a widely used construction methodology for high rise structures such as skyscrapers, pylons, silos or marine foundations that benefits from its high construction speed and the absence of cold joint that may affect the durability of the structure. The concrete is directly in contact with the formwork from its fresh

state to a set state without any demolding agent. During sliding, possible micro-cracking/lump formation can happen on the wall surface. These defects are most probably related with the concrete adhesion on the formwork. These issues should be solved and prevented to avoid a reduction of the durability of the structures that could turn into strong damages if not properly treated.

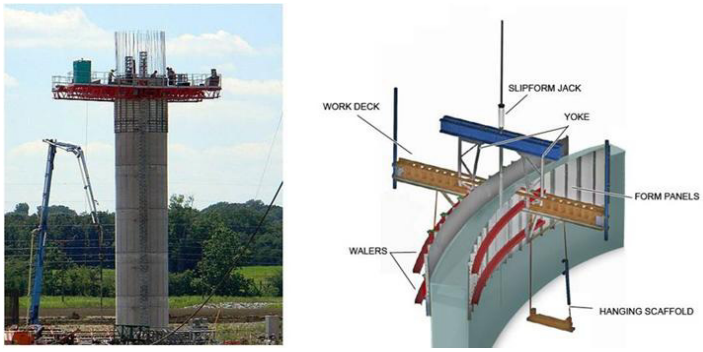

Figure 1. Slipforming illustration.

Usually, the industrial formworks are about 1.2 meters height and the average lifting speed is around 15 - 25 centimeters per hour.
The aim of the study is to determine the physical phenomena which govern friction and adhesion of concrete to the metallic surface. It has been shown that friction between the concrete and the formwork is mainly influenced by pore water pressure: water consumption caused by cement hydration will induce capillary suction which is assumed to play a major role on the interface [2]. Pore water depression can increase granular stresses acting on the particles assembly as described by Terzaghi equation [3].

This study aims to design tools studying the influence of pore water pressure on the shear stress of cement based materials/formwork interface.

2. Pore water pressure and granular stress (Terzaghi equation)

Thanks to Terzaghi equation, suction can be related to the normal force in case of saturated conditions. Terzaghi [1] describes that the total stress, σ (kPa) is equal to the sum of the effective stress σ' (granular stress, kPa) and the pore water pressure, u_w (kPa):

$$\sigma = \sigma' + u_w \quad (1)$$

The total stress of the concrete is considered in this study as almost constant. Therefore, the effective stress of the concrete only varies with concrete pore water pressure [4]. Terzaghi equation is illustrated in **Figure 2**. At constant total stress, negative pore water pressure increases the stress σ' acting on the granular skeleton (which is the case in the early stage of hydration). Unlike water pressure, the granular effective stress is able to transmit shear stress to the concrete itself, or to any support, depending on the friction level.

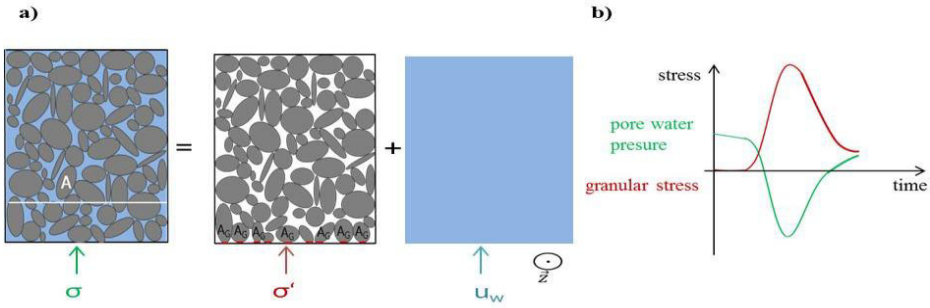

Figure 2. Terzaghi equation illustration.

3. Experimental procedures

3.1 Materials and mixing procedure

The aim of the study is to understand the physical phenomena involved in the lifting resistance exerted by the concrete during the slipforming; therefore we chose usual materials: a Portland cement (CEM I 52.5N PM-ES CP2 NF), with 37v% of a fine sand (PE2LS 0/0.315µm) to help the mixing (also to reduce heating during mixing). A low Water/Cement ratio (W/C=0.3) is used to reduce strongly the pore water pressure. In order to obtain a low W/C ratio and a good rheology, a common polycarboxylate plasticiser admixture was used: Glenium 27 from BASF (0.063wt%/cement).

In the fresh state, the mortar is fluid (slump ASTM is 260 mm), and its air volume fraction is 2.7%.

The designed mortar was prepared with a Perrier mixer with the same mixing protocol in order to ensure tests reproducibility. The sand was first mixed with part of the water at low speed (140 rpm) during 1 minute. Then, after a waiting period of 4 minutes, cement is introduced and mixed at low speed during 1 minute. The rest of water is introduced during 30 seconds at low speed. Finally, the material is mixed at high speed (180 rpm) during 2 minutes.

3.2 Devices and procedures

Two devices are used for the experiments. The first one gathers multiple physical phenomena as it is more representative of the real process. The second one aims at piloting and observing specific phenomena in order to isolate physical phenomena and understand the origin of the friction.

The first device consists of a parallelepiped box, filled with mortar. One face of the box, attached on a traction machine, can be moved and is made of the material that represents the formwork interface. A load cell permits to measure the global interfacial shear load (Figure **3**). It is also fitted with pore pressure sensors [5] and force transducers to estimate those critical physical parameters. It allows to improve the understanding of the impact of suction on granular/interfacial friction and to assess its relative influence on the total stress. The advantage of this apparatus is to benefit from a total lifting run of 380 mm. For each lifting step, the lifting speed is 1 $mm.s^{-1}$ for a move of 5 mm. The time at rest is 565 seconds between each step. The average lifting speed is then $0.5mm.min^{-1}$. The total test lasts around 12 hours.

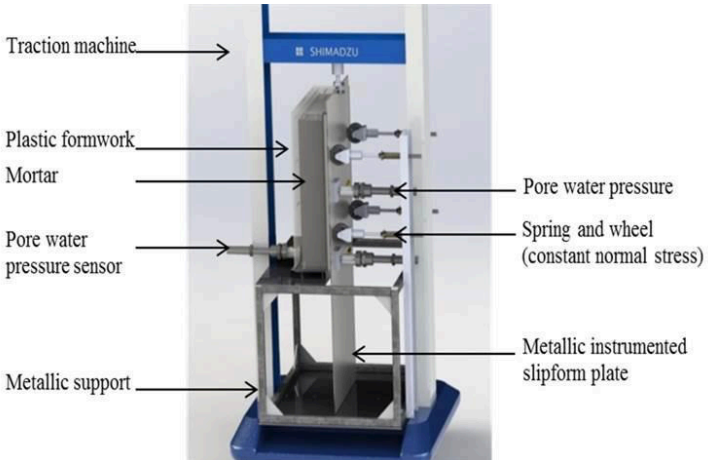

Figure 3. Vertical shear stress device developed to study slipforming operations.

The second device is composed of a small cylindrical box where the material is under controlled depressure. The objective is to measure shear stress evolution of the material under pore water depressure. The measuring cell is placed on a rheometer with a vane tool to observe rheological evolution (essentially yield stress) and a cylindrical tool to characterize tribology properties. The system is equipped with pore water pressure sensor and a system creating a depressure by removing water inside the material. The measuring cell is 50 mm high and 50 mm diameter to ensure the homogeneity of the material. This device is complementary to the vertical shear stress device because it will permit to separate the adhesion phenomena created by pore water pressure and the hydrates physical bonds to the metallic surface [6]. It will also allow comparing the material cohesion (yield stress) with its adhesion to a given support. We are not presenting results with this device in this paper.

4. Experimental results and discussions

4.1 Degree of hydration

Hydration degree over time was determined using calorimetry measurements: it is defined as the ratio between the cumulated heat flow (which is the surfaces under the curve of the evolution of the heat flow per gram of cement over time) and the total theoretical enthalpy of the hydrates (ΔrH=353 J/g for C_3S hydration which is the major hydrate); see **Figure 4**.

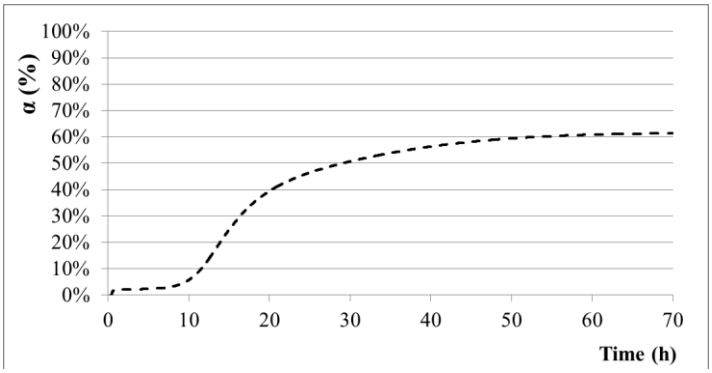

Figure 4. Degree of hydration in function of time (after cement/water contact).

Cement kinetic hydration is slow until 10 hours, then it is really fast until 20 hours, reaching 40 % of the state of hydration. After this transition period, the hydration is slower and reaches 60 % at 70 hours.

The degree of hydration is essential for the study because it shows where the maximum of water consumption is. It shows that only little water consumption, thus few hydrates created, induces suction.
In addition to hydration degree measurements, it should be noticed that it is *isothermal* calorimetry, this means that if temperature is not control in other experiment for example, the hydration development will be different.

4.2 Friction evolution

The time evolution of the effective stress and tangential shear stress are plotted in Figure **5**. (obtained with the vertical shear stress device presented above in Figure **3**). We observe that the order of magnitude of the effective stress (dotted line) is really higher than the tangential shear stress (continuous line).
It seems that there is proportionality between tangential shear stress and the pore water pressure until 7 hours of hydration. Considering a constant total shear stress, as proposed by Terzaghi theory (saturated conditions), the granular stress should fluctuate with the opposite of the pore water pressure. This is in agreement with our measurements until 7 hours when the water network becomes discontinuous (thus Terzaghi equation cannot be applied because we are not in saturated condition). Thus, comparing the two different y-scales of Figure **5**, a friction coefficient of about 0.4 can be determined. After the simultaneous evolution there is a separation, this occurs when the water network is not continuous anymore and the air network is linked, this is called air entry value [7]. Those first results have to be confirmed.

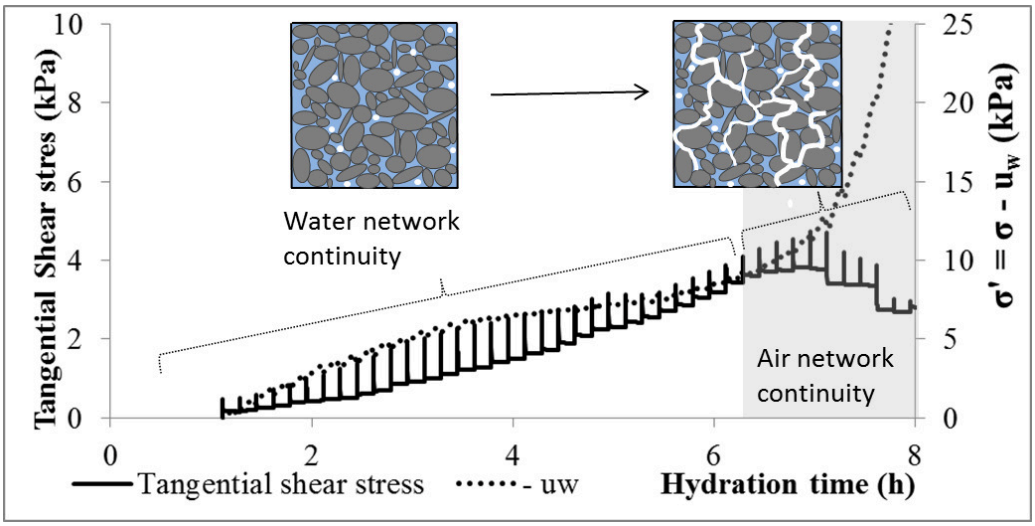

Figure 5. Calibrated pore water pressure and shear stress evolution measured with the experimental device.

This increase of the interfacial stress can be due to mortar stiffening. The granular stress increases due to water suction and hydrates formation at the interface.

Results on the second device are expected to demonstrate the influence of pore water pressure on the shear stress properties of the material using rheology and tribology data. The small device presents the advantages to control the influences of physical phenomena.

5. Conclusion and perspectives

A first estimation of the frictional coefficient between concrete and a metallic formwork has been evaluated thanks to a design device. Terzaghi equation was used under saturated condition. Nonetheless, pore water pressure was measured inside the material and the future objective is to measure it at the interface.
A new device has been described in order to appreciate the shear stress evolution properties under controlled pore water pressure which seems to be mainly at the origin of friction on concrete/formwork interface.

Acknowledgements
The authors also wish to thank Alexandre Menguy who made the drawings of the experimental device.

References
[1] Fossa, K. T. Slipforming of Vertical Concrete Structures. Friction between Concrete and Slipform Panel. (Fakultet for ingeniørvitenskap og teknologi, 2001).
[2] Hammer, T. A., «The use of pore water presure to follow the evolution from fresh to hardened concrete », 2006 (e-ISBN: 2351580028) RILEM Publications SARL.
[3] L. K. Mettler, F. K. Wittel, R. J. Flatt, et H. J. Herrmann, « Evolution of strength and failure of SCC during early hydration », *Cem. Concr. Res.*, vol. 89, p. 288-296, nov. 2016.
[4] S. Ghourchian, M. Wyrzykowski, et P. Lura, « A poromechanics model for plastic shrinkage of fresh cementitious materials », *Cem. Concr. Res.*, vol. 109, p. 120‑132, juill. 2018.
[5] T. Lecompte, A. Perrot, V. Picandet, H. Bellegou, et S. Amziane, « Cement-based mixes: Shearing properties and pore pressure », Cem. Concr. Res., vol. 42, no 1, p. 139‑147, janv. 2012.
[6] N. Roussel, G. Ovarlez, S. Garrault, et C. Brumaud, « The origins of thixotropy of fresh cement pastes », *Cem. Concr. Res.*, vol. 42, n° 1, p. 148‑157, janv. 2012.
[7] V. Slowik, M. Schmidt, et R. Fritzsch, « Capillary pressure in fresh cement-based materials and identification of the air entry value », *Cem. Concr. Compos.*, vol. 30, n° 7, p. 557‑565, août 2008

SynerCrete'18 International Conference on Interdisciplinary Approaches
for Cement-based Materials and Structural Concrete
24-26 October 2018, Funchal, Madeira Island, Portugal

PROPERTIES OF CEMENT WITH INCREASED LITHIUM CONTENT

Theodor Staněk [(1)], Alexandra Rybová [(1)], Anežka Zezulová [(1)], Martin Boháč [(1)]

(1) Research Institute for Building Materials, Brno, Czech Republic

Abstract
Lithium consumption in the production of batteries and accumulators for energy storage is increasing. It can be foreseen that the amount of waste with higher content of this metal will grow. Cement industry is one of the major consumers of several types of waste and secondary raw materials, therefore it is desirable to study the impact of lithium on the properties of clinker and cement. Under laboratory conditions, it has been found that lithium has a significant impact on clinker melt formation and on formation of main clinker phases. Moreover, cements with sufficient technological parameters were prepared from clinkers burned at 1350 °C with Li_2O up to 1 wt.%. The research was conducted by means of XRD, DTA, optical and electron microscopy.

1. Introduction

The influence of LiO_2 on the properties of Portland clinker and cement has not been properly studied yet. It is desirable to look at this issue deeper due to the possibility of use of lithium-containing raw materials in cement production.
Lithium behaves differently from sodium and potassium. It forms non-volatile Li_2O at higher temperatures and mainly it decreases the temperature of melt formation. The presence of Li_2O changes the course of the burning process during which lime dissolves in the liquid phase and results in higher reactivity. The negative effect is that Li_2O inhibits the conversion of C_2S to C_3S. The effects of Li_2O are more intense compared to Na_2O and K_2O [1]. According to [2], these effects takes place when Li_2O addition is higher than 1 %.
Saraswat et al [3] stated that Li_2CO_3 addition lowers the decomposition temperature of $CaCO_3$ and the process takes place in two steps. When the addition of dopant is 1 %, CaO formed at low temperature reacts with SiO_2 to form the β-C_2S even at 750 °C. The reaction is completed at 1350 °C, with formation of β-C_2S and small amounts of γ-C_2S. Addition of 5 % dopant

lowers the final reaction temperature down to 1290 °C, the reaction products are β-C_2S and small amounts of C_3S.
Kolovos et al [4] examined addition of 2.5 % Li_2O into clinker raw meal. After sintering at 1450 °C, the samples were examined using SEM. Distinct differences compared to reference clinker were observed, concerning specifically the size and shape of belite grains. The alite crystals were coarse (size of 80-200 μm), prismatic and deposited in an idiomorphic underlay of belite. Belite distribution around alite grains was in a shape of fish bone composed of mix of elongated and roundish grains. Li oxides easily form eutectic mixtures with SiO_2. According to the authors, Li effect on crystallization and development of silicates in clinker causes very unique belite configuration.
As an admixture (in adequate amount), Li can reduce the alkali-silica reaction in concrete, mainly in form of salts like LiOH or Li carbonates. It can be possible that Li in clinker has similar effect. [1]
Taylor [5] stated that lithium salts are strong accelerators of hydration process.

2. Materials and methods

Raw meals were prepared from chemically pure phases so that the effect of Li_2O addition on temperature of clinker melt formation and phase composition can be observed. As Li_2O source Li_2CO_3 was used. All together 7 raw meals were prepared with different Li_2O content in burned clinkers (0, 0.5, 1, 2, 3, 4 and 5 wt.%). The addition of Li_2O replaced a part of CaO. Reference raw meal composition was 78.07 % $CaCO_3$, 15.85 % SiO_2, 3.71 % Al_2O_3 and 2.36 % Fe_2O_3.
Raw meals were examined by DTA Netzsch Perseus STA 449 apparatus with temperature increase 10 °C/min up to 1450 °C.
Raw meals were burned in forms of tablets with temperature increase was 10 °C/min up to 1450 °C with 4 hours hold. Cooling was done in 2 different ways. Fast cooling – immediate pulling out of furnace and cooling by water. Slow cooling – clinker remains in furnace till 1400 °C then it is pulled out and cooled down in laboratory conditions.
Phase analyses of clinkers were done by X-ray diffraction method on the Bruker D8 Advance apparatus with Cu anode (λKα = 1.54184 Å) and variable divergence slits at Θ-Θ Bragg-Brentano reflective geometry. Quantitative phase analyses were done by Rietveld method using Topas software.
Clinker microstructure was observed on the surface of polished section etched by acetic acid [6] in reflective light of polarization microscope Nikon Eclipse LV100. Some phases were also observed by SEM by back scattered electrons (BSE) on apparatus JEOL JSM-7600F.
Another experiments were done using industrial raw meal which is not chemically pure. The raw meal was doped with 0.5 and 1 wt. % of Li_2O in form of Li_2CO_3. Basic chemical parameters of the raw meal are LSF = 96, SR = 2.53 and AR = 0.74 (LSF – Lime saturation factor, SR – Silica ratio, AR – Alumina-iron ratio). Residuum on 0.09 mm sieve is 12 wt. %.
Reference industrial raw meal was burned up to 1450 °C. Meals with Li_2CO_3 addition were burned up to 1350 °C. Clinker was cooled at laboratory condition.
Quantitative phase composition of these clinkers was evaluated by microscopic point counting method on polished section etched by acetic acid. The following specific weights of

clinker phases were used for vol. % to wt. % recalculation: C_3S – 3.15; C_2S – 3.28; C_3A – 3.03; C_4AF – 3.77; free CaO – 3.35 $g.cm^{-3}$.
Clinkers with addition of gypsum as a setting regulator were ground in laboratory ball mill to the same specific surface (400 m^2/kg). Specific surface was determined by Lea and Nurse permeability method according to British standard BS 12:1958. Standard mortar bars were prepared according to EN 196. Strength development (EN 196-1) and heat of hydration (EN 196-8) were determined after 2, 7, 28 days.

3. Results and discussion

3.1 Thermal processes in raw meal

DTA measurement shows endotherm of Li_2CO_3 decomposition even in the raw meal with the lowest Li_2O content – the minimum of the endotherm is at 643 °C. In the raw meal with the highest Li_2O content, the peak of Li_2CO_3 decomposition is at 662 °C. $CaCO_3$ decomposes at 875 °C in the reference raw meal. In raw meals with higher Li_2CO_3 content, the endotherm is split as stated in [2,3]. Raw meal with the highest Li_2O content has two minimums of this double endotherm at 820 and 860 °C. Temperature of melt formation decreases rapidly with Li_2O content in raw meal (see Tab. 1).

Table 1: DTA results of raw meals in °C.

Raw meal	RM-0Li	RM-0.5Li	RM-1Li	RM-3Li	RM-5Li
Temperature of melt formation onset	1333	1252	1218	1174	1157
Temperature of minimum of melt formation endotherm	1404	1365	1352	1325	1320

3.2 The influence of Li_2O on the clinker phase composition

The burned clinkers show that Li_2O significantly lowers viscosity of melt. Clinkers with 1 and 2 wt.% Li_2O were considerably more sintered than clinker without Li_2O or with 0.5 wt.% Li_2O. Clinkers with higher Li_2O content were greatly melted and coloured by lithium to brown-pink.
The phase composition of individual clinkers burned from pure raw meals with graded Li_2O contents is given in Tab. 2. The number in clinker designation shows theoretical Li_2O content in clinker if there is no partial evaporation during burning.
The results have shown decrease of alite amount and increase of belite and free lime in clinkers with Li_2O that were cooled slowly. As can be seen by microscope, alite crystals decompose to submicroscopic mixture of belite and free lime even in clinkers with the lowest Li_2O addition. Almost all of the alite is decomposed in clinkers with more than 3 wt.% of Li_2O. In case of fast cooling this phenomenon is nearly supressed. Therefore, there is no inhibition of conversion C_2S to C_3S as stated in [1] but the decomposition of formatted C_3S to C_2S and C takes place.
This phenomenon, which is connected to burning conditions and cooling of clinker, will be the subject of following research. Fig. 1 and 2 show examples of microstructure of burned clinkers. Due to lower viscosity of burned clinkers nucleation decreases and alite crystals

grow faster. The crystals are very big – more than 200 μm and their outer lines are imperfect. For example, addition of SO_3 has similar effect [7].

Table 2: Quantitative phase composition of clinkers in wt.% evaluated by X-ray diffraction analysis (amount of phase during fast cooling / slow cooling) - C_3S (alite) – $3CaO{\cdot}SiO_2$, C_2S (belite) – $2CaO{\cdot}SiO_2$, C_3A – $3CaO{\cdot}Al_2O_3$, C_4AF – $4CaO{\cdot}Al_2O_3{\cdot}Fe_2O_3$, C (lime) – free CaO.

Clinker designation	**C_3S**	**C_2S**	**C_3A**	**C_4AF**	**C**
C-0Li	73.1/70.6	9.2/11.5	11.4/12.2	5.9/5.4	0.4/0.3
C-0.5Li	70.6/69.4	12.6/14.0	7.6/7.0	8.3/8.9	0.9/0.7
C-1Li	72.3/27.9	11.4/48.4	5.9/1.6	6.7/9.3	2.8/12.8
C-2Li	76.9/33.7	8.8/48.5	7.0/2.1	2.7/2.9	4.6/12.8
C-3Li	77.3/2.8	13.2/67.1	1.3/2.6	1.8/0.6	6.4/26.9
C-4Li	67.8/1.6	21.2/61.8	2.2/2.2	1.5/1.7	7.3/32.7
C-5Li	50.3/0.0	38.7/56.7	2.3/2.1	0.9/4.0	7.8/37.2

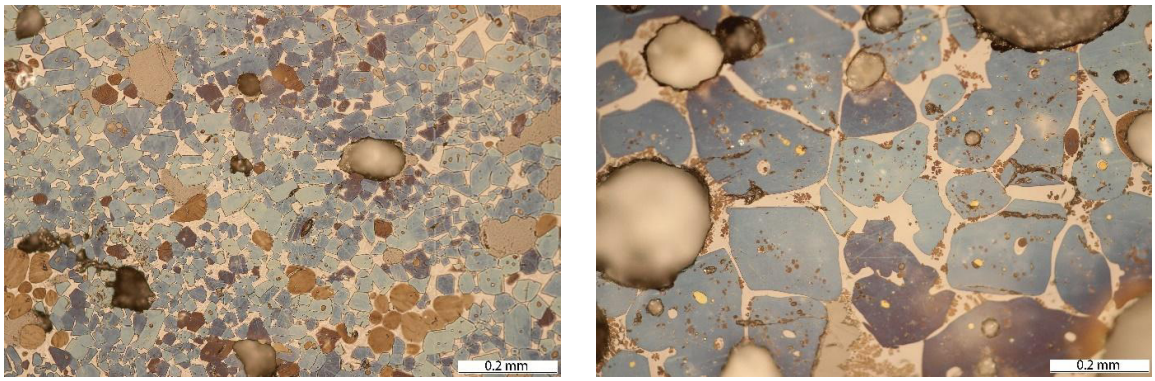

Figure 1: Microstructure of burned clinkers. Left – clinker C-0Li (fine blue alite crystals, nests of brown round belite grains in the right bottom corner). Right – clinker C-2Li with fast cooling (big alite crystal, small belite grains in white ground mass).

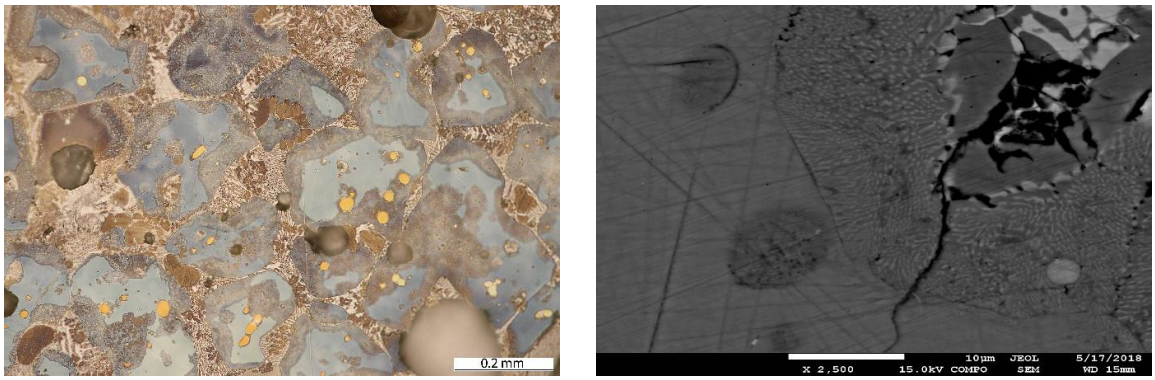

Figure 2: Left – microstructure of clinker C-2Li with slow cooling (big alite crystals with obvious zones of decomposition, fine dendric belite can be seen in ground mass). Right – a part of alite with decomposition zone taken by BSE.

3.3 The influence of Li_2O on the properties of cement

Microscopical determination of quantitative phase composition of clinkers for cement preparations can be seen in Tab. 3. The basic parameters of these cements are given in Tab. 4. Phase composition of these clinkers confirms results from chapter 3.2 – increase of Li_2O results in decrease of alite content which decomposes to submicroscopic belite and free lime. This phenomenon is also evident in scanning electron microscopy (see Fig. 2).
The results in Tab. 4 shows that higher degree of sintering and greater content of belite in clinkers containing Li_2O cause worse grinding ability by up to 18% – expressed as grinding time on the same specific surface. Setting of the cement prepared from clinker containing Li_2O is a little faster than reference cement CEM-0Li/P.

Table 3: Quantitative phase composition of clinkers in wt. % determined by X-ray diffraction analysis.

Clinker designation	C_3S	C_2S	C_3A	C_4AF	C	C_3S decomposed
C-0Li/P	69.2	14.1	2.8	13.9	0.0	0.0
C-0.5Li/P	51.5	20.6	6.0	13.7	0.7	6.9
C-0.5Li/P*	51.8	25.9	6.1	13.8	2.5	*
C-1Li/P	52.6	23.8	5.2	7.3	0.9	9.4
C-1Li/P*	53.0	31.1	5.3	7.4	3.3	*

* Composition with recalculation of decomposed C_3S to C_2S and C.

Table 4: Basic parameters of prepared cements.

Cement designation	Specific surface [m^2/kg]	Grinding time [mins]	Normal consistency [%]	Initial setting time [hours : mins]	Final setting time [hours : mins]
CEM-0Li/P	400	195	28.0	3 : 40	4 : 40
CEM-0.5Li/P	399	220	27.7	3 : 20	4 : 00
CEM-1Li/P	400	230	27.7	2 : 30	3 : 10

The most important properties of cements are their compressive strengths, which are mentioned in Fig. 3. Short-term strengths after two days are approximately the same for all cements. In later stages of hydration, the strengths of the Li_2O-containing cements are lower by about 28% after 7 days and by about 20% after 28 days compared to cements without Li_2O. However, it should be noted that Li_2O-containing clinkers were burned at a lower temperature by 100 °C than the clinker for reference cement. From this perspective, the cements can be classified as low-energy with very high strength and they fulfil requirements for the 42.5R strength class according to EN 197-1. In addition, the cements have a favourably reduced hydration heat as can be seen in Fig. 3.

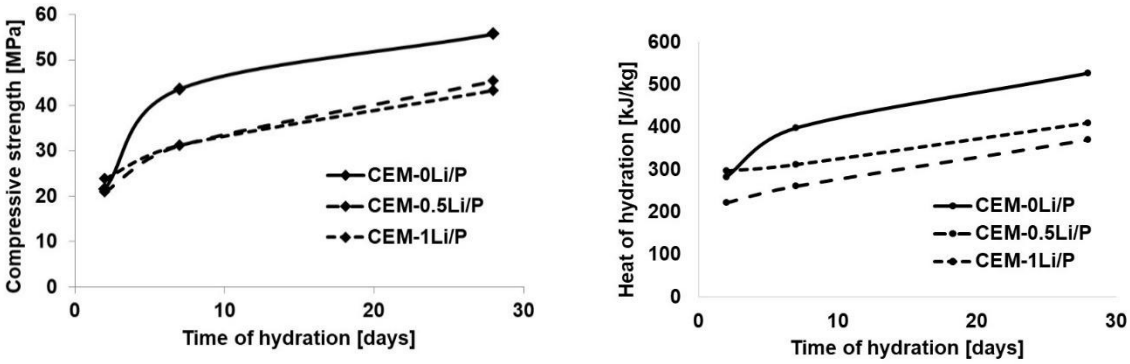

Figure 3: Left – development of compressive strength according to EN 196-1. Right – heat of hydration determined by dissolution method according to EN 196-8.

4. Conclusions

The presence of lithium in raw meal has a significant mineralization effect on the formation of clinker. It causes a significant decrease of melt formation temperature and decreases the viscosity of melt. This enables burning of clinker at lower temperatures with sufficient alite content. Lowering the viscosity causes a reduction in nucleation and an increase in the growth rate of alite crystals. Therefore, less alite crystals of large dimensions are formed.
Higher additions of Li_2O have a significant negative effect during slow cooling and cause decomposition of alite to a submicroscopic mixture of belite and free lime.
It has been found that clinkers with 1 wt. % addition of Li_2O can be burned at temperature lower by 100 °C with similar properties as conventional clinker. Cements prepared from these clinkers have parameters of CEM I 42.5 R when grinded to the standard fineness.

Acknowledgement
This research was done within the project No. 16-08959J financed by the Czech Science Foundation.

References

[1] Role of Minor Elements in Cement: Manufacture and Use. Javed I. Bhatty (Ed.), PC Association, Skokie (1995)
[2] Kolovos, K. et al, The effect of foreign ions on the reactivity of the $CaO–SiO_2–Al_2O_3–Fe_2O_3$ system. Part II: Cations, Cem Concr Res 32 (2002), 463-469
[3] Saraswat, P. et al, Thermal studies of the $CaCO_3$:SiO_2 (2:1) system containing lithium as dopant. Termochim Acta 97 (1986) 313-320
[4] Kolovos, K. et al, SEM examination of clinkers containing foreign elements. Cem Concr Comp 27 (2005) 163-170
[5] Cement chemistry. H. F. W. Taylor (Ed.), Academic press, London (1990)
[6] Chromý, S., Anfärben des freiem CaO und Silikate in anschliffen von Portlandklinker. Z-K-G, 27(1974), 79-84
[7] Maki, I. and Goto, K., Factors influencing the phase constitution of alite in Portland cement clinker. Cem Concr Res 12 (1982), 301-308

SynerCrete'18 International Conference on Interdisciplinary Approaches
for Cement-based Materials and Structural Concrete
24-26 October 2018, Funchal, Madeira Island, Portugal

PROPOSAL OF A TEST SET UP FOR SIMULTANEOUS APPLICATION OF AXIAL RESTRAINT AND VERTICAL LOADS TO SLAB-LIKE SPECIMENS: SIZING PRINCIPLES AND APPLICATION

José Gomes [(1)], Miguel Azenha [(1)], José Granja [(1)], Rui Faria [(2)], Carlos Sousa [(2)], Behzad Zahabizadeh [(1)], Ali Edalat-Behbahani [(1)], Dirk Schlicke [(3)]

(1) University of Minho, School of Engineering, ISISE, Guimarães, Portugal
(2) Faculty of Engineering of the University of Porto, CONSTRUCT, Porto, Portugal
(3) Institute of Structural Concrete, Graz University of Technology, Graz, Austria

Abstract
Cracking control in reinforced concrete (RC) is a key factor to ensure proper service life behaviour. However, current design recommendations are unable to provide straightforward methodologies for crack width prediction in RC structures subjected to the combined effects of applied loads and restrained deformations, which is a common situation in civil engineering. This is motivated by the lack of knowledge about the complex interactions that take place between self-imposed deformations, viscoelasticity and the effects of applied loads in the process of crack development.
A major challenge in studying these combined effects is the validation of numerical simulations with real scale experimental data. For that purpose, an experimental system for testing real scale RC slabs subjected to the above-mentioned conditions was developed. This system is capable of inducing a prescribed axial restraint to the slab, in correspondence to a high restraint degree that induces cracking in view of expectable shrinkage. At the same time, the setup enables the application of vertical loads. The experimental results obtained in this work allowed for the validation of the test setup, as well as the suitability of the slab geometry and reinforcement.

1. Introduction

Cracking in RC structures is an acceptable phenomenon when controlled, but it is one of the main factors that affect structural durability when crack width exceeds the recommended limits. The design of RC structures that meet safety, functionality and aesthetic requirements

during their lifespan, without additional maintenance costs, depends also on adequate design practices that allow engineers to properly predict expectable crack widths.
Even though there is a wide body of design codes and recommendations providing practices for predicting the crack width due to applied loads or imposed deformations, they do not provide unambiguous rules for estimation of crack width under the combined effects of applied loads and restrained shrinkage. Different simplified approaches based on the application of CIRIA C660 [1], simplified combinations of the Eurocode framework, deformation-based methods [2] and explicit crack width calculations in composed bending with a percentage of the cracking axial force [3] may lead to differences in reinforcement for controlling crack width as large as 50% [4]. In view of such challenges, several authors have used the finite element method (FEM) to perform nonlinear numerical analyses in RC structures subjected to the combined effect of applied loads and restrained shrinkage, to quantify the stresses and forces which occur due to these effects [5-8]. These works, although very important to better understand the stress/crack development mechanism of such structures, are still lacking the experimental validation of long-term real scale tests.
This paper intends to show the development of an experimental system for testing real scale RC slabs under the above-mentioned effects. The paper starts by explaining the principles behind the design of the test specimens and the system requirements. After describing the test setup and procedures, the results of the preliminary test are discussed, and the suitability of the test setup and necessary improvements are addressed. This paper is a short version of the report of the research project IntegraCrete on the same matter [9].

2. Sizing and requirements

The main requirement of the developed testing system is the ability to provide an axial controlled restraint to a slab-type specimen, while simultaneously allowing it to be loaded with sustained bending/shear. It was intended to simulate a stretch of slab on a highly restrained condition, whilst monitoring the restraining forces, the in-plane and out-of-plane deformations and the reinforcement strain.
The design of the tested specimen corresponded to the simulation of a real-case one-way slab supported by transverse beams, under high axial restraint. Spans of 4.0m were considered for the slab, and a sizing considering permanent loads of 2kN/m^2 (acting together with the self-weight) and variable loads corresponding to class A of EN1991-1-1 [10] (2kN/m^2 plus 1.2kN/m^2 relative to movable partitions) was performed. The slab was designed for the ultimate and service limit states according to EN1992-1-1 [11], which resulted in a 0.10m thick slab, reinforced for bending with ϕ8//0.10 in the bottom face. This provides adequate behaviour without direct consideration of restraint, which was considered a design start point.
As the experimental setup was devised to test the slab under simply supported conditions, the 4.0m span was corrected to match the distance in between zero bending moments, which corresponds to approximately 3/5 of the span. Therefore, the test setup has a free span of 2.4m. The slab is supported by a perpendicular rod at each extremity (Fig. 1), and even though cracking is expected in such region due to stress concentration, the control region for restraint will be limited to 1.4m in the mid-span. The specimen is 0.50m wide, as to ensure a width-to-height ratio of 1/5, and therefore have a standard slab-type behaviour.

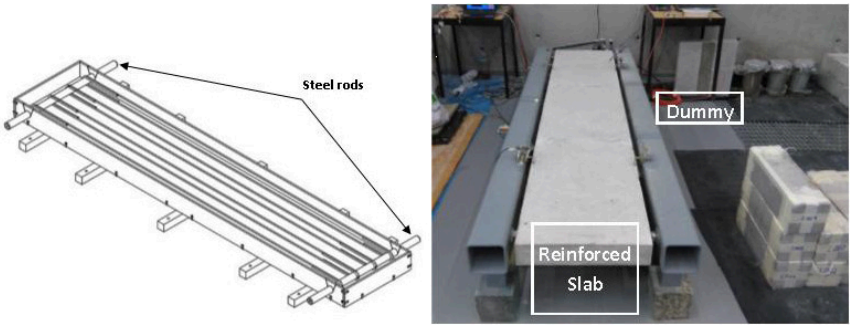

Figure 1: Slab formwork and steel rods (left); test setup (right).

3. Test set up and procedures

The long-term experiment that simultaneously combine the effect of self-induced deformations together with applied loads is conducted through the instrumentation of two specimens: a RC slab tested on the restraint frame and an unrestrained complementary plain concrete specimen (dummy) (Fig. 1). Furthermore, nine cubes (15cm edge) and three cylinders (15cm diameter; 30cm length) of the same batch were used for characterization of the concrete at different ages (compressive strength according to EN12390-3 [12] and E-modulus according to LNEC E397 [13]). The above-mentioned test setup, designed according to Section 2 to ensure the necessary performance requirements, is described next.

3.1 Geometry and materials

The slab, made of a C20/25 concrete strength-grade class, is 2.6m long and has a transversal cross-section of $0.5\times0.1m^2$. A free span of 2.4m is assured by two 40mm steel rods embedded in the slab at mid-height and connected to the restraint frame (see Fig 1).

Even though the design of the slab reinforcement that has been addressed in Section 2 foresees a solution of 8mm rebars spaced by 100mm, for this prototype slab both top and bottom flexural reinforcement are materialized with 8mm rebars transversely spaced by 125mm (larger than 100mm as initially planned due to a placement mistake, which was however considered acceptable for the sake of this prototype testing stage). A secondary transverse reinforcement of 6mm rebars spaced by 300mm was applied, to fulfil the rule of 20% of the principal reinforcement, as recommended by EN1992-1-1 [11]. The described reinforcement has a concrete cover of 22mm. The complementary specimen is made of plain concrete of the same batch of the slab, has the same cross section ($0.1\times0.5m^2$) and is 0.5m long. This specimen is not restrained, being simply placed vertically next to the restrained slab.

The slab was cast and tested in an experiment room without specific control of temperature or humidity. Recorded temperatures during test indicate variations between 20-28ºC. Environmental humidity ranged 50-70%. Concrete was kept from drying before demoulding of the slab and dummy (at 7 days) using a plastic foil. From 7 days onwards, the slab was subjected to drying at all surfaces.

3.2 Restraining device

The slab is simply supported and its axial deformation is restrained by controlling the axial force of the slab using hydraulic actuators, placed inside a metallic frame and connected to the

steel rod embedded in the slab. This frame is constituted by two 2.65m long rectangular hollow section (RHS) steel profiles with outer dimensions of 140×140mm^2 and an inner hollow region of 124×124mm^2, supported by two 0.15m long RHS with outer dimensions of 80×80mm^2 and an inner hollow region of 72×72mm^2 (Fig. 2).

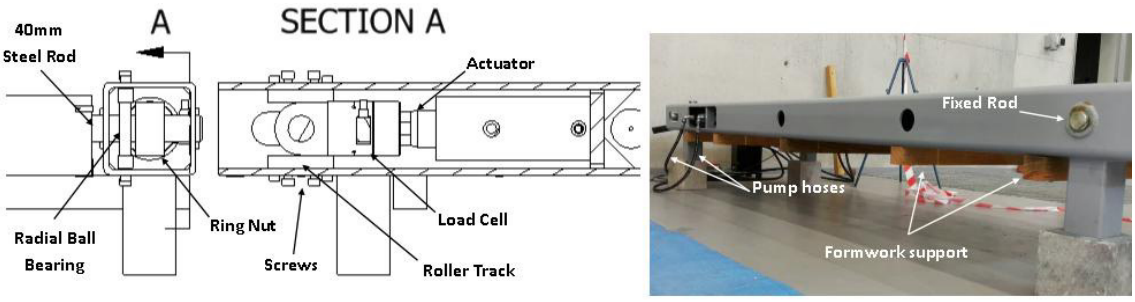

Figure 2: Restraining device: inside the metallic frame (left) and overview (right).

Each longitudinal RHS has five drills on the bottom to enable the fixation of the formwork in the frame with wooden slats. On the lateral side there are two 40mm diameter holes to insert both fixed and moving steel rods. The positioning of the moving rod is done with a radial ball bearing between two roller tracks, whose position is adjusted with 4 socket head cap screws (Fig 2). For application of the axial load to the slab, two double effect hydraulic actuators supplied by a manual hydraulic pump are used, each with a 100kN capacity in compression and a 50kN capacity in traction, connected to the moving steel rod embedded in the slab.
Information about self-induced deformations of the slab are given by the dummy, and in both specimens the temperature and deformations are measured by means of electrical resistance stain gauges for rebar stress/strain assessment, a vibrating wire strain gauge (VWSG) acquiring the dummy deformation, linear variable displacement transformers (LVDT's) for slab deflection and longitudinal strains measurement and resistance temperature detectors (RDT's). The axial force applied by the actuators is measured by two load cells connected to the 40mm steel rod through a ring nut (Fig. 2).
On each side of the slab, one LVDT is fixed to a bracket, partially embedded in the concrete with a metallic clamp, and the concrete deformation in the central region of the slab is measured using a steel cable in tension, fixed between the other bracket and a steel plate in contact with the LVDT, as the steel plate is connected to the LVDT bracket with two springs (Fig. 3). With this spring system it was possible to measure the longitudinal strains of the slab during the application of the axial load.

4. Results

The test specimens were cast and left undisturbed for 7 days, with the actuators fully inactive (and free to move). At the age of 7 days (~174h), both the slab and dummy were demoulded and a tensile axial load of approximately 16kN was applied. The result of such load application in both load cells and longitudinal LVDTs is shown in Fig. 4. The longitudinal strain of 10-15με measured by the LVDTs was consistent with the corresponding calculated value, taking into consideration the geometry of the slab and the modulus of elasticity of the rebars and concrete [14] (200GPa and 26.3GPa, respectively): ~12 με, although a more

precise concrete strain measuring device must be devised for next experiments in order to minimize the noise-to-signal ratio of the system.
At the age of 59 days the slab was loaded with 14 concrete blocks adequately spaced to avoid arch effects, and to simulate a quasi-permanent load combination (live load of 2.96kN/m^2). The blocks were placed sequentially from the mid-span towards the supports, leading to the formation of a single crack at mid-span, with a width of approximately 0.2mm, as shown in Fig. 4. As it was expected, the measured crack was wider than what is predicted from the EN1992-1-1 [11] formulation (~0.07mm), since the combined effect of restrained shrinkage and applied loads has to be taken into account.

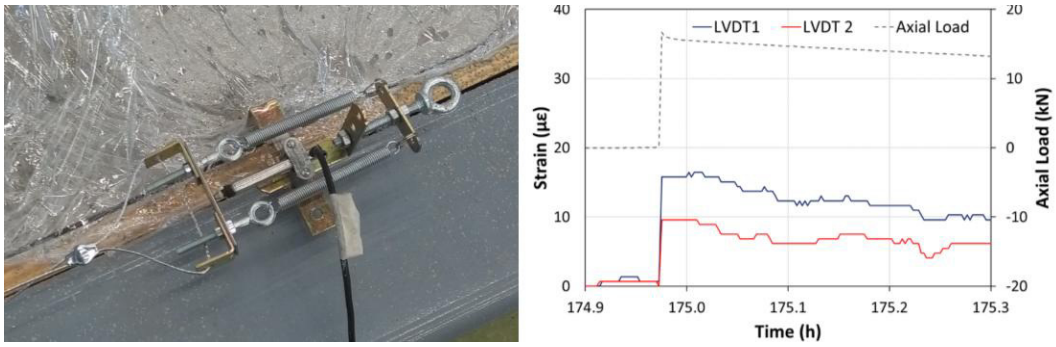

Figure 3: Concrete strain measurement setup (left) and results after axial loading (right).


Figure 4: Load blocks (left) and crack at midspan after application of the load blocks (right).

5. Conclusions

The current work describes the arrangement and preparation of the experimental setup designed for conducting long-term tests with real scale slabs subjected to the combined effect of applied loads and restrained shrinkage deformations.
The formwork support solution proved to be adequate, in the sense that it was possible to easily mount it and demould it in the restraining frame. The geometry of the specimens was accurate and therefore viable.
So far, the monitoring devices showed satisfying results at past key moments. Although there is some oscillation on the strain measurements, this was mostly caused by the fact that the experiment was not conducted in a controlled temperature chamber. This will be overcome in the next setup application. Even though the LVDT measurement system shown performed well, there are still operational drawbacks that can jeopardize reliability and thus deserve improvement in order to minimize the noise and the influence of the curvature of the slab in

the measurement. The loading frame/setup has demonstrated capacity to impose and keep/control of the axial load, with an example application being demonstrated herein.
In general, it can be claimed that the trial experiment has shown to be successful and that relevant hints for improvement were obtained. The production of a second setup is envisaged for a wider program to be conducted on long term.

Acknowledgements
This work was financially supported by: Project POCI-01-0145-FEDER-007457 (CONSTRUCT - Institute of R&D in Structures and Construction) and by project POCI-01-0145-FEDER-007633 (ISISE), funded by FEDER funds through COMPETE2020 - Programa Operacional Competitividade e Internacionalização (POCI), and by national funds through FCT - Fundação para a Ciência e a Tecnologia. FCT and FEDER (COMPETE2020) are also acknowledged for the funding of the research project IntegraCrete PTDC/ECM-EST/1056/2014 (POCI-01-0145-FEDER-016841). The financial support of COST Action TU1404 through its several networking instruments is also gratefully acknowledged.

References
[1] Bamforth, P.B., C660: Early-age thermal crack control in concrete, in CIRIA, UK (2007)
[2] Schlicke, D. and Tue, N.V., Crack width control–verification of the deformation compatibility vs. covering the cracking force, Proc. MSSCE2016/Service Life Segment, Denmark (2016)
[3] Camara, J. and Luís, R., Structural Response and Design Criteria for Imposed Deformations Superimposed to Vertical Loads, Proc. *fib* Congress, Italy (2006)
[4] Azenha, M. and Granja, J., Seminar: Design of reinforcement for RC elements under the combined effect of applied loads and restrained shrinkage. E-book of presentations. 2017: Zenodo. http://doi.org/10.5281/zenodo.800693
[5] Luis, R., Análise e dimensionamento de estruturas de betão com sobreposição de cargas e deformações impostas, MSc thesis; Universidade Técnica de Lisboa (2005)
[6] Carvalho, J.F., Estudo da fendilhação em lajes restringidas devido ao efeito conjunto da retração e das ações distribuídas no piso, MSc thesis, Universidade do Porto (2013)
[7] Felisberto, E.A.d.O., Análise de lajes maciças de edifícios atendendo aos efeitos da retração restringida e às ações gravíticas, MSc thesis, Universidade do Porto (2015)
[8] Carvalho, R., Rumo à análise 3D pelo método dos elementos finitos do efeito combinado de ações diretas a da retração impedida em lajes de betão armado, MSc thesis, Universidade do Minho (2017).
[9] Gomes, J. et al, Task 4 – Setting up for long term experimental framework, IntegraCrete Report, Universidade do Minho (2017)
[10] CEN, Eurocode 1 EN 1991-1-1 Actions on structures - Part 1-1: General actions -Densities, self-weight, imposed loads for buildings, CEN: Brussels (2004)
[11] CEN, Eurocode 2 EN 1992-1-1 Design of concrete structures Part 1-1 General rules and rules for buildings, CEN: Brussels (2004)
[12] IPQ, Ensaios do betão endurecido: Parte 3 - resistência à compressão de provetes NP EN 12390-3, IPQ: Caparica (2011)
[13] LNEC, Especificação LNEC E397: Betões. Determinação do Módulo de Elasticidade em Betões. Lisboa (1993)
[14] Beer, F. P. and Johnston Jr., E.R., Mechanics of materials. 3rd ed., McGraw Hill, USA (2001)

SynerCrete'18 International Conference on Interdisciplinary Approaches
for Cement-based Materials and Structural Concrete
24-26 October 2018, Funchal, Madeira Island, Portugal

RESISTANCE TO SULFATE AND ACID ATTACK OF SELF-COMPACTING CONCRETE WITH RECYCLED AGGREGATES

Said Kenai [(1)], Mohamed Omrane [(1, 2)]

(1) University of Blida 1, Algeria
(2) University of Djelfa, Algeria

Abstract
Natural aggregates are sometimes lacking around big cities but construction and demolition waste debris are available to manufacture recycled aggregates. The durability performance of SCC with natural aggregates is well investigated. However, the durability of SCC with recycled aggregates under aggressive environments such as sulfate and acid attacks that could be encountered in structures near the sea, in aggressive soils or sewage treatment plants needs to be elucidated. In this paper, SCC mixes with only natural aggregates (SCCN) or 50% natural aggregates and 50% recycled coarse and aggregates (SCCR) were immersed in 3% hydrochloric acid (HCl) and 5% sodium sulfate (Na_2SO_4) and the weight loss measured as well as visual inspection and XRD tests. The experimental results indicate that recycled aggregated reduced the resistance to aggressive environment. The addition of 15% to 20% of natural pozzolan mitigated this negative effect.

1. Introduction

Recycled aggregates from construction and demolition waste (CDW) production worldwide is important. In 2014, the total waste generated in the EU-28 by all economic activities and households amounted to 2 503 million tons; of which 34.7% comes from CDW activities (Eurostat, 2017) [1]. The performance of concrete with recycled aggregates from CDW has been investigated extensively [2]. However, their incorporation in self-compacting concrete is less investigated especially under the effect of aggressive environments. Self-compacting concrete is highly flowable concrete with high paste content and hence cement replacement materials such as slag, natural pozzolan, limestone fillers and metakaolin are used. SCC with both recycled aggregates and mineral additions could be considered as an eco-concrete as it reduces the CO_2 emission by reducing the cement content and reduces the consumption of

natural aggregates and hence help reducing the depletion of natural resources. The addition of mineral admixtures also mitigates some of the drawbacks of recycled aggregates addition such as reduction of compressive and tensile strength, increase of water and air permeability, a decrease in chloride penetration resistance and a decrease in sulfate attack [2-4]. In this paper, the resistance of SCC with recycled aggregates and natural pozzolan under acid and sulfate attack is investigated. These aggressive environments could be encountered in many structures like foundations on aggressive soils and slabs in industrial sites.

2. Materials and experimental program

CEM II/A-L 42.5R with a fineness of 300 m^2/kg was used. A local natural pozzolan (PZ) from volcanic sediments in Beni–Saf quarry in the west of Algeria was crushed in a laboratory mill to a fineness of 400 m^2/kg was used to partially replace cement. The chemical composition of cement and natural pozzolan is shown in Table 1. Concrete slabs (25 MPa grade) of 1m x 1m x 0.1m were manufactured in the laboratory and crushed at the age of 28 days. The crushed material was sieved to obtain the various recycled aggregate fractions. 50% substitution by weight of both fine and coarse natural aggregates by fine and coarse recycled aggregates was adapted. The ratio of replacement for natural pozzolan were (5%, 10% and 15%) for natural self-compacting concrete (NSCC) and (5%, 10%, 15% and 20% for recycled self-compacting concrete (RSCC) by mass of cement. The water/binder ratio was kept constant at 0.42 and an Ether polycarboxylates super-plasticizer (SP) that complies with EN 934-2 was used. The concrete mix proportions are summarized in Tables 2 and 3.
The resistance to aggressive environments was evaluated by the measurement of the loss in mass after immersion in sulfate solutions (5% sodium Na_2SO_4) or in 3% acid solutions (hydrochloric acid (HCl)), was measured after 1, 7, 14, 21, 28, 90 days and 180 days of immersion. The solutions were renewed after each weighing. Specimens were examined visually for any sign of deterioration and XRD analysis were performed on the outer face in contact with the aggressive solutions after immersion for 180 days.

Table.1: Chemical composition of cement and natural pozzolan

Compound (%)	CaO	SiO_2	Al_2O_3	Fe_2O_3	MgO	Na_2O	K_2O	SO_3	L.O.I
Pozzolan	12.4	43	19	9.5	4	3.0	1.4	--	6.5
Cement	63.6	20.5	5.8	2.6	0.9	0.4	0.9	3.3	--

Table 2: Mixes of SCC with natural aggregates (SCCN)

	SCCN0	SCCN5	SCCN10	SCCN15
Cement (kg)	468	447	425	404
Water (l)	197	196	195	194
Pouzzolane (kg)	0	19	39	59
Sand (kg)	907	907	907	907
Gravel 3/8 (kg)	265	265	265	265
Gravel 8/15(kg)	530	530	530	530
SP (kg)	5.14	5.13	5.11	5.09
W/B ratio	0.42	0.42	0.42	0.42

Table 3: Mixes of SCC with recycled aggregates (SCCR)

	SCCR0	SCCR5	SCCR10	SCCR15	SCCR20
Cement (kg)	458	438	416	396	374
Water (l)	192	192	191	190	190
Pouzzolane (kg)	0	19	38	58	77
Sand * (kg)	841	841	841	841	841
Gravel* 3/8 (kg)	265	265	265	265	265
Gravel*8/15(kg)	530	530	530	530	530
SP (kg)	3.67	3.65	3.64	3.63	3.61
W/B ratio	0.42	0.42	0.42	0.42	0.42

**50% natural and 50% recycled.*

3. Results and discussion

The rheological performance and mechanical test results are reported elsewhere [5]. SCC with recycled aggregates with good rheological properties was obtained when the recycled aggregates content was limited to 50%. The SCCN and SCCR mixtures containing PZ develop a comparable compressive strength to mixtures without PZ at 120 days of age.

3.1 Resistance to sulfates

Figures 1 and 2 shows the variation of mass loss with immersion duration in the sulfate solution for both SCCN and SCCR specimens. For short term immersion (less than 4 weeks), the level of degradation for both types of concrete (SCCN and SCCR) were comparable. However, after 90 days, a slight difference is noticed. SCCN mixes showed a lower mass loss by 18.82% as compared to SCCR mixes. The addition of natural pozzolan enhances the resistance to sulfate attack for both SCCN and SCCR mixes. The loss of mass at 180 days as compared to reference concrete was reduced by 12.2%, 13.7 and 22.62% for SCCN mixes with 5%, 10% and 15% of PZ, respectively. The loss of mass after180 days of immersion for SCCR mixes with 5%, 10%, 15% and 20% of PZ was 1%, 2.28%, 2.28% and 6.1%, respectively. The XRD analysis showed the presence of large quantity of gypsium (g) and etringite (E) (Fig. 3). The intensity of gypsium does not show a significant difference between the two types of concrete with and without recycled aggregates. The portlandite is consumed by the sulfate attack. The attack by Na_2SO_4 forms the gypsium which in its turn participates to the formation of secondary ettringite from C_3A and monosulfoaluminates. The incorporation of natural pozzolan increases the resistance to sulfate attack as it reacts with the portlandite of the hydrated cement to form C-S-H, reduces the capillary pores and reduces the diffusion of sulfate ions into concrete. The beneficial effect of using natural pozzolan is clearly seen on Figs.4 &5 where the visual deterioration is reduced.

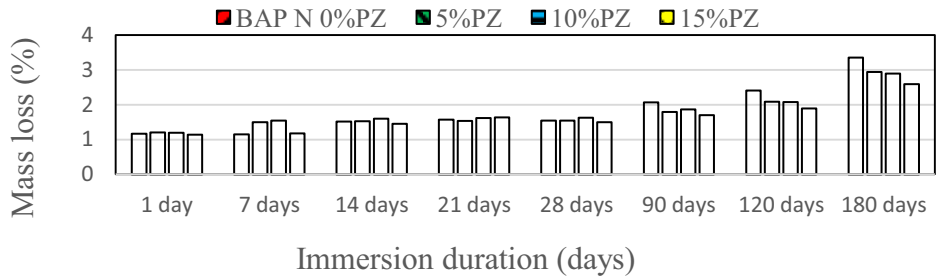

Figure 1: Mass loss of SCCN mixes after immersion in 5% Na_2SO_4 solution.

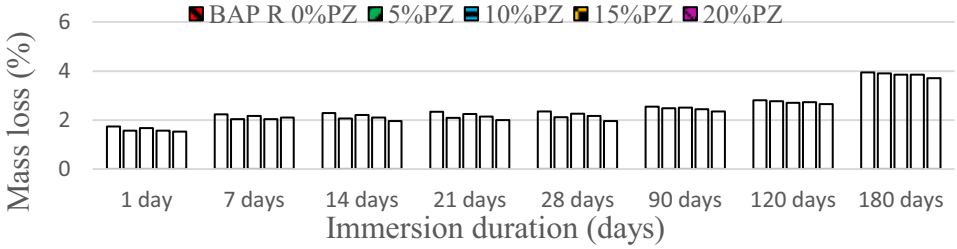

Figure 2: Mass loss of SCCR mixes after immersion in 5% Na_2SO_4 solution.

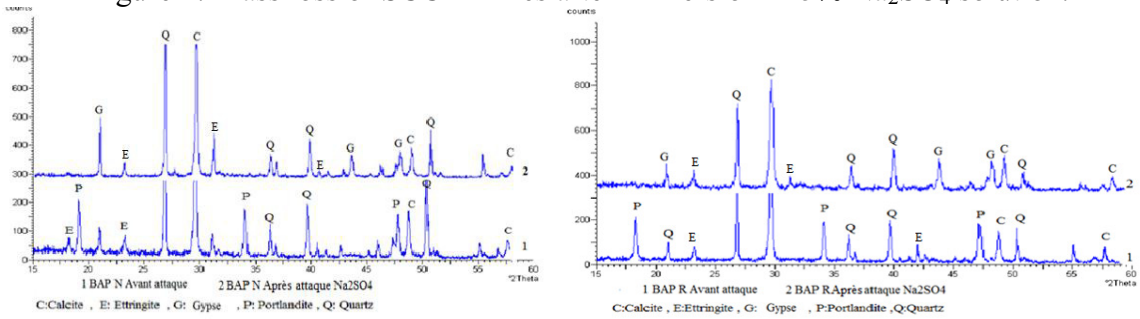

(a) (b)

Figure 3: XRD spectrum of (a) SCCN and (b) SCCR mixes before and after immersion in 5%Na_2SO_4.

Figure 4: SCCN specimens degradation before and after immersion in 5%Na_2SO_4 solution.

Figure 5: SCCR specimens degradation before and after immersion in 5%Na_2SO_4 solution.

3.2 Resistance to acids

Figures 6 and 7 summarized the variation of mass loss with the increase of period of immersion in HCl solution. Similarly to sulfate attack, the performance under acid attack for up to 4 weeks of immersion was comparable. For both SCC with natural and recycled aggregates, a slight difference is noticed after 12 weeks,. The loss of mass was more important for SCCR mixes (24.63%) than SCCN mixes. This shows the low performance of recycled aggregates under HCl acid attack contrary to the beneficial effect on the resistance to the more aggressive 5% sulfuric acid (H_2SO_4) solution reported elsewhere [5]. However, the addition of natural pozzolan enhances the resistance to acid. After 180 days of immersion, the reduction in mass loss was 1.38% and 8.77% for SCCN with 5% and 15% of PZ respectively. The reduction in mass loss was comparable for SCCR mixes with 3.16%, 4.81 and 20% for 5%, 15% and 20% PZ, respectively. The XRD spectrum shows the disappearance of the portlandite after HCl attack (Fig.8). When acid is in contact with cement hydration products, it will react with calcium hydroxide ($Ca(OH)_2$) to form a highly soluble chloride calcium salt. The beneficial effect of adding natural pozzolan is also demonstrated as PZ reacts with portlandite to form C-S-H, fills the pores and reducse the lixiviation. The visual inspection of the specimens also conformed the beneficial effect of natural pozzolan.

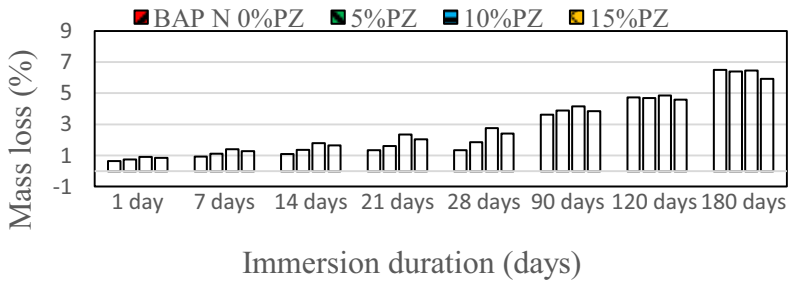

Figure 6. Mass loss for SCCN specimens after immersion 3% HCl solution.

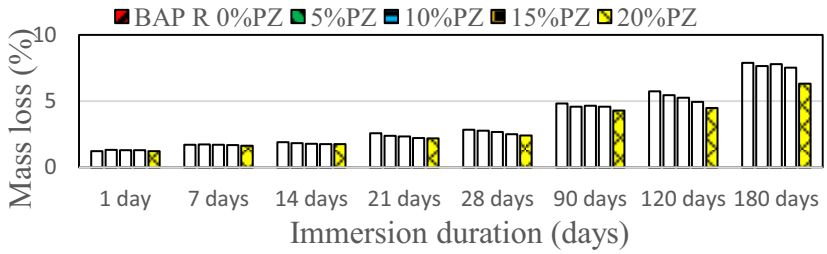

Figure 7: Mass loss for SCCR specimens after immersion 3% HCl solution.

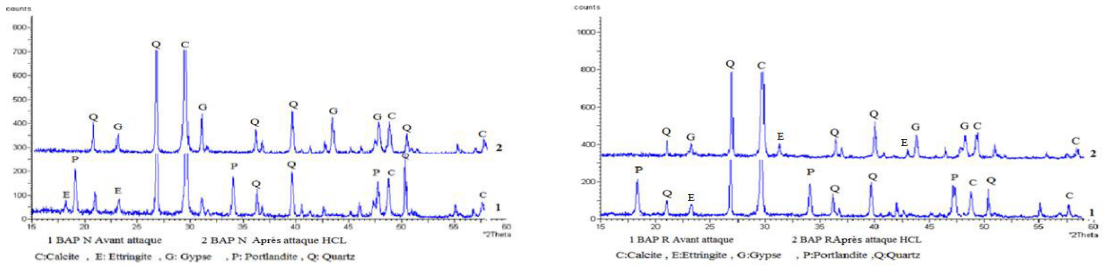

(a) (b)

Figure 8: XRD spectrum of (a) SCCN and (b) SCCR mixes before and after immersion in 3%HCl.

4. Conclusion

The replacement of natural aggregates with recycled aggregates in SCC mixes produced mixes with acceptable rheological and mechanical performance when the substitution level was limited. The resistance to sulfate and acid attacks of mixes with recycled aggregates was lower than that of mixes with natural aggregates as higher mass losses were observed. However, the incorporation of 15% to 20% natural pozzolan increased the resistance to both sulfate and acid attack and compensated partially the detrimental effect of recycled aggregates.

References

[1] Eurostat (2017). Waste statistics in Europe.
[2] Kenai, S. Recycled aggregates, chapter 3 in Waste and supplementary cementitious materials in concrete, edited by Siddique, R. and Cachim, P., Elsevier, 2018, pp. 81-121.
[3] Dodds, W., Goodier, C., Christodoulou, C., Austin, S., Dunne, D. (2017). Durability performance of sustainable structural concrete: Effect of coarse crushed concrete aggregate on microstructure and water ingress. Construction and Building Materials 145, pp. 183–195.
[4] Kapoor, K., Singh, S.P., Singh, B. (2017). Permeability of self-compacting concrete made with recycled concrete aggregates and metakaolin. Journal of Sustainable Cement-Based Materials, 6(5), pp. 293-313.
[5] Omrane, M., Kenai, S., Kadri, E.H, Ait-Mokhtar, A Performance and durability of self-compacting concrete using recycled concrete aggregates and natural pozzolan. Journal of Cleaner Production 165 (2017) 415-430.

SynerCrete'18 International Conference on Interdisciplinary Approaches
for Cement-based Materials and Structural Concrete
24-26 October 2018, Funchal, Madeira Island, Portugal

SELF-COMPACTING CONCRETE WITH RECYCLED CONCRETE AGGREGATE AS ECOLOGICAL MATERIAL

Iva Despotović[(1)], Ksenija Janković[(2)], Dragan Bojović[(2)], Marko Stojanović[(2)]

(1) Belgrade University College of Apllied Studies in Civil Engineering and Geodesy, Serbia
(2) IMS Institute, Belgrade, Serbia

Abstract
The concept of sustainable development, which in addition to social and economic aspects, includes energy saving, environmental protection and the conservation of exhaustible natural resources, is a strategic goal of many economic sectors including the particular contribution expected from the construction. Self-compacting concrete contains a certain amount of powdered materials – fillers. There are various possibilities of selecting this component. If we used any of the industrial by-products, such as fly ash or silica fume, we would solve the problem of depositing these materials, and thus made concrete ecological material. The research subject presented in this paper are the properties and technology of self-compacting concrete in the fresh and hardened state, made with various mineral additives: lime, fly ash, and silica fume, wherein the aggregates used, are both natural and recycled aggregates.

1.Introduction

Construction industry uses vast amounts of natural resources, simultaneously producing significant amounts of construction waste, so that it has a great impact on the environment. Annual production of concrete in the world has reached 10 billion tons, classifying concrete in the most widely used building material. Having in mind the fact that 70 % of concrete is aggregate, it is clear what the quantity of natural and crushed aggregates requires. Uncontrolled exploitation of aggregates from rivers seriously disrupts aquatic ecosystems and habitats, while the production of crushed natural aggregates increases harmful gas emissions, primarily of CO_2, which are responsible for the greenhouse effect. These gases are formed during blasting rocks and during the transportation of aggregates to the usually distant urban areas. On the other hand, the amount of construction waste generated during the construction and demolition of buildings is growing rapidly, deepening the problem of disposing this

waste, which is usually solved by making planned landfills (which occupy large areas of land and disposal is costly) or illegal dumps.
One of the solutions of the mentioned problems is recycling deposited building materials, primarily concrete. This idea is not new and developed countries, like Japan, the Netherlands, Belgium and Denmark achieve a high percentage of recycling of construction waste. Recycled concrete aggregates are mostly used in road engineering, for different fillings and making non-structural elements (curbs, fences, etc). Because of the uneven quality, the possibility of various impurities to rest during recycling, larger water absorption and lower bulk density, compared to natural aggregates, recycled aggregates require a series of tests and special technology of concrete making.
Self-compacting concrete contains a certain amount of powdered materials – fillers. There are various possibilities of selecting this component. If we used any of the industrial by-products, such as fly ash or silica fume, we would solve the problem of depositing these materials, and thus made concrete ecological material.

2. Materials

Self – compacting concrete (SCC), according to many authors "the most revolutionary discovery of concrete industry of the 20th century", does not need vibrating when placing and compacting. It is estimated that when using self–compacting concrete instead of vibrated concrete, the need for workers is reduced by about 10 %; when using prefabricated elements, construction time is shorter by about 5 %, and demand for workers decreased by about 20 %; when applying sandwich elements (steel – concrete) time saving is 20%, and savings in the labour force 50%. The main disadvantages of the use of self – compacting concrete are higher material prices, stricter quality requirements and increasing pressure on the formwork compared to vibrated concrete [1].
The initiators of the idea of applying **fly ash**, resulted from coal burning, in concrete were McMillan and Powers (1934). At the end of 40s the experiments carried out in the UK (Fulton and Marshal) led to the construction of dams Lednock, Clatworthy and Lubreoch, with fly ash as a cement additive. All these structures are after 60 years in excellent condition [2].
Silica fume is formed during melting quartz at high temperature in an electric arc furnace, wherein silicon or ferrosilicon occurs. Due to its nature, even a small addition of silica fume significantly changes physical and chemical properties of concrete. The customary dosage of 8- 10% by weight of cement means between 50 000 and 100 000 microspheres of dust per cement grain, which directly increases the cohesion of concrete. Because of higher specific area and higher content of silicon dioxide, silica fume is much more reactive than fly ash or granulated slag. This increased reactivity initially increases hydration rate of C_3S cement mineral, but after two days the process becomes normal.
Lime is more widely used as a cement additive than a concrete additive. The presence of lime causes the acceleration of the hyd**r**ation process and hydration shrinkage of concrete in the first few hours, because the particles of lime are used as additional cores for hydration.
The use of **recycled aggregates** in structures is not new. Buck (1977) defines its beginning in the period immediately after the Second World War, when there was a tremendous need for building new facilities and infrastructure and at the same time, clearing the existing ruins. After that, the use of recycled aggregates stopped but during 70s the US started to re-use

recycled aggregates in non-construction purposes, mainly as fill material and different fillings in road engineering [3]. Due to the above mentioned reasons, testing of recycled aggregates (not just concrete) and their application are more relevant today than ever, because the need for aggregates globally reached 26.8 billion tons per year [4]. For example, the US annually recycles about 149 million tons of concrete waste. According to the data from the annual report of the European Association for aggregates (2010), recycled aggregates make 5% of the total production of aggregates in the European Union, where Germany is the largest producer, followed by Great Britain (49 million tons), the Netherlands (20 million tons) and France (17 million tons). In Australia, around 50% of the concrete waste is recycled, while in Japan, the impressive 98% of concrete waste is turned into recycled aggregate [5]. It is estimated that in the Republic of Serbia, about 1 million tons of construction waste and demolition waste is annually produced. This waste ends up in landfills of municipal waste, and is also used as inert material for coverage of waste at landfills. Recycling construction waste actually does not exist [6].

3. Experimental research

For the purposes of the experimental work, nine three-fraction concrete mixes have been made. Cement PC 42.5 has been used as well as mineral additives: lime (120 kg/m^3), fly ash (from the power plant, 120 kg/m^3), and silica fume (52 kg/m^3); natural aggregate, recycled aggregate obtained by crushing demolished retaining wall. Control concrete was made with each of the additives and a natural aggregate; in mixes K50, P50 and S50, fraction 8/16mm was replaced by the recycled aggregate, and in mixes K100, P100 and S100, both coarse fractions (4/8 and 8/16) were replaced by recycled fractions. In all the mixes, superplasticizer ViscoCrete 5380 (manufacturer SIKA) has been used. The criterion in the designing mixes was to achieve the same consistency of concrete, i.e. slump-flow class SF2, which includes the usual uses of concrete and involves spreading from 66 to 75cm. When used recycled aggregate, the amount of water which was absorbed by the aggregate in 30 minutes (II fraction 2.22%, III fraction 1.5%) was added, although this principle could not be consistently applied.

3.1 Test results

The test results for concrete in the fresh state are shown in Table 1.

Table 1: Test results for concrete in the fresh state

Concrete mix	Density kg/m3	Slump-flow cm	T500 s	L-box H1/H2	Sieve segregation %
EK	2418	73	4	1	12.4
EP	2288	70	4	0.94	11
ES	2416	66	6	0.91	6.8
K50	2362	70	5	0.96	12
P50	2279	70	5	0.95	7.8
S50	2324	67	5	0.94	5.2
K100	2347	69	5	1	10
P100	2298	66	6	0.91	5.5
S100	2359	66	6	0.92	7.5

Testing compressive strength was carried out on the cubes with edges of 15cm. The test results for compressive strength after 2, 7 and 28 days are shown in Chart 1.

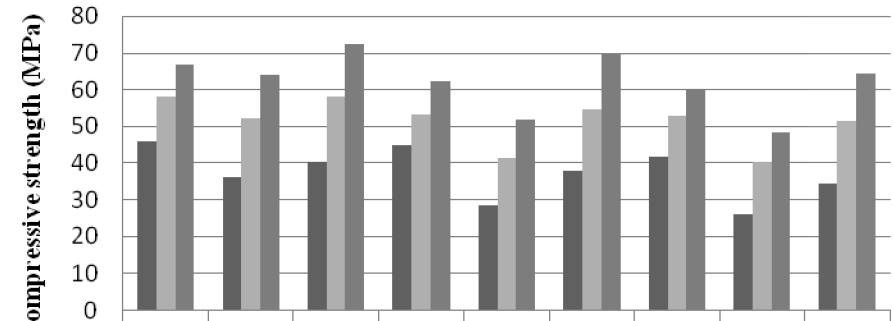

	EK	EP	ES	K50	P50	S50	K100	P100	S100
2 days	46	36.34	40.4	44.82	28.68	37.75	41.86	26.2	34.38
7 days	58.24	52.18	58.05	53.12	41.24	54.67	52.86	40.18	51.59
28 days	66.68	64	72.31	62.17	51.7	69.7	60.3	48.2	64.5

Figure 1: Compressive strength.

Shrinkage test was done on the samples of dimensions 12x12x36cm. 72 hours after the samples are made they are taken out from the water and exposed to thermo hygrometric conditions. We chose it to be 70 ± 5 % air humidity and a constant temperature of 20± 4 °C. First measurement was done 72± 0.5 h hours after the samples were made, and then after 4 and 7 days. After this, further measurements were done after every seven days, until the process stabilized. The results of shrinkage tests after 4, 7, 14, 21, 28, and 35 days, are shown in Chart 2.

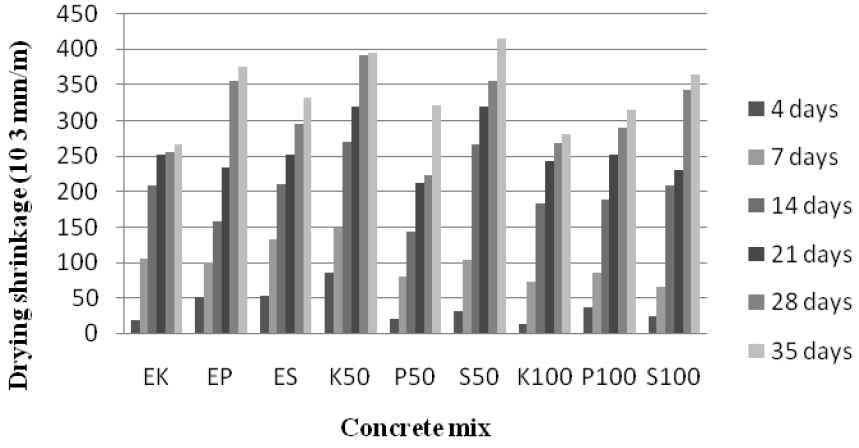

Figure 2: Shrinkage.

Scanning electron microscopy (SEM analysis) enables to "look into" the structure of concrete made and to better explain the results obtained by testing (Figure 1). Water absorption test was done on the samples of dimensions 12x12x36cm, by the method of gradual immersion. The results are in the range of 0.85% (mix S50) to 2.12% (mix EP). The highest water absorption was recorded in the mixes with fly ash, and the lowest in the mixes with silica fume, which is absolutely in accordance with the achieved concrete structure**,** which was,

according to SEM analyses, the most porous in concrete mixes with fly ash. Average water absorption in mixes with silica fume was 0.9%, in mixes with lime 1%, and in mixes with fly ash 2%.

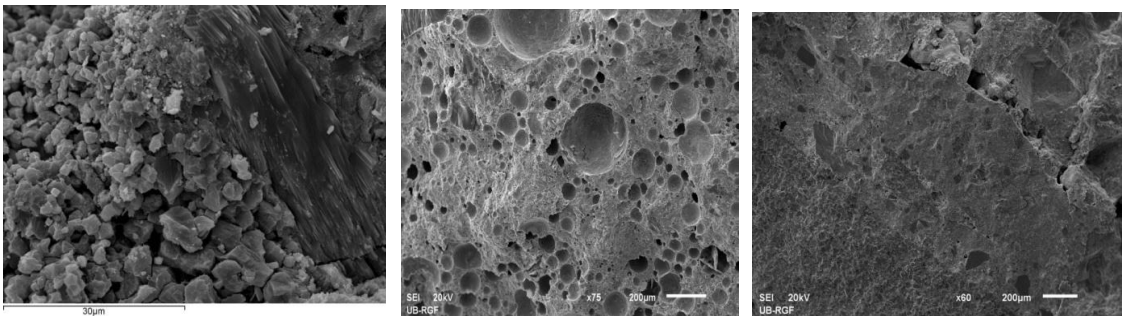

Figure3: Structure of concrete with lime, fly ash and silica fume

4. Discussion

Properties of self-compacting concrete are affected both by a kind of mineral additive and a kind of the applied aggregate. Best properties of self-compacting are achieved by using lime. These concrete mixes had the best fluidity and viscosity, after passing through reinforcement they were absolutely horizontal, but because of the largest spreading, they had minimum segregation resistance. Mixes with fly ash had the best ratio of diameter of spreading (fluidity) and segregation resistance. Since they are very small and have very large area of grain (15 000 to 20 000 m^2/kg), particles of silica fume significantly increase concrete cohesion and adversely affect the fresh concrete self-compacting. Use of recycled aggregates, due to a sharp-edged shape of grains which increases adhesion, also adversely affects the properties of self-compacting concrete, so it was necessary to intervene in the sense of reducing III or increasing I fraction by 5%, in order to achieve the desired consistency.

Effect of silica fume: as concrete starts to bind and harden, pozzolanic activity of silica fume becomes the dominant reaction. Due to the high specific area and higher content of silicon dioxide, silica fume is much more reactive than fly ash. This increased reactivity will initially significantly intensify hydration rate of C_3S cement fraction, but after two days the process becomes normal. As silica fume reacts and forms calcium silicate hydrates, voids and pores in the concrete are filled, wherein crystals formed connect the space between cement particles and aggregate grains. If this effect is added by the physical presence of silica fume in the mix, it is clear that the concrete matrix will be very homogenous and dense, resulting in improved strength and impermeability, which is clearly seen in SEM pictures.

When fly ash is added to concrete, there is pozzolanic reaction between the silicon dioxide (SiO_2) and calcium hydroxide ($Ca(OH)_2$) or lime, which is a by-product of hydration of Portland cement. Weak pozzolanic reaction occurs during the first 24 hours at a temperature of 20˚C. That is why, for a given amount of cement, with increasing fly ash content, lower early compressive strength is achieved. The presence of fly ash slows the reaction of alite in Portland cement at an early stage. Slower early strengths of concrete with fly ash prevent its application where high early strength is expected, which can be solved by using accelerator.

The effect of lime: SEM analyses show the presence of lime particles in concrete even after 28 days, and on the other hand, two day increment of strength confirms that these particles

constitute the core for hydration C_3S and C_2S, so that they accelerate the reactions of hydration, which supports the thesis that lime is chemically inert. Available data from the literature, like own previous researches [7] show that it is difficult to predict or find regularities when shrinkage of concrete is in question. The measurements done show that the largest shrinkage was found in the concrete mix with silica fume and III recycled fraction, S50, and the smallest in the control concrete with lime EK, wherein the difference is 56%. No regularities can be drawn from these results. The main problem of using recycled aggregate is its increased porosity, caused by the remained old cement paste on aggregate grains. The amount of recycled aggregate affects the absorption of water in the sense that with increasing the amounts of recycled aggregates, the percentage of water absorption is also increased, as a consequence of greater porosity.

5. Conclusion

Using all three tested mineral additives, high performance self-compacting concretes can be obtained. Silica fume is ahead, but having in mind economic and ecological component of fly ash, as well as relatively small difference in the obtained results, fly ash should necessarily be taken into account. Besides, the use of recycled aggregates (with increased testing) makes these concretes ecological rightly considered. Insufficient research in this area opens up a wide range of options for further testing, in terms of variations in the amount of cement, combining different additives, etc.

Acknowledgements
The work reported in this paper is a part of the investigation within the research project TR 36017 "Utilization of by-products and recycled waste materials in concrete composites in the scope of sustainable construction development in Serbia: investigation and environmental assessment of possible applications", supported by the Ministry for Education, Science and Technological Development, Republic of Serbia. This support is gratefully acknowledged.

References

[1] Corinaldesi V., Moriconi G., Influence of mineral additions on the performance of 100% recycled aggregate concrete, Construction and Building Materials, 23 (2009) 2869–2876.
[2] Newman J., Chao B.S., Advanced concrete Technology, Elsevier, 2003, 280.
[3] Meyer C., The greening of the concrete industry, Cement & Concrete Composites 31 (2009), 601-605.
[4] www.waste-environment.vin.bg.ac.rs
[5] Janssen G., Hendrik C.F., Sustainable use of recycled materials in building construction, Advances in Building Technology, Volume 2 (2002), 1399 – 1407.
[6] Trumić M., Trumić M., Uloga pripreme u reciklaži otpada i održivom razvoju Srbije, Stanje i perspektive pripreme mineralnih sirovina u Srbiji, Izdavač: Inženjerska Akademija Srbije, Beograd, (2011), 73-93.
[7] Despotović I., Uticaj različitih mineralnih dodataka na osobine samougrađujućeg betona, PhD thesis, Građevinsko- arhitektonski fakultet, Niš 2015.

SynerCrete'18 International Conference on Interdisciplinary Approaches
for Cement-based Materials and Structural Concrete
24-26 October 2018, Funchal, Madeira Island, Portugal

STANDARD AND INNOVATIVE CHARACTERIZATION OF STRENGTH, STIFFNESS, AND NON-AGING CREEP OF CONCRETE AT EARLY AGES

Mario Ausweger [(1)], Eva Binder [(1)], Olaf Lahayne [(1)], Roland Reihsner [(1)], Gerald Meier [(2)], Martin Peyerl [(2)], Bernhard Pichler [(1)]

(1) TU Wien – Vienna University of Technology, Austria
(2) Smart Minerals GmbH, Vienna, Austria

Abstract
Quantitative knowledge regarding the early-age evolutions of strength, stiffness, and creep properties of concrete are important for structures that are loaded already a few days after production. This was the motivation to characterize six concretes at early ages. The concretes were made of three types of cements (CEM II / A-M (S-L) 42.5N, CEM II/A-S 42.5R, and CEM I 52.5 R) and two types of aggregates (quartzite and limestone). The content of entrained air ranged from 2 % to 6 %. The standard tests included nondestructive loading-unloading experiments and destructive cube compression tests, performed 1, 3, 7, 14, and 28 days after production. The innovative experiments were performed according to the test protocol by Irfan-ul-Hassan et al. [1]. Three-minutes-long compression tests were performed once every hour, starting 24 hours after production and ending at material ages amounting to 8 days. Thus, each specimen was subjected to a series of 168 ultra-short creep experiments. Three minutes are *long* enough such that significant creep deformation is measured, and *short* enough such that the microstructure is virtually constant, i.e. that the chemical reaction between the cementitious binder and water does not progress significantly. Thus, each test provides access to the *non-aging* creep behavior of a specific material microstructure. Test evaluation is based on linear viscoelasticity, under explicit consideration that significant creep strains develop already during the short loading phase. Evaluation of more than 1000 three-minutes-long compression tests provided access to the hydration-induced evolutions of the elastic Young's modulus and the creep modulus of the tested concretes [2].

1. Introduction

For concrete structures which are loaded a few days after production, the strength, stiffness, and creep properties are of interest at the time of loading. The focus of this paper is to experimentally characterize six concretes within the first 28 days after production. Standard tests are performed according to the Austrian standard [3]. As for non-standard test methods, regularly-repeated short-term testing at early ages has become popular, see [3] as well as [4-6]. The individual tests are so short that the chemical reaction between the binder and the water does not progress significantly. Thus, each individual test provides access to the macroscopic properties of one specific material microstructure. The strategy for evaluation of ultra-short creep tests by Irfan-ul-Hassan et al. [1] is mechanically appealing, because it distinguishes rigorously between time-independent *elastic* and time-dependent *creep* deformation. In this context, it is considered that significant creep deformation develops not only during periods of constant loading, but also *during* short loading and unloading events. The availability of hundreds of ultra-short creep tests on cement pastes [1] was the motivation to perform top-down identification of creep constants of microscopic hydrate needles [7]. The latter represent the products of the chemical reaction between the binder and the water. Based on one and only one set of power-law creep *constants* of the hydrates, a multiscale model allowed for reproducing hundreds of ultra-short creep tests on cement pastes [7]. In addition, the identified creep constants of hydrates also allowed for predicting the evolution of deformation of a 30 years old cement paste subjected to a 30 days long creep test [7]. This success was the motivation to upscale the creep behavior from the scale of cement paste to the scales of mortars and concretes [8]. Thereby, it was shown that oven-dried sand and aggregates take up water during mixing of the raw materials, and that this water migrates back from the open porosity of the sand grains and the aggregates to the cement paste matrix during the hydration process [8]. Thus, the evolution of non-aging creep properties of cementitious materials at early ages could be deciphered based on the combination of repeated ultra-short creep testing with a careful test evaluation protocol and modern multiscale modeling. This was the motivation, to apply the same combined experimental-modeling strategy also to polymer modified cement pastes [9,10].
The present contribution combines standard and innovative test methods in order to gain quantitative insight into the early-age evolutions of strength, stiffness, and creep properties of six modern concretes with variable contents of entrained air. This way, a rich database of experimental results is produced supporting follow-up multiscale modeling activities in the future.

2. Materials

The experimental campaign involves six concrete mixes, see Table 1. They are made of three types of cement and two types of aggregates. The mass density of the quartzite and limestone aggregates is 2.65 g/cm^3 and 2.72 g/cm^3, respectively. An air entrainment agent was used to arrive at an air content between 2 % and 6 %.

Table 1: Composition of the six concretes.

Concrete type	cement	w/c	aggregates
C30/37	CEM II / A-M (S-L) 42.5 N	0.48	quartzite / limestone
C35/45	CEM II / A-S / 42.5 R	0.45	quartzite / limestone
C40/50	CEM I / 52.5R	0.42	quartzite / limestone

3. Standard testing of strength and stiffness

In order to quantify the compressive strength and the unloading modulus at material ages amounting to 1, 3, 7, 14, and 28 days after production, standard tests were carried out according to the European standards, see the Austrian application document [3]:

- The compressive strength is quantified by means of cube compression test. Dividing the cube compressive strength by the factor 1.2 delivers the cylinder compressive strength.
- The unloading modulus is quantified as the average of at least three unloading cycles on a cylindrical specimen, whereby the unloading modulus is the quotient of the stress and strain differences observed during unloading from 1/3 to 1/30 of the compressive strength.

In order to study the effect of curing conditions, two types of strategies for storage of specimens were used. Both of them referred to quasi-isothermal curing at 20 ºC:

- Standard storage: The specimens remained in the mold for at least 16 hours and a maximum of three days. After demolding, the specimens were stored under water up to a material age of seven days. After that, specimens for compressive strength tests were exposed to the ambient air, while specimens used for quantification of the unloading modulus were stored always under water.
- Sealed storage: The specimen remains in the mold for about 24 hours. After demolding, the specimens were sealed by several layers of food preservation foil, in order to avoid significant drying.

For the standard testing methods, each concrete mixture was produced with an air content of either 2 % or 6 %. Exemplary experimental results are shown in Fig. 1.

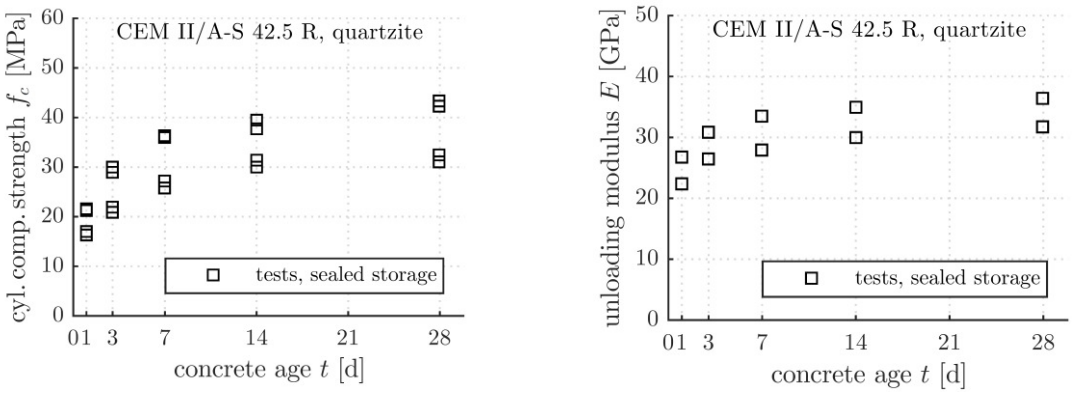

(a) (b)

Figure 1: Experimental results of the standardized tests for the C35/45 concrete with quartzite and air contents of 2 % and 6 %, see the larger and the smaller values, respectively.

4. Innovative testing of stiffness and creep properties

In order to characterize the early-age development of stiffness and creep properties, the experimental protocol of Irfan-ul-Hassan et al. [1] is used. This test protocol includes hourly repeated three-minutes-long creep tests under uniaxial compression. The test setup consists of a serial arrangement of one specimen (diameter = 7 cm, height = 30 cm) and two metal cylinders, for achieving a central load application [1]. Five linear variable differential transducers (LVDTs, type Hottinger Baldwin) are used for the quantification of the deformation. The first three-minutes-long creep test on the sealed specimens is carried out 24 hours after their production. Hourly testing is repeated until the tested specimens reach an age of eight days. Each specimen undergoes 168 loading-unloading cycles during the first week after production. In order to ensure that the specimens remain undamaged, the maximum forces are selected such that the loading does not exceed 20 % of the strength of the specimen at the time of testing. The Young's modulus and the creep modulus of the microstructure present at the time of testing can be quantified based on the force readings and the averaged LVDT readings.

Concretes respond to any applied stress is a viscoelastic fashion, i.e. with a spontaneous *elastic* and a time-dependent *creep* deformation response. The viscoelastic behavior of concrete can be described by a power-law creep function, see also [11]:

$$J(t-\tau) = \frac{1}{E} + \frac{1}{E_c}\left(\frac{t-\tau}{t_{ref}}\right)^{\beta}, \tag{1}$$

were E denotes the Young's modulus, E_c the creep modulus, $t-\tau$ the time elapsed since sudden loading, $t_{ref} = 1\,\text{day}$ a constant reference time, and β a dimensionless creep exponent. Macroscopic creep of cementitious materials results from the viscoelastic behavior of microscopic hydrate needles which are reaction products of cement and water. Micromechanical investigations have shown that the hydrate needles have constant creep properties. Thus, also their creep exponent is a time-independent material constant: $\beta = 0.25$ [7]. Furthermore, Königsberger et al. [7] showed that the same exponent also applies at the much larger scale of cement paste. This is the motivation to set the creep exponent β for concrete also equal to 0.25. Thus, only the elastic modulus and the creep modulus need to be identified from the measured data of each three-minutes-long creep test. Given that significant creep deformation already develops during the short loading period, it is necessary to calculate the viscoelastic strain response for a variable stress history. Since the examined specimens are loaded with a maximum of 20 % of the compressive strength, there is a linear relationship between stresses and strains. Thus, Boltzmann's superposition principle can be used:

$$\varepsilon_{mod}(t) = \sum_{i=1}^{n} J(t-\tau)\,\Delta\sigma(\tau_i)\,, \tag{2}$$

were the modeled strain $\varepsilon_{mod}(t)$ results from the sum of the individual strains due to sudden stress jumps $\Delta\sigma$. In an ideal creep test, in which the load is applied infinitely fast, the sum in Eq. (2) would reduce to one single term. In a real experiment, however, the loading cannot be

applied infinitely fast. Thus, the loading process is subdivided into a sequence of many small stress jumps, see [1] for further details.
The Young's modulus E and the creep modulus E_c are identified for each individual creep test. This is done by minimizing the sum of squared error, E_{srss}, between the experimentally determined strains $\varepsilon_{exp}(t_i)$ and the modeled strains $\varepsilon_{mod}(t_i)$:

$$E_{srss}(E, E_c) = \sqrt{\frac{1}{N}\sum_{i=1}^{N}\left[\varepsilon_{exp}(t_i) - \varepsilon_{mod}(t_i)\right]^2} \rightarrow min. \tag{3}$$

Therein, N is the total number of experimental readings considered for test evaluation during the load application phase *and* the subsequent load holding phase. The optimization problem in Eq. (3) is solved iteratively. At first, search intervals for the Young's modulus and the creep modulus are defined and subdivided in seven equidistant values. For all $7 \cdot 7 = 49$ parameter combinations, representing a search grid, the error function in Eq. (3) is evaluated. The combination of values for E and E_c, which results in the smallest error value, is treated as an initial estimate of the optimum solution. Depending on the position of this estimate within the search grid, the grid is shifted and/or refined, in order to define a new search grid. Thus, a sequence of progressively refined search grids is used, until both the Young's modulus and the creep modulus are identified up to an accuracy of 0.001GPa.
The optimization procedure was applied to each individual three-minutes-long creep test. As a result, the evaluation of the test data allows for a quasi-continuous quantification of the early-age development of Young's modulus and creep modulus. Covering air contents from 2% to 6%, the specimens exhibit similar evolutions of their stiffness and creep properties. Exemplary experimental results referring to the C35/45 concretes with quartzite are shown in Fig. 2.

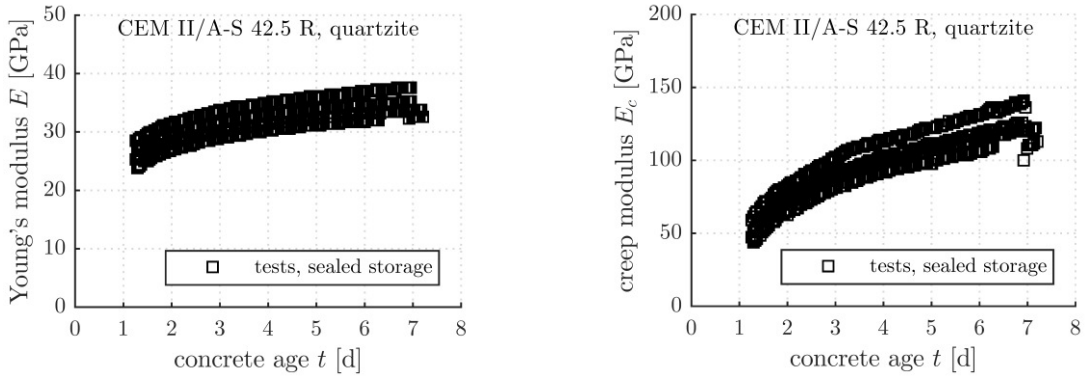

(a) (b)

Figure 2: Exemplary experimental results of the innovative tests for the C35/45 concrete with quartzite and air pore contents in the range from 2% to 6%; information on the exact value of the air content is not available; due to the page-limit not all results are shown.

5. Summary and conclusions

Standard and innovative testing methods were combined for the experimental characterization of six concretes within the first 28 days after production. The standard tests provide quantitative insight into the evolution of strength and stiffness. The innovative short-time creep tests provide access to the stiffness and the non-aging creep properties at early ages. The stiffness evolutions from both testing methods are in good agreement, see Fig. 1(b) and 2(a). The testing campaign comprises some 120 strength tests, 60 stiffness tests, and more than 1000 short-time creep tests. The resulting database will be used for the development and validation of future multiscale models.

Acknowledgment
Financial support by the Austrian Research Promotion Agency (FFG), provided within VIF-project 850554 "ÖBB – Österreichischer Betonbenchmark zur Steigerung der Vorhersage-qualität mechanischer Eigenschaften moderner Betone" is gratefully acknowledged.

References

[1] M. Irfan-ul-Hassan, B. Pichler, R. Reihsner, Ch. Hellmich: Elastic and creep properties of young cement paste, as determined from hourly repeated minute-long quasi-static tests, Cement and Concrete Research, 82, 36-49 (2016).
[2] M. Ausweger: Quantification and prognosis of early-age development of strength, stiffness, and creep properties of modern Austrian concretes, Master Thesis, TU Wien – Vienna University of Technology, Austria (2017).
[3] ONR 23303: Prüfverfahren Beton (PVB) – Nationale Anwendung der Prüfnormen für Beton und seine Ausgangsstoffe (2010).
[4] P. Karte, M. Hlobil, R. Reihsner, W. Dörner, O. Lahayne, J. Eberhardsteiner, B. Pichler: Unloading-based stiffness characterisation of cement pastes during the second, third and fourth day after production, Strain, 51 (2015), 156-169.
[5] B. Delsaute, C. Boulay, J. Granja, J. Carette, M. Azenha, C. Dumoulin, G. Karaiskos, A. Deraemaeker, S. Staquet: Testing concrete E-modulus at very early ages through several techniques: An inter-laboratory comparison, Strain, 52 (2016), 91-109.
[6] B. Delsaute, C. Boulay, S. Staquet: Creep testing of concrete since setting time by means of permanent and repeated minute-long loadings. Cement and Concrete Composites, 73, 75–88, (2016).
[7] M. Königsberger, M. Irfan-ul-Hassan, B. Pichler, Ch. Hellmich: Downscaling based identification of nonaging power-law creep of cement hydrates, Journal of Engineering Mechanics (ASCE), 142, 04016106 (2016).
[8] M. Irfan-ul-Hassan, M. Königsberger, R. Reihsner, Ch. Hellmich, B. Pichler: How water-aggregate interactions affect concrete creep: A multiscale analysis, Journal of Nanomechanics and Micromechanics (ASCE), 7(4), 04017019 (2017).
[9] L. Göbel, A. Osburg, B. Pichler: The mechanical performance of polymer-modified cement pastes at early ages: ultra-short non-aging compression tests and multiscale homogenization, Construction and Building Materials, 173 (2018) 495-507.
[10] L. Göbel, M. Königsberger, A. Osburg, B. Pichler: Viscoelastic behavior of polymer-modified cement pastes: Insight from downscaling short-term macroscopic creep tests by means of multiscale modeling, Applied Sciences, 8(4), 487 (2018).

SynerCrete'18 International Conference on Interdisciplinary Approaches
for Cement-based Materials and Structural Concrete
24-26 October 2018, Funchal, Madeira Island, Portugal

STRESS DISTRIBUTION IN RESTRAINED RING TEST DUE TO DRYING AND AUTOGENOUS SHRINKAGE

Semion Zhutovsky [(1)]

(1) National Building Research Institute – Faculty of Civil and Environmental Engineering
Technion – Israel Institute of Technology, Haifa 32000, Israel

Abstract
Cracking of concrete is crucial from point of view of both durability and mechanical properties. With the extensive use of high-performance concretes that have low water to cement ratios, cracking sensitivity of concrete becomes even more important concern. Testing of concrete shrinkage restrained by steel ring turned into a standard for evaluation of the concrete potential for cracking. The stress at cracking in concretes with w/c ratios of 0.7, 0.45, 0.33, 0.25 and 0.21 was determined by means of restrained ring test and compared with the splitting tensile strength. The results show the significant change of stress to strength ratio at cracking with the change of water to cement ratio. Analysis of stresses was performed considering two types of shrinkage: drying shrinkage and autogenous shrinkage. Because drying shrinkage is driven by external drying that causes moisture gradient across the specimen and autogenous shrinkage is driven by internal drying – self-desiccation – that is uniformly distributed, stress distribution caused by these two types of shrinkage is significantly different. The analysis of the distribution of stresses in the restrained concrete ring due to autogenous and drying shrinkage provides a good explanation of the observed experimental data.

1. Introduction

Cracking of concrete is an important issue for both durability and mechanical performance of concrete structures[1]. The extended use of high performance concretes (HPC) which are more sensitive to cracking has generated renewed interest in the early age cracking of concretes [2,3]. It has become clear that the cracking potential of concrete cannot be estimated just by the shrinkage [4,5]. Although shrinkage of concrete is the driving force for cracking, it is not the only parameter which needs to be considered. This understanding is especially

important in the view of the development of special technologies to control cracking, such as internal curing and shrinkage reducing admixtures [6–8]. As the result, new testing techniques have been developed to asses directly the cracking based on set-ups which can provide quantitative information beyond the time to cracking [9–13].
Testing of concrete shrinkage restrained by steel ring turned into a standard for evaluation of the concrete potential for cracking [13]. The ASTM C1581 test is one example [14]. The potential for cracking in such test is determined using either criterion of the net time to cracking or average stress rate. In addition to the thermal strains, two types of shrinkage need to be considered in evaluating cracking potential: drying shrinkage and autogenous shrinkage [15]. Drying shrinkage is driven by external drying from the concrete surface. Such drying causes moisture gradient across the specimen. Accordingly, drying shrinkage strain, at the early ages, is distributed from the maximum at the surface to the minimum at the inner core of the concrete. Autogenous shrinkage, on the other hand, is driven by internal drying called self-desiccation. For this reason, autogenous shrinkage strain in sealed concrete is uniformly distributed. In case of restrained shrinkage, due to the difference in the driving forces stresses distribution caused by these two types of shrinkage is significantly different. However, in the restrained shrinkage ring test, the stress is estimated as an average based on the measurements of the strain gages that are bonded to the inner surface of the restraining steel ring. Thus, the test results do not consider the distribution of stresses in the concrete sample.
Restrained ring test was performed on concretes with w/c ratios of 0.7, 0.45, 0.33, 0.25, and 0.21 and stress at cracking was compared with the splitting tensile strength. Experimental results show that in the case of the concretes with high water to cement (w/c) ratio, cracking takes place at a stress which is 37 to 56% higher than the splitting tensile strength, while the concretes with low water to cement ratio, the stress at cracking can be about 21% lower than the splitting tensile strength. This can be explained by the fact that the ratio of drying to autogenous shrinkage changes significantly with the reduction of water to cement ratio [16]. To support this assumption, analysis of stress distribution in restrained ring sample due to drying and autogenous shrinkage was performed. The results of stresses distribution provide a good explanation to the observed phenomena.

2. Materials and methods

2.1 Mixture composition

The mix composition is given in Table 1. The mix notation designate w/c ratio, so that 21, 25, 33, 45 and 70 stand for w/c ratios of 0.21, 0.25, 0.33, 0.45, and 0.70, respectively. In all mixes Portland cement CEM I 52.5 N was used. The mix compositions were adjusted with superplasticizing admixture to keep the workability similar. The superplasticizer was Rheobuild 2000 admixture produced by WR Grace, USA. The concretes were made with 14 mm maximum size dolomite as a coarse aggregate and sea sand as a fine aggregate.

2.2 Testing procedure

The potential for cracking was determined by restrained shrinkage ring test following the standard procedure of ASTM C1581-04, 2004 [14]. Concrete was cast into the ring mold with 330 mm and 406 mm inner and outer diameters, respectively, and 150 mm height. The specimens were demolded and exposed to drying at one day in a controlled environment of

50±4% RH and 20±2°C. The measurements included continuous monitoring of the strain developed in the steel ring. The results of the ring tests were obtained in terms of strain-time curves. Cracking was identified by a sharp sudden decline in the strain. Cracking sensitivity was quantified according to the ASTM C 1581 in terms of the time to cracking and stress rate to cracking, determined at the time of cracking. Splitting tensile strengths were tested on cube specimens of 50 mm size at 1, 7, 28, and 90 days. The specimens for strength tests were demolded after 1 day and cured at conditions identical to those of the rings.

Table 1 Concrete composition (kg/m^3)

Mix Notation	Cement	Mix Water	Sand	Gravel
21	667	140	532	1145
25	600	150	562	1145
33	506	167	572	1145
45	450	203	504	1191
70	291	213	652	1191

3. Results and discussion

3.1 Cracking potential and stress to strength ratio at cracking

The strain that was measured in the restraining steel was used to evaluate the stress in the concrete according to equation proposed by See et al. [9]:

$$\sigma_t(t) = E_s \varepsilon_s(t) \frac{r_{ic} h_s}{r_{is} h_c} \quad (1)$$

where $\varepsilon_s(t)$ is an elastic strain in steel ring at a time t, E_s is the modulus of elasticity of steel ring, r_{is} and r_{ic} are internal radii of steel ring and of the concrete ring, respectively, h_s and h_c are thicknesses of steel ring and of the concrete ring, respectively.

In Figure 1, the stresses calculated according to the equation (1) for all concrete mixes are given. The data for sensitivity to cracking is presented in Figure 2 for both criteria, time to cracking and stress rate to cracking. The Figure 2 presents also the classification as outlined in the ASTM standard. Since the classification according to each of these criteria do not always coincide with each other, the integrated criterion suggested by Kovler and Bentur [13] was used, which is obtained by dividing the stress rate by the net time to cracking. The effect of w/c ratio on the integrated cracking potential criterion is presented in Figure 3. The data in this figure clearly shows the effect of reduction of w/c ratio on the increase of cracking sensitivity, as well as a demarcation line between the HPC and NSC which can be identified in the proximity to w/c ratio of 0.4. Figure 2 demonstrates that for HPC the tendency for increased cracking sensitivity rises steeply with the reduction of w/c ratio, while for NSC the reduction of w/c ratio results in an only modest increase in cracking potential. The increased cracking sensitivity of HPC should be emphasized in the view of the logarithmic base of the cracking criteria scale.

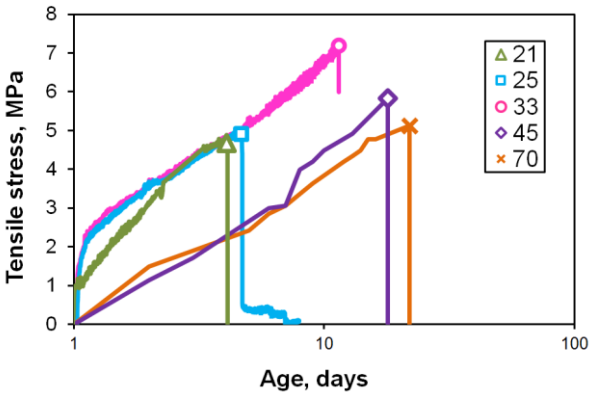

Figure 1: Stress build-up in concretes during the ring test

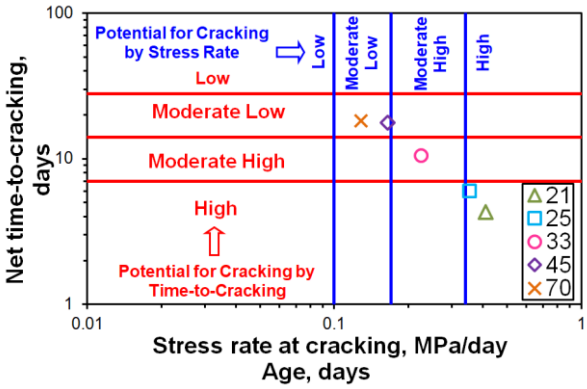

Figure 2: Cracking sensitivity of concretes by the standard cracking potential criteria

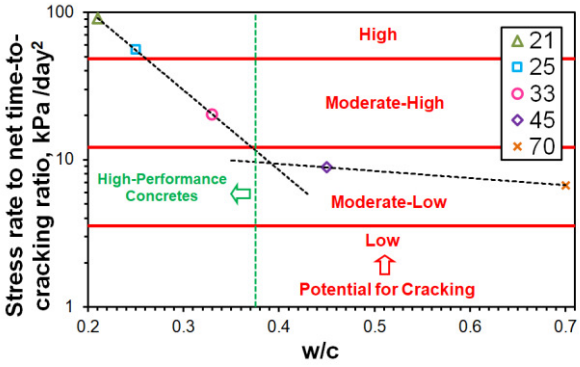

Figure 3: Cracking sensitivity of concrete by the integrated cracking potential criterion

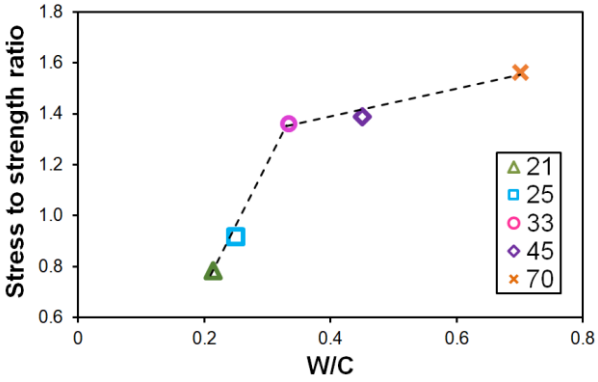

Figure 4: Stress to strength ratio at of concrete at cracking

In Figure 1, it can be clearly seen that the stress build-up rate is very high in the first few days in the concretes with w/c ratio of 0.33 and lower. This is consistent with the demarcation boundary in Figure 2. The obvious explanation for the big difference between the higher and lower w/c ratio concretes is in the autogenous shrinkage which takes place mainly within the first day or two. The occurrence of cracking can be expected to take place when the tensile strength and stress curves intersect. This is indeed roughly the case, but there are some variations which have significance. The ratio of the stress at cracking to is splitting tensile strength shown in Figure 4. In the case of the higher w/c ratio, cracking takes place at a stress which is about 56, 39 and 37% higher than the strength, for w/c ratios of 0.70, 0.45, and 0.33, respectively. While at the lower w/c ratios of 0.25 and 0.21 concrete cracks at a stress which is 8 and 21% lower than the splitting tensile strength, respectively. This difference in trends might be explained on the basis of the nature of shrinkage in the ring test. In the higher w/c ratio concretes, shrinkage is induced by external drying and the result is stress distribution in the ring due to the fact that the outer surface is shrinking first, leading to a stress gradient resulting in cracking which starts at the outer surface and gradually penetrates inwards. In the lower w/c ratio concretes, the shrinkage is largely due to internal drying, which is uniform, and it is therefore expected that cracking will start at the inner surface of the ring in these concretes.

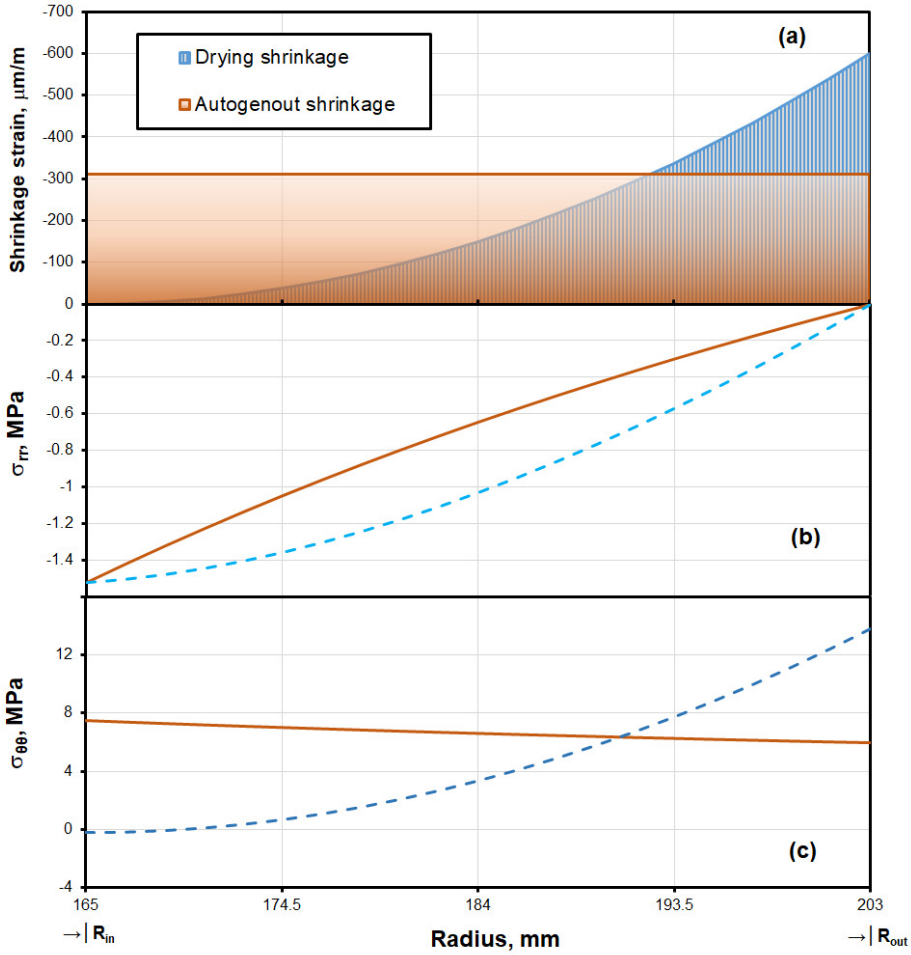

Figure 5: Stresses distribution induced by autogenous (solid lines) and drying (dotted line) shrinkage

3.2 Analysis of strains

Let us consider two distributions of shrinkage strains as shown in Figure 5a: (i) uniform strain distribution caused by autogenous shrinkage and (ii) parabolic strain distribution (for the sake of simplicity) caused by drying shrinkage. Solving equilibrium equation for plain stresses in the concrete ring with boundary conditions of zero radial displacement at the inner radius and zero radial stress at the outer radius we obtain the stress distributions as shown in Figure 5 b and Figure 5 c. Note that the relative magnitude of autogenous and drying shrinkage was adjusted to give the same normal radial pressure on the steel ring, i.e. the strain gages on the steel ring will measure the same strain, which will result in the same average stress in the concrete ring calculated according to the equation (1). However, as can be seen in Figure 5 c, the distribution of tangential stresses in the concrete ring is significantly different for the cases of autogenous and drying shrinkage. When shrinkage is induced by external drying, the outer surface is shrinking first, leading to a stress gradient resulting in cracking which starts at the outer surface and gradually penetrates inwards. The crack can be arrested in its propagation, especially when considering that the higher w/c ratio concretes are somewhat ductile. As a result, the mode of failure resembles more flexural type behavior, where the calculated

flexural strength is higher than the "pure" tensile one. In the case of autogenous shrinkage is the tensile stress distribution is uniform and the volume of concrete subjected to tensile stress is larger. Thus, the probability of cracking is higher and the cracking occurs when the tangent stress at the inner ring surface reaches tensile strength, and perhaps lower, considering the more brittle nature of these concretes. In this way, the difference in stresses distribution in concrete ring caused by autogenous versus drying shrinkage can satisfactorily explain the phenomena of strength to stress ratio change with the change of w/c ratio observed in Fig. 4.

References

[1] A. Bentur, S. Igarashi, K. Kovler, Prevention of Autogenous Shrinkage in High- Strength Concrete by Internal Curing Using Wet Lightweight Aggregates., Cem. Concr. Res. 31 (2001) 1587–1591.
[2] E. Holt, M. Leivo, Cracking risks associated with early age shrinkage, Cem. Concr. Compos. 26 (2004) 521–530.
[3] A. Bentur, K. Kovler, Evaluation of early age cracking characteristics in cementitious systems, Mater. Struct. 36 (2003) 183–190.
[4] S.A. Altoubat, D.A. Lange, Creep, shrinkage, and cracking of restrained concrete at early age, ACI Mater. J. 98 (2001) 323–331.
[5] S.A. Altoubat, D.A. Lange, The Pickett effect at early age and experiment separating its mechanisms in tension, Mater. Struct. Constr. 35 (2002) 211–218.
[6] S. Weber, H.W. Reinhardt, A New Generation of High Performance Concrete: Concrete with Autogenous Curing, Adv. Cem. Based Mater. 6 (1997) 59–68.
[7] O.M. Jensen, P.F. Hansen, Water-Entrained Cement-Based Materials II: Experimental Observations, Cem. Concr. Res. 32 (2002) 973–978.
[8] S. Zhutovsky, K. Kovler, A. Bentur, Effect of hybrid curing on cracking potential of high-performance concrete, Cem. Concr. Res. 54 (2013).
[9] H.T. See, E.K. Attiogbe, M.A. Miltenberger, Shrinkage Cracking Characteristics of Concrete Using Ring Specimens, ACI Mater. J. 100 (2003) 239–245.
[10] E.K. Attiogbe, H.T. See, M.A. Miltenberger, Cracking Potential of Concrete under Restrained Shrinkage, in: Adv. Cem. Concr. Vol. Chang. Cracking, Durab., Engineering Conferences International, Copper Mountain, CO, USA, 2003: pp. 191–200.
[11] K. Kovler, J. Sikuler, A. Bentur, Restrained shrinkage tests of fibre-reinforced concrete ring specimens: effect of core thermal expansion, Mater. Struct. 26 (1993) 231–237.
[12] K. Kovler, Testing System for Determining the MechanicBehavior of early age concrete under restrained and free uniaxial shrinkage, Mater. Struct. 27 (1994) 324–330.
[13] K. Kovler, A. Bentur, Cracking Sensitivity of Normal- and High-Strength Concretes, ACI Mater. J. 106 (2009) 537–542.
[14] ASTM C1581-04, Standard Test Method for Determining Age at Cracking and Induced Tensile Stress Characteristics of Mortar and Concrete under Restrained Shrinkage, American Society for Testing and Materials, 2004.
[15] K. Kovler, S. Zhutovsky, Overview and future trends of shrinkage research, Mater. Struct. Constr. 39 (2006).
[16] E. ichi Tazawa, S. Miyazawa, Experimental Study on Mechanism of Autogenous Shrinkage of Concrete, Cem. Concr. Res. 25 (1995) 1633–1638.

SynerCrete'18 International Conference on Interdisciplinary Approaches
for Cement-based Materials and Structural Concrete
24-26 October 2018, Funchal, Madeira Island, Portugal

STUDY ON CHARACTERISTICS OF TENSILE STRENGTH OF CONCRETE CONSIDERING TEMPERATURE DEPENDENCE IN MASS CONCRETE STRUCTURES

Hiroki Izumi [(1)], Jun-ichi Arai [(1)], Toshiaki Mizobuchi [(1)]

(1) Department of Civil and Environmental Engineering, Hosei University, Japan

Abstract
It is important to grasp mechanical and thermal properties in order to verify the possibility of thermal cracking. In this study, for the purpose of improving the accuracy of analysis in prediction of cracking caused by thermal stress, it was investigated that the direct tensile strength and thermal properties considering temperature history inside concrete member may be applied as a design values for the analysis of prediction of cracking caused by thermal stress. From results of these experiments, in early age, the direct tensile strength under mass curing which is considered temperature history inside concrete member is higher than the splitting tensile strength under standard curing. However, the direct tensile strength under mass curing is lower than the splitting tensile strength under standard curing after 7 days. At 28 days, the strength of former was about 20% lower than that of latter. And the thermal expansion coefficient was estimated using measured values of strain and temperature. In this paper, it was reported that the test method of direct tensile strength considering temperature history inside concrete member was proposed and that the accuracy of analysis for the prediction of thermal cracking by using this method would be improved.

1. Introduction

It is necessary to grasp mechanical and thermal properties of concrete exactly for improving of precision of the prediction for thermal cracking. Since thermal cracking occur when the tensile stress of concrete exceeds the tensile strength, it is particularly important to estimate the tensile stress and tensile strength definitely. Currently the tensile strength is required by the splitting tensile test. However, there is problem that the tensile stress does not occurs uniformly as a constraint stress is generated in the neighbourhood of loading point in the splitting tensile test. Further since specimens of standard curing under water of 20℃ are used,

it cannot consider effects of temperature inside mass concrete member. Therefore, the tensile strength should be required by the direct tensile test using specimen considering the temperature history. In this study, the test method of direct tensile strength under mass curing which was conveniently obtained in site was proposed.

2. Outline of Experiment

2.1 Case studied

In this study, since the subject of investigation is mass concrete structure, six types of cement described in Guidelines for Control of Cracking of Mass Concrete 2016 published by Japan Concrete Institute (hereinafter referred to as JCI2016). For each cement, water to cement ratio was set to three levels of 45%,50% and 60%. In this experiment, the target slump was 8±1.5cm and the target air content was 4.5±1.0%. For each cement, unit content of water to satisfy the required quality of these fresh concrete was selected. Table 1 shows case studied.

2.2 Experimental method

Method of investigation of mechanical properties. The test device to evaluate thermal and mechanical properties using insulation container is shown in Fig. 1. The specimens of the both side in the device were used for the direct tensile test to investigate the tensile properties considering influence of temperature history inside mass concrete member. The direct tensile test was carried out at age of 3 days, 7 days, 14 days, 28 days using three specimens for each age. Loading rate is 0.05 N/sec by using oil pressure type universal testing machine. Further the compressive test and the splitting tensile test were carried out at age same as the direct tensile test.

Method of investigation of thermal properties. The temperature history measured by the specimen, which is ø300 mm × 400 mm high, in the middle of the insulation container was used for the identification analysis by the temperature analysis to investigate insulation temperature rise properties. The formula described in JCI2016 were refed to estimate adiabatic temperature rise characteristics. And the relationship between the temperature amount of change and the strain amount of change used to calculate coefficient of thermal expansion.

Table 1: Concrete mixes investigated in this study.

kinds of cement	mark	water cement ratio	unit quantity (kg/m^3)	
		W/C (%)	water W	cement C
Normal Portland cement	N45	45	157	349
	N50	50	158	316
	N60	60	154	257
Moderate Portland cement	M45	45	157	349
	M50	50	157	314
	M60	60	157	262
Low-heat Portland cement	L45	45	157	349
	L50	50	157	314
	L60	60	157	262
High-early-strength Portland cement	H45	45	157	349
	H50	50	157	314
	H60	60	157	262
Portland blast-furnace cement B class	BB45	45	157	349
	BB50	50	154	308
	BB50	60	154	257
Fly ash cement B class	FB45	45	157	349
	FB50	50	157	314
	FB60	60	157	262

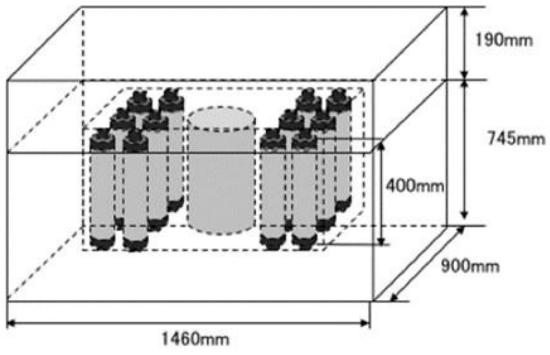

Figure 1: Layout of insulation container to evaluate thermal and mechanical properties conveniently.

3. Results of experiment

3.1 Mechanical properties

Tensile strength. Figure 2 shows one case of the result of comparison between the direct tensile strength development considering influence of temperature history inside mass concrete member and the splitting tensile strength development under water of 20°C (BB50). The direct tensile strength is higher than the splitting tensile strength by the effect of temperature rise until age of 7 days. However the splitting tensile strength is higher than the direct tensile strength after age of 7 days. Though it is different by a kind of the cement, the splitting tensile strength is higher the direct tensile strength at age of 28 days in most cases. There is 20% of differences between the splitting tensile strength under water of 20°C and the direct tensile strength considering influence of temperature history inside mass concrete member at age of 28 days. Figure 3 shows example of the relationship between the splitting tensile strength under standard curing and the direct tensile strength considering influence of temperature history inside mass concrete member in all cases. The direct tensile strength considering influence of temperature history inside mass concrete member is lower than the splitting tensile strength under water of 20°C in area of that the splitting tensile strength under water of 20°C is beyond 2 N/mm^2. And the direct tensile strength considering influence of temperature history inside mass concrete member is higher than the splitting tensile strength under standard curing in area of that the splitting tensile strength under water of 20°C is within 2 N/mm^2. This is because the direct tensile strength development given a temperature history is early. Considering the mentioned above point, if the direct tensile strength considering influence of temperature history inside mass concrete member is near to structure body strength, it is evaluated the safe side for occurring cracking in area of that the tensile strength is within 2 N/mm^2 and the danger side for occurring cracking in area of that the tensile strength is beyond 2 N/mm^2.

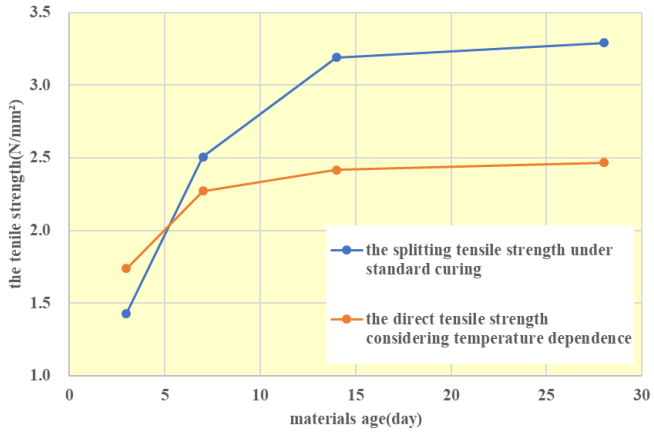

Figure 2: Tensile strength development considering influence of temperature history (BB50).

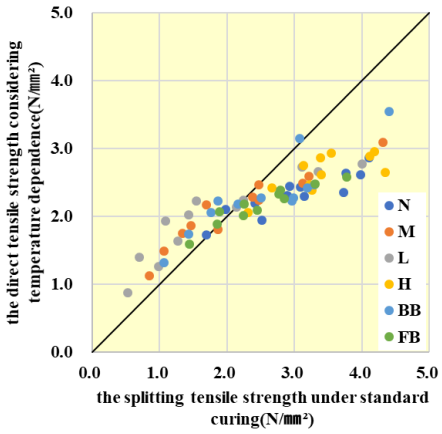

Figure 3: The relationship between the splitting tensile strength and the direct tensile strength.

The estimated formula on the strength development of direct tensile strength. The direct tensile strength development coefficient Eq. (1) and the direct tensile strength development

equation in management materials age 28 days considering influence of temperature history inside mass concrete member and a kind of cement are made based on the compressive strength development equation described in JCI2016 using the result of the direct tensile test.

$$f_s(t_e) = ((t_e - S_f)/(A+B(t_e - S_f)) \times f_t(t_n) \quad (1)$$

where :
t_e: effective material age(day)
t_n: manegement materials age of cocrete under standard curing(day)
$f_t(t_e)$: the direct tensile strength at effective materials age t_e
A, B: coefficient expressed the tensile strength supported a kind of cement
S_f: effective materials age expressed the hardening origin supported a kind of cement
$f_t(t_n)$: the direct tensile strength at manegement materials age t_n

Table 2 shows each coefficient of the estimated formula on the strength development of the direct tensile strength and the estimated formula on the strength development of the direct tensile strength considering a kind of cement at manegement materials age 28 days made using result of the direct tensile test. The tensile strength of structure can be estimated directly by using the estimated formula on the strength development of the direct tensile strength.
Figure 4 shows one case of the result of comparison between the tensile strength calculated using the estimated formula on the strength development of the direct tensile strength shown in Table 2 and using the estimated equation described in JCI2016(N50). the estimated formula on the strength development of the direct tensile strength made from the test result is nearer to the experimental value than that described in JCI2016.

Table 2 : Coefficients determined for strength development formula.

	A=α1+β1(C/W)		B=α2+β2(C/W)		S_f	f'_t=P1+P2(C/W)	
	α1	β1	α2	β2		P1	P2
N	6.27	-1.49	0.64	0.19	0.37	1.17	0.75
M	11.2	-2.25	0.11	0.70	0.42	-0.13	1.42
L	16.5	-4.87	0.47	0.17	0.50	0.23	1.17
H	16.6	-6.52	0.96	0.00	0.30	2.62	0.14
BB	4.58	0.74	0.27	0.32	0.42	-1.66	2.24
FB	8.40	-2.30	0.75	0.10	0.47	1.85	0.32

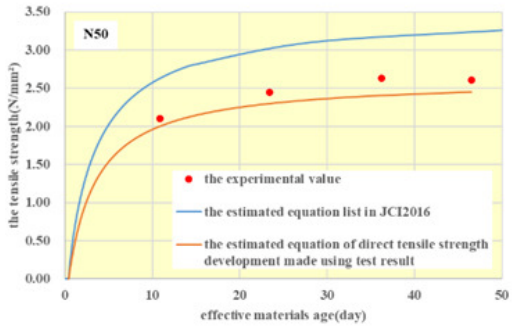

Figure 4: The result of comparison of tensile strength calculated using the estimated formula

3.2 Thermal properties

Insulation temperature rise properties. Properties of Adiabatic temperature rise are estimated by the identification analysis by the temperature analysis using the results of temperature history. Figure 5 shows comparison between the quantity of end insulation temperature rise calculated by using the estimated equation described in JCI2016 and that of the experimental value in all case. The quantity of end insulation temperature rise calculated by using the estimated equation described in JCI2016 is about 20% lower than that of the experimental value of insulation container regardless of a kind of cement and water cement ratio.

Coefficient of thermal expansion. In this study, it is examined that coefficient of thermal expansion calculated by the experimental value is the apparent coefficient of thermal expansion included a self-shrinkage strain, because the experimental strain of test to evaluate thermal properties is including self-shrinkage strain. In this study, the apparent coefficient of thermal expansion is calculated by dividing part about the same an incline in temperature rise area and descent area into four sections which is temperature rise section ①,② and temperature descent section ①,②. Table 3 shows the apparent coefficient of thermal expansion in each case. Although there is unevenness by a few water cement ratio, the apparent coefficient of thermal expansion is organized every a kind of cement.

Table 3: Apparent coefficient of thermal expansion.

a kind of cement	unit cement content (kg/m3)	the coefficient of thermal expantion (μ/℃)							
		temperature rise area①		temperature rise area②		temperature descent area①		temperature descent area②	
		experimental value	average	experimental value	average	experimental value	average	experimental value	average
N	349	18.19	19.88	7.13	7.18	23.54	20.45	10.76	11.07
	316	20.31		7.16		20.98		9.63	
	257	21.14		7.26		16.84		12.83	
M	349	7.70	10.31	6.43	6.63	15.52	14.68	10.85	11.64
	314	10.48		5.96		16.21		12.56	
	262	12.76		7.49		12.32		11.52	
L	349	5.51	10.03	4.17	5.06	16.50	13.61	16.40	14.22
	314	9.79		5.44		13.84		13.98	
	262	14.79		5.55		10.50		12.27	
H	349	12.93	12.97	3.90	5.14	9.66	5.04	11.53	11.05
	314	13.99		5.31		3.12		10.72	
	262	12.00		6.21		2.34		10.89	
BB	349	14.62	14.09	6.82	7.36	6.68	5.58	14.98	13.60
	308	14.52		7.94		4.08		13.69	
	257	13.14		7.34		5.98		12.13	
FB	349	11.16	11.68	6.88	6.93	4.56	13.09	12.23	12.29
	314	10.63		6.86		23.88		12.29	
	262	13.25		7.06		10.82		12.35	

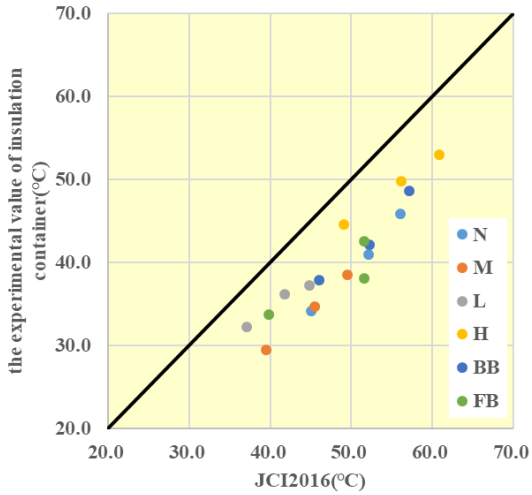

Figure 5: Comparison of ultimate adiabatic temperature rise.

4. Thermal stress analysis

Thermal stress analysis was performed by using the experimental value. The analysis model of Box Calvert. The analysis model is 10 meters in height, 10 meters in width, 1 meters of wall-thicknesses, 10 meters in construction length.

The comparison between the case of using the experimental values as the design value and the case of using the value of JCI2016 was shown below. Figure 6 shows comparison between the cracking index described in JCI2016 and the cracking index of the result of the direct tensile test in all case. The cracking index of the result of the direct tensile test is great less in comparison with that described in JCI2016 in a kind of cement in a case of Moderate Portland cement and Low-heat Portland cement. In the area that is less than it of smallest cracking index to considered as a boundary line about having cracking outbreak or not 1.0, the cracking index of the result of the direct tensile test is less than that described in JCI2016 around 0.1 in case of a kind of cement of Normal Portland cement, High-early-strength Portland cement, Portland blast-furnace cement B class and Fly ash cement B class.

From results mentioned above, when it is supposed that the direct tensile strength considering influence of temperature history inside mass concrete member is near to structure body

strength, there is possibility to evaluate outbreaking cracking in the danger side by using the splitting tensile strength under water of 20℃. It is necessary to examine the modulus of elasticity having the need to distinguish the tensile strength and the compressive strength and the creep greatly influencing generation stress in early age which are value for design of thermal stress analysis to express structure body strength.

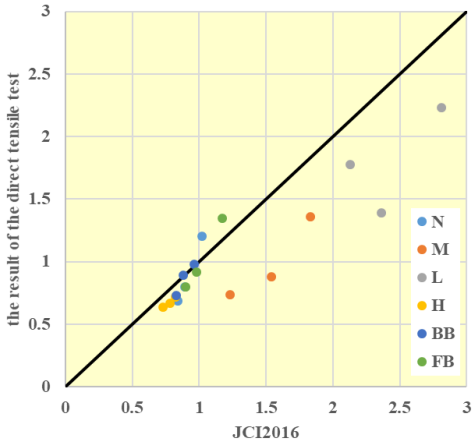

Figure 6: Comparison between the cracking index described in JCI2016 and the cracking index of the result of the direct tensile test in all case.

5. Conclusion

In this study, the direct tensile test using insulation container was conducted to investigate mechanical and thermal properties in mass concrete structure. The results are shown below.

1. In early age, the direct tensile strength under mass curing considering temperature history inside concrete member is higher than the splitting tensile strength under water of 20℃. However, at 28 days, the strength of former was about 20% lower than that of latter.
2. There is possibility to evaluate the tensile strength in the danger side for occurring cracking in area of that the tensile strength is beyond 2 N/mm^2.
3. The estimated formula on the strength development of the direct tensile strength was proposed made it possible to estimate tensile strength inside concrete member directly.
4. If the direct tensile strength considering influence of temperature history inside mass concrete member is near to structure body strength, there is possibility to evaluate outbreaking cracking in the danger side caused by result of the thermal analysis described in JCI2016 and that used experimental results.

References

[1] Tunashima, T. et al, The tensile properties of the concrete using various cement, Concerete Engineering Annual Memoirs 32(1) (2010)
[2] Takeuchi, N. et al, Basic study on properties of evaluation of concrete using insulation container, Concerete Engineering Annual Memoirs 33(1) (2011)
[3] Senba, R. et al, Examination about critical limit of concrete cracks using various cement, Concerete Engineering Annual Memoirs 37(1) (2015)

SynerCrete'18 International Conference on Interdisciplinary Approaches
for Cement-based Materials and Structural Concrete
24-26 October 2018, Funchal, Madeira Island, Portugal

SULPHATE-INDUCED CORROSION OF STEEL REINFORCEMENT IN FRESH CALCIUM SULPHOALUMINATE BINDERS: PRELIMINARY STUDIES

Yegor Morozov [(1)], Simone Pellegrini [(2)], Sergio Lorenzi [(3)], Fátima Montemor [(1)]

(1) Centro de Química Estructural, Instituto Superior Técnico, Universidade de Lisboa, Lisbon, Portugal
(2) Security Building Service S.R.L., Via Santi Filippo e Giacomo, Covo (Bergamo), Italy
(3) Department of Engineering, University of Bergamo, Bergamo, Italy

Abstract
Ordinary Portland cement (OPC) production is the largest contributor to global emissions. Main strategies to reduce the environmental impact include optimization of clinker production and grinding, usage of alternative fuels and raw materials, and, finally, shift to blended cements. Nevertheless, such measures can shorten emissions just for 30-40 %, thus, alternative binders and their mixtures with OPC are recently in focus. Among those, calcium sulphoaluminate cements (CSA) are attractive for emissions minimization, and show unique properties, but they lack durability studies and the understanding of embedded steel reinforcement behaviour.
The corrosion behaviour of steel was tentatively tested in solutions that simulate liquid phase at various stages of binder hydration. In static tests, steel samples were immersed in solutions of constant composition, while in dynamic tests it was changed to mimic the evolution of key parameters, i.e. pH and sulphates, in a way it happens during binder hydration. The preliminary results suggested that the corrosion of plain mild steel reinforcement would start instantly in CSA binders upon water addition, due to simultaneously low pH and high sulphate concentration, and, despite favourable conditions in hydrated state, corrosion would proceed further, since no long-term repassivation was observed.

1. Introduction

The construction sector is one of the greatest sources of carbon dioxide emissions, and the production of ordinary Portland cement (OPC) alone accounts for 6-8 % of its global output.

Today around 900 kg of CO_2 is released per each tonne of Portland clinker, which hardly can be lowered below 800 kg [1, 2]. The main strategies to reduce environmental impact target optimization of clinker production and grinding, the usage of alternative fuels and raw materials, and a shift to blended cements [2-4]. The intensive introduction of high performance concrete and concrete composites into construction practice reduced the amount of concrete required to support the same load [2, 5], improved durability and increased the service life of structures [2], decreasing the demand for cement both in short- and long-term respectively. Nevertheless, these measures are limited, thus alternative binders are in focus [3, 6].
Calcium sulphoaluminate cement (CSA) is particularly attractive. CSA clinker is produced at about 1250 °C, which is 200 °C lower compared to OPC [2, 7-12], need just 800 kJ/kg, and it is accompanied by the release of just ca. 340 kg of CO_2 per tonne of clinker [6, 9-13], which together with better grindability [13] make it discernibly advantageous in terms of energy conservation and emissions reduction. Besides, various industrial by-products can be used as raw materials, enhancing the sustainability of CSA production [13]. They are perfect for pre-cast construction due to high early strength and rapid hardening [2, 10], which together with high frost resistance of fresh mixes is valuable in cold weather. CSA is used in shrinkage-compensating formulations, or for self-stressing concrete [2, 6, 7, 14]. However, fresh CSA concretes have lower workability, as they require more water, but it is higher, when compared to OPC-slag blended concretes [11]. Nevertheless, self-consolidating CSA formulations, such as for self-levelling floors, can be easily obtained using proper admixtures. CSA binders are less alkaline compared to OPC, being safer against alkali-aggregate reactions and are suitable for glass-fibre composites [2, 15]. But the principal difference to OPC is the intrinsic immunity of CSA materials against sulphate attack [10, 11], which together with lower porosity [16], should result in higher durability and performance. On the other hand, lacking portlandite in the composition, CSA concretes could be susceptible to carbonation with an adverse effect on the passivation of steel reinforcement, as it has been proven for blended cements [17]. Long-term durability of CSA in terms of steel reinforcement corrosion is not well studied [2, 15].
Regardless of lower porosity and lower chloride ingress, compared to OPC [16, 18], high corrosion rates of embedded carbon steel rebars were previously observed since early beginning of testing [18], but no viable explanation was given. Thus, we assumed that the composition of CSA binder and pore solution, is the cause for the corrosion of carbon steel reinforcement.
The principal components of CSA binders are ye'elimite – $3CaO{\cdot}3Al_2O_3{\cdot}CaSO_4$, calcium sulphate and belite, with their variable ratio to determine controlled shrinkage or expansion. Thus, CSA contain significant amount of sulphate-rich phases (17 wt. % of SO_3 vs 2.6 wt. % in OPC [2, 6, 7, 13, 19, 20]) that may release sulphate ions into pore solution. Previously, a combined action of sulphate and chloride ions on steel rebars was studied [21], but the behaviour of steel in the presence of sulphates alone has not been studied yet.
Pore solution composition for CSA and OPC binders at various stages of hydration was previously reported [7, 19, 22-24]. Though dissolved sulphate values are similar in the end of hydration – 10 mM and 4.5 mM respectively for OPC and CSA, in the beginning of hydration (0.5 h), OPC binders have in average more dissolved sulphates with respect to CSA analogues – 110 vs 20 mM. On the opposite, hydroxide concentration in the beginning of CSA hydration is 2.3 orders lower compared to OPC, evidenced by pH of 10.5 vs 12.8 respectively. However, after 8 hours of CSA cement hydration pH increases, reaching 12.5 in

average vs 13.6 for OPC. Therefore, regardless lower absolute value of dissolved sulphates, CSA binders are characterized by significantly lower pH, thus higher sulphate-to-hydroxide ratio.
Based on intensive analysis of the state-of-the-art, it has been assumed that the corrosion of mild steel reinforcement in fresh CSA binders is caused by the combination of low pH and relatively high concentration of sulphates in pore solution of CSA mortars and concretes. We believe that sulphate ions adsorb on the steel surface followed by the formation of soluble species, causing thinning and destruction of passive oxide film followed by the formation of corrosion pits in a similar manner as chlorides do [17, 25]. Since hydroxides stabilize passive oxide film, it is assumed, that the deleterious action of sulphate ions is inversely proportional to the concentration of hydroxides in pore solution, and a critical ratio between sulphate and hydroxide ions should exist, which separates corrosion and non-corrosion regions. The determination of that threshold is a fundamental task to confirm or disprove the assumptions made above over the mechanism of steel corrosion in CSA-based mortars and concrete.
Since the corrosion of steel is the main culprit for reduced durability of reinforced concrete structures due to cracking caused by expansive corrosion products, to find a scientific solution of the problem, or at least to propose a preventive repair methodology, the origin of mild steel reinforcement corrosion in fresh CSA-based cementitious materials must be comprehensively understood. Mild steel rebars were tentatively tested in simulating solutions to mimic conditions encountered in binders at various stages of CSA hydration. While in static corrosion tests steel samples continuously immersed in the solutions of constant composition, in dynamic corrosion tests the composition was changed in programmed way to reflect the evolution of key corrosion parameters, i.e. pH and dissolved sulphates, as it occurs during hydration of CSA. This paper overviews only preliminary findings of electrochemical tests, such as circuit potential (OCP) monitoring and electrochemical impedance spectroscopy (EIS) [26-28].

2. Materials and experimental procedures

Low carbon steel CK45K reinforcement rebar (in wt.%: C 0.4, Mn 0.7, Si 0.2, S max. 0.05, P max. 0.05, balance – Fe) of 1.2 cm in diameter was cut perpendicularly to the axis with a water-cooled circular sand saw. Copper wire was attached to the inner side of steel piece with a silver paint, and the pieces were embedded into epoxy resin. Samples were polished under water using SiC papers up to 1000 grit at 500 rpm, rinsed with deionized water and ethanol, dried with compressed air. Finally, 3M™ Scotchrap™ 50 tape was applied over polished surface, defining the exposed area of 0.24 cm^2. At least three identical samples were prepared for all the tests and conditions.
Corrosion tests were performed in air at 25ºC in 0.316, 3.16 and 31.6 mM NaOH solutions, containing or not 1.00, 10.0 and 200 mM of K_2SO_4. Electrochemical tests, – OCP and EIS, were performed in three-electrode arrangement (Pt wire as counter electrode - CE, saturated calomel electrode as a reference electrode, and steel sample as a working electrode - WE) using Autolab PGSTAT302N. OCP were recalculated vs standard hydrogen electrode (SHE) potential. For EIS single sinusoidal potential perturbations of 10 mV (rms) amplitude were applied vs OCP within the frequency range 50 kHz to 5 mHz. The impedance data were fitted with ZView.

3. Results and discussion

The results of OCP monitoring of exposed steel rebars in 0.316 mM NaOH suggested that corrosion immediately started even in the presence of just 1 mM of sulphates. OCP declined gradually till final values of -420 – -460 mV, suggesting severe corrosion. On the other hand, in the absence of sulphates, initial OCP values were 100-160 mV higher, and increased with time till 8.3 mV, indicating the passive state. EIS spectra, obtained after 7 hours of immersion, showed notable differences. In high frequency region (2-50 kHz), where the response from solution dominates, |Z| decreased with sulphates addition. In middle frequency range (1-10 Hz), where the response mainly comes from oxide film, impedance modulus values declined, as the number and size of corrosion pits increased – $|Z|_{3.15Hz}$ were 3630, 700, 168 and 105 Ohm·cm^2 for 0, 1, 10 and 200 mM K_2SO_4 respectively, accompanied by lessening of the capacitive response of oxide film, evidenced from phase angle Bode plot. The greatest difference was seen for $|Z|_{5mHz}$, proportional to polarization resistance, R_P. Steel exposed to sulphate-free solution evidenced high value of 670 kOhm·cm^2 in the opposite to the samples in solutions containing sulphates, in which the values were 2.5 - 3.5 orders lower – 4.2, 2.9 and 1.2 kOhm·cm^2, indicating active corrosion of steel reinforcement, intensified with the increase of sulphates.

While the corrosion tests carried out in 0.316 mM were designed to mimic the liquid phase of CSA binders at very beginning of cement hydration, testing in 3.16 mM NaOH solutions simulated the conditions encountered between 2 and 64 hours of hydration. Tenfold increase in hydroxide concentration improved the corrosion resistance of steel, and not only in sulphate-free, but also in 1 mM K_2SO_4 a gradual OCP growth was found. In the latter case, mild steel depassivation occurred and corrosion initiated between 52.4 and 53.0 hours, evidenced by a drop from 66.5 to -331 mV, finally reaching -396 mV (64 hours) vs 90.2 mV (66 hours) for the reference. The samples immersed in 10 and 200 mM K_2SO_4 since early beginning showed gradual decrease in OCP, reaching values of -471 and -501 mV in the end of the test.

These results fully corroborated with EIS findings. $|Z|_{5mHz}$, measured for mild steel in pure 3.16 mM NaOH, increased with time and reached 1.36 MOhm·cm^2 after 2 days, being a bit higher, when compared to 1.27 MOhm·cm^2 for the sample in 1 mM K_2SO_4 solution, in which a sharp three-order drop was observed after 53 hours, reaching similar values for 10 and 200 mM sulphate solutions – 1.9, 1.4 and 1.3 kOhm·cm^2 respectively. The middle frequency range EIS response followed the trend at low frequencies: high impedance values and phase angle close to 90°, were observed for steel in passive state, while corroding samples showed both low impedance and phase angle values, due to the progressive damage of the oxide film.

Finally, corrosion studies were performed in 31.6 mM NaOH (pH 12.5) solutions containing sulphates to simulate pore media encountered in CSA and OPC mortars and concretes in the end of cement hydration. According to cumulative electrochemical results in 31.6 mM NaOH, mild steel could tolerate small amount of dissolved sulphates. In fact, the passive state of steel was observed in all 31.6 mM NaOH solutions, evidenced by gradual increase of OCP since the beginning of corrosion tests, until passive film breakdown occurred after 18-22nd and 5-6th days of immersion respectively for steel samples in solutions of 10 and 200 mM K_2SO_4, evidenced the drop in OCP due to aggressive action of sulphates as sulphate-hydroxide ratio increased. On the other hand, in the presence of 1 mM K_2SO_4 mild steel reinforcement

remained passive until the end of corrosion test (30th day), confirmed by high OCP, by far exceeding 115 mV (SHE), similar to the reference sample in sulphates-free solution.
The results of corrosion tests suggested that in order to ensure persistent passivation of steel, the concentration of hydroxide ions should exceed that of sulphates about 18 times, serving a guide for the critical ratio. The combined findings suggested that sulphate-induced corrosion of common mild steel reinforcement would start instantly in CSA-based materials at early stages of hydration due to high sulphate-to-hydroxide ratio, well above proposed safe threshold, although the conditions in hydrated state are favourable for steel passivation (Fig. 1).

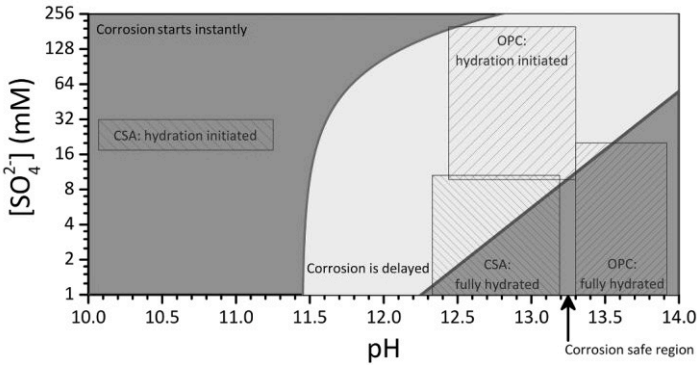

Figure 1: Sulphate-induced corrosion diagram of mild steel

To understand whether re-passivation of steel would occur, as the environment becomes less aggressive, passing from the region of severe corrosion to no corrosion region (Fig. 1), dynamic corrosion testing in solutions of variable composition was performed, and they suggested that regardless of the perfect conditions for the passivation of steel in hydrated matrix, CSA binders fail to provide chemical protection of rebars, since due to corrosion emerged at early stages of hydration, caused simultaneously by elevated amount of dissolved sulphates and low pH, the corrosion of the reinforcement will likely progress, despite short-term repassivation observed.

4. Conclusions and Future work

The corrosion behaviour of plain carbon steel reinforcement was studied in solutions that simulate liquid phase of calcium sulphoaluminate cement at various stages of hydration. Two types of tests were carried out. In static corrosion tests steel rebars were studied in solutions of constant fixed composition, while in dynamic corrosion tests their composition was changed with time to mimic the evolution of pH and sulphates as it occurs during hydration of calcium sulphoaluminate cement. The deleterious role of sulphate ions on the passivity of steel has been proven. To guarantee a persistent protection of steel, the concentration of hydroxide ions should exceed that of sulphates about 18 times. The results suggested that the corrosion of steel would start instantly, stipulated by low pH and high concentration of dissolved sulphates, exceeding threshold, and, despite favourable conditions for passivation in the hydrated state of calcium sulphoaluminate cement based materials, corrosion of the reinforcement would proceed further, since no long-term repassivation was observed.
Therefore, the corrosion of steel reinforcement in calcium sulphoaluminate cement based materials is their greatest single limitation, and its elimination is the most crucial, indispensable requirement for wide market acceptance and successful application in construction practice. Therefore, in our future research, we aim to search for viable scientific and technologic solutions or preventive repair methodologies to minimize the risk of reinforcement corrosion to meet the life expectancy level of conventional OPC-based concretes.

Acknowledgements

The authors acknowledge Fundação para a Ciência e Tecnologia for funding PhD grant SFRH/BD/88016/2012 and Centro de Química Estructural (UID/QUI/00100/2013), as well as acknowledge CA15202 for financial support.

References

[1] J.G.J. Olivier, G. Janssens-Maenhout, M. Muntean, J.A.H.W. Peters, Trends in global CO_2 emissions: 2015 Report, Institute for Environment and Sustainability of the European Commission's Joint Research Centre, 2015.
[2] P.C. Aïtcin, Binders for Durable and Sustainable Concrete, Taylor & Francis, 2007.
[3] M. Schneider, M. Romer, M. Tschudin, H. Bolio, Sustainable cement production — present and future, Cem. Concr. Res., 41 (2011) 642-650.
[4] J.S. Damtoft, J. Lukasik, D. Herfort, D. Sorrentino, E.M. Gartner, Sustainable development and climate change initiatives, Cem. Concr. Res., 38 (2008) 115-127.
[5] V.S. Ramachandran, Concrete Admixtures Handbook: Properties, Science, and Technology, Noyes Publications, 1995.
[6] P. Barnes, J. Bensted, Structure and Performance of Cements, Second Edition, Taylor & Francis, 2002.
[7] F. Winnefeld, B. Lothenbach, Hydration of calcium sulfoaluminate cements - Experimental findings and thermodynamic modelling, Cem. Concr. Res., 40 (2010) 1239-1247.
[8] F.P. Glasser, L. Zhang, High-performance cement matrices based on calcium sulfoaluminate–belite compositions, Cem. Concr. Res., 31 (2001) 1881-1886.
[9] P. Arjunan, M.R. Silsbee, M.R. Della, Sulfoaluminate-belite cement from low-calcium fly ash and sulfur-rich and other industrial by-products, Cem. Concr. Res., 29 (1999) 1305-1311.
[10] K. Quillin, Performance of belite–sulfoaluminate cements, Cem. Concr. Res., 31 (2001) 1341-1349.
[11] S. Ioannou, K. Paine, L. Reig, K. Quillin, Performance characteristics of concrete based on a ternary calcium sulfoaluminate-anhydrite-fly ash cement, Cem. Concr. Compos., 55 (2015) 196-204.
[12] Y.S. Liao, X.S. Wei, G.W. Li, Early hydration of calcium sulfoaluminate cement through electrical resistivity measurement and microstructure investigations, Construction and Building Materials, 25 (2011) 1572-1579.
[13] M.C. Gonçalves, F. Margarido, Materials for Construction and Civil Engineering: Science, Processing, and Design, Springer International Publishing, 2015.
[14] L. Zhang, F.P. Glasser, Hydration of calcium sulfoaluminate cement at less than 24 h, Adv Cem Res, 14 (2002) 141-155.
[15] M.C.G. Juenger, F. Winnefeld, J.L. Provis, J.H. Ideker, Advances in alternative cementitious binders, Cem. Concr. Res., 41 (2011) 1232-1243.
[16] G. Bernardo, A. Telesca, G.L. Valenti, A porosimetric study of calcium sulfoaluminate cement pastes cured at early ages, Cem. Concr. Res., 36 (2006) 1042-1047.
[17] L. Bertolini, B. Elsener, P. Pedeferri, Corrosion of Steel in Concrete: Prevention, Diagnosis, Repair, Wiley, 2004.
[18] D. Kalogridis, G.C. Kostogloudis, C. Ftikos, C. Malami, A quantitative study of the influence of non-expansive sulfoaluminate cement on the corrosion of steel reinforcement, Cem. Concr. Res., 30 (2000) 1731-1740.
[19] B. Lothenbach, F. Winnefeld, Thermodynamic modelling of the hydration of Portland cement, Cem. Concr. Res., 36 (2006) 209-226.
[20] B. Lothenbach, F. Winnefeld, C. Alder, E. Wieland, P. Lunk, Effect of temperature on the pore solution, microstructure and hydration products of Portland cement pastes, Cem. Concr. Res., 37 (2007) 483-491.
[21] V.K. Gouda, W.Y. Halaka, Corrosion and Corrosion Inhibition of Reinforcing Steel: II. Embedded In Concrete, Br. Corros. J., 5 (1970) 204-208.
[22] A. Vollpracht, B. Lothenbach, R. Snellings, J. Haufe, The pore solution of blended cements: a review, Mater. Struct., 49 (2016) 3341-3367.
[23] P. Chaunsali, Early-age hydration and volume change of calcium sulfoaluminate cement-based binders, Doctor of Philosophy in Civil Engineering Dissertation, University of Illinois, 2015
[24] M. Andac, F.P. Glasser, Pore solution composition of calcium sulfoaluminate cement, Adv Cem Res, 11 (1999) 23-26.
[25] P. Marcus, V. Maurice, H.-H. Strehblow, Localized corrosion (pitting): A model of passivity breakdown including the role of the oxide layer nanostructure, Corros. Sci., 50 (2008) 2698-2704.
[26] K. Hladky, L.M. Callow, J.L. Dawson, Corrosion Rates from Impedance Measurements - an Introduction, Br. Corros. J., 15 (1980) 20-25.
[27] M.F. Montemor, Estudo da deterioração por corrosão de estruturas de betão armado, PhD Dissertation, Instituto Superior Técnico, Universidade Tecnica de Lisboa, 1995
[28] P. Marcus, F.B. Mansfeld, Analytical Methods In Corrosion Science and Engineering, CRC Press, 2005.

SynerCrete'18 International Conference on Interdisciplinary Approaches
for Cement-based Materials and Structural Concrete
24-26 October 2018, Funchal, Madeira Island, Portugal

THE DEVELOPMENT OF THE EARLY-AGE ELASTIC MODULUS IN CEMENT-MATERIALS WITH DIFFERENT WATER COEFFICIENT

Romana Halamová [(1)], Dalibor Kocáb [(1)], Barbara Kucharczyková [(1)], Petr Daněk [(1)]

(1) Brno University of Technology, Brno, Czech Republic

Abstract
The effect of the composition of cementitious materials on the resulting value of the modulus of elasticity is a matter of common knowledge. However, the issue of what factors affect it during early age is still not well understood. The paper deals with the development of the modulus of elasticity in cement composites at an early age. The measurements were performed on cement pastes with varying water-cement ratio. The influence of plasticizer content was also investigated. Prism-shaped specimens with the dimensions of 40×40×160 mm and Vicat ring-shaped specimens were manufactured for the purposes of the experiment. The modulus of elasticity was determined based on a continuous measurement of the ultrasonic transit time during the first 24 hours of ageing. The measurement was started immediately after filling the measurement cell with the fresh material and took 24 hours. The internal temperature of the specimens was measured simultaneously, which provided information about the hydration process of the material. All the prismatic test specimens were removed from moulds at an age of 24 hours and tested for the dynamic modulus of elasticity by the ultrasonic pulse velocity test at the age of 24, 48 and 72 hours. The measurement of the dynamic modulus of elasticity was supplemented with a static test performed on the prismatic test specimens at the age of 24 and 72 hours.

1. Introduction

Concrete is a common construction material which possesses great compressive strength. In the beginning of its existence, it consisted of cement, aggregate, and water, and only later did it start to be enhanced by various additives and admixtures, resulting in considerable advancement in concrete technology [1]. However, the composition of concrete was not the only thing that saw marked development; approaches to designing concrete structures have also undergone substantial changes. The trend of the past few years has been the construction

of (in some aspects) unorthodox, revolutionary, or at times even megalomaniac land structures and long-span bridges, which combine an emphasis on a low environmental impact and pleasant aesthetics. Modern concrete structures are increasingly taller, longer and slenderer [2]. It so happens that, aside from compressive strength, other properties enter the foreground of attention, e.g., durability, shrinkage, and especially deformation resistance, which is typically represented by the modulus of elasticity [3, 4, 5]. This property has recently become the subject of examination at research centres as well as in general construction practice. There are also a number of factors that affect the value of the modulus of elasticity, which can be divided into two basic groups [6]. The first group of factors includes the composition of the fresh mixture (mainly the type, amount, fraction, and quality of aggregate) and the conditions in which the concrete matures (ambient temperatures, curing time and technique, etc.) [7]. The second group involves the influences of the test methods used to determine the value of the elastic modulus. These factors have impact especially on the results of measurements which values deviate more or less from the real material's characteristic. In terms of the testing principle, these methods can be divided into static and dynamic [8]. Most test methods measure hardened composites (a material of a specific strength). In many cases, such as early formwork removal, rapid construction, or the installation of pre-stressing cables, it is useful to know how the value of the elastic modulus develops in concrete which has not yet fully hardened. This can be tested using the ultrasonic pulse velocity test, which is also the focus of this paper.

2. Experiment

The goal of the experiment was to determine the influence of the w/c ratio and plasticiser content on the value of the modulus of elasticity in cement pastes younger than 72 hours.

2.1 Materials and specimens

Prior to the experiment six cement pastes were mixed for the purposes of testing using cement CEM I 52.5 R produced by cement plant Mokrá (Czech Rep.). The first three pastes contained no plasticiser and had a w/c ratio of 0.33, 0.40, and 0.50. They were identified as CP33, CP40, and CP50. The lowest w/c ratio corresponded to the theoretical minimum of water required for the cement to hydrate fully. The other three pastes had the same w/c ratio as the first three; however, they also contained polycarboxylate-based plasticiser Sika ViscoCrete 4035 at an amount of 1 % of cement weight. They were designated as CPP33, CPP40, and CPP50.

Each paste was made into a one specimen in the shape of the Vicat ring, which were used for the continuous measurement of the dynamic modulus of elasticity (henceforth E_{cu}) using the ultrasonic pulse velocity test over the first 24 hours, and eight prisms with the dimensions of 40 × 40 × 160 mm used for measuring the modulus of elasticity at ages from 24 to 72 hours. The first four prisms were used for determining the dynamic and static modulus of elasticity (henceforth E_c) at an age of 24 hours. The other four then served for the determination of E_{cu} at an age of 48 hours. The same specimens were then used for E_{cu} and E_c at 72 hours of age counted from the moment the cement was mixed with water. The prism specimens were covered with a PE foil while they aged and were stored in standard laboratory conditions at a temperature of (22±2) °C and RH = (55±5) %.

2.2 Test methods

Measuring the modulus of elasticity during the first 24 hours. After each of the cement pastes has been mixed, a Vicat ring was filled with the fresh mixtures and placed in the measuring chamber of a Vikasonic ultrasonic apparatus produced by the company Schleibinger [9] (pictured in Fig. 1 left). This ring, having been filled with a cementitious material, is placed between two transducers operating at 54 kHz, one of which functions as the transmitter and the other as the receiver of an ultrasonic pulse. Following parameters of the ultrasonic pulse were set before the start of measurement: pulses transmission frequency of 60 impulses per minute, impulse voltage of 2000 V, reading frequency of 10 s. The transit time was determined as the time when the amplitude of the signal exceeds the pre-set threshold. The apparatus is primarily designed for measuring the setting time, but unlike the traditional Vicat apparatus, it can continuously and non-invasively measure setting while monitoring the material's internal temperature together with the ultrasonic transit time. Given the fact that the instrument is designed so that the distance of the measuring base does not change during use, the continuous measurement of ultrasonic transit times can be used to calculate the ultrasonic pulse velocity and subsequently determine the values of the dynamic modulus of elasticity over the set time period according to the following formula [9]:

$$E = \rho \cdot v^2, \tag{1}$$

where E is the dynamic modulus of elasticity in MPa, ρ is bulk density in kg/m^3 and v is the ultrasonic pulse velocity in km/s. Changes in the internal temperature of the material well demonstrates the progress of cement hydration. The use of the Vikasonic is discussed in greater detail e.g. in [10].

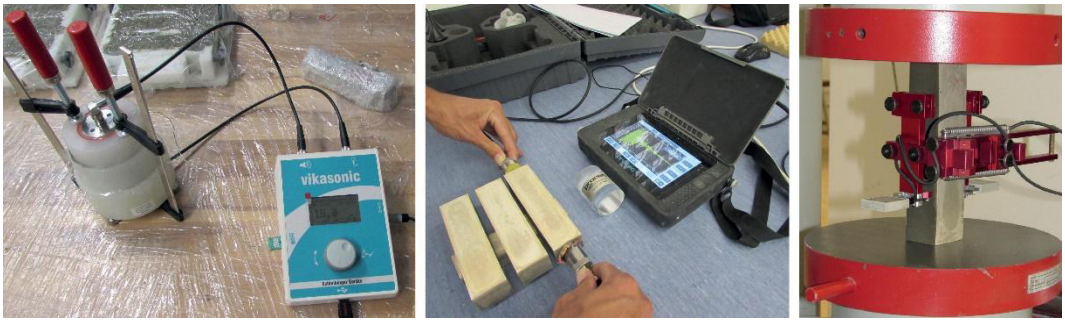

Figure 1: The Vikasonic ultrasonic device (left), ultrasonic pulse velocity test using Pundit PL-200 (middle) and static test (right).

Measuring the modulus of elasticity at an age of 24 through 72 hours. The measurements were performed on prism specimens with the dimensions of 40 × 40 × 160 mm, which were demoulded 24 hours after the cement was mixed with water. The first four specimens were measured for the modulus of elasticity at an age of 24 hours. The remaining four were wrapped in PE foil and left in standard laboratory conditions for later testing. The modulus of elasticity was determined by the ultrasonic pulse velocity test first – the measurements were made using the Pundit PL-200 apparatus manufactured by Proceq (see Fig. 1 middle) and the elastic modulus E_{cu} was calculated according to ČSN 73 1371 [11] using the formula:

$$E_{cu} = \rho \cdot v_L^2 \cdot \frac{(1+\mu)\cdot(1-2\cdot\mu)}{1-\mu}, \quad (1)$$

where E_{cu} is the dynamic modulus of elasticity in MPa, ρ is bulk density in kg/m^3, v_L is the ultrasonic pulse velocity in km/s and μ is the dynamic Poisson's ratio, which was estimated on the basis of a supplementary measurement of resonance frequencies using the same specimens. The second stage focused on determining the static modulus of elasticity E_c. The test was performed in accordance with ISO 1920-10 [12]. The specimens were loaded using the DELTA 6-300 press manufactured by FORM+TEST. The deformations were measured along a base of 80 mm using displacement transducers connected to a data logger (Fig. 1 right). The test of E_c was concluded by determining the compressive strength.
At the age of 48 hours, the remaining four prisms were tested for E_{cu}. Once the tests were finished, the prisms were again wrapped in a PE foil until the age of 72 hours when they were once again tested for both the static and dynamic modulus of elasticity.

3. Results and discussion

3.1 Results of the dynamic modulus of elasticity in first 24 hours

The measurement results obtained using the Vikasonic are plotted in Fig. 2.

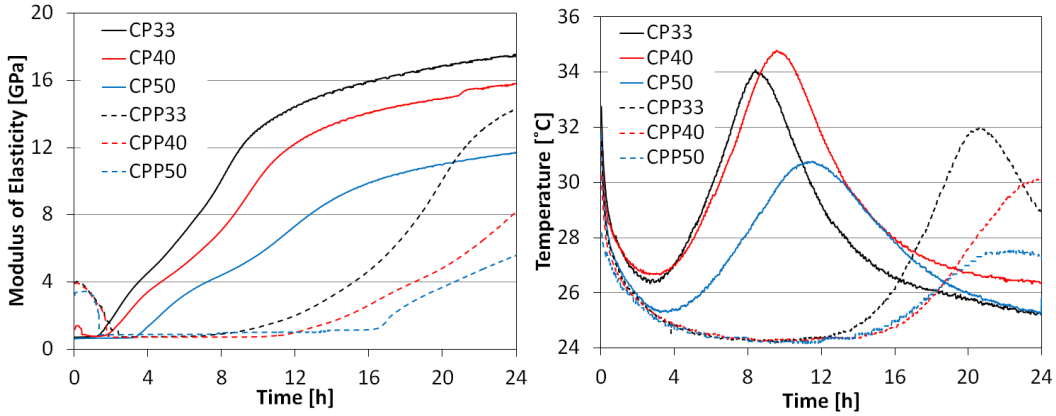

Figure 2: Progress of the dynamic modulus of elasticity of the cement pastes (left) and progress of the internal temperature (right) over the first 24 hours of age.

The diagrams show that as the w/c ratio rises, the values of the dynamic modulus of elasticity grow more slowly and the temperature peak also occurs at a later time. The cement pastes that contained plasticiser saw a significant delay in setting compared to pastes with no plasticiser content, which can be clearly seen in the development of internal temperature (Fig. 2 right). This was also visible in the markedly lower values of the dynamic modulus of elasticity during the monitored period (first 24 hours of age), see Fig. 2 left. The continuous measurement captured also the very early stage of hydration period (end of the first hydration peak) when the viscosity of the material was changing from the fluid to thixotropic state. This process was very well visible in the case of cement pastes with the plasticizer, when the initial value (at the start of measurement) of the modulus of elasticity corresponded to the ultrasonic

pulse velocity of approx. 1420 m/s which was close to the value of the ultrasonic pulse velocity of water. The subsequent changes in viscosity and formation of material's microstructure caused damping of the ultrasonic waves which was reflected in the decrease in the elastic modulus value. During the dormant period there were no changes in the value of elastic modulus. The subsequent growth of the elastic modulus started with the growth of the internal temperature (see Fig. 2).

3.2 Results of the dynamic modulus of elasticity from 24 to 72 hours after mixing

The average values of the measured elastic moduli E_{cu} and E_c taken from measurements performed on four test specimens are plotted as bar charts in Fig. 3; the error bars represent a sample standard deviation. The relative values of elastic modulus are summarized in Tab. 1.

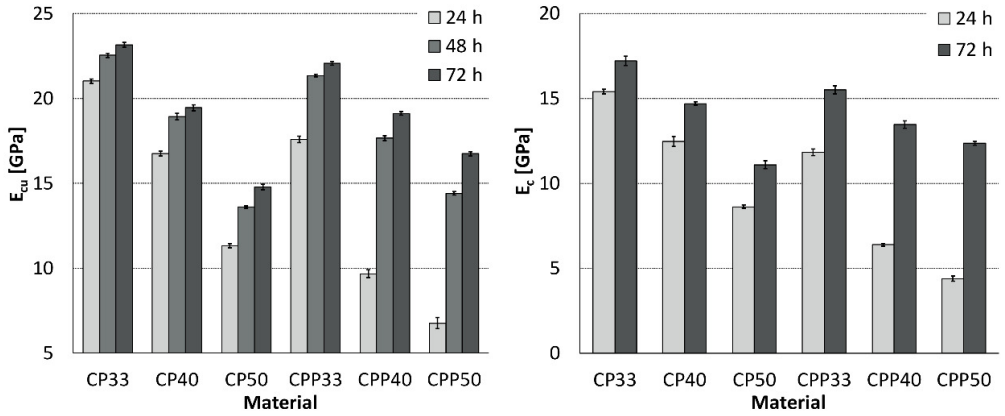

Figure 3: Results of the dynamic modulus of elasticity determined by the ultrasonic pulse velocity test and static modulus of elasticity (right).

Table 1: Relative values of elastic modulus: 100% is CP33 at the age of 24 hours.

Elastic Modulus	Age [h]	Material					
		CP33	CP40	CP50	CPP33	CPP40	CPP50
E_{cu}	24	100.0	79.7	53.9	83.6	46.0	32.1
	48	107.2	90.1	64.7	101.5	84.0	68.5
	72	110.2	92.5	70.3	104.9	90.9	79.7
E_c	24	100.0	81.0	56.0	76.7	41.4	28.5
	72	111.8	95.4	72.0	100.6	87.4	80.2

It can be said that the increasing trend of the elastic modulus was very similar in all the cement pastes without plasticiser (regardless of the w/c ratio); only their final absolute values differed – the lower the w/c ratio, the higher the values of elastic modulus. All the cement pastes with a content of plasticiser also exhibited a similar trend in the development of the modulus of elasticity (regardless of the w/c ratio), which, however, was markedly different from the development in pastes without plasticiser. During the first 24 hours the increase in pastes containing plasticiser was very slow, accelerating only over the second day of age. After that, the values of the elastic modulus increased much more rapidly.

4. Conclusion

The experiment results showed the influence of w/c ratio and plasticiser on the development of the modulus of elasticity in young cement pastes. This case study showed that the pastes made from CEM I 52.5 R with plasticiser registered a significant retardation in the early growth of the modulus of elasticity compared to pastes without plasticiser, especially during the first 24 hours. However, only one kind of plasticiser has been used in the production of cement pastes. Other products may show different results.
It appears that the ultrasonic apparatus is well suited for determining the dynamic modulus of elasticity during the setting of cement composites. The question still remains, however, how to determine the Poisson's ratio, which influences the value of the elastic modulus E_{cu}. Hardened composites allow its value to be obtained e.g. by measuring resonance frequencies, as was done in the case of this paper.

Acknowledgements
This paper has been written as part of the project No. GA17-14302S "Experimental analysis of the early-age volume changes in cement-based composites", supported by the GA0 - Czech Science Foundation and project No FAST-J-18-5516 "Determination of modulus of elasticity in the early phase of maturing of cement composites and their thermal expansion".

References

[1] Neville, A. M. and Brooks, J. J., Concrete technology, Prentice Hall, Harlow (2010)
[2] Collepardi, M., The New Concrete, first ed., Grafiche Tintoretto, Treviso (2006)
[3] Yldirim, H. and Sengul, O., Modulus of elasticity of substandard and normal concretes, Constr. Build. Mater. 25 (2011), 1645-1652
[4] Zhou, Y. et al, A fundamental study on compressive strenght, static and dynamic elastic moduli of young concrete, Constr. Build. Mater. 98 (2015), 137-145
[5] Kucharczyková, B. et al, Experimental Analysis on Shrinkage and Swelling in Ordinary Concrete, Advances in Materials Science and Engineering (2017), ID 3027301
[6] Huňka, P. et al, Test and technological influences on modulus of elasticity of concrete, Procedia Engineering 65 (2013), 266-272
[7] Křížová, K. and Hela, R., Selected technological factors influencing the modulus of elasticity of concrete, World Academy of Science, Engineering and Technology, Turkey, 6 (2014), 557-559
[8] Halamová, R. and Kocáb, D., Review of the Possibilities of Determining the Modulus of Elasticity and Poisson's Ratio in the Early Stage of Cement Composite Ageing, 10th Int. Scientific Conference of Civil and Environmental Engineering, Slovakia (2018), 1-7
[9] Vikasonic – Measuring the Early Setting and Hardening with Ultrasonic Waves Measuring,http://www.schleibinger.com/cmsimple/en/?Setting_and_Maturity:Ultrasonic_Setting_Measurement
[10] Rozsypalová, I. et al, Monitoring of the Setting and Early Hardening with Ultrasonic Waves, to be published 2018
[11] ČSN 73 1372 Non-destructive testing of concrete – Testing of concrete by resonance method, ČNI, Prague (2011) (in Czech)
[12] ISO 1920-10 Testing of concrete – Part 10: Determination of static modulus of elasticity, ISO, Geneva (2010)

SynerCrete'18 International Conference on Interdisciplinary Approaches
for Cement-based Materials and Structural Concrete
24-26 October 2018, Funchal, Madeira Island, Portugal

THE USE OF ACOUSTIC METHODS TO DESCRIBE THE BEHAVIOUR OF CEMENT PASTES IN THE EARLY STAGE OF AGEING

Michaela Hoduláková [(1)], Libor Topolář [(1)], Barbara Kucharczyková [(1)], Dalibor Kocáb [(1)]

(1) Brno University of Technology, Faculty of Civil Engineering, Brno, Czech Republic

Abstract
Monitoring of properties of cement-based composites at an early age (approximately during the first 48 hours after mixing cement with water), understanding the hydration processes of the cement paste, and identifying various mechanisms, including potential formation of microcracks during hardening, are essential steps to ensure the quality of cement-based composites and to guarantee their long lifetime. The processes that occur at this early age significantly influence the resulting properties of cement-based composites. Various methods used today to expand the understanding of early hydration include, for example, non-contact complex resistivity, thermogravimetric X-ray computed tomography, scanning electron microscopy, ultrasound or the acoustic emission method. The paper deals with the use of the acoustic emission method to describe the behaviour of cement-based composites during the first 48 hours after mixing cement with water. The acoustic emission sensors allow the detection of elastic waves which may occur during the formation of hydration products, water cavitation, or during the formation and spreading of microcracks (e.g. as a result of plastic shrinkage). The acoustic emission method allows continuous monitoring of the hydration process throughout the experiment and by using the acoustic emission method, there is no need to stop the hydration process to allow its monitoring.

1. Introduction

Monitoring the behaviour of composite building materials and structures is an important part of not only the production process (in course of their setting, hardening, and ageing), but also of the actual usage of the structure during its lifetime (compressive and bending stresses, cyclic loading, etc.). The description of the behaviour of composite building materials and

structures in laboratory, semi-laboratory, production, and practical use serves both research and development goals as well as practical purposes. To achieve this goal, the scope of current development and the use of the already existing methods should be expanded and non-standard methods and procedures should be employed. Non-destructive acoustic method, the acoustic emission method, is one of those non-standard methods which was utilized in the paper [1, 2].

The acoustic emission method (AE) belongs among the most advanced methods for material engineering and fatigue applications. The source of the AE signal can originate in many phenomena depending on the type of the material. For metals, the sources of the acoustic emissions can originate in dislocation movements, cracks, fractures, and even corrosion processes. In concrete, the AE signals can be generated by microscopic and macroscopic defects as well as by tearing or shifting of the reinforcement. In composites, the AE comes from matrix cracking, delamination, matrix separation from fibres, fibre tearing, and fibre pulling. Most acoustic emission sources are associated with defects. Detection and monitoring of these emissions is commonly used to predict material failure [1 – 4].

The AE event (Fig. 1) is emitted by irreversible dislocation and degradation processes in the microstructure and macrostructure of the material. The released energy is transformed into a mechanical stress impulse propagating throughout the material as an elastic longitudinal or transverse wave. A signal detected on the AE sensor and converted to an electrical signal is described as an AE signal [5].

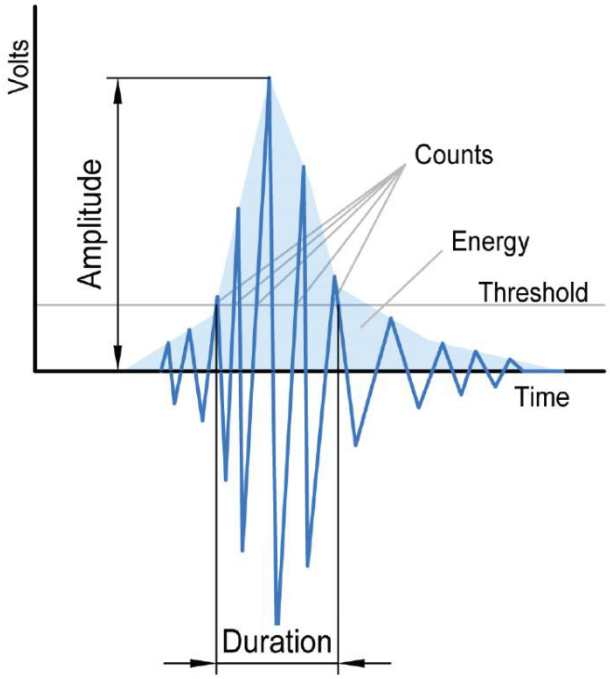

Fig. 1 AE events with measured parameters.

In parametric description of individual AE events, the aim is primarily to detect the emission source and to obtain as much information as possible about the progress of the AE signal. The

progress of the AE events is described in the basic parameters, the standard EN 1330-9 defines the following AE signal parameters [6]:

- hit - detection of one discrete signal (Fig. 1) on one AE channel;
- acoustic emission detection threshold - the voltage level that must be exceeded to detect a discrete signal;
- arrival time - time when the discrete signal first exceeds detection time;
- duration - time difference between the first and last exceeding of the detection threshold by the discrete signal;
- number of events - number of events of the discrete signal that exceeds the detection threshold in one polarity;
- maximum amplitude - maximum voltage deviation during the duration of the discrete signal;
- rise time - time difference between the first exceeding of the threshold and the maximum amplitude of the discrete signal;
- energy - the integral of the squared AE signal over the duration of the discrete signal.

In addition to these parameters, it is recommended to record the values of other significant parameters or physical quantities along with the individual AE events that correspond to the created internal stresses (e.g. force, temperature, etc.). Within the evaluation of experiments discussed in this paper, the focus was paid to the amplitudes of the AE signal [7].

2. Materials and experimental setup

For the purpose of the experiment, cement pastes were produced and placed into a Vicat ring. Individual specimens of the cement pastes were produced from two types of cement (CEM I 42.5 R and CEM I 52.5 R) with the water/cement coefficient of 0.40. Three test specimens were manufactured from each cement, i.e. there were six specimens manufactured in total. Two specimens from each set were submerged in a paraffin oil to prevent a water evaporation from the specimens' upper surface during the maturation. The upper surface of the remaining specimen of each set was exposed to free desiccation. All measurements started approx. 0.5 hours after the cement was mixed with water.
During recording and processing of the AE signals within the experiments, the Dakel system XEDO was used, which was developed by the company ZD Rpety-Dakel [8]. In general, the acoustic emission sensors are mostly attached directly on the surface of measured specimen or structure. This was, however, not possible in this particular case due to the fresh mixture of water with cement. In such cases, the acoustic waveguides are used as a support for the sensor. This configuration has a significant disadvantage – a loss of the signal on the sensor-waveguide interface [9, 10]. In the performed experiment, this disadvantage was eliminated by usage of specially constructed waveguides with an incorporated acoustic emission sensor, see Fig. 2. This approach led to the elimination of the signal attenuation and other possible disturbances of the signal at the interface of the waveguide and the sensor. The sensor-

waveguide was coated with a thin layer of beeswax before measurement, which enabled the safe extraction of the waveguide after the measurements were finished.

Fig. 2 Photo of placement of the AE sensors.

3. Results and discussions

The results are presented in figures where the curve shows the differential temperature inside the specimen (ΔT), which was calculated as the difference between the internal temperature measured in the specimen and the ambient temperature. Points show the AE amplitude (U_{AE}). (Note: no comparison can be made between the specimens submerged in oil and the specimens exposed to free desiccation of one type of cement because different AE sensor sensitivity was set).
Generally, the higher the AE amplitude is, the larger changes in the inner structure of the specimen are in progress. In the case of a solid phase, a higher amplitude indicates the formation of a larger structural failure.

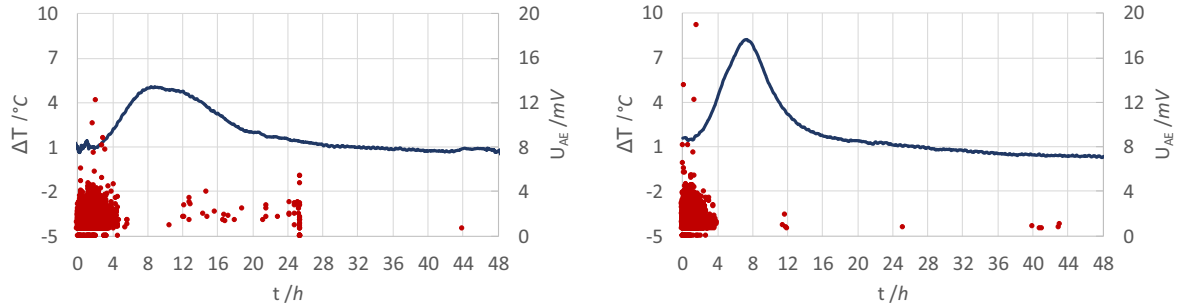

Fig. 3 Specimens submerged in oil (left CEM I 42.5 R; right CEM I 52.5 R).

Comparing the curves in Fig. 3 for the specimens submerged in oil, it can be seen that the specimens from CEM I 52.5 R exhibited higher inner temperature and also reached the relative setting time earlier. The relative setting time was estimated based on the measured curves as the time it takes to reach approximately half of the maximum of the temperature peak The AE results show that the specimen from CEM I 42.5 R exhibits a higher number of

minor structural changes during the first 4.5 hours of mixing when compared to the specimen with the CEM I 52.5 R cement. This difference can be due to a faster creation of hydration products in the CEM I 52.5 R specimen, which also led to higher amplitudes. After reaching the maximum temperature, it can be seen that the acoustic activity of either specimen is much lower than the activity at the beginning of the measurement. Nevertheless, the results indicate that certain significant structural changes still occur after the maximum temperature was reached, particularly in the specimen with the CEM I 42.5 R cement.

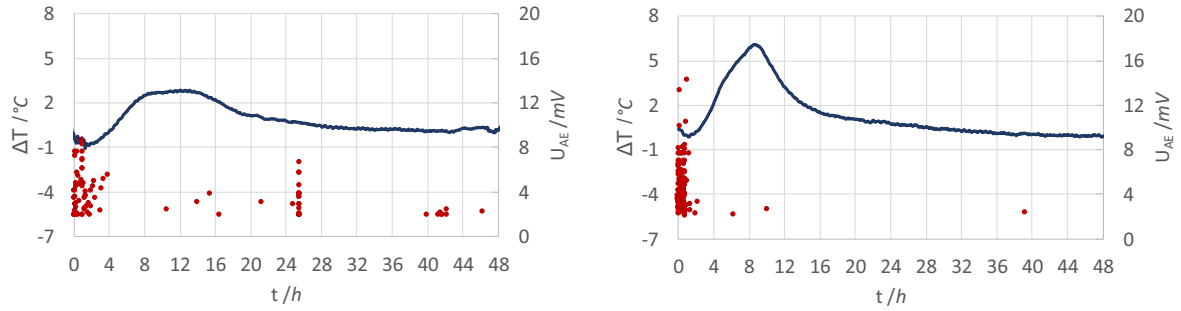

Fig. 4 Freely setting specimens (left CEM I 42.5 R; right CEM I 52.5 R)

The situation is different in the case of the specimens that were exposed to free desiccation (Fig. 4). Firstly, lower temperatures by almost two degrees were reached within the specimens. This was caused by cooling of the surface of the specimens due to evaporation of water. Secondly, the delay in the setting time of about 1.5 hours was recorded for CEM I 42.5 R and 0.5 hours for CEM I 52.5 R. The AE measurements show that the specimens made from CEM I 52.5 R exhibit higher amplitudes in a shorter time period than the specimens made from CEM I 42.5 R.

4. Conclusions

The AE method appears to be an appropriate supplementary tool for determining the formation of new products and later even microcracks during maturation of cementitious composites. It can be said that the formation of more significant bonds in the cementitious matrix and later of microcracks generate higher AE signal amplitude values. The use of the AE method for continuous monitoring of cementitious composites can help to expand the understanding of structural changes in course of setting. The use of sensor-waveguides seems appropriate for monitoring the setting process of fresh mixtures. The sensor-waveguide allows the sensor to be placed in the early stage of the setting of cementitious composites while improving the sensitivity of the sensor, making the received waves more detectable.
Currently, supplemental measurements are performed, which focus on the strength and elastic modulus development expressed by the process of the ultrasonic pulse velocity measured during the maturation of the cement paste. As the next step, the degree of hydration will be determined for the times where the AE events are detected. It is expected that these results provide more details about the AE events which appear during material maturation.

Acknowledgement
This outcome has been achieved with the financial support of the Czech Science Foundation under project no. 17-14302S "Experimental analysis of the early-age volume changes in cement-based composites".

References

[1] Grosse, Ch.U. and Ohtsu, M., Acoustic emission testing. Springer, Berlin (2008)
[2] Kopec, B. et al, Nondestructive testing of materials and constructions [in Czech]. CERM, Brno (2008)
[3] Bentur, A. (Ed.), Report 25: Early Age Cracking in Cementitious Systems-Report of RILEM Technical committee TC 181-EAS: Early age cracking shrinkage induced stresses and cracking in cementitious systems (Vol. 25), Rilem Publications (2003)
[4] Malhotra, V.M. and Carino, N.J., Handbook on Nondestructive Testing of Concrete Second Edition, CRC press (2003)
[5] Miller, R.K. et al, Acoustic Emission Testing. Nondestructive testing handbook – 6, American Society for Nondestructive Testing (2005)
[6] ČSN EN 1330- 9 (015005), Non-destructive testing - Terminology - Part 9: Terms used in acoustic emission testing, Úřad pro technickou normalizaci, metrologii a státní zkušebnictví, Praha (2001)
[7] Sikorski, W., Acoustic emission – research and applications. InTech, Rijeka (2013)
[8] Dakel - Systém XEDO. Dakel - O nás [online]. Copyright © [cit. 11.07.2018]. Available on: http://www.dakel.cz/index.php?pg=prod/dev/xedo
[9] Topolář, L., Quantification of Micro-cracks by Acoustic Emission Method during Setting and Hardening of Concrete. In Ecology and New Building Materials and Products. Advanced Materials Research vol. 1000 (2014), 199-202
[10] Topolář, L. et al, Using acoustic emission methods to monitor cement composites during setting and hardening. Applied Sciences - Basel, 7(5): 451, (2017), 1-11

SynerCrete'18 International Conference on Interdisciplinary Approaches
for Cement-based Materials and Structural Concrete
24-26 October 2018, Funchal, Madeira Island, Portugal

TIME DEPENDENT OF YOUNG'S MODULUS OF CONCRETE IN VERY EARLY AGE

Tatsuya Usui [(1)], Hitoshi Takeda [(2)] ,Hiroshi Murata[(3)], Takuya Tani[(1)]

(1) Infrastructure Technology Research Department, Technology Center, Taisei Corporation, Japan
(2) Production Engineering Technology Department, Technology Center, Taisei Corporation, Japan
(3) Urban Engineering Research Department, Technology Center, Taisei Corporation, Japan

Abstract
In the thermal stress analysis, the concrete stress is calculated from the early age. Therefore, it is considered that the influence on the concrete stress is great if the compressive strength and the Young's modulus in early age changes. However, these experimental data prior to 1 day of age have rarely been reported, because an appropriate measurement method has not been established. In this study, the Young's modulus of concrete was measured from very early age to 28 days material age based on JISA1149. The measurement was carried out with the ordinary cement concrete and the blast furnace cement concrete, and concrete temperatures were 20°C and 40°C to study the influence of cement types and concrete temperatures. As a result, it has been confirmed that the Young's modulus at 1.0N/mm^2 or less was smaller than the regression formula of JCI guidelines by 1/10-1/100 and clearly different from the regression equation of JCI guideline.

1. Introduction

The estimated equation of autogenous shrinkage of concrete which is used for thermal stress analysis has been formulated starting from the initial setting time in JCI mass concrete guideline[1]. On the other hand, the relationship between compressive strength and Young's modulus of concrete has been set based on experimental data of after 1 day of age which are the concrete compression strength 3 N/mm^2 or more and the Young's modulus 7 GPa or more. This is because the concrete strain can be continuously measured before the initial setting time is cured by using an embedded strain gauge, whereas in the case of the Young's modulus,

the method for preparing specimens, the measuring and calculating method which compressive strength is smaller than before 1 day of age have not been established. In the thermal stress analysis, it is thought that the effect of the temporal change of the compressive strength and the Young's modulus at the age of early ages is large, because the stress is calculated from the initial stage of concrete curing. However, almost no experimental data has been reported. In this study, the Young's modulus was measured from the very early age by improving the molding method based on the past research. The measurement of the Young's modulus was aimed at ordinary cement concrete and blast furnace cement concrete. In addition, the effect of cement types and concrete temperatures were investigated by measuring at concrete temperatures of 20 °C and 40 °C.

2. Method for measuring Young's modulus

2.1 Materials and Mix proportion of concrete

The mix proportion of the concrete is shown in Tab. 1 and the materials are shown in Tab. 2. As the binder, ordinary Portland cement and blast furnace slag fine powder were used. The mix proportion of the concrete was the ordinary cement concrete and the blast furnace cement concrete. The blast furnace cement concrete was replaced the blast furnace slag by 40% of the ordinary cement. In addition, the water binder ratio was 55%, the slump was 15 ± 2.5 cm, and the air volume was 4.5 ± 1.5%.

Table 1: Mix proportion of concrete

Binder	Slump (cm)	Air (%)	W/B (%)	s/a (%)	Unit weight [kg/m^3]					
					W	C	BFS	S	G	Ad
N	15	4.5	55	47.5	166	302		863	963	3.02
BB				47.5	164	179	119	861	961	2.98

Table 2: Properties of concrete materials

Symbol	Material	Property
C	Ordinary portland cement	Density 3.16g/m^3 Specific surface area 3300cm^2/g
BFS	Blast-furnace slag	Density 2.83g/m^3 Specific surface area 4050cm^2/g
S	Fine aggregate	Sarturated surface-dry density 2.63g/m^3
G	Coarse aggretegate	Sarturated surface-dry density 2.65g/m^3
Ad	Air entraining and water reducing adent	Lignin acid binding agent

2.2 Test method for very early age

(1) Test starting material age

In order to confirm the measurable start age of the Young's modulus, the initial set time of the condensation and the termination time were measured based on JIS A 1147 [2]. The concrete was used in two mix proportions, and curing temperatures were carried out at two conditions of 20°C and 40°C. In the test at the curing temperature of 20°C, the temperature of mixed concrete was set to 20°C. In the test at the curing temperature of 40°C, the temperature of mixed concrete was set from 35°C to 40°C by warming mixing water, cement and aggregate. After the concrete was mixed, slump, air volume, unit volume mass, and temperatures were measured. After that, mortar was screened from the concrete, and the penetration resistance value was measured under curing temperatures of 20°C and 40°C.

The test results are shown in Fig. 1.Under the curing temperature of 20°C, the ordinary Portland cement concrete had a slightly shorter termination time than the blast furnace cement concrete, but at the curing temperature of 40°C, there was almost no difference in two mix proportions. On the basis of the obtained test results, the Young's modulus was measured from aging for 7 hours at the curing temperature of 20 °C and 4 hours at the curing temperature of 40°C.

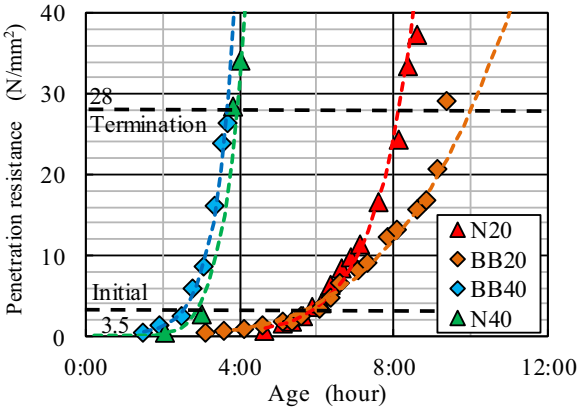

Binder	Initial	Termination
N20	5:50	8:00
BB20	6:10	9:25
N40	3:05	3:55
BB40	2:35	3:40

20 : Curing temperature20℃
40 : Curing temperature40℃

Figure 1: The penetration resistance value

(2) Preparation of concrete specimen and loading speed

The age of the test material and the number of specimens are shown in Tab. 3. Specimens were cylindrical shapes with a diameter of 100 mm and a height of 200 mm, and steel molds were used. For the specimens with a the curing temperature of 20°C, the mixed concrete which temperatures were of 20°C was driven into the steel mold. After driving, the upper surface was covered with Teflon sheets to seal the specimens until the material age of demolding tests starting, and the curing was performed in a thermo-hygrostat chamber at the temperature of 20°C and the humidity of 80%.

Table 3: Age of test material and number of specimens

Age	Temp20℃		Age	Temp40℃	
	Loading method			Loading method	
	0.1mm/min	0.6 N/mm²/sec		0.1mm/min	0.6 N/mm²/sec
7hr	1		4hr	1	
8hr	1		6hr	1	
9hr	1		8hr	1	
10hr	1		10hr	1	
12hr	1		12hr		1
14hr	1		14hr		1
16hr	1		16hr		1
24hr		3	24hr		1
2d		3	2d		3
3d		3	3d		3
28d		3	28d		3

For the specimens with the curing temperature of 40°C, the mixed concrete which temperatures were from 35 to 40°C was driven into the mold, and the top surface was covered with Teflon sheets and sealed until the starting age of the test. Thereafter, it was cured in a

thermo-hygrostat chamber at the temperature of 40°C and the humidity of 80%. As devises at demolding, in the case of the specimens up to 10 hours at the curing temperature of 20°C and 40°C (hereinafter, referred to as "very early age"), Teflon sheets were affixed to the inside of the steel formwork to prevent the concrete from adhering to the steel mold when demolding. At the time of the loading test, the side Teflon sheets were removed, and the test was carried out. (Fig. 2(c)) Finishing of the upper surface of the specimens before covering with the Teflon sheets, the parallelism between upper and lower surfaces of the specimen was ensured by pressing the steel lid after the completion of water generation was confirmed. (Fig. 2(b))

In the measurement of very early age, it is difficult to conduct a test at a loading speed of 0.6 ± 0.2 N/mm^2/sec according to JIS A 1149, because the compression strength is very small and the amount until the maximum load is large. From this reason, displacement was controlled and the displacement speed was set to 0.10 mm/min based on the previous research [3]. The measurement of the Young's modulus other than the very early age was carried out based on JIS A 1149, because compressive strength of concrete is sufficiently high. The Young's modulus was calculated according to JIS A 1149.

(a) Molding of specimen (b)Demolding (c)Loading

Figure2: Examination at the very early age

3. Results and discussions

The relationship between compressive stress and strain obtained from the measurement test of the Young's modulus of the very early age is shown in Fig. 3, and the relationship between compressive strength and strain obtained in JIS A1149 at the curing temperature of 20°C is shown in Fig. 4. From these results, it can be confirmed that the strain is more distorted until the compressive stress becomes maximum at the concrete of the very early age, and it is distinctly different from concrete of a general compressive strength. For the Young's modulus, the secant Young's modulus was calculated.

The relationship between the compressive strength and the Young's modulus is shown in Fig. 5 and Fig.6. In the figure, the regression equation obtained from the test results of the Young's modulus after 1 day of age using the concrete of the same mix proportion as this test in the past study[4] is shown. It can be confirmed that there is one correlation between the compressive strength and the Young's modulus regardless of the formulation, the cement type and the curing temperature. Also, since one correlation is shown, it can be confirmed that the difference between the displacement speed control and the load speed control measurement method is very small. According to Fig.5(a), the relationship between the compressive strength and the Young's modulus seems to be in good agreement with the regression equation[4], but in the range of the compressive strength 0 to 3.0 N/mm^2 (Fig.5(b)), The

Young's modulus obtained by the test shows a value slightly smaller than the regression equation. In particular, it can be seen that when the compressive strength is 1.0 N/mm^2 or less, it differs greatly. In the case where the vertical axis (Young's modulus) is taken as a logarithm (Fig.6(b)), it can be confirmed that the Young's modulus at 1.0 N/mm^2 or less is smaller by 1/10-1/100 than the regression equation. This is because the regression equation is calculated based on the test results after 1 day of age. Also, paying attention to the compressive strength of 0 to 0.75 N/mm^2, the Young's modulus in this range increases exponentially. It clearly shows a different tendency from the expression characteristics of the Young's modulus at the compressive strength of 1.0 N/mm^2 or more, suggesting that the Young's modulus development greatly changes around 0.75 to 1.0N/mm^2 of the compressive strength. Since the recommended formula in the JCI guidelines is set based on the test data after 1 day of age, it is considered that it is important to set an estimation formula that considers the test data of very early age.

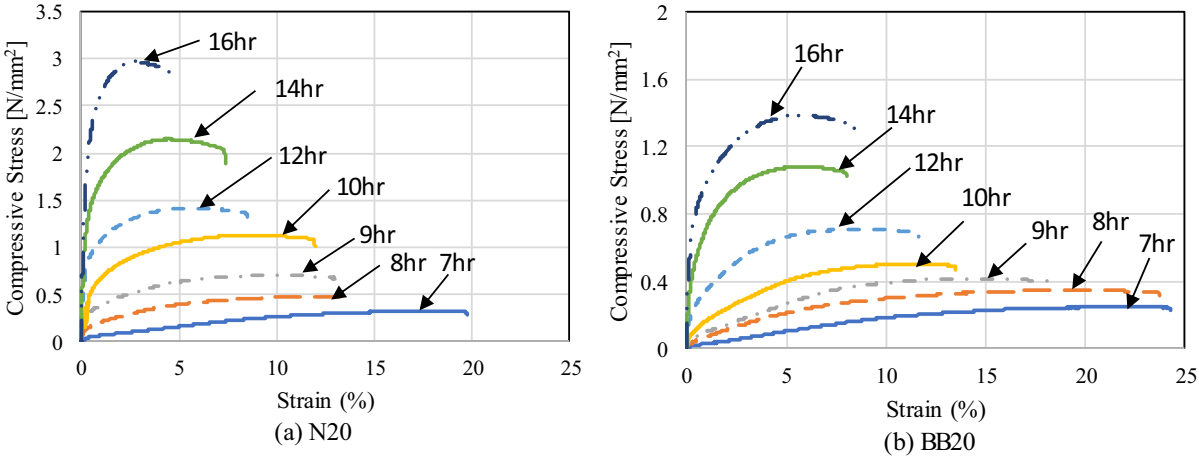

Figure 3: Relationship between compressive stress and strain (very early age)

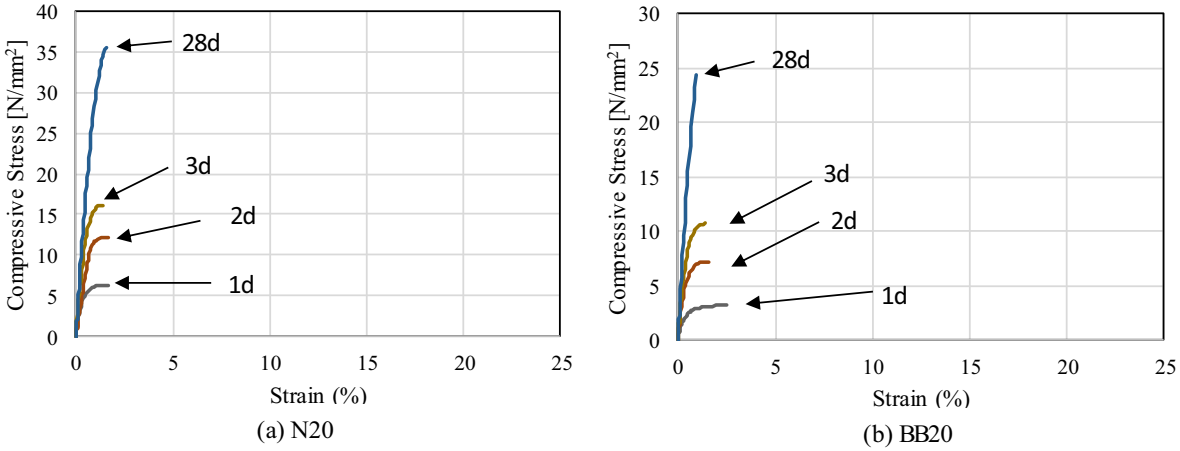

Figure 4: Relationship between compressive stress and strain (JIS A1149)

4. Conclusions

From the test results in this study, it was clarified that the relationship between the compressive strength and the Young's modulus greatly differ in the Young's modulus

expression characteristics at very early age. Especially in the region where the compressive strength is 0.75 N/mm^2 or less, the increase in the Young's modulus increases exponentially as it is the curing process of concrete. It is thought that it is important to consider the difference in the Young's modulus expression in order to improve the accuracy of temperature stress analysis at very early age.

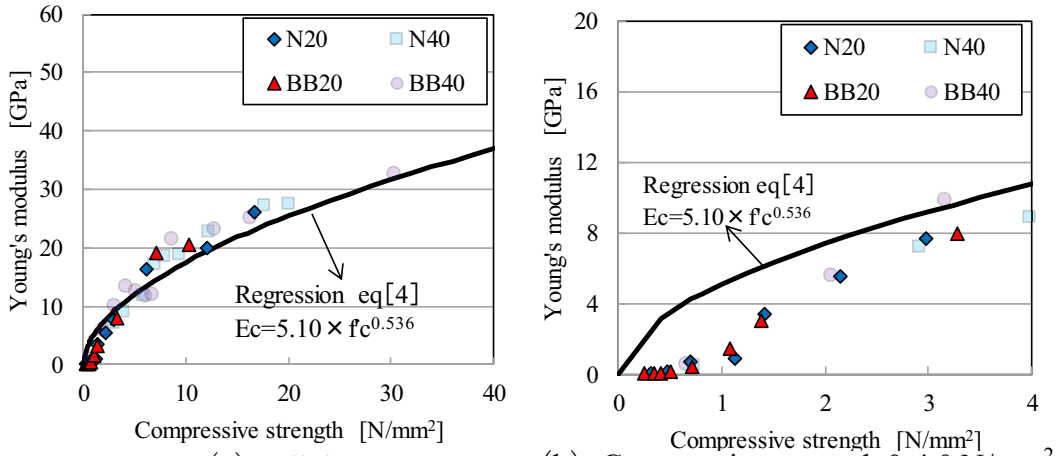

(a) All data (b) Compressive strength 0-4.0 N/mm^2

Figure 5: The relationship between compressive strength and Young's modulus

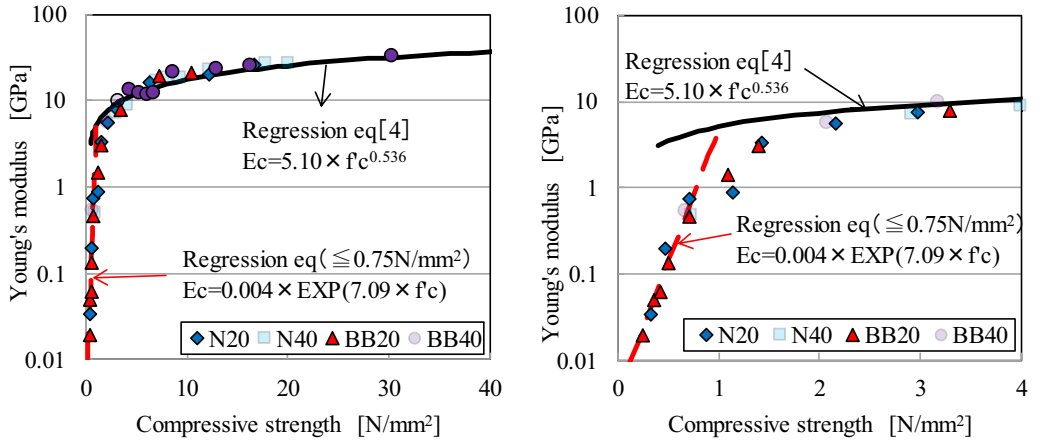

(a) All data (b) Compressive strength 0-4.0 N/mm^2

Figure 6: The relationship compressive strength and Young's modulus (Logarithmic display)

References

[1] JCI：Guidelines for Control of Cracking of Mass Concrete 2016, 2017.4

[2] JISA1147：Method of test for time of setting of concrete mixtures by penetration resistance

[3] Takuya TANI, Tomoyuki AOKI, Toyokazu OGAWA, Hitoshi TAKEDA, Yoshiaki FUJII: Study on Deformation Characteristics of Young-Age Tunnel Shotcrete, Journal of MMIS Vol.128,p.113-120

[4] Tatsuya USUI, Shigeyoshi MIYAHARA, Tsuyoshi MARUYA, Takeshi OTOMO: Study on Autogeneous Shrinkage and shrinkage Stress of Concrete using Ground Granulated Blast-Furnace Slag under Different Curing Temperature Conditions, Journal of Japan Society of Civil EngineersE2, vol.70, No.1, pp92-103, 2014.3

SynerCrete'18 International Conference on Interdisciplinary Approaches
for Cement-based Materials and Structural Concrete
24-26 October 2018, Funchal, Madeira Island, Portugal

UTILISING EXCAVATED ROCK MATERIAL FROM TUNNEL BORING MACHINES (TBMS) FOR CONCRETE

Torjus Berdal [(1)], Pål Drevland Jakobsen [(1)], Stefan Jacobsen[(1)]

(1) The Norwegian University of Science and Technology (NTNU), Norway

Abstract

There are more than 2000 completed road, railroad and hydropower tunnels in Norway, with a current annual production of more than 7 million solid cubic metres excavated rock. The road and railroad tunnels are consumers of concrete, which is utilised for rock support, water- and frost protection. A small portion of the excavated rock affiliated with Norwegian tunnelling is used as concrete aggregate, while the major part of the rock is used for landfill. This paper reviews the potential of utilising excavated rock obtained by tunnel boring machines (TBM) as concrete aggregates, including results from recent European TBM projects that have utilised the excavated rock for concrete aggregates. Finally we present test results from excavated rock material from two new (including one ongoing) Norwegian TBM projects. Particle Size Distribution (PSD) of the filler / fines fraction and effect of the fines fraction (< 0.125mm) of the rock material on flow of fresh filler modified cement paste were measured. The reuse in concrete of excavated rock from 8 different recent European TBM projects varied from zero to 100 %. Reviewed PSDs and own PSD measurements show that TBM PSDs vary within wide ranges. Content of fines < 0.1 mm content can be more than 20 % of the total TBM and even higher when the coarsest material is used as feed in production of crushed aggregate. The newest project reviewed, the Norwegian Follo line, is generating the finest material with 50 % < 4 mm indicating the importance of rock quality in addition to TBM-technology for fines generation. The flow results of filler modified paste show that the TBM fines from the two projects with size 0-0.125 microns have very similar effect on fresh cement paste flow properties as a replica limestone filler with similar PSD composed from 3 different filler fractions.

1. Introduction

Most of the tunnels in Norway are excavated by the conventional drill and blast method. Furthermore, they are mostly less than 1000 m and the excavated rock has mainly been used for landfill, or even dumped in the sea. Around 30 of the tunnels in Norway were excavated by tunnel boring machines (TBMs) [1]. Hydropower tunnels are the main user of TBMs, as the TBM enables a smooth tunnel cross-section with reduced head-loss in comparison with drill and blast tunneling. Figure 1a) shows a typical TBM cutterhead. Currently the Norwegian Railroad Authorities are utilizing 4 TBMs for a major railroad project from Oslo towards the suburb Ski. Last year the same client achieved the breakthrough of the new Ulriken TBM railroad tunnel project in the city of Bergen. Thus, infrastructure owners in Norway are starting to utilize TBM more commonly for tunneling. One central question is how are the possibilities to utilize excavated rock material locally, for example as aggregate for the tunnel's permanent concrete rock support and linings.
The aims of this paper are 1) to give an overview of the potential of utilising excavated rock material obtained from TBMs for use as concrete aggregates. Knowing the magnitude of the challenge is important to assess the societal impact. 2) Present how various recent TBM projects have utilised the excavated rock for concrete aggregates as input to discuss technical prospects for future reuse of the residues also including fines and not just the coarse parts that are presently used as feed for crushed rock processing plants. 3) Discuss how local aggregates can be exploited more in connection with tunnel projects. The results of the paper are based on a literature review, collection of laboratory data from old, recent and ongoing TBM projects, own laboratory studies of PSD of fines, sand and coarser fractions, as well as laboratory measurements of the effect of filler from TBM debris on flow of fresh filler modified paste. The quality of fines have a proportionally much larger influence than the quality of coarse aggregate on rheology of concrete [2] and therefore we start with the fines in this work. The work is entirely based on the MSc thesis of Torjus Berdal [3]. The key question, which is, whether this reuse can be done within economic benefits is not addressed.

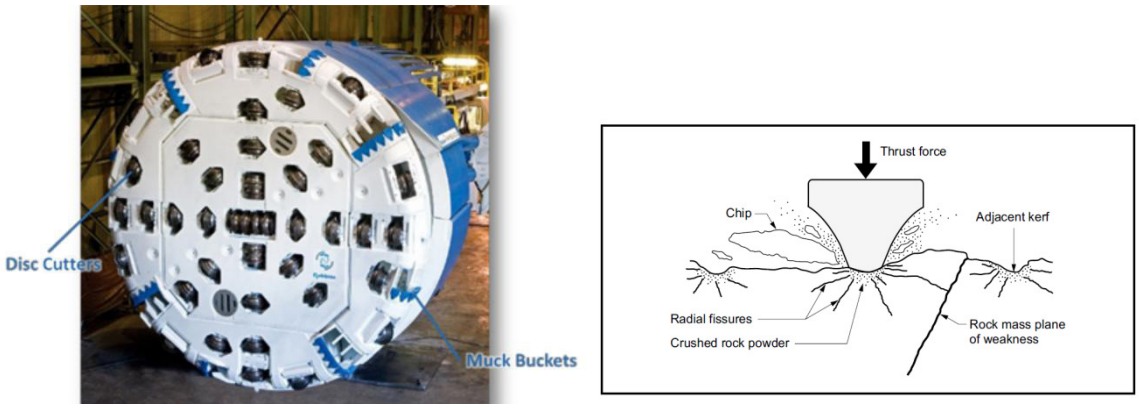

Figure 1: a) TBM cutterhead designed for hard rock excavation. Courtesy of the Robbins company [1] , b) Idealised rock breaking principle under disc cutters after Bruland [1]

2. Generation of debris, utilization and PSD

The rock breaking of hard rock TBMs is done by rotating the cutterhead equipped with disc cutters and applying high axial forces (200 – 315 kN per disc cutter) while the cutterhead is rotating. The axial force enables a crushing zone between the disc cutter and the rock face as well as inducing radial fractures into the rock mass. When the radial fissures range to a natural plane of weakness or a mechanical induced fissure from another disc cutter, chipping occurs, see Figure 1b.
TBM debris, when intended used for concrete aggregates, needs to be handled similarly in quality control as ordinary concrete aggregate. Particle size distribution (PSD) of fines, sand and coarser fractions is hence one of the most important aggregate quality parameters. PSDs were therefore reviewed and measured with dry and wet sieving on various TBM debris materials and with X-ray sedigraph on fines, or filler which is the terminology used in concrete technology. Nine different newer TBM projects (Railway- and Hydropower tunnels) in 5 European countries were reviewed as well as 30 older TBM projects (25 Norwegian, 5 Swiss)**.** Regarding the other continents, no data on TBM-debris were found in Asia, Oceania or America in this study [3]**.** Table 1 shows an overview of 8 different TBM projects with varying degrees of reuse in concrete from almost zero to 100 %. So in practice the variation in reuse is large.

Table 1: TBM projects with confirmed utilisation of TBM excavated rock in concrete [3]

Project name	**Duration (year)**	**Minimum utilization fraction (mm)**	**Utilization of excavated rock (%)**
Zugwald	N/A-1998	16	16
Gotthard base tunnel	1999-2016	0	23
Lötschberg	1999-2007	0	29.1
Linthal	2010-2015	0	100
Nanth de Drance	2008-2016	0	25
Breheimen	1986-1989	10	N/A
Follo Line	2016-2021	20	10*
Koralm KAT2	2013-2023	16	17

* The utilisation of excavated rock for concrete purposes has stopped at the Follo line due to sulphur content ≈ 0.1 %

A literature review from various sources has compared PSDs from hard rock TBM projects between 1977 and 2018 from Switzerland or Norway. The number of projects and time span of the projects enables high reliability, in terms of varying geology, TBM operation and TBM development. Figure 2 shows an overview of PSDs from the major Norwegian and Swiss TBM projects. Fines contents vary from< 5% to > 20 % and maximum particle size vary from < 10 to > 100 mm so these are clearly very variable materials. In addition, it is important to remember that use of coarse debris particles as feed in rock crushing plants will further increase the amount of fines. Careful selection of process technology for reuse of TBM debris is very important to limit the problem of fines generation and optimize particle shape.

Although particle shape was not investigated in this study it needs to be addressed in concrete aggregate production. An interesting observation from figure 2 is that the Follo line, which is a new project, is generating the finest sieve curve (50% < 4 mm). The reason for this could be related to the TBM operation (relative low load per disc cutter), the brittleness of the rock mass and/or the TBM cutterhead design. Anyway, this project shows how a modern TBM with carefully distanced cutter discs and a high thrust force for maximum penetration rates is not enough to generate coarser sieve curves. The geology and petrography seem to influence the outcome of TBM debris quality to a large extent.

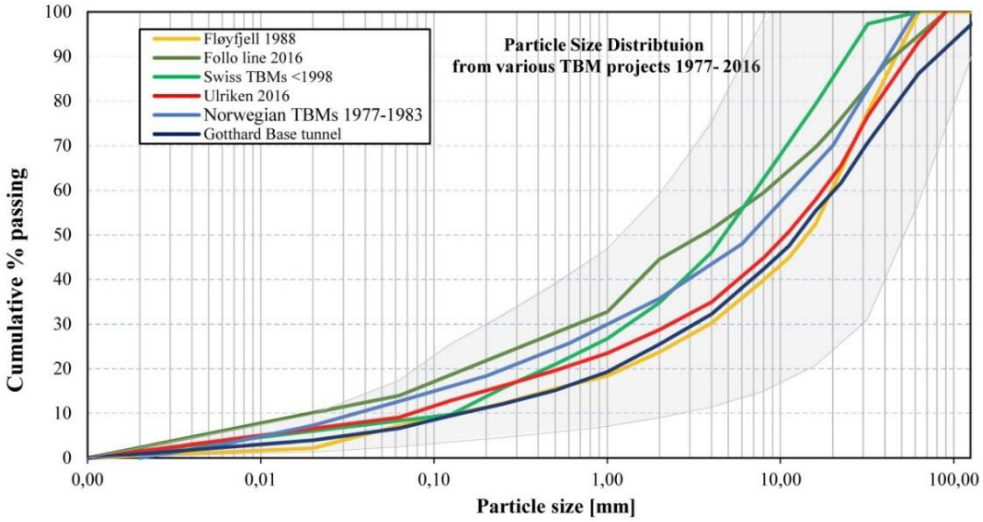

Figure 2: PSD from various hard rock TBM projects showing mean curves. Grey area represents possible variation for a single sieve curve

Observations in optical microscope of debris from Ulriken revealed that fines could adhere to the surfaces of larger (sand) particles to various extents, possibly due to the TBM process itself. This may cause negative effects on concrete properties (bond etc) as well as affect the measured PSDs. Therefore, both wet and dry sieving were done on 1 kg samples. These showed a +2.46% increase on the 0.125 mm sieve and +5.79% increase on the 0.063 mm sieve when wet sieving compared to when dry sieving. This seems to verify the visual observations of fines adhering to the surfaces of larger particles.

3. TBM filler vs limestone filler – PSD measurements and cement paste

TBM filler from Ulriken TBM project was collected on site in October 2017. The fraction <0.125mm was sieved out. Then the PSD was investigated with X-ray sedimentation using Micromeritics SediGraph III PLUS. With the known PSD of the TBM filler, the same PSD curve was composed with three different fractions of a crushed limestone filler. The reference limestone filler had been produced prior to the TBM material and separated through air classification and divided into coarse (40/250µm), medium (20/60µm) and fine (0/20µm) fractions. Figure 3 (left) shows the PSD of the TBM filler that was replicated with limestone filler with the method presented in [4]. A filler modified cement paste which would resemble that in a B45M40 concrete was designed for the purpose of measuring effect of TBM filler on

flow properties in terms of mini-slump flow value and flow resistance [5]. The mini cone had bottom diameter: 89 mm, top diameter: 39 mm, height 70 mm. The cement content in the mix would resemble a cement content of 360 kg/m^3 in a 1 m^3 concrete mix. Table 2 shows composition with mass ratios water/cement = 0.40 and filler/cement = 0.36.

Table 2: Cement paste composition used with TBM filler and limestone filler

Constituents	**Kg**	**Density(kg/m3)**
Norcem CEM II/A-V	2.288	3020
Water	0.915	1000
Superplastizer (0.9%)	0.021	1050
Filler (TBM/Limestone)	0.818	2700

2 litre cement paste mixes were prepared in the lab according to the procedure [6]. The slump-flow measurements were performed on a transparent plexiglass plate and assured no leakages between matrix and cone. In addition FlowCyl values were measured [5]**.** The latter method is similar to the Marsh cone and the resulting flow resistance number λ_Q (0 - 1) correlates well to plastic viscosity whereras slump flow correlates to yield stress [2,6]. Table 3 gives average results of 2 parallel mixes for each of the 5 studied fillers: 4 TBM fillers and 1 reference limestone filler. The results show marginal differences between the mixes. The slightly better workability of the replica limestone filler with similar PSD is in line with previous findings that limestone filler can have a favourable effect on workability compared to other minerals [6].

Table 3: λ_Q and Mini-slump results, each value is average of two parallel mixes

Constituents	**λ_Q**	**Mini-slump(cm)**
Limestone	0.745	27.2
TBM Ulriken 1	0.807	23.4
TBM Ulriken 2	0.808	22.8
TBM Ulriken 3	0.806	21.3
TBM Follo	0.817	21.3

Figure 3 also shows that the replica lime stone filler has slightly lower content of the very finest particles which also contributes to the slightly higher mini slump flow and lower flow resistance number λ_Q seen in Table 3. The photos in Figure 3 show very stable edges on the slump flow samples.

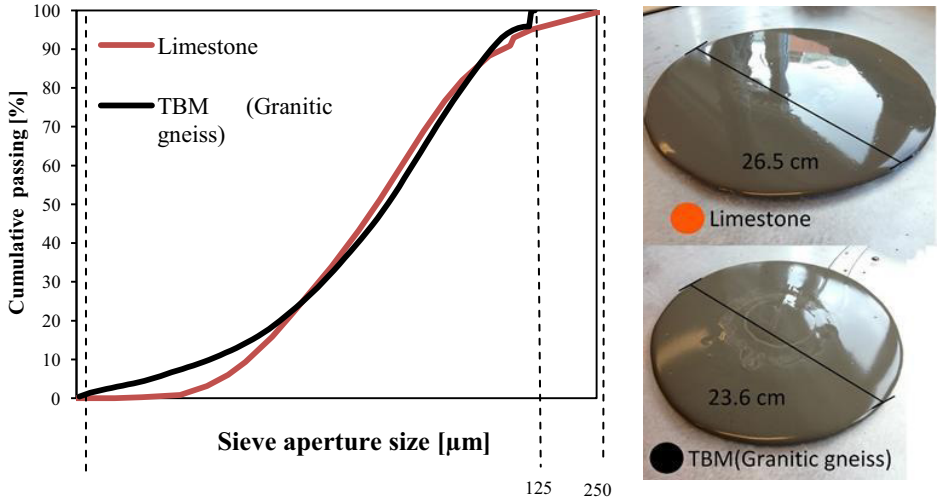

Figure 3: PSD of the filler from TBM debris and replica limestone (left) Mini slump measurements with stable edges (right)

4. Conclusive remarks

This paper presents early findings associated with the potential of using excavated rock material obtained by TBM for concrete aggregates, as well as summarising the potential of recent TBM projects in Norway related to concrete aggregates. The authors believe that further research and development with the civil construction industry, as well as contractual incentives can increase the use of excavated rock, and reduce the waste-problems that are associated with tunnelling.

References

[1] Jakobsen, P.D., Log, S., Skjeggedal, T., Hansen, A.M., Palm, A., Short introduction to the use of TBM. Kort innføring i bruk av TBM (in Norwegian only). NFF. (2015)
[2] Cepuritis, R, Development of crushed sand for concrete production with microproportioning, PhD thesis, Norwegian University of Science and Technology (2016)
[3] Berdal, T, Use of excavated rock material from TBM tunnelling for concrete Proportioning, Master thesis, Norwegian University of Science and Technology (2017)
[4] Cepuritis R., Jacobsen S. and Onnela T., Sand production with VSI crushing and air classification: Optimising fines grading for concrete production with micro-proportioning, Minerals Engineering Vol 78 (2015) 1-14
[5] Mørtsell E., Modelling the effect of concrete part materials on concrete consistency. PhD thesis, Norwegian University of Science and Technology (1996)
[6] Cepuritis, R., Jacobsen, S., Smeplass, S., Mørtsell, E., Wigum, B. & Ng, S. Influence of crushed aggregate fines with micro-proportioned particle size distributions on rheology of cement paste. Cement and Concrete Composites Vol 80 (2017), 64-79

SynerCrete'18 International Conference on Interdisciplinary Approaches
for Cement-based Materials and Structural Concrete
24-26 October 2018, Funchal, Madeira Island, Portugal

WATER ABSORPTION CHANGES IN MORTARS WITH CRYSTALLINE ADMIXTURE EXPOSED TO ACID ENVIRONMENT

Victoria Eugenia García-Vera[(1)], Antonio José Tenza-Abril[(2)], Marcos Lanzón[(1)], Afonso Miguel Solak[(2,3)], Concepción Pla[(2)], David Benavente[(4)]

(1) Department of Architecture and Building Technology, Technical University of Cartagena, Murcia, Spain
(2) Department of Civil Engineering, University of Alicante, Alicante, Spain
(3) CYPE Ingenieros S.A., Alicante, Spain
(4) Department of Earth and Environmental Science, University of Alicante, Alicante, Spain

Abstract
In industrial cities, a common attack in concrete is sulfuric acid attack. Sulfuric acid is particularly corrosive due to the sulfate ion in addition to the dissolution caused by the hydrogen ion causing the deterioration of the cementitious materials. To improve acid attack resistance in those materials, the matrix must be dense, with low permeability, use in the production a sulfate resistant cement or high alumina cement, etc. Crystalline admixtures are used as a waterproofing product because they improve the protection of the cementitious materials filling the capillaries preventing the penetration of liquid by crystals formation that fill the capillary pores and micro-cracks, blocking the water entrance. The main objective of this work is to study the behaviour of mortars produced with the same quantity of cement, water, fine aggregate and including different percentages of crystalline admixture (1%, 1.5% and 2%) in an aggressive environment (sulfuric acid solution - 3% w/w). Changes in the mass, density, porosity and capillary absorption coefficient after 28 and 56 days of fully submerged in H_2SO_4 solution. From the results obtained, we can observe a noticeable better performance of the mortars with crystalline admixtures.

1. Introduction

Nowadays, cementitious materials are in contact to acids because of the environmental pollution —soils, seawater or treatment plants [1, 2]. In industrial cities, a common attack in concrete is sulfuric acid attack. Sulfuric acid is particularly corrosive due to the sulfate ion in

addition to the dissolution caused by the hydrogen ion causing the deterioration of the cementitious materials. There are numerous studies about acid attack in concrete; however, already is a challenge to find high durability performance mortars in aggressive environments. To improve acid attack resistance in those materials, the matrix must be dense, with low permeability, use in the production a sulfate resistant cement or high alumina cement, etc [3-5]. There are strategies aimed at extending the durability of cementitious materials against acid attacks, and try to increase the impermeability of these materials by introducing water-repellent admixture. Some of the most commonly investigated hydrophobic admixtures for mortars include metallic soaps, e.g. calcium stearate, zinc stearate, sodium oleate, and silanes [6]. Crystalline admixtures are commonly used as a waterproofing product to improve the protection of the concrete. The crystals formed grow and fill the capillary pores and micro-cracks, blocking the water entrance preventing the penetration of liquid.
The main objective of this work is to study the behaviour of mortars produced with the same quantity of cement, water, fine aggregate and including different percentages of crystalline admixture (1%, 1.5% and 2%) in an aggressive acid environment (sulfuric acid solution - 3% w/w). Changes in the mass, density, porosity and capillary absorption coefficient after 28 and 56 days of fully submerged in H_2SO_4 solution.

2. Materials

Four types of mortars were studied: i) control mortar; ii) mortar with 1% xypex by cement weight (Xypex Admix C-100 NF); iii) mortar with 1.5% xypex by cement weight; and iv) mortar with 2% xypex by cement weight. The dosage used for the mortars was one part cement (CEM I / 52.5R), 0.45 parts water and three parts of fine limestone aggregate. For adequate workability of the mortars, 1.2 % of superplasticizer (Sika ViscoCrete-5980) by cement weight was added.

3 Methods

3.1 Manufacturing, curing process and acid sulfuric attack simulation

Twelve normalized specimens (40 x 40 x 160 mm) were prepared per each type of mortar. First, the water-repellent admixtures were added to the dry mass (cement and sand) and were well mixed for 1 minute with an automatic mortar mixer. Then, water was added and mixed for another 4 minutes respecting the velocities and times of the standard EN 196-1 [7]. Mortars were kept in laboratory conditions for 24 hours and then they were demoulded. All the samples were cured for 28 days in a temperature and humidity controlled chamber at 20 °C and 95% RH. When the curing period had finished, all specimens were exposed to two different media. The first one was a H_2SO_4 solution (3% w/w) to study the behaviour of mortars regarding the attack of this aggressive. The second medium consisted in submerging the samples in distilled water until the testing age. This last condition has been used as a reference for comparing the effects of aggressive attack to an optimum hardening condition. Solution was renewed in periods of 7 days.
To change the acid sulfuric solution i) the specimens were extracted from aggressive medium, and were gently brushed with tap water to eliminate rests of material weakly adhered to the

surface; ii) the acid sulfuric solution was renewed; and iii) the specimens were reintroduced into the new solution. The temperature of the aggressive medium and the distilled water were keep constant at 20ºC.
The test time has been coded as follows: $t_{m(e)}$. Where *m* is the age of the mortar and *e* the exposure time to aggressive medium (28 days after the manufacture corresponds to 0 days of acid exposure). The tests were conducted in two periods at 28 days [$t_{56(28)}$] and 56 days [$t_{84(56)}$] days of exposure.

3.2 Mass variation

To study the mass variation of the mortars exposed to acid, the specimens were weighed weekly up to 49 days after. The mass of the specimen was obtained after complete drying in an oven at 105 °C for 24 h. The following masses were obtained: 28 days after the manufacture and before starting the simulation (0 days of acid exposure) [$t_{28(0)}$]; at 7 days [$t_{35(7)}$]; 14 days [$t_{42(14)}$]; 21 days [$t_{49(21)}$]; 28 days [$t_{56(28)}$] and 49 days [$t_{77(49)}$] of acid attack exposure. The percentage of mass loss were calculated taken into account the initial weights [$t_{28(0)}$] as:
$M_c = [(m_e – m_0) / m_0] \cdot 100$
Where M_c is the mass change; m_0 is the initial mass of the specimen before being exposed to the chemical solution; m_e is the mass of specimen after exposure time *e*.

3.3 Study of the capillary water absorption of the mortars

The capillary absorption test was performed according to the standard EN-1015-18 [8]. Before the test, samples were subjected to a pre-conditioning procedure, which firstly consisted of a complete drying in an oven at 105 °C for 24 h, and from then to the start of the test they were saved in a hermetically sealed recipient with silica gel.
The lateral sides of the specimens were sealed to restrict the water flow along the longitudinal axis. The water flux through the sample was measured by partial immersion of the specimens at a depth of 5±1 mm. Throughout the test, water level was kept constant and the container was hermetically closed.The capillary absorption coefficient was calculated using the measurements for 10 and 90 min. The test was performed at 28 [$t_{56(28)}$] and 56 [$t_{84(56)}$] days of exposure to the aggressive medium. According to the standard, the water absorption coefficient is the line slope that joins the points corresponding to 10 minutes and 90 minutes in the curve that represents the mass variation of water absorbed per unit area as a function of the square root of time, i.e. the coefficient was computed using the formula:
$C = (M_2 - M_1) / (A \cdot (t_2^{0.5} - t_1^{0.5}))$
where: C is the capillary water absorption coefficient, $k/(m^2 \cdot min^{0,5})$; M_1 is the specimen mass after the immersion for 10 minutes; M_2 is the specimen mass after the immersion for 90 minutes; A is the surface of the specimen face submerged in the water in m^2; t_2 corresponds to 90 minutes and t_1 to 10 minutes.

4. Results

4.1 Mass variation

Fig. 1 plots the mass variation rates of the specimens soaked in H_2SO_4 solution compared with the mass before the immersion up to 56 days. It can be seen that the percentage of mass

loss in the mortars is similar in all the samples (-22%, -24 and -26% in mortar with 1%, 1.5% and 2% of crystalline admixture in its composition respectively).

4.2 Density and porosity

Fig 2a) and b) plot the density and porosity percentage variation due to the exposure of the mortar to the acid attack during 28 days and 56 days compared with mortars immersed in water (actual values are listed in Tab. 1). As can be seen in Fig.2a, the reduction in the density of the mortar at 28 days is similar in all the mortars.

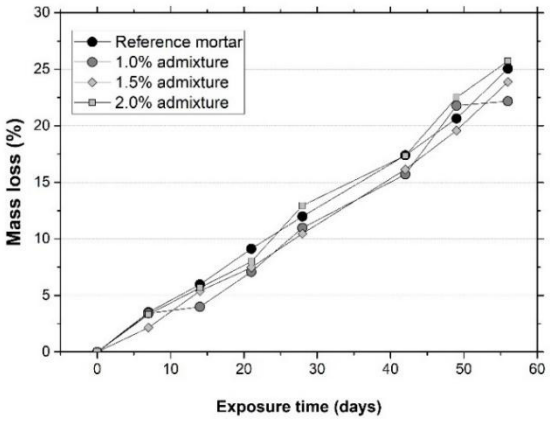

Figure 1: Percentage of mass loss in the mortars.

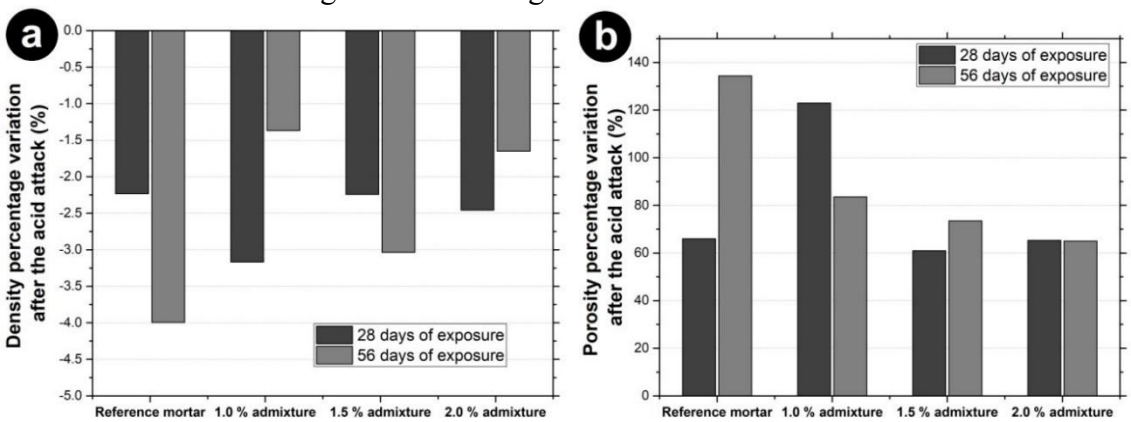

Figure 2: a) Density percentage variation and b) porosity percentage variation after the acid attack after 28 and 56 days of exposure. The bars are normalised to the values obtained in the same mortar immersed in water at the same age.

Table 1. Results obtained in the tests.

	% Mass loss		Dry density (kg/m3)				Porosity (%)			
	H_2SO_4		Water	H_2SO_4	Water	H_2SO_4	Water	H_2SO_4	Water	H_2SO_4
Days of immersion	**28**	**56**	**28**	**28**	**56**	**56**	**28**	**28**	**56**	**56**
Reference mortar	12,0%	25,0%	2301	2247	2348	2261	8,3%	13,8%	5,4%	12,1%
Admix. (1%)	11,0%	22,2%	2302	2223	2288	2246	6,2%	13,9%	6,3%	11,8%
Admix. (1,5%)	10,5%	23,9%	2307	2273	2345	2292	8,2%	12,5%	5,7%	8,8%
Admix. (2%)	13,0%	25,7%	2339	2285	2351	2319	7,0%	11,4%	5,0%	8,2%

However, after 56 days of exposure, the mortars that contains crystalline admixtures the impact of the reduction of the density is less compared with the reference mortar without admixture. The porosity of the mortars exposed to acid solution increased (Fig. 2b). As observed with density, the increase in porosity in mortars with crystalline additions is much less at 56 days than at 28 days and lower than the reference mortar probably due to the formation of crystals throughout the pores and capillary.

4.3 Capillary absorption

Fig. 3 shows the capillary water absorption coefficient of the mortars at 28 days (exposed and non-exposed to acid solution). As can be observed, the mortars with crystalline admixture exhibited less capillary absorption than the reference mortar in both conditions (immersed in water and immersed in acid solution).

Again, the crystalline formation throughout the capillary prevents the penetration of water. They usually consist in a certain dispersion of the complex chemical active substances that dissolve in water interacting with the products of hydration of Portland cement to form sparingly soluble compounds and filling the pore space [9]. Small newly formed needles are mostly located in the walls of capillaries and cavities, making it narrower. The composition of needle-like calcium hydrosilicates [9]. Figure 4 shows the X-ray diffraction pattern of the mineral admixture used to produce the mortars. No peaks attributed to any crystallised compound can be identified except a broad diffraction halo (amorphism of between 20° and 30°). Further research is needed to understand the mechanism that could be associated to the crystal formation (X-Ray diffraction, SEM imaging, and pore size distribution) that influences the reduction of water absorption in mortars exposed to acid environment.

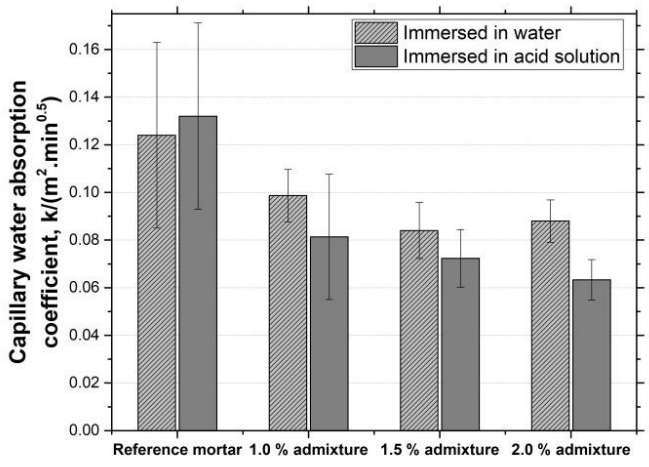

Figure 3: Capillary water absorption coefficient at 28 days [$t_{56(28)}$].

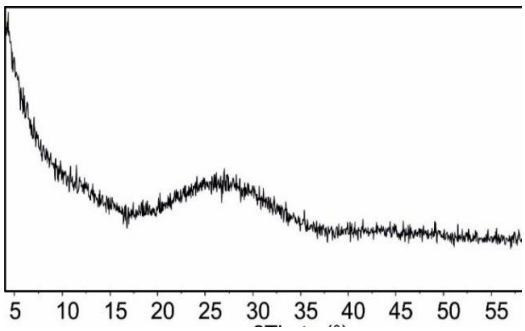

Figure 4: XRD pattern of the mineral admixture.

5. Conclusions

In this work, the effects of acid attack on physical properties of containing crystalline admixtures mortars were analysed. From the results presented in this study the following conclusions are drawn:

- Accordingly mass loss in H_2SO_4 solution, the effect of crystalline admixtures on sulfate attack is small because it is similar in all the mortars.
- However, after 56 days of acid exposure, the mortars with crystalline admixture in its composition presented less reduction of the density and lower increase of the porosity. In addition, the capillary water absorption coefficient were lower in the mortars with crystalline admixture compared with the reference mortar after the acid attack.

Acknowledgements
This research was funded by the University of Alicante (GRE13-03) and (VIGROB-256).

References

[1] Santhanam, M., Cohen, M.D. and Olek, J., Sulfate attack research — whither now?, Cem Concr Res 31,6 (2001), 845-851
[2] RILEM TC 211 – PAE, Performance of Cement-based materials in aggressive aqueous environments, State-of-the-Art, 10 (2013)
[3] Irassar, E.F., Di Maio, A. and Batic, O.R., Sulfate attack on concrete with mineral admixtures, Cem Concr Res 26, 1 (1996), 113-123
[4] González, M.A. and Irassar, E.F., Ettringite formation in low C3A Portland cement exposed to sodium sulfate solution, Cem Concr Res 27,7 (1997), 1061-1072
[5] Irassar, E.F., Sulfate attack on cementitious materials containing limestone filler – a review, Cem Concr Res 39,3 (2009), 241-254
[6] Nunes, C. and Slízková, Z., Freezing and thawing resistance of aerial lime mortar with metakaolin and a traditional water-repellent admixture, Constr Build Mater 114 (2016)
[7] EN 196-1:2005, Methods of testing cement - Part 1: Determination of strength, CEN, (2005)
[8] EN-1015-18, Methods of test for mortar for masonry - Part 18: Determination of water absorption coefficient due to capillary action of hardened mortar (2002)
[9] Kapustin, F., Pomazkin, E., Spiridonova, A. and Oleinik, V., Impact of Waterproofing Permeable Capillary Mixtures on Cement Stone. In book: Progress in Materials Science and Engineering, (2018), 99-106.

SynerCrete'18 International Conference on Interdisciplinary Approaches
for Cement-based Materials and Structural Concrete
24-26 October 2018, Funchal, Madeira Island, Portugal

X-RAY MICROTOMOGRAPHIC IMAGES OF FIBRE CONCRETE COMPOSITES FABRICATED USING DIFFERENT METHODS

Zbigniew Ranachowski [(1)], Marcin Lewandowski [(1)], Krzysztof Schabowicz [(2)], Tomasz Gorzelańczyk [(2)], Stanislav Kudela Jr [(3)], Tomas Dvorak [(3)]

(1) Institute of Fundamental Technological Research, Polish Academy of Sciences, Pawińskiego 5B, 02-106 Warsaw, Poland
(2) Faculty of Civil Engineering, Wroclaw University of Science and Technology, Wybrzeże Wyspiańskiego 27, 50-370 Wrocław, Poland
(3) Institute of Materials and Machine Mechanics, Slovak Academy of Sciences, Dubravska Cesta 9, P.O. Box 95, 830-08 Bratislava, Slovakia

Abstract
The fibres constituting the reinforcement of the fibre cement composites are of small diameter and colourless and thus difficult to recognize inside the cementitous matrix applying the optical or electron microscopy. Seven fibre cement composite specimens fabricated applying different methods were object of investigation. The X-ray microtomography enabled the authors to perform the following research applying the X-ray microtomographic technique. The length and shape of the fibres could be assessed on specimens' cross–sections. Applying the 3D visualization it was possible to present the fabrication errors resulting in the non–homogenous distribution of fibres within the specimen volume.

1. Introduction

In the paper the microstructure of different kinds of fibre cement composites was investigated using the X-ray microtomographic (micro–CT) technique. Organic fibre cement composites are widely implemented despite of the complexity of its fabrication process. The cellulose fiber cement board (FCB) siding is commonly used as a replacement for wood siding, as it is less expensive and more durable, and has lower maintenance costs [1]. The FCB also referred to as precast fabrication, are becoming more and more important in the entire construction sector. Common applied fibers are of 2.5 to 3 mm of length and of 30 – 50 μm in diameter [2]. In some FCB of lower quality short fibres derived from recycled cellulose of ca. 1 mm

long are used. The methods of fabrication, mechanical properties, durability and microstructure of the standard fibre cement composites are described in [3–5].

2. X-ray microtomography

X-ray microtomography (micro-CT) offers the ability to create different modes of microstructure imaging of investigated specimens with a resolution of ca. 1 – 5 μm per voxel (volumetric pixel). The early study of pore size distribution and of pore connectivity in concrete samples using this method was performed by Lu et al. in 2005 and presented in [6]. Several papers concern the application of micro-CT technique in testing the properties of concrete. Garboczi [7] reconstructed the aggregate shapes in concrete with voxel resolution of 0.4 mm3. This enabled the author to approximate the real shapes by its mathematical models to built the stereological model of entire population of aggregates. Schabowicz et. al. [8] applied the microtomography to assess the quality of fabricated cellulose fibre-cement boards. Lanzón et al. [9] used the micro-CT method to test the specimens made of concrete with low-density additions: expanded perlite, expanded glass and cenospheres (hollow microspheres). Stock et. al. [10] analysed the progression of sulfate attack within the cement paste by examining the microtomograms. It was found that recognized damage levels in specimens exposed to a Na_2SO_4 solution in different conditions varied from 0 (no damage) to 4 (extreme damage).
The equipment for insight into specimens' microstructure with micro-CT technique is produced at present by a few firms and these apparatus are capable to perform tests on the small pieces of few millimetres size or on large elements of a few meters. They include the microfocal source of X-ray radiation, the movable table to place a specimen and the flat panel with a radiation detector, which resolution usually equals 2000 × 2000 pixels. The microstructure of is visualized on the cross-sections (tomograms) of the investigated specimen using grey scale convention related directly to the amount of local radiation absorption of the material. The grey scale covers several tens of grey levels and is ordered from white related to maximum of absorption to black related to the minimum, respectively. Unhydrated cement particles and aggregate grains are objects of the greatest absorption. The hydratation products that cover major part of the cement matrix present slightly lower absorption ability. The next in the line are hydrated calcinates and at the end of the scale are the organic fibres (if present) and the regions of high porosity. The advantage of micro-CT technique is a possibility of reconstruction of 3-dimensional image of investigated objects and to determine the volumetric part of the material occupied by bulk matrix, aggregates, voids, cracks, fibres etc.

3. Experimental

The authors analysed five specimens made of different FCB compositions. According to the determined micro-CT scanning procedure, i.e. 50 X magnification, cylindrical cores 7 mm in diameter and 7 mm in height were cut from the larger blocks. Prior to analysis, the fibre cement composite specimens were tested using the additional procedures to evaluate their performance.
Materials 'A' – 'D' were the fabricated façade boards made using accumulative rolling

technology, known as the Hatscheck process [3]. Material 'A' was characterized by low moisture absorbability (8–10%) and the bending strength of boards was 11–13 MPa. The concentration of fibres cellulose fibres by weight in that was 6 % (wt.) of good quality 3 mm long cellulose fibres. Material 'B' was made using the same technology as material 'A', but contained 6 % (wt.) recycled cellulose short fibres ca. 1 mm long and thus the bending strength of boards was lower: 8,5–10 MPa. Material 'C' was of fabricated using the similar technology as of 'A' type but by another producer using the other type of fibres. Material 'C' was coloured in the volume that increased its density. Material 'D' was obtained by the accelerated production technology applying the Hatscheck process and autoclaving. The research presented below has revealed non-uniform, laminar distribution of fibers in it. Material 'E' was fabricated using another technology, i.e. extrusion what caused the increased tendency of agglomerating of the fibres.

The microstructure of all the specimens were tested using Nanotom 30 microtomograph by General Electric at the Institute of Materials and Machine Mechanics in Bratislava. The following parameters were set: lamp voltage - 115 kV, lamp current – 95 microamps, shot exposition time – 750 ms. Scanning performed by the authors resulted in a large set of tomograms (specimen cross-sections), performed every 5 μm of the specimen height. This set of tomograms consisted of 1200 cross-sections, 1200 × 1200 pixels each. The recorded data allows presenting a greater number of cross-sections within the single graph using a quasi 3D projection. However, the total number of bytes related to the consecutive voxels in such a dataset would be 1.5×109 bytes, and would require additional lengthy processing. Therefore, a specific subset was taken from the entire dataset, preferably cube-shaped for further processing. The resulting subset is referred to as a ROI (Region Of Interest). Cracked areas in the proximity of the specimen surface, usually damaged by a drilling tool were left outside of that area. The study included ROIs 9003 (729,000,000) voxels each, representing 4 × 4 × 4 mm cubes and virtually extracted from the analysed specimens. 800 scans constituting the single ROI occupied the equivalent surface of 128 cm^2. The equipment and the dedicated software was capable of producing the data sets defining the microstructure of the specimen in the form of: a) three-dimensional projections of the specimens showing 4 × 4 × 4 mm cubes of the tested specimen and b) digital specimen images (i.e. BMP files), representing cross-sections of tested object in transverse or lengthwise direction to the mean axis of the cylindrical specimen. Example three-dimensional projections of 4 × 4 × 4 mm cubes virtually cut from specimens 'B' and 'D' are presented in Figures 1 and 2.

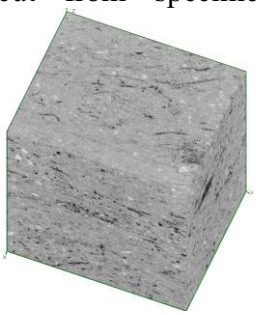

Figure 1. Three-dimensional projection of the 4 × 4 × 4 mm piece of specimen 'B'. Some ca. 1 mm long fibres are visible in the bulk of the material.

Figure 2. Three-dimensional projection of the 4 × 4 × 4 mm piece of specimen 'D'. Its layered structure was a result of autoclaving after completing of combining of layers in the fabrication sequence after Hatscheck process.

One can determine several 1 mm short cellulose fibres in the former of the Figures and in the latter –specific layered structure of material 'D', being a result of autoclaving after completing of combining of layers in the fabrication sequence.
Cross-sections of the specimens of type 'A' and 'C' are depicted in Figures 3, 4. Long fibres of ca. 3 mm are visible in Fig. 3. The fibre diameter and length seems to be lower in specimen 'C' than that determined in specimen 'A'. The cross-section of the FCB specimen coded 'E' is shown in Figure 5. The fibres form distinct agglomerates (curls) here, what was caused by extrusion used during the fabrication process.

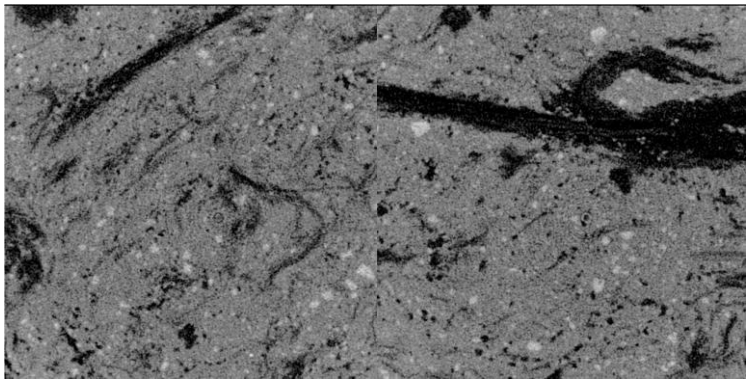

Figure 3. Examples of ca.3 mm long cellulose fibres depicted in micro-CT cross-sections elaborated in specimen 'A'.

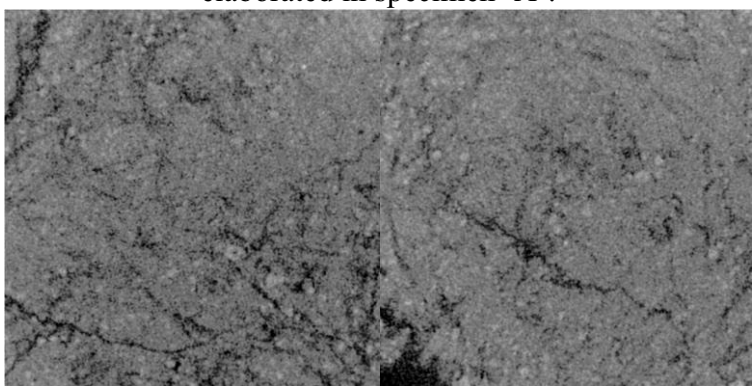

Figure 4. The cross-section of the FCB specimen coded 'C'. The fiber diameter and length seems to be lower than that presented in Fig. 3.

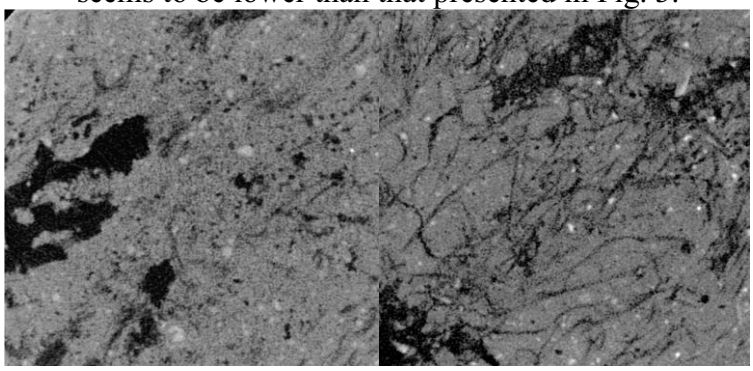

Figure 5. The cross-section of the FCB specimen coded 'E'. The fibres form agglomerates (curls), what is caused by extrusion used during the fabrication process.

The other way to present the information included in the specimens' ROIs described above is to perform the brightness distribution of all voxels , i.e. (729,000,000) constituting the ROI ensembles. It was found experimentally that the magnitudes of brightness in different regions were included in the following ranges: the area of voids and fibres: 0 - 50 [arbitrary units, a.u.], fillers: 50 - 140 [a.u.], dense phases (unhydrated cement and fine aggregate grains: 140 - 170 [a.u.]. The greyscale brightness distribution (GBD) of all voxels belonging to the investigated ROIs are shown in Figures 6 and 7 to demonstrate the ability of GBD to determine the different microstructure differences among the investigated compositions. It is worth noting that the presence of dense phases (and their amount) can be observed as the peaks on the right side of the distributions mentioned above. By contrast, the potential presence of voids and cracks can be observed as the narrow peaks on the left end of GBD dependence.

It can be concluded that GBD dependencies constructed for the compositions fabricated applying standard Hatscheck method and extrusion techniques (specimen 'C' and 'E') are of similar shape however extrusion resulted in the more tight composition (the curve 'E' is shifted to the right) and probably the large fibre agglomerates are the reason of the remarkable peak at the left part of the graph. The composition 'D', presented in Fig. 2., which underwent the autoclaving process is characterised by different type of GBD curve.

Types of dark coloured and thus of low brightness (0-50 a.u.) fibres can be traced in Figure 7. Specimen 'A' containing 6 % of good quality ca. 3 mm long cellulose fibres (see Fig.3) is represented by GBD curve moved to the left comparing to that representing specimen 'B' containing 6% recycled cellulose short fibres ca. 1 mm long (see Fig. 1). Both specimens were fabricated applying the similar, standard Hatscheck technique what resulted in similar shape of curves depicted in Fig. 7.

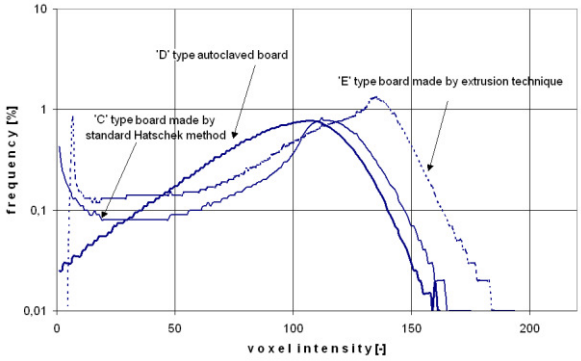

Figure 6. The dependence of greyscale brightness distribution determined for specimens fabricated applying different methods whose micro-CT scans of the microstructure were presented in previous Figures.

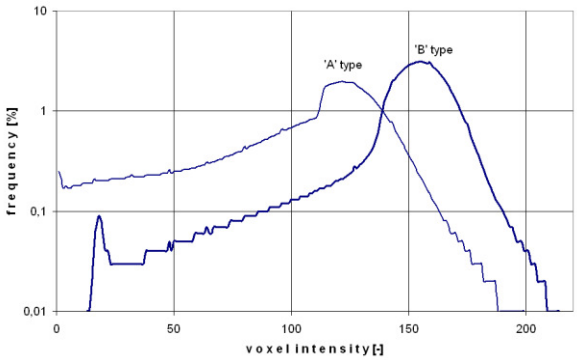

Figure 7. The dependence of greyscale brightness distribution determined for specimens compositions fabricated applying standard Hatscheck method and different fibre types.

4. Conclusions

The micro-CT method applied in the research delivered the large amount of digital data enabling various schemes of it processing. The methods of data presentation include: three-

dimensional projections of the internal specimens microstructure, planar cross–sections at chosen specimen depth or comparative greyscale brightness distribution graphs. The technique presented in the paper appeared to be effective for determining of the certain micro structural properties of tested material, i.e.: microstructure compactness, volume homogeneity, and types of fabrication processes. The presented method can be then recommended as the efficient means for investigation and design of different fibre cement compositions.

References

[1] BS EN 12467:2004, Fibre-cement flat sheets. Product specification and test methods (2013)
[2] Ardanuy M., Claramunt J., Toledo Filho R. D., Cellulosic fiber reinforced cement-based composites: A review of recent research, Construction and Building Materials 79 (2015), 115–128, doi.org/ 10.1016/j.conbuildmat.2015.01. 035
[3] Cooke T., Formation of Films on Hatschek Machines. Bondelwood and Fibre Composites Conference, Idaho (2002), http:// www.fibrecementconsulting.com/publications/publi-cations.htm.
[4] Cooke A. M., Durability of Autoclaved Cellulose Fiber Cement Composites. Conference on Inorganic Bonded Wood and Fibre Composites, Idaho (2000), http:// www.fibrecementconsulting.com/publications/publi-cations.htm
[5] Akhavan A., Catchmark J., Rajabipour F., Ductility enhancement of autoclaved cellulose fiber reinforced cement boards manufactured using a laboratory method simulating the Hatschek process, Construction and Building Materials 135, (2017), 251–259
[6] Lu S., Landis E. N., Keane D. T., X-ray microtomographic studies of pore structure and permeability in Portland cement concrete, Materials and structures. 39 (2006), 611-620, doi.org/ 10.1617/s11527-006-9099-1
[7] Garboczi E. J., Three-dimensional mathematical analysis of particle shape using X-ray tomography and spherical harmonics: Application to aggregates used in concrete, Cement & Concrete Research 32 (2002), 1621-1638
[8] Schabowicz K., Ranachowski Z., Jóźwiak-Niedźwiedzka D., Radzik Ł., Kúdela Jr. S., Dvorak T., Application of X-ray microtomography to quality assessment of fibre cement boards, Construction and Building Materials 110 (2016), 182-188
[9] Lanzon M., Cnudde V., de Kock T., Dewanckele J., X-ray microtomography (μ-CT) to evaluate microstructure of mortars containing low density additions, Cement & Concrete Composites 34 (2012), 993-1000
[10] Stock S. R., Naik N. K., Wilkinson A. P., Kurtis K. E., X-ray microtomography (micro-CT) of the progression of sulfate attack of cement paste, Cement & Concrete Research 32 (2001), 1673-1675
[12] Nakashima Y., Kamia S., Mathematica Programs for the Analysis of Three-Dimensional Pore Connectivity and Anisotropic Tortuosity of Porous Rocks using X-ray Computed Tomography Image data, Journal of Nuclear Science and Technology 44 (2012), 1233-1247
[13] Provis, J. L., Myers R. J., White C. E., X-ray microtomography shows pore structure and tortuosity in alkali-activated binders, Cement & Concrete Research 42 (2012); 855-864

GEOPOLYMERS AND ALKALI-ACTIVATED MATERIALS

SynerCrete'18 International Conference on Interdisciplinary Approaches
for Cement-based Materials and Structural Concrete
24−26 October 2018, Funchal, Madeira Island, Portugal

ACOUSTIC EMISSION PARAMETERS OF ALKALI ACTIVATED FLY ASH SPECIMENS WITH HEMP FIBRES UNDER STATIC LOADING

Libor Topolář [(1)], Hana Šimonová [(1)], Barbara Kucharczyková [(1)]

(1) The Brno University of Technology, Faculty of Civil Engineering, Brno, Czech Republic

Abstract
This paper deals with the effect of the different amount of hemp fibres added to fine-grained composite based on alkali activated fly ash matrix on the values of acoustic emission signals parameters obtained during the fracture tests. The prisms specimens with nominal dimension 40 × 40 × 160 mm and initial central edge notch were subjected to tests in three-point bending configuration. The four magnetic sensors were placed on each specimen and acoustic emission signals were recorded during the loading. The obtained results indicate that the specimens with hemp fibres exhibit a larger number of acoustic emission events than reference specimens without the fibres. It can be most likely connected to pull-out or break of the hemp fibres. The addition of hemp fibres causes the attenuation of the AE signals and the reduction of the amplitude values.

1. Introduction

Currently, environmental aspects are much more pursued, therefore there is the increased effort to develop new environmentally friendly innovative building materials as an alternative to ordinary Portland cement-based concrete. The alkali activated materials (AAMs) belongs to a promising alternative to traditional cement [1, 2]. The manufacture of AAMs is more effective in reducing CO_2 emissions and energy consumption in comparison to the ordinary cement [3, 4], because of the industrial by-products like as blast furnace slag or fly ash is used. The major disadvantage of AAMs is an increased shrinkage during hardening period, which finally results in a decrease in values of tensile and bending properties/strengths [5, 6]. The addition of different types of fibres into alkali activated matrix might lead to the reduction of the cracking tendency and improvement of tensile properties of these materials, likewise as it is in the case of the fibre-reinforced ordinary Portland cement-based materials [7−9].

The above mentioned environmental friendly trend of research induces the use of a sustainable alternative to steel and synthetic fibres. Natural fibres produced from different types of plants (e.g. hemp, flax) belong to a relatively cheap alternative [10−12]. The main advantages of natural fibres are their biodegradability, their resources are renewable, neutral toward CO_2 emissions. On the other hand, natural fibres still have several drawbacks that limit their wider use. One of the most important is the dependence on their physical and mechanical properties on growing, harvesting and processing methods. Moreover, the use of natural fibres reinforced composites for civil engineering applications requires additional information about the damage mechanisms within these materials [13]. Therefore, in this paper, authors pay their attention to the effect of the different amount of hemp fibres added to fine-grained composites based on the alkali activated fly ash matrix on their behaviour during the fracture test. While the effect of fibres is expressed by the values of acoustic emission signals parameters obtained during the loading tests.

The acoustic emission method belongs to non-destructive methods which can be used to monitoring of active defects that occur inside the monitored structure. The inactive defects and the shape of the investigated structure do not have a decisive influence on the creation of AE signals. One of the AE measurement advantages is the capability to observe the damage propagation in real time during the specimens loading [14]. For the purpose of the AE measurements evaluation, it is necessary to analyse several parameters of an AE waveform, such as a number of events, counts, duration, amplitude and energy of AE signals. Counts refer to the number of pulses emitted by the measurement circuitry if the signal amplitude is greater than the threshold. Depending on the magnitude of the AE event and the characteristics of the material, one hit may produce one or many counts. The duration of AE signal is the time between the first and last overstepping of the threshold value. The amplitude is the greatest measured voltage of the signal which determines the detectability of the AE signal. The signals with amplitudes below the operator-defined minimum threshold value will not be recorded. The energy of AE signals is directly proportional to the area under the AE waveform [14].

2. Materials and methods

The prism specimens with nominal dimensions 40 × 40 × 160 mm made of alkali activated fly ash mortars were studied. In total three set of specimens were tested. The first one was a reference set, designated as AAFAM, another two sets contained different volume percentage
of hemp fibres (0.5 and 1.0 %), designated as AAFAM_0.5 and AAFAM_1.0, respectively. The power plant fly ash (450 g), sodium silicate solution as alkali activator (306 g), river sand (1350 g) with a maximum grain size of 8 mm, water (70 g) and hemp fibres (6.25 and 12.5 g) with a length of 10 mm were used to produce the test specimens. The specimens were provided with a central edge notch with the depth of approximately one-third of the prism height and subsequently tested in the three-point bending fracture test configuration. The loading procedure was performed with the requirement of a constant increment of displacement which was set to 0.02 mm/min. In this way, the diagram of loading force F in

relation to the crack mouth opening displacement *CMOD* during the fracture test was recorded. The recorded *F−CMOD* diagrams for all specimens are shown in Fig. 1; three specimens were tested from each set.

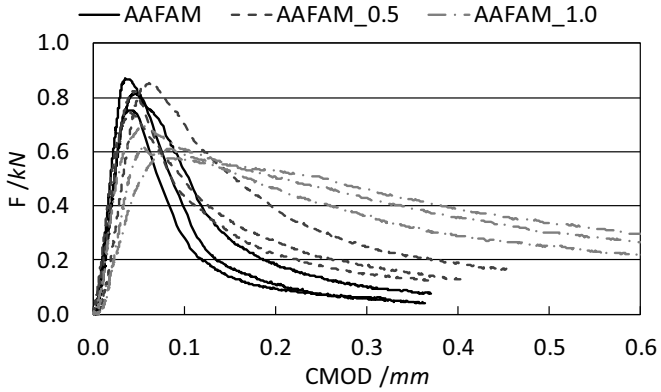

Figure 1: *F−CMOD* diagrams for all specimens

The acoustic emission (AE) signals (during the fracture tests) were detected using four magnetic sensors (MDK-13) which were placed for all specimens at the same positions, see Fig. 2. The AE sensors were magnetically attached to the pre-prepared metal strips glued onto the surface of the individual specimens. Moreover, AE signals were amplified by a 35 dB amplifier and transmitted to the universal measuring and diagnostic system DAKEL-XEDO which was developed by the Czech company ZD Rpety-Dakel. DAKEL-XEDO equipment allows record and digital processing of AE signals as well as measurement of additional physical parameters e.g. temperature, resistance, force etc.

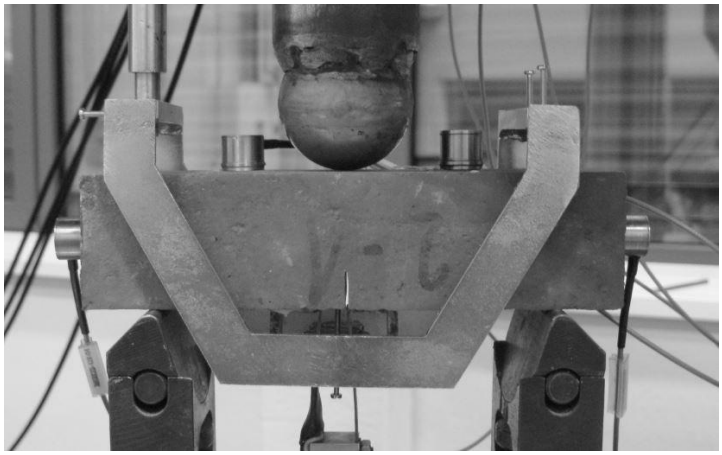

Figure 2: Fracture test configuration and positions of AE sensors.

3. Results and discussion

In this paper, the number of AE events, the duration of the AE signal, and the AE signal amplitude were selected to describe the effect of the different amount of hemp fibres in the fine-grained AAFAM composites on the values of AE signals parameters obtained during the

fracture tests. The results are shown in Figs. 3−5 in the form of bar charts representing mean values with error bars representing standard deviations values. The charts on the left always present the results obtained during the loading process from the start up to the maximum load (peak of the load-deflection diagram see Fig. 2) and the charts on the right the results obtained from the whole measurement, i.e. from the start or loading until the specimen's fracture.
The Fig. 3 shows the number of AE events for the individual sets. The number of AE events represents the approximate amount of defects (microcracks, cracks, etc.) formed in the material inner-structure. In the initial part of loading (up to the maximum load, Fig. 3, left), a decrease of a number of AE events was observed with the increasing amount of hemp fibres. The results obtained from the whole measurements exhibit a many-times higher number of AE events for specimens with the hemp fibres in comparison to the reference one. Furthermore, it is evident that the number of AE events increases with the increasing amount of hemp fibres. This is probably associated with a gradual rupture of the hemp fibres or they're pulling out from the matrix, therefore the higher amount of fibres produces the higher number of AE events.

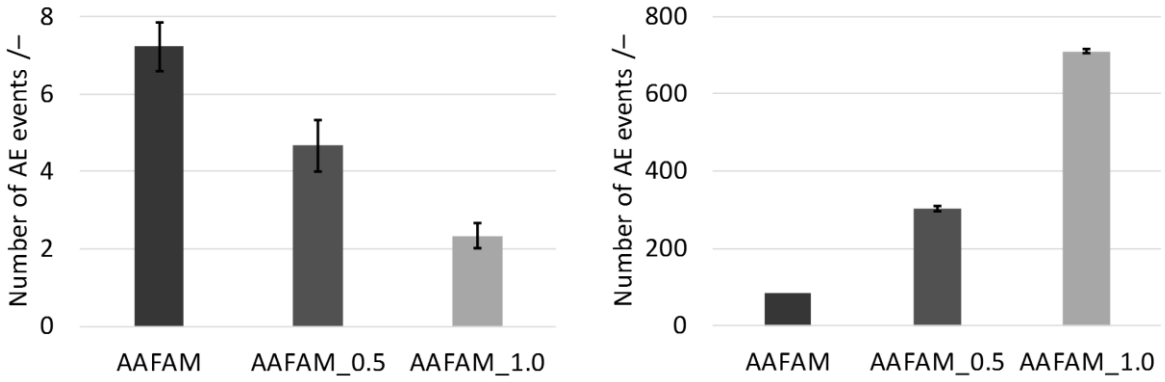

Figure 3: Number of AE events for individual specimen sets (up to maximum load (left) and from the whole measurement).

The Fig. 4 demonstrates that the duration of the AE signals is reduced by the addition of hemp fibres. The addition of hemp fibres causes the attenuation of the AE signals, therefore the AE signals are shorter. For the reference specimens (AAFAM) without hemp fibres, the AE signals propagate more easily and therefore produces higher AE signal duration values. The results also show that the AE signals attenuation was essentially the same for both amounts of fibres.

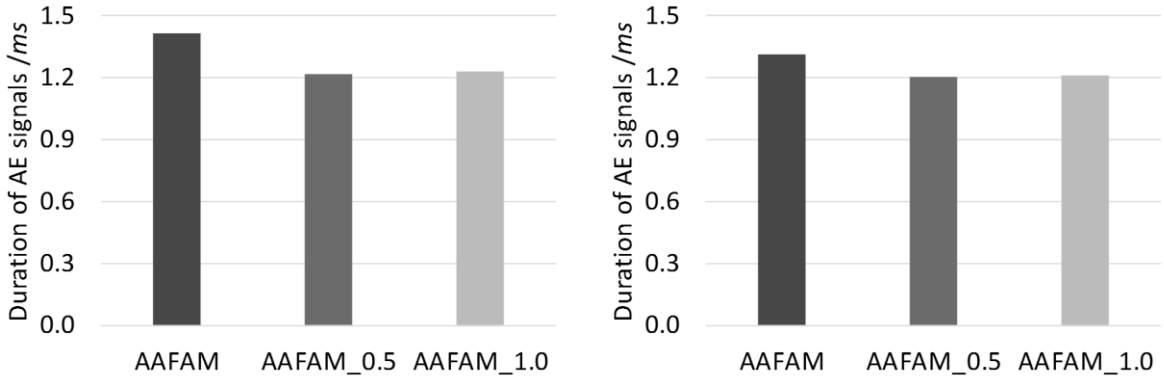

Figure 4: Duration of AE signals for individual sets (up to maximum load (left) and from the whole measurement).

The Fig. 5 shows the effect of hemp fibres addition on the values of AE signals amplitudes. The obtained trend is similar as in the case of the duration of AE signals. The higher amount of hemp fibres in the mixture causes attenuation of the AE signal which resulted in the reduction of the amplitude values.

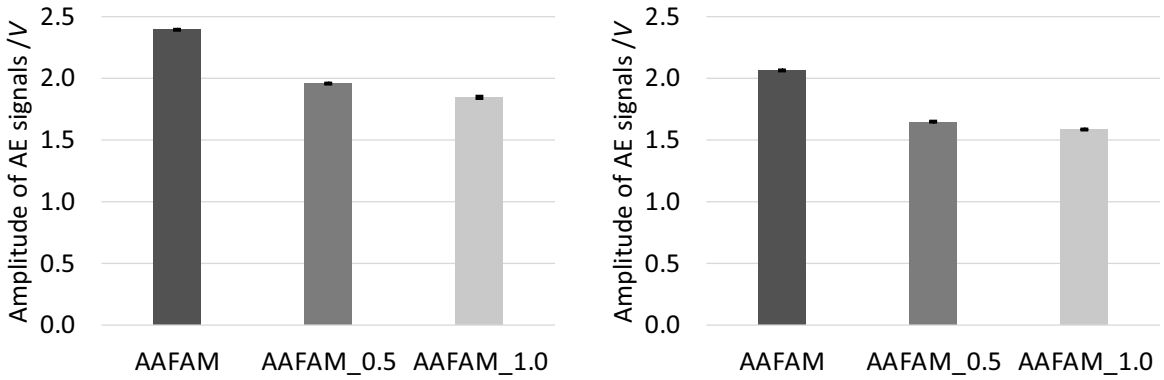

Figure 5: Amplitude of AE signals for individual sets (up to maximum load (left) and from the whole measurement).

4. Conclusions

This paper presented evaluation of the experimental tests focused on the analysis of selected parameters of AE signals recorded during the three-point bending fracture test of alkali activated fly ash composites reinforced with hemp fibres. The AE method seems to be an effective tool for the detection of the disturbances in the inner-structure of the alkali activated composites during the fracture test. The selected parameters of the AE signals show the different behaviour of the individual sets of specimens depending on the amount of hemp fibres in the mortar.

The conclusions of this article can be summarized as follows:

- The addition of hemp fibres reduces the number of AE events before the maximum load is reached. In the case of whole measurement evaluation, it can be suggested that the

hemp fibres addition causes the increase in the number of AE events, which is associated with the gradual rupture of the fibres and their pulling out from the matrix.

- The addition of hemp fibres reduces the duration of the AE signals due to a greater signal attenuation.
- The addition of hemp fibres also causes a decrease in the values of AE signals amplitude.

Acknowledgement
This outcome has been achieved with the financial support of the Czech Science Foundation, project No. 18-12289Y "Advanced characterization of crack propagation in composites based on alkali activated matrix".

References

[1] Provis, J. L. and van Denventer, J. S. (eds), Alkali activated materials: state-of-the-art report, RILEM TC 224-AAM, Springer, Dordrecht (2014).
[2] Shi, C. et al, Alkali-activated cements and concretes, Taylor & Francis, London (2006).
[3] Keun-Hyeok, Y. et al, Assessment of CO_2 reduction of alkali-activated concrete, J Cleaner Production 39 (2013), 265–272.
[4] McLellan, B. C., et al, Costs and carbon emissions for geopolymer pastes in comparison to ordinary Portland cement, J Cleaner Production 19 (2011), 1080–1090.
[5] Cincotto, M. A. et al, Effect of different activators type and dosages and relation with autogenous shrinkage of activated blast furnace slag cement, Proc. of the 11th International Congress on the Chemistry of Cement, Durban, South Africa (2003)1878–1888.
[6] Ye, H. eta al, Understanding the drying shrinkage performance of alkali-activated slag mortars, Cement and Concrete Composites 76 (2017), 13–24.
[7] Li, B. et al, The Mechanical Properties of Polypropylene Fiber Reinforced Concrete, Journal of Wuhan University of Technology-Mater. Sci. Ed. 19 (2004), No. 3, 68−71.
[8] Ravikumar, C. S. et al, Effect of Fibres in Concrete Composites, International Journal of Applied Engineering Research 10 (2015), No. 1., 419−430.
[9] Nedeljkovic, M. et al, Development and application of an environmentally friendly ductile alkali-activated composite, J Cleaner Production 180 (2018), 524–538.
[10] Schwarzova, I. et al, Sustainable hemp-based composites for the building industry application, AIP Conference Proceedings, Vol. 1866, No. 1, 040036 (2017).
[11] Zhou, X. and Kastiukas, G., Engineering Properties of Treated Natural Hemp Fiber-Reinforced Concrete, Frontiers in Building Environment 3 (2017), Article 33, 1–9.
[12] Merta, I. and Tschegg, E. K., Fracture energy of natural fibre reinforced concrete, Construction and Building Materials 40 (2013), 991–997.
[13] Lau, K. T. et al, Properties of natural fibre composites for structural engineering applications. Composites Part B: Engineering, 136 (2018), 222-233.
[14] Ohtsu, M., Acoustic emission and related non-destructive evaluation techniques in the fracture mechanics of concrete: fundamentals and applications, Woodhead Publishing (2015).

SynerCrete'18 International Conference on Interdisciplinary Approaches
for Cement-based Materials and Structural Concrete
24-26 October 2018, Funchal, Madeira Island, Portugal

ALKALI ACTIVATED MATERIALS: REVIEW OF CURRENT PROBLEMS AND POSSIBLE SOLUTIONS

Adeyemi Adesina [(1)]

(1) Concordia University, Montreal, Canada

Abstract
Focus on alkali-activated materials (AAMs) have increased in recent years due to its possibility to be a substitute for the ordinary Portland cement (OPC). However, the development of AAM that would be a viable substitute for OPC is still impeded due to several problems faced during its production, and properties of the resulting AAMs. Finding a substitute for OPC is imminent as a result of its contribution of about 7% to the world's human-induced carbon dioxide emission. The amount of emission is expected to increase in the coming years due to increase in development all over the world. Therefore, it is necessary to develop alternative green binder that would contribute less emission to the environment while conserving natural resources deposit.
This review explored the current problems hindering the universal acceptance and large-scale application of AAMs. It was concluded that with more research and development on user-friendly activators with low embodied energy and carbon, AAMs will be able to compete as a viable substitute for OPC.

1. Introduction

Alkali-activated materials (AAMs) have gained huge attention recently in the concrete industry due to its viability to be used as a replacement for the conventional ordinary Portland cement (OPC). AAMs are obtained by activating an aluminosilicate precursor with an alkaline activator. The need for replacement of OPC in concrete is imminent due to its high embodied carbon and energy [1]. Approximately 1 tonne of carbon dioxide is emitted with an equivalent amount of OPC produced [2]. The carbon dioxide emission is from the calcination of raw materials and high amount of energy used during OPC's production. As OPC is the main binder in concrete, and billions of tonnes of concrete produced annually; OPC's production contributes between 5 – 10% of the total world anthropogenic greenhouse gases emission [3].

Higher strength and durability properties of AAMs compared to OPC concrete has made it attract huge research from the concrete industry. And majorly, AAMs has shown the possibility of having a huge reduction in carbon dioxide emissions between 55 – 75% of conventional OPC concrete [4]. In addition, AAMs conserves the natural deposits of raw materials such as limestone, as the aluminosilicate materials used for AAMs are by-products of other industrial processes. However, this green advantage is posed with several limitations. Some of the major limitations are quick setting times and high drying shrinkage. These limitations have inhibited the universal acceptance and commercial use of AAMs. Depending on the aluminosilicate materials used, AAMs can be further divided. For example, alkali-activated slag (AAS) is a type of AAMs which uses slag as the aluminosilicate precursor. As the component in AAMs is different from that of OPC, its chemical composition and process differ also [5, 6].
This review is aimed at exploring the major limitations of AAMs, and possible solutions for the limitations. It is anticipated that this review will be a great reference for researchers, construction managers and engineers in the field of construction in general.

2. Current AAMs problems

The problems currently faced by AAMs are evident in the fresh and hardened properties of AAM. Some of the fresh properties limitations are short set times and extremely low flowability. While some of the hardened properties limitations are high drying shrinkage and low volume stability. Some of the major limitations are further explained as follows;

2.1 Short setting time

Two major factors have been identified to affect the setting time of AAMs. These factors are the type of activator and the activator content [7]. Short setting time in AAMs is observed when sodium silicate is used as an activator. Earlier studies [8, 9] reported flash setting of AAMs when activated with sodium silicate. However, the quick setting of AAMs is more pronounced in those activated with sodium silicate compared to sodium hydroxide. The setting times of AAMs activated with a combination of sodium silicate and sodium hydroxide is longer than when activated with only sodium silicate [10]. Short set time caused by sodium silicate activation has been attributed to the initial formation of calcium silicate hydrate. Whereas, the extended setting time observed in AAS activated with sodium hydroxide and sodium carbonate is as a result of the formation of polysilicates hydrates and calcium carbonate respectively [11, 12]. Increase in the ambient temperature has been recorded to shorten the setting time of AAS [4]. However, no significant effect was found on the setting time of AAS when sodium silicate and sodium hydroxide was used to activate AAS. The difference in the effect of ambient temperature on the setting time of different AAS activated with various activator has been attributed to the difference in the chemical composition of the activator [4].

2.2 Elevated curing temperature

AAMs with low calcium aluminosilicate precursors such as class F Fly ash fly ash requires an elevated temperature to accelerate the dissolution of the monomers. In order to achieve a similar strength of AAM made with fly ash compared to that of OPC, an elevated temperature

between 60 to 80^0 C is required [7, 13]. Though the elevated temperature is not required for high calcium aluminosilicate precursors such as slag. However, it has been reported that curing AAMs made with slag reduces the high drying shrinkage associated with it [10]. This elevated temperature requirement has limited the practical large-scale application of AAMs for different applications. However, elevated curing is reasonable in applications such as precast concrete, where the concrete is made in the plants, and it is easier to control the variables during production. Use of elevated temperature curing however consumed huge amount of energy and release more carbon dioxide to the environment thereby increasing the overall embodied energy and carbon of AAMs.

2.3 High drying shrinkage

Shrinkage in AAMs has been found to be higher than that of OPC, especially those with slag as aluminosilicate precursors, and activated with sodium silicate [14, 15]. Formation of gel that is rich in silica has been attributed to the high shrinkage in slag activated with sodium silicate [16, 17]. As the rich silica gel loses moisture during drying, it causes microcracks within the AAS paste. Also, higher shrinkage in AAMs has been attributed to its high quantity of mesopores compared to that of OPC [18].

2.4 Non-user friendly activator

Based on open literature, sodium silicate and sodium hydroxide are the most used activators for AAMs [1-5]. These common activators are expensive, corrosive and the highest contributor of embodied energy and carbon to AAMs. The high cost associated with AAMs activated with these activators have discouraged contractors in embracing this sustainable material. In addition, the high embodied energy and carbon of some of the common activators (i.e. sodium silicate and sodium hydroxide) have eliminated the advantage of using AAMs as a sustainable building material. Also, the corrosiveness of these activators will prevent its large-scale transportation and application as special handling will be required.

2.5 Unknown long-term durability and performance

Most durability properties of concrete are associated with its permeability, which can be measured through its water absorption. Generally, AAMs has been reported in most studies to be more resistant to several detrimental forces in the environment that affects its durability. However, to date, there's no consensus on the water absorption of AAMs due to limited data availability and variation in the available data. For example, Bernal et al [19] and Yang et al [20] concluded that the water absorption of slag activated with sodium silicate is higher than that of OPC. However, some other studies [21, 22] recorded a contradicting observation in which the water permeability was lower than that of OPC. Albitar et al [23] also reported a lower water absorption for AAMs. These contrasting results and lack of extensive long-term results have discouraged project managers and contractors to embrace this innovative sustainable material (i.e. AAMs). Another durability aspect that there's no consensus yet is the alkali-aggregate reaction (AAR). Though the aluminosilicate precursors used for AAMs are used to curb AAR in conventional concrete, contradicting results exists in the open literature. Several studies reported lower AAR expansion in AAM when reactive aggregates are used. However, Bakharev et al. [24] reported that higher expansion when reactive aggregates were used. It should be noted that AAMs usually contain higher amount alkali due to activator used, therefore the probability of AAR to occur is higher. There exist

specifications to limit the equivalent sodium oxide in OPC to 0.8% to prevent the occurrence of AAR, however, AAMs contain a higher amount of sodium oxide equivalent. Resistance to AAR in AAMs reported in some studies might be as a result of the high alkali present in AAMs been bounded to the hydration products formed, thereby reducing the overall alkalinity in the pore solution [25, 26]. However, the practical proof exists of the quantity of alkali bounded to formed products [27].

2.6 Supply market for raw materials

Compared to limestone which is the main raw material for OPC, the aluminosilicate materials use of AAMs are not readily available everywhere, and the type available varies from different geological location. For examples, rice husk ash is readily available in India, whereas its production is limited in Canada, and slag and fly ash is more readily available. This variation in large quantity availability limits the universal use of AAMs compared to that of OPC.

2.7 Lack of universal specification and standard for AAMs

Most construction and research involving AAMs currently use the specifications and standards available for OPC, and OPC concrete. However, it has been found that some of these standards/ tests give false results as the chemistry of AAMs are different from that of OPC. Byfors et al [28], Bakharev [10], and Deja [29] observed that the carbonation rate of alkali-activated slag (AAS) concrete is faster than that of OPC using accelerated carbonation test. However, it concluded that this accelerated test used for OPC is not suitable for AAMs as it overestimates the carbonation of AAMs [30, 31].

2.8 Efflorescence

Effloresce is the whitish product that is formed on the surface of the concrete. The formation of this whitish products in AAMs has been associated with the use of high concentration of sodium hydroxide as an activator for AAMs [58] The whitish product is bicarbonate crystals formed as a result of the reaction of alkali that leached with the carbon dioxide in the environment. Ideally, low amount of bicarbonate formation on the surface of AAMs does not pose any danger to its durability and mechanical properties [58]. But the high formation of this whitish product might be detrimental to the hardened properties of the AAM. Also, high amount of bicarbonate crystals on the surface of AAM would affect its aesthetics. Use of sodium sulphate as activator might also lead to the formation of alkali sulphates on the surface of AAMs. This formation of alkali sulphate is as a result of the low solubility of sodium sulphate [32].

3. Possible solutions to AAMs problems

Use of retarding admixtures employed for OPC concrete can be used to extend the setting time of AAS as there exits currently retarding admixtures made specifically for AAMs. As using sodium silicate is mainly responsible for most quick set times in AAMs, use of alternative activators such as sodium carbonate which produces similar set times similar to that of OPC will be a viable option. Shrinkage in AAMs can be controlled by the use of alternative activators instead of the conventional sodium silicate. For example, the use of sodium carbonate to activate slag has been found to reduce the shrinkage of AAS to give

shrinkage similar to that of OPC [14]. Other possible ways to reduce the shrinkage in AAMs includes the use of shrinkage reducing admixtures (SRAs) [33, 34], internal curing [33], heat curing [16, 35]. Use of supplementary cementitious materials (SCMs) [35, 36] can also reduce the shrinkage of AAMS. Also, air entrainers used for OPC concrete has been found to reduce the shrinkage in AAS [37]. Use of OPC by 10% by mass of the aluminosilicate material used has also been reported to reduce the shrinkage of AAMs [38]. Also, moist curing of AAMs has been found to reduce shrinkage significantly as it prevents rapid loss of moisture from the AAM matrix [18]. Other shrinkage mitigation techniques include fibre reinforcement [39], use of lightweight aggregates, high aggregate content, etc.
Proper moist curing and use of activators with lower concentrations would prevent the formation of high amount of bicarbonate crystals (i.e. efflorescence) on the surface of AAM concrete. Curing of AAMs at relative humidity higher than 95% has been found to prevent the formation of efflorescence [32].

4. Conclusions

This review showed that AAMs is a good substitute for OPC if all its limitations can be overcome. Based on this review, the following conclusions can be drawn;

- Use of alternative green activators will go a long way in eliminating most of the challenges faced by the fresh and hardened properties of AAMs
- Shrinkage in AAMs can be controlled with proper moist curing, use of shrinkage reducing admixture, and good mix design which employs the use of high coarse aggregate content
- Involvement of different stakeholders in the concrete industry will propel more acceptance of AAMs as an alternative sustainable building material.

References

[1] Flower, D., and Sanjayan, J. Greenhouse gas emissions due to concrete manufacture," 26 International Journal of Life Cycle Assessment, (2007) 282- 288
[2] Cabeza, F et al, Low carbon and low embodied energy materials in buildings: a review Renew. Sustain. Energy Rev., 23 (2013), 536-542
[3] Scrivener, K.L and Kirkpatrick, R. J., Innovation in use and research on cementitious material Cem. Concr. Res., 38 (2008), p.128-136
[4] Zivicz, V., Effects of type and dosage of alkaline activator and temperature on the properties of alkali-activated slag mixtures Construction and Building Materials Vol. 21, 7, 2007, 1463-1469
[5] Pacheco-Torgal, F., et al Alkali-activated binders: A review: Part 1 Historical background, terminology, reaction mechanisms and hydration products Constr. Build. Mater.(2008), 1305-1314
[6] Zhang, et al. Compositional, microstructural and mechanical properties of ambient condition cured alkali-activated cement Constr. Build. Mater., 113 (2016), 237-245
[7] Duxson, P et al. Geopolymer technology: the current state of the art J Mater Sci, 42 (2007),
[8] Cheng, Q.H., and Shondeep L. S., A study of rheological and mechanical properties of mixed alkali activated slag pastes. Advn Cem Bas Mat (1994), 178–84.
[9] Gifford P. M., and Gillot, J. E., ASR and alkali carbonate reaction in activated blast furnace cement concrete. Cem Concr Res (1996) 21–6.
[10] Bakharev, T. Resistance of alkali-activated slag concrete to carbonation Cem. Concr. Res., (2001),1277-1283
[11] Hong S. Y. et al. Studies on the hydration of alkali activated slag. In: Proceedings of the third Beijing international symposium on cement and concrete, vol. 2. Beijing; (1993.)1059–1042.

[12] Brylicky W et al. Alkali activated slag cementitious material for drilling operation. In: Proceedings of the ninth international congress on the chemistry of cement, v. 3. New Delhi; (1992). 312–318.
[13] Palomo, A. et al. Alkali-activated fly ashes, a cement for the future, CCR, 29 (8) (1999), 1323-1329
[14] Cartwright, C. et al Shrinkage characteristics of alkaliactivated 2slag cements, J. Mater. Civ. Eng. (2014), 401-407
[15] Ye, H., and Radlinska, A. Shrinkage mechanisms of alkali-activated slag, Cement and Concrete Research, (2016), 126-135
[16] Shi, C. et al Alkali-activated Cements and Concretes Taylor and Francis, London a. New York (2006)
[17] Wu, C. Properties and application of alkali-slag cement," Journal of Chinese Ceramic Society, (1993).
[18] Collins F, Sanjayan J. G. Microcracking and strength development of alkali-activated slag concrete. Cem Concr Compos (2001), 345–52.
[19] Bernal, S. et al Performance of an alkali-activated slag concrete reinforced with steel fibers Constr. Build. Mater., (2010), 208-214.
[20] Yang, K., et al. Establishment of a preconditioning regime for air permeability and sorptivity of alkali-activated slag concrete Cem. Concr. Compos., 73 (2016), pp. 19-28.
[21] Mithun, B.M. and Narasimhan, M.C. Performance of alkali activated slag concrete mixes incorporating copper slag as fine aggregate J. Cleaner Prod., (2016), 837-844
[22] Bernal, S. et al Performance of an alkali-activated slag concrete reinforced with steel fibers Constr. Build. Mater., (2010), 208-214
[23] Albitar, M. et al Durability evaluation of geopolymer and conventional concretes Constr. Build. Mater., 136 (2017), 374-385
[24] Bakharev T. et al Resistance of alkali-activated slag concrete to alkali-aggregate reaction. Cem Concr Res (2001), 331–4
[25] Krivenko, P. Sodium sulphate based slag alkaline cements, Proceedings of 3rd Beijing International Symposium on Cement and Concrete, Beijing, (1993). 1032-1037
[26] Tailing, B., and Brandstetr, J. Present state and future of alkali activated slag concrete, Proceeding of 3rd International Conference on Fly ash, Silica Fume, Slag and Natural Pozzolanas in Concrete, Trondheim, (1989) 1519-1546.
[27] Mesto, J. Alkali reaction of alkali activated Finish blast furnace slag, Silic. Indus. (1982), 123 -127.
[28] Byfors, K. et al Durability of concrete made with alkali-activated slag, Third International Conference Proceedings. Fly Ash, Silica Fume, Slag, and Natural Pozzolans in Concrete (1989), 1429–1466.
[29] Deja, J. Carbonation aspects of alkali activated slag mortars and conc. Silic Ind., (2002), 37-42.
[30] Bernal, S. A et al. Accelerated carbonation testing of alkali-activated slag/metakaolin blended concretes: effect of exposure conditions Mater. Struct., (2014), 653-669.
[31] Bernal, S.A. et al. Gel nanostructure in alkali-activated binders based on slag and fly ash, and effects of accelerated carbonation Cem. Concr. Res., (2013), 127-144.
[32] Wang S. D, et al Factors affecting the strength of alkali-activated slag. Cem Concr Res (1994).
[33] Saliba J. et al. Influence of shrinkage-reducing admixtures on plastic and long-term shrinkage. Cem. Concr. Compos. (2011), 209–217.
[34] Rajabipour F. et al Interactions between shrinkage reducing admixtures (sra) and cement paste's pore solution. Cem. Concr. Res. (2008), 38:606–615.
[35] Aydin S., and Baradan B. Mechanical and microstructural properties of heat cured alkali-activated slag mortars. Mater. Des. (2012), 374–383.
[36] Rajabipour F. et al Interactions between shrinkage reducing admixtures (sra) and cement paste's pore solution. Cem. Concr. Res. (2008), 38:606–615.
[37] Bakharev et al. Effect of admixtures on properties of alkali-activated slag concrete. Cem Concr Res (2000) 367–74.
[38] Fu-seng W et al Study on modification of the high-strength slag cement material. Cem Concr Res (2005), 1344–8.
[39] Mangat, P.S., and Bordeian, S. Shrinkage of fibre reinforced alkali activated composites. Cem. Concr. Compos., in press

SynerCrete'18 International Conference on Interdisciplinary Approaches
for Cement-based Materials and Structural Concrete
24-26 October 2018, Funchal, Madeira Island, Portugal

ALKALI-ACTIVATED BLEND OF CALCINED LATERITIC SOIL AND WASTE MARBLE SLURRY

Luca Valentini [(1)], Ludovico Mascarin [(1)], Enrico Garbin [(1)], Maria Chiara Dalconi [(1)]

(1) Department of Geosciences, University of Padova, Italy

Abstract
This contribution illustrates some preliminary results of a project focussed on the use of alkali-activated materials obtained from clays of different mineralogical composition, sampled in different localities in non-commercially exploited outcrops. Tests performed by alkali activation (using sodium silicate with added sodium citrate) of a calcined clay, consisting of 66% smectite, 22% volcanic glass and accessory phases gave encouraging results, showing that alkali activated materials with excellent mechanical properties can be produced from cheap, widely distributed raw materials, without previous beneficiation. The results also showed that both mechanical properties and workability could be enhanced by the use of marble slurry, a waste material from marble quarrying and cutting, which adds environmental value to the designed mix.
Here, we focus on the use of lateritic soils sampled in Yaoundé, Cameroon, as a raw material for the production of alkali-activated binders. This choice is motivated by the need of investigating the feasibility of producing robust, low-CO_2 cements from raw materials that are widely available across Africa, with the aim of boosting the sustainable development of this continent, in line with recent actions for the collaboration between African Union and European Union.
Some preliminary results of the microstructural and mechanical characterization of these materials as well as their kinetic and thermodynamic modelling will be illustrated.

1. Introduction

The scientific literature on sustainable binders, alternative to Portland cement, has become consolidated. The two main lines of research being pursued comprise zero-clinker to low-clinker binders. The first group mostly encompasses the use of alkali-activated aluminosilicates, the main ones being fly ash, ground granulated blast furnace slag and

metakaolin [1]. The second group of binders is obtained by blending the same aluminosilicates with different amounts of OPC [2]. Given the lack of geographically homogeneous availability (fly ash, slag) or economic viability (metakaolin), in the last few years the use of calcined clays blended with OPC has been explored [3]. In such a scenario, research into the alkali activation of calcined clays still represents a niche.
In this contribution, we investigate the potential use, as sustainable binders, of alkali activated calcined clays of different chemical and mineralogical composition. Clay is an economically viable raw material and is homogeneously distributed geographically. Moreover, clay materials are particularly abundant in soils in many developing countries (Fig. 1) and represent, therefore, in important resource for the growing economies. In this context, we explore the performance of lateritic clays sampled in Cameroon as raw materials for the production of alkali activated cement, relying on previous findings that showed the possibility of obtaining an excellent mechanical performance by alkali activation of calcined smectites, blended with calcium carbonate slurry, a waste material deriving from marble quarrying and cutting [5].

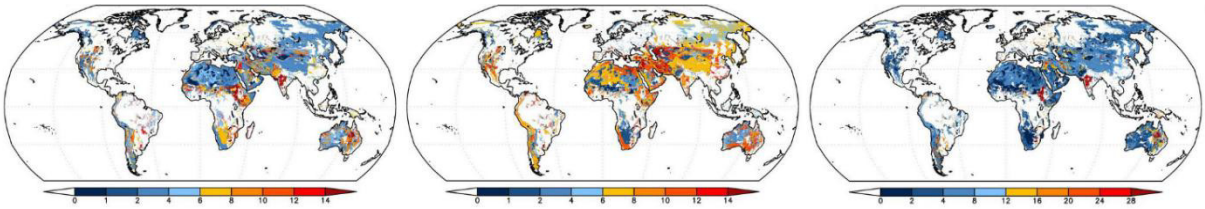

Figure 1: Concentration of clay minerals in soils (left to right: kaolinite, illite, smectite). Data from [4].

2. Material and methods

XRF compositions of the lateritic clay and marble slurry (oven dried at 60 °C) used are reported in Tab. 1. The XRD composition of the clay is: 60% kaolinite, 30% quartz, 8% goethite, 1% anatase, 1% calcite. Recalculating the chemical composition from this phase assemblage leads to an underestimation of Fe > 2%, suggesting that part of the iron might be incorporated in an amorphous phase or adsorbed to kaolinite surfaces. The high amount of iron yields an intense reddish coloration to the clay.

Table 1: XRF composition.

	SiO_2	TiO_2	Al_2O_3	Fe_2O_3	MnO	MgO	CaO	Na_2O	K_2O	P_2O_5
Clay	62.1	1.8	24.6	10.1	0.0	0.2	0.1	0.0	0.2	0.1
Slurry	0.0	0.0	0.1	0.0	0.0	0.6	55.9	0.0	0.0	0.0

Clay calcination was performed at 800 °C for 5 hours, with a heating rate of 10 °C/min. Dehydroxylation of goethite induced the formation of hematite.
The dried marble slurry consists of 100% calcite with some Mg impurities and was pre-mixed in different amounts with clay and a fixed amount of sodium silicate pentahydrate

($Na_2SiO_3 \cdot 5H_2O$) used as an alkaline activator. The addition of dry sodium silicate rather than a previously prepared alkaline solution was preferred, in order to facilitate mixing and enhancing workability. The water-to-solid ratio was 0.5. The different mixes are summarized in Tab. 2.
Additional samples were prepared by blending a commercial metakaolin with an amount of finely ground quartz corresponding to that measured by XRD for the lateritic clay, with the aim of decoupling the effect of quartz from that of Fe-bearing phases.

Table 2: Mix composition (wt%).

	Clay	Marble slurry	Sodium silicate	Water
Sample 1	44.44	0	22.22	33.33
Sample 2	37.78	6.67	22.22	33.33
Sample 3	31.11	13.33	22.22	33.33

The fresh pastes were kept in teflon moulds for two days at ambient temperature and 95% relative humidity. After demoulding, the samples were cured at the same temperature and humidity conditions. One day before compressive strength testing, the samples were kept at ambient humidity. Powder XRD was performed to study the phase assemblage of the reacted materials and polished thin sections were prepared for SEM-EDS analyses. Simulations of the phase assemblage at thermodynamic equilibrium were performed using the software GEMS (http://gems.web.psi.ch/) and the database provided in [6].

3. Results

Samples obtained using the above mix compositions displayed low values of the 7 days compressive strength (4.3 – 4.5 MPa). The samples presented severe fracturing that may be ascribed to the presence of excess sodium silicate (the Na/Al of the three mixes varies between 0.98 and 1.4). It has to be noted, however, that the samples prepared by blending commercial metakaolin and quartz displayed values of the compressive strength up to 11.3 MPa, suggesting a detrimental effect of iron. Also, by reducing the amount of sodium silicate added to the lateritic clay, from 22.22 wt% to 11.11 wt% (Na/Al = 0.49 – 0.70), the 7 days compressive strength increased up to 13.0 MPa.
The EDS spot chemical composition of the matrix is reported in the Na-Al-Si system in Fig. 2 and compared to the N-A-S-H chemical composition predicted by the thermodynamic model. A good level of agreement exists for the systems with additions of marble slurry, whereas a slightly higher Na/Si is predicted by the thermodynamic model for the system in the absence of marble slurry.
Precipitation of up to 3% trona ($Na_2CO_3 \bullet NaHCO_3 \cdot 2H_2O$), formed by carbonation of the alkaline pore solution, is observed by means of powder XRD at 28 days.

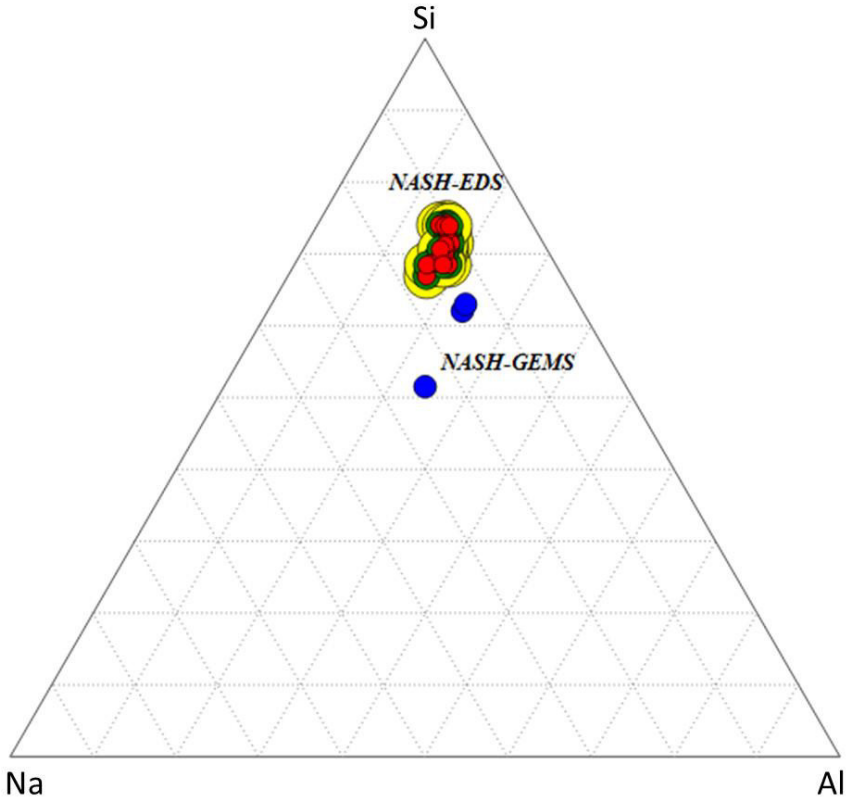

Figure 2: Chemical composition of the matrix, as measured by SEM-EDS and of the N-A-S-H product, as predicted by the GEMS thermodynamic model (blue circles, black in greyscale print).

4. Conclusions and perspectives

This research draws on previous experience on the alkali activation of locally sampled smectitic clays to test the performance of calcined lateritic clay soils from Cameroon as raw materials for the production of sustainable binders. Although preliminary results gave low compressive strengths at one week, it could be observed that the mechanical performance could be significantly improved by adjusting the Na/Al ratio of the mix. Moreover, comparison with samples prepared by alkali activation of a blend of commercial metakaolin and quartz, in the same proportion of that of the lateritic clays, suggests that the presence of iron in clay soils may hinder the development of compressive strength.

It will be worth exploring further the possible role of calcined clays of different mineralogical and chemical composition for the production of alkali activated binders. We are currently testing the properties of alkali-activated calcined clays from Tunisia, consisting of kaolinite-illite mixtures and other additional phases. Preliminary tests using a blend of calcined clay and marble slurry gave a compressive strength of 24 MPa at one week.

This results show that a careful consideration of the chemical and mineralogical composition of such impure systems and subsequent adjustment of the mix proportion is mandatory.

The possibility of exploiting locally available raw materials for the African market is intriguing, and in line with current strategies of scientific collaboration between African Union and European Union [7].

References

[1] Siddique, R. and Khan, M. I., Supplementary Cementing Materials, Springer, Berlin, Germany (2011)
[2] Provis, J. L. and van Deventer, J. S. J., Alkali Activated Materials, State-of-the-Art Report, RILEM TC 224-AAM, Springer, Berlin, Germany (2014)
[3] Scrivener, K. L.; Favier, A., Calcined Clays for Sustainable Concrete. Proceedings of the 1st international conference on calcined clays for sustainable concrete. Springer, Berlin, Germany (2015)
[4] Nickovic, S. et al., Mineral composition in arid soils: A global distribution. AGU Fall Meeting, abstract no NH53A-1254 (2010)
[5] Valentini, L. et al., Alkali-activated calcined smectite clay blended with waste calcium carbonate as a low-carbon binder, J Cleaner Prod 184 (2018) 41-49
[6] Myers, R. J. et al., Thermodynamic modelling of alkali-activated slag cements, Appl Geochem 61 (2015) 233-247
[7] European Commission, Science for the AU-EU Partnership: building knowledge for sustainable development (2017)

SynerCrete'18 International Conference on Interdisciplinary Approaches
for Cement-based Materials and Structural Concrete
24-26 October 2018, Funchal, Madeira Island, Portugal

CHARACTERIZATION OF THE SELF-HEALING EFFECT THROUGH PORE STRUCTURE AND DURABILITY OF ALKALI-ACTIVATED CEMENT CONCRETE

Pavel Krivenko [(1)], Igor Rudenko [(1)], Oleh Petropavlovskyi [(1)], Oles' Lastivka [(1)]

(1) Kyiv National University of Construction and Architecture, Scientific Research Institute for Binders and Materials, Povitroflotskyi prospect 31, Kyiv 03037 Ukraine

Abstract
The paper considers the effect of constituents of alkali-activated cements (AAC) and the chemical admixtures on formation of effective porosity of concrete as a criterion for the AAC matrix to self-heal. The durability of concrete is performed by its frost resistance. Minimization of open capillary porosity was considered as the determining factor for reducing amount of ice in pores and predetermining a corresponding decrease in stresses. The influence of the anionic part of AAC's alkaline component on the features of pore structure of concrete is shown. Thus, sodium carbonate causes greater open capillary porosity of compared to sodium silicates. An increase of granulated blast-furnace slag in AAC from 50 to 100 % and adequate increase alkaline component determine decrease in the volume of open capillary pores with higher volume of micro- and conditionally closed pores. This phenomenon determines increasing AAC concrete's ability to self-heal under the cyclic action of freezing and thawing. It was determined negative changes in the pore structure of AAC concretes modified with polyesters. It has been proposed to use alternative admixtures of the polyether type.

1. Introduction

One of the ways to avoid disadvantages of cements with high slag contents is to add alkali metal compounds in order to produce alkali-activated cement (further, AAC) [1, 2, 3].
A key factor which determines performance properties and durability of concrete is its porosity. However, if strength of concrete depends on a total porosity, freeze/thaw resistance and durability are determined chiefly by capillary porosity [4]. The tendency to simplify concrete technologies causes the use of plasticizers, which application is problematic with

AAC because of high alkaline medium [5]. The basis for designation of the main active ingredient of plasticizers for AAC concretes was proposed [6].
It is known the natural ability of cement materials to eliminate cracks, i.e. (improved) autogenous self-healing mainly due to hydration of unhydrated cement and carbonization of $Ca(OH)_2$ [7]. The peculiarity of AAC in comparison with OPC is the tendency to higher volume of micropores (gel pores) and to reduce capillary porosity due to gradual formation in porous space of alkaline and alkaline- alkali-earth hydroaluminosilicates, which causes self-healing [8]. An important aspect is to ensure self-healing of AAC concrete with its modification by plasticizers, i.e. providing high frost resistance.
The purpose of this paper is to investigate the features of pore structure which determine autogenous self-healing of plasticized AAC concrete under the action of cyclic freezing and thawing.

2. Raw materials and testing techniques

The AACs varying in contents of ground granulated blast furnace slag (further, slag) between 50 and 100 % as per national standard of Ukraine were used [9].
Slag (basicity modulus M_b = 1.1, content of glass phase 56 %) and portland cement clinker were used as aluminosilicate components of the AACs, their chemical compositions are shown in Tab. 1. Soda ash (Na_2CO_3) and sodium metasilicate pentahydrate ($Na_2SiO_3 \cdot 5H_2O$) were used as alkaline components of the AACs. It is required to use sodium lignosulfonate (further, LST) in order to provide the required setting times and strength of AAC.

Table 1: Chemical composition of AACs components.

Component	**Oxides, % by mass**								
	SiO_2	**Al_2O_3**	**Fe_2O_3**	**MnO**	**MgO**	**CaO**	**Na_2O**	**SO_3**	**LOI**
Clinker	21,3	5,7	4,62	-	1,2	64,9	0,3	0,86	0,12
Slag	39,0	5,9	0,3	0,5	5,82	47,3	-	1,54	-

The AAC compositions are shown in Tab. 2. Fineness of the AACs (by Blaine) was 4500 cm^2/g.
In order to change a consistency of the AAC concrete mixtures from class S1 (that of the reference composition) to class S4 at t= 20±2 ºC the chemical admixtures were used (% by AAC): type 1 – surfactant based on polyacrylate esters ("Dynamon SR 2", Mapei) – 1.2 %; type 2 - surfactant based on polyether (polyethylene glycol "PEG-400", JSC "Barva") – 1.3 %; type 3 - surfactant based on sodium gluconate ("Mapetard SD 2000", Mapei) – 1.0 %.
The mentioned surfactants are compatible with LST as components of complex admixtures (further, CA), used to ensure low water consumption of concrete mixtures with decrease in the surface tension of porous fluid. It is known that the latter circumstance facilitates migration of porous fluid, respectively, reducing the capillary stress that causes shrinkage [10].
The standard composition of the AAC concrete was taken in accordance with [11], kg/m^3: cement - 350; silica sand - 740; granite gravel: 350 (5/10) and 810 (10/20); water - 165.
Porosity (P) of AAC concretes was studied in accordance with methodology of the national standard of Ukraine [12]. The concrete cubes (100 mm) after 28 days of hardening (t= 20±2

°C, RH= 95±5 %) were dried up to a constant weight at *t*= 105±5 °C. Then, the concrete specimens were saturated with water until a constant weight at *t*= 20±2 °C. The values of porosity, i.e. volumes of open capillary pores (P_o) and conditionally closed pores (P_c), were calculated from the values of average density and water absorption of the concrete specimens.

Table 2: Compositions of AAC.

# of composition	Basic composition
1	50 % slag, 50 % clinker, 2 % Na_2CO_3, 1 % LST
2	50 % slag, 50 % clinker, 3 % $Na_2SiO_3 \cdot 5H_2O$, 1 % LST
3	69 % slag, 31 % clinker, 2,5 % Na_2CO_3, 1 % LST
4	69 % slag, 31 % clinker, 3,5 % $Na_2SiO_3 \cdot 5H_2O$, 1 % LST
5	88 % slag, 12 % clinker, 3 % Na_2CO_3, 1 % LST
6	100 % slag, 4,7 % Na_2CO_3, 0,8 % LST

Freeze/thaw resistance was studied in accordance with the third test method prescribed by the national standard of Ukraine [13]. The concrete cubes (100 mm) after 28 days (*t*= 20±2 °C, RH= 95±5 %) were saturated with 5 % solution of NaCl at *t*= 18±2 °C and after that were subjected to freezing at *t*= -50±5 °C. Thawing was also done in 5 % solution of NaCl. Class of concrete in freeze/thaw resistance was designated as a number of alternate freezing and thawing at which a mean compressive strength decreased by no more than 5 %. The freeze/thaw resistance of concrete was assessed by the correspondence between permissible number of freezing-thawing cycles on the used accelerated method and on first (basic) method prescribed in mentioned standard. The differences of the first method are specimens saturation medium (water), the medium and the freezing temperature (air, *t*= -18±2 °C), the thawing medium (water).

3. Results and discussions

The use of polyester-based CA in the AAC concretes containing 50 % of slag lead to slight increase of P_o in comparison with the reference composition – for example, from 8.1 up to 8.8 % using soda ash (Fig. 1). With increase of slag content in AACs up to 88 % the effectiveness of this CA in concrete tended to significantly decrease and was accompanied by increase of P_o up to 11 %.

At the same time, there was observed general tendency to increasing effectiveness of pore structure of the concrete, i.e. to decrease P_o with increase in slag content and, accordingly, with increase in the required content of alkaline component in AACs (Fig. 1). In this case, the increasing P_c determines formation of more dense structure with advanced self-healing.

Modification of the AAC concretes by polyester-based admixtures in case of AAC with 50 % of slag (compositions #1 and #2) provided class F200 in freeze/thaw resistance (Fig. 2), i.e. highest class for the most demanding concrete structures in unheated buildings undergoing alternate freezing-thawing and operating at ambient temperature (-20 to -40) °C (exposure class XF4). However, with increase in slag contents up to 69 % the efficiency of this type of admixture tended to decrease. This was accompanied by lack in self-healing of the structure, P_o increased (up to 9.6 %) and freeze/thaw resistance declined (class F150).

Polyethylene glycol did not significantly affect pore structure of concrete in case of AACs containing 88 % of slag (Fig. 1). Significant self-healing function of concrete structure defined class F200 in freeze/thaw resistance. With an increase of slag up to 100 %, the structural parameters did not significantly change: P_o increases from 7.3 % to 7.7 % and P_c from 2.4 % to 2.6 % respectively. Due to additional volume of artificial air micropores this fact caused increasing self-healing of concrete and provided class F200 (Fig. 2).

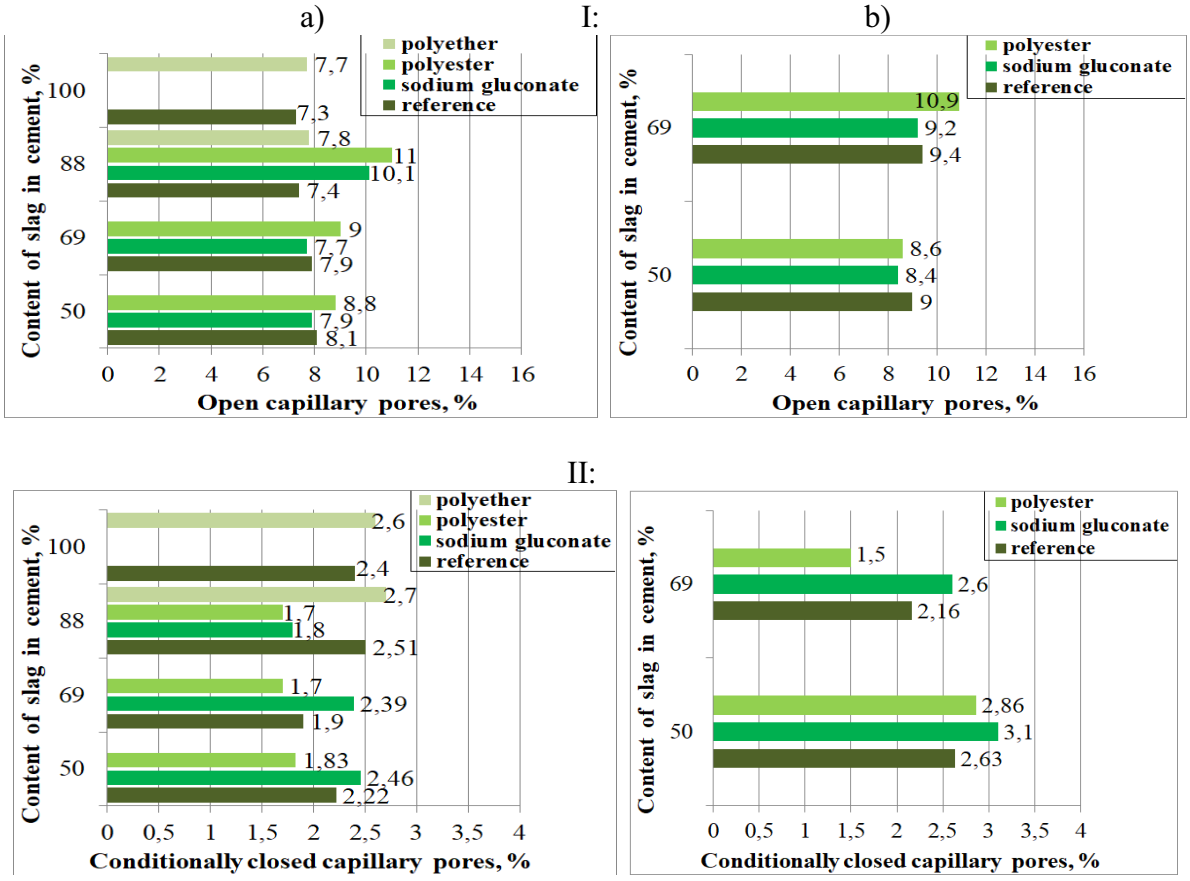

Figure 1: Volumes of open capillary pores (I) and conditionally closed capillary pores (II) of the AAC concrete vs. type of surfactant as ingredient of CA and slag contents in the AACs, % (see Tab. 2): a) #1, #3,#5, #6; b) #2, #4.

Sodium gluconate as ingredient of CA did not change the pore structure of concrete with 50 – 69 % slag in AAC essentially (Fig. 1). Thus, with 50 % slag in AAC P_o = 8.1 % for the reference composition and P_o = 7.9 % with the admixture. With an increase in the amount of slag up to 69 %, there was even some decrease in the volume of these pores. As a result, provided class for frost resistance of concrete was F200 (Fig. 3). However, this type of admixture in concretes with 88 % of slag in AAC deteriorated pore structure and P_o increased up to 10 % with reducing the frost resistance to class F150.

The replacement of the anion in AACs alkaline component from carbonate to silicate caused higher porosity of concrete both the reference composition and the modified ones by the mentioned surfactants (Fig. 1). This fact caused minor ability of concrete to self-healing and lack in frost resistance of concrete with high volume of slag in AAC (Fig. 3).

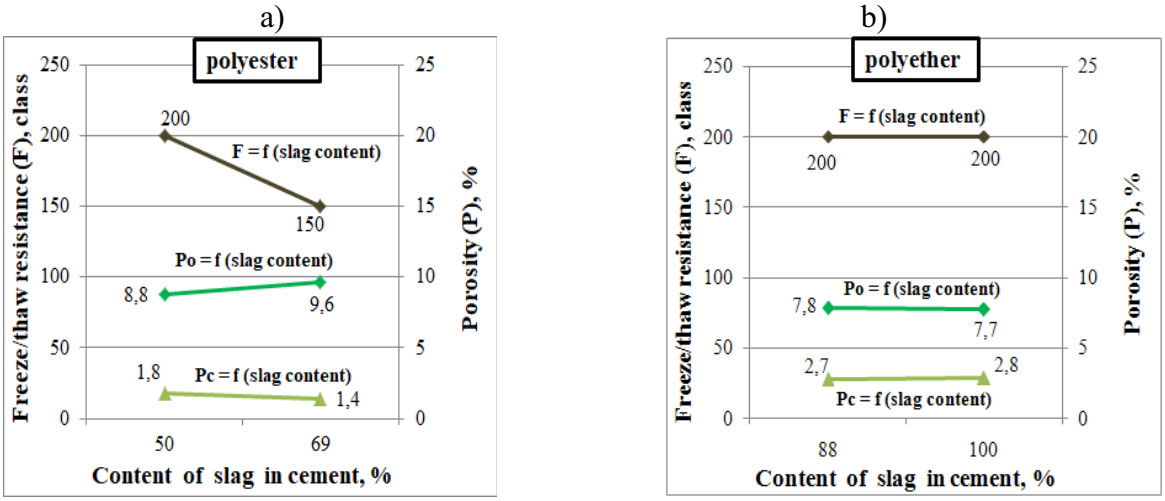

Figure 2: Open capillary porosity (P_o), conditionally closed porosity (P_c) and freeze/thaw resistance (F) of the AAC concretes vs. main active substance of plasticizing admixture as ingredient of CA and slag content in AAC (see Tab. 2): a) #1, #3; b) #5, #6.

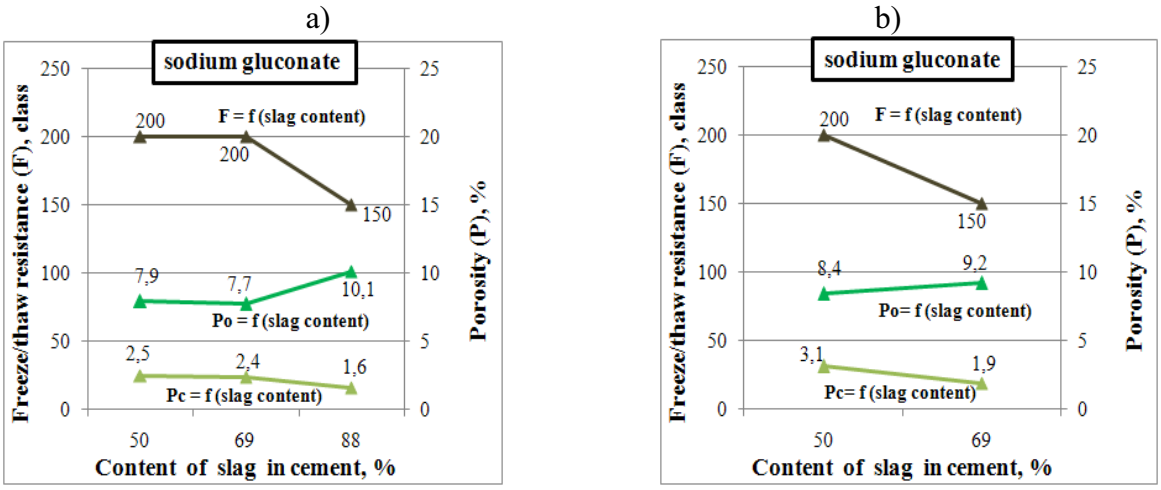

Figure 3: Open capillary porosity (P_o), conditionally closed porosity (P_c) and freeze/thaw resistance (F) of the AAC concretes plasticized by sodium gluconate vs. slag content in AAC (see Tab. 2): a) #1, #3, #5; b) #2, #4.

4. Summary

It was found out that the ability of plasticized AAC concrete to (improved) autogenous self-healing, also under the cyclic freezing and thawing, can be provided by the features of pore structure, namely by minor volume of open pores and correspondingly high volume of conditionally closed capillary pores. In general, this phenomenon is observed with an increase in volume of slag in AAC with consequently maintenance in the required dosage of alkaline component. In this case, the polyesters become ineffective as plasticizers while the admixtures based on polyethers or alkaline salts of carboxylic acid in presence of sodium

lignosulfonate positively affect the formation of additional volume of micropores in the structure of concrete. This creates a reserve for the self-healing function of concrete, i.e. formation of air space for migration of water during cyclic freezing/thawing.

Acknowledgements
The authors would like to acknowledge the contribution of the COST Action CA15202. http://www.sarcos.enq.cam.ac.uk

References

[1] Glukhovsky, V.D. et al, Fine Alkali-Activated Slag Cement Concretes, Vysscha Shkola Publishing, Ukraine (1981)
[2] Krivenko, P.V., Alkali-activated alumosilicates: past, present and future, Proceed. the 4-th Meeting on Chemistry and Life, Brno University of Technology, Brno (2008), 1-5
[3] Krivenko, P.V. et al, Features of Alkali-Activated Slag Portland Cement, Proceed. 1-st Int. Conf. on the Chemistry of Construction Materials, October 7-9, Berlin, Germany (2013), 453-456
[4] Stark, J. Wicht, B., Dauerhaftigkeit von Beton, Weimar: Hochschule für Architektur u. Bauwesen, Weimar, Schriften 100 (1995)
[5] Krivenko, P. et al, Plasticizing alkaline cements: state-of-the-art and solutions, Proceed. the 14-th Int. Congress on the Chemistry of Cement, China (2015)
[6] Krivenko, P., Runova, R., Rudenko, I., Skoryk, V., Omelchuk, V., Analysis of plasticizer effectiveness during alkaline cement structure formation, EasternEuropean journal of Enterprise Technologies 4(6-88) (2017), 35-41
[7] Tittelboom, K. V. et al, Most recent advances in the field of self-healing cementitious materials, 4th International conference on Self-Healing Materials (ICSHM 2013), Belgium (2013), 406-413
[8] Krivenko, P., Physico-chemical bases of alkali-activated slag cement durability, Cement 11 (1990), 2-5
[9] National standard of Ukraine DSTU B V.2.7-181:2009 Alkaline cements. Specification
[10] Palacios, M., Puertas, F., Effect of shrinkage-reducing admixtures on the properties of alkali-activated slag mortars and pastes, Cem Concr Res 37 (2007) 691–702
[11] National standard of Ukraine DSTU B V.2.7-171:2008 (EN 934-2:2001. NEQ). Admixtures for concretes and mortars. General specification (that meets EN 934-2:2001 "Admixtures for concrete. mortar and grout – Part 2: Concrete admixtures – Definitions. requirements. Conformity, marking and labelling")
[12] National standard of Ukraine DSTU B. V.2.7-170:2008 Building materials. Concretes. Methods for determining of average density, humidity, water absorption, porosity and water resistance
[13] National standard of Ukraine DSTU B V.2.7-47-96 Building materials. Concretes. Method for determination of freeze/thaw resistance

SynerCrete'18 International Conference on Interdisciplinary Approaches
for Cement-based Materials and Structural Concrete
24-26 October 2018, Funchal, Madeira Island, Portugal

DURABILITY OF CALCIUM SULFOALUMINATE – PORTLAND CEMENT BLENDS

Gultekin Ozan Ucal [(1)], Mehmet Kemal Ardoga [(1)], Melike Sucu [(2)], Tughan Delibas [(2)], Ismail Ozgur Yaman [(1)]

(1) Middle East Technical University, Ankara, Turkey
(2) Cimsa Cement Co., Mersin, Turkey

Abstract
Calcium sulfoaluminate cement (CSAC) is a low-energy cement with lower carbon footprint than ordinary portland cement (PC), and it may be a better alternative in certain applications where rapid setting or shrinkage compensating properties are desired. In this study, performance of PC-CSAC blends were investigated by preparing eight sets of mortar and concrete blends with CSAC/PC ratios of 0/100, 5/95, 10/90, 20/80, 30/70, 40/60, 50/50, 100/0. Their alkali-silica reactivity was determined on mortar specimens, and drying shrinkage, compressive strength development, rapid chloride ion permeability, and porosity were investigated on concrete specimens. As a result of the experimental investigation, 100% CSAC showed properties superior to both 100% PC and blended mixtures in most of the determined properties. It was observed that although blending CSAC with PC increases the 1-Day strength of concrete, its later-age performance was adversely affected. It appeared that the blend with 30% CSAC had the lowest performance.

1. Introduction

Cement industry is responsible for around 5% of global humanmade CO_2 emissions [1]. Production of one ton of PC results in 0.87 ton of CO_2 emission on average [2]. PC production is also an energy-intensive process, with PC clinker consuming around 3.8 GJ/t of energy [3].
Main phases in calcium sulfoaluminate cement (CSAC) clinker are tetracalcium trialuminate sulfate ($C_4A_3\$$) and belite (C_2S), and principal hydration product is ettringite, which results in a relatively low pH final product due to the absence of calcium hydroxide [4]. CSAC can be produced by calcination of limestone, clay, bauxite and gypsum [4,5]. Due to a reduction in

production temperature from 1450 ^{o}C to 1250 ^{o}C and lower limestone content in raw mixture, ~1 GJ/t of energy saving in clinker production, and 25-35% lower CO_2 emission would be achievable by utilizing CSAC instead of PC [6].
Past studies had shown that blending CSAC with PC may increase the hardening rate [7], early strength [8], and reduce drying shrinkage [8,9], relative to using PC only. This study aims to contribute to the literature by investigating several performance characteristics of various CSAC/PC blends in mortar and concrete.

2. Experimental Program

This was an experimental study that investigated the effects of CSAC content in CSAC/PC blended mortar and concrete on several performance characteristics, by examining the results of 8 different mixtures containing CSAC/PC ratios of 0/100, 5/95, 10/90, 20/80, 30/70, 40/60, 50/50, 100/0. For ease of display, each mixture will be denoted with its CSAC/cementitious material ratio in the following sections.
For concrete batches, cement dosage of 400 kg/m^3 was selected and consistency was kept constant by changing water content to attain a slump of 21.5±1.5 cm.

2.1 Materials

Commercially available CSAC and CEM I/42.5R (PC) were used in this study. The chemical composition and the compound composition of the cements are provided in Tab.1 and 2. Properties of 0-4mm limestone fine aggregate (FA), 5-12mm limestone coarse aggregate (CA1), and 12-25mm limestone coarse aggregate (CA2) are shown in Tab. 3. 810 kg/m^3 of FA, 405 kg/m^3 of CA1, and 405 kg/m^3 of CA2 were used in all batches.

Table 1: Chemical composition of cements

Cement	SiO_2	Al_2O_3	Fe_2O_3	CaO	MgO	K_2O	Na_2O	SO_3	LOI	Cr_2O_3	Mn_2O_3
CSAC	7.53	27.51	0.73	39.06	2.39	0.44	0.8	19.62	0.76	0.06	0.19
PC	19.17	5.2	2.606	63.3	2.4	0.84	0.29	3.2	0.0292	0.06	3.28

Table 2: Compound composition of CSAC

$C_4A_3\$$		C_2S	C$	MgO
Orthorhombic	Cubic			
44.3	11.9	22.8	19.8	1.1

Table 3: Properties of aggregates

	Fine Aggregate	Coarse Aggregate	
		(5-12 mm)	(12-25 mm)
Specific gravity (SSD)	2.67	2.69	2.71
Absorption capacity (%)	1.2	0.3	0.2
Moisture content (%)	0.2	0.2	0.2

Reactive fine aggregate complying with ASTM C1260 grading requirements was used to determine the alkali-silica reactivity of mortar mixtures [10].

2.2 Methods Employed during the Experimental Investigation

Alkali-silica reactivity of mortar mixtures was determined in accordance with ASTM C1260 [10] by using three 25x25x285 mm mortar bars for each mixture.

To observe the effect of CSAC content on drying shrinkage, 75x75x320 mm concrete prisms were allowed to cure at 100% RH for 30 days, then stored at 35+-5% RH for the next 28 days unrestricted. Length of each prism was measured initially, at the end of curing, and 28 days after the curing. The average reading of three prisms was reported as the result for each mixture.

To monitor compressive strength development, 100x200 mm concrete cylinder specimens were tested at 1, 3, 7, and 28 days in accordance with ASTM C39 [11]. The average reading of three cylinders was reported as the result for each mixture.

Rapid chloride permeability test was employed to determine the ion permeability of specimens [12]. 28 and 90 days conductivity values were measured by using four 100x50 mm concrete disc specimens for each test.

Permeable porosity was calculated by using three 100x50 mm concrete disc specimens in accordance with ASTM C642 [13], except only cold water-saturated and immersed masses were used to determine apparent density.

3. Results and Discussion

Slump, water-to-cement ratio, air content, and fresh density values of concrete mixtures are shown in Tab. 4. Rapid setting property of CSAC started affecting workability of concrete after 20% CSAC. Therefore, use of set retarder admixture is advised with CSAC replacement ratios over 20%.

3.1 Drying shrinkage

Specimen length after demolding is recorded as initial length. Length change after 30 days of curing, after concrete prisms were taken out of the 100% RH condition is shown in Tab. 5. It was seen that addition of CSAC to concrete resulted in expansive behavior during curing, with maximum expansion recorded for 30% and 100% CSAC specimens. However, this situation was reversed upon drying. All blends except 5% CSAC undergone a larger final shrinkage than PC concrete (%0 CSAC). Only 100% CSAC concrete specimens were longer than their initial length after drying. This test confirmed that CSAC by itself shows shrinkage compensating properties, however, blending CSAC and PC actually increased drying shrinkage of concrete.

3.2 Alkali-silica reactivity

Length change of mortar specimens at the end of the 16^{th} day is shown in Tab. 6. It was observed that all blends expanded more than PC mortar, with an increasing trend up to 30% CSAC. Even though the aggregate was known to be reactive, expansion of 100% CSAC mortar was well below ASTM's safety limit of 0.1%, which was believed to be caused by the lower pH of the product upon hydration due to the absence of calcium hydroxide.

Table 4: Fresh concrete properties

	Slump (cm)	Water-to-cement ratio	Air content (%)	Density (kg/m^3)
0% CSAC	21.0	0.60	2.5	2318
5% CSAC	20.5	0.60	2.0	2341
10% CSAC	23.0	0.60	2.5	2337
20% CSAC	21.0	0.60	2.4	2313
30% CSAC	21.0	0.56	2.7	2297
40% CSAC	21.5	0.57	2.3	2327
50% CSAC	20.5	0.61	2.5	2293
100% CSAC	21.5	0.58	2.1	2298

Table 5: Length change of concrete prisms after curing and drying

	0% CSAC	5% CSAC	10% CSAC	20% CSAC	30% CSAC	40% CSAC	50% CSAC	100% CSAC
After 30 days curing (%)	-0.004	0.012	0.014	0.026	0.034	0.026	0.014	0.034
28 days of drying after 30 days of curing (%)	-0.030	-0.022	-0.038	-0.076	-0.126	-0.085	-0.040	0.008

Table 6: Length change of mortar specimens at the end of ASR test

	0% CSAC	5% CSAC	10% CSAC	20% CSAC	30% CSAC	40% CSAC	50% CSAC	100% CSAC
Length change (%)	0.67	0.74	0.81	1.12	1.25	1.16	0.85	0.04

3.3 Compressive strength

1, 3, 7, and 28 days compressive strength of concrete cylinder specimens are shown in Tab. 7 along with standard deviations for each set. Although CSAC addition enhanced the 1-Day strength of concrete at all ratios, only 40% and 100% CSAC specimens yielded higher compressive strength than PC specimens after 28 days. Overall, blending CSAC and PC did not improve the later-age compressive strength of concrete.

Table 7: 1, 3, 7, and 28 days compressive strength of concrete specimens

Strength (MPa)	0% CSAC	5% CSAC	10% CSAC	20% CSAC	30% CSAC	40% CSAC	50% CSAC	100% CSAC
1-Day	7.8[1.1]	10.5[0.5]	9.8[1.2]	13.7[0.3]	11.4[0.2]	9.6[0.6]	12.2[0.9]	29.4[2.5]
3-Day	20.9[1.6]	24.1[1.6]	23.7[0.6]	18.5[0.5]	18.6[0.6]	21.9[1.0]	17.8[0.3]	36.9[1.1]
7-Day	26.4[2.4]	29.9[1.4]	26.7[1.6]	23.0[1.6]	27.5[0.5]	30.3[0.3]	24.3[2.8]	43.3[0.2]
28-Day	40.5[0.6]	38.9[0.2]	34.6[1.2]	27.8[1.2]	31.3[1.6]	42.6[0.6]	34.8[4.1]	44.9[2.4]

* Numbers in brackets are the standard deviation of 6 specimens

3.4 Ion permeability

As an indication of chloride ion permeability, the electrical conductivity of concrete specimens was tested. Passing charge values at 28 and 90 days are shown in Tab. 8. It was observed that CSAC had a reduction effect on electrical conductivity when the replacement level is at least 40%. On the other hand, it was noted that 30% CSAC performed the worst at both ages. Thus, the replacement ratio is an important factor that affects ion permeability in CSAC-PC blends.

Table 8: Electrical conductivity of concrete specimens

Charges Passed (Coulomb)	**0% CSAC**	**5% CSAC**	**10% CSAC**	**20% CSAC**	**30% CSAC**	**40% CSAC**	**50% CSAC**	**100% CSAC**
28-Day	5741	6118	5732	5339	8138	4328	2644	4149
90-Day	4374	4831	4431	5257	5610	3776	1744	2687

3.5 Porosity

The permeable porosity of concrete specimens is shown in Tab. 9. While CSAC concrete had lower permeable porosity than the rest of the mixtures, blending PC and CSAC did not result in a notable trend on porosity relative to PC concrete.

Table 9: Permeable porosity of concrete specimens

	0% CSAC	**5% CSAC**	**10% CSAC**	**20% CSAC**	**30% CSAC**	**40% CSAC**	**50% CSAC**	**100% CSAC**
Permeable porosity (%)	15.4	16.8	17.8	18.3	15.1	14.7	17.9	10.4

4. Conclusion

At the end of this study, it was observed that CSAC appeared to be a superior alternative to PC consistently performing better than both PC and CSAC-PC blends. However, blending PC and CSAC did not improve the overall performance of the final product at any replacement amount. 30% replacement of PC with CSAC resulted in the worst performance. Hydration characteristics and microstructure will be further investigated, to reveal the underlying reasons for the behavioral change of the cement blends. Moreover, the following conclusions were drawn within the scope of this experimental program:

- Although CSAC-PC blends showed expansive behavior during curing, they experienced higher shrinkage after drying relative to PC.
- Blending CSAC with PC increases alkali-silica reactivity of mortar relative to PC.
- CSAC addition to PC increased the 1-Day compressive strength of concrete at all replacement ratios, however, later-age strength was negatively affected by blending, with only 40% CSAC having a higher 28-Day compressive strength than PC.
- Replacing at least 40% of PC with CSAC resulted in a decrease of concrete's electrical conductivity.

- Blending CSAC with PC did not yield a notable trend in permeable porosity of concrete.

References

[1] Hendriks, C.A. et al, Emission reduction of greenhouse gases from the cement industry, Proceedings of the 4th International Conference on Greenhouse Gas Control Technologies, Interlaken, Austria, IEA GHG R&D Programme, UK, (1998)
[2] Damtoft, J.S., Lukasik, J., Herfort, D., Sorrentino, D., Gartner, E.M., Sustainable development and climate change initiatives, Cem Concr Res 38 (2008), 115-127
[3] Tokyay, M., Cement and Concrete Mineral Admixtures, CRC Press, Boca Raton, (2000)
[4] Odler, I., Special Inorganic Cements, first ed., Taylor and Francis Group, New York, (2000)
[5] Chen, I.A., Juenger M.C.G., Incorporation of coal combustion residuals into calcium sulfoaluminate-belite cement clinkers, Cem Concr Compos 34 (2012), 893–902
[6] Hanein, T., Galvez-Martos, J.L., Bannerman, M.N., Carbon footprint of calcium sulfoaluminate clinker production, J Clean Prod 172 (2018), 2278-2287
[7] Trauchessec, R., Mechling, J.-M., Lecomte, A., Roux, A., Le Rolland, B., Hydration of ordinary portland cement and calcium sulfoaluminate cement blends, Cem Concr Compos 56 (2015), 106-114
[8] Gastaldi, D. et al, Hydraulic behaviour of calcium sulfoaluminate cement alone and in mixture with Portland cement, Proc. 13th Int. Congr. Chem. Cem., Spain (2011)
[9] Chaunsali, P., Mondal, P., Influence of calcium sulfoaluminate (CSA) cement content on expansion and hydration behavior of various ordinary portland cement- CSA blends, J Am Ceram Soc 98 (2015), 2617-2624
[10] ASTM C1260, Standard Test Method for Potential Alkali Reactivity of Aggregates (Mortar-Bar Method), American Society for Testing and Materials, USA (2014)
[11] ASTM C39, Standard Test Method for Compressive Strength of Cylindrical Concrete Specimens, American Society for Testing and Materials, USA (2017)
[12] ASTM C1202, Standard Test Method for Electrical Indication of Concrete's Ability to Resist Chloride Ion Penetration, American Society for Testing and Materials, USA (2017)
[13] ASTM C642, Standard Test Method for Density, Absorption, and Voids in Hardened Concrete, American Society for Testing and Materials, USA (2013)

SynerCrete'18 International Conference on Interdisciplinary Approaches
for Cement-based Materials and Structural Concrete
24-26 October 2018, Funchal, Madeira Island, Portugal

EARLY-AGE CRACKING TENDENCY OF ALKALI-ACTIVATED SLAG BINDERS COMPARED TO ORDINARY PORTLAND CEMENT

Farah Rifai [1, 2], Aveline Darquennes [3], Benoist Muzeau [1], Lavinia Stefan [4], Farid Benboudjema [2]

(1) SECR, CEA, Université Paris-Saclay, Gif-sur-Yvette, France
(2) LMT Cachan – ENS Cachan – Paris-Saclay University, Cachan, France
(3) INSA Rennes, 20 Avenue des Buttes de Coesmes, Rennes
(4) Orano, NWM, Technical Department, Paris La Défense, France

Abstract
Alkali-activated binders are increasingly used in civil engineering for different structural applications. Their thermo-chemo-mechanical behaviour (activation process, hydration reactions and mechanical properties' evolution) is investigated in the literature. However, few studies addressing their cracking tendency can be found. This paper focuses on the cracking risks induced by thermal and delayed strains' restriction, at materials' early age. First, the results of an experimental campaign comparing the early-age behaviour of an alkali-activated slag mortar to that of an OPC based mortar are discussed. Second, a simplified approach allowing comparing the cracking tendency of both materials is proposed. The alkali-activated mortar undergoes autogenous shrinkage strains higher then OPC mortar and showing an increase even at long term. However, its basic creep strains are more important than OPC mortar, tested in the same conditions. This implies a higher capacity of stress relaxation for the alkali-activated slag mortar. Regarding the evolution of mechanical properties, Young modulus and tensile strengths of the alkali-activated mortar are lower of those of OPC based mortar at all ages. A simplified cracking index comparison applied at this stage of study shows comparable cracking risks of both materials at 7 days, higher risks for alkali-activated slag mortar at 28 days.

1. Introduction

Ground granulated blast furnace slag (GGBFS) is a by-product of steel manufacturing, used as an alkali-activated hydraulic binder. The substitution of Ordinary Portland Cement (OPC)

binders by this type of material represents essentially an ecological advantage due to the reduction in CO2 emissions. Additionally, these materials constitute relevant alternative of OPC binders in some specific industrial applications [1]. The advancement of Hydration reactions and the evolution of micro-structural properties of alkali-activated slag materials have been extensively studied in the literature. A large dependency both on the chemical and physical properties of the activated GGBFS, and the type and concentration of the alkaline activator used can be observed [2], [3]. Additionally, high autogenous shrinkage was demonstrated comparing to OPC [4], [5]. Nevertheless, few studies have addressed the creep behaviour of this type of binders [6]. Thus cracking tendency, related to the eventual restriction of the volumetric changes of the hydraulic binders (especially at early-ages when these changes are the most important), needs to be investigated. This is essential in order to study the durability of any structural application.

2. Experimental campaign

The experimental comparison presented here covers hydration heat release, delayed strains' evolution and mechanical properties' (mechanical strengths and Young's modulus) evolution of the mortars. The described experiments and measurements are conducted on samples kept in autogenous conditions, in a controlled room at 23±1ºC.
The hydration heat determined in the same conditions allows comparing cracking tendency related to self-restriction of thermal strains in massive structures. A higher temperature gradient between the core and the surface leads to higher cracking risks. Autogenous shrinkage strains are considered as driving factor for cracking in restrained conditions, whereas basic creep is related to stress relaxation and thus decreasing cracking risks). Finally, the mechanical properties allow to evaluate the forces generated in the binders in restrained conditions and then to determine the subsequent cracking risks.

2.1 Materials

The tested hydraulic binders are prepared with the same water to binder (w/b) and sand to binder (s/b) ratios of 0.5 and 2 respectively. The alkali-activated mortar consists of a ground granulated blast furnace slag (GGBFS) – LA – activated with NaOH solution (2.5 M). 0.3% of setting retarder by mass of slag are added. Ordinary Portland Cement (OPC) mortar – SR0 – consists of a sulphates free formulation (CEM I 52.5 N-SR0 CE PM-CP2 NF). The choice of the latter OPC-based mortar is based on the relatively low hydration heat. Siliceous fine aggregate sand (0.1/1.2) is used.

2.1 Early-age hydration heat release

An isothermal micro-calorimetric test is performed using a "Tam Air Isothermal Calorimeter" with a precision of 20 μW at 22°C. The reference samples used for heat measurements consist of sand and distilled water. Mix proportions are calculated to have the same heat capacity of the binders.
The results obtained for both binders are shown in Fig.1 and Fig.2. The alkali-activated slag mortar presents shorter induction period implying faster formation of hydration products with respect to OPC-based mortar. This affects the advancement of hydration reactions, as the larger amount of hydration products formed can slow down water diffusion and therefore the

hydration process of anhydrous grains. This explains the earlier settlement of reactions heat flux of alkali-activated slag mortars.

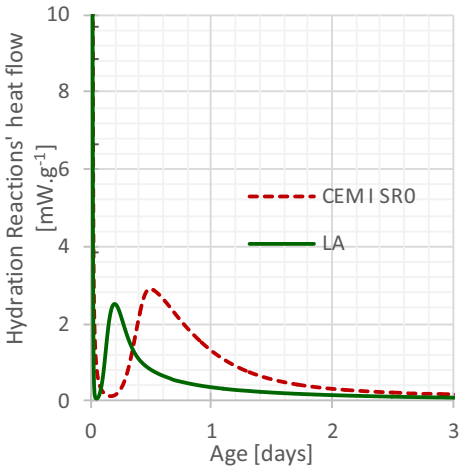

Figure 1: Comparison of hydration reactions' heat flow of studied mortars

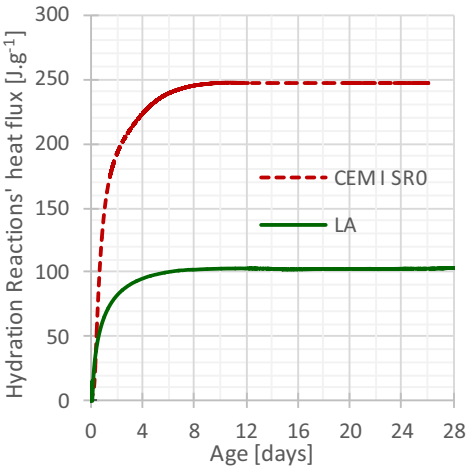

Figure 2: Comparison of hydration reactions' heat flux of studied mortars

Concerning the amount of heat released during the hydration process, the alkali-activated slag mortar show an important advantage with respect to OPC-based mortar. The total amount of heat measured at 28 days is around 100 and 250 $J.g^{-1}$ respectively. The lower amount of heat implies lower temperature gradient in massive structures and thus lower cracking tendency due to thermal self-restriction.

2.2 Time evolution of mechanical properties

Three-point flexural test are performed according to NF-EN-196-1 (2006), on three different 4x4x16 cm specimens, in order to compare the binders' tensile strength at 3, 7 and 28 days. Additionally, compression tests are conducted according to NF-EN-1015-11 (2000), on three different 11x22 cm cylindrical samples, at 3, 7 and 28 days. Three extensometers fixed to the samples allow the measurement of compressive strains in the elastic phase and the subsequent calculation of the binders' static Young modulus. Results are illustrated in Fig. 3 and Fig.4.

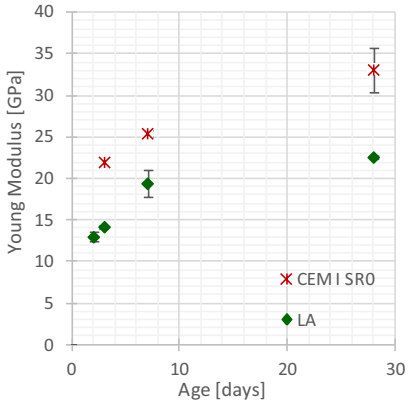

Figure 3: Comparison of the evolution of Young modulus of studied mortars

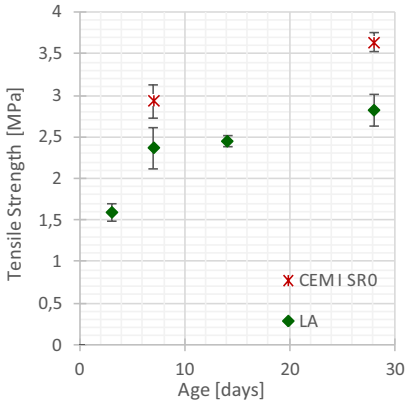

Figure 4: Comparison of the evolution of tensile strengths of studied mortars

OPC-based mortar shows higher stiffness and strength than alkali-activated slag mortar at all tested ages. Even though the lower stiffness represents an advantage with respect to the value of restriction-generated stress, the lower tensile strength of alkali-activated slag mortar can indicate higher cracking tendency of the material.

2.3 Time evolution of delayed strains

The autogenous shrinkage strains of tested mortars are continuously measured on three different 4x4x16 cm specimens, using linear variable differential transformer (LVDT) sensors. The basic creep is determined under compressive stress. 7x7x28 cm specimens kept in autogenous conditions. Two samples are loaded, at the age of 7 and 28 days, at 30% of their compressive strength at the respective ages, during 30 days. Both delayed strain measurements are performed in the controlled room at 23±1ºC.

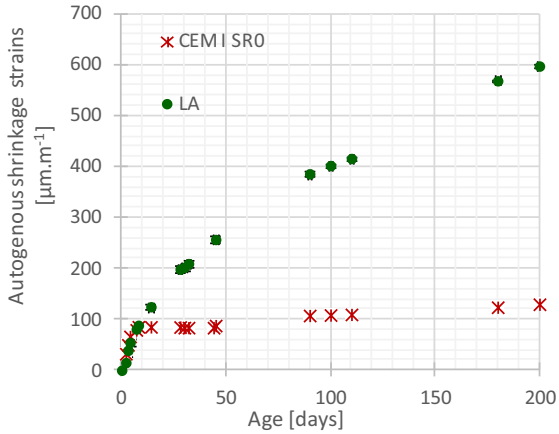

Figure 5: Comparison of autogenous shrinkage strains' measurements of studied mortars

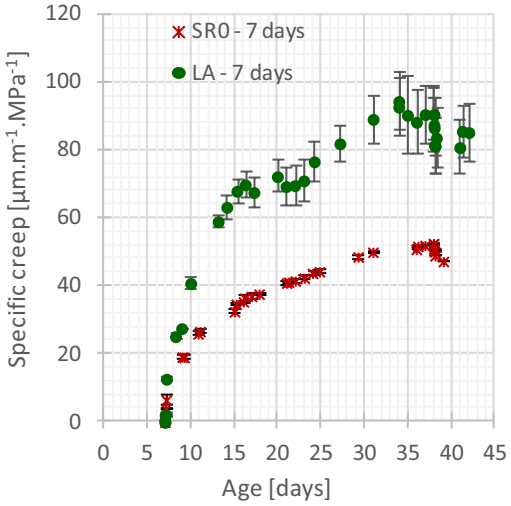

Figure 6: Comparison of creep compliance of studied mortars at 7 days (value of creep strains by MPa compressive force)

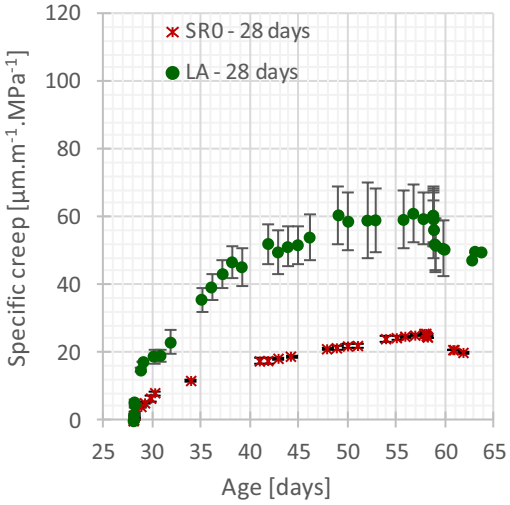

Figure 7: Comparison of creep compliance of studied mortars at 28 days (value of creep strains by MPa compressive force)

The mean values of measurements of autogenous shrinkage are illustrated in Fig.5. Similar behaviour can be detected at early-age for both mortars (up to 14 days of hydration).

Afterward, OPC-based mortar show stabilization in the shrinkage strains while alkali-activated slag mortar continues to shrink significantly. This was also observed in the literature in the case of drying shrinkage and is still being investigated [5], [7].
Specific creep is shown in Fig.6 and Fig.7 instead of basic creep strains, for the specimens loaded at 7 and 28 days respectively. It consists of basic creep strains (by deducing autogenous shrinkage and elastic strains from total measured strains, then dividing by the applied compressive load). The results show significantly higher creep capacity for the alkali-activated slag mortar, at both ages. This could be explained, by the higher amount of C-S-H forming the alkali-activated slag systems especially that the long term part of basic creep is usually explained by the mechanical sliding of C-S-H [8]. The decrease in creep capacity with the advancement of hydration (with time) is observed for the alkali-activated slag as well as for OPC-based mortar.

3. Evaluation of early-age cracking tendency (CI)

Based on the experimental results discussed in the previous section, a cracking index approach is applied to compare the cracking tendency of the binders. It considers a fully restrained configuration with constant materials' properties [9]. The thermal strains are not taken into account.
The restriction is expressed in terms of elastic $\boldsymbol{\varepsilon^{e}}(t)$ [µm.m^{-1}], autogenous shrinkage $\boldsymbol{\varepsilon^{sh}}(t)$ [µm.m^{-1}] and basic creep $\boldsymbol{\varepsilon^{bc}}(t)$ [µm.m^{-1}] strains as in Eq. (1).

$$\boldsymbol{\varepsilon}(t) = \boldsymbol{\varepsilon^{e}}(t) + \boldsymbol{\varepsilon^{sh}}(t) + \boldsymbol{\varepsilon^{bc}}(t) = 0 \quad (1)$$

Where $\boldsymbol{\varepsilon}(t)$ [µm.m^{-1}].is the total strain tensor at the age t [days]. By introducing the creep coefficient ϕ defined as in Eq. (2), in 1D:

$$\phi\,(t) = \frac{\varepsilon^{bc}(t)}{\varepsilon^{e}(t)} \quad (2)$$

The relationship between elastic and shrinkage strains reads Eq. (3):

$$\varepsilon^{e}(t) = \frac{-\,\varepsilon^{sh}(t)}{1+\phi\,(t)} \quad (3)$$

Applying Hooke Law in 1D, Eq. (4) can be obtained:

$$\sigma(t) = -\,1e^{-3} \times E(t) \times \varepsilon^{e}(t) = \frac{E(t) \times \varepsilon^{sh}(t)}{1+\phi\,(t)} \quad (4)$$

Where $\sigma(t)$ [MPa] is the generated stress tensor and $E(t)$ [GPa] the material's Young modulus. The cracking index $CI\,(t)$ comparing the generated tensile stress to the tensile strength f_t [MPa] of the material can then be expressed as in Eq. (5):

$$CI\,(t) = \frac{\sigma(t)}{f_t} = \frac{E(t) \times \varepsilon^{sh}(t)}{f_t \times (1+\phi\,(t))} \quad (5)$$

The results of calculations are reported in Tab.1, where the creep coefficient and the cracking index are exposed (creep coefficient is calculated according to creep measurements at 7 days). They show lower cracking tendency of alkali-activated slag mortar at early-age (7days), higher tendency at later ages (28 days). The high autogenous shrinkage of alkali-activated material is responsible of these observations.

Table 1: Comparison of cracking index of studied mortars at 7 and 28 days

	Age [days]	$\phi(t)$ (-)	$CI(t)$ (MPa)
LA r	7	1.02	0.33
	28	1.45	0.65
CEM I SR0	7	0.57	0.44
	28	0.81	0.43

4. Conclusions and perspectives

The study presented here discussed essentially an experimental comparison of early-age behaviour between an alkali-activated slag mortar and an OPC-based mortar, including the compressive basic creep strains. The alkali-activated material showed lower hydration heat, fast evolution of the system at early ages and quick settlement of mechanical properties. However, the autogenous shrinkage strains continue to grow even at the long term. The creep capacity of OPC-based mortar is shown to be lower than alkali-activated slag mortar. At early-ages, the latter binder seems to be subjected to lower cracking the risks. At later ages, the high autogenous shrinkage strains increase these risks despite the material's great creep capacity.

Acknowledgments
The authors would like to thank Miss Ginger El Tabbal for contributing in the experimental campaign during her Master Research final project.

References

[1] Bai, Y., Collier, N., Milestone, N. B., and Yang, C. H., The potential for using slags activated with near neutral salts as immobilisation matrices for nuclear wastes containing reactive metals, J. Nuclear Materials 413 (2011), 647-654.
[2] Wang, S., Scrivener, K., and Pratt, P, Factors affecting the strength of alkali-activated slag, Cem Concr Res 24 (1994), 1033-1043.
[3] Fernández-jiménez, A., Palomo, J G., Puertas, F., Alkali-activated slag mortars Mechanical strength behaviour, Cem Concr Res 29 (1999), 1313-1321.
[4] Cartwright, C., Rajabipour, F., Radli, A., Shrinkage Characteristics of Alkali-Activated Slag Cements, J. Mat. Civ. Eng. 27 (2014), 1-7.
[5] Melo Neto, A. A., Cincotto, M. A., Repette, W., Drying and autogenous shrinkage of pastes and mortars with activated slag cement, Cem Concr Res 38 (2008), 565-574.
[6] Collins, F.G., Sanjayan, J.G., Workability and mechanical properties of alkali activated slag concrete, Cem Concr Res 29 (1999), 455-458.
[7] Ye, H., Cartwright, C., Rajabipour, F., Radlińska, A., Understanding the drying shrinkage performance of alkali-activated slag mortars, Cem Concr Comp. 76 (2017), 13-24.
[8] Ulm, F., Acker, P., Le point sur le fluage et la recouvrance des bétons, Bulletin des Laboratoires des Ponts et Chaussées (1998), 73-82.
[9] Darquennes, A.; Benboudjema F., Behavior of activated ternary binders under autogenous condition, 2nd International Workshop on Durability and Sustainability of Concrete Structures, 6-7 June 2018, Izmailovo Congress Centre.

SynerCrete'18 International Conference on Interdisciplinary Approaches
for Cement-based Materials and Structural Concrete
24-26 October 2018, Funchal, Madeira Island, Portugal

EFFECT OF BAUXITE CONTENT AND FINENESS ON COMPRESSIVE STRENGTH OF VOLCANIC ASH-BASED GEOPOLYMER MORTARS

Léonel N. Tchadjié [(1)], Stephen O. Ekolu [(1)]

(1) Department of Civil Engineering Science, University of Johannesburg, South Africa

Abstract
The particle size, mineralogical and chemical composition of starting materials are important factors affecting their geopolymeric reactivity. This study investigated the effect of bauxite fineness and content on the early compressive strength of volcanic ash-based geopolymers. Geopolymer mortars were prepared using volcanic ash with or without 5 to 20 wt% bauxite as a partial replacement. The bauxite used in the study was of three fineness levels comprising 0, 5 and 29 % retained on 45 μm sieve. Bauxite provided the source of alumina while sodium silicate solution was used as the alkaline activator. The results revealed that incorporation of bauxite decreased the overall SiO_2/Al_2O_3 molar ratio in the geopolymer products. The 7-day compressive strength of 50 mm cube mortars varied between 30.3 and 44.5 MPa. A strength increase of up to 46.9 % was attained with 15 wt% bauxite content of fineness level 0 to 5 % retained on 45 μm sieve.

1. Introduction

Portland cement is a hydraulic binder mostly used in civil engineering construction. The production of this binder requires much energy and leads to significant release of CO_2 to the atmosphere. The production of one ton of Portland cement releases about 0.85 tons of CO_2. Up to 8% of the world's CO_2 emission is attributed to the cement industry [1]. To reduce the environmental footprint linked to this industry, the development of alternative sustainable, low-CO_2 construction materials is essential. Geopolymers are the foremost alternative binders currently being developed with a view of promoting environmental benefits in the construction industry [2]. They offer attractive possibilities for commercial applications due to their impressive properties such as fast hardening, high early compressive strengths, high acid resistance, long-term durability and low cost [3]. Also, the optimal production of these

materials requires less energy, reducing the CO_2 resulting from Portland cement production by 80% [2]. According to previous works, the properties of geopolymers are affected by several factors such as the nature of starting materials including their mineralogical and chemical composition, the amorphous content, particle size, curing temperature, composition of alkaline solution and the liquid to solid ratio [4, 5].

In recent years, there has been a growing trend to use raw materials of volcanic origin in geopolymer synthesis, due to their abundant availability in some regions. Volcanic scoria are igneous rock deposits formed during volcanic eruptions and are widely available in various regions such as in the Rift valley region of East Africa, Cameroon in West Africa, etc. [6–8]. These materials are generally of low cost and of low environmental impact. However, geopolymers obtained from volcanic scoria exhibit relatively long setting times, high shrinkage, efflorescence and low compressive strength [9]. This characteristically low reactivity of these materials is related to their low amount of alumina (Al_2O_3) and low amorphous phase content [10]. It is well-known that availability of Al_2O_3 significantly affects the properties of geopolymers. Greater availability of Al_2O_3 during the reaction influences the gel homogeneity, contributing to the formation of a more homogeneous gel and better strength development [11]. Previous work has shown that bauxite can be used as a source of Al_2O_3 to modify the SiO_2/Al_2O_3 ratio in the raw material, during geopolymer synthesis [12, 13] However, bauxite in its natural state tends to exhibit low geopolymeric reactivity. For instance, Djobo et al. [12] investigated the effects of partial replacement of volcanic ash by 10 to 30 wt% bauxite. They found that bauxite addition of up to 10 wt% reduced the initial setting time, lowered the efflorescence and led to a 5 % increase in the 28-day compressive strength of paste specimens. Further increase of bauxite replacement beyond 10 % was found to be detrimental to compressive strength. As such, enhancing the reactivity of bauxite before using it as a source of Al_2O_3 in geopolymerization should be of interest. This purpose can be achieved by employing various methods such as mechanical grinding, thermal treatment, physical separation, and chemical activation [4], of which mechanical activation by grinding is the most commonly employed technique [14].

The primary objective of this study was to determine the effect of bauxite fineness and content on the early compressive strength of volcanic ash-based geopolymers. Different levels of bauxite fineness were prepared by grinding the material in a ball mill.

2. Experimental details

2.1 Materials

Volcanic ash (VA) was used as the aluminosilicate raw material while bauxite (BX) was used to increase the availability of Al_2O_3 during geopolymer synthesis. BX and VA were oven-dried at 105°C for 24 h then crushed and ground. BX was ground in a ball mill to three fineness levels of 0, 5 and 29 % retained on 45 μm (No. 325) sieve. The same procedure was followed for VA. The chemical compositions of these raw materials are presented in Table 1. Silica sand of fineness modulus 2.5 was used as fine aggregate for preparing mortar samples. The alkaline activator solution used was a mixture of 12 M sodium hydroxide and sodium silicate solutions, prepared to achieve a silicate modulus (SiO_2/Na_2O) of 1.4. After mixing,

the activator solution was kept for at least 24 h to allow equilibration and the depolymerization of sodium silicate species. The sodium hydroxide solution was obtained by dissolving technical grade sodium hydroxide pellets in distilled water. The sodium silicate used was a commercial product obtained from PQ Silicas South Africa (pty) Ltd. Its physico-chemical characteristics were 29.05% SiO_2, 8.81% Na_2O, 62.14% H_2O, pH of 11.73, viscosity of 378 cP, specific gravity of 1.40 at 20°C, and SiO_2/Na_2O weight ratio of 3.3.

Table 1: Chemical composition of raw materials: VA-volcanic ash, BX-bauxite

Oxides (wt%)	**SiO_2**	**Al_2O_3**	**Fe_2O_3**	**CaO**	**TiO_2**	**MgO**	**K_2O**	**Na_2O**	**P_2O_5**	**LOI**
VA	45.94	15.58	13.68	9.00	2.86	7.10	1.43	3.75	0.60	-0.52
BX	2.31	39.56	28.09	0.07	6.68	0.23	-	-	0.23	21.60

2.2 Preparation of geopolymer mortars

To prepare the geopolymer mortars, bauxite was initially dry-mixed with VA for 3 mins using a laboratory mortar mixer, to homogenize the mixture. The alkaline activator solution was then gradually added and mixing continued for another 2 mins. Thereafter, silica sand was added and further mixing done for 3 mins. A liquid to powder ratio of 0.6 and sand to powder ratio of 2.25 were used in preparing all the mortar mixtures. Details of the mixtures are presented in Table 2. After mixing, the mortar slurry was rapidly poured into 50 × 50 × 50 mm moulds and tamped by hand in accordance with ASTM C 109. To prevent water evaporation, the freshly cast cubes in their moulds were sealed into polyethylene bags and cured at 80 °C for 7 days in an oven. Afterwards, the specimens were demoulded, cooled to room temperature and tested for compressive strength.

Table 2: Mix proportions of geopolymer mortars

Mix -ID	**BX fineness (retained on 45 µm sieve)**	**BX(wt%)**	**BX(g)**	**VA(g)**	**SiO_2/Al_2O_3**	**Liquid/ Powder**	**Silica Sand (g)**
Mix 1	0	0	0	310.0	5.0	0.6	698
		5	15.5	294.5	4.4	0.6	698
		10	31.0	279.0	3.9	0.6	698
		15	46.5	263.5	3.5	0.6	698
		20	62.0	248.0	3.1	0.6	698
Mix 2	5	0	0	310.0	5.0	0.6	698
		5	15.5	294.5	4.4	0.6	698
		10	31.0	279.0	3.9	0.6	698
		15	46.5	263.5	3.5	0.6	698
		20	62.0	248.0	3.1	0.6	698
Mix 3	29	0	0	310.0	5.0	0.6	698
		5	15.5	294.5	4.4	0.6	698
		10	31.0	279.0	3.9	0.6	698
		15	46.5	263.5	3.5	0.6	698
		20	62.0	248.0	3.1	0.6	698

3. Results and discussion

The 7-day compressive strength results of geopolymer mortars containing varied bauxite content with different levels of fineness, are shown in Figure 1. Also included in Figure 1 are error bars from data of replicate tests. It is evident that there was increase in compressive strength for all fineness levels, at 5 wt% bauxite content. At higher bauxite contents exceeding 5 wt%, the finer bauxite gave the highest compressive strength gain. The fineness levels of 0 and 5 % retained on 45 μm sieve, showed compressive strength increase for all bauxite contents of up to 20 wt%. In the converse, the low fineness of 29 % retained on 45 μm, had a negative effect leading to strength reduction at high bauxite contents exceeding 5 wt%. The highest compressive strength of 44.5 MPa was obtained at a bauxite fineness level of 0 % retained on 45 μm, with 15 wt% bauxite content. This value corresponds to 46.9 % strength increase over that of the control.

The incorporation of bauxite to VA changes the bulk chemical composition of the geopolymer products. The overall SiO_2/Al_2O_3 molar ratio varied from 5.0 in the control sample to 3.1 in the mixtures containing 20 wt% bauxite (Table 2). Furthermore, it is well known that the SiO_2/Al_2O_3 molar ratio has a major impact on strength development in geopolymers. Also, the particle size distribution of raw materials affects their geopolymeric reactivity. So, the observed increase in compressive strength due to incorporation of bauxite (Figure 1), can be attributed to reduction of the SiO_2/Al_2O_3 molar ratio in the system, thereby allowing greater dissolution of bauxite particles with increase in its fineness. These two factors induced greater geopolymerization and formation of a more compact microstructure. The observed results in the present study agree with those obtained by Tchakoute et al.[15] who claimed that addition of Al_2O_3 to VA promoted the dissolution of aluminosilicate species, thereby forming higher amounts of geopolymeric gel, in turn leading to increase in compressive strength of the geopolymers. The relatively lower compressive strength observed at the fineness of 29 % retained on 45 μm, is likely due to an increase in the proportion of less reactive bauxite particles in the system. It may be noted that the presence of excessively high amounts of Al_2O_3 species at early stages of the geopolymerization reaction, may hinder the dissolution of silica particles from VA, while favouring the participation of the Al_2O_3 in formation of the geopolymer network. This process leads to low strength development [16].

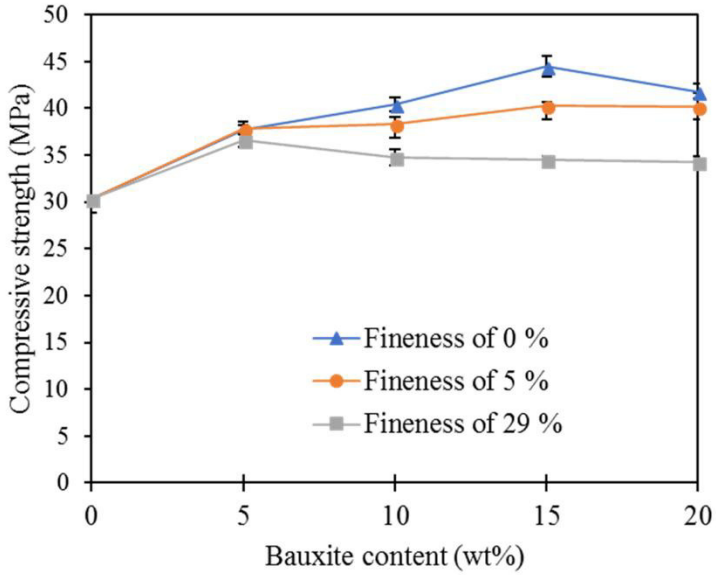

Figure 1: Compressive strengths of volcanic ash-based geopolymer mortars of various bauxite contents and fineness levels.

4. Conclusion

In this work, the effects of bauxite content and fineness on compressive strength of volcanic ash-based geopolymer mortars were studied. It has been observed that incorporation of bauxite to volcanic ash, leads to a significant enhancement in geopolymeric reactivity, depending on the level of bauxite fineness. As the fineness level of bauxite increased, greater compressive strength gain was observed up to a certain amount of bauxite content. The highest improvement in strength development was obtained with 10 to 15 wt% bauxite content at fineness levels of 0 to 5 % retained on 45 µm sieve. The combined effect of SiO_2/Al_2O_3 molar ratio and particle size influenced the observed strength development. Further studies involving characterization of the geopolymer samples using X-ray diffraction (XRD) and Fourier Transform Infrared Spectroscopy (FTIR) are being undertaken so as to explain the microstructural changes that occurred during geopolymerisation.

Acknowledgements
This paper is part of the PhD study of Leonel Noumbissie Tchadjie, conducted under the NRF-TWAS Doctoral Scholarship grant no. 99993. The candidate thanks the National Research Foundation (NRF) of South Africa for offering him this grant and study opportunity. The authors are grateful to Professor Paul Tematio of the Department of Earth Sciences of University of Dschang for providing bauxite samples.

References

[1] Mclellan, B. C., Williams, R. P., Lay, J., Van Riessen, A., and Corder, G. D., Costs and carbon emissions for geopolymer pastes in comparison to ordinary portland cement, J. Clean. Prod. 19 (2011), 1080–1090.
[2] Davidovits, J., Geopolymer Chemistry and Applications 3rd edition, France (2011).
[3] Provis, J. L., and Bernal, S. A., Geopolymers and related alkali-activated materials, Annu. Rev. Mater. Res. 44 (2014), 299–327.
[4] Tchadjie, L. N., and Ekolu, S. O., Enhancing the reactivity of aluminosilicate materials toward geopolymer synthesis, J. Mater. Sci. 53 (2018), 4709–4733.
[5] Naghizadeh, A., and Ekolu, S. O., Investigation of mixture factors influencing alkali-silica reaction in fly ash-based geopolymer mortars, International Conference on Advances in Construction Materials and Systems, India (2017), 395–400.
[6] Ekolu, S. O., Thomas, M. D. A., and Hooton, R. D., Studies on Ugandan volcanic ash and tuff, Proceedings of the First International Conference on Advances in Engineering and Technology, Uganda (2006), 75–83.
[7] Kamseu, E., Leonelli, C., Perera, D. S., Melo, U. C., and Lemougna, P. N., Investigation of volcanic ash based geopolymers as potential building materials, InterCeram Int. Ceram. Rev. 58 (2009), 136–140.
[8] Naghizadeh, A., and Ekolu, S. O., Pozzolanic materials and waste products for formulation of geopolymer cements in developing countries : a Review, Concr. Bet. 151 (2017), 22–31.
[9] Tchakoute, H. K., Elimbi, A., Yanne, E., and Djangang, C. N., Utilization of volcanic ashes for the production of geopolymers cured at ambient temperature, Cem. Concr. Compos. 38 (2013), 75–81.
[10] Lemougna, P. N., Melo, U. F. C., Delplancke, M., and Rahier, H., Influence of the chemical and mineralogical composition on the reactivity of volcanic ashes during alkali activation, Ceram. Int. 40 (2014), 811–820.
[11] Weng, L., Sagoe-Crentsil, K., Brown, T., and Song, S., Effects of aluminates on the formation of geopolymers, Mater. Sci. Eng. B 117 (2005), 163–168.
[12] Djobo, J. N. Y., Elimbi, A., Manga, J. D., and Li, I. B. D., Partial replacement of volcanic ash by bauxite and calcined oyster shell in the synthesis of volcanic ash-based geopolymers, Constr. Build. Mater. 113 (2016), 673–681.
[13] Martin, A., Pastor, J. Y., Palomo, A., and Fernández, A., Mechanical behaviour at high temperature of alkali-activated aluminosilicates (geopolymers), Constr. Build. Mater. 93 (2015), 1188–1196.
[14] Wei, B., Zhang, Y., and Bao, S., Preparation of geopolymers from vanadium tailings by mechanical activation, Constr. Build. Mater. 145 (2017), 236–242.
[15] Tchakoute, H. K., Elimbi, A., Mbey, J. A., Sabouang, C. J. N., and Njopwouo, D., The effect of adding alumina-oxide to metakaolin and volcanic ash on geopolymer products : A comparative study, Constr. Build. Mater. 35 (2012), 960–969.
[16] Hajimohammadi, A., Provis, J. L., and Van Deventer, J. S. J., Effect of alumina release rate on the mechanism of geopolymer gel formation, Chem. Mater. 22 (2010), 5199–5208.

SynerCrete'18 International Conference on Interdisciplinary Approaches
for Cement-based Materials and Structural Concrete
24-26 October 2018, Funchal, Madeira Island, Portugal

EFFECT OF COMPACTING PRESSURE AND CARBONATION DURATION ON CARBON DIOXIDE ACTIVATED BINDERS

Pedro Humbert [(1)], João Castro Gomes [(1)]

(1) University of Beira Interior, Covilhã, Portugal

Abstract
Alternative binders and hardening reactions are methods to reduce greenhouse gases emissions, energy and water consumption. Waste-based carbon dioxide activated binder represents a potential solution as an environmental friendly construction material. To achieve efficient mechanical properties and optimal mixture design, a preliminary comparison about the effect of compacting pressure and carbonation duration on carbon dioxide activated binders was studied. An electric arc furnace slag from the national steel industry in Portugal and a Portland cement CP-I were used as binders. This work shows the compressive strength development of a slag-based and Portland cement-based binders under different compacting pressures and carbonation durations. Compressive strength present stronger development due higher compacting pressures and longer carbonation duration however, its development ratio was decreasing after two hours under carbon dioxide atmosphere. The carbon dioxide activation has highly dependence on both studied factors, compacting pressure and carbonation duration, which enhance the compressive strength development.

1. Introduction

Europe has adopted the Circular Economy Package which aims to close the loop of product lifecycles by improving recycling and re-use efficiency supporting the sustainable development with advantages for the environment and the economy [1]. The steel industry has great role in economy but, produce a huge amount of waste, the main one is the steel slag which has an annual production worldwide around 130 million tons [2]. Construction industry already reuse the steel slag as aggregate on few construction purposes such as concrete, asphalt, road bases and surfaces [3]. However, the amount of steel slag disposed in landfills is not reducing overtime.

Solutions for reduce and eliminate wastes' landfills have been investigated worldwide [4]. Alternative binders such as geopolymers, alkali-activated and carbon dioxide activated, follow sustainable development and Circular Economy guidelines as these binders use mainly wastes as raw material, less water and energy on its production, and sometimes store carbon dioxide in its matrix [5,6]. Carbon dioxide activated binder is a construction material made by calcium and magnesium rich wastes mixed with water (10%) and activated under carbon dioxide atmosphere, besides of its environmental qualities, its mechanical properties evidence the Portland cement replacement potential for structural applications [7].
Carbon dioxide activated binder have been investigated by some researchers which studied its synthesis and properties [8], mechanical performance [9], pore structure [10] and flexural fracture [11] under specified conditions. This experimental program aims to improve the steel slag carbonation kinetics and efficiency by moulding the samples under different compacting pressures and carbonating the samples for different durations. The effect of the sample compactness on the compressive strength development and the compressive strength development rate will be analysed. Optimal condition was used with Portland cement for comparison purpose.

2. Experimental program

2.1 Materials and procedures

An electric arc furnace slag was received from the national steel industry at Maia and Aldeia de Paio Pires, Seixal, Portugal. A Portland cement CEM II/B-L 32.5 N was also used. The as-received slag was left to dry at 60°C for 24 hours in an oven then, crushed into a mal size using a crusher mill and finally, pulverised into powder using a ball mill. The slag powder was sieved through a sieve of 45μm and subjected to density and Blaine tests which showed a result of 3.7712 g/cm^3 and 529 m^2/kg respectively. Portland cement was also subjected to density and Blaine tests which showed a result of 2.977 g/cm^3 and 382 m^2/kg.
The sieved powder and the Portland cement were subjected to an energy dispersive spectroscopy (EDS) analysis to determine its chemical composition where evidenced that the steel slag is rich in calcium (CaO), iron (Fe_2O_3) and silica (SiO_2) with some other minor oxides on its composition, the Portland cement is also rich in calcium (CaO) and silica (SiO_2) with some other minor oxides. Density, Blaine number and chemical composition of both powders are shown in Tab. 1.

Table 1: Powders characterisation.

Material	Oxides						Density (g/cm^3)	Blaine number (m^2/kg)
	CaO	SiO2	Al2O3	MgO	SO3	Fe2O3		
Steel slag	30.21	14.18	12	5,58		29.51	3.771	529
OPC	62.2	12.31	3.08	1.27	4.33	2.42	2.977	382

Twenty-one steel slag cylindrical samples were moulded and tested under seven different conditions, three different compacting pressures and five different carbonation durations. Three Portland cement cylindrical samples were moulded and tested under the optimal condition. The samples were compacted with 10, 20 and 30 MPa of compacting pressure into

a mould of 20mm of diameter and 40mm of height with a water to solid ratio of 0.1. The samples were subjected to carbonation curing right after casting with a concentration of 100% of CO_2 inside the chamber with 0.5 bar of partial pressure. The carbon dioxide used had 99.9% of purity and was injected to the chamber for 2, 4, 8, 12 and 24 hours being replenished as it was being consumed by the samples. The chamber was inside an oven at 40°C of temperature. After curing, the samples were taken from the chamber to dry inside an oven for 20 hours at 40°C of temperature and then subjected to compressive strength test in a rate of 0.05 kN/second. Table 2 shows the different used carbonation conditions with their respective labels.

Table 2: Carbonation conditions.

Carbonation conditions	Identification and carbonation condition									
	ID	CC	ID	CC	ID	CC	ID	CC	ID	CC
Compacting pressure (MPa)	c1	10	c2	20	c3	30				
Duration (hours)	t1	2	t2	4	t3	8	t4	12	t5	24

EDS analysis was done to compare the carbon dioxide uptake between steel slag and Portland cement binders. Non-carbonated and carbonated powders from Portland cement and steel slag were analysed and had their atomic mass of carbon compared to measure the carbon dioxide uptake.

3. Results and discussion

Compressive strength results evidenced that compacting pressure and carbonation duration has strong influence on the carbon dioxide activated binder's compressive strength development. Compacting the sample with 30 MPa showed a compressive strength of 72.1 MPa, 58.1% higher than compacting with 10 MPa which achieved 45.6 MPa however, the compressive strength development between 20 to 30 MPa was only 1.98% higher showing that after 20 MPa of compacting pressure the gain in compressive strength is minimal. The compactness of the sample influences on the compressive strength development once the binder will have its porosity reduced as much pressure is applied during compaction however, after certain point is hard to reduce the porosity or there will be less water to diffuse the carbon dioxide through the binder.

Table 3: Compressive strength.

Carbonation parameters	Identification and compressive strength (MPa)									
	ID	CS	ID	CS	ID	CS	ID	CS	ID	CS
Compacting pressure	c1	45.6	c2	70.7	c3	72.1				
Duration	t1	26.7	t2	37.5	t3	55.8	t4	60.8	t5	72.1
Optimal conditions	os	72.1	opc	63.4						

The carbonation duration analysis showed that during the first two hours the compressive strength development rate was 13.35 MPa/hour reducing to 0.9 MPa/hour during the last

twelve hours. After eight hours of carbonation the carbon dioxide activated binder already achieved 55.8 MPa. Table 3 present all compressive strength results and the compressive strength development rate correlated with the carbonation duration.
The optimal condition was under 30MPa of compacting pressure and with 24 hours of carbonation. Under the same conditions the Portland cement showed 63.4MPa of compressive strength which was 12.07% lower than the steel slag compressive strength. This result evidence that the steel slag has higher reactivity under the carbon dioxide environment than the Portland cement.
The carbon dioxide uptake was calculated considering the atomic weights of the elements [12] and the carbon weight found by the EDS analysis on the Portland cement and steel slag powders before and after the carbonation curing. The carbonated samples were under the optimal conditions. The steel slag sample reached a carbon dioxide uptake of 6.89% while the Portland cement sample reached 6.34% which was 7.98% lower than the steel slag CO_2 uptake. Tab. 4 shows the carbon weight before and after carbonation and the carbon dioxide uptake of the carbonated samples.

Table 4: Carbon dioxide uptake.

Sample	Carbon weight (%)	CO2 uptake (%)
Steel slag	3.1	
Portland cement	6.3	
Os	4.98	6.89
Opc	8.03	6.34

4. Conclusions

This study has reported experimental results and analysis about the influence of compacting pressure and carbonation duration on cement-free steel slag carbon dioxide activated binders compressive strength development. The following conclusions can be drawn from this investigation:

- Compacting pressure up to 20 MPa has strong effect on compressive strength development of the carbon dioxide activated binders. Higher compacting pressure does not represent sensible compressive strength increase.
- The carbon dioxide activated binder continuously develops its compressive strength within time. However, the compressive strength development rate decrease overtime after eight hours the development is less than 1.5 MPa/hour.
- The steel slag CO_2 activated binder showed good potential to be used as Portland cement replacer for construction materials applications due its mechanical properties. Moreover, the binder has great role on the sustainable production, besides the industrial waste valorisation, this construction material stores steel slag and uptake up to 6.89% of carbon dioxide.
- Further investigation is necessary to develop proper applications and analyse the size effect of the carbonation on the inner part.

References

[1] European Commission, Press release - Closing the loop: Commission adopts ambitious new Circular Economy Package to boost competitiveness, create jobs and generate sustainable growth, NewEurope (2015), 13-15. http://neurope.eu/wires/closing-the-loop-commission-adopts-ambitious-new-circular-economy-package-to-boost-competitiveness-create-jobs-and-generate-sustainable-growth/.
[2] van Zomeren, A. et al, Changes in mineralogical and leaching properties of converter steel slag resulting from accelerated carbonation at low CO2pressure, Waste Manag. 31 (2011), 2236–2244
[3] Piatak, N.M. et al, Characteristics and environmental aspects of slag: A review, Applied Geochemistry 57 (2015), 236-266
[4] Kajaste, R. and Hurme, M., Cement industry greenhouse gas emissions - Management options and abatement cost, J. Clean. Prod. 112 (2016), 4041-4052
[5] Sedira, N. et al, A review on mineral waste for chemical-activated binders: mineralogical and chemical characteristics, Min. Sci. 24 (2017), 29-58
[6] Zhang, D. et al, Review on carbonation curing of cement-based materials, J. CO2 Util. 21 (2017), 119-131
[7] Humbert, P.S. et al, Cement-Free Binder Activated by Carbon Dioxide: Potential and Challenges, 3o Congr. Luso Bras. Mater. Constr. Sustentaveis, Portugal (2018)
[8] Das, S. et al, Synthesis and Properties of a Novel Structural Binder Utilizing the Chemistry of Iron Carbonation, ACS Appl. Mater. Interfaces. 6 (2014), 8295-8304
[9] Mo L. et al, Mechanical performance and microstructure of the calcium carbonate binders produced by carbonating steel slag paste under CO2 curing, Cem. Concr. Res. 88 (2016), 217-226
[10] Das, S. et al, Pore- and micro-structural characterization of a novel structural binder based on iron carbonation, Mater. Charact. 98 (2014), 168-179
[11] Das, S. et al, Flexural fracture response of a novel iron carbonate matrix - Glass fiber composite and its comparison to Portland cement-based composites, Constr. Build. Mater. 93 (2015), 360-370
[12] Meija, J. et al, Atomic weights of the elements 2013 (IUPAC Technical Report), Pure Appl. Chem. 88 (2016), 265-291

SynerCrete'18 International Conference on Interdisciplinary Approaches
for Cement-based Materials and Structural Concrete
24-26 October 2018, Funchal, Madeira Island, Portugal

EFFECT OF GREEN ACTIVATORS ON THE PROPERTIES OF ALKALI ACTIVATED MATERIALS: A REVIEW

Adeyemi Adesina [(1)]

(1) Concordia University, Montreal, Canada

Abstract
The most common types of activators used for alkali activated materials (AAMs) are sodium hydroxide and sodium silicate. These activators have been found to be corrosive, viscous, expensive, and with high embodied energy and carbon. In addition, the properties of these activators have made the large-scale applications of AAMs possible as a result of the special handling and side effects it has on the properties of the resulting AAM.

Therefore, this review explored the use of alternative green activator used for AAMs, and the effects it has on its properties. A green activator herein is classified as an activator that has a less embodied energy and carbon compared to sodium silicate and sodium hydroxide. This study shows the possibility of producing a greener AAM with enhanced strength and durability properties. In addition, it was observed that there's a considerable cost reduction with the use of the green activators compared to the convectional ones.

1. Introduction

The high emission of carbon dioxide due to production of ordinary Portland cement (OPC) has opened way for various sustainable initiatives that can be used to reduce these high emission. These initiatives vary from partial and total replacement of OPC, to use of alternative fuels and optimization of OPC's production processes. However, the one with the most promising possibility of reducing a significant amount of carbon dioxide are alkali activated materials (AAMs). Alkali activated materials creates an avenue for 100% replacement of OPC in concrete, and uses waste materials as one of the major components. AAMs are achieved by alkali activation of aluminosilicate precursors with an alkali source. Examples of aluminosilicate precursor used for AAMs are slag, fly ask, metakaolin, rice husk

ash, etc. The alkali activation results in dissolution of aluminate and silicate monomers from the precursor, and a gel which hardens is formed. The common types of alkali activators commonly used for AAMs eliminates the sustainable advantage of AAMs over OPC, as they are its major contributor of carbon dioxide.
The most commonly used activators used are sodium silicate and sodium hydroxide. These activators are mostly used due to its resulting high strength. However, these activators produce poor fresh and hardened properties that has limited the universal acceptance and large scale application of AAMs. The major poor properties ensued from the use of sodium silicate and sodium hydroxide are quick setting and high drying shrinkage. Quick setting of alkali activated slag (AAS) which is a type of AAM has been found to result in low workability and flowability of the AAM [12, 13]. In addition, these activators are expensive, corrosive, and are the highest contributor of embodied energy in AAM preventing the advantage of using AAM as binder in concrete [2,5].
As there exists no review in open literature that focuses on the use of green activators in AAMs, this review explores the use of activators that can be classified as green activators, and the effects they have on the resulting properties of the AAMs. AAMs used herein refers to different types of AAMs which use different types of aluminosilicate precursors. Where significant, the type of AAMs is mentioned. It is anticipated that this review will open a pathway for more application and research on the use of green activators.

2. Green activators

Activators classified as green in this article have a significant lower embodied carbon and energy compared to that of sodium silicate and sodium hydroxide. Also, these green activators are more user friendly (i.e. less corrosive), and cheaper. Some types of green activators are further explored, alongside with their effect on the properties of the resulting AAMs.

2.1 Sodium carbonate

Compared to sodium silicate and sodium hydroxide, sodium carbonate exists naturally in the environment, and can be extracted from sodium carbonate and trona mines [19]. Also, it can be obtained through a chemical procedure (i.e. Solvay) [18]. In addition, it is approximately 3 times cheaper than sodium silicate and sodium hydroxide [9].
However, activating aluminosilicate precursors with sodium carbonate results in lower early age strength compared to those activated with common activators (i.e. sodium silicate and sodium hydroxide). This lower early strength has been attributed to initial formation of sodium calcium carbonate which delays the activation reaction [4]. Sodium carbonate also results in lower drying shrinkage of AAM compared to those activated with sodium silicate.
AAMs activated with sodium carbonate shows a more practical set time compared to those activated with sodium silicate [4]. The extended set time has been attributed to the initial formation of calcium carbonate, which also results in lower early age strength as mentioned earlier. Also, sodium carbonate lower pH (i.e. 12.6) compared to that of sodium silicate (i.e. 13.4) and sodium hydroxide (i.e. 13.8) is responsible for the extended setting time. Wang et al [22] also attributed the lower early strength of slag activated with sodium carbonate to the activator's lower pH. Slag activated with sodium carbonate has been able to result in higher

strength at later ages (i.e. 28 days) which makes it a great alternative for sodium silicate and sodium hydroxide where high early strength is not required [4]. The later higher strength has been attributed to the formation of carbonated compounds which results in a more densified microstructure [4]. Other studies also recorded late higher strength of up to 60MPa at 28 days when sodium carbonate was used to activate slag.

2.2 Magnesium oxide

Slag activated by 10 - 20% of magnesium oxide has been found to have strength about four times that of those activated with calcium hydroxide [16]. However, between 5 – 10% magnesium oxide, the 28 days of the resulting AAM was found to be lower than those activated with calcium hydroxide. Use of magnesium oxide to activate slag has been found to reduce shrinkage and cracking capability of the resulting AAM [16].

Despite the great potential of using magnesium oxide as a green alternative activator for AAMs, it should be noted that the chemical composition of magnesium oxide varies considerably from different locations [1]. Birchal et al. [1] and Mo et al. [11] recorded variations in AAMs properties when different types of magnesium oxide was used. Therefore, proper initial tests should be carried out to determine the optimum proportions for a specific magnesium oxide before a large-scale production is carried out

Though high energy is consumed, and carbon dioxide is emitted during the manufacture of magnesium oxide, the very low amount (i.e. about 10% the mass of the binder) required to activate AAMs still makes the resulting AAM more sustainable compared to OPC [22].

2.3 Sodium sulphate

The common activators used for AAMs (i.e. sodium silicate and sodium hydroxide) cannot be mined directly from the environment, therefore they required several industrial processes that are energy intensive and emit large amount of carbon dioxide into the environment. On the other hand, sodium sulphate can be obtained from natural resources, which eliminates the negative impact production of the common activators have on the environment [14]. Similar to sodium carbonate, AAMs activated with sodium sulphate show low early age strength [23]. This is due to the low alkalinity of the sodium sulphate [14]. Increasing the sodium oxide equivalent of sodium sulphate from 1 to 3% resulted in a significant increase in the early age strength of AAMs [14, 15]. However, at 28 days, there's no significance difference between samples activated with 1% and 3% sodium oxide equivalent. Using 1% sodium oxide equivalent to activate slag, Douglas and Brandstetr [3] obtained a 24 hours strength similar to that of OPC

AAMs activated with sodium sulphate exhibited longer setting times compared to those activated with sodium silicate and sodium hydroxide. In addition, AAMs activated with sodium sulphate show excellent workability similar to that of OPC [14], and higher fire resistance [15]. This shows to use sodium sulphate as activator for large scale AAMs applications. However, AAMs activated with sodium sulphate exhibited higher drying shrinkage compared to that of OPC, but lower than those activated with sodium hydroxide and sodium silicate [14]. Use of shrinkage reducing admixtures (SRA), OPC, hydrated lime, or fly ash can be used to control the drying shrinkage in AAMs activated with sodium sulphate. A reduction of 43.64% and 58.73% in drying shrinkage was recorded when hydrated lime and OPC was used respectively [14]. Sodium sulphate is also more economical in terms of cost and availability compared to the common activators

2.4 Calcium hydroxide

Calcium hydroxide has a lower alkalinity compared to that of sodium silicate, sodium hydroxide and sodium carbonate. This lower pH has resulted to lower strength gain of AAMs activated with calcium hydroxide due to slower dissolution of silicate and aluminate monomers from aluminosilicate precursors [8, 24]. When calcium hydroxide is used as AAMs activator, an optimum activator level has to be determined as this type of activators does not behave like other activators where increasing the concentration leads to higher strength. This is as a result of the low solubility of calcium hydroxide in water, which results in an insignificant change in alkalinity when higher amount is dissolved in water as observed in Figure 1 [10]. These results are also similar to Jeonung et al. [7] study where they observed no significant gain in strength when the concentration of the calcium hydroxide was increased

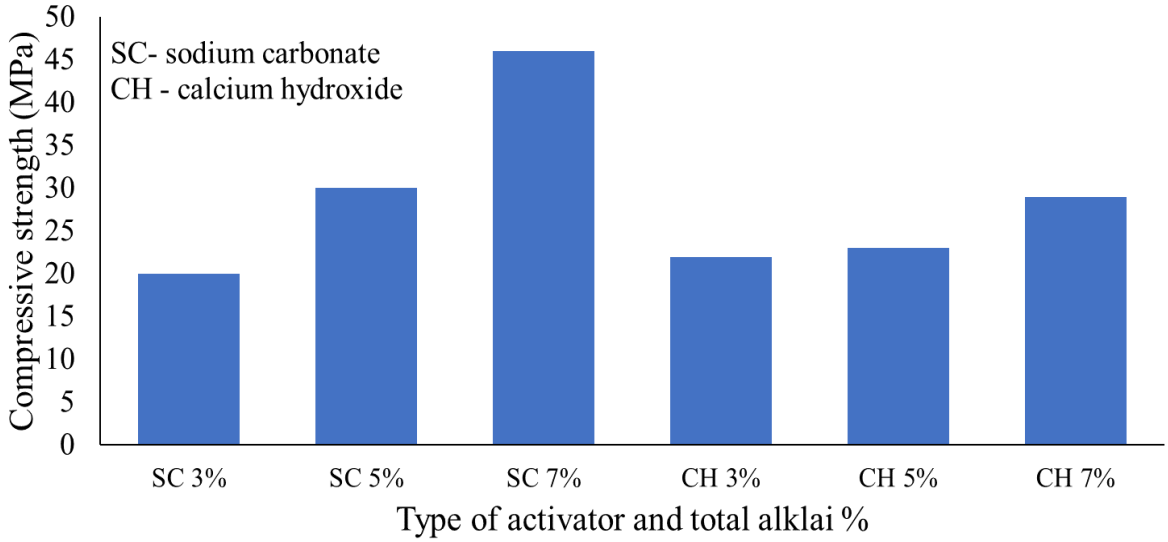

Figure 1: 28 days compressive strength of different types of activator and total alkali percentage (data from [10])

Calcium hydroxide is a more user-friendly activator as it safe to handle, less expensive, and readily available for purchase in household stores. Calcium hydroxide is approximately 6 times cheaper than sodium hydroxide [6]. Use of sodium sulphate with calcium hydroxide as AAM activator has been reported to improve the strength of the AAM significantly [17]. The improved strength has been attributed to the formation of ettringite which densify the microstructure, thereby leading to higher strength [17]. A study carried out by Jeong et al. [7] showed that the early strength of AAMs activated with calcium hydroxide can be improved by addition of supplementary activators. The supplementary activators used were gypsum, sodium hydroxide, sodium carbonate and sodium sulphate. However, the later age strength was not improved with the addition of supplementary activators. Yang et al [24] used longer curing duration to improve the later age strength of AAM which employs slag as the aluminosilicate precursor. The improved later age strength can be attributed to a more stabilized calcium silicate hydrate

3. Conclusions

Based on the short review on the effect of green activators on the properties of AAMs, the following conclusion can be made;

- Use of sodium hydroxide and sodium silicate as activators for AAMs is not a sustainable option, as these common activators cannot be obtained from natural resources, and their production process is energy intensive, and emits carbon dioxide to the environment
- In cases where high early strength is not required, activating AAMs with sodium carbonate is a greener alternative, as it results in similar strength at later ages compared to those activated with sodium silicate and sodium hydroxide
- Binary and ternary application of green activators will result in practical early age and later age strength. In addition, the combination of the green activators at right percentages will help to improve the overall durability of AAMs
- More research in the field of green activators is still required as very limited research is available, majority of all the studies in AAMs employs the use of sodium silicate and sodium hydroxide as activators

References

[1] Birchal, V. et al effect of magnesite calcination conditions on magnesia hydration Miner Eng, (2000), 1629-1633
[2] Deventer, J.S.J. et al Chemical research and climate change as drivers in the commercial adoption of alkali activated materials Waste Biomass Valoriz., (2010), 145-155
[3] Douglas E, Brandstetr J. A preliminary study on the alkali activation of ground granulated blast-furnace slag. Cem Concr Res, (1990), 746–56
[4] Fernández-Jiménez, A. et al. Alkali-activated slag mortars: mechanical strength behavior Cem. Concr. Res., (1999), 1313-1321
[5] Habert, G et al. An environmental evaluation of geopolymer based concrete production: reviewing current research trends J. Clean. Prod., (2011), 1229-1238
[6] ICIS Indicative Chemical Prices A–Z (2015) http://www.icis.com/chemicals/channel-info-chemicals-a-z
[7] Jeong, Y. et al Influence of four additional activators on hydrated-lime [Ca(OH)2] activated ground granulated blast-furnace slag Cement and Concrete Composites (2016) 1-10
[8] Kim, M. S. et al Use of CaO as an activator for producing a price-competitive non-cement structural binder using ground granulated blast furnace slag Cem. Concr. Res., (2013), 208-214
[9] Kostick D. S. Soda Ash: Statistics and Information U.S. Geological Survey (2013)
[10] Maghsoodloorad, H. et al Recycling phosphorus slag as a precursor for alkali-activated binder; Impact of type and dosage of activator, Journal Ceramics-Silikáty, (2014), 227 - 236
[11] Mo, L et al. Effects of calcination condition on expansion property of MgO-type expansive agent used in cement-based materials Cem Concr Res, (2010), 437-446

[12] Pacheco-Torgal, F. et al Alkali-activated binders: a review. Part 2. About materials and binders manufacture Constr Build Mater, (2008), 1315-1322
[13] Palacios, M and Puertas,F Effect of superplasticizer and shrinkage reducing admixtures on alkali-activated slag pastes and mortars, Cem. Concr. Res. (2005), 1358-1367
[14] Rashad, A. M. Influence of different additives on the properties of sodium sulfate activated slag Const and Buil Mat, (2015), 379–389
[15] Rashad, A. M. et al Chemical and mechanical stability of sodium sulfate activated slag after exposure to elevated temperature. Cem Concr Res, (2012), 333–43.
[16] Shen W. et al Magnesia modification of alkali-activated slag fly ash cement. J Wuhan Univ Technol Sci Ed, (2011), 121–5.
[17] Shi, C and Day, R Chemical activation of lime-slag blends V.M. Malhotra (Ed.), Fly Ash, Silica Fume, Slag, and Natural Pozzolans in Concrete – Proceedings, Fifth International Conference, vols. 1 and 2, American Concrete Institute, Detroit (1995), pp. 1165-1177
[18] Shi, C. et al, D. Alkali-activated Cements and Concretes Taylor & Francis, Oxon (2006)
[19] U.S. Geological Survey Mineral Commodity Summaries: Soda Ash (2013)
[20] Wang, J et al Influence of the combination of calcium oxide and sodium carbonate on the hydration reactivity of alkali-activated slag binders. Journal of Cleaner Production, (2018), 622-629
[21] Rashad Alaa M. An exploratory study on sodium sulfate-activated slag blended with Portland cement under the effect of thermal loads. J Therm Anal Calorim, (2014), 4345-4347
[22] Wang S. D, et al Factors affecting the strength of alkali-activated slag. Cem Concr Res (1994), 1033–43.
[23] Xueqan, W. et al. Early activation and properties of slag cement. Cem Concr Res (1990), 961–974.
[24] Yang, K. H. et al Hydration products and strength development of calcium hydroxide-based alkali-activated slag mortars Constr. Build. Mater., (2012), 410-419

SynerCrete'18 International Conference on Interdisciplinary Approaches
for Cement-based Materials and Structural Concrete
24-26 October 2018, Funchal, Madeira Island, Portugal

EFFECT OF TEMPERATURE ON RHEOLOGICAL PROPERTIES OF ALKALI ACTIVATED BRICK POWDER BASED PASTES

Martin Vyšvařil [(1)], Pavla Rovnaníková [(1)]

(1) Brno University of Technology, Faculty of Civil Engineering, Brno, Czech Republic

Abstract
The effect of temperature on flow properties and viscoelastic properties of brick powder based pastes prepared by alkaline activation of red clay brick waste is monitored in this paper. A different effect of temperature with respect to its classic rheological influence was ascertained. Elevated temperature has a considerable impact on the yield stress, viscosity and thixotropy of brick pastes, which turn to be more pseudoplastic and rheopectic. Raising temperature accelerates the geopolymer curing kinetics and contributes to the more rigid structure of the resulting geopolymeric gel.

1. Introduction

Alkali activated materials are formed by alkaline activation of suitable aluminosilicate precursors (e.g metakaolin, blast furnace slag, fly ash). Ceramic and red clay brick wastes are considered to be efficacious aluminosilicate materials, which can be used as alternative to metakaolin and fly ash [1-4]. Bricks waste is usually rich in glass and burned clays, consisting in dehydrated aluminosilicates not only in crystalline phase but also in amorphous state which is important for alkaline reaction. In recent years, large volumes of brick dust have been produced with the development of building elements for the construction of low-energy houses. As activators, a wide range of alkaline solutions can be applied: NaOH, Na_2CO_3, sodium silicate (water glass), sodium aluminate, or their potassic equivalents. The elevated temperature promotes the alkali reaction, the temperature of 60 to 90 °C is mostly used, although even at ambient temperature an aluminosilicate gel is formed by brick powder activation [3]. In order to develop a building material that could be used as a cement replacement for specific applications, the understanding of its rheological behaviour at fresh state is fundamental. Some studies on alkali activated materials based metakaolin, fly ashes or blast furnace slags showed that similarly to cement pastes, these materials display viscoelastic

behaviour with thixotropic properties [5-8]. In spite of the common alkali activation of aluminosilicates at elevated temperatures, very few studies have been conducted regarding the effect of temperature on rheological properties of alkali activated materials. In metakaolin based geopolymers, increasing the temperature also produces an increase of viscosity and yield stress [9].
In this study, the effect of temperature on the rheological properties of brick powder based pastes prepared by alkaline activation of red clay brick waste is monitored. The influence of the composition of activation solution (varied silicate modulus) on the flow properties and the viscoelastic properties of pastes has been also studied.

2. Materials

A brick powder from the grinding of calibrated thermal insulating brick elements from the HELUZ Brickworks factory, v.o.s., plant in Hevlín, was used to prepare test specimens. The powder was used as-received, just the particles larger than 1 mm were removed by sieving. The chemical and phase composition of the brick powder as well as the particle size distribution and fundamental physical parameters were presented in the previous study (ceramic powder H) [10]. Fresh brick pastes were prepared from the brick powder with three dosages of activating solutions (potassium silicate, supplied by Vodní sklo, a.s., Czech Republic, and KOH p. a., by Penta Chemicals, a.s.). The silicate modulus (M_s) of the activator varied from 1.0 to 1.4; the water content – sum of dosed water and water present in potassium silicate solution – was equal in all mixes. The recipes were based on preliminary experiments performed with varying activator composition and dosage. The varying dosage of liquid activator means varying Si/Al and K/Al ratio in the prepared materials. The testing specimens were prepared by mixing of brick powder and alkaline activator prearranged from potassium silicate solution, KOH and tap water (Tab. 1). The mixtures were homogenized by hand stirring for 1 minute.

Table 1: Composition of mixtures.

Mixture	**Brick powder (g)**	**Potassium silicate (g) M_s = 3.0**	**KOH (g)**	**H_2O (ml)**	**M_s (-)**
BP-K-1.0	50	20	6.3	5	1.0
BP-K-1.2	50	20	4.6	5	1.2
BP-K-1.4	50	20	3.5	5	1.4

3. Experimental methods

The rheological investigation including the characterization of flow properties and viscoelastic properties of pastes were carried out on the hybrid rheometer Discovery HR-1 (TA Instruments) in the Peltier Concentric Cylinder system with a DIN rotor with rough surface lowering the slippage and segregation of mixes during measurements. TRIOS 4.0.2.30774 software was used for a data evaluation [11]. The standard gap for DIN cylinder (5.917 mm) was adopted. The measurements were done at 20, 40 and 60 °C.

3.1 Flow properties

The brick suspension was placed into the measurement system at the end of the mixing cycle and the rheological measurements were started after a period of rest of 60 s. The testing routine was composed of a shear rate increase (from 0.1 to 100 s^{-1}) applied through 30 steps with 15 s of measuring time at each shear rate followed by a decrease of shear rate on the same conditions. The results of flow measurements were expressed as shear rate vs. shear stress (flow curves) and the Herschel-Bulkley model Eq. (1) was applied to descending branches of the flow curves to fit the experimental data and to describe the pastes rheological behaviour [12]:

$$\tau = \tau_0 + k\dot{\gamma}^n \quad (1)$$

where τ is the shear stress, $\dot{\gamma}$ is the shear rate, τ_0 corresponds to the yield stress, k is the consistency coefficient, and n is the fluidity index which characterizes shear-thinning (n < 1) or shear-thickening (n > 1) behaviour of a material. Thixotropy or rheopexy of pastes were determined as an area between flow curves using TRIOS software.

3.2 Viscoelastic properties

Time evolution of the viscoelastic properties of pastes were evaluated by small amplitude (0.01%) oscillation tests measuring elastic (G') and viscous (G'') modulus. If the elastic behaviour dominates the viscous one ($G' > G''$), the sample exhibits a certain rigidity. Conversely, if $G'' > G'$, the sample shows the character of a liquid without a consistent chemical or physical network-of-forces [12]. Since one of the purposes of this study is to determine the variation over time of the viscoelastic parameters according to the geopolymer composition, it is important to determine the linear viscoelasticity region (LVR) in order to prevent structural decomposition of the geopolymerized network. The LVR is the region in which measurements are non-destructive to the microstructure of a material and it ends at a critical strain γ_c. The strain of 0.01% used in the oscillation tests is lower than the critical strain for all brick pastes studied. The rheological characterization was completed by frequency sweep tests with increasing the frequency from 0.1 Hz to 10 Hz. Experimental data were reported in terms of complex modulus (G^*) and loss tangent (tan δ) defined as follows Eqs. (2–3):

$$G^* = \sqrt{(G')^2 + (G'')^2} \quad (2)$$

$$\tan\delta = G''/G' \quad (3)$$

4. Results and discussion

4.1 Flow properties

The course of flow curves (Fig. 1) dramatically changed with increasing temperature indicating the change from thixotropic (time-dependent shear-thinning) to rheopectic (time-dependent shear-thickening) behaviour of brick powder pastes. Strong rheopexy can be revealed on the flow curve of BP-K-1.4 sample measured at 60 °C. Increasing M_s tended to the rheopectic character of brick powder pastes. This is also evident on the thixotropy values in Tab. 2. The shape of descending branches of the flow curves indicates continual conversion

from dilatant to pseudoplastic behaviour of the pastes with increasing temperature and M_s, respectively. The last-mentioned is confirmed by the downtrend of the flow index values, *n*, (Tab. 2). The yield stress and the consistency coefficient (which can be compared to plastic viscosity of the material) of pastes increased with increasing temperature and M_s; this is in agreement with the metakaolin based geopolymers [9] and the generally known inverse dependence of alkali-activated paste workability on the increasing silicate modulus of alkali activator.

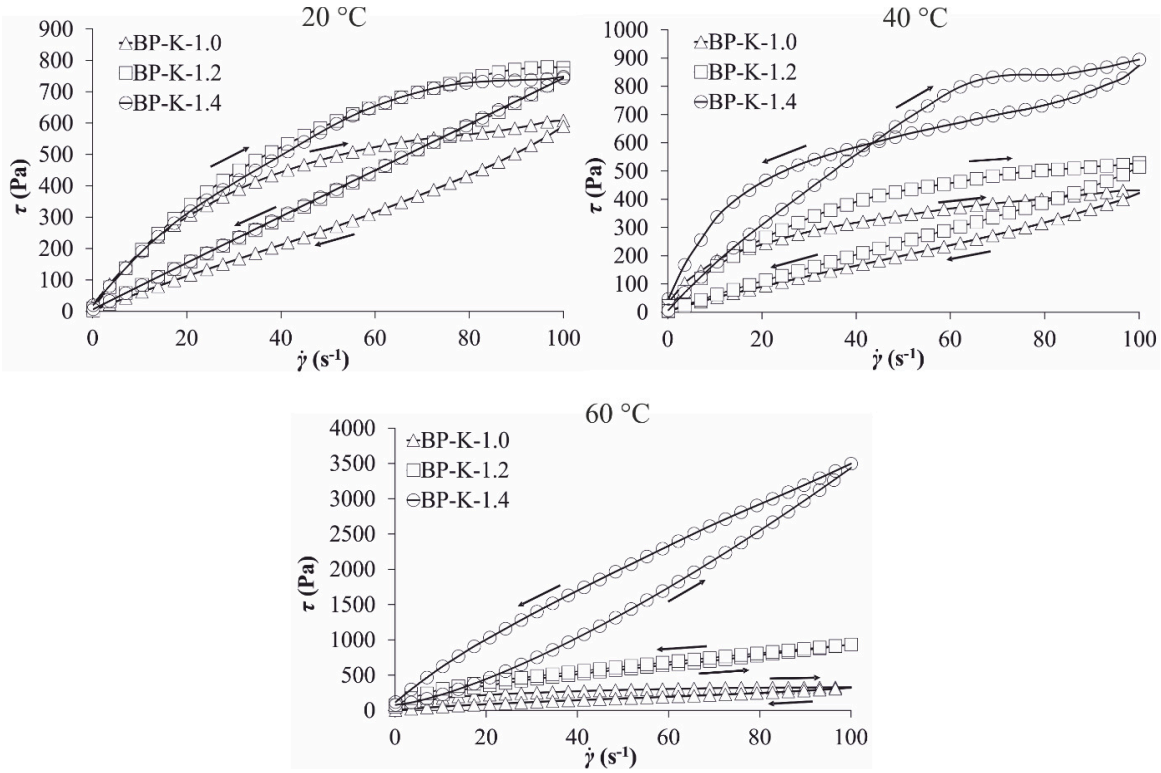

Figure 1: Flow curves of brick powder pastes measured at temperatures of 20, 40 and 60 °C.

Table 2: Rheological parameters of brick powder based pastes.

Mixture	τ_0 **(Pa)**	***k* (Pa s)**	***n* (-)**	**Thixotropy (Pa s)**	t_{SG} **(s)**	***G**** **(Pa)**	**tan** δ **(-)**
BP-K-1.0 (20 °C)	6.03	2.55	1.17	16 233	1 060	300	1.07
BP-K-1.0 (40 °C)	13.96	2.92	1.06	13 084	921	356	1.05
BP-K-1.0 (60 °C)	19.79	5.21	0.88	9 951	826	4 936	0.69
BP-K-1.2 (20 °C)	7.98	3.35	1.03	16 200	591	399	0.99
BP-K-1.2 (40 °C)	14.75	4.13	1.01	11 565	432	816	0.98
BP-K-1.2 (60 °C)	74.93	51.08	0.61	-3 896	429	7 034	0.66
BP-K-1.4 (20 °C)	12.29	7.55	0.99	14 433	257	754	0.67
BP-K-1.4 (40 °C)	47.50	63.65	0.92	357	190	10 534	0.59
BP-K-1.4 (60 °C)	91.81	78.76	0.36	-45 705	119	222 939	0.31

4.2 Viscoelastic properties

Fig. 2 shows the time evolution of the viscoelastic parameters (G' and G'') during a small amplitude oscillation test. Geopolymer gel formation was monitored by a time point t_{SG} at the intersection of the curves of G' and G'' (gel point). Before the gel point, samples show the behaviour of a liquid with $G'' > G'$, after the gel point, the samples show gel-like or solid behaviour with the existence of interactions between the constituents [12]. The results (Tab. 2) confirmed that elevated temperature accelerates the geopolymer curing kinetics and that the gel point was observed at earlier times. In addition, it has been found that the increasing silicate modulus results in faster gel formation and more rigid structure (the elastic component (G') varies rapidly than the viscous component (G'')).

The results of frequency sweep tests (Tab. 2) proved the relationship between elevated temperature and the stiffness of brick pastes; the ratio between dissipation and elasticity increased (growing G^*) with increasing temperature and the pastes became more rigid and more viscous. Since the tan δ of the pastes decreased, the brick paste showed higher and higher proportion of the elastic component (G') with increasing temperature and M_s suggesting that the pastes had a stronger structure more resistant to external interference.

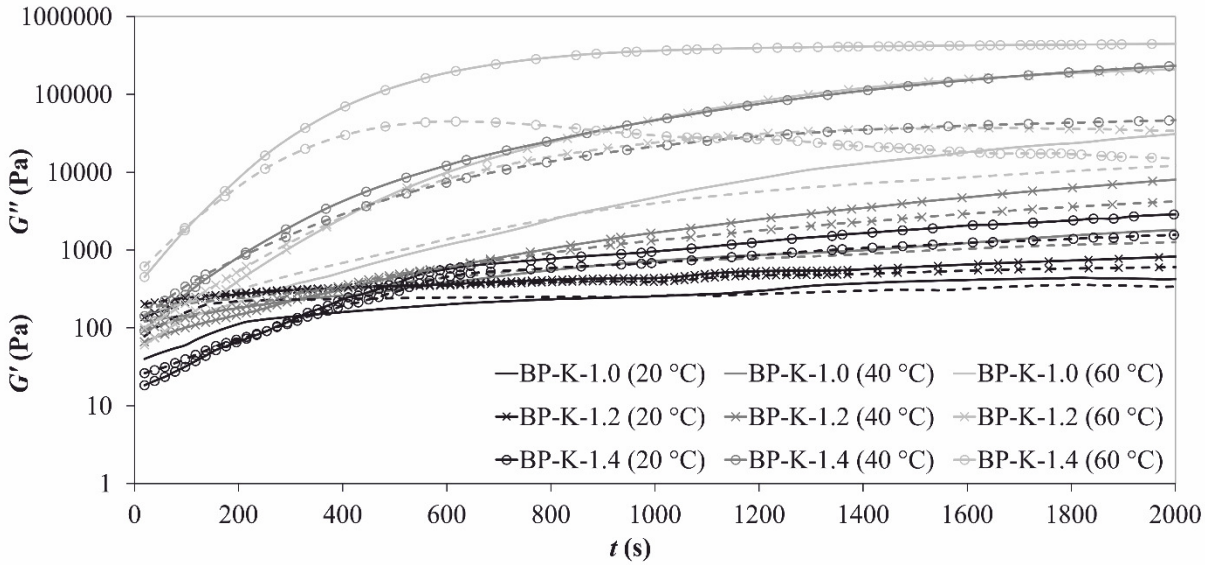

Figure 2: Time evolution of storage modulus (G'; continuous curves) and loss modulus (G''; dash curves) for the brick powder based pastes.

5. Conclusions

In this study, it is shown that:

- Brick powder based pastes prepared at ambient temperature by alkaline activation of red clay brick waste are highly thixotropic fluids with relatively low yield stresses and viscosities.
- Elevated temperature has a considerable impact on the yield stress, viscosity and thixotropy of brick pastes, which turn to be more pseudoplastic and rheopectic. Raising

temperature accelerates the geopolymer curing kinetics and contributes to the more rigid structure of the resulting geopolymeric gel; this is a different effect of temperature with respect to its classic rheological influence.

- Increasing silicate modulus of alkali activator tends to the rheopectic character of brick powder pastes; the pastes become more rigid and more viscous. The increasing viscosity of the activator solution at rising M_s is the main reason for it. This also leads to the acceleration of gel formation in brick pastes.
- The effect of temperature and silicate modulus of alkali activator is similar as on metakaolin geopolymerization.

Acknowledgments
This outcome has been achieved with the financial support of the GA ČR research project 16-02862S and due to the Ministry of Education, Youth and Sports under the „National Sustainability Programme I" – the project No. LO1408 „AdMaS UP – Advanced Materials, Structures and Technologies".

References

[1] Reig, L. et al, Alkaline activation of ceramic waste materials, Waste Biomass. Valoriz. 4 (2013) 729-736
[2] Reig, L. et al, Properties and microstructure of alkali-activated red clay brick waste, Constr. Buil. Mater. 43 (2013) 98-106
[3] Bignozzi, M.C. et al, Ceramic waste as new precursors for geopolymerization, Adv. Sci. Tech., 92 (2014) 26-31
[4] El-Fadaly, E. et al, Eco-friendly cement from ceramic waste geopolymerization, Natur. Soc. Sci., 2 (2014) 195-210
[5] Palacios, P. et al, Rheology and setting of alkali-activated slag pastes and mortars: Effect of organic admixture, ACI Materials Journal, 105 (2008) 140-148
[6] Palomo, A. et al, Properties of alkali-activated fly ashes determined from rheological measurements, Adv. Cem. Res. 17 (2005) 143-151
[7] Abdalqader, A. and Al-Tabbaa, A., Rheological Properties of Sodium Carbonate - Activated Fly Ash/Slag Pastes with Different Superplasticisers, 27th Biennial National Conference of the Concrete Institute of Australia in conjunction with the 69th RILEM Week, Australia (2015), 1105-1115
[8] Poulesquen, A. et al, Rheological behavior of alkali-activated metakaolin during geopolymerization, J. Non-Cryst. Solids. 357 (2011) 3565-3571
[9] Romagnoli, M. et al, Rheology of geopolymer by DOE approach, Constr. Build. Mater. 36 (2012) 251–258
[10] Keppert, M. et al, Red-clay ceramic powders as geopolymer precursors: Consideration of amorphous portion and CaO content, Appl. Clay Sci. 161 (2018) 82-89
[11] http://www.tainstruments.com/trios-software/
[12] Mezger, T.G., The Rheology Handbook, 4th ed., Vincentz Network, Germany (2014)

SynerCrete'18 International Conference on Interdisciplinary Approaches
for Cement-based Materials and Structural Concrete
24-26 October 2018, Funchal, Madeira Island, Portugal

EXPERIMENTAL STUDY OF THE CHEMICAL DEFORMATION OF METAKAOLIN BASED GEOPOLYMER

Zhenming Li [(1)], Guang Ye [(1)]

(1) Section Materials and Environment, Faculty of Civil Engineering and Geosciences, Delft University of Technology, Delft, the Netherlands

Abstract
Chemical deformation is an important material property which influences the autogenous deformation of the materials. While geopolymer is emerging as an eco-friendly alternative to ordinary Portland cement (OPC), few studies have been conducted on the chemical deformation of this material. In this paper, the chemical deformation of a metakaolin (MK) based geopolymer is studied. Unlike OPC paste which exhibits monotonous chemical shrinkage, metakaolin-based geopolymers can show chemical shrinkage and chemical expansion at different stages of curing. X-ray diffraction (XRD) and Fourier transform Infrared Spectrophotometer (FTIR) tests were conducted to characterize the geopolymer paste cured at different ages in order to explain the mechanisms of different chemical deformation behaviors. It was confirmed that the early age chemical shrinkage was mainly due to the dissolving of MK, where the density of MK plays an important role. The chemical expansion taking place in the second stage was mainly associated with the formation of Al-rich products. The chemical shrinkage in the late age was related to the formation of Si-rich products in literature, but this finding was not confirmed in this study. The understanding of chemical deformation of geopolymers is helpful to explain the autogenous deformation of geopolymers.

1. Introduction

Geopolymer has emerged as an eco-friendly alternative to OPC. OPC has been widely utilized in construction for many centuries with stable properties but the CO_2 emission produced by cement industry is becoming a serious issue hindering the application of this material. Geopolymer, in contrast, can be made from industrial by-products or other inexpensive aluminosilicate materials, to which little or no CO_2 footprint is usually attributed. To serve as a qualified binder in construction, geopolymer needs to have good volume stabilities.

However, the autogenous deformation property of geopolymers remains an unsolved issue. To better understand the autogenous deformation of geopolymers, research attention needs to be paid on the chemical deformation, since it essentially influences the driving force of autogenous deformation [1]. Li et al. [2] have studied the chemical deformation evolution and mechanism of a geopolymer made from a highly reactive MK with a typical Si/Al ratio around 1. They found that the metakaolin based geopolymer (MKG) experiences three stages of chemical deformation, i.e. chemical shrinkage in the first stage which was mainly due to dissolution of the precursor, chemical expansion in the second stage which was strongly associated with the formation of Al-rich (nano-) zeolites and chemical shrinkage again in the final stage due to the reorganization and polymerization of the Al-rich products to form Si-rich gels. To verify the applicability of their theories in explaining geopolymers synthesized from different precursors, this paper concentrates on the chemical deformation of a geopolymer made of MK with different reactivity and a different Si/Al ratio. The reaction products of the MKG paste are characterized.

2. Materials and experiments

2.1 Materials

The MK used as precursor was from Argeco (France), with a particle size range of 0.15-142 μm and a d_{50} of 69.4 μm. The chemical compositions of MK determined by X-ray fluorescence spectrometry (XRF) are shown in Tab. 1. The reactive SiO_2 and Al_2O_3 contents in MK were determined by chemical dissolution treatment. The MK was dissolved in dilute hydrochloric acid solution and were afterwards treated with boiling solution of sodium carbonate. The obtained residue was rinsed, heated up to 950 °C and then was cooled to room temperature in a desiccator before subject to XRF test. The dissolved fraction corresponding to the mass loss after chemical dissolution treatment is determined as the amorphous phase content. The amount of reactive SiO_2 and Al_2O_3 was shown in Tab. 2. The mole ratio of SiO_2/Al_2O_3 in the reactive part of MK is 0.65.

The activator was prepared by mixing solid NaOH and liquids (sodium silicate and distilled water) in a closed plastic bottle to prevent evaporation. The solution was then allowed to cool for 24 hours before mixing with MK. The mixture proportions of the MKG paste are presented in Tab. 3.

Table 1: Chemical compositions of MK and insoluble residue.

Oxide weight (%)	SiO_2	Al_2O_3	CaO	Fe_2O_3	K_2O	TiO_2	ZrO_2
MK	55.14	38.43	0.55	2.60	0.17	1.12	0.05
Insoluble residue	83.65	12.61	0.12	0.79	0.23	2.43	0.11

Table 2: Reactivity of MK (wt%).

Components (%)	I.R.	Reactive content	Total SiO_2	Reactive SiO_2	Total Al_2O_3	Reactive Al_2O_3
MK	51.23	48.77	55.14	12.29	38.43	31.97

Table 3: Mixture proportions of MKG paste.

	SiO_2 (mol)	Al_2O_3 (mol)	Na_2O (mol)	H_2O (g)
MK	1.23	1.88	--	--
Activator	1	--	1.5	350
MKG	2.23	1.88	1.5	350

2.2 Experiments

The densities of MK and the insoluble residue were measured by pycnometer. The chemical deformation of the paste was measured from casting till 2 weeks according to gravimetry method, with the detailed procedure described elsewhere [2]. The chemical deformation value was described as the absolute volume change of the paste per gram of the reactive part of the precursor. XRD was conducted by using a Philips PW 1830 powder X-ray diffractometer, with Cu Kα (1.5406 Å) radiation, tube setting to be 40 kV and 40 mA, a step size of 0.030°, and a 2θ range of 5–70°. FTIR was performed by using a Spectrum TM 100 Optical ATR-FTIR spectrometer over the wavelength range of 600 to 4000 cm^{-1} with a resolution of 4 cm^{-1}.

3. Results and discussion

3.1 Chemical deformation evolution

The evolution of chemical deformation of MKG is shown in Fig.1 (a). For the convenience of comparison, the chemical deformation of the geopolymer synthesized from another kind of MK (denoted as MKG2) studied in [2] is shown in Fig.1 (b). It can be seen that the chemical deformations of the two MKGs both experience three stages of evolutions, i.e. chemical shrinkage in the first few hours, chemical expansion in the subsequent stage and chemical shrinkage again in the third and final stage. No evident change was observed after 2 weeks of curing. These results indicate that the three-stage evolution of chemical deformation seems an intrinsic behavior of MKGs rather than a phenomenon dependent on the properties of precursors. The development of chemical deformation of geopolymers is essentially different from that of OPC, where OPC always exhibits a monotonous chemical shrinkage in the whole age of curing. The absolute volume change of OPC is called chemical shrinkage, but the one of geopolymers can only be called chemical deformation due to the expansion observed.
Despite of the same trend followed by the chemical deformations of the two MKGs, the magnitudes of the first-stage chemical shrinkages of these two mixtures differ a lot. This difference will be emphasized in next section.

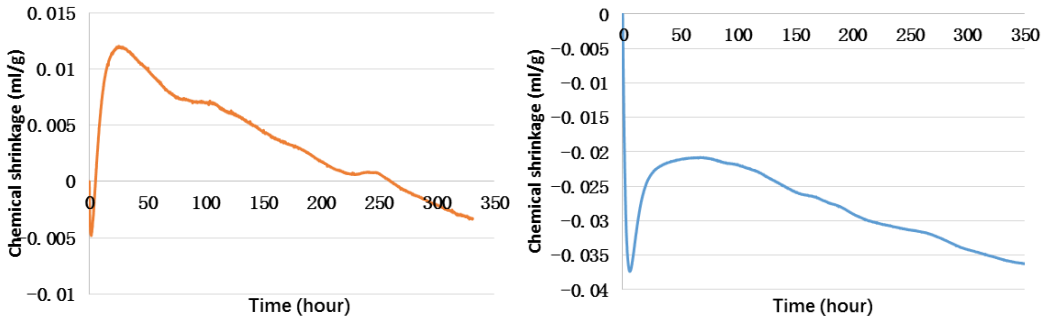

Figure 1: Comparison of chemical deformations of MKG from this study (a) and MKG2 from [2] (b).

3.2 Explanation of the chemical deformations in different stages

3.2.1 Chemical shrinkage in the first stage (the first few hours after casting)

According to [2], the first stage chemical shrinkage of MKG was mainly due to the dissolution of the precursor. To verify this hypothesis, 120g of MK was mixed with 1200g of alkali activator with continuous stirring. The volume change of the suspension during mixing was measured according to Le Chatelier method. The volume change (ml) divided by the mass (g) of the reactive part of MK is shown in Fig.2.

It can be seen that the volume of the suspension decreased in the first half an hour of mixing. Due to the low concentration of MK in the solution, the dissolution of MK should be the dominant reaction in this period. After half an hour of mixing, the volume of the suspension began to increase, indicating that the concentrations of the dissolved species reached a threshold and the polymerization among them began to occur. Therefore, the volume reduction of 0.0044 ml/g at the time 0.5 hour can be considered as an approximation of the chemical shrinkage caused by dissolution of MK. In fact, the value of 0.0044 ml/g is quite close to the chemical shrinkage of MKG in the first stage which is 0.0048 ml/g as shown in Fig.1 (a). This result supports the hypothesis proposed in [2] that the early age chemical shrinkage of MKGs is mainly due to the dissolution of MK.

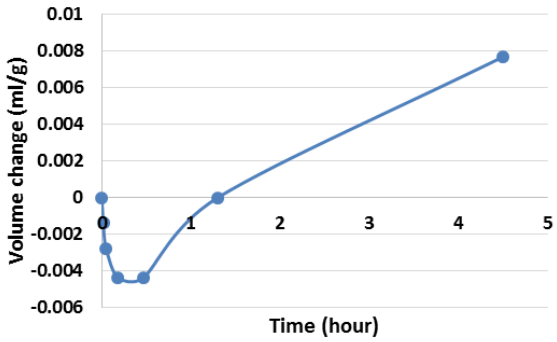

Figure 2: Volume change during dissolution of MK.

Moreover, the chemical shrinkage due to dissolution of MK can also be approximated by calculation. If we assume the reaction products after dissolving of MK are simply monomers, $Si(OH)_4$ and $Al(OH)_3$, without considering the ionization or the polymerization of these species, the dissolution of MK can be described as Eq. (1). The chemical formula of MK is expressed as $(SiO_2)0.65{\bullet}Al_2O_3$ because the SiO_2/Al_2O_3 ratio of the reactive part of MK is 0.65.

$$(SiO_2)0.65{\bullet}Al_2O_3 + 4.3\ H_2O + 2\ OH^- \longrightarrow 0.65\ Si(OH)_4 + 2Al(OH)_4^- \quad (1)$$

The chemical deformation associated with Eq.(1) can be calculated based on the density of reactive MK and the molar volumes of H_2O, OH^-, $Si(OH)_4$ and $Al(OH)_3$. Based on the densities of MK and insoluble residue measured by pycnometer method, the density of the reactive part of MK can be calculated to be 2.37 g/ml. The molar volumes of $Si(OH)_4$ and $Al(OH)_3$ are assigned as 58.68 ml/mol and 42.3 ml/mol, respectively, according to the data in literatures [3–5]. The chemical deformation associated with Eq. (1) is calculated to be -0.034 ml/g, i.e. chemical shrinkage of 0.034ml/g. This is qualitatively consistent with the experiment results which also show chemical shrinkage in the first stage. However, the value 0.034ml/g is much higher than the measured chemical shrinkage of MKG in the first stage

which is 0.0048 ml/g. This is because the calculation above assumes the precursor was 100% dissolved while in real alkali activation only a part of the MK was dissolved in the first hours. Even though the dissolution of MK proceeded with elapse of time, the chemical shrinkage induced by later dissolution was compensated by the chemical expansion which occurred in the second stage, hence the experimentally measured chemical shrinkage in the first stage reached only 0.004 - 0.005 ml/g.

The calculation also indicates that a key parameter influencing the early age chemical shrinkage of MKG is the density of the reactive part of the precursor, which determines the volume of the reactants before reaction. The big difference between the densities of the precursors used in this study and in [2], which are 2.37 g/ml and 2.09 g/ml, respectively, explains the big difference between the first-stage chemical shrinkages of the two MKGs shown in Fig.1.

3.2.2 Chemical expansion in the second stage (from 3 to 50 hours curing)

The FTIR spectra of the MKG pastes at different curing times are shown in Fig.3. The main band of the spectrum of raw MK located at around 1045 cm^{-1} is assigned to the asymmetric stretching vibration of Si-O-T bonds (T= tetrahedral Si or Al). After 4 hours of activation, the main band shifts to around 940 cm^{-1}, which is attributed to the formation of NASH gels [6], indicating that the MK was largely dissolved and the reaction products began to form in this period. At the curing age of 16 hours and 30 hours, the humps at 680 cm^{-1}, 740 cm^{-1} and 860 cm^{-1}, which represent the vibrations of Al-O bonds in AlO_4 tetrahedral groups, become apparent, indicating that a large amount of Al was incorporated into the polymerized structures. These reaction products are normally denoted as "Al-rich" products [7]. The formation of Al-rich products corresponds to the chemical expansion occurring in this stage, indicating that the finding proposed in [2] that the chemical expansion occurring in the second stage of geopolymerization is associated with the formation of Al-rich products is also applicable to the present MKG.

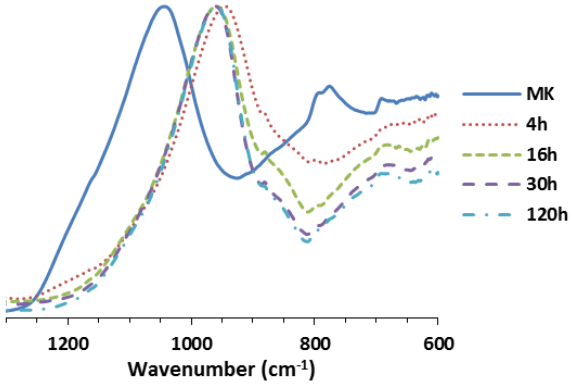

Figure 3: FTIR spectra of MK and MKG pastes cured for 4 hours, 16 hours, 30 hours and 120 hours.

3.2.3 Chemical shrinkage in the final stage (after about 50 hours curing)

The formation of Si-rich gels was reported to be responsible on the chemical shrinkage happening in the final stage of geopolymerization [2]. However, this hypothesis cannot be confirmed in this study by only the FTIR results. As shown in Fig.3 (a), the spectra of 30h and 120h are indistinguishable, although the reactions were ongoing and the chemical

shrinkage was continuously developing in this period. It is suggested that techniques like nuclear magnetic resonance (NMR) need to be utilized to detect the Si coordination environments of the MKG pastes cured at different ages.

3.3 Perspective

In [8], the autogenous deformation of the MKG paste with the same mixture design as in this study was investigated. Autogenous expansion after final setting time (2.3 hours after mixing) and subsequent autogenous shrinkage after 1 day of curing were observed, but the mechanisms behind these behaviors were not clearly understood. The chemical expansion and the chemical shrinkage observed in this study may help to explain the autogenous expansion and autogenous shrinkage of MKG, respectively.

4. Conclusions

The MKG experienced three stages of chemical deformation regardless of the reactivity of the precursor. The chemical shrinkage in the first stage was mainly due to the dissolving of precursor. MK with higher density of the reactive part was supposed to have lower chemical shrinkage in this period. The chemical expansion occurred subsequently was associated with the formation of Al-rich products, which may consist of nano-zeolites that cannot be detected by X-ray. The chemical shrinkage in the late age may be due to the reorganization and polymerization of the previously formed entities, where further research is needed.

References

[1] O.M. Jensen, P.F. Hansen, Autogenous deformation and RH-change in perspective, Cem. Concr. Res. 31 (2001) 1859–1865. doi:10.1016/S0008-8846(01)00501-4.
[2] Z. Li, S. Zhang, Y. Zuo, W. Chen, G. Ye, Chemical deformation of metakaolin based geopolymer, Cem. Concr. Res. (2018) (Submitted).
[3] J.G. Reynolds, The Density of Aqueous Sodium Hydroxide- Sodium Aluminate Solutions : Data Review and Model Development, in: WM'06 Conf., 2006.
[4] T. Ikkatai, N. Okada, K.K. Showa, Viscosity, specific gravity, and equilibrium concentration of sodium aluminate solutions, Extr. Metall. Alum. 1 (1963) 159–173.
[5] J. Li, C.A. Prestidge, J. Addai-Mensah, Viscosity, density, and refractive index of aqueous sodium and potassium aluminate solutions, J. Chem. Eng. Data. 45 (2000) 665–671. doi:10.1021/je000025d.
[6] W.K.W. Lee, J.S.J. van Deventer, Use of infrared spectroscopy to study geopolymerization of heterogeneous amorphous aluminosificates, Langmuir. 19 (2003) 8726–8734. doi:Doi 10.1021/La026127e.
[7] P. Duxson, A. Fernández-Jiménez, J.L. Provis, G.C. Lukey, A. Palomo, J.S.J. van Deventer, Geopolymer technology: the current state of the art, J. Mater. Sci. 42 (2007) 2917–2933. doi:10.1007/s10853-006-0637-z.
[8] Z. Li, P. Gao, G. Ye, Experimental study on autogenous deformation of metakaolin based geopolymer, in: 2nd Int. RILEM/COST Conf. Early Age Crack. Serv. Cem. Mater. Struct., Brussels, 2017: pp. 209–214.

SynerCrete'18 International Conference on Interdisciplinary Approaches
for Cement-based Materials and Structural Concrete
24-26 October 2018, Funchal, Madeira Island, Portugal

FLEXURAL BEHAVIOR AND STRENGTHENING OF GEOPOLYMER CONCRETE BEAMS REINFORCED WITH GFRP BARS USING CFRP SHEETS

Abdalla Elbana [(1)], M. Talha Junaid [(1)], Salah Altoubat [(1)]

(1) Department of Civil and Environmental Engineering, University of Sharjah, UAE

Abstract
Fiber Reinforced Polymers (FRP) are a relatively new material, and some behavioral aspects are not yet studied, especially pertaining to flexural and serviceability behavior in structural members. On the other hand, researchers have found that Geopolymer concrete has significantly high mechanical properties making it suitable for structural applications. A combination of FRP and Geopolymer should result in a durable, sustainable, and environment-friendly. This paper has two main aims. Firstly, to study the flexural behavior and serviceability of geopolymer concrete beams reinforced with Glass Fiber Reinforced Polymer (GFRP) bars. Secondly, to investigate the applicability of carbon fiber reinforced polymer (CFRP) as a strengthening regime for such systems. A total of six 2.1meter beams were tested under quasi-static four-point flexural tests for this purpose. Two identical beams were tested to failure. The remaining 4 beams were partially damaged and then repaired and strengthened with CFRP sheets using four different strengthening regimes. The CFRP strengthening system restored the capacity of the damaged beams, however, the contribution of GFRP rebars and CFRP sheet in load carrying capacity is not as efficient as in beams with conventional reinforment strengthened with CFRP. This could be attributed to the stress-strain relationship of CFRP and GFRP that is distinctly different from each other.

1. Introduction

Geopolymers are formed when an alumina and silica-rich source material is activated with a strong metallic alkaline. The source material is usually fly-ash (class F or C), naturally occurring clays, and furnace slag from the production of metals. Generally, sodium, potassium and calcium hydroxides or silicates, or a combination of these is used as activator solutions. Geopolymer concrete is highly sustainable and cost-effective since it is

manufactured from industrial waste materials. Researchers have found that Geopolymers could be a possible replacement of conventional concrete[1-9]. Conventional steel reinforcement is prone to corrosion thus leading to non-durable concrete structures. Recently, glass fiber-reinforced polymer (GFRP) reinforcement bars have become an alternative to the traditional rebars. GFRP has superior durability properties being a noncorrosive material and superior mechanical properties, such as high tensile strength and low self-weight [10]. A combination between GFRP and GPC should result in a durable, sustainable, and cost-effective system. Moreover, externally bonded Carbon fiber reinforced polymers (CFRP) are used for strengthening or repairing of existing concrete members to improve load-resistance as well as serviceability. The current research aims at studying the behavior of flexural members composed of the different materials described above, and their interaction with each other. To this end, six (6) beams made with GPC and reinforced with GFRP bars in flexure and shear were tested. Two beams were tested to failure and served as reference beams for the remaining testing. The other 4 beams were loaded to induce substantial damage and repaired by CFRP sheets using different strengthening regimes and then tested to failure. The results of this testing program help in understanding the flexural behavior of such a composite system and the interaction of these materials with each other.

2. Materials

Commercially available fly ash class-F and ground granular blast furnace slag (GGBFS) was used as a binder for making geopolymer concrete. 12 molar sodium hydroxide solution was prepared by dissolving sodium hydroxide pallets with tap water 24 hours prior using. An extra pure sodium silicate solution was used with chemical compositions of $27.2\%\ SiO_2$, $8\%\ Na_2O$, and 64.8% water. The sodium hydroxide to sodium silicate ratio is 1.8 and the GGBFS content of the total binder is 20%. Geopolymer concrete mix proportions are summarized in Tab. 1. The 28 days average compressive strength of geopolymer concrete is 34.1 MPa.

GFRP bars under the product name MateenBar provided by Pultron Composites UAE were used in this study. The nominal diameters used were 16 mm for moment reinforcement (f_{fu}*= 690 MPA ε_{fu}^{*}= 0.0135 and $E_f = 51 \pm 2.5$) and bar size 10 mm for shear stirrups reinforcement. All beams are equipped with two 10 mm bars in the compression zone. Straight GFRP bars without anchor head with a deformed surface were used.

Table 1: Geopolymer concrete mix proportions

Component	20 mm C.A.	10 mm C.A.	5 mm F.A.	Dune Sand	NaOH (12M)	FA	Na_2Sio_3	GGBFS	Water	Superplasticizer
Quantity (Kg/m^3)	540.8	302.5	582.2	289.4	55.1	99.2	340	85	47	4

A high strength, high elastic modulus, and uni-directional carbon fiber reinforced polymer sheet provided by CONMIX LTD was used for strengthening the damaged beams. The carbon fiber sheets were externally bonded to the soffit of the beam as per ACI 440.R2-08 [11] guideline for installation. CFRP material has a tensile strength of 4000 MPa and a tensile modulus of 230 GPa with an ultimate elongation of 1.80% as specified by the supplier. Grout

and injection resin as provided and installed by CONMIX LTD under the brand name Recon FCE and Recon LVE was used to repair damaged beams.

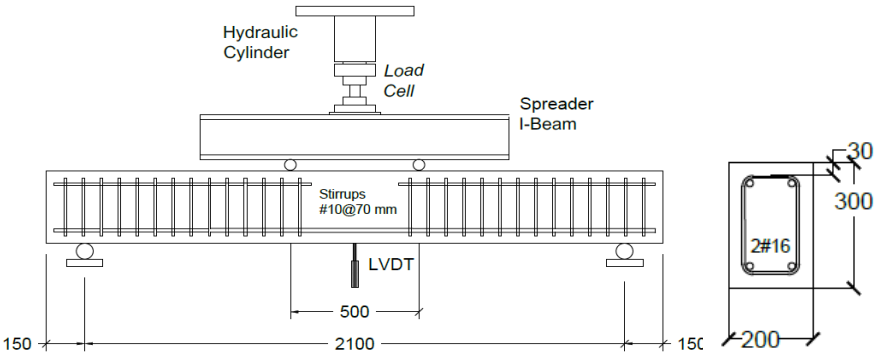

Figure 1: Schematic diagram of test set up and reinforcement details (dimensions are in mm)

3. Methodology

All beam specimens were tested under four-point bending static test. The load was applied through a spreader beam (Fig. 1) by a 1500 KN capacity hydraulic jack. The beams were simply supported with a clear span and shear span of 2100 mm and 800 mm, respectively. Displacement controlled load was applied at 0.01 mm/sec rate. The distance between the two loads was 500 mm. Two beams were loaded to failure. The remaining four beams are loaded to 50% of the experimental ultimate moment to substantially damage them. The damaged beams were repaired by injecting the cracks with epoxy and strengthened with different schemes using CFRP sheets as explained in the next section. A total of six GPC beams reinforced with GFRP bars were tested in this program. Each beam is 2.4m long and a simply supported span of 2.1m with a section of 200mm by 300mm. The beams were reinforced with 2#16 bars in flexure and #10@70mm in shear and designed to fail in flexure. In the constant moment zone, no stirrups or compression bars were provided, so as not to affect the strain and crack development on the pure bending zone. Fig. 1 summarizes the test setup and reinforcement details of the beams. Two such beams were tested to failure and their results were used as a reference for the other 4 beams, which were initially loaded to 50% of the moment capacity. This loading caused substantial damage to the test specimens. These four beams were then repaired and strengthened using two layers of CFRP sheets and the schemes summarized in Tab. 2. A linear variable differential transformer (LVDT) was placed at the midspan section, to measure the incremental midspan deflection. Two strain gauges were installed at the center of the flexural GFRP reinforcement (M). The CFRP sheet were instrumented with four strain gauges, two in the midspan F1, and one at the half shear span F2, and one at the U-wrap side F3 depth (at the same depth of the longitudinal reinforcement).

Table 2: beam specimens and Strengthening Schemes

Ref	Strengthening length	Strengthening profile
GPC-LF and GPC-LU	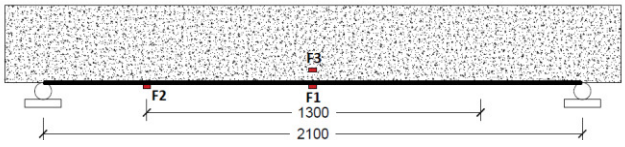	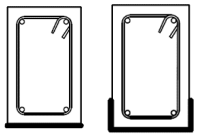
GPC-SF and GPC-SU	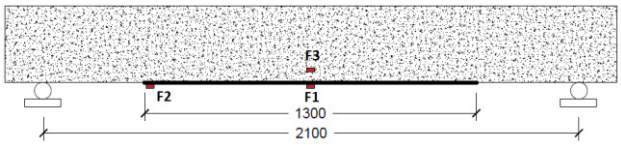	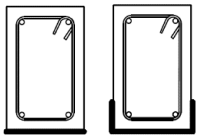

**F3 is placed at CFRP only for U-shape*

4. Results and Discussion

Tab. 3 summarizes the observed experimental failure modes of each specimens. All beams were designed to be under-reinforced in flexure, however, the beams experimentally behaved as over-reinforced and failed due to concrete crushing because the GFRP properties reported by the manufacturer were conservative. For the reference beams GPC-R1 and GPC-R2 the strain values of the strain gauges (M2 and M3) installed in the middle of the two flexural GFRP bars (2#16) exceeded the guaranteed rupture strain (ε_{fu}^{*}=0.0135) provided by the manufacturer at these applied loads before concrete crushing. However, the GFRP bars did not physically rupture at this strain values and contributed to the load carrying capacity of the beams until concrete crushing. Long flat and long U-wrap strengthened beams GPC-LF and GPC-LU failed due to CFRP sheet rupture at the constant moment zone. While beams that has short strengthening system (GPC-SF and GPC SU) failed due to concrete cover delamination which initiated at either end of the CFRP sheet. This failure is due to the short development length (less than that recommended by ACI 440.R2-08 [11] which failed to develop an effective CFRP stress. After CFRP failure, all the strengthened beams continued to resist the applied load until the GFRPs' ε_{fu}^{*} was reached, shortly followed by concrete crushing.
Tab. 3 summarizes the experimental flexural capacities at CFRP ($M_{\text{n, CFRP}}$), GFRP ($M_{\text{n, GFRP}}$), and concrete crushing ($M_{\text{n, CC}}$) failure. The experimental flexural capacity $M_{\text{n, GFRP}}$ for each specimen is obtained when the strain of GFRP exceeds ε_{fu}^{*} provided by the manufacturer. The Flexural capacity of the strengthened beams changed by -18.4, -5.5%, -63.8%, -60% for GPC-LF, GPC-LU, GPC-SF, GPC-SU from the reference beams respectively. The U-wrapped beams in GPC-LU and GPC-SU experienced 15.7% and 8% improvement in flexural capacities over GPC-LF and GPC-SF respectively. This may be due to the transfer of some of the tensile stresses to the sides by the strengthening system. The flexural capacity of GPC-SU and GPC-SF is dramatically lower than the reference beams because of the early cover delamination failure caused insufficient development length. Nevertheless, the strengthened beams continued to resist loads after CFRP failure until the GFRP reaches its ε_{fu}^{*} followed by concrete crushing failure. This may be attributed to the substantial difference in the CFRP and GPRP modulus of elasticity values, therefore, CFRP carries a substantially higher amount of load, while GFRP bars are not strained to a similar extent. It is only after CFRP sheet fails that the GRRP bars contribute significantly towards the tensile load carrying function.

Table 3: Experimental failure mode and load level at CFRP, GFRP, and concrete crushing.

Sample	$M_{n, CFRP}$	$M_{n, GFRP}$	$M_{n, CC}$	Failure Mode
GPC-R1	-	53.9	63.9	Concrete Crushing
GPC-R2	-	58.9	66.4	Concrete Crushing
GPC-LF	53.2	56.8	73.6	CFRP Rupture
GPC-LU	61.6	56.4	62.4	CFRP Rupture
GPC-SF	23.6	58.8	62.0	Cover Delamination
GPC-SU	25.6	50.8	78.4	Cover Delamination

Fig. 2 presents the relationship between the applied load and mid-span deflection. The first loading phase of all 6 beams represents the elastic behavior which corresponds to the beam's uncracked condition. After cracking the load-deflection curve shows a slight nonlinearity with a reduced slope up to a load at concrete crushing for control beams or at CFRP sheet failure for the strengthened beams. The strengthened beams have steeper load-deflection curve because of the enhanced stiffness that is provided the CFRP strengthening system. GPC-LF and GPC-LU experienced an abrupt drop in the applied load resistance after CFRP rupture failure this is due to the sudden change in stiffness of the system. While GPC-SF and GPC-SU showed a slight drop in load due to the peeling of the concrete cover. All the 4 strengthened beams continued to resist additional load as the GFRP continues to strain after CFRP failure. This continued up to the load at which the ε_{fu}^{*} of GFRP bars was achieved followed by concrete crushing at the absolute peak load.

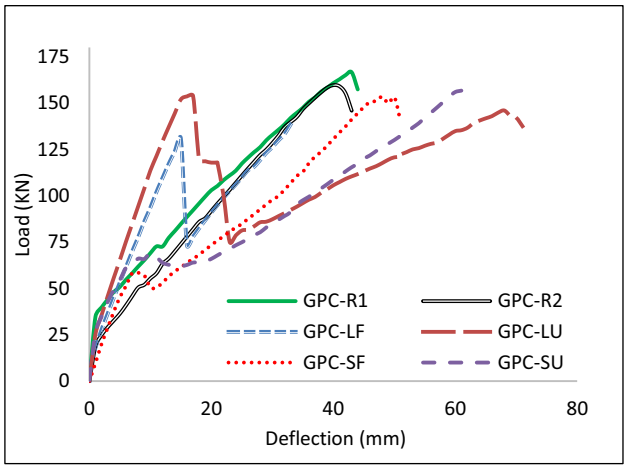

Figure 2: Load-Deflection relationship

5. Summary and Conclusion

This paper studied the performance of concrete beams reinforced with GFRP rebars and strengthened with CFRP sheet under four points quasi-static loading. Failure modes, flexural capacities, and load-deflection relationship were determined. The findings of this experimental program are summarized as below:

- The observed failure mode of the control beams is concrete crushing. However, the strain at GFRP bars exceeded its ε_{fu}^{*} before crushing failure indicating that the specified ε_{fu}^{*} is conservative.

- Externally bonded CFRP sheet in a GFRP-CFRP system works very differently from that of CFRP-steel system. In conventional cases after steel yielding the bars will exhibit plastic behavior and will continue to contribute to load carrying capacity side by side with CFRP sheets. However, in case of GFRP reinforced beams which are CFRP strengthened, the moment carrying capacity of the beams did not change significantly from the reference beams because the GFRP bars have a much lower modulus value than the CFRP sheets. However, for such systems, the original capacity of the beams is restored, provided sufficient development length is ensured for the CFRP sheets.
- For long strengthening schemes, both flat and U-shaped, the failure happens due to CFRP rupture. This shows the effectiveness of the long strengthening schemes in utilizing the strain capacity of the CFRP sheets. In case of short strengthening schemes, premature failure was experienced.
- The long strengthening schemes, both flat and U-wrap, restored the load carrying capacity of the damaged beams because proper development length was provided.
- For the short flat and short U strengthened beams experienced a decrease in moment resisting capacity. This indicates that such schemes are detrimental to the section capacity and must not be used.
- The CFRP strengthening system provided a stiffer member and reduced the ultimate deflection at CFRP failure to almost half of the ultimate deflection of the reference beams.

References

[1] Elbana, A., Evaluation of flexural behavior of reinforced concrete beams with glass fiber reinforced polymer (GFRP) bars, in Department of Civil and Environmental Engineering. 2018, University of Sharjah. p. 108.
[2] Junaid, M.T., et al., Aspects of the deformational behaviour of alkali activated fly ash concrete at elevated temperatures. Cement and Concrete Research, 2014. 60: p. 24-29.
[3] Junaid, M.T., et al., A mix design procedure for low calcium alkali activated fly ash-based concretes. Construction and Building Materials, 2015. 79: p. 301-310.
[4] Davidovits, J. and J.L. Sawyer, Early high-strength mineral polymer. 1985, Google Patents.
[5] Davidovits, J., Geopolymer cement. A review. Geopolymer Institute, Technical papers, 2013. 21: p. 1-11.
[6] Provis, J. and J. van Deventer, Alkali Activated Materials State-of-the-Art Report, J. Provis and J.S.J. van Deventer, Editors. 2014, RILEM.
[7] Junaid, M.T., A. Khennane, and O. Kayali, Stress-Strain Behaviour of Alkali Activated Fly Ash Concrete at Elevated Temperatures, in 2nd International Conference on Advances in Cement and Concrete Technology in Africa. 2016: Tanzania. p. 301-308.
[8] Rangan, B., Fly ash-based geopolymer concrete. Your Building Administrator, 2008. 2.
[9] Junaid, M.T., O. Kayali, and A. Khennane, Response of alkali activated low calcium fly-ash based geopolymer concrete under compressive load at elevated temperatures. Materials and Structures, 2017. 50(1): p. 50.
[10] 440, A.C. Guide for the design and construction of structural concrete reinforced with FRP bars. 2007. American Concrete Institute.
[11] Institute, A.C., Guide for the Design and Construction of Externally Bonded FRP Systems for Strengthening Concrete Structures, in ACI 440.2R-08. July, 2008, ACI Committee 440.

SynerCrete'18 International Conference on Interdisciplinary Approaches
for Cement-based Materials and Structural Concrete
24-26 October 2018, Funchal, Madeira Island, Portugal

HYBRID ALKALI-ACTIVATED PORTLAND CEMENTS

Lukáš Kalina [(1)], Vlastimil Bílek Jr. [(1)], Lada Bradová [(1)], Radoslav Novotný [(1)], Tomáš Opravil [(1)], František Šoukal [(1)]

(1) Brno University of Technology, Materials Research Centre, Brno, Czech Republic

Abstract
The most promising way to improve the sustainability of cement is to produce blended Portland cements with supplementary cementitious materials. Blast furnace slag (BFS) is one of significant pozzolan sources used worldwide in blended cements which contributes to lowering the environmental impact of cement industry. On the other hand, the replacement of Portland clinker is connected with undesirable effects such as the reduction of early strength development. In order to overcome this disadvantage, the study deals with the development of hybrid cements in which the utilization of solid waste alkaline activator quickly awakens the pozzolanic properties of BFS. New types of blended alkali activated cements were designed to meet the European standard EN 197-1 and classified to the Blastfurnace CEM III cements in accordance with the mechanical, physical and chemical requirements. The alkali activation caused an increase of early compressive strength in comparison with reference cement and at the same time the initial setting time was delayed which is also interesting from the point of view of concrete production. Moreover, this non-traditional hybrid alkali-activated Blastfurnace cement provides considerable ecological and economical potential.

1. Introduction

The cement industry is one of the most carbon-intensive industries required to produce Portland clinker which is the key component of ordinary Portland cement (OPC). The industry predicts that the global cement production will reach 5.9 billion tons by 2020 which represents more than 4.8 Gt of CO_2 emissions [1]. The global approach to reducing the carbon footprint of cement includes several options. Firstly, the alternative fuels and/or raw materials should be used. Further the replacement of Portland clinker with supplementary cementitious materials (SCMs) is suggested. The development of alternative binders not based on Portland clinker represents the third option and finally the capture of CO_2 emitted by cement plants

could be another solution [2]. In most parts of the world, the utilization of SCM is particularly advantageous, especially if the "low-carbon" materials such as industrial waste products are used. Blast furnace slag (BFS), a by-product from pig iron production, or fly ash from coal combustion provide a viable way to substitute Portland clinker [3]. On the other hand, blended cements with high content of SCMs can slow down the early strength development which represents considerable drawback in practical applications [4]. Apart from low clinker content, one of the potential solutions is the production of new cement binders, like hybrid alkaline cements. Hybrid alkali-activated Portland cements aim at combining the positive characteristics of traditional OPC materials with those of alkali-activated materials (AAMs), generating materials with enhanced durability and mechanical properties [5]. These facts were also confirmed in the study of Gelevera and Munzer [6] who focused on alkali-activated Portland clinker/BFS blends in which the increase of BFS content in conjunction with alkali silicate solution led to higher compressive strength and frost resistance as well.
The production of hybrid binders can be achieved in two different approaches. The first option is the activation of aluminosilicate materials (mixture of OPC and SCM) with high alkaline solution which is the conventional procedure for AAMs preparation. Whereas the second possibility consists in the production of special type of cement with incorporated alkaline activator mixed in solid form with other cement components. The binder formed in this way provides two major benefits. It can be activated only with water and subjected to certain criteria it can be classified to Blastfurnace CEM III/C cements in accordance with European standard EN 197-1 [7]. Moreover, such developed non-traditional hybrid cement fulfils the ecological and economical aspects due to the utilization of waste alkaline activator. The verification of mechanical, physical and chemical properties of the new type of hybrid alkali-activated Portland cement is the main purpose of this study.

2. Experiment

2.1 Materials and sample preparation

The hybrid alkali-activated Portland cements were composed of Portland clinker (HeidelbergCement Czech Republic, Ltd.), blast furnace slag (ArcellorMittal Ostrava, Ltd.) and dried, milled technological waste from waterglass production (Vodní sklo, Ltd.). The chemical compositions of raw materials are summarized in Tab. 1.

Table 1: Chemical composition (wt. %) of used raw materials as determined using XRF.

	CaO	**SiO_2**	**Al_2O_3**	**Na_2O**	**K_2O**	**MgO**	**SO_3**	**Fe_2O_3**	**TiO_2**	**MnO**
Portland clinker	64.9	20.7	5.4	0.3	0.6	1.3	3.0	3.3	0.3	0.2
BFS	41.1	34.7	9.1	0.4	0.9	10.5	1.4	0.3	1.0	0.6
WG-waste*	0.1	84.2	0.4	14.2	0.2	–	–	0.6	0.3	–

*The waterglass waste (WG-waste) contains 7.89 wt. % of Na_2O and 16.03 wt. % of SiO_2 in soluble fraction determined according to conductometry titration.

The cement samples were designed according to the EN 197-1 standard for Blastfurnace CEM III/C cements. The content of Portland clinker was lowered to the minimum required

quantity (5 wt. %). The rest of binder was formed by BFS, WG-waste and minor additional constituents as shown in Tab. 2. The WG-waste was added to the hybrid cement with given Na_2O/BFS ratio (0.3; 0.6; 0.9 and 1.2), therefore the tested samples were named according to that.

Table 2: Designed compositions of reference and hybrid cements (wt. %).

	REF.	**H-0.3**	**H-0.6**	**H-0.9**	**H-1.2**
Portland clinker	5.00	5.00	5.00	5.00	5.00
BFS	94.34	89.92	86.74	83.78	81.02
WG-waste (additive)	–	4.42	7.60	10.56	13.32
additional constituents	0.66	0.66	0.66	0.66	0.66

2.2 Testing methods

The compressive strengths of cement mortars were determined in accordance with EN 196-1 [8] at 7 and 28 days with w/c = 0.5. The standard siliceous sand was used in the amount of three times higher than the weight of cement. After 24 h of moist curing, the specimens were demolded and cured at 25 °C in water conditions. The initial setting time as well as the expansion were tested in accordance with EN 196-3 [9]. The total content of sulfate, recalculated to SO_3, was obtained using the combustion analyzer (G4 ICARUS HF). The amount of chlorides was measured according to EN 196-21 [10]. Sulfate as well as chloride contents are the chemical requirements for the appropriate type of cement (CEM III). The loss on ignition and insoluble residue were determined according to EN 196-2. The process of hydration mechanism was explained by means of TAM Air isothermal calorimeter (TA instruments) at the temperature of 20 °C.

3. Results and Discussion

3.1 Chemical and physical properties of hybrid cements

Table 3 shows the chemical as well as physical properties of hybrid cements. With respect to the EN 197-1 standard, all hybrid cements meet the requirements for CEM III cement types. The loss on ignition and insoluble residue increased with higher content of alkaline activator mainly due to the siliceous sand present in WG-waste. The amount of insoluble residue with higher WG-waste (samples H-0.9; H-1.2) does not meet the EN 197-1 standard, which could be solved by the addition of effective ingredients in the form of fully soluble solid sodium silicate leading to lower the contribution of WG-waste with insoluble siliceous sand. Conversely, the sulfate and chloride content decreased with higher Na_2O/BFS ratio which is related to lower amount of BFS containing these elements. The interesting results could be observed in case of initial setting time. Hybrid cements exhibited significant differences compared to reference sample. It was determined that lower content of alkalis contributed to the acceleration of setting time, however higher content (samples H-0.9; H-1.2) delayed it significantly. This behaviour is closely associated with different hydration mechanism discussed further. The expansion measurements did not show any substantial changes.

Table 3: Chemical and physical characteristics of reference and hybrid cements.

sample	Loss on ignition (≤ 5%)	Insoluble residue (≤ 5%)	Sulfate content as SO_3 (≤ 4%)	Chloride content (≤ 0.1%)	Initial setting time (≥ 75 min)	Expansion (≤ 10 mm)
REF.	0.96	–	0.61	0.031	162	0.9
H-0.3	1.25	2.27	0.58	0.028	158	0.4
H-0.6	1.57	4.74	0.56	0.022	142	0.3
H-0.9	1.68	7.31	0.55	0.022	187	0.2
H-1.2	1.70	8.97	0.53	0.015	324	0.5

The values in italics are the requirements for CEM III cement type according to EN 197-1 standard [7].

3.2 Mechanical properties of hybrid cements

The amount of WG-waste addition plays the key role not only in chemical and physical properties of hybrid cements but also affects the compressive strength development significantly. The percentage comparison of compressive strength between hybrid cements and reference sample is shown in Fig. 1. The results were obtained after 7 and 28 days with regards to prescribed values for early and standard strength as defined in the EN 197-1 standard [7]. It is obvious that the small amount of alkaline activator decreased the compressive strength down to certain limit. Nevertheless, if the Na_2O/BFS ratio rose to 0.9 (sample H-0.9), the compressive strength approached the reference sample. Moreover, the sample H-1.2 exhibited better results in comparison with the reference sample after 7 and 28 days.

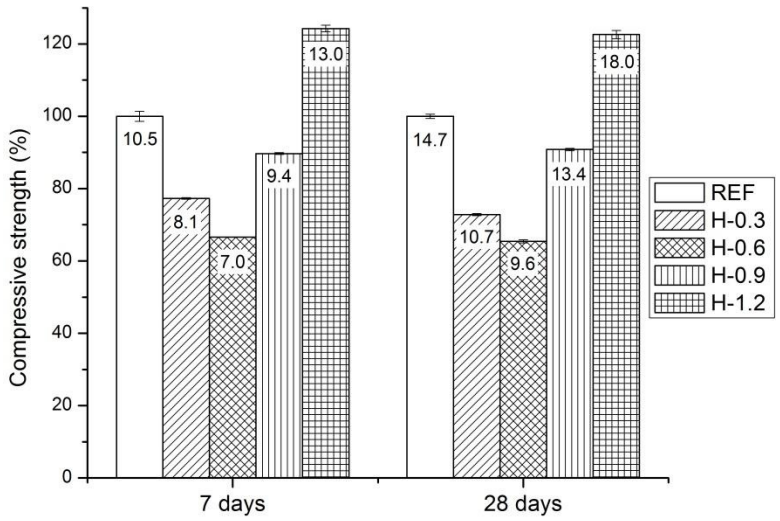

Figure 1: Compressive strength comparison of hybrid cements with reference sample without alkaline activator (values in columns represent the compressive strength in MPa).

3.3 Hydration process of hybrid cements

The hydration process which is closely related to the mechanical properties of cements, is shown in Fig. 2. The calorimetric curves characterizing the heat flow can be observed in Fig. 2A. The first peak (zoomed area) occurring during the first 30 minutes is associated with the wetting and dissolution of BFS and Portland clinker grains. The results suggest that higher content of alkaline activator leads to better dissolution of cementitious particles. Thereafter, the induction period took place. It is well observed that small amount of alkaline activator contained in samples H-0.3 and H-0.6 shortens the induction period. Contrary, higher Na_2O/BFS ratio (H-0.9; H-1.2) delays the C-S-H gel creation in comparison with the reference sample. The total amount of heat evolution (Fig. 2B) is particularly associated with the quantity of C-S-H gel formation. Higher addition of WG-waste resulted in higher amount of C-S-H gel but only in early stages of hydration process. Whereas, the evolution of hydration heat very quickly slowed down in case of hybrid cements, the reference sample exhibited almost linear increase of heat. In other words, it can be expected that the amount of binder phase will be higher in reference sample compared to hybrid cements with lower content of alkaline activator after a long time. These results correspond to compressive strength development after 7 and 28 days when only the sample with the highest WG-waste addition exceeded the values of early and standard strengths of reference sample.

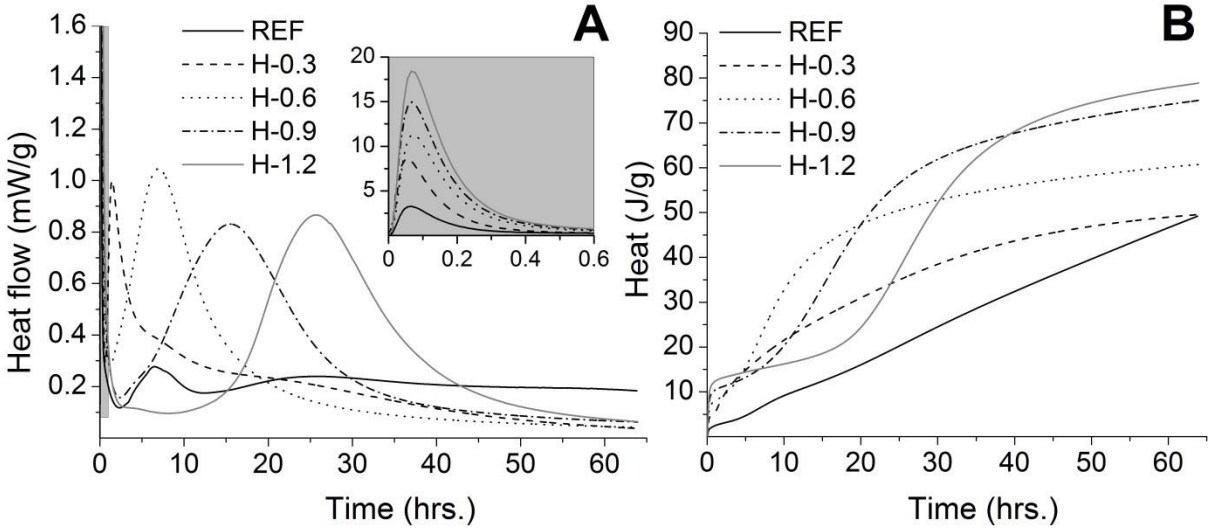

Figure 2: Evolution of heat flow (A) and total heat (B) of hybrid cements and reference sample without alkaline activator.

4. Conclusion

The results show that hybrid cements with alkaline activator in the form of WG-waste are a promising option to reduce the Portland clinker content in cements which contributes to the production of more ecological as well as economical type of cements belonging to CEM III/C class. Especially, the hybrid cements with the weight ratio Na_2O/BFS = 1.2 achieved better mechanical properties in early and long-term ages compared to standard CEM III/C cement.

Acknowledgments
This outcome has been achieved with the financial support by the project: Materials Research Centre at FCH BUT- Sustainability and Development, REG LO1211, with financial support from the National Programme for Sustainability I (Ministry of Education, Youth and Sports) and GA17-03670S "Development of shrinkage reducing agents designed for alkali activated systems", with financial support from the Czech Science Foundation.

References

[1] Gupta, A., Cement Primer Report, Carbon War Room (2011)
[2] Gartner, E. and Hirao, H., A review of alternative approaches to the reduction of CO_2 emissions associated with the manufacture of binder phase in concrete, Cem Concr Res 78 (2015), 126-142
[3] Lothenbach, B. et al, Supplementary cementitious materials, Cem Concr Res 41 (2011), 1244-1256
[4] Donatello, S. et al, The early age hydration reactions of hybrid cement containing a very high content of coal bottom ash, J Am Ceram Soc 97 (2014), 929-937
[5] Rivera, J.F. et al, Hybrid cement based on the alkali activation of by-products of coal, J Construction 13 (2014), 31-39
[6] Gelevera, A.G., and Munzer, K., Alkaline Portland and slag Portland cements. Krivenko, P.V. (ed.) Proceedings of the First International Conference on Alkaline Cements and Concretes, Ukraine (1994), 173-179
[7] EN 197-1:2005, Cement – Part 1: Composition, specifications and conformity criteria for common cements, European committee for standardization, EU (2005)
[8] EN 196-1:2016, Methods of testing cement – Part 1: Determination of strength, European committee for standardization, EU (2015)
[9] EN 196-3:2016, Methods of testing cement – Part 3: Determination of setting times and soundness, European committee for standardization, EU (2016)
[10] EN 196-21:1992, Methods of testing cement. Determination of the chloride, carbon dioxide and alkali content of cement, European committee for standardization, EU (1992)
[11] EN 196-2:2013, Methods of testing cement. Chemical analysis of cement, European committee for standardization, EU (2013)

SynerCrete'18 International Conference on Interdisciplinary Approaches
for Cement-based Materials and Structural Concrete
24-26 October 2018, Funchal, Madeira Island, Portugal

INFLUENCE OF SODIUM HYDROXIDE CONCENTRATION ON MECHANICAL PARAMETERS OF FLY ASH-BASED GEOPOLYMER

Natalia Paszek [(1)], Marcin Górski [(1)]

(1) Silesian University of Technology, Gliwice, Poland

Abstract
Geopolymer is considered to be the new alternative to the ordinary Portland cement concrete. Some of its characteristics surpass OPC concrete parameters. Additionally, it should be emphasised that geopolymer is an environmentally friendly material since it is based mainly on wastes and the CO_2 emission during its production is limited because of lack of the cement in the composition. Geopolymer parameters can be influenced by many factors. In the paper, the influence of NaOH concentration on the compressive and flexural strength of fly-ash based geopolymer is considered. Tests were carried out on right rectangular prism samples made from five mixtures containing fly ash, sodium silicate and sodium hydroxide of varying concentrations: 6, 8, 10, 12 and 14 mol/L. Compressive and flexural strength tests were performed after 7 days. Tests showed that compressive strength generally increases with the increase of NaOH concentration. No obvious dependence between flexural strength and NaOH concentration was found.

1. Introduction

Geopolymer is an aluminosilicate material formed during geopolymerization process by activation of oxides of aluminium and silicon minerals or aluminosilicate minerals by alkalis [1]. The term "geopolymer" was applied firstly by a French material scientist Joseph Davidovits in the early 1980s [2]. According to Davidovits, geopolymeric materials can be treated as "polymers" because of the ability to polycondensate and to adopt the final shape rapidly in the low temperatures. The prefix "geo" stands for the fact that they are hard and resistant materials able to withstand high temperatures [3]. Regularly, when talking about geopolymer, the ecological aspect of the matter is brought up. Geopolymer is considered to be a new alternative binder without cement in the composition which allows for energy and greenhouse gases emission savings. According to different estimations, the CO_2 emission

during geopolymer production can be lowered in comparison to the concrete production by 9% to 80% [4,5]. The gross disparity between estimations results mainly from the different scientific approach to the calculations, different basic assumptions and finally, different meaning of keywords "geopolymer" and "concrete" which hide the versatile range of materials having various compositions. The next reason why geopolymer is considered to be environmental friendly material is the fact that it can be based on industrial and mining wastes. It means that geopolymer production not only does not consume raw materials like limestone, marl or chalk which are used for cement production [6] but also allows for wastes utilisation. Almost every country produces wastes which can state the main component of geopolymer. It means that in nearly each country geopolymer can be a response to the problem of wastes utilisation. Furthermore, production of geopolymer is possible almost everywhere without transport of wastes for long distances what would be senseless from the ecological point of view. Some kinds of wastes are specific for particular parts of the world and cannot be easily found in the others. Portuguese scientists found out that residues which are by-products of the Panasqueira tungsten mine can be effectively used as a precursor in geopolymer concrete [7]. Geopolymer is likewise believed to be the solution for the excess of the oil sand wastes in Canada [1]. In some cases, geopolymer is not only the way of economic and ecological wastes utilisation but also gives a possibility to immobilise toxic substances present in wastes [3,8]. According to this, the necessity of toxic red mud waste utilisation was one of the main reasons why scientists tried to add it to the geopolymer concrete [9].
Fly ash is one of the most popular industrial by-products used as a precursor in geopolymer. Fly ash is produced all over the world and consists mainly of silicon and aluminium oxides what makes it an excellent material for geopolymeric reaction. Nonetheless, it should be emphasised that properties and chemical composition of fly ash can differ in dependence on its source [10]. Consequently, there is no one optimal composition for all fly ash-based geopolymers. Exact parameters of geopolymer containing fly ash from the new source cannot be predicted on the base of literature examples either. Additionally, mechanical characteristics of geopolymer are affected by many factors starting from the choice of exact composition and ending with the curing conditions [10].
The primary goal of the paper is to present the influence of NaOH concentration on the compressive and flexural strength and density of the fly ash-based geopolymer. Fly ash used in the experiment comes from the Polish power plant and is a by-product of the black coal combustion.

1.1 Influence of NaOH concentration on the geopolymer strength – State of Art

Many scientists investigated the influence of sodium hydroxide concentration on the geopolymer strength. Tests results presented in the scientific literature show that impact of NaOH concentration on geopolymer strength cannot be easily predicted since it depends on many factors, mainly on the kind of the precursor.
According to the Wang et al. [11], both compressive and flexural strength of metakaolin-based geopolymer increase with the increase of NaOH concentration. Prepared mixtures contained metakaolin, sodium silicate and sodium hydroxide in concentrations: 4, 6, 8, 10 and 12 mol/L. The most significant increase in compressive strength was noticed between samples activated by NaOH of 8 and 10 mol/L. The increase in flexural strength was approximately monotonic. The similar dependence was also noticed by Stevenson 2005 [12]. In that experiment differences between results of samples containing NaOH of different

concentrations were more significant. The compressive strength of samples made of mixture activated with NaOH of concentration 10 mol/L was over 5 times greater than of concentration 7 mol/L. The compressive strength of samples containing NaOH of concentration 12 mol/L increased once more about 1,5 times.
As it was proved by tests, the influence of NaOH concentration on the compressive strength of fly ash-based geopolymers is depended on the sodium silicate to NaOH ratio. Sathonsaowaphak et al. 2009 [13] compared results obtained on samples activated by sodium silicate and NaOH mixed in ratios 1,5 and 0,67. Concentrations of NaOH were equal to: 5; 7,5; 10; 12,5 and 15 mol/L. In the first case (sodium silicate to NaOH ratio equal to 1,5), the monotonic increase of compressive strength from about 18 MPa to 35 MPa was registered. All samples activated by sodium silicate and NaOH in ratio 0,67 obtained higher compressive strengths, but the influence of NaOH concentration was not monotonic this time. Firstly, there was registered a significant increase in compressive strength between samples activated with NaOH of concentration 5 and 7,5 mol/L. Then, the compressive strength decreased slightly for samples activated with NaOH of concentration 10 mol/L, increased for next part (NaOH concentration 12,5 mol/L) and decreased again.
The similar experiment was conducted by Chindaprasirt et al. 2007 [14]. The lignite fly ash-based geopolymer was activated by a mixture of sodium silicate and sodium hydroxide at concentrations 10, 15 and 20 mol/L. In case of samples containing sodium silicate and sodium hydroxide mixed in ratios 1,0 and 3,0, the compressive strength increased with the increase of NaOH concentration. Samples activated with sodium silicate mixed with NaOH in ratio 0,67 obtained the same compressive strength for NaOH concentrations 10 and 20 mol/L and higher strength for NaOH concentration 15 mol/L. Almost opposite dependence was registered for samples containing 1,5 times more sodium silicate than NaOH.
Another experiment performed on fly ash-based geopolymer activated only by sodium silicate this time was presented by Alvarez-Ayso et al. 2008 [15]. During the test, fly ash was mixed with NaOH of concentrations 5, 8 and 12 mol/L. The experiment showed that compressive strength increases significantly with the increase of NaOH concentration.
On the contrary to examples showed above, geopolymer based on the waste glass powder from crushed glass bottles achieves higher compressive strength for smaller NaOH concentrations [16].

2. Laboratory tests

The main goal of the laboratory tests was to establish the influence of NaOH concentration on flexural and compressive strength and the density of fly ash-based geopolymer. The flexural strength test was conducted on right rectangular prism samples of dimensions 4x4x16cm. Compressive strength test was carried out on halves of samples broken during the flexural strength test according to the European standard EN 196-1:2016 [17].

2.1 Mixture composition

Each mixture contained the same components used in the same quantity. The exact mixture composition is presented in Tab. 1. Fly ash was the only one precursor. Sodium silicate and sodium hydroxide were used in a role of activators. The only variable was the NaOH

concentration. There were prepared five mixtures containing NaOH of concentrations 6, 8, 10, 12 and 14 mol/L.

Table 1: Mixture composition.

	Fly ash	Sodium silicate	Sodium hydroxide
Quantity [kg/m^3]	1133	664	219
Contribution [%]	56,2	32,9	10,9

2.2 Samples preparation

Mixtures activated by NaOH of different concentration were prepared separately. Sodium hydroxide solution was prepared 24 hours before mixtures preparation by dissolving sodium hydroxide in solid form in demineralized water. The procedure for samples preparation was the same for all mixtures. Sodium hydroxide was mixed with sodium silicate by 5 minutes and then poured into the vessel with the fly ash. All components were mixed with a mechanical mixer. The mixture was placed into forms, covered and kept in the climatic chamber for 24 hours in the temperature of 60°C and humidity of 40%. After 24 hours samples were demoulded and kept at the room temperature for the next 6 days.
Curing regime was chosen on the base of experience taken from literature. Both curing time and curing temperature has an influence on mechanical properties of geopolymer. Many scientists believe that 60°C is the optimal curing temperature [18,10].

2.3 Test results

Compressive and flexural strength test results are presented respectively in Fig. 1 and Fig. 2.

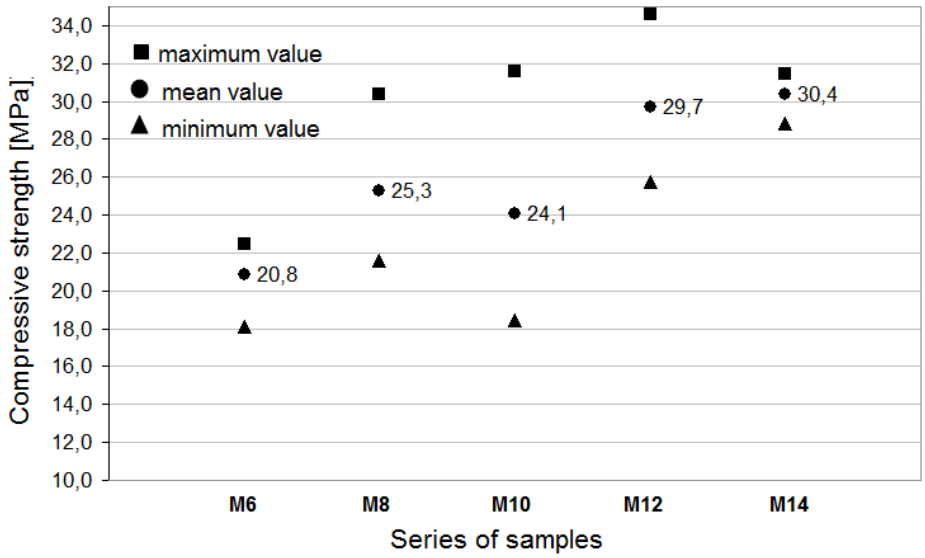

Figure 1: Compressive strength of geopolymer samples after 7 days.

The conducted test showed that compressive strength of fly ash-based geopolymer increase with the increase of NaOH concentration. The only exception is the compressive strength of samples containing NaOH of concentration 10 mol/L which average value is slightly smaller than the average compressive strength of samples activated with NaOH of concentration

8 mol/L. Additionally, results of samples activated with NaOH of concentration 10 mol/L had the most significant standard deviation. The highest compressive strength was obtained by samples activated with NaOH of concentration 14 mol/L. The standard deviation of these results was smallest.

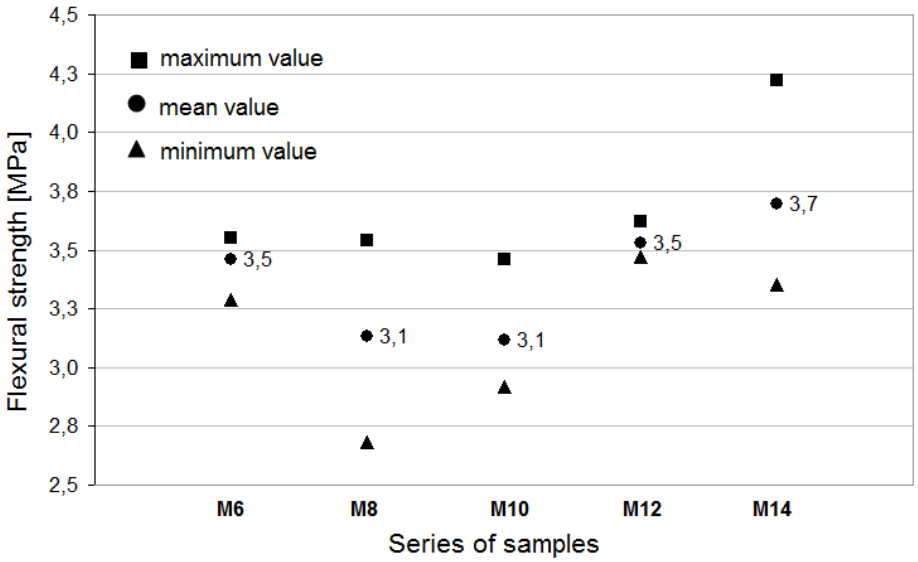

Figure 2: Flexural strength of geopolymer samples after 7 days.

No obvious connection between NaOH concentration and flexural strength was registered. The highest flexural strength was observed for series of samples M14 but also the most significant standard deviation for these results was registered.
No dependence between NaOH concentration and density of fly ash-based geopolymer samples were registered either. Differences between densities of samples from different series were small. Average value of all densities was equal to 1720 kg/m^3. This is relatively low value in comparison to the density of cement mortar.

3. Summary

During the experiment, the influence of NaOH concentration on flexural and compressive strength and density of geopolymer was investigated. Test results showed that compressive strength of examined fly ash-based geopolymer generally increases with the increase of NaOH concentration. The highest compressive strength was obtained by samples containing NaOH of concentration 14 mol/L and the smallest by samples containing NaOH of concentration 6 mol/L. No straight dependence between flexural strength and NaOH concentration was registered. Similarly, due to the test results, the density of geopolymer is not connected with NaOH concentration.

Acknowledgements
REMINE H2020-MSCA-RISE, support of the Polish Ministry of Science and Higher Education for Department of Structural Engineering, Silesian University of Technology (Grant No. BK-237/RB6/2018) and project 341284/PnH /2016

References

[1] Rao, F. and Liu, Q., Geopolymerization and its Potential Application in Mine Tailings Consolidation: A review, Min Proc Ext Met Rev 36 (2015), 6
[2] Provis J. L. and van Deventer J. S. J., Alkali Activated Materials. State-of-the-Art Report, RILEM TC 224-AAM, London (2014)
[3] Davidovits, J., Geopolymers: Inorganic polymeric new materials, J Therm Anal Calorim 37 (1991), 1633-1656
[4] Tuner, L. and Collins, F., Carbon dioxide equivalent (CO2-e) emissions: A comparison between geopolymer and OPC cement concrete, Constr Build Mater 43 (2013), 125-130.
[5] von Weizsacker, E., Hargroves, K., Smith, M. H., Desha, C. and Stasinopoulos, P., Factor Five: Transforming the Global Economy Through 80% Improvements in Resource Productivity, Earthscan, London (2009)
[6] Neville, A., Właściwości betonu, Kraków (2000)
[7] Pacheco-Torgal, F., Castro-Gomes, J. and Jalali, S., Tungsten mine waste geopolymeric binder: Preliminary hydration products investigations, Constr Build Mater 23 (2009), 200-209
[8] Boca Santa, R. A. A., Soares, C. and Riella, H. G., Geopolymers with a high percentage of bottom ash for solidification/immobilization of different toxic metals, J Hazard Mater 318 (2016), 145-153
[9] Toniolo, N., Rincon, A., Avadhut, Y. S., Hartmann, M., Bernardo, E. and Boccaccini, A. R., Novel geopolymers incorporating red mud and waste glass cullet, Mater Lett 219 (2018), 152-154
[10] Hardjito, D. and Rangan, B. V., Development and properties of low-calcium fly ash-based geopolymer concrete. Research Report GC 1 Faculty of Engineering Curtin University of Technology, Perth (2005)
[11] Wang, H., Li, H. and Yan, F., Synthesis and mechanical properties of metakaolinite-based geopolymer, Colloids Surf, A Physicochem Eng Asp 268 (2005), 1-6, 2005
[12] Steveson, M., Relationships between composition, structure and strength of inorganic polymers. Part I: Metakaolin-derived inorganic polymers, J Mater Sci 40 (2005), 2023-2036
[13] Sathonsaowaphak, A., Chindaprasirt, P. and Pimraksa, K., Workability and strength of lignite bottom ash geopolymer mortar, J Hazard Mater 168 (2009), 44-50
[14] Chindaprasirt, P., Chareerat, T. and Sirivivatnanon, V., Workability and strength of coarse high calcium fly ash geopolymer, Cement Concrete Comp 29 (2007), 224-229
[15] Alvarez-Ayso, E., Querol, X., Plana, F., Alastuey, A., Moreno, N., Izquierdo, M., Font O., Moreno, T., Diez, S., Vazquez, E. and Barra, M., Environmental, physical and structural characterization of geopolymer matrixes synthesised from coal (co-)combustion fly ashes, J Hazard Mater 154 (2008), 175-183
[16] Pascual, A. B., Tognonvi, M. T. and Tagnit-Hamou, A., Waste glass powder-based alkali-activated mortar, Int J Res Eng Technol 3 (2014), 15-19
[17] EN 196-1:2016, Method of testing cement – Part 1: Determination of strength, Brussels (2016)
[18] Bing-hui, M., Zhu, H., Cui, X. M., He, Y. and Gong, S. Y., Effect of curing temperature on geopolymerization of metakaolin-based geopolymers", Appl Clay Sci, 99 (2014), 144-148

SynerCrete'18 International Conference on Interdisciplinary Approaches
for Cement-based Materials and Structural Concrete
24-26 October 2018, Funchal, Madeira Island, Portugal

INVESTIGATION ON STRENGTH DEVELOPMENT IN GEOPOLYMER MADE OF POWER PLANT FLY ASH SUSPENSION

Szymon Dawczyński [(1)], Anita Kajzer [(1)], Marcin Górski [(1)]

(1) Silesian University of Technology, Gliwice, Poland

Abstract
In general, the geopolymers have potential to compete with cement-based materials because of their good mechanical parameters as well as because they are considered as environmentally friendly materials. It is not only because of the reduction of carbon dioxide during the production process (which reduces greenhouse effect) but also because of a large amount of industrial wastes (like fly ashes, mine tailings or metallurgical slags) which are consumed. Paper presents laboratory investigation on geopolymeric binder made of fly ash suspension, metakaolin, and recycled ground glass. The geopolimerisation reaction was activated with the use of a 10M solution of sodium hydroxide mixed with sodium silicate. The researches were focused on strength development in the first two weeks just after the day when samples were prepared. The curing time in the climatic chamber was 24 hours in a temperature of 60°C and humidity 40%. The prism samples 40x40x160 mm were used for flexural strength tests and halves of broken prisms were used for compression strength tests. These tests were performed after 1, 3, 7 and 14 days after samples preparation. In both cases, it was noted that the strength was increased with the increasing of curing time (in case of flexural strength from 1.29 to 2.58 MPa, and in case of compressive strength from 19.05 to 21.99 MPa).

1. Introduction

Nowadays, concrete is the most frequently used structural material all over the World. This is obvious due to its very good strength parameters, good performance, and durability, as well as the relatively low cost of production. From the ecological point of view, the most significant disadvantage of concrete is the fact that during the production process of cement (a key ingredient of concrete), a significant amount of carbon dioxide is released to the atmosphere. This is the result of two issues: first one is related to decomposition of $CaCO_3$ (limestone) into

CaO (lime) and CO_2 by providing the heat, and the second one is associated with the combusting of fossil fuels in order to obtain the energy necessary to ensure the correct course of the clinker burning process (the required temperature may reach even up to 1500°C) [1]. Unfortunately, every percent of this harmful gas released into the atmosphere contributes to poisoning the environment and climate change, which affects our lives directly. More detailed information about CO_2 emission from cement production can be found in [2], and in general about global emission in [3, 4]. Taking into consideration the carbon dioxide emission, as well as the need for natural resources, the possibility of replacing concrete with other, more environmentally friendly material is very attractive. Such an alternative may be geopolymers or in general alkali-activated materials (AAM). From the mechanical point of view, geopolymers have similar strength properties as ordinary concrete has [5]. However, interesting is that they also have other features that far outweigh cement-based materials. One of them is high-temperature resistance. Davidovits tests [6] showed that geopolymers composed of metakaolin, sodium, and potassium silicate were able to withstand the temperature even up to 1400°C. They are also more heat-stable than concrete – the binding water which builds up vapour pressure in the event of fire results in spalling or cracking. Depending on the mix composition, a temperature that can withstand varies between 800-1400°C. Also, another interesting fact – geopolymers are highly resistant to chemicals like acids, chlorides, and sulphates. Ready products that contain metakaolin or fly ash exhibit high resistance to sulphuric acid, nitric and hydrochloric acids in comparison to OPC concrete. The tests [7] indicated that geopolymers activated with sodium hydroxides had better resistance than those activated with a solution of sodium silicate.
Even though the geopolymers are known for several dozen years, still there are no standards or formal regulations regarding their structural use as well as designing and testing procedures. This paper presents laboratory tests focused on strength development in time, as a contribution to the complex description of these materials.

2. Mixture and samples preparation

Geopolymers are obtained as a product of the chemical reaction between aluminosilicate material (precursor) and alkaline solution (activator). Some additions are often added to the mixture to improve the geopolymer properties. There are many possibilities in proportioning of components in dependence on what result we expect or what is our primary aim.

2.1 Precursor

The precursor used in this mixture is a carbon suspension. It is fly ash obtained from Bełchatów Power Plant – the largest brown coal power plant in the world. The power plant is located in the central part of Poland, and it is the largest emitter of carbon dioxide in this country. The fly ash suspension is an ash/dust depositing on electrofilters in huge boilers which is a product of burning brown coal. This fly ash is extremely fine material, what makes that it has higher reactivity. This feature is essential to the geopolymerization process.
The fuel that is used for energy production is brown coal from a nearby open-cast mine. The most important effect of the power plant's operation is the emission of a large amount of pollutants like: sulphur dioxide, nitrous oxide, carbon monoxide and ashes. For this reason, four-chamber electrofilters were installed in every block. The ash is captured by electrofilters,

then it is transmitted through the pipeline system into the reservoir, and finally, it is transmitted to special humidifiers. In the next step, it is served to the mine excavation by conveyor belt.
Because of the volume of produced wastes, the fly ash from those electrofilters was chosen to be the primary product of the mix to prepare geopolymer samples. An additional advantage is the fact that if more fly ash is used in the mixture, the volume of metakaolin can be reduced. A large amount of metakaolin in the mix results in higher energy consumption which is another problem of this type of mixtures.
The exact composition of fly ash suspension from Bełchatów Power Plant is shown in Tab. 1.

Table 1: Oxide composition of fly ash suspension.

Oxides	**Mass (%)**
SiO_2	39.56
CaO	23.45
Al_2O_3	20.05
SO_3	7.27
Fe_2O_3	5.72
TiO_2	1.83
MgO	1.54
Na_2O	0.42
K_2O	0.17

2.2 Activator

The combination of sodium hydroxide and sodium silicate was used as a chemical activator of the geopolymerisation reaction. Pellets for preparation of the NaOH solution had 99.5% of purity and molar mass equal to 40 g/mol. As a combination of these pellets and demineralized water, it was obtained a solution with the concentration of 10M. The sodium silicate was the R-145 type with the purity higher than 99%. The molar ratio was between 1.6 and 2.6, while the density was about 1.45 g/cm^3. The ratio of sodium silicate to sodium hydroxide was equal to 2.0.

2.3 Additives

The carbon fly ash suspension was combined with recycled ground glass and metakaolin. The ground glass in powder form was obtained as a result of crushing glass bottles in Los Angeles machine. The percentage share of the solid precursor in the mixture was about: carbon fly ash suspension 80%, recycled ground glass 10% and metakaolin 10%.

2.4 Mixture

The exact mass of all components was weighed with a laboratory scale with the accuracy of 1.0 mg. All dry components were mixed, and then the precursor and activator were combined

and mixed. The ratio of precursor to activator was equal to 1.0, while the ratio of precursor to sodium silicate was equal 1.5.
The fresh geopolymeric mixture was cast in a mould made of Plexiglas (PMMA) because it is characterized by high alkaline reaction so it might react with steel. All the samples were tightly covered because previous studies [8] have shown that it may influence the strength properties and it prevents the shrinkage cracking in the top layer of the samples. In the next step, the mould was placed in the climatic chamber with a constant temperature of 60°C and humidity 40%. The higher temperature of curing usually influences positively on final mechanical properties (both flexural and compression strength) [9] because it accelerates the geopolimerisation reaction. The exact curing temperature which has the most favourable consequences on the final strength of geopolymers was checked during the laboratory investigation [8]. All samples were prepared exactly in the same way and from the same mixture and then put into the climatic chamber for 24 hours. After the first day of heat curing, samples were put in the ambient temperature (20°C) up to the day of testing.

3. Test results

In case of cement-based materials, the tests are usually carried out 28 days after the samples preparation. However, because there are no geopolymer standards and test procedures at the moment, it cannot be explicitly stated what the optimal time for testing the strength properties is. For this reason, the impact of time (from the moment of samples preparation to the time of conducting test) on strength parameters, was examined in this paper. The tests have been made on the basis of the standard procedures described in [10]. The flexural strength, as well as the compression strength, were investigated after 1, 3, 7 and 14 days from the moment when the samples were made.

3.1 Flexural strength test

It was the regular three-point flexural test with the span length between the supports equal to 100mm. The load was applied on the upper surface of the sample, in the middle of the span length. An example of the failure of the geopolymer sample is shown in the Fig. 1 left. While in Fig. 2 there are presented average values of bending strength for each set of samples.

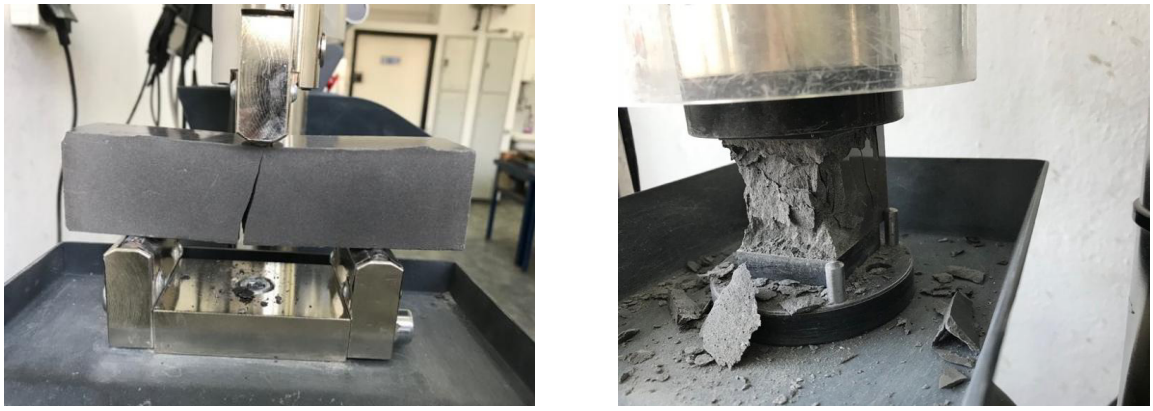

Figure 1: Left: an example of the flexural failure, Right: an example of compression failure.

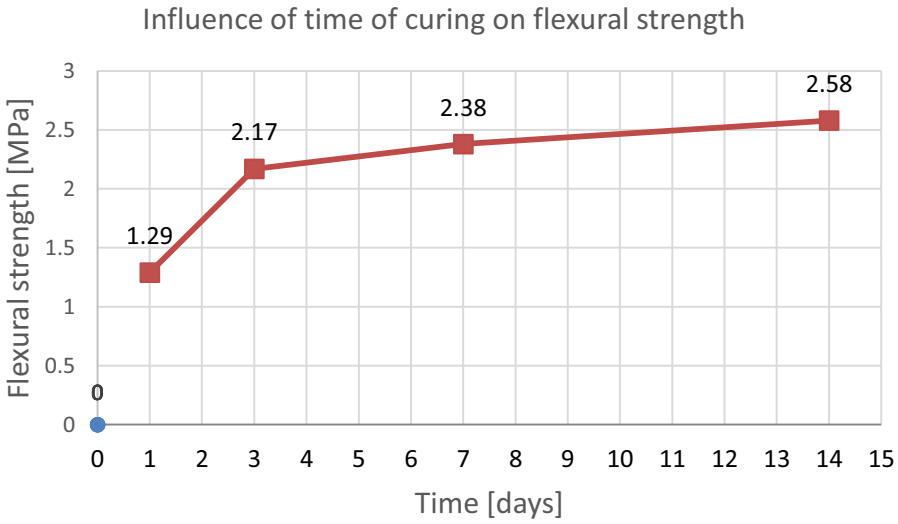

Figure 2: Results of three-point bending test.

3.2 Compression strength test

An example of the compression failure of the geopolymer sample is shown in the Fig. 1 right. The values of compression strength were determined from the destructive forces magnitudes. The results of those tests are presented in Fig. 3.

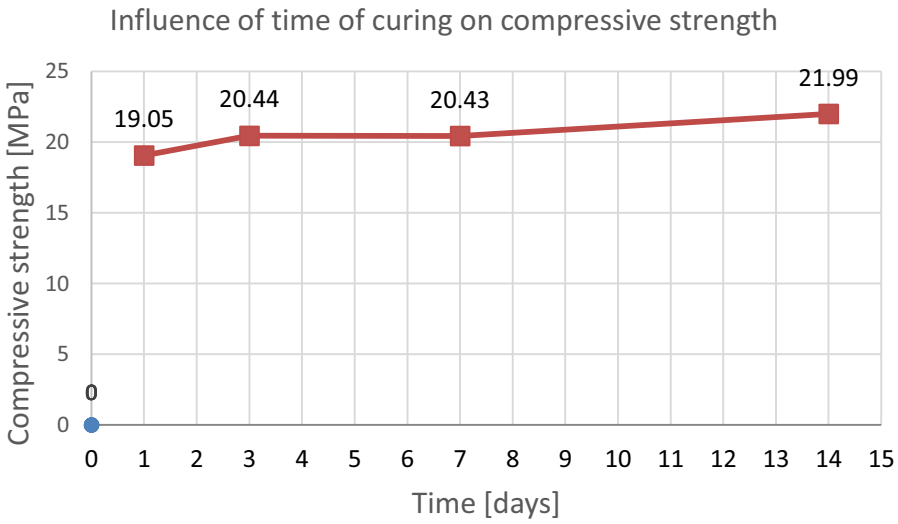

Figure 3: Results of the compression test.

4. Final remarks

Geopolymers are a broad group of materials with good mechanical properties. In case of flexural strength, it could be observed that with the increasing of curing time also the strength

increased. The most significant increase was observed between 1st and 3rd day – the growth has reached over 68%. Between 3rd and 7th day (the period was twice larger), the growth was equal to 9.7%. While in the last period – between 7th and 14th day – the flexural strength growth was only 8.4%. Of course, also it would be interesting to know the strength value after 28 days (like in the case of cement-based materials), but these tests are still ongoing.
In case of compressive strength results, it can be observed that in two periods – between 1st and 3rd day and between 7th and 14th day – the strength increase in relative terms was equal 7.3% and 7.6%, but in absolute values, it was only 1.39 MPa and 1.56 MPa respectively.
The presented results indicate that structural behaviour of geopolymers is different from the structural behaviour of any other cement-based materials.
Cement is still the most - known and used material in the world. Especially in the construction industry. However, geopolymers have the potential to compete with those products due to their good mechanical, psychical and chemical properties. The most important feature of this material is the possibility of using the industrial wastes as well as the reduction of CO_2 emission. Its environmentally friendly performance is very much needed nowadays.

Acknowledgement
This paper has been prepared with the financial support of the Silesian University of Technology (BK-235/RB6/2017); European Union's Horizon 2020 Research and Innovation Staff Exchange (RISE) programme (Marie Skłodowska-Curie Actions) under grant agreement no. 645696, project REMINE (Reuse of Mining Waste into Innovative Geopolymeric-based Structural Panels, Precast, Ready Mixes and Insitu Applications) and Polish Ministry of Science and Higher Education project no. 341284/PnH /2016.

References
[1] Crow, J.M., The concrete conundrum, Chem. World March (2008), 62-66
[2] Andrew, R. M., Global CO_2 emissions from cement production, Earth Syst. Sci. Data 10 (2018), 195-217
[3] Le Quéré, C. et al., Global Carbon Budget 2016, Earth Syst. Sci. Data 8 (2016), 605-649
[4] Le Quéré, C. et al., Global Carbon Budget 2017, Earth Syst. Sci. Data 10 (2018), 405-448, in review
[5] Dawczyński, S., Górski, M., Krzywoń, R., Geopolymers as an alternative ecological material for buildings, Proceedings of the 14th International Conference on New Trends in Statics and Dynamics of Buildings, Slovakia (2016), 374-378
[6] Davidovits, J., Geopolymers – Inorganic polymeric new materials, Jour. of Therm. Anal. 37 (1991), 1633-1656
[7] Provis, J.L., van Deventer, J.S.J., Alkali Activated Materials, Springer (2014)
[8] Dawczyński, S., Soczyński, M., Górski, M., Feasibility and strength properties of the geopolymeric binder made of fly ash suspension, 64 Scientific Conference Krynica Zdrój, Poland (2018), in review
[9] Adam, A.A., Horianto, The effect of temperature and duration of curing on strength of fly ash based geopolymer mortar, Proc. Engin. 95 (2014), 410-414
[10] PN-EN 1015-11:2001: Methods of test for mortar for masonry – Part 11: Determination of flexural and compressive strength of hardened mortar, Poland (2001)

SynerCrete'18 International Conference on Interdisciplinary Approaches
for Cement-based Materials and Structural Concrete
24-26 October 2018, Funchal, Madeira Island, Portugal

SELF-SENSING PROPERTIES OF ALKALI-ACTIVATED SLAG COMPOSITE WITH CARBON NANOTUBES

Pavel Rovnaník [(1)], Maria Míková [(1)], Ivo Kusák [(1)], Pavel Schmid [(1)], Libor Topolář [(1)]

(1) Brno University of Technology, Brno, Czech Republic

Abstract
Conductive concrete is produced by addition of conductive filler to ordinary concrete. Electrically conductive concrete allows analysing stress and strain variation in structures by means of resistivity measurements. The study of self-sensing properties of conductive concrete is now of great importance to its application in civil engineering. Since there is very limited information about electrical properties of alkali-activated materials as alternative binders to Portland cement, this paper presents the study on basic electrical and self-sensing properties in compression of alkali-activated slag composite with carbon nanotubes as conductive filler. The results showed that addition of carbon nanotubes reduced the electrical resistance of alkali-activated slag, however, it did not improve its sensing properties.

1. Introduction

Development of multifunctional materials is within the scope of many researchers in order to fulfil the demand for smart structures. Among these functionalities, strain and damage sensing, heating control, absorption of electromagnetic waves or weight control of moving objects can be mentioned. A certain level of conductivity is necessary in order to achieve these functional properties of structural composites, and for this reason, conductive admixtures are usually added [1]. Despite the fact that much effort was already devoted to design, observations and utilization of electrically enhanced cement-based materials that can be used as smart materials, there does not exist any complex research focused on alkali-activated materials enhanced in such way.
The present study aims to investigate the self-sensing properties of alkali-activated slag (AAS) mortars with multi-walled carbon nanotubes (MWCNTs) as conductive admixtures under compressive loading. The results are compared to reference AAS mortar without MWCNTs treated under the same conditions. This work relates to our previous study that

analysed the influence of MWCNTs on the electrical properties of AAS without mechanical loading [2].

2. Experimental part

2.1 Materials

The alkali-activated slag was composed of granulated blast furnace slag supported by Kotouč, s.r.o. (CZ) finely ground to the specific surface of 383 m^2/kg with the mean particle size of 15.5 μm and solid sodium silicate Susil MP 2.0 (Vodní sklo, CZ) as an activator. Quartz sand with a maximum grain size of 2.5 mm was used as aggregate. MWCNTs were added in the form of well-dispersed aqueous dispersion containing 1 wt.% of MWCNTs (Graphistrengths CW 2-45, Arkema, France). In order to prepare the aqueous dispersions, the procedure prescribed by the producer was followed. MWCNT pellets were dissolved in hot water and dispersed bundles of MWCNTs were further disintegrated by a mechanical homogenizer (3 h at 14000 rpm).

Alkali-activated slag was prepared according to the following procedure. Sodium silicate activator was suspended and partially dissolved in water. Since no additional water is used in case of CNT 0.4 mixture, sodium silicate was dissolved directly in the dispersion of MWCNTs. Then, slag and quartz aggregate were added and the mixture was stirred in a planetary mixer for about 5 min to prepare a fresh mortar. Finally, additional water or dispersion of MWCNTs was mixed into fresh alkali-activated slag mortar. The composition of mixtures is presented in Tab. 1.

Table 1: Mixture proportions

	REF	CNT 0.1	CNT 0.4
Slag (g)	600	600	600
Susil (g)	120	120	120
Sand (g)	1800	1800	1800
1% MWCNTs (g)	0	60	240
Water (mL)	240	180	0

Investigation of self-sensing properties was performed on 100 × 100 × 100 mm cubes with embedded gauze electrodes. The electrodes were made of copper having the wire thickness of 1 mm and the mesh size of 2.5 mm. The size of the electrodes was 80 × 120 mm and the span between electrodes was 40 mm.

After 24 h the hardened specimens were immersed in a water bath at 20 °C for another 27 days. The cubes for the measurement of sensing properties were stored at ambient conditions for 30 days before testing in order to reach moisture equilibrium.

2.2 Methods

Prepared prismatic samples were characterized by impedance spectroscopy in the range of 40 Hz to 1 MHz using sinusoidal signal generator Agilent 33220A and dual-channel oscilloscope

Agilent 54645A [3]. The output voltage of the signal generator was 5.5 V. Input values of electrical capacity and resistance of oscilloscope were 13 pF and 1 MΩ, respectively. These instruments were assembled for fully automated measurement. In order to perform impedance analysis, the prismatic specimens were placed between parallel brass electrodes (30 × 100 mm) with the distance of 40 mm.
Measurement of sensing properties during compressive load was carried out on a FORM+TEST Prüfsysteme hydraulic testing machine with the measuring range 0–3000 N. The cubic specimens were loaded perpendicular to the plane of the Cu-electrodes (Fig 1). In the experiment, cyclic loading and releasing of the samples was performed linearly with loading rate 400 N s^{-1} and in the range 5–50 kN which corresponds to approx. 8% of the maximum compressive stress. Finally, in the last experiment, these cubes were loaded linearly with loading rate 200 N s^{-1} up to failure.

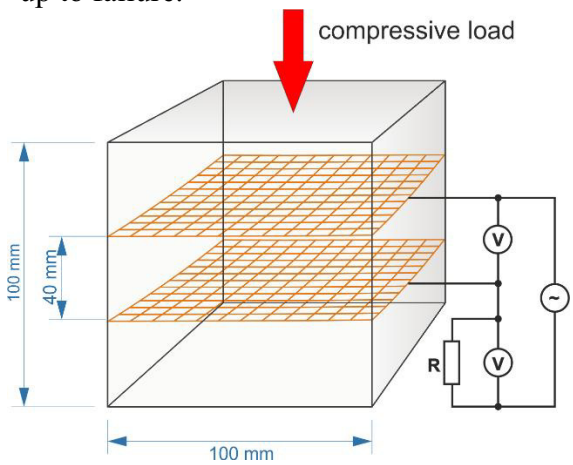

Figure 1: Experimental configuration during the compressive loading tests

For the measurement of electrical resistance of loaded samples in AC field, a sinusoidal signal generator Agilent 33220A and two multimeters Agilent 34410A were used. These appliances were arranged according to the scheme (Fig. 1) and connected via USB hub to the computer for fully automated measurement. The frequency of AC field was 1 kHz and voltage of the sinusoidal generator was 5 V. The electrical current was calculated from the voltage measured on one of the voltmeters and the reference resistance R which was exactly 6796 Ω. The electrical resistance of the measured sample was computed from the electric current flowing through the exact resistance R and the voltage that was measured separately on the test sample using Ohm's law and taking into account the internal resistance of the voltmeter.
The universal measurement and diagnostic system DAKEL-XEDO© (ZD Rpety-Dakel company) was used for the acoustic emission (AE) measurements. The guard sensors eliminated noise that is generated from outside the area of interest. In this work, three acoustic MIDI emission sensors (type IDK-09) were used, all having identical frequency range and being attached to the surface by beeswax.

3. Results and discussion

Self-sensing properties of building materials stem from the change of conductive network inside composites, so the change in resistivity is able to characterize the sensing behaviour.

For this purposes, the fractional change in resistivity (FCR) is used as a relative measure to describe self-sensing properties under different loading conditions. It can be calculated as follows:

$$FCR\ (\%) = \frac{R - R_0}{R_0} \cdot 100 \quad (1)$$

where R is electrical resistance and R_0 is the initial electrical resistance. The initial resistance of AAS composite decreased with increasing content of MWCNTs (Tab. 2), which is in accordance with previously reported work [2].

Table 2: Initial electrical resistance of AAS composites

	REF	CNT 0.1	CNT 0.4
R_0 (Ω)	18700	12880	8800

In order to compare the self-sensing properties of alkali-activated slag and cement mortars, cubic specimens with embedded Cu-electrodes were subjected to repeated compressive loading at a fixed maximum of 5 MPa. This range fits into the elastic part of loading and does not cause any irreversible changes in microstructure. Totally ten loading cycles were accomplished in order to collect enough data of electrical resistance. The curves drawn in Fig. 2a show the response of electrical properties, which are expressed as fractional change in resistivity, to the applied compressive load. As the compressive stress increases the electrical resistance decreases, which is in accordance with other studies reported for the cement based composites with conductive filler [4, 5–7]. During compressive loading, the resistance decreased due to the healing of microcracks and defects formed by drying shrinkage. During unloading, it increased due to defect aggravation. Alkali-activated slag shows the fractional change in resistivity of 2.1% during repeated loading with the amplitude of 45 kN and the baseline signal is very stable for selected conditions. Although MWCNTs decrease resistivity of AAS matrix, self-sensing properties of AAS composites with MWCNTs appeared to be similar to those observed for the reference AAS mortar. The fractional change in resistivity was only 1.2% for the composite with 0.1% of MWCNTs and 2.6% for the composite with 0.1% of MWCNTs. The baseline signal of these two composites continuously increased, which was more obvious for the mixture with higher nanotubes content. This effect was reported also for a cement mortar during repeated loading and is attributed to its irreversible damage [5].

Fig. 2b shows the fractional change in resistivity during compressive loading till failure. The FCR of reference AAS mortar is quite extraordinary because it has a local maximum. At first, the resistance linearly decreased up to 6 MPa but then it increased again and reached its maximum at 24 MPa. In the range 14–35 MPa the resistance even exceeded the reference value but with higher compression, it gradually decreased up to failure, at which it increased abruptly. Sudden increase in resistance is caused by interruption of conductive routes at the failure point and this behaviour has already been reported for conductive cement composites [4]. Such behaviour is probably caused by the formation of some preliminary defects under compression causing an opening of microcracks and partial destruction of conductive routes which results in the increase of electrical resistance. When the monotonous compression

proceeds the conductive routes are reconstructed due to defect healing and the electrical resistance decreases again till failure. There is no significant difference between curves recorded for the reference AAS mortar and AAS composites with MWCNTs. However, the increase in FCR starts at lower compressive stress and the local maximum is higher and closer to the beginning compared to reference mortar.

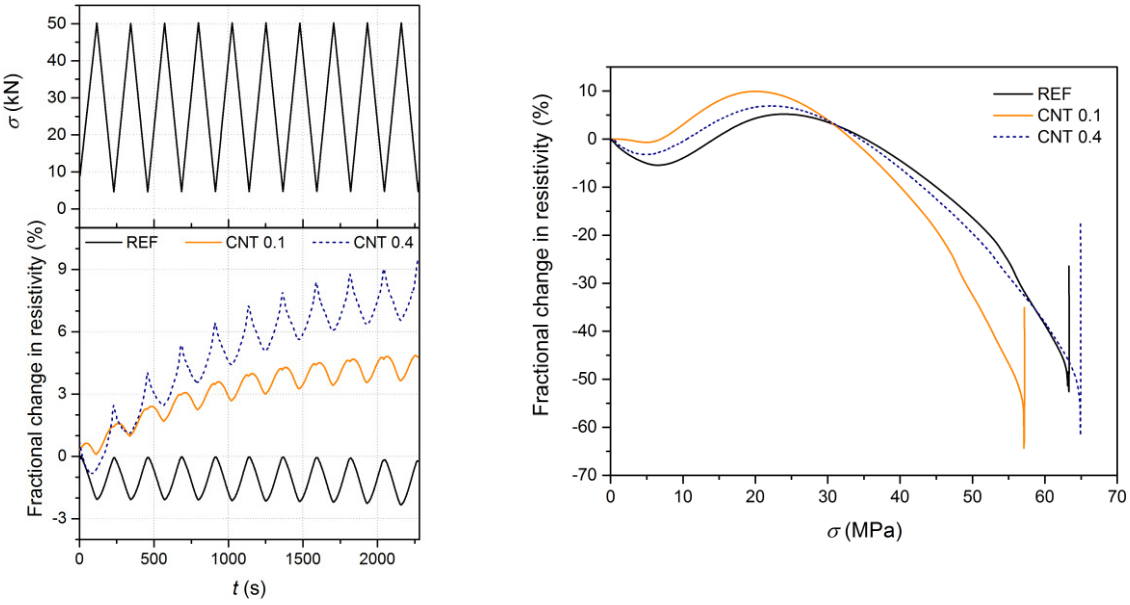

a) **b)**

Figure 2: Fractional change in resistivity of alkali-activated slag composites: a) during repeated compressive loading; b) during compressive loading till failure

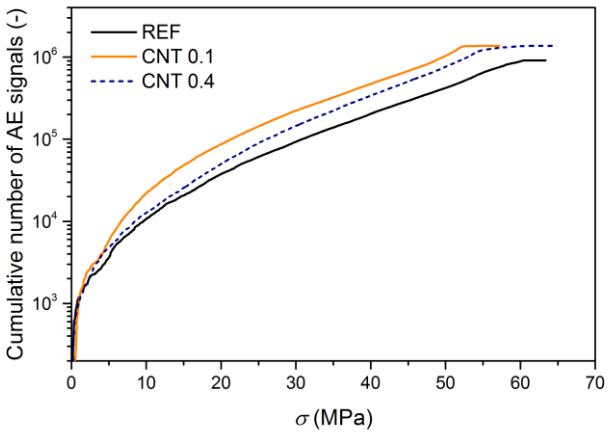

Figure 3: Cumulative number of recorded AE signals versus compressive stress

The acoustic emission (AE) method is considered to be a "passive" non-destructive technique because it identifies defects while they are being developed during the test. This technique has quite unique ability to detect crack formation and propagation occurring not only on the surface but also deep inside the material. To detect defects formation, we focused on a number of signals overshooting a pre-set threshold level. The cumulative number of AE

signals versus compressive stress is presented in Fig. 3. All three curves are quite similar, however, the total number of AE signals of AAS composites with MWCNTs is higher by $5 \cdot 10^5$. The increase in AE signals recorded for CNT 0.1 sample at compressive stress higher than 5 MPa corresponds to the increase in fractional change in resistivity. This also supports a presumption that the local maximum on FCR curves is caused by the microcrack formation and partial deterioration of the mechanical properties.

4. Conclusions

In this paper, self-sensing properties of alkali-activated slag composites with two different amounts of MWCNTs under compressive loading were investigated. The properties were compared with reference AAS mortar without MWCNTs. The experimental and analytical results have led to the following conclusions:

- Addition of carbon nanotubes to AAS mixture led to a significant decrease in electrical resistance of AAS mortars.
- Self-sensing properties under repeated compressive loading can be observed for all three mixtures, however, the addition of MWCNTs does not improve sensing properties of AAS mortar.
- The composites with MWCNTs showed a permanent damage during repeated loading, which is reflected in a gradual increase in basic FCR.
- FCR decreased during compression till failure, however, it showed a local maximum, which is associated with microcrack formation. This conclusion is also supported by AE measurements.

Acknowledgements
This outcome has been achieved with the financial support of the Czech Science Foundation, project No. 16-00567S, and the MEYS CR under the "National Sustainability Programme I", project No. LO1408 (AdMaS UP).

References

[1] Han, B., Yu, X., Ou, J., Self-sensing concrete in smart structures, Butterworth-Heinemann (2014)
[2] Kusák, I., Luňák, M. and Rovnaník, P., Electric conductivity changes in geopolymer samples with added carbon nanotubes, Proceedia Eng 151 (2016) 157-161
[3] Kusák, I., Luňák, M. and Schauer, P., Tracing of concrete hydration by means of impedance spectroscopy (New tool for building elements testing), Appl Mech Mater 248 (2013) 370-378
[4] Wen, S. and Chung, D. D. L., Pressure-sensitive properties and microstructure of carbon nanotube reinforced cement composites, Cem. Concr. Compos. 29 (2007) 377-382
[5] Cao, J., Wen, S. and Chung, D. D. L., Defect dynamics and damage of cement-based materials, studied by electrical resistance measurement, J Mater Sci 36 (2001) 4351-4360
[6] Li, G. Y., Wang, P. M. and Zhao, X. H., Pressure-sensitive properties and microstructure of carbon nanotube reinforced cement composites, CemConcrCompos 29 (2007) 377-382
[7] Wen, S. and Chung, D. D. L., Electric polarization in carbon fibre-reinforced cement, Cem Concr Res 31 (2001) 141-147

SynerCrete'18 International Conference on Interdisciplinary Approaches
for Cement-based Materials and Structural Concrete
24-26 October 2018, Funchal, Madeira Island, Portugal

SOLIDIFICATION/STABILIZATION OF PORT SEDIMENTS CONTAMINATED BY HEAVY METALS AND TBT USING SLAG-BASED BINDERS

Tanya Gutsalenko [(1)], Alexandra Bourdot [(1)], Peter Seymour [(2)], Laurent Frouin [(2)], Mohend Chaouche [(1)]

(1) LMT, CNRS/ENS-Cachan/Paris-Saclay University, Cachan, France
(2) Ecocem Ltd. F1, Dublin, Ireland

Abstract
Dredge sediments from marine basins represent an environmental issue. Indeed, they are often contaminated with heavy metals and/or organic pollutants. Thus, they are considered as hazardous waste and must undergo treatments to stabilize them and if possible to valorize them. The Dublin Port sediments are contaminated with heavy metals and TBT (Tributyltin) related to port activities (paintings used for boats). In this study, the Solidification/Stabilization method is used because of its technical, environmental and economic benefits. Compression tests were performed on the composites of sediments-OPC-GGBS. The results are correlated with XRD analyses and micro-tomography observations. Regarding the plain OPC based samples, the degradation of the strength can be attributed to the decrease of the amount of some hydration products, may be attributed to internal carbonation resulting from eventual decomposition of organic matter at high pH. This led then porosity increase in comparison to the GGBS-based binder, which microstructure is denser. The stability of contaminant compounds solidified in hydraulic binders was considered through leaching tests. The leachates were analyzed using ICP-MS technique for HM and GC-MS analyses to follow the evolution of TBT and its derivatives throw. The results show a positive effect of GGBS based binder in stabilizing contaminated sediments.

1. Introduction

The port activities induce sediment accumulation in basins. In order to maintain a viable navigation within the port structures, it is essential to carry out dredging operations to evacuate the sediments accumulating in their basins. Much of this sediment is once again

dumped at sea. Nevertheless, marine basins are polluted due to mining, chemical, mechanical industry, agriculture industry emissions, port activities (paintings used for boats). Therefore some of sediments are polluted with heavy metals (HM) and/or organic pollutants (PCBs, PAHs, TBT). Thus, they are considered as hazardous waste and are regulated in Europe by the Decree of August 9, 2006 which defines threshold values N1 and N2 for heavy metals, PCB, HAP, and TBT. They must undergo treatments to stabilize them and if possible to valorize them.

In this study, the Solidification/Stabilization method using a hydraulic binder for sediments valorization is considered because of technical, environmental and economic benefits. On this way, Granulated ground blast furnace slag (GGBS) based binders is used for their effectiveness in immobilizing various heavy metals [1]. GGBS is expected to impact immobilization through several mechanisms: the porosity of the binder is finer (due in particular to its pozzolanic activity), presence of hydrotalcite like phases that are characterized by high immobilization capacity, etc.

Three different hydraulic binders of Portland cement-Granulated ground blast furnace slag (GGBS) were used for the Dublin port sediments valorization: Portland cement (OPC) and Portland cement-Granulated ground blast furnace slag (GGBS) at two different GGBS contents. Compression tests were performed on the composites of sediments- OPC-GGBS at 28 and 90 days. The results are correlated with XRD analyzes and micro-tomography observations. The Dublin Port sediments are contaminated with heavy metals (As, Cu, Ni, Zn, Pb, Cr) and TBT (Tributyltin) related to port activities (paintings used for boats). The stability of heavy metal compounds contained in the sediments solidified in hydraulic binders was considered through leaching tests. Each mixture was analyzed using ICP-MS technique. In the same way, the paper presents preliminary results from leaching tests carried out to follow the evolution of TBT and its derivatives. The organic compounds were analyzed by GC-MS.

2. Materials

Sediment sampling took place at Alexandra basin (Dublin Port) at around 1.5 m depth. The sediment comprises mainly very fine fractions with the average diameter of about 40 μm. The sediment consisted of both organic and inorganic components. The main inorganic crystalline components observed by X-ray diffraction (Co Kα, $\lambda = 1.79°$) were mainly Quartz, Calcite, Muscovite, and clays. The clays are composed mainly of Illite (59%) associated with chlorite (25%) and kaolinite (14%). Smectite is present as trace (2%). The average value of the organic carbon (TOC) in the Dublin sediment is 35.3 g/kg. The sediment is characterized by the presence of several heavy metals as Zn, Cu, Ni, Cr, Pb and As. The initial TBT, DBT and MBT contents in the sediment were 205, 78.9 and 34.3 μ(Sn)/kg/sec, respectively (according to [2]). The TBT concentration in the Dublin port sediment is superior to the first threshold level N1 of 100 μg/kg/sec defined by the Decree of August 9, 2006. Consequently, its reimmersion is in question, therefore, the stabilization is proposed using cement-GGBS binders. The cation exchange capacity (CEC) for the exchangeable ions Al^{3+}, Ca^{2+}, Fe^{2+}, K^{+}, Mg^{2+}, Mn^{2+}, Na^{+}, determined according to [3] is 21.3 cmol/kg.

The sediment, noted F0 in the paper, was first sieved to remove the aggregates larger than 4 mm. Then, the sediment sample was let to settle over 24 hours and the bleeding water was

removed. All the samples were prepared with sediments having water content of 45±1.5%wt and density of 1400±70 kg/m^3.
The hydraulic binders considered consisted of mixtures of Portland cement (OPC) and slag (GGBS) from ECOCEM Ireland. Three different hydraulic binders were mixed with sediments. The mixtures are reported in Table 1. F1 correspond to Portland cement (OPC) binder, F2 and F3 are Portland cement-Granulated ground blast furnace slag (GGBS) mixtures at two different GGBS contents. Initially, the binder is mixed with water with a w/b ratio 0.5. Samples F1 to F3 are obtained by mixing 150 kg of total binder with 1 m^3 of sediment.

Table 1: Sediment-Binder mixtures and compressive strength Rc at 28 and 90 days

Mixture	Binder content (%)		Rc (MPa)	
	Cement	GGBS	28 days	90 days
F1	100	0	1.90±0.14	0.77±0.08
F2	50	50	1.90±0.14	2.53±0.22
F3	15	85	1.10±0.07	2.00±0.13

3. Methods

The compressive strength of the sediment–binder samples was determined at both 28 and 90 days. X-Ray microtomography imaging (voxel size 7.5 x 7.5 x 7.5 µm) was performed to observe the microstructure.
The leaching tests of heavy metals were performed according to compliance test from NF EN 12457-2 standard [4]. This consisted in dispersing 90±5g of solid particles of sediment-binder in 900 ml of demineralized water (pH=5-7.5 and conductivity <0.5 mS/m) for 24 hours at 10 rpm (horizontal rotation) in a room at controlled temperature 24°C±1°C. For each mixture three samples were prepared and analyzed using ICP-MS technique.
The semi-dynamic leaching tests of TBT and its derivatives were performed for monolithic waste according to NEN 7375 [5]. The cylindrical specimen of ø40 x 40 mm is immersed in a leachant (demineralized water (5<pH<7.5) with a conductivity <0.1 mS/m) that is renewed after specified intervals. The leachant volume (in cm^3) used for each interval was 8× the surface area of the specimen (in cm^2). The water solution was analyzed after each exchange using GC-MS according to XP T 90-250 [2].

4. Results and discussion

4.1 Mechanical strength

The compressive strength of the samples is reported in Table 1. At 28 days the strength is not modified when replacing 50% of OPC with GGBS. Increasing the replacement level of OPC by GGBS leads to a significant decrease of the strength at 28 days. On the other hand, at longer term (90 days) the strength of the samples with GGBS exceeds that of cement-based mixtures. In addition, the strength of the GGBS-based materials increases between 28 and 90 days while that of the OPC-based samples decreases. This phenomenon can be explain by examining the XRD results (Fig. 1). The greatest amount of Portlandite is formed between 7

and 30 days, but then the peaks decreased significantly. The Ettringite phase completely disappeared after 60 days of storage. C_4AH_x phase reached its maximum at 45 days and then decreased. The decrease of the amount of these hydration products may be attributed to internal carbonation resulting from eventual decomposition of organic matter at high pH. This led then porosity increase (Fig. 2) and degradation of the strength.

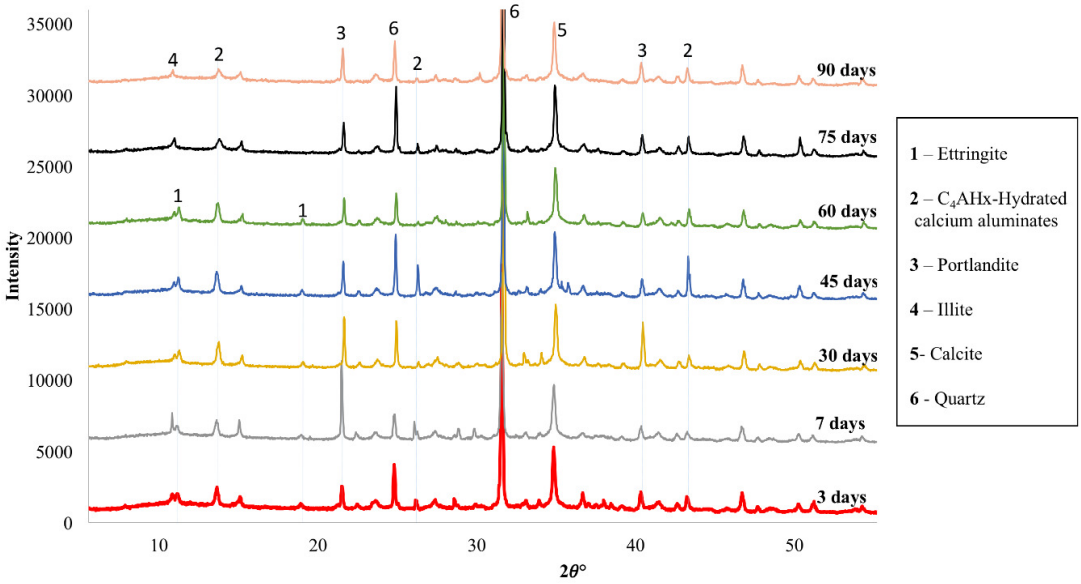

Figure 1: XRD of F1 mixture over time

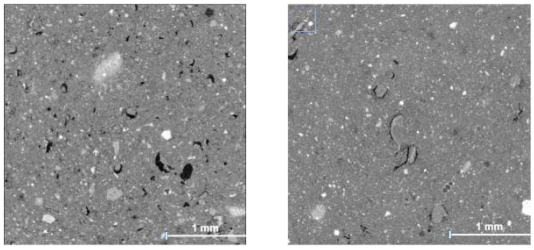

Figure 2: Microstructure of F1 (left) and F3 (right) mixtures from X-ray micro-tomography

4.2 Heavy metals leaching tests

The leaching test results for the HMs are reported in Fig. 3. Surprisingly the leachability of the HMs from the plain sediment (F0) is quite low. This suggests that they should be present in rather stable compounds. The effect of the binder depends on the HM considered. For instance As, Cr, Pb and Zn are quite efficiently immobilized with all the binders. On the other hand, Cu and Ni are rather destabilized in the presence of the binder. It can be noticed that the destabilizing effect decreases when the level of OPC substitution with GBBS increases. These trends seem to be related to the pH of the samples (Fig. 3). The highest pH is obtained with the OPC based sample F1 (around 12.5). Overall the pH decreases when increasing the fraction of GGBS. The lowest pH is obtained with F3. As already observed in other studies [6], the dissolution of metal species is highly pH dependent. Most metal species are soluble at very low pH. Nevertheless, actually, solubility of metals such as Cu significantly increases also at high pH [7]. This may be a primary explanation for the significant increase of leachability of this metal in a cementitious environment.

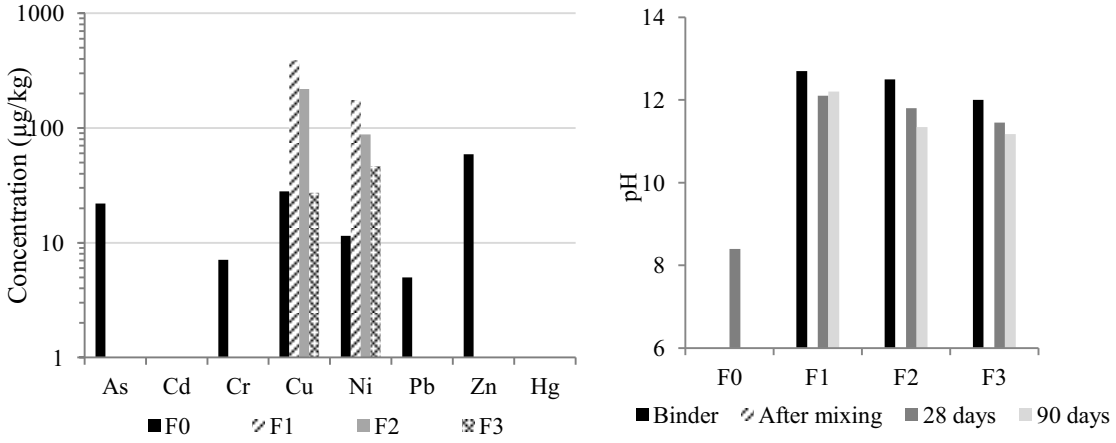

Figure 3: Amount of leached heavy metals and pH for the different mixes.

4.3 TBT leaching tests

The TBT leaching test for 3 months were conducted on sediment-binder mixes, the results are presented in Fig. 4. TBT, MBT and DBT are quite efficiently immobilized with all the binders.

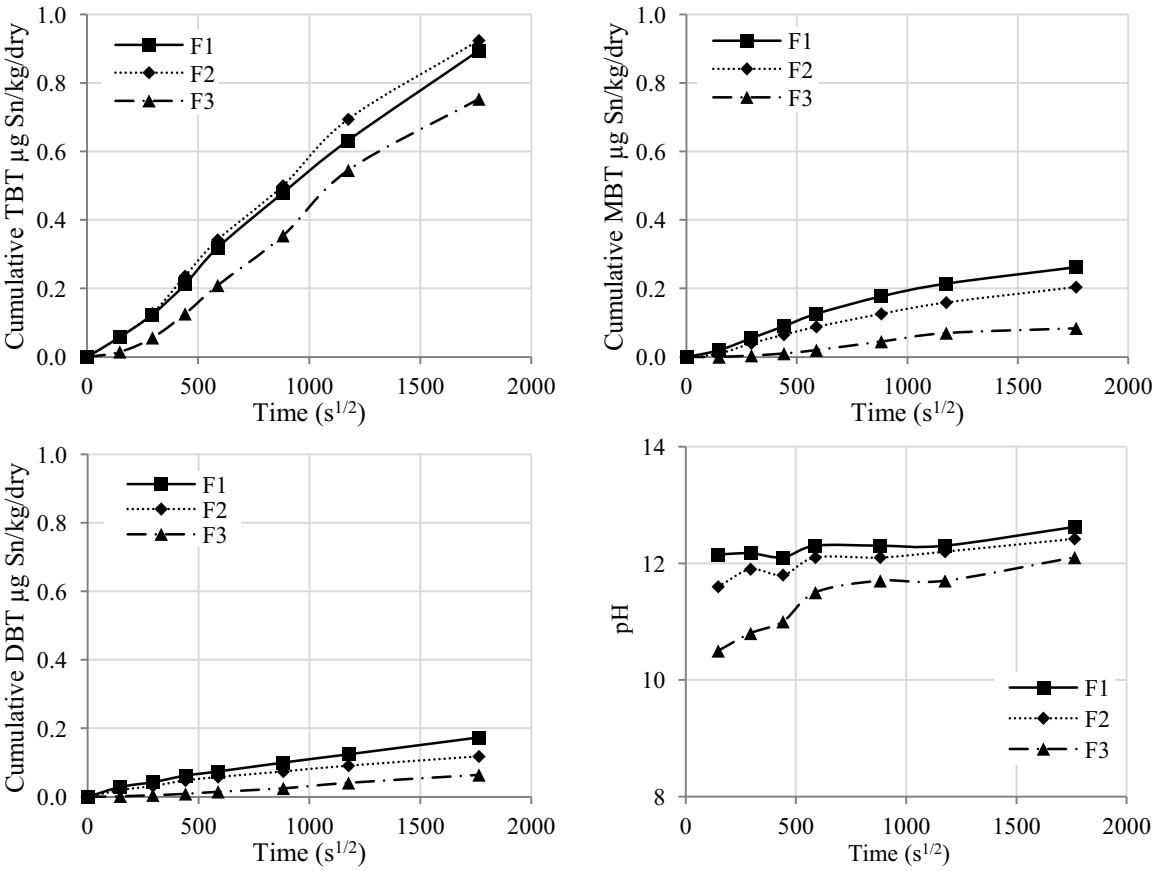

Figure 4: Leaching measurement of TBT, MBT and DBT and pH for the different mixes.

The compounds could stay strongly adsorbed to clays minerals, oxides and hydroxides, and organic material. It can be noticed that the destabilizing effect decreases when the level of OPC substitution with GBBS increases. These trends seem to be related to the pH of the samples (Fig. 4). The highest pH is obtained with the OPC based sample F1 (around 12.5). Overall the pH decreases when increasing the fraction of GGBS. The lowest pH is obtained with F3. The effect of pH on TBT or DBT adsorption was already studied by [8,9] and showed a destabilization at low and high pH. However the gap between pHs for the different mixes is decreasing with time whereas the concentration gap of pollutant is increasing. Therefore, pH does not seem to be the only parameter influencing the leachability of TBT and its derivatives.

5. Conclusion

The study proposed the valorization of polluted sediment by solidification in cement-GGBS binder. Mechanical strength values are quite interesting as soil application using GGBS. Leaching tests were performed on Dublin port sediment embedded in binders with different contents of GGBS. It was found that the leachability of most heavy metals contained in the sediment under initially neutral pH conditions is quite low. Regarding the leachability of TBT and its derivatives with time, the values are very weak. The values are the lowest using high percentage of GGBS in binder. Consequently, the results indicated that the heavy metals and TBT within the sediment are embedded in stable compounds using high level of GGBS.

References

[1] Deja J., Immobilization of Cr^{6+}, Cd^{2+}, Zn^{2+} and Pb^{2+} in alkali-activated slag binders, Cem Concr Res 32 (2002), 1971–1979
[2] AFNOR XP T90-250, Water quality - Determination of selected organo-tin compounds in sediments - Gas chromatography method, Association Française de Normalisation, France (2006)
[3] AFNOR NF EN ISO 23470, Soil quality — Determination of effective cation exchange capacity (CEC) and exchangeable cations using a hexamminecobalt trichloride solution, Association Française de Normalisation, France (2011)
[4] NF EN 12457-2, Characterization of waste — Leaching — Compliance test for leaching of granular waste materials and sludges — Part 2: One stage batch testat a liquid to solid ratio of 10 l/kg for materials with particle size below 4 mm (without or with size reduction), Association Française de Normalisation, France (2002)
[5] EA NEN 7375, Leaching characteristics of moulded or monolithic granular building and waste materials 'The tank test', Environment Agency, UK (2004)
[6] Spence R. D. and Shi C., Stabilization and solidification of hazardous, radioactive and mixed wastes, Boca Raton, CRC Press (2004), 382pp
[7] Chatain V., Blanc D., Borschneck D., and Delolme C., Determining the experimental leachability of copper, lead, and zinc in a harbor sediment and modeling, Environ Sci Pollut Res 20 (2013), 66–74
[8] Burton E. D., Phillips I. R., and Hawker D. W., Sorption and Desorption Behavior of Tributyltin with Natural Sediments, Environ Sci Technol 38 (2004), 6694–6700
[9] Hoch M., Alonso-Azcarate J., and Lischick M., Assessment of adsorption behavior of dibutyltin (DBT) to clay-rich sediments in comparison to the highly toxic tributyltin (TBT), Environ Pollut 123 (2003), 217–227

BIO-BASED MATERIALS

SynerCrete'18 International Conference on Interdisciplinary Approaches
for Cement-based Materials and Structural Concrete
24-26 October 2018, Funchal, Madeira Island, Portugal

ALGINATE-BACILLUS SUBTILIS BASED REPAIR MATERIALS FOR SEALING CRACKS IN CONCRETE

Masahiko Ide [(1)], Keiyuu Kawaai [(1)], Isao Ujike [(1)]

(1) Ehime University, Ehime, Japan

Abstract
Recently, repair materials associated with microbial induced calcium carbonate precipitation (MICP) have been intensively studied in the field of self-healing concrete. We have proposed a liquid-based repair system comprising microorganism and organic carbon sources mixed with alkali buffering solution. This study examined crack repair methods using alginate gel films (1.0-1.5 wt%) mixed with healing agents under wet and dry actions. The healing agents consist of bacillus subtilis as aerobic microorganism and glucose as an organic carbon source, thereby producing insoluble calcium carbonate precipitation in the gel films in the presence of calcium ions. The results showed that water permeability was significantly lowered for the cases of alginate gel films with MICP, thus suggesting that the precipitates could enhance the resistance against water pressure of the gel films formed on the cracked surface.

1. Introduction

In recent years, bio-based materials for repairing cracks in concrete through the metabolic processes of microorganisms and enzymes have been intensively studied [1-3]. According to past research reported by Kawaai et al., 2017 [4], precipitation of calcium carbonate in alkaline environment has been confirmed by precipitation test using aerobic Bacillus subtilis (natto) encapsulated in calcium alginate capsules. Sodium alginate extracted from brown seaweed could provide viscosity in aqueous solution, which varies depending on the concentrations. When sodium alginate dissolved in a liquid is used for repairing cracks in concrete, there is a strong possibility that the alginate reacts with calcium ions available on the cracked surface, thus forming a polymer comprising calcium alginate via ion-link on the cracked surface. This could result in in-situ encapsulation for the microorganism and nutrients in the cracks. Generally, there are two types of microorganisms, anaerobic and aerobic microorganisms. The former can metabolize an organic carbon sources in an oxygen-free

environment. On the other hand, the latter requires oxygen for the metabolic activity. In this study, we selected Bacillus subtilis (natto) as an aerobic microorganism. The liquid-based mixture is supposed to be applied to concrete structures in tidal zones under marine environment. Dissolved oxygen is expected to be available during the dry and wet cycles. Based on the above background, this study examines the effect of crack repair using the viscosity modified mixture containing the Bacillus subtilis (natto) and nutrients via liquid-based approach under dry and wet conditions

2. Experimental program

2.1 Materials

First, culture solution of Bacillus subtilis (natto) containing sodium alginate is stirred using a stirrer for 30 minutes until the sodium alginate dissolves. Subsequently, Tris buffer solution or glucose is added. The concentrations of each constituent of the mixtures are shown in Tab. 1. The experimental parameters include the presence (N1 mixtures) and absence (W mixture) of Bacillus subtilis (natto), the concentration of sodium alginate ranging from 1.0 to 1.5 wt%. The use of Tris buffer solution with concentrations of 0.1 mol/L is also considered as testing parameters. In this study, 4 mixtures were totally prepared.

Table 1: Concentrations of each constituent of mixtures.

	Mixtures	Sodium Alginate (%)	Glucose (mol/L)	Tris buffering solution (mol/L)
N1	1.0-N1-G1-T0	1.0	0.4	-
	1.5-N1-G1-T0	1.5	0.4	-
	1.5-N1-G1-T1	1.5	0.4	0.10
W	1.5-W-G0-T0	1.5	-	-

2.2 Cultivation of bacillus subtilis (natto)

In this study, Bacillus subtilis (natto) was cultivated using culture media mainly comprising NH_4Cl, NH_4NO_3, Na_2SO_4, $MgSO_4$, $CaCl_2$, K_2HPO_4, KH_2PO_4 in this study. The round rod shape of Bacillus subtilis (natto) forms one spore per one bacterial cell in the bacterial body. Spores are formed when it becomes an environment not suitable for growth such as oxygen, water and nutrient sources. And then, they become dormant and inactive. However, if the environment is set, the spore dormancy state ends, and germination begins. And then it becomes vegetative cell and the activity starts. Therefore, the Bacillus subtilis (natto) has higher resistance to environmental fluctuation compared to other microorganisms. Also, the metabolic activity of the Bacillus subtilis (natto) in a highly alkaline environment of pH 12 has been confirmed [4]. In this study, the culture solution of the Bacillus subtilis (natto) after 24 hours was used as repair mixtures. Before preparing the mixtures, the dissolved oxygen concentration in the culture solution was measured to confirm the metabolic activity of Bacillus subtilis (natto).

2.3 Specimen preparation and exposure tests via dry and wet cycles

In this study, a mortar specimen with a water cement ratio of 50% and unit water content of 316 kg/m^3 and unit weight of crushed sand 1264 kg/m^3 was prepared using a cylindrical mold of ϕ 50×100 mm. Specimens were demolded in 24 hours after casting and sealed curing was carried out until the age of 28 days. In order to simulate the cracks generated in the concrete member, split cracks were induced using a loading machine. The experimental set-up is similar to tensile strength test. The crack width was targeted from 0.2 to 0.4 mm. The dry and wet exposure test was carried out through dry conditions (12 hours) and wet conditions (12 hours). Dry and wet cycles were repeated using either distilled water or distilled water containing NaCl (3%).

2.4 Observations by microscope, FE-SEM and FT-IR analysis

Cracked surface including crack width, distribution of calcium carbonate precipitates and the presence of Bacillus subtilis (natto) was observed via microscope and FE-SEM. Three pictures were taken in each specimen, and the maximum and average crack widths of each image were measured. And the precipitates produced by the metabolic activity of Bacillus subtilis (natto) were analyzed by a Fourier transform infrared spectrophotometer (hereinafter referred to as FT-IR).

2.5 Water permeability tests

Water permeability test was carried out using specimens subjected to dry and wet exposure tests using distilled water containing NaCl. It was tested before and after the specimens were repaired. The water pressure was set as high as 25 kPa and the amount of water flowing through the crack is measured by weighing machine for 10 minutes.

3. Experimental results and discussion

3.1 Exposure tests via dry and wet cycles using distilled water

For the mortar specimens repaired with each mixture, the materials formed on the cracked surface were firstly observed by microscope. The observations were made before repaired, 1 week later before the specimens were exposed to the dry and wet cycles. As shown in Fig. 1, precipitates in a white colour were clearly observed by microscope on the specimens repaired with the mixture of 1.5-N1-G1-T0. The specimens were exposed to the room conditions controlled at 20°C for a week. They were also visually confirmed after the dry and wet exposure tests. In contrast to the results, such precipitates were not observed on the specimens repaired with the mixture of 1.5-W-G0-T0 without the Bacillus subtilis (natto) for a week after the mixture was poured onto the cracked surface. They were not visually observed even after the dry and wet exposure tests. Therefore, the results suggest that the white precipitate can be produced through the metabolic processes of the Bacillus subtilis (natto) in the gel films formed on the cracked surface. It is noted that the addition of glucose in the mixtures is essential for the metabolic processes and MICP in the gel films.

3.2 Exposure tests via dry and wet cycles using distilled water containing NaCl

As shown in Fig. 1, precipitates in a white color were clearly observed by microscope on the specimens repaired with the mixture of 1.5-N1-G1-T0. The specimens were exposed to the dry and wet exposure tests for a week. In contrast to the result, such precipitates were not

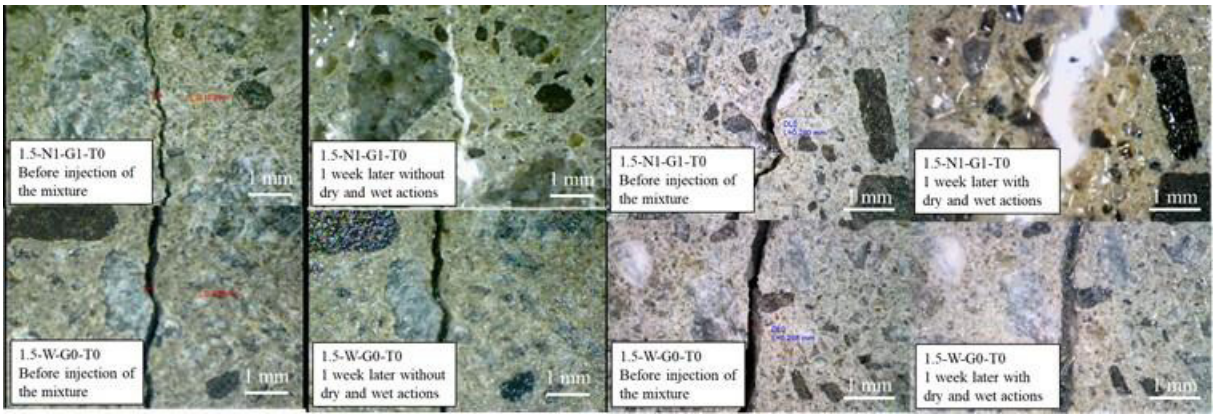

Figure 1: Cracked surface repaired with the liquid-based mixtures.
(Left: distilled water, Right: distilled water containing NaCl)

observed on the specimens repaired with the mixture of 1.5-W-G0-T0 without the Bacillus subtilis (natto) for a week after the mixture was poured onto the cracked surface. They were not visually observed even after the dry and wet exposure tests. Therefore, the results suggest that the white precipitate can be formed in the gel films through the metabolic processes of the Bacillus subtilis (natto) under the saline environment.

3.3 FT-IR analysis

Fig. 2 shows the results of FT-IR measurements using samples containing white precipitates taken from the cracked surface repaired with the mixtures (1.0-N1-G1-T0 and 1.5-N1-G1-T0) which were exposed to dry and wet cycles using either distilled water or distilled water containing NaCl. Also shown is a spectrum obtained by calcium carbonate for the reference. In the case of the reference spectrum of calcium carbonate, one of the peak is prominent at the wavenumbers of 872 cm^{-1}. Based on the results obtained by the samples tested in this study, similar peaks exist in the samples tested in the experiments. Thus, the results indicate the presence of calcium carbonate in/on the gel films formed on the cracked surface during the testing periods irrespective of the mixtures formulated in this study.

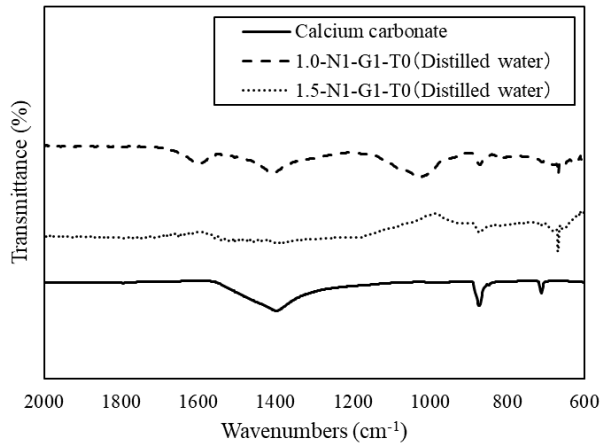

Figure 2: Results of FT-IR.

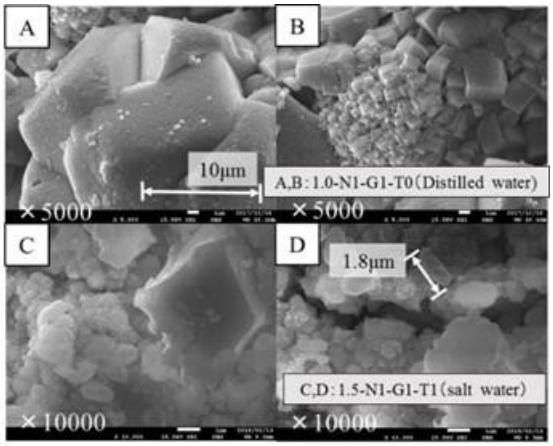

Figure 3: FE-SEM observations.

3.4 FE-SEM observations

In order to confirm the precipitates comprising calcium carbonate formed in/on the gel films, samples including white precipitates were collected from the materials in the vicinity of cracks. Some pictures observed by FE-SEM for 1.0-N1-G1-T0 and 1.5-N1-G1-T1 are shown in Fig. 3. It is noted that FE-SEM images show the materials exposed to the dry and wet cycles for 2 weeks. As can be seen in Fig. 3 (A) and (B), the size of crystals reached about 10 μm at maximum for the testing periods. In addition to this, Fig. 3 (C) and (D) show the presence of the Bacillus subtilis (natto) of about 1.8 μm long in the vicinity of those crystals. Based on the observations made on the samples, it is certain that the calcium carbonate precipitates through the microbial metabolic processes taking place in/on the gel films formed on the cracked surface under the dry and wet environment.

3.5 Water permeability tests

Three specimens for each case were tested for the water permeability to confirm the consistency of the results. The amount of water flowing through the cracked parts of the specimens was weighed for 10 minutes, and average values were calculated. Fig. 4 shows the results of water permeability measured after repaired and average crack width of the specimens. As can be seen, the sealing effect is found to be obtained in the cases of specimens with the crack width ranging from about 0.2 to 0.4 mm. Of the total 8 specimens (1 specimen for 1.5-W-G0-T0 was omitted), the water permeability of 6 specimens was observed to be negligible, thus indicating that the resistance against ingress of water and water pressure was significantly improved by the repair. In particular, the specimens repaired with the mixtures mixed with Bacillus subtilis (natto) resulted in a significant decrease in the water permeability. The results suggest that the calcium carbonate precipitated in/on the alginate gel films formed on the cracked surface is highly effective in improving the water permeability. In addition, even in the specimens repaired with 1.5-W-G0-T0 without Bacillus subtilis (natto), the water permeability was decreased by about 70% on average. The results indicate the gel films of calcium alginate formed on the cracked surface could solely contribute to the improvement of water permeability possibly by absorbing moisture and swelling. Although the sealing effect for the long-term was unclear in this study, which could be dependent on the

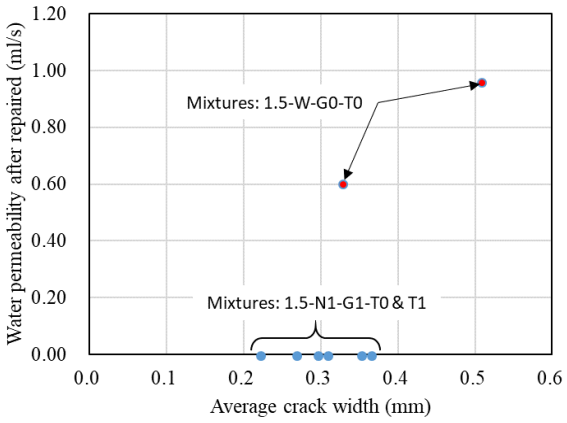

Figure 4: Results of water permeability test.

concentrations of glucose and Tris buffer solution. Therefore, we will continue to examine long-term effect for sealing cracks under dry and wet actions for future research.

4. Conclusion

(1) Based on the observations made by microscope and FE-SEM, calcium carbonate precipitates through the metabolic activity of Bacillus subtilis (natto) cultivated in this study in/on the gel films of calcium alginate formed on the cracked surfaces with cracking width ranging from 0.2 to 0.4 mm under dry and wet actions.
(2) Water permeability test was carried out using specimens repaired with mixtures mixed with and without Bacillus subtilis (natto). Calcium carbonate precipitated in/on the gel films of calcium alginate formed on the cracked surface is found to show beneficial effect in sealing cracks and decreasing water permeability. Although the sealing effect was observed to some extent in the cases of specimens repaired with only gel films of calcium alginate without Bacillus subtilis (natto), the results suggest that precipitation of calcium carbonate by the microbial metabolism further enhances the sealing effect of cracks in concrete.

Acknowledgement

This study is financially supported by JSPS KAKENHI Grant-in-Aid for Young Scientists (A), Grant numbers JP17H04933.

References

[1] H. Jonkers et al., Application of bacteria as self-healing agent for the development of sustainable concrete, Ecological Engineering, 36 (2010), 230-235.
[2] P.Y. Putri et al., Effect of Temperature on Precipitation Rate of Calcium Carbonate Produced through Microbial Metabolic Process of Bio Materials, Civil Engineering Dimension, 18 (2016), 103-108.
[3] J. Wang, D. Snoeck, S. Van Vlierberghe, W. Verstraete, N. De Belie, Application of hydrogel encapsulated carbonate precipitating bacteria for approaching a realistic self-healing in concrete, Construction and Building Materials, 68 (2014), 110-119.
[4] K. Kawaai et al., Alginate capsules encapsulating aerobic and anaerobic microorganism for repairing cracks in concrete, 6th International Conference on Self-Healing Materials, web (2017).

SynerCrete'18 International Conference on Interdisciplinary Approaches
for Cement-based Materials and Structural Concrete
24-26 October 2018, Funchal, Madeira Island, Portugal

EFFECT OF ANISOTROPY ON THERMAL AND HYGRIC PREPERTIES OF HEMP COMPOSITE.

Florence Collet [(1)], Sylvie Prétot [(1)], Brahim Mazhoud [(1)], Christophe Lanos [(1)]

(1) Université de Rennes, LGCGM, Rennes, France

Abstract
This study investigates the effect of anisotropy on thermal and hygric properties of hemp - clay composite.
The clay based binder is made of fines from aggregate washing mud. It is stabilized with 5% of Portland cement and 5% of lime based binder (Thermo®). The aggregates are CAVAC Biofibat® hemp shiv. The hemp to binder mass ratio is 0.5, representative of wall formulation. The specimens are produced by casting with successive layers, compacted at 0.1 MPa. The density of hemp-clay composites is about 445 kg/m^3 after stabilization at (23°C, 50%RH).
The thermal conductivity is measured with a hot wire at dry state. The measurements are performed placing the wire in planes perpendicular to or parallel to the compaction direction. The anisotropy induces 16.8 % of discrepancy between the two measurement directions.
The moisture buffer value (MBV) is measured following the Nordtest protocol. After stabilization at 23°C, 50 %RH, the specimens are exposed to daily cyclic variations (8 hours at 75 %RH , 16 hours at 33 %RH). The MBV is calculated from the mass variation through the exposed surface under relative humidity step. The anisotropy induces 27 % of discrepancy between moisture flux parallel and perpendicular to the compaction direction.

1. Introduction

In order to meet the requirements of sustainable development, hemp composites are developed to be used as non load bearing material in building envelop. They show low density, low thermal conductivity and high moisture buffering capacity [1]. Such materials can be precast (building blocks or elements) or implemented on site by casting or spraying. All these implementation techniques lead to anisotropy of materials which is both due to the shape of aggregates and to the successive layers (compacted or not). William et al. [2]

demonstrate a significant anisotropy within hemp concrete thanks to image analysis method. This anisotropy impacts all multi-physical properties of materials. It was investigated on thermal conductivity of hemp concrete and on mechanical properties of hemp concrete [3-7] but not on hygric properties, to our knowledge. So, this study investigates the effect of anisotropy on thermal conductivity and moisture buffer value of washing fine – hemp.

2. Material and methods

2.1 Material

The studied material is a hemp - clay composite. The clay based binder is made of fines from aggregate washing mud taken from a gravels production site. After decanting, the mud is dried in an oven at 100°C. After drying, the material is milled with a knife mill. The powder is then sieved with a square mesh of 2 mm side to remove the larger particles. The fines are stabilized with 5% of Portland cement and 5% of lime based binder (Thermo®), following the stabilisation study performed in [8][9].

The bio-sourced aggregates are CAVAC Biofibat® hemp shiv. They were characterised following the Rilem protocol [10]. The particle size distribution is given Fig. 1. Their width ranges from 0.14 to 6.8 mm, and their length from 0.6 to 40.6 mm. Their elongation (width/length) ranges from 0.09 to 0.90 with a medium value of 0.26.

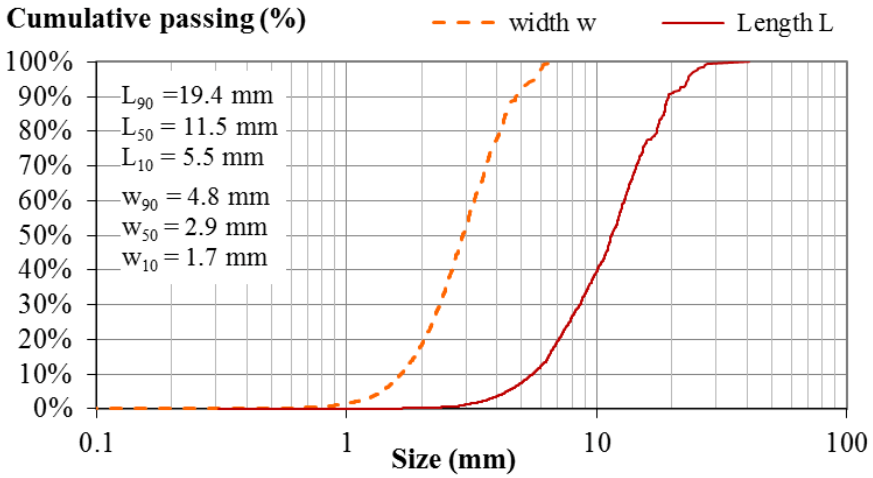

Figure 1: Particle size distribution of hemp shiv

The hemp to binder mass ratio is 0.5, representative of wall formulation.

For the production, the hemp shiv is weighed and mixed by hand for about 2 min in a container with water to hemp mass ratio of 0.4. At the same time, binder powder and water are mixed with the mixer to form a binder paste. The cubic specimens (10*10*10 cm^3) are produced by casting with successive 5 cm thick layers. Each layer is compacted at 0.1 MPa. The specimens are demoulded after 6 days and are stabilised in a climate room at (23°C, 50%RH).

The average bulk density after stabilisation is 443 $kg.m^{-3}$, with a variation coefficient of 2.45 % between the 9 specimens. This value is close to the one found in previous work [8]. This underlines the reproducibility of the washing fine – hemp composite production.

2.2 Measurement of thermal conductivity

The thermal conductivity is measured at dry state. After drying in an oven at 60°C, the specimens are stabilized in a desiccator were the measurements are performed at ambient temperature. The measurements are performed with a 5 centimetres long hot wire. This transient method consists in analysing the temperature rise versus heating time (Eq. 1).

$$\Delta T = \frac{q}{4\pi\lambda}(\ln(t) + C) \quad (1)$$

Where ΔT is the temperature rise (°C), q is the heat flow per meter ($W.m^{-1}$) and λ is the thermal conductivity ($W.m^{-1}.K^{-1}$), t is the heating time (s) and C is a constant including the thermal diffusivity of the material.

The measurement is performed with the sensor sandwiched between two specimens. To investigate the effect of anisotropy, the measurements are performed placing the wire in planes perpendicular to or parallel to the compaction direction (Fig. 2). The heat flow (212 mW) and heating time (120 s) are chosen to reach high enough temperature rise (>10°C) and high correlation coefficient (R^2) between experimental data and fitting curve. These settings meet the requirements of the manufacturer, the expected accuracy is thus better than 5%. For each sensor position, the measurements are performed on two pairs of specimens. The thermal conductivity of a pair of specimens is the average of five values with a coefficient of variation lower than 5%. The thermal conductivity is the average value of the two pairs of specimens.

Figure 2: Measurement of thermal conductivity – wire position :
λ_1 wire perpendicular to the compaction direction, λ_2 wire parallel to the compaction direction

2.3 Measurement of Moisture Buffer Value (MBV)

The moisture buffer value (MBV) is measured following the Nordtest protocol [11]. Specimen are sealed on all but one surfaces. In order to investigate the effect of anisotropy, the open surface allows moisture flux to be parallel or perpendicular to compaction direction. The open surface area is measured by image analysis (Fig. 3).

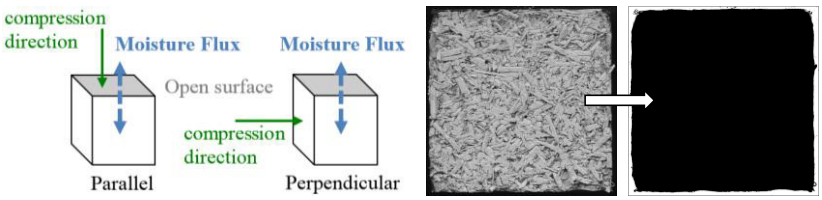

Figure 3: Measurement of moisture buffer value -
left : moisture flux direction versus compaction direction, right : image treatment

The specimens are firstly dried at 60°C and then stabilised at 23°C, 50%RH to begin the test from the adsorption curve. After stabilization, specimens are exposed to daily cyclic variation

of ambient relative humidity (8 hours at 75%RH and 16 hours at 33 %RH) in a climate chamber (Vötsch VC4060). The moisture buffer value is then calculated from their moisture uptake and release with:

$$MBV = \frac{\Delta m}{A \times (RH_{high} - RH_{low})} \quad (2)$$

Where MBV is the moisture buffer value (g/(m². %RH)), Δm is the moisture uptake/release during the period (g), A is the open surface area (m^2), $RH_{high/low}$ is the high/low relative humidity level (%).

Temperature and relative humidity are measured continuously with sensor SHT75; the average air velocity in the surroundings of the specimens is 0.13 m/s with standard deviation of 0.06 m/s for the horizontal velocity and is 0.04 m/s with standard deviation of 0.02 m/s for the vertical one. The specimens are weighed out of the climatic chamber five times during absorption period and two times during desorption one. The readability of the balance is 0.01 g, and its linearity is 0.01 g. The accuracy of the moisture buffer value is thus about 5%. The measurement is performed on five specimen for perpendicular configuration and on four specimens four parallel one. The MBV is the mean value of all specimen on the three stable cycles.

3. Results and discussion

3.1 Thermal conductivity

Fig; 4 gives the thermal conductivity of washing fines – hemp composites versus wire position.

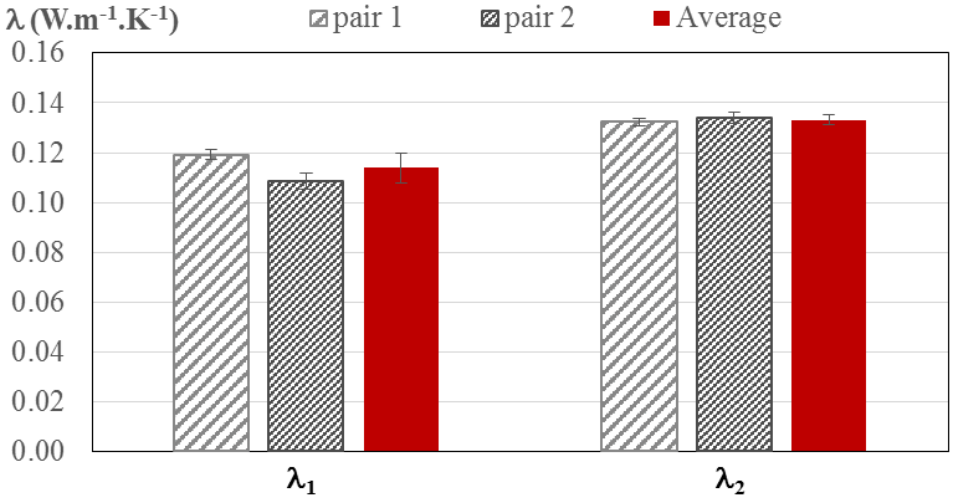

Figure 4: Thermal conductivity of washing fines-hemp composites versus anisotropy - λ_1 wire perpendicular to the compaction direction, λ_2 wire parallel to the compaction direction

For the two directions of measurement, the results obtained on the two pairs of specimens are close. When the wire is perpendicular to the compaction direction, the average thermal

conductivity is 0.114 $W.m^{-1}.K^{-1}$. This value is the same as the one found in previous work [8]. It underlines the reproducibility of the material and its thermal performances. When the wire is parallel to the compaction direction, the average thermal conductivity is 0.133 $W.m^{-1}.K^{-1}$. This value is 1.168 times higher than the previous one and underlines the effect of anisotropy on the thermal conductivity of washing fine – hemp composite. Such results are also observed on hemp composites by several authors. The effect of anisotropy is more or less important with ratios between thermal conductivities ranging from 1.01 to 1.10 in [3], from 1.13 to 1.33 in [4, 5] and from 1.20 to 1.30 in [6], in link with different formulations and productions.

Finally, on thermal point of view, such composite shows lower performances when its implementation leads to heat flux perpendicular to the compaction direction. So, the best way to implement it is to induce compaction direction parallel to heat flux. This can be reach by implementing it by spraying [7] or by precasting.

3.2 Moisture Buffer Value

The moisture buffer value of washing fine – hemp versus moisture flux direction is given in Fig. 5.

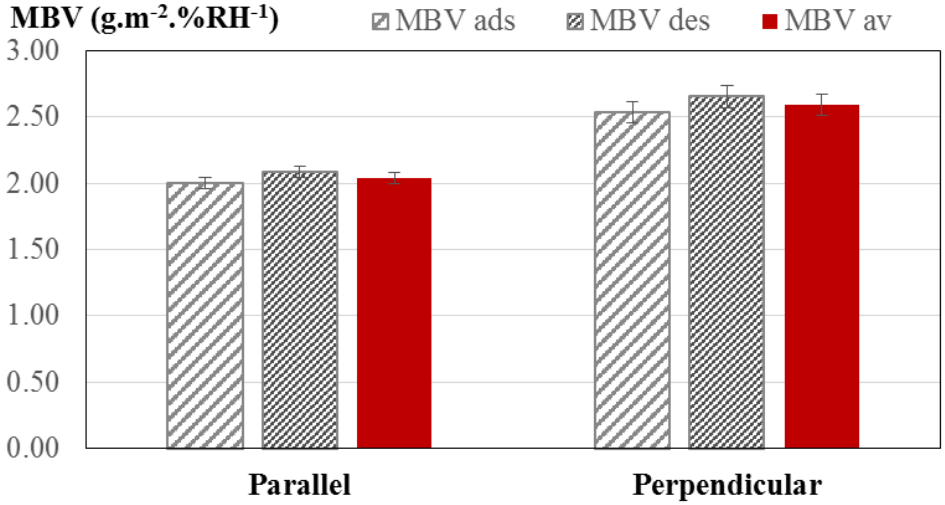

Figure 5 : Moisture Buffer Value of washing fines-hemp composites versus anisotropy – moisture flux parallel or perpendicular to the compaction direction

When the moisture flux is parallel to the compaction direction, the average moisture buffer value is 2.04 $g.m^{-2}.\%RH^{-1}$. This value is lower than the value found in previous study where the specimen were not firstly dried (2.24 $g.m^{-2}.\%RH^{-1}$ in [8]). This difference is probably due to different initial water content of the material. Actually, as shown in [12], the hygric history impacts the hygric behaviour of materials. When the moisture flux is perpendicular to the compaction direction, the MBV is 27 % higher (2.59 $g.m^{-2}.\%RH^{-1}$). So, the best way to take advantage from this material is to implement it in order to have moisture flux perpendicular to the compaction direction. This can be reached with framing technique where the composite is poured and more or less compacted.

4. Conclusion

This study underlines the effect of anisotropy on thermal conductivity and moisture buffer value of washing fine – hemp composite produced by moulding and compacting successive layers.
The thermal conductivity exhibits 16.8 % of discrepancy between the two measurement directions. For moisture buffer value, the discrepancy reaches 27 %.
So, implementation way can be recommended. However, the best performance is not obtained for the same orientation of the material on hygric and on thermal point of view.

References

[1] S. Amziane, F. Collet, M. Lawrence, V. Picandet, C. Lanos, S. Marceau, S. Pavia, Bio-aggregates Based Building Materials, Springer Netherlands, Amziane Sofiane and Collet Florence, (2017).
[2] J. Williams, M. Lawrence, P. Walker, A method for the assessment of the internal structure of bio-aggregate concretes, Construction and Building Materials. 116 (2016) 45–51.
[3] C. Niyigena, Variabilité des performances de bétons de chanvre en fonction des caractéristiques de la chènevotte produite en Auvergne, phdthesis, Université Blaise Pascal - Clermont-Ferrand II, (2016).
[4] Dinh, T.M., Magniont, C., Coutand, M., and Escadeillas, G.. Hemp concrete using innovative pozzolanic binder. In ICBBM, (Clermont-Ferrand, France), (2015) 265-270.
[5] V. Nozahic, S. Amziane, G. Torrent, K. Saïdi, H. De Baynast, Design of green concrete made of plant-derived aggregates and a pumice–lime binder, Cement and Concrete Composites. 34 (2012) 231–241.
[6] T.T. Nguyen, V. Picandet, P. Carre, T. Lecompte, S. Amziane, C. Baley, Effect of compaction on mechanical and thermal properties of hemp concrete, Eur. J. Environ. Civ. Eng. 14 (5) (2010) 545–560.
[7] S. Elfordy, F. Lucas, F. Tancret, Y. Scudeller, L. Goudet, Mechanical and thermal properties of lime and hemp concrete ("hempcrete") manufactured by a projection process, Construction and Building Materials. 22 (2008) 2116–2123.
[8] B. Mazhoud, Elaboration et caractérisation mécanique, hygrique et thermique de composites bio-sourcés, phD Thesis, INSA de Rennes (2017).
[9] B. Mazhoud, F. Collet, S. Prétot, et C. Lanos, « Characterization and comparison of thermal and hygric properties of hemp-clay composite and hemp-lime concrete », International Conference On Materials and Energy, ICOME 2016, La Rochelle, France, (2016).
[10] S. Amziane, F. Collet, M. Lawrence, C. Magniont, V. Picandet, M. Sonebi, Recommendation of the RILEM TC 236-BBM: characterisation testing of hemp shiv to determine the initial water content, water absorption, dry density, particle size distribution and thermal conductivity, Materials and Structures. (2017) 50:167.
[11] Rode, C., Peuhkuri, R.H., Mortensen, L.H., Hansen, K.K., Time, B., Gustavsen, A., Ojanen, T., Ahonen, J., Svennberg, K., and Arfvidsson, J. Moisture buffering of building materials - BYG·DTU R-126, (2005).
[12] Y. Aït Oumeziane, Evaluation des performances hygrothermiques d'une paroi par simulation numérique : application aux parois en béton de chanvre, phD Thesis, INSA de Rennes (2013).

SynerCrete'18 International Conference on Interdisciplinary Approaches
for Cement-based Materials and Structural Concrete
24-26 October 2018, Funchal, Madeira Island, Portugal

EVALUATION OF THE POTENTIAL OF CORN AND SUNFLOWER BARK PARTICLES AS BIO-AGGREGATES FOR LIGHTWEIGHT CONCRETE

Alexandra Bourdot[(1)], Camille Magniont[(1)], Méryl Lagouin[(1)], Guillaume Lambaré[(1)], Laurent Labonne[(2)], Philippe Evon[(2)]

(1) LMDC, Université de Toulouse, INSAT, UPS, Toulouse, France
(2) LCA, Université de Toulouse, INP-ENSIACET, Toulouse, France

Abstract
Biomaterials are an alternative to non-renewable materials. Hemp shives allowed developing an industrial sector favorable to sustainable development. Hence, hemp concrete is currently used as filling material in a timber frame (cast onsite, sprayed or precast). Nevertheless, hemp shiv, the reference biobased aggregate, has a limited availability. It is thus necessary to consider other bio-aggregates largely and locally available. Sunflower and corn stalks were selected for their large availability in south-west of France. The objective of this paper is to evaluate the potential of these two agricultural by-products as alternative bio-aggregates for vegetal lightweight concrete throw the determination of aggregate properties and the study of chemical interactions between plant particles water-soluble compounds and a pozzolanic binder. The results revealed a strong deleterious effect of corn water-soluble compounds on the setting and the hardening mechanisms of the pozzolanic binder. A 24 hours long setting delay was not only observed but an almost complete inhibition of the hardening was also highlighted by the mineralogical analysis and the evolution of the mechanical performances. Sunflower particles could be a good candidate for hemp shives substitution, since their characteristics are similar and their impact on the binder setting and hardening is moderate.

1. Introduction

The building sector is responsible for major environmental impacts (consumption of non-renewable raw materials, emission of greenhouse gases and waste production). As a consequence, the design and characterization of innovative eco-friendly building materials has become a priority. The incorporation of bio-based raw materials could be a response to this

environmental challenge since they are renewable, are mainly by-products of local crops, and are carbon neutral. Over the last fifteen years, these environmental benefits have contributed to the development of a specific building material called hemp concrete. This composite combines a mineral binder and a plant aggregate: hemp shiv, i.e. the ligneous by-product resulting from the mechanical extraction of technical fibers from hemp stalk. Nevertheless, although hemp has been considered as the reference agro-resource for bio-aggregates based building materials, its availability is limited. Therefore, it is necessary to consider other bio-aggregates largely and locally available.
The present study aims to evaluate the potential of two agricultural by-products (corn and sunflower bark particles) as alternative bio-aggregates for vegetal lightweight concrete. Sunflower and corn stalks were selected for their large availability in south-west of France. Corn is the second most cultivated cereal in France, generating large quantities of by-products: 5.2 Mt of stalks in 2015. Sunflower is grown for its seeds to produce vegetal oil with about 614,000 ha cultivated nationwide. 230,000 tons of by-products were produced each year due to this agricultural crop. In comparison, only 17,000 t/year of hemp by-products are available [1].
The first part of the study focused on the plant particles characterization. According to the recommendations of RILEM TC 236-BBM [2], bulk density, particles size distribution and water absorption capacity were determined on hemp shives and on bark particles extracted from corn and sunflower stalks. In a second part, the impact of the water-soluble components extracted from the different bio-aggregates on the setting and hardening mechanisms of the lime-metakaolin binder was investigated.

2. Materials and methods

2.1 Bio-aggregates

Two bio-aggregates are evaluated : corn and sunflower bark particles compared to hemp shives. The samples are presented in Fig.1.
Alternative aggregates result from the combination of a preliminary stage of grinding of the entire stalk and a second phase of separation of the pith from the bark using a tilted conveyor belt and a blowing system. The bark particles under 1 mm were then eliminated by sieving.

Figure 1: Photographs of the three studied bio-aggregates: hemp shives (A), corn (B) and sunflower (C) bark particles

2.2 Mineral binder

The binder is composed of 70 %wt of metakaolin and 30 %wt of aerial lime. Metakaolin, a pozzolanic admixture, is mainly composed of quartz, silicon and aluminium oxides with an

amorphous silicoaluminate mineralogical form. The aerial lime is around 92% $Ca(OH)_2$. Potassium sulfate and a superplastizer glycerol carbonate (GC) were added.

2.3 Aggregate characterization

The physical characterization of plant particles (bulk density, water absorption and particle size distribution) was realized according to RILEM Technical-Committee 236 – BBM (Bio Based Building Materials) recommendations [2].

2.4 Experimental methods on binder pastes

Four different mixtures were tested and differed by the nature of the mixing solution: a control paste was made with demineralized water, and the other three pastes were mixed with the filtrate of bio-aggregates. The filtrates were obtained after immersion of crushed particles (under 1 mm) in demineralized water for 48h with a water to particles ratio 15. The distillated water or filtrate to binder ratio was 0.55. The potassium sulfate to binder ratio was 0.03 and the superplatizer to binder ratio was 0.016.

After mixing, the binder paste was cast in 40 x 40 x 160 mm^3 moulds complying with NF-EN 196-3 [3]. The samples were then demolded at 3 days, cut in three samples and continuously cured in a room at 20 °C and RH > 95% until the date of the test. The pastes are noted Hemp_P, Corn_P, and Sunflower_P. Compressive strength tests were conducted after 3, 14 and 150 days with a constant loading speed of 2.4 kN/s according to NF-EN 196-1 [4].

The setting process of the pastes was studied by isothermal calorimetry using TAM AIR 3116 microcalorimeter. The paste was elaborated manually with components at 20°C outside the calorimeter. Heat flow due to the setting reactions was recorded during 6 days.

The mineralogical evolution was carried out by X-ray diffraction and thermogravimetric analyses. The measuring system was a Bruker D8 Advance diffractometer using Kα (λ=1.542 Å) copper anticathode. The 2-Theta values ranged from 4° to 70° and were recorded at a 0.02° step with an acquisition time of 0.25 s per step. Thermogravimetric analyses were performed on a thermal analyser NETZSCH STA 449 F3 Jupiter® operating at a heating rate of 10°C/min up to 1000°C. For each age, the hydration is stopped by immersion in liquid nitrogen and freeze-drying.

3. Results and discussion

3.1 Bio-aggregates properties

The bulk densities of bio-aggregates are 154.2 ± 0.6 kg/m^3, 120.2 ± 1.0 kg/m^3, 168.2 ± 4.5 kg/m^3, for hemp, corn and sunflower particles, respectively.

The fitted curves and histograms of particle size distribution are presented in Fig. 2.

Fig. 2 reveals that hemp shives present a very narrow particle size distribution in comparison with corn or sunflower bark particles. This could be corrected by a more adequate calibration process for these alternative aggregates in order to eliminate the longer particles. Their circularity is also lower than for hemp particles in particular for corn particles. This result is consistent with bulk density measurement. Corn particles are more elongated and consequently induce a larger interparticular porosity responsible for a lower bulk density.

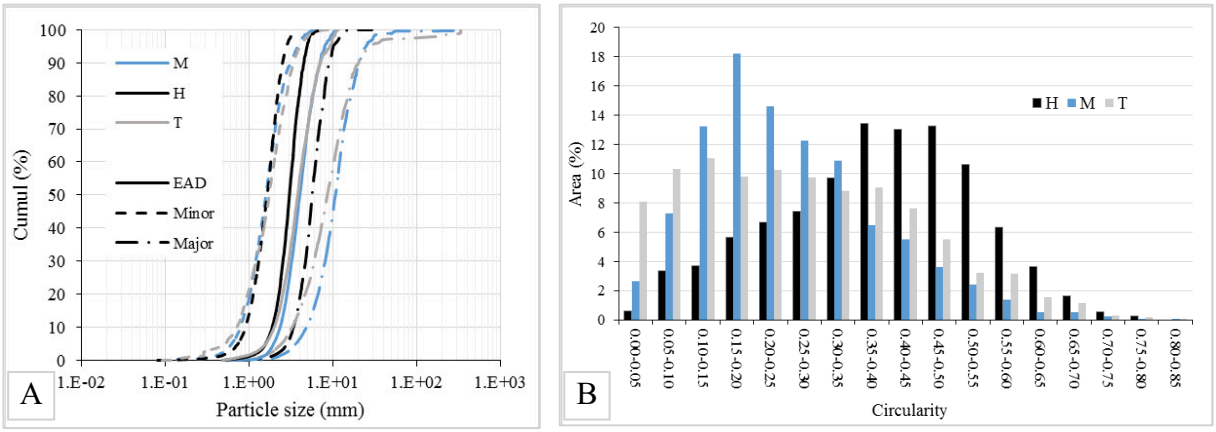

Figure 2: Particle size distribution (A) and circularity (B) of hemp, corn and sunflower particles

The kinetics of water absorption of the three plant particles have been assessed and are plotted in Fig. 3. The figure presents the evolution of the water content of plant particles with the time of immersion and as a logarithmic function of time. The three bio-aggregates present high water absorption capacity, from 250 to 300 %wt after 48h immersion. Fig. 3B evidences distinct initial rate of absorption (IRA) between the particles. After 1 minute, hemp and sunflower aggregates already retain more than 150 %wt while corn particles only absorb 100 %wt. This could be a benefit for corn particles at the time of mixing with the mineral binder.

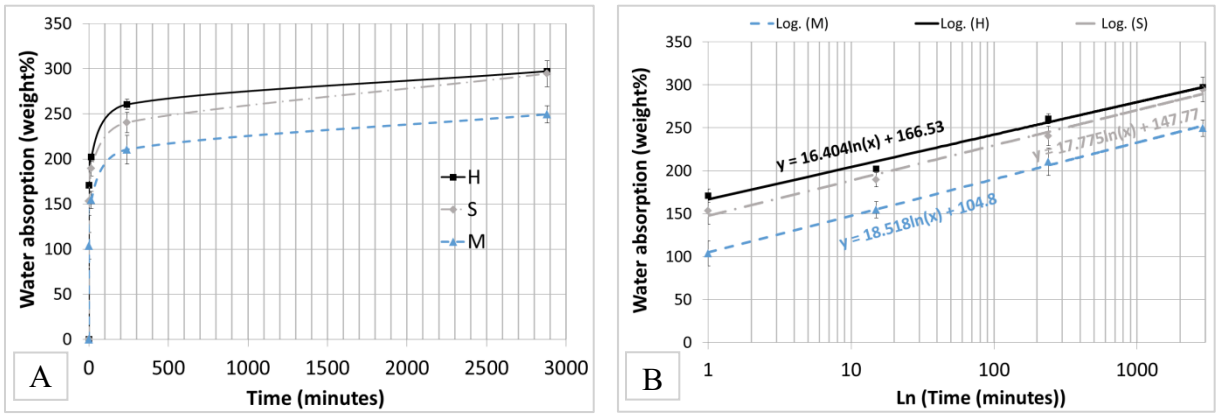

Figure 3: Water absorption curves as a function of time: linear (A) and logarithmic (B) scale

3.2 Interactions between bio aggregates extractives and pozzolanic binder

3.2.1 Composite setting study

The isothermal calorimetry tests results are presented in Fig. 4. The heat flow curves highlight the impact of bio-aggregate extractives on the setting mechanisms of the pozzolanic matrix. Two phases are noted. The first ① corresponds to the exothermic reaction between potassium sulphate and calcium ions forming ettringite. The second ② is attributed to the pozzolanic reaction. Regarding hemp and sunflower pastes, a slight delay is observed. In addition, the heat flow intensity related to the reaction is reduced. However, the setting reaction tooks place. The corn extractives induce the highest impact by a delay of 27 hours and a significant reduction of the heat flow intensity related to the reaction implying partial inhibition of the setting and hardening mechanisms of the pozzolanic binder. This effect was previously reported in the literature during the hydration of Portland cement in the presence of wood, hemp or lavender.

3.2.2 Mechanical performance of pastes

The compressive strengths of pastes are presented in Fig. 5. The results show that the filtrates of bio-aggregates can strongly influence binder pastes strengths. The effect of extractives can be observed from 3 days with a compressive strength value for control paste (CP) of 15.2 MPa while for the other pastes made with extractives the values are lower. Hemp and sunflower filtrates moderetaly impact the 3 days strength (11.7 Mpa). On the contrary, the model pastes with corn filtrate only reach 1.0°MPa. This decrease noticed at 3 days is still observed after 150 days of curing. At that age, the reduction of compressive strength in comparison with control paste is about 27, 14 and 88 % for hemp, sunflower and corn based pastes, respectively.

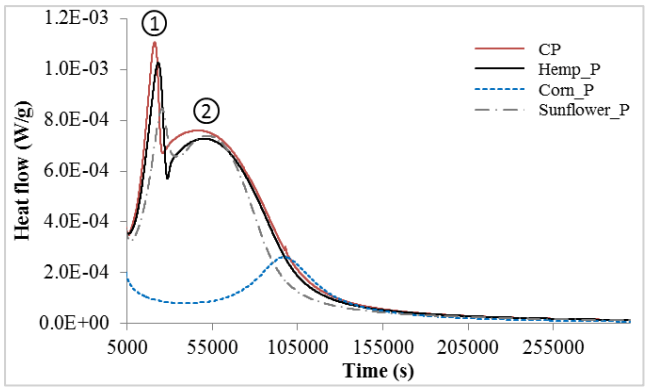

Figure 4: Heat flow by isothermal calorimetry of model pastes.

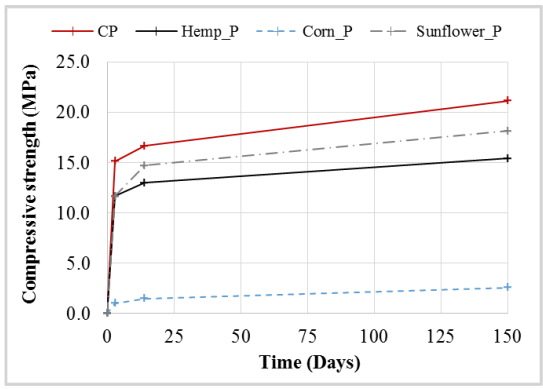

Figure 5: Compressive strength of model pastes at 3, 14 and 150 days.

3.2.3 Mineralogical evolution

The short term effect of bio-aggregate extractives was studied by XRD and TGA in order to explore the hardening mechnisms of model pastes. Differential TGA curves realized 24 hours after mixing are plotted in Fig. 6A.

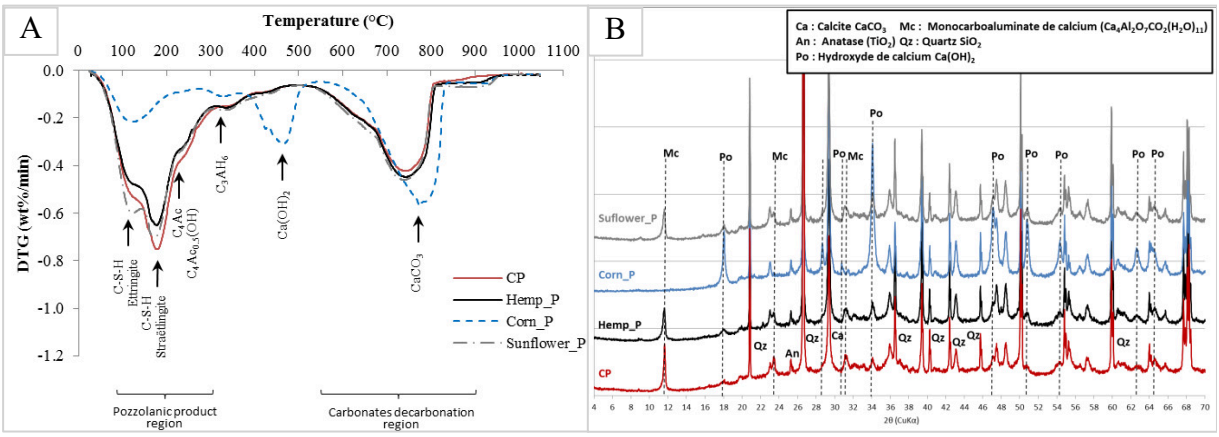

Figure 6: Differential TGA curves (A) and XRD analyses (B) of model pastes after 24h.

Extractives have a significant impact on the pozzolanic reaction development by reducing the amount of reaction products. The difference between the pastes based on hemp and sunflower extractives, and the control paste is mainly related to the peaks in a temperature range of 100-250°C. These peaks are attributed to the dehydratation of C-S-H, ettringite and straëtlingite.

The small peak at 250°C is attributed to calcium carboaluminates phases: calcium aluminium oxide carbonate hydrate, $Ca_4Al_2O_6CO_3(H_2O)_{11}$ (noted C_4Ac) and calcium aluminium oxide hemi-carbonate hydroxide hydrate, $(Ca_4Al_2O_6(CO_3)_{0.5}(OH)(H_2O)_{11.5}$ (noted $C_4Ac_{0.5}(OH)$) [5]. No significant delay is observed in the consumption of portlandite (430°C) in these pastes. On the contrary, in the paste based on corn extractives, a large amount of residual portlandite is observed after 24 hours. A deficit in the formation of C-S-H and straetlingite phases is also evidenced. These phenomena may be responsible for the decrease in mechanical performances. Finally, the increased presence of carbonates could be related to the release of carbon dioxide induced by the alkaline degradation of corn particles, which was responsible for the carbonation of portlandite [6]. These results are consistent with XRD analyses (Fig. 6B) that show similar crystallised compounds between control, hemp and sunflower pastes while corn paste is distinguished by the absence of calcium carboaluminates and the presence of portlandite.

4. Conclusion

This study aims to evaluate the potential of bark particles of sunflower and corn as bio-aggregates for lightweight concrete. It has been shown that:

- Particle size distribution of sunflower and corn particles could be corrected through a calibration process, notably based on the elimination of the longer particles.
- Corn particles present a limited water absorption capacity. This could be valorized in association with a clay matrix for example. On the contrary, the deleterious effect of corn extractives on the setting and hardening mechanisms of the pozzolanic binder would largely reduce the mechanical performances of vegetal concrete designed with these two components.
- Sunflower bark particles appear to be a good candidate for hemp shives substitution since their characteristics are close and their impact on the setting mechanisms of the pozzolanic binder negligible.

References

[1] Laborel-Préneron A., Magniont C., and Aubert J.-E., Characterization of Barley Straw, Hemp Shiv and Corn Cob as Resources for Bioaggregate Based Building Materials, Waste Biomass Valor (2017), 1–18

[2] Amziane S., Collet F., Lawrence M., Magniont C., Picandet V., and Sonebi M., Recommendation of the RILEM TC 236-BBM: characterisation testing of hemp shiv to determine the initial water content, water absorption, dry density, particle size distribution and thermal conductivity, Mater Struct Constr 50 (2017), 1-11

[3] AFNOR NF EN 196-3, Methods of testing cement – Part 3 : Determination of setting times and soundness, Association Française de Normalisation, France (2017)

[4] AFNOR NF EN 196-1, Methods of testing cement – Part 1: Determination of strength, Association Française de Normalisation, France (2006)

[5] Magniont C., Escadeillas G., Oms-Multon C., and De Caro P., The benefits of incorporating glycerol carbonate into an innovative pozzolanic matrix, Cem Concr Res 40 (2010), 1072–1080

[6] Govin A., Peschard A., and Guyonnet R., Modification of cement hydration at early ages by natural and heated wood, Cem Concr Compos 28, (2006), 12–20

SynerCrete'18 International Conference on Interdisciplinary Approaches
for Cement-based Materials and Structural Concrete
24-26 October 2018, Funchal, Madeira Island, Portugal

EVOLUTION OF HEMP CONCRETE PROPERTIES EXPOSED TO DIFFERENT TYPES OF ENVIRONMENTS

Guillaume Delannoy [(1)], Sandrine Marceau [(1)], Philippe Glé [(2)], Etienne Gourlay [(2)], Marielle Guéguen-Minerbe [(1)], Sofiane Amziane [(3)], Fabienne Farcas [(1)]

(1) Université Paris-Est, MAST, CPDM, IFSTTAR, Marne-la-Vallée, France
(2) Cerema, Laboratory of Strasbourg, Strasbourg Cedex 2, France
(3) Université Clermont Auvergne, Institut Pascal, Clermont-Ferrand Cedex 1, France

Abstract
Vegetal aggregates-based materials, as hemp concrete, are used to improve thermal insulation, acoustical and hygrothermal performances for a better living comfort in buildings, by using renewable resources. Hemp concrete is frequently used. However, the lack of knowledge about its long-term performances is a limitation to the development of the material. Therefore, the objective of this study of durability is to identify the ageing mechanisms of hemp concrete by using a pluridisciplinary and multiscale approach. Hemp concrete is aged for two years under two different environmental conditions, the factors of ageing used are temperature and variations of relative humidity. The evolution of functional properties (thermal, acoustical and mechanical) is followed and related to the evolution of microstructure and chemistry of the different components. The results show that under static laboratory conditions, the properties of hemp concrete are stable with time. The accelerated ageing allows changes in the functional properties with time, due to modifications of the binder chemistry and of the microstructure of vegetal aggregates, with an action of microorganisms.

1. Introduction

Hemp concrete is an insulating material used for its thermal, hygrothermal and acoustic properties [1]. It is composed of plant aggregates, called hemp shiv, which are coated and bound by a thin layer of mineral binder, whose thickness is less than 0.5 mm. The microstructure, and in particular the high porosity of shiv, brings the functional properties of the material [2].
Feedbacks on real constructions [3] made it possible to identify problems of implementation in the first constructions, which have since been largely corrected, in particular after the publication of building codes [4]. Therefore, the question of the evolution of the long-term performances of the material arises. Former studies focused on the durability of hemp concretes. In order to observe changes in functional properties or microstructure, accelerated aging is used with variations of relative humidity [5, 6], immersion in water [7] or freeze-

thaw cycles [8, 9]. The presence of water is indeed a risk factor for the durability of hemp concrete. Indeed, the hydrophilic nature of hemp shiv induces a swelling of the particles, and thus constraints at the interface between the vegetal components and the binder [10]. Moreover, in the presence of water and mineral binders, a high pH value can be achieved within the material, leading to alkaline degradation [11] as well as mineralization of plants [12]. The relative humidity value applied also has an impact on the evolution of the binder, and in particular on the kinetics of carbonation [13].
Too short aging periods (<75 days) explain the small variations in properties observed in the durability studies that set hygrometry as an aging factor [14]. Nevertheless, this type of aging is closer to the real conditions of use of the materials, and does not modify their integrity. Indeed, a leaching of organic or mineral materials is observed during the immersion cycles, which correspond rather to accidental conditions such as water damage in a building. It is for this reason that the study presented in this article uses accelerated aging consisting of humidification and drying cycles, by applying relative humidity variations, at a temperature favourable to the potential development of microorganisms. A multi-scale and multi-disciplinary approach makes it possible to highlight and link possible evolutions of functional properties (thermal, acoustic and mechanical performances) with the evolution of the microstructural and physicochemical properties of hemp concretes. In order to study the impact of the formulation on all long-term properties, two binders, with a different chemical composition and commonly used on worksites are chosen.
Firstly, the characterization of the functional, microstructural and chemical properties is presented as a function of time, depending on the type of aging. Then, these results are discussed by making the link between characterizations at different scales

2. Materials and methods

2.1 Materials and manufacturing

A commercial hemp shiv sold for insulation applications is selected for this study. A: commercially formulated binder (FL), based on natural lime (70%) and hydraulic and pozzolanic binders (30%), is selected.
Formulation of hemp concretes is set according to the building codes of hemp construction for a wall formulation [4]. The binder/shiv ratio is 2, and the total water/binder ratio is 1. The fresh density of hemp concretes is set to 530 $kg.m^{-3}$. Samples are demoulded after 7 days, and after 83 days of drying at 65% RH and 20°C, the dried density is about 350 $kg.m^{-3}$. Hemp concretes containing the formulated binder based on lime are called HC-FL.

2.2 Aging protocols

After curing, the test pieces are divided into two lots and are placed under two different environments for 2 years, defined from the results of the Marceau et al. [6]

- The first batch is used as reference (REF) and is stored in a room at 50% RH and 20°C.
- The second batch is submitted to accelerated aging (A_{WD}), corresponding to cycles of relative humidity from 40 to 98% at a constant temperature of 30°C in a climatic chamber.

The properties of the material are measured before aging (A_0) and then regularly over a period of 2 years (3, 6, 12, 18 and 24 months) on samples previously dried 48h at 40°C.

2.3 Aging protocols

Thermal conductivity measurements are conducted using a transient measurement technique (Hot Disk method) at 24 °C on five specimens for each formulation (measurement time 80 s, power 0.1 W).
The sound absorption coefficient α is measured using a Kundt tube (Acoustitube AFD) over a frequency range of 250 to 2000 Hz on five specimens. α (f) is between 0 (no absorption) and 1 (total absorption).
Concrete samples are mechanically tested in compression (10 cm in diameter and 20 cm in height) using a Zwick press with controlled displacement at 3 mm/min.
An analysis of the mineral phases is carried out by thermogravimetric analysis.
Open air porosity is measured using a porosimeter as described in [2] on 4 specimens.
Microstructural analysis is performed using a Quanta 400 FEI scanning electron microscope in SE and BSE mode.

3. Results

3.1 Functional properties

The evolution of thermal conductivity of hemp concrete for both types of aging is shown in Fig. 1. For the reference aging, no change in thermal conductivity is observed. In contrast with A_{WD} aging, an increase in thermal conductivity is visible.

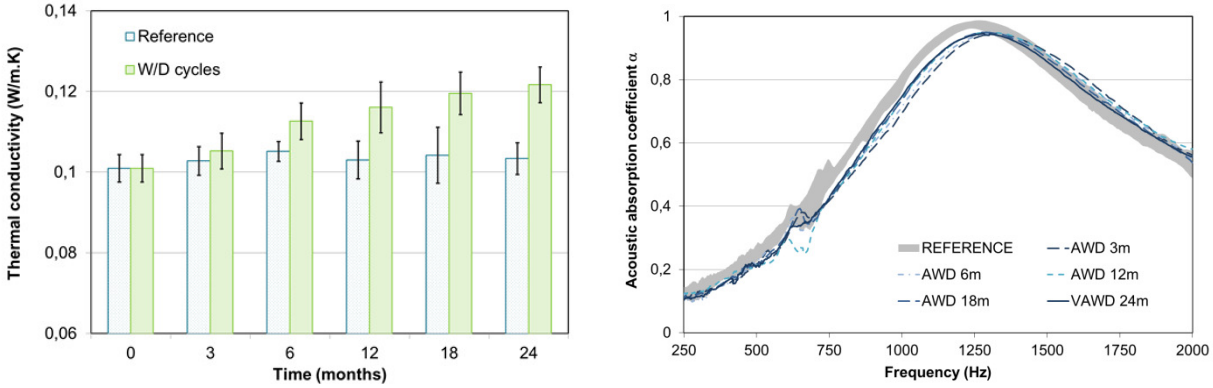

Figure 1: Evolution of the thermal conductivity and of the acoustic absorption coefficient in both environments.

Similarly, no significant evolution of the acoustic absorption coefficient is observed for the reference samples (Fig. 1). The results are therefore represented as an area representing the spindle of all measurements between 0 and 24 months. For aging A_{WD}, we observe a shift of the curve towards the higher frequencies, with a decrease of the maximum value. This stall occurs between 0 and 3 months, the other curves do not vary significantly.
The compressive strength results of hemp concrete specimens are shown in Fig. 2. In view of the results and of their dispersion, no change in the mechanical behaviour is observed. The weak mechanical resistance observed comes from a poor hydration of binder which is inhibited by extractible molecules of hemp, such as sugars [2].

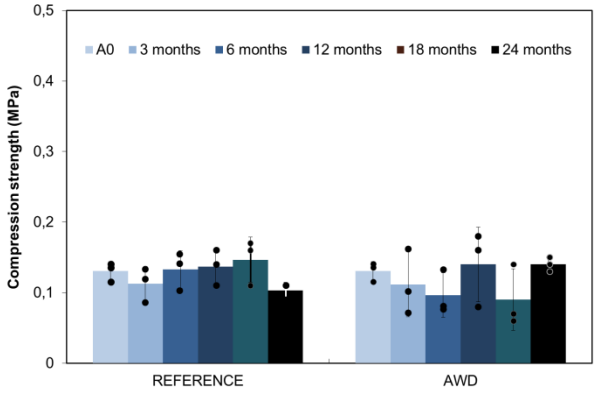

Figure 2: Evolution of the compression strengths in both environments

3.2 Physical properties

The mass variation of the test pieces is shown in fig. 3 Due to the low mechanical strength of the samples, some vegetal particles are released during their handling. In the reference environment, this induces an initial mass loss of around 3%. In spite of this, during the A_{WD} cycles, an increase in mass is visible over time. This increase occurs up to 18 months, then the mass seems to stabilize until 24 months. Considering an equivalent mass loss as observed for the reference specimens, the weight gain of samples stored in A_{WD} environment can be estimated at 10%.

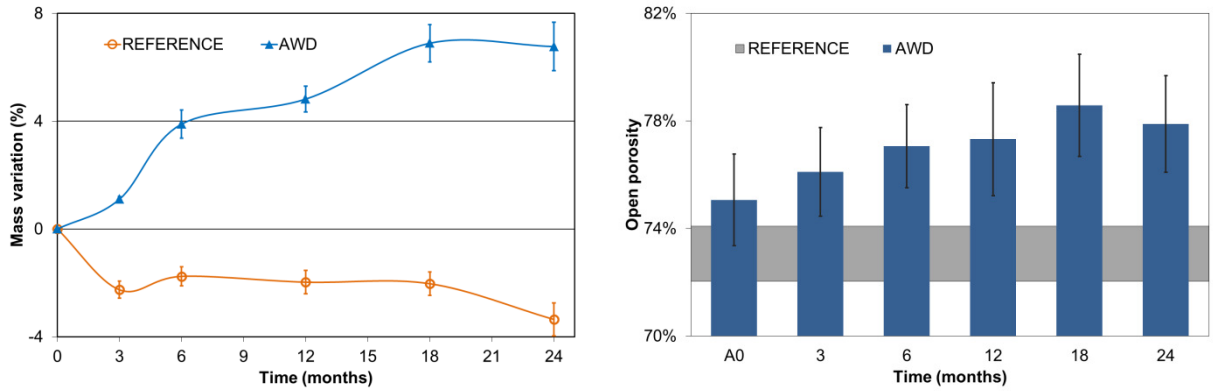

Figure 3: Evolutions of the mass and of the open porosity as a function of time

The open porosity accessible to the air is stable for the reference environment (Fig. 3). On the other hand, the value of open porosity increases of 4% in A_{WD} aging until 18 months then seems to have reached its maximum.

The observations with a scanning electron microscope were carried out on longitudinal and cross sections (Fig. 4). Perforations are visible in the plant walls (Fig. 4c), as well as hyphae (Fig. 4a) and penetration of the binder into the porosity of the aggregates (Fig. 4b and d).

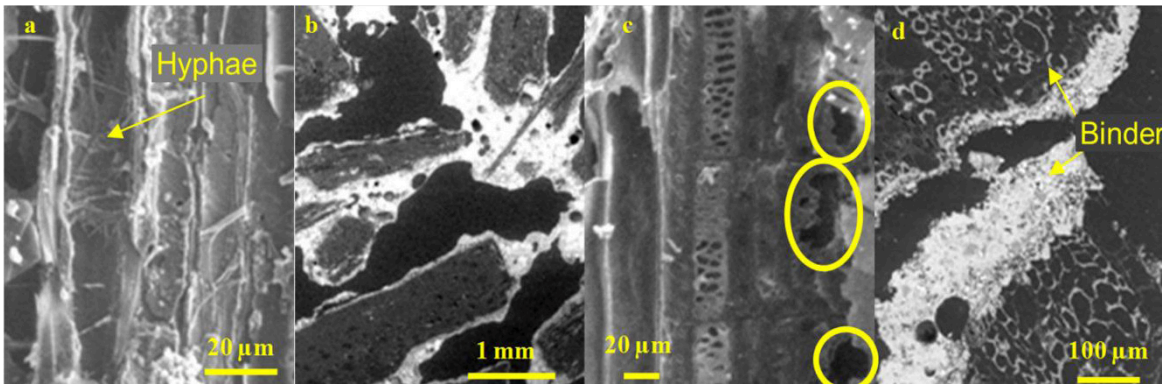

Figure 4: Observation of concrete microstructure by scanning electron microscopy

3.3 Chemical properties

The synthesis of the results of the thermogravimetric analyses on the mineral part is presented in Fig. 5 on the binder powder, at A_0 and during aging A_{WD}. It is observed that between the binder powder and the results at A_0, the hydration is not complete, as observed previously [2]. For this concrete, hydration is low at A_0 and most of the initial portlandite has carbonated. During aging A_{WD}, the hydration and carbonation of the binder slowly resume.

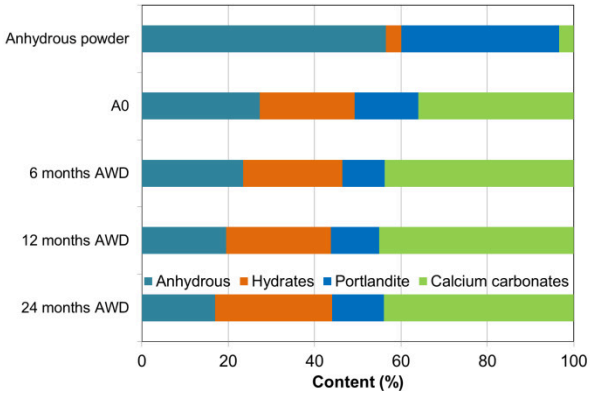

Figure 5: Evolution of the chemical composition on the binder during A_{WD} aging

4. Conclusion

The first conclusion of this study is that under reference conditions, no change in functional, microstructural or chemical properties is observed for 2 years. The material remains stable over time under these conditions.

The application of an accelerated aging protocol to hemp concrete under hygric stress has made it possible to highlight changes in functional, microstructural and chemical properties. Two major mechanisms seem to operate simultaneously: a densification of the mineral part by hydration and carbonation of binders during aging, as well as a degradation of the shiv by microorganisms. The densification of the mineral part leads to an increase in the mass of concretes, but also in their thermal conductivity. The attack of the vegetal particles is visible by an increase of the open porosity, the degradation of the plant wall allowing the access to an intraparticular porosity initially closed.

The presence of lime in the binder causes the modification of the mineral part by carbonation and by mineralization of the shiv porosity. These changes affect functional properties, such as acoustic behaviour, portlandite being water soluble and subject to migration under water stress. This binder is also sensitive to carbonation, which leads to a build-up and therefore an increase in thermal conductivity.
Finally, no evolution of the mechanical properties is observed, the effects of the hydration and carbonation recovery being counterbalanced by a weakening of the plant.

References

[1] Amziane, S. and Collet, F., Bio-aggregates Based Building Materials, RILEM State-of-the-Art reports, Vol. 23, Springer, Dordrecht (2017)
[2] Delannoy, G. et al, Influence of binder on the multiscale properties of hemp concretes, European Journal of Environmental and Civil Engineering (2018), 1-17
[3] Agence Qualité Construction, Isolants biosourcés: points de vigilance (2016)
[4] Construire en chanvre, Règles professionnelles d'exécution, SEBTP, Paris (2012)
[5] Arizzi, A. et al., Predicting the long-term durability of hemp-lime renders in inland and coastal areas using Mediterranean, Tropical and Semi-arid climatic simulations, Science of Total Environment 542 (2016), 757-770
[6] Marceau, S. et al., Influence of accelerated aging on the properties of hemp concretes, Construction and Building Materials 139 (2017), 524-530
[7] Sentenac, C. et al., Investigation on the performance and durability of treated hemp concrete with water repellent, Proceedings of the 2nd International Conference on Bio-based Building Materials, Clermont-Ferrand, France (2017), 20-28
[8] Walker, R. et al., Mechanical properties and durability of hemp-lime concretes, Construction and Buildings Materials 61 (2014), 340-348
[9] Sassoni, E. et al., Experimental study on the physical–mechanical durability of innovative hemp-based composites for the building industry, Energy and Building 104 (2015), 316-322
[10] Nozahic, V., Vers une nouvelle démarche de conception des bétons de végétaux lignocellulosiques basée sur la compréhension et l'amélioration de l'interface liant / végétal, PhD Thesis, Université de Clermont-Ferrand (2012)
[11] Wei, J. and Meyer, C., Degradation mechanisms of natural fiber in the matrix of cement composites, Cement and Concrete Research 73 (2015), 1-16
[12] Chabannes, M., Studying the hardening and mechanical performances of rice husk and hemp-based building materials cured under natural and accelerated carbonation, Construction and Building Materials 94 (2015), 105-115
[13] Marceau, S. and Delannoy, G., Durability of Bio-based concretes in Bio-aggregates Based Building Materials, RILEM State-of-the-Art reports 23, Eds. Amziane, S. and Collet, F., Springer, Dordrecht (2017), 167-187
[14] Gourlay, E., Caractérisation expérimentale des propriétés mécaniques et hygrothermiques du béton de chanvre, PhD Thesis, Université de Lyon (2014)

SynerCrete'18 International Conference on Interdisciplinary Approaches
for Cement-based Materials and Structural Concrete
24-26 October 2018, Funchal, Madeira Island, Portugal

INFLUENCE OF FILLER EFFECT AND POZZOLANIC REACTION OF BIOMASS ASHES ON MECHANICAL PROPERTIES OF CEMENT MORTARS

Vlastimir Radonjanin[(1)], Mirjana Malešev[(1)], Slobodan Šupić[(1)], Miroslava Radeka[(1)]

(1) Faculty of technical sciences, University of Novi Sad, Serbia

Abstract
The contribution of pozzolana in cement-based materials (concrete and mortar) can be categorized into: (i) physical or filler effect which is attributed by the fineness of the particles and (ii) chemical or pozzolanic effect which is attributed by the pozzolanic reaction. Various types of biomass, from agro-industrial processes, generate ashes through their combustion. These ashes, under certain conditions (chemical configuration, level of fineness), can have pozzolanic and/or filler activity in cementitious composites. In this study, the influence of filler effect and pozzolanic reaction of wheat straw ash (WSA), soya straw ash (SSA) and mixed soya and wheat straw ash (WSSA) was analysed. In the first phase pozzolanic activity and activity index of these ashes were tested and results have shown that SSA and WSSA have lower pozzolanic activity and activity index compared to wheat straw ash. That is why authors of this paper have tried to improve their filler effects by additional grinding in a lab ball mill. Filler effect was checked by testing of compressive strength of mortars in which 10 and 25% of cement was replaced with grinded ashes. Additional grinding had a positive impact on the activity index of WSSA, but in the case of SSA, it was close below the required value.

1. Introduction

Cement is the principal raw material for the concrete production, by which manufacturing leads to severe environmental problems, primarily caused by CO2 emission. The emission of CO2 is estimated as 1 tonne of CO2/1 tonne of cement produced which makes 8% of the total global emission. In addition, production of cement requires high energy and generates considerable costs; hence cement nowadays becomes unsuitable for the sustainable development in civil engineering [1].

Several research has been conducted on finding alternative materials that can be used as cement replacement, such as the disposable and less valuable wastes from industry and agriculture, whose potential benefits can be realized through recycling, reuse and renewing regimes [2]. Some studies showed that certain agro-waste materials could be utilised as a cement replacement in cement based materials. The utilization of agricultural waste can provide the alternative needed to make the industry more environmentally friendly and sustainable.

In Autonomous Province (AP) Vojvodina, in a northern part of Republic of Serbia, biomass is commonly utilized through combustion for heat generation. Wheat straw, soya straw and sunflower husk are major energy biosources and, by their combustion, large quantities of biomass ash are generated. This ash represents a potential source for the production of alternative mineral binders with cementitious properties.

The activity of these ashes, used as a binder in cement-based composites, is mainly influenced by amorphous silica content and fineness. In this study, the influence of filler effect and pozzolanic reaction of biomass ashes (wheat straw ash, soya straw ash and mixed soya and wheat straw ash) on mechanical properties of cement mortars was investigated.

2. Experimental research - Phase 1

Biomass ashes, used in this experimental study, were collected from three producers of biomass ash in Vojvodina. In the first phase of the experiment, following properties of ashes were tested:

- Basic physical properties (density, specific surface area),
- Chemical composition,
- Pozzolanic activity,
- Activity index.

The following materials were used in the study:

- Portland cement CEM I 42,5R (Lafarge-BFC Serbia),
- Wheat straw ash (WSA), "Mitrosrem", Sremska Mitrovica, Serbia, Fig. 1,
- Mixed wheat and soya straw ash, the ratio 50:50, (WSSA), "Soya Protein", Bečej, Serbia, Fig. 2,
- Soya straw ash (SSA), "Hipol", Odžaci, Serbia, Fig. 3,
- CEN Standard sand in accordance with EN 196-1,
- Distilled water.

Figure 1: View of biomass ashes after grinding, a) WSA, b) WSSA, c) SSA

2.1 Physical properties and chemical composition

After grinding for 6 hours, all types of biomass ashes had densities cca 2.400 kg/m^3, while specific surface area (Blaine) exceeded 5.000cm^2/g. Physical properites of tested biomass ashes are shown in Tab. 1.

Table 1: Physical properites of tested biomass ashes.

	Density (kg/m^3)	**Specific surface (Blaine) (cm^2/g)**
WSA	2.380	5.800
WSSA	2.370	5.500
SSA	2.400	5.200

The chemical composition of tested biomass ashes is given in Tab. 2. Ashes WSA and WSSA have relatively high silica content, exceeding 50%, while soya straw ash is characterized with lower silica content (13.8%), which should reflect on its pozzolanic activity.

Table 2: Chemical composition of biomass ashes (wt% of ash) [3].

	SiO_2	Al_2O_3	Fe_2O_3	CaO	MgO	Na_2O	K_2O	LOI
WSA	53.21	4.00	2.69	13.45	1.90	0.41	12.05	10.19
WSSA	51.93	0.19	1.39	14.28	2.07	0.43	18.43	9.27
SSA	13.80	1.76	1.45	47.53	7.76	0.07	5.23	18.60

With respect to the chemical composition, higher amorphous silica content results in the higher pozzolanic reactivity of ashes. Materials with very high silica content and large surface area intensively react with the water and the calcium hydroxide, generated during the hydration of cement, to produce additional C–S–H, which is the main strength contributing compound in cement-based composite. C-S-H gel makes denser microstructure of biomass ashes containing cement-based material.

2.2 Pozzolanic activity

The pozzolanic activity was tested on specimens prepared according to the procedure given in SRPS B.C1.017-2001. Results are given in Tab. 3. The class of pozzolanic activity was determined based on 7 day compressive (fp) and flexural (fzs) strength of standard mortar prisms (SRPS B.C1. 018-2001). Mortars were prepared with biomass ash, slaked lime and standard sand, (Figure 18), with following mass proportions: msl:mbash:mqs=1:2:9 and water/binder ratio 0,6 (where: msl – mass of slaked lime; mbash – mass of biomass ash; mqs – mas of CEN standard sand). After compacting, specimens were hermetically packed and cured 24h on 20°C, then 5 days on 55°C. After cooling of specimens in next 24h up to 20°C, compressive and flexural strength were tested.

Table 3: Pozzolanic activity of biomass ashes.

	$f_{zs,mean}$ [MPa]	S_{dev}	$f_{zs,min}$[MPa]	$f_{p,mean}$ [MPa]	S_{dev}	$f_{p,min}$ [MPa]	CLASS
WSA	3.4	0.22	3.3	11.0	0.49	10.3	**10**
WSSA	3.6	0.05	3.3	9.3	0.30	8.75	**5**
SSA	1.6	0.17	1.45	4.06	0.08	3.84	/

Testing of pozzolanic properties showed that wheat straw ash has medium pozzolanic activity of Class 10, mixed soya and wheat straw ash has lower pozzolanic activity - Class 5, while soya straw ash has low pozzolanic activity that is not sufficient to express through Class. These classes are used to measure pozzolanic activity based on the strength of cementitious mixtures containing the pozzolan with lime. They are one of the parameters in the selection and classification of pozzolans. Higher Class of pozzolanic activity will probably lead to the better reactivity of these materials in cementitious systems.

2.3 Activity index

Activity index was studied on specimens prepared according to the standard EN 450-1. Results are given in Tab. 4. Activity index is a ratio of the compressive strength of standard mortar prisms, prepared with 75%wt cement and 25%wt fly ash by mass, to the compressive strength of standard mortar prisms prepared with 100% cement, when tested at the same age. According to the criteria, activity index at 28 days and at 90 days shall not be less than 75% and 85%, respectively. Wheat straw ash exhibited even higher compressive strength in relation to the reference mortar's strength, which can be attributed to the filler effect of small particles of wheat straw ash. Ashes WSSA and SSA didn't fulfil criteria, as their activity indexes were below required value. This is due to the insufficient pozzolanic activity of soya-based biomass ashes.

Table 4: Activity index of biomass ashes.

	$f_{p,28d}$ [MPa]	Index, 28d (%)	$f_{p,90d}$ [MPa]	Index, 90d (%)
C	50.26	-	54.53	-
WSA	52.39	**104.24**	58.96	**108.12**
WSSA	32.65	64.90	41.80	76.60
SSA	28.3	56.3	test in progress	

The results indicate that SSA and WSSA have lower pozzolanic activity and insufficient activity index compared to WSA. As pozzolanic reactivity depends heavily on the size of the material particles, the next stage in the experimental research was an attempt to improve filler effects of these biomass ashes by additional grinding in a lab ball mill.

3. Experimental research - Phase 2

Ashes WSSA and SSA were additionally grinded for 18 hours (total of 24 hours) in a lab ball-mill, thereby achieving Blaine fineness: 15.000cm^2/g. The ashes were further used for activity index test, by testing of compressive strength of mortars, in which 10 and 25% of cement was replaced with grinded ashes. This approach enabled recording the pure effect of fineness on soya straw ash reactivity (filler effect).
Additional grinding of biomass ashes had a positive impact on activity index of WSSA ash, by both replacement levels (10 and 25%). Activity indexes were 91.7% and 94.3% for replacement levels 10% and 25%, respectively. Within this process, activity index of WSSA ash at the replacement level of 25%, was increased by 29% (from 64,9 to 91,7%), hence the criterion for activity index at the age of 28 days, according to EN 450-1, was satisfied (>75%) – Fig. 4.
Activity index of SSA was over 75% at the replacement level of 10%, whereas additional grinding increased index by 7%. At the replacement level of 25%, additional grinding increased index by 19% (from 56,3 to 69,9%); however, it was still below the required value (69.6<75%) – Fig. 5.

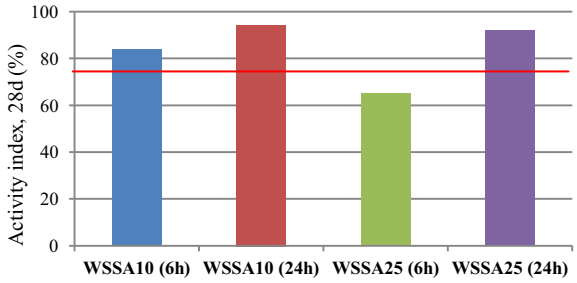

Figure 4: Activity index of WSSA.

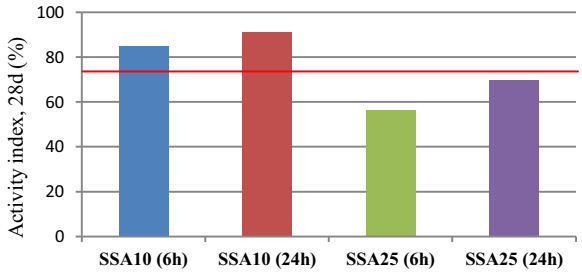

Figure 5: Activity index of SSA.

4. Conclusions

In this study, pozzolanic properties and activity index of agro-waste materials, originating from AP Vojvodina: wheat straw ash, soya straw ash and mixed soya and wheat straw ash were tested in order to investigate the possibility of their application in cement based composites.
Results show that wheat straw ash has high pozzolanic activity of Class 10 and high activity index, while soya straw ash and mixed soya and wheat straw ash have lower pozzolanic activity and activity index. In order to define possible use of soya-based biomass ashes, authors of the paper tried to improve filler effect of these types of ashes by additional grinding in a lab ball mill. Additional grinding had a positive impact on the activity index of WSSA, as it was increased by 29%, satisfying criterion at the age of 28 days. In the case of SSA, activity index was increased by 19%; however, it was close below the required value.
Main reason of low pozzolanic activity of soya-based biomass ash lies in its low silica content (13,8%). Therefore, in the third phase, an attempt to stimulate pozzolanic activity of soya straw ash and improve its activity index will be performed by using mineral admixture with

high amount of amorphous silica – silica fume, as a substitute for part of biomass ash. This research should provide reasons for use of inert biomass ashes in cement composites.

Acknowledgements
The paper presents the part of research realized within the project "Theoretical and experimental research and improvement of educational process in civil engineering" conducted by the Department of Civil Engineering and Geodesy, Faculty of Technical Sciences, University of Novi Sad.

References
[1] Josephin A. et al, Experimental investigation on rice husk ash as cement replacement on concrete production, Construction and Building Materials127 (2016), 353–362
[2] Aprianti E. et al, Supplementary cementitious materials origin from agricultural wastes – A review, Construction and Building Materials 74 (2015), 176–187
[3] Malešev M. et al, Physical and mechanical properties of cement mortars with biomass ashes as SCM, International RILEM Conference on Materials, Systems and Structures in Civil Engineering - Conference segment on Concrete with Supplementary Cementitious Materials, Technical University of Denmark, Lyngby, Denmark (2016), 223-233.
[4] SRPS EN 196-6: Methods of testing cement - Determination of fineness
[5] SRPS EN 196-1: Methods of testing cement - Determination of strength
[6] SRPS B.C1.018.2001 - Non-metal mineral raw material: Testing of pozzolanic activity
[7] EN 450-1:2012: Fly ash for concrete. Definition, specifications and conformity criteria

SynerCrete'18 International Conference on Interdisciplinary Approaches
for Cement-based Materials and Structural Concrete
24-26 October 2018, Funchal, Madeira Island, Portugal

IN-PLANE RACKING STRENGTH OF TIMBER WALLS FILLED WITH HEMP CONCRETE

Husam Wadi [1,2], Sofiane Amziane [1,2] , Evelyne Toussaint [1,2] , Mustapha Taazount [1,2]

(1) Université Clermont Auvergne, Institut Pascal, Clermont-Ferrand, France
(2) CNRS, Aubière, France

Abstract
The use of low carbon material in structures improves the insolation level and sound absorption and also decreases the weight of building. In response to this need, the use of bio-aggregate such as hemp shives is increasing in Europe and especially in France. Hemp concrete is now used in construction as a sustainable and carbon neutral infill wall material around timber-framed construction. This study focuses on the effect of wall dimensions on the in-plane racking strength of timber frame walls filled with hemp concrete. Two wooden geometrical configurations were used as wall units, the first was diagonal bracing walls under compression, and the second was vertical stud walls. These two types of timber walls are most widely used as structural elements in construction subjected to lateral loads. In this research, an experimental investigation of large-scale timber walls both with and without hemp concrete was carried out to investigate the contribution of this filling material against the lateral loads. The hemp walls then compared to empty frames to determine the real contribution of hemp concrete in the lateral strength of the timber wall. Based on the results obtained from the experimental tests, this study confirms, firstly, that hemp concrete has a small participation against lateral loads with wall dimensions 2.5 m height and 1.2 length. However, several studies found that hemp concrete has a high racking strength. In fact it cannot be generalized that hemp concrete has always a significant strength in timber wall. The filling material could not work mechanically against lateral load without a complete form of compression diagonal zone which make the material loaded under shear forces. This zone is related to the dimensions of the wall and is present when the ratio between the height and the length of the wall (L/h) ≥1. Within this limit, the material mechanically works, otherwise, the results are totally different.

1. Introduction

Construction and public projects nowadays are facing a significant challenges of reducing energy consumption due to the large amount of using daily services such as heating, electricity and hot water in the residential and commercial buildings especially in Europe. For this purpose, many buildings regulations try to use now bio-base materials with a high quality of physical properties in construction sectors. The use of low carbon material in structures will firstly, improve the insolation level and sound absorption and secondly, will decrease the weight of building because this natural material considered as a lightweight aggregate. In response to this need, the use of bio-aggregate such as hemp, flax and sunflower is increasing in Europe and especially in France [1]. Wood is one of the most widely used building materials in many countries in the world, because it has a good physical properties and environmentally friendly [2]. Timber walls are frequently used as a structural system in the buildings designed to withstand lateral loads and transfer these forces to the foundations with ductile behaviour [3]. Timber shear wall consists of timber frame and sheathing board, connected by fasteners. The sheathing board may be made of a variety of materials, such as Oriented Strand Board [4-7]. Hemp particles are a natural low carbon material used to reduce energy consumption in buildings [5]. Nowadays this natural material is used in construction as infill wall material within timber framed construction in Europe and especially in France [5].

2. Theoretical approach

Two different shapes of timber walls were considered in this study, vertical stud and diagonal bracing walls (see Fig. 1 & 2). A linear elastic behaviour of the wall-unit were assumed in this approach, also the deformations are caused by only external force. By applying the virtual work transformation by unit-load theorem (F), the total top displacement of the wall unit (Δ) can by calculated as:

$$\Delta = \frac{\partial W}{\partial F} \tag{1}$$

where W is the elastic strain energy stored in the wall and provided by an external horizontal load F applied on the top of the wall unit. In the present case, the total strain energy consists of three internal forces: a normal force N, shear force V and an internal moment M as illustrated in Eq. (2). By taking the material characteristics into account, then the total horizontal displacement (Δ_1) in vertical stud wall can be calculated as a function of the internal forces by Eq. (3), also the total horizontal displacement (Δ_2) in the diagonal bracing wall can be calculated by Eq. (4) using the same principle.

- For vertical stud timber frame: $F(kN) = 0.0083 \times \Delta_1$ (mm)
- For diagonal bracing element: $F(kN) = 2.7 \times \Delta_2$ (mm)

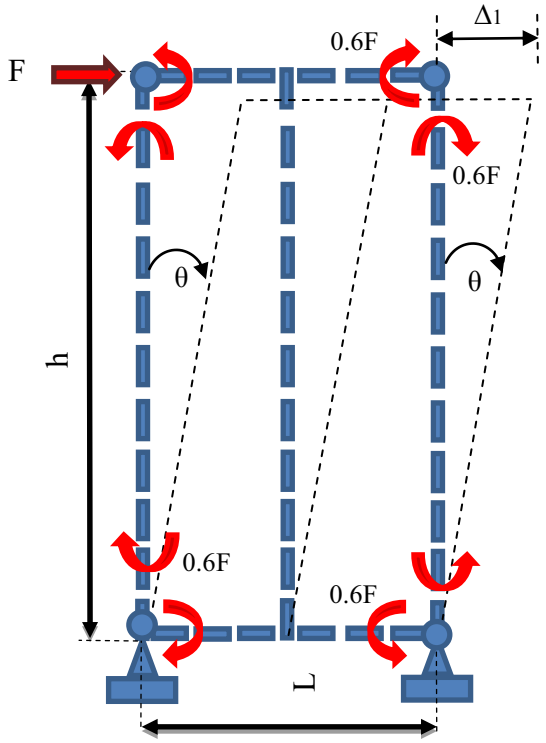

Figure 1: Loaded and unloaded state of vertical stud wall unit.

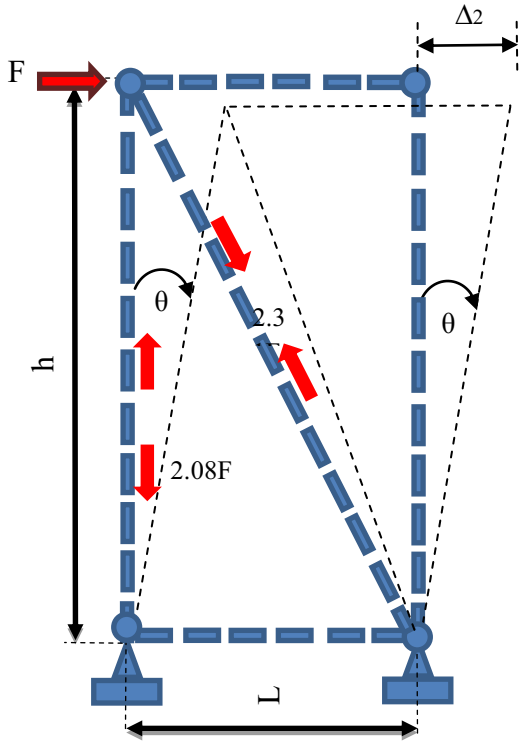

Figure 2: Loaded and unloaded state of diagonal bracing wall unit.

$$W = \frac{1}{2}\left[\frac{1}{E_{0,05}\,I}\int M^2(x)\,dx + \frac{1}{E_{0,mean}\,A}\int N^2(x)\,dx + \frac{1}{G_{mean}\,\acute{A}}\int V^2(x)\,dx\right] \quad (2)$$

$$\Delta_1(m) = \left[\left(\frac{0.964}{E_{0,05}\,I}\right) + \left(\frac{5.72}{E_{0,mean}\,A}\right) + \left(\frac{3.85}{G_{mean}\,A'}\right)\right]F(N); \quad A' = \frac{2}{3}A \quad (3)$$

$$\Delta_2(m) = \left[\left(\frac{1.26\times10^{-5}}{E_{0,05}\,I}\right) + \left(\frac{25.5}{E_{0,mean}\,A}\right) + \left(\frac{1.0\times10^{-4}}{G_{mean}\,A'}\right)\right]F(N) \quad (4)$$

$$\Delta_i(m) = (a_M + a_V + a_N)F(N) \quad (5)$$

It was obvious that on the first hand, normal and shear forces in the vertical stud walls are negligible compared to the value of internal moments (1.2×10^{-4}). On the second hand, shear forces and internal moments are negligible in the diagonal bracing case compared to the value of normal forces (3.5×10^{-7}) as presented in previous Figures (Fig. 1 & 2).

3. Experimental Results

3.1 Vertical stud wall

The empty vertical stud wall was considered as a control frame for comparing with hemp walls (see Fig. 3). The maximum load bearing capacity of the empty frame was around 0.18 kN (Fig. 4). It was obvious that the theoretical approach describe the elastic behaviour of the wall and matches the initial experimental behaviour experimental results. Vertical stud hemp walls (V-H) were tested with the same set up and method as illustrated in Fig. 5. The average load bearing capacity of the vertical stud hemp wall was around 2 kN (Fig. 6).

Figure 3: Empty vertical stud frame in test.

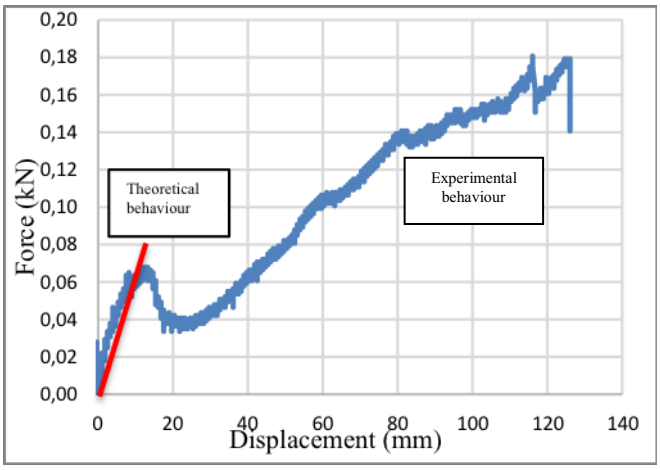

Figure 4: Force-Displacement behaviour for frame only.

Figure 5: Vertical stud hemp wall in test.

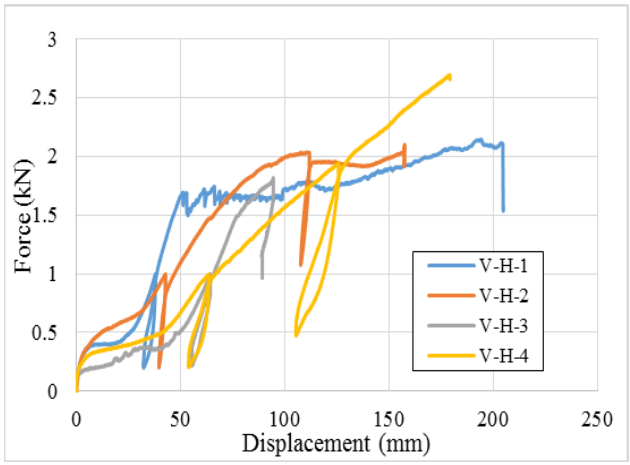

Figure 6: Force-Displacement behaviour for vertical stud hemp wall.

4.2 Diagonal bracing walls

The load bearing capacity of empty diagonal bracing walls was presented below in Fig. 8 by force-displacement plots. The average maximum load bearing capacity of diagonal bracing wall was 10.78 kN. The theoretical behaviour of diagonal bracing wall did not show the same behaviour of the experimental results (Fig. 8), this difference is related to the joint consideration. It is clear from the results that the experimental behaviour of the wall is less rigidity than the mathematical approach. Figure 10 presents the lateral strength of diagonal bracing walls filled with hemp concrete (D-H) and obviously, the hemp concrete did not contribute in the lateral strength with the diagonal bracing wall and no clear contribution of the hemp concrete in both cases in the lateral resistance as infill material in the diagonal configuration.

Figure 7: Diagonal bracing walls in test.

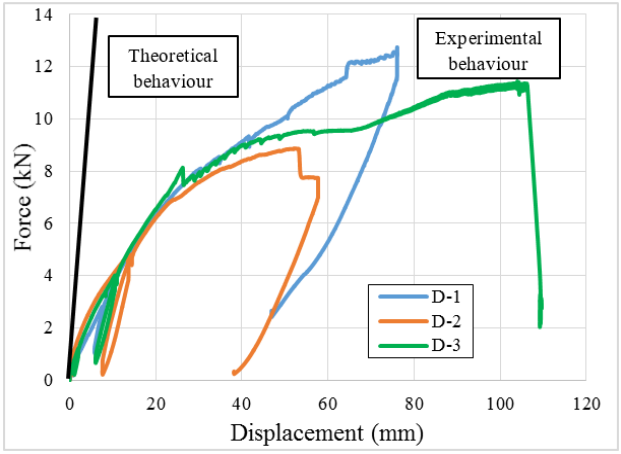

Figure 8: Force-Displacement behaviour for diagonal bracing walls.

Figure 9: Diagonal bracing hemp walls in test.

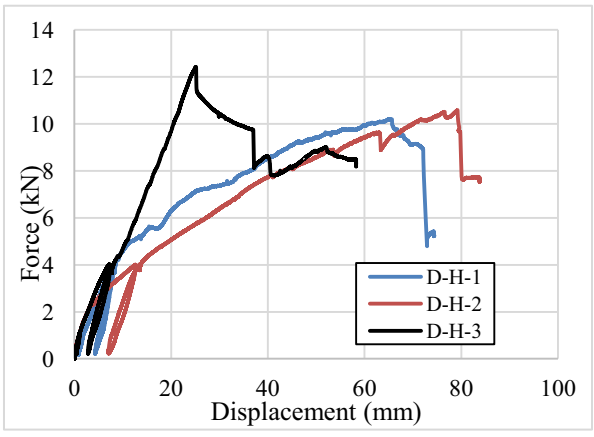

Figure 10: Force-Displacement behaviour for diagonal bracing hemp walls.

5. Analysis and conclusion

Obviously, the two shapes have a completely different behaviour with the filling material. On the first hand, the participation of hemp concrete has more than ten times in vertical stud wall comparing to the empty frame, on the other hand, the participation of hemp concrete is around zero in the diagonal bracing. Simply, the forces did not transmit to the filling material in the diagonal bracing due to the high rigidity of the whole system. However, in case of vertical stud wall which is less rigidity, the forces easily transmit to the filling material and make it participate in the lateral strength. Despite the contribution of hemp concrete with vertical stud wall, still this contribution is insufficient. In fact, the dimensions of the timber wall (L/h) play a main role to make the filling material load under shear forces. Several studies found that hemp concrete has a high racking strength. This study confirms that the contribution of hemp concrete in the lateral strength of the timber wall depends significantly on the length of the wall as the height is constant. Also installing hemp concrete in a very high rigid system will prevent transmitting forces to the filling materials and decrease its participation in the lateral resistance, the more rigid the wall is, the less resistant hemp is.

References

[1] Amziane, S. and Arnaud, L. Eds., Bio-aggregate-based building materials: applications to hemp concretes, Holboken: ISTE Ltd., London, UK (2013)
[2] Premrov, M. and Kuhta M., Influence of fasteners disposition on behavior of timber-framed walls with single fibre-plaster sheathing boards, Constr Build Mater 23 (2009), 2688-2693
[3] Loo, W.Y. et al, A numerical study of the seismic behavior of timber shear walls with slips-friction connectors, Engineering Structures 34 (2012), 233-243
[4] Vessby, J. et al, Coupled and uncoupled nonlinear elastic finite element models for monotonically loaded sheathing-to-framing joints in timber based shear walls. Engineering Structures 32 (2010), 3433-3442
[5] Gross, C. and Walker P., Racking performance of timber studwork and hemp-lime walling, Constr Build Mater 66 (2014), 429-435
[6] Bevan, R. et al, Hemp lime construction: a guide to building with hemp lime composites. IHS BRE Press (2008)
[7] Wadi, H. and Amziane S., Mechanical behaviour of unclassified timber walls against horizontal forces, 35èmes Rencontres universitaires de génie civil de l'AUGC, Nantes, France (2017)
[8] Christopher, G. and Pete, W., Racking performance of timber studwork and hemp-lime walling. Constr Build Mater 66 (2014), 429-435
[9] Hans, S. et al, Mechanical behaviour of wooden framework buildings with sprayed hemp concrete, Proc. ICBBM: 2nd International Conference on Bio-based Building Materials (3BM), Clermont-Ferrand, France (2017)

SynerCrete'18 International Conference on Interdisciplinary Approaches
for Cement-based Materials and Structural Concrete
24-26 October 2018, Funchal, Madeira Island, Portugal

LIFE CYCLE ASSESSMENT OF BIO-BASED CONSTRUCTION PANELS WITH MAGNESIUM BINDER

Maris Sinka [(1)], Aleksandrs Korjakins [(1)], Diana Bajare [(1)], Genadijs Sahmenko [(1)]

(1) Riga Technical University, Riga, Latvia

Abstract
The hemp-lime concrete as a self-bearing thermal insulation material has a low thermal conductivity and neutral CO_2 emissions. However, the strength limitation of lime binder is an issue to use this material as a load-bearing material. Magnesium oxychloride binders are of considerably higher strength level and better bio-compatibility compared to the lime-based binders. In this study, magnesium oxychloride binders were used in combination with hemp shives as a filler to produce composite materials to be used in production of construction panels on industrial scale. These panels consist of an outer and inner border layer and a middle thermal insulation layer. The life cycle assessment of such panels was performed, analysing various impacts on the environment in the production process and comparing it to usual materials with similar thermal transmittance properties. Results of the research showcase that the magnesium-hemp concrete can be used in production of bio-based construction panels because the strength of their outer layers can reach more than 1.0 MPa at 450 kg/m^3 density and thermal conductivity for inner layer – 0.062 W/m·K at 210 kg/m^3 density. It was proved in the research that the magnesium-hemp panel represents reduced impact on environment by CO_2 emissions 6 times less compared to usual construction materials.

1. Introduction

The construction industry is one of the largest emitters of CO_2 [1] mainly because of the production of traditional construction materials and insufficient building insulation with resulting energy demand [2]. It also contributes negatively to other environmental impact categories [3].
To reduce this negative impact materials with low thermal conductivity and reduced impact on environment are necessary. One group of such materials is bio-based insulation composites

that uses agricultural waste products as the primary filler, hemp concrete is one of the most studied materials in this group. It is a mixture of hemp shives and usually hydraulic lime, it is a self-bearing thermal insulation material with low thermal conductivity (lower than 0.064 W/m·K) [4] and neutral or negative CO_2 emissions [5]. However, the hydraulic lime binder used in this material is of limited strength because of compatibility issues with bio-based filler, so to ensure broader use of the bio-based materials, a binder of higher strength and better bio-compatibility is required.

Magnesium oxychloride cement (MOC) is a binder that can be used to produce bio-based materials with higher mechanical strength compared to lime binder. This is because magnesium oxychloride cement has better compatibility with organic fillers [6] compared to lime based binders creating highly alkaline environment that enables organic substances, such as lignin, to be released from filler. The MOC is usually used for production of sheeting boards containing wood fibres and perlite [7] or to create various bio-composites with wood [6].

Magnesium oxychloride cement is produced by combining magnesium oxide with magnesium chloride brine solution; it forms $MgO–MgCl_2–H_2O$ ternary system [8] respectively. Magnesium oxychloride cement can also reach higher mechanical strength than lime: 120 [9] to 140 MPa [8]. Magnesium carbonate decomposes at lower temperatures than calcium carbonate, about 700 °C, which releases less CO_2. However, no CO_2 is sequestered when magnesium oxide reacts with magnesium chloride as opposed to lime binders.

2. Materials and Methods

In this study multi layered bio-based construction panel is proposed as a solution to optimally use material properties using less dense middle layer for insulation and denser outer layers for envelope purposes (Fig. 1.). The panels can be used as a load-bearing panels with structural timber frame. Magnesium binder is used for bio-based composites with varying ratio of shives:binder, to control density. Mixtures are created in laboratory conditions (Fig. 1.) and tested, the results acquired are used for conducting Life cycle assessment of the panel and comparing it to traditional building materials.

Mechanical properties of biocomposites were tested with Zwick Z100 universal testing machine, pressure was applied with 10 mm/min speed, compressive strength was recorded at 10% relative deformations (according to LVS EN 826). Thermal conductivity was measured with LaserComp FOX600 heat flow meter.

Hemp shives used in this research are manufactured by local producers, their granulometry has been optimized for hemp concreate in previous research [10]. Caustic magnesium oxide CCM RKMH-F from Austrian company "RHI AG Ltd" is used with 76% MgO purity. Hardener magnesium chloride hexahydrate containing 47% $MgCl_2$ is used in this research.

A forced action mixer was used to produce the test samples. At the beginning of production process, the hemp shives are blended with water at a ratio 1:1.25 of volume, to hydrate the hemp shives ensuring that the water would not be eventually reduced from the binder. After adding magnesium oxide and magnesium chloride it is mixed for three minutes, after which samples are placed for two days into molds, and after demolding they are drayed in laboratory conditions - 20±2 °C and 40±10 % RH – until constant volume is reached.

Figure 1: Proposed panel prototype with three different density layers (left), experimental panel scaled model (right)

Table 1: Composition and properties of different panel layers

	Shives, kg	Binder, kg	Average density, kg/m^3	Thickness, mm	Thermal conductivity, W/m·K	Target compressive strength, MPa
Outer layer	3.77	9.64	452.2	30	0.112	1.00
Middle-insulation layer	36.42	28.65	210.1	290	0.062	0.15
Inner layer	6.28	10.50	332.5	50	0.077	0.35

3. Results and Life cycle assessment

In the scope of this research Life cycle assessment was carried out according to ISO 14040/44 guidelines which consist of the following steps: 1. Definition of goal and scope; 2. Inventory analysis; 3. Impact analysis; 4. Interpretation.

3.1. Definition of goal and scope

Goal of this research is to assess the life cycle of a multi-layer construction panel produced of experimental magnesium-hemp concrete, by evaluating impact of material on the greenhouse gas emissions and comparing it with the traditionally used construction materials.

The LCA calculation programme SimaPro 8 and the Ecoinvent 3.0 data base that have been used for most of the related processes, was used for assessment. Calculations were performed according to the CML-IA baseline method.

To compare the life cycle of magnesium-hemp material with that of other materials there must be a comparable functional units of alternative materials. As thermal insulation is the primary function of the material, functional unit is defined with U value – 0.18 W/m^2·K. Dimensions of the panel are based on experimental results in Tab. 1., outer layer is 30mm, middle-insulation layer is 290 mm, inner layer is 50 mm.

Alternative materials with similar U values were chosen to be the 500 mm 300 kg/m^3 blocks of aerated concrete without additional thermal insulation, 300 mm 375kg/m^3 blocks of aerated concrete with 100 mm 120kg/m^3 rock wool insulation, and 440 mm thick ceramic blocks with 100 mm 120kg/m^3 of rock wool insulation. Transportation for all the materials was set at 100 km.

None of the materials created specific additional emissions in the usage phase so they are not considered in this research, thus "Cradle-to-gate" system is used for analysis [10].

3.2. Inventory analysis

When possible, the data was used from the Ecoinvent database, as well as the required data from the previous researches about life cycle assessment of the hemp construction materials [10] and other related papers [11], [12].

3.3. Life cycle impact assessment and interpretation

After life cycle impact assessment, it is possible to analyse separately emissions created by the magnesium-hemp functional unit and its separate processes. It can be seen that impact of different major components of the panel (such as different density layers and wooden frame) is similar, with exception of Global warming potencial (GWP) where middle layer has negative CO_2 emissions due to highest shives:binder ratio (Tab. 2.). Compared by thickness, outer and inner layers have proportionally greater impact in all categories as middle layer due to the elevated levels of binder. The binder is responsible for 70-75% of all impacts of middle layer and 80-90% of inner and outer layer impacts, due to highly energy intensive binder production.

Even though the hemp shives absorb more CO_2 than is produced during the cultivation and processing period, these processes also release carbon dioxide in atmosphere that could be reduced. The largest part of emissions (around 45%) from hemp cultivation comes from mineral fertilisers, both in their production and in use, so their reduction would be necessary - for example, by using covering crops, complementing the nitrogen fertiliser after braiding of plants, broader use of tests to determine optimal nitrogen level in the ground, etc., as agriculture already is second largest GHG emitting industry in Latvia with 24% of total emissions [13].

Compared to all alternative materials bio-based panel emit 6 times lower amounts of CO_2, only 12.6 kg/CO_2 eq. per m^2 of wall (Fig. 2., Tab. 2.). This is mainly due to absorbed CO_2 amounts by hemp shives in the growth process and because of considerable amount of energy used in production of construction blocks [14] that makes up the largest part of functional unit of alternative materials.

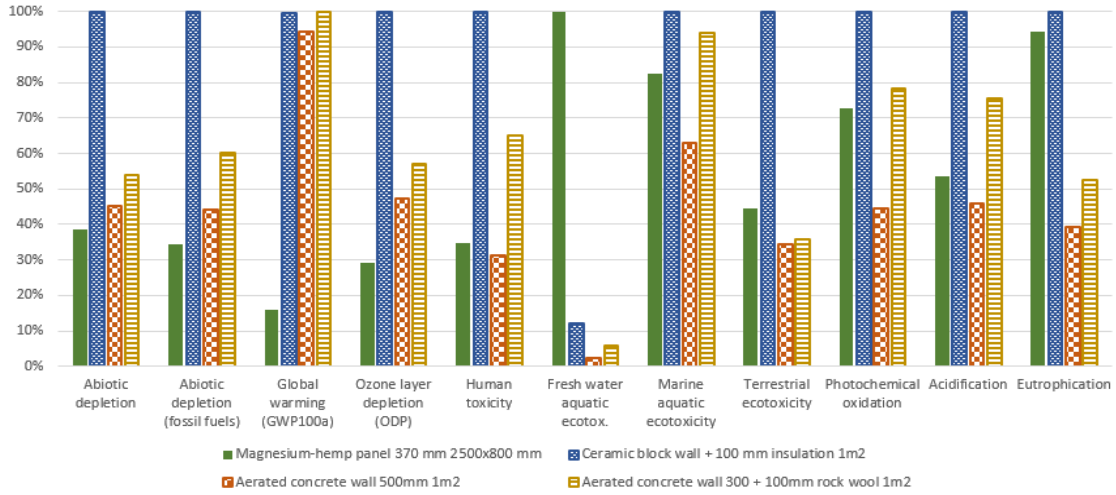

Figure 2: CML-IA baseline environmental impact results of magnesium-hemp panel and alternative materials

Considering other impact categories, panel has lower or similar impact in all categories except Fresh water aquatic ecotoxicity and Eutrophication (Fig. 2.). Eutrophication is due to the fertilizer use and could be reduced by lowering amount of fertilizer applied by using techniques described above. Fresh water aquatic ecotoxicity impact comes from magnesium oxide production that has high amounts of emissions to water oxide in Ecoinvent database, as it is based on iron mining. The impact of magnesium oxide is around 200 times higher than for similar binders as cement of lime according to the database, but no sources in literature indicate such difference, so it should be viewed with caution.

4. Conclusions

To answer the growing need for construction materials with lowered environmental impact a new type of material is needed. Bio-based construction materials can answer this need, as their environmental impact is low, due to usage of large volumes of agricultural waste as filler and due to their thermal properties, that allows to provide optimal building insulation. In the paper it was proposed to use these materials in wall insulation panels with constructive wooden frame, hemp shives as a filler and an alternative binder – magnesium oxychloride cement.

Properties of various density magnesium-hemp material were tested experimentally. Material has compressive strength of around 0.15 MPa at low densities of 210 kg/m^3 that allow to achieve thermal conductivity of 0.062 W/m·K. To achieve 1 MPa compressive strength a 450 kg/m^3 density is needed with λ value 0.112 W/m·K. These properties can allow for material to be used in wall insulation panels in three layers – outer envelope layers and middle thermal insulation layer, and to achieve U value of 0.18 W/m^2·K at 370 mm panel thickness.

LCA for magnesium-hemp panel were done and environmental impact compared with alternative materials. In most categories panel shows lower impact than alternative construction block materials, in GWP it has the largest advantage, as hemp shives absorbs CO_2 in the growing process, thus having 6 times lower emissions - only 12.6 kg/CO_2 eq. per 1 m^2 panel. Highest impact of the panel is in the Fresh water aquatic ecotoxicity and Eutrophication. The former is due to high amounts of emissions to water for magnesium oxide in Ecoinvent database, as it is based on iron mining. Compared to similar binders as cement or lime, these emissions are about 200 times higher and should be interpreted with consideration. Eutrophication is due to fertilizer used for hemp production, impact is 95% of ceramic block impact and 2 times higher than aerated concrete impact.

Table 2: CO_2 emissions in detail for studied and other materials 1 m^2 (upper), emissions in detail for each part of studied material (lower)

Proposed materials	Magnesium-hemp panel	Ceramic block	Aerated concrete	Aerated concrete with insul.	-
kg CO_2 eq	12.62	78.66	74.55	79.05	-
Components of the studied material	Outer layer	Middle layer	Inner layer	Wooden frame	Transport
kg CO_2 eq	5.06	-6.28	3.68	9.39	0.77

Acknowledgements
The financial support of European Regional Development Fund project Nr.1.1.1.1/16/A/007 "A New Concept for Sustainable and Nearly Zero-Energy Buildings" is acknowledged.

References
[1] Kylili, A., M. Ilic, and P. A. Fokaides, Whole-building Life Cycle Assessment (LCA) of a passive house of the sub-tropical climatic zone, Resour. Conserv. Recycl. 116 (2017), 169–177
[2] Li, H. X., L. Zhang, D. Mah, and H. Yu, An integrated simulation and optimization approach for reducing CO 2 emissions from on-site construction process in cold regions, Energy Build. 138 (2017), 666–675
[3] Hossain, M. U., C. S. Poon, Y. H. Dong, and D. Xuan, Evaluation of environmental impact distribution methods for supplementary cementitious materials, Renew. Sustain. Energy Rev. 82 (2018), 597–608
[4] Walker, R., S. Pavia, and R. Mitchell, Mechanical properties and durability of hemp-lime concretes, Constr. Build. Mater., 61 (2014), 340–348
[5] Arrigoni, A., R. Pelosato, P. Meli, G. Ruggieri, S. Sabbadini, and G. Dotelli, Life cycle assessment of natural building materials: the role of carbonation, mixture components and transport in the environmental impacts of hempcrete blocks, J. Clean. Prod. 149 (2017), 1051–1061
[6] Zhou, X. and Z. Li, Light-weight wood-magnesium oxychloride cement composite building products made by extrusion, Constr. Build. Mater. 27 (2012), 382–389
[7] Manalo, A., Structural behaviour of a prefabricated composite wall system made from rigid polyurethane foam and Magnesium Oxide board, Constr. Build. Mater. 41 (2013), 642–653
[8] Xu, B., H. Ma, C. Hu, S. Yang, and Z. Li, Influence of curing regimes on mechanical properties of magnesium oxychloride cement-based composites, Constr. Build. Mater. 102 (2016), 613–619
[9] Li, Y., H. Yu, L. Zheng, J. Wen, C. Wu, and Y. Tan, Compressive strength of fly ash magnesium oxychloride cement containing granite wastes, Constr. Build. Mater. 38 (2013), 1–7
[10] Sinka, M., P. Van Den Heede, N. De Belie, D. Bajare, G. Sahmenko, and A. Korjakins, Comparative life cycle assessment of magnesium binders as an alternative for hemp concrete, Resour. Conserv. Recycl. 133C (2018), 288–299
[11] Stramkale, V., Multipurpose hemp for bioproducts and biomass. Latgale Agriculture Research Centre. Latgale Agriculture Research Centre, Vilani, Latvia (2015)
[12] Turunen, L. and H. M. G. van der Werf, Life Cycle Analysis of Hemp Textile Yarn, Comparison of Three Hemp Fiber Processing Scenarios and a Flax Scenario, INRA-French Natl. Inst. Agron. (2006)
[13] Gancone, A., J. Pubule, M. Rosa, and D. Blumberga, Evaluation of agriculture eco-efficiency in Latvia, Energy Procedia 128 (2017), 309–315
[14] Yang, D., L. Fan, F. Shi, Q. Liu, and Y. Wang, Comparative study of cement manufacturing with different strength grades using the coupled LCA and partial LCC methods—A case study in China, Resour. Conserv. Recycl. 119 (2017), 60–68

SynerCrete'18 International Conference on Interdisciplinary Approaches
for Cement-based Materials and Structural Concrete
24-26 October 2018, Funchal, Madeira Island, Portugal

MARKET POTENTIAL OF WOOD BIOMASS ASH UTILISATION IN CEMENT COMPOSITES - CROATIAN CASE STUDY

Nina Štirmer [(1)], Ivana Carević [(1)], Bojan Milovanović [(1)], Ana Baričević [(1)]

(1) University of Zagreb, Faculty of Civil Engineering, Zagreb, Croatia

Abstract
The growing trend of using biomass as a renewable energy source (RES) results in a growth of the wood biomass ash (WBA) as a by-product. Considering the increasing amount of WBA as well as the costs of its disposal, it is necessary to establish its sustainable management.
The WBA quality varies depending on the biomass used in power plants, combustion technology and the location where collection of WBA is done. One of the possible solutions of the WBA´s disposal problem is an application in cement composites. Since WBA differs from the coal fly ash and does not satisfy the existing regulation for use of fly ash in cement, determination of the potential and adequacy of WBA as a cement replacement and/or mineral admixture in cement composites is needed.
This paper presents detailed analysis of market conditions in Croatia regarding possible use of WBA in cement composites. Estimation of the WBA production in Croatia has been made based on data gathered from energy power plants. A survey for assessing current demands of the cement and concrete industry has been carried out and the extent to which the market is ready to accept WBA is evaluated.

1. Introduction

To achieve a sustainable future, the European Union (EU) has committed to the targets set in the EU's Renewable Energy Directive, meaning that a 20 % of the total energy required will come from renewable sources by 2020. For a period beyond 2020, the Revised Renewable Energy Directive [1] is already introduced and activities are proposed to cut emissions in the Union by at least 40% below 1990 levels by 2030. As the most significant renewable energy source in the EU, solid and gaseous biomass fuelled power plants are expected to contribute in achieving the set goals [2].

Croatia belongs among the countries of large biomass potential and part of biomass could be used for production of energy. The Energy Strategy of the Republic of Croatia [3] was adopted to define the development of Croatian Energy sector by 2020 and with a goal to build, under the conditions of uncertainty in the global energy market and scarce local energy resources, a sustainable energy system. Within the Energy Strategy, it was defined that a part of the available biomass shall be used as feedstock in biomass combustion power plants, preferably cogeneration plants, to assure the total power of 85 MW by 2020 (Figure 1).

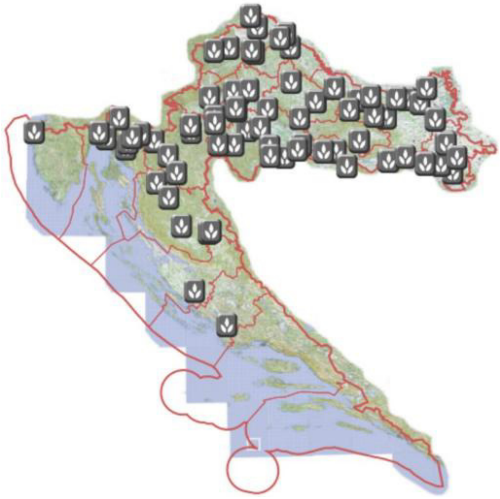

Figure 1: Locations of the biomass plants planned by 2020 in Croatia [4]

Based on the official data from the Croatian Energy Market Operator (CEMO), currently in the Republic of Croatia there are 14 plants with the total installed capacity of 28.955 MWe. However, the CEMO database contains only data for plants connected to the public power network. The plants that produce the energy for their own production needs (such as wood industry drying ovens, etc.) or district heating plants that produce only thermal energy and are not included in the CEMO database. Therefore, the database of CEMO was supplemented by the review of published papers where in total 22 biomass plants were confirmed running at the time of writing this paper. Additional data was collected through survey conducted within 13 biomass plants and 11 concrete producers.

The aim of the research was to determine the available quantities of wood biomass ash (WBA) in Croatia and their potential for the future application in the construction industry. Research is carried out as part of the research project *Transformation of Wood Biomass Ash into Resilient Construction Composites (*TAREC^2). TAREC^2 involves a detailed characterization of available WBA in the Republic of Croatia (biomass origin, combustion technology, ash type) with the aim of detecting wood biomass plants whose WBA has potential for application in the construction sector.

2. Types & quantities of wood biomass ash

Croatia has a large wood industry, and therefore the potential of using biomass as fuel. A total of 48% of the territory of the Republic of Croatia is covered by forests. Biomass is mainly

obtained from sawdust, wood and paperboard industry. As the biomass, the following types of wood are often used: beech and oak, then hornbeam, and to a lesser extent poplar and mixed woods, spruce, willow and fir.
This research and survey concentrated to wood biomass ash (WBA) which is obtained by combustion of forest biomass and non-contaminated waste wood. Different types of combustors are being used in Croatian biomass plants, but grate combustors are most often (69.2 %), then fluidized bed combustors (23.1 %) and pulverized fuel combustors (7.7 %). Combustion temperature ranges from 500 to 1000°C, with an average value of 800°C. The biomass plants are in operation for an average of 7580 hours or approximately 316 days per year with the average biomass consumption of 5 t/h.
The greatest influence on the quality and the quantity of WBA produced has the type of biomass feedstock used. Respondents stated that 15 % of surveyed biomass plants use pure wood chips, while 85 % use other types of wood biomass as well, such as wood chips with impurities like soil, etc. None of the respondents uses residues from agriculture, herbaceous plants or wood pellets and briquettes.
Surveyed biomass plants produce in total 15,190 tons of WBA per year. Consumption of wood biomass in the representative biomass plant can easily be calculated based on the acquired data. If the representative biomass plant is in the operation 7580 hours per year and the consumption of wood biomass is 5 t/h, then 37,900 tons of wood biomass is averagely consumed per one biomass plant. This means that the combustion of 1 t of the wood biomass on average produces 3.1% of WBA.
Based on the data available from the survey, a projection of the total wood biomass consumption and the WBA production in Croatia was performed. Proportionally to the installed power in biomass plants, it is estimated that the consumption of wood biomass is 676,786 tons per year and that the total amount of WBA in the existing biomass plants is 20,890 tons.

3. Cement consumption and concrete production

The conducted surveys show that approximately 35,000 tons per year of mineral admixtures are used for cement production; mostly slag, limestone and fly ash. Most commonly used cement types are: CEM I – 18 %, CEM II – 64 % and CEM III – 18 %. According to the survey results, concrete is mainly produced with the following compressive strength classes: C25/30 and C30/37 (each represented with 91%), then C20/25, C35/45 and C40/50 all represented with 64 % within surveyed producers. As additional concrete properties, producers mainly specify water permeability, freeze-thaw resistance, abrasion and resistance to chemicals. To assure improved concrete properties, 27% of the respondents use mineral additives such as silica fume, fly ash and metakaolin.

4. Application of WBA in concrete production

Today's commercially available cements typically contain about 20% of supplementary cementitious materials – such as fine-milled limestone, granulated slag and fly ash from coal-combustion thermal power plants. European standard EN 450-1:2013 [5] and US standard

ASTM C618 [6] prevent the use of fly ashes that are not obtained by combustion of coal, i.e. limit the use of WBA as a mineral additive in the production of cement. Nevertheless, the standard EN 450-1:2013 [5] allows the use of fly ash produced by parallel co-combustion. Following, many studies have been focused on the use of ash obtained by combining coal and wood [7]. Given that the chemical composition of the WBA is different from fly ash obtained from the combustion of coal and does not meet the existing regulations, a detailed characterization of WBA is required to determine the potential and appropriateness of WBA in cement composites.

State of the art review on the application of WBA in the construction industry concludes that WBA contains higher amounts of CaO, K_2O, P_2O_5 and MgO compared to fly ash from coal. According to [8], WBA has irregular particles while other types of ash (fly ash from coal, milled ash obtained from coal and wood biomass) show approximately spherical shapes (Figure 2). WBA particles are coarser than cement particles and are more porous and irregular in shape [9]. In addition, increasing the WBA share in concrete showed increase of the initial and final setting time as well as postponed hardening [10,11,12]. This may be desirable when postponed setting is required [7] or for use in massive concrete [12]. However, results vary depending on the type of WBA used [9].

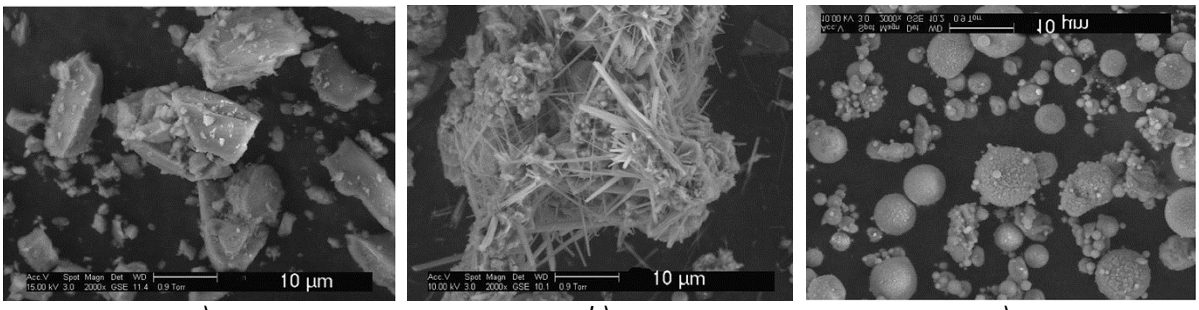

a) *b)* *c)*

Figure 2: SEM analysis: a) cement, b) WBA i c) 80 % of coal fly ash (class C) mixed with 20 % of WBA [13]

Maximum recommended cement replacement with WBA is 20 %, as further increase of WBA has negative influence on the properties of cement composites. Based on significant degradation of properties, some authors recommend a maximum replacement up to 10%. Especially, if durability properties are considered. Namely, analysis of the durability properties shows that the optimal proportion of cement substitution by WBA is 5%. Substitution in larger shares (up to 10% of cement) causes an increased water absorption. Carevic et al. [14] suggest that mixtures with WBA content below 10 % have satisfying behaviour when exposed to the aggressive environment XF4 (56 cycles) [15]. Others, state that WBA has no adverse effects on freezing and thaw resistance [9,10,16]. Similar conclusions were obtained for the influence of WBA on the chloride diffusion. According to [17], the chloride diffusion coefficient decreases with the increase in WBA content. On contrary, according to [9] the WBA does not have an adversely effect on the chloride resistance of the concrete. Using WBA as a swelling admixture, due to the large share of free CaO and MgO, is yet to be research. However, swelling that occurs due to the WBA incorporation in concrete can be used to alleviate the problem of autogenous shrinkage

occurring in cement composites with a very low water-cement ratio. Flexural and compressive strength of cement composites is reduced as the WBA content increases.
Further research is needed to assure distinguished understanding of the WBA influence on both, mechanical and durability properties of cementitious composites. Nevertheless, following the conducted literature review, it can be concluded that based on its characteristics WBA can be used as: (a) alternative raw material for the production of clinker; (b) mineral admixture in cement production and (c) a mineral admixture in the manufacture of cement composites (as a partial cement replacement).

5. Conclusions

Based on the conducted surveys and proportionally to the installed power in biomass plants in Croatia, an annual consumption of wood biomass is estimated to approximately 680,000 tons. Furthermore, total amount of WBA produced in the active biomass plants is 20,890 tons per year. This quantity could be used to satisfy the needs of approximately 20 concrete productions plants with an average production of 50,000 m^3 of concrete per year. For example, in only 1 concrete plant by replacing 10% of cement, 1500 t of WBA can be used annually. The inert particles of WBA can be used as a substitute for a fine aggregate fraction (sand). However, such implementation in the construction industry must be followed by the strict and regular quality control due to the variable quality of WBA.

References

[1] European Commission, Proposal for a Directive of the European Parliament and of the Council on the promotion of the use of energy from renewable sources (recast) (2017)
[2] European Commission, State of play on the sustainability of soli d and gaseous biomass used for electricity, heating and cooling in the EU, SWD (2014) 259 final, Comm. Staff Work. Doc. (2014)
[3] Croatian Council, Energy Strategy of the Republic of Croatia, Official Gazette 130 (2009)
[4] Ministry of Economy, Labour and Entreneurship of the Republic of Croatia, Renewable Energy Sources – review – Interactive map 62 (2012). [Online]. Available: http://oie-aplikacije.mingo.hr/InteraktivnaKarta/. [Accessed: 01-Jan-2016].
[5] HRN EN 450-1, Fly ash for concrete -- Part 1: Definition, specifications and conformity criteria, Croatian Standards Institute, Croatia (2013)
[6] ASTM C 618, Standard Specification for Coal Fly Ash and Raw or Calcined Natural Pozzolan for Use, American Society for Testing and Materials, USA (2010)
[7] M. Berra, T. Mangialardi, and A. E. Paolini, Reuse of woody biomass fly ash in cement-based materials, Constr. Build. Mater. 76 (2015), 286–296
[8] J. Rosales, M. Cabrera, M. G. Beltrán, M. López, and F. Agrela, "Effects of treatments on biomass bottom ash applied to the manufacture of cement mortars," *J. Clean. Prod.*, vol. 154, pp. 424–435, 2017
[9] S. Chowdhury, M. Mishra, and O. Suganya, The incorporation of wood waste ash as a partial cement replacement material for making structural grade concrete: An overview, Ain Shams Eng. J. 6 (2) (2015), 429–437

[10] C. B. Cheah and M. Ramli, The implementation of wood waste ash as a partial cement replacement material in the production of structural grade concrete and mortar: An overview, Resour. Conserv. Recycl. 55 (7) (2011), 669–685
[11] A. U. Elinwa and Y. A. Mahmood, Ash from timber waste as cement replacement material, Cem. Concr. Compos. 24 (2) (2002), 219–222
[12] F. F. Udoeyo and P. U. Dashibil, Sawdust Ash as Concrete Material, J. Mater. Civ. Eng. 14 (2) (2002), 173–176
[13] S. Wang, L. Baxter, and F. Fonseca, Biomass fly ash in concrete: SEM, EDX and ESEM analysis, *Fuel* 87(3) (2008), 372–379
[14] I. Carević, I. Banjad Pecur, and N. Stirmer, Utilization of Wood Biomass Ash (WBA) in the Cement Composites, in ICBBM 2017 - Proceedings of the 2nd International Conference on Bio-based Building Materials (2017), 196–201
[15] HRS CEN/TS 12390-9 Testing hardened concrete -- Part 9: Freeze-thaw resistance with de-icing salts – Scaling, Croatian Standards Institute, Croatia (2016)
[16] S. Wang, E. Llamazos, L. Baxter, and F. Fonseca, Durability of biomass fly ash concrete: Freezing and thawing and rapid chloride permeability tests, Fuel 87 (3) (2008), 359–364.
[17] M. D. L. Garcia and J. Sousa-Coutinho, Strength and durability of cement with forest waste bottom ash," Constr. Build. Mater. 41 (2013), 897–910

SynerCrete'18 International Conference on Interdisciplinary Approaches
for Cement-based Materials and Structural Concrete
24-26 October 2018, Funchal, Madeira Island, Portugal

MECHANICAL PERFORMANCE, SHRINKAGE AND WEATHERING OF TREATED HEMP CONCRETE

Mohammed Sonebi [(1)], C. Sentenac [(1)], Sofiane Amziane [(2)]

(1) Queen's University Belfast, Belfast, UK
(2) University Clermont Auvergne, Polytech Clermont-Ferrand, France

Abstract
This paper investigated the effects of aggregate treated with linseed oil and two types of binders (calcic lime and Prompt Natural Cement binder-Vicat). The particle distribution, the absorption of particles, the capillarity absorption of hemp concrete and the compressive strength at 7, 14 and 28 days were determined. The results showed that with higher density treated samples get a higher compressive strength. In addition, hydraulic performance was tested with the capillarity test and highlighted the great decrease of sorption coefficient on treated samples. Concerning the autogenous shrinkage, the results of treated samples shrinkage were higher than no-treated ones. Finally, the durability performance test included the full water immersion showed that treated samples with linseed oil are better compared to none-treated. These treated samples absorbed less water, therefore less degradation and softening of the specimens.

1. Introduction

Hemp concrete principal weakness point is the strength in compression but the lack of information concerning the durability performance of this material can also be an explanation for the professional's reluctance to use bio-based concrete [1-3]. These ten last years have conducted several studies on hemp concrete to improve its properties this included the binders effect on mechanical strength but also the compaction effects [1, 2]. Matrix additions and aggregates treatments were also conducted to improve hemp concrete performances [1, 2]. The durability and cure conditions stay the less studying properties [7, 8] but this lack of information can be an explanation for the professional's reluctance to use bio-based concrete.
In this study, the effect of linseed oil (LO) as treatment of aggregates was investigated. Few studies have already been conducted on this treatment [1, 2] but in our case hemp concrete

has been made with two different binders: Cement Vicat (V) and a composite binder based on calcic lime (C). The mix composition for this study was similar for all mixes and each treated aggregates type was compared to a normal hemp (NH) concrete sample for every performance. In total, four mixes were investigated:

- LOV : Vicat binder with linseed oil treatment on hemp shiv
- NHV : Vicat binder with normal hemp shiv
- LOC : Calcic lime binder and additions with linseed oil treatment on hemp shiv
- NHC : Calcic lime binder and additions with normal hemp shiv.

2. Materials, mix compositions and test methods

Hemp shiv was used for this work. Hemp shiv used in the experimental program was Yorkshire hemp in UK. The first binder used in this study was Vicat Cement. Linseed oil is yellow oil obtained from the dried, ripened seeds of the flax plant. Linseed oil is a drying oil; meaning it can polymerize into a solid form. Because of polymerisation it took time to drying process, therefore after mixing the oil with the aggregates, they were left for 20 days to be dry. The linseed oil (LO) amount was evaluated by 0.5 mass ratios with aggregates. The sample was homogenised every day to ensure the homogenous of drying process.
According to the French professional rules for hemp concrete structures [9], shuttered wall mix composition was tested in this investigation with water/aggregates = 3, Binder to aggregates = 2 and water to binder = 1.5.
The water absorption and bulk density were measured according the protocols to RILEM TC 236 [2]. Water absorption test is particularly interested in this study to compare treatments effects on particles water absorption.
The compressive strength was determined on cubes of 50 mm size tested with a displacement of loading rate of 3 mm/min.
The capillary absorption was measured of cube 100 mm at 14 and 28 days after manufacture. During this curing time samples are placed in a control room at 20°C of temperature and e relative humidity of 55%.
Basically, this test is used to measure the volume and weight change of the hemp concrete under several drying and wetting cycles. It enables to simulate the weather conditions, at the end of all the cycles the influence of these cycles on the strength in compression is measured. Samples used in this case are 100mm cubes, four samples for each mixed are needed: two in the air and two for weathering cycles. The autogenous shrinkage was measured on prism of 50x50x200 mm^3 to measure the variation of length of the samples at different ages.

3. Results and discussion

3.1 Water absorption and bulk density

In this part the water absorption was measured on normal hemp shiv (NH) and treated hemp shiv with linseed oil (LO). Fig. 1 presents the variation of water absorption.

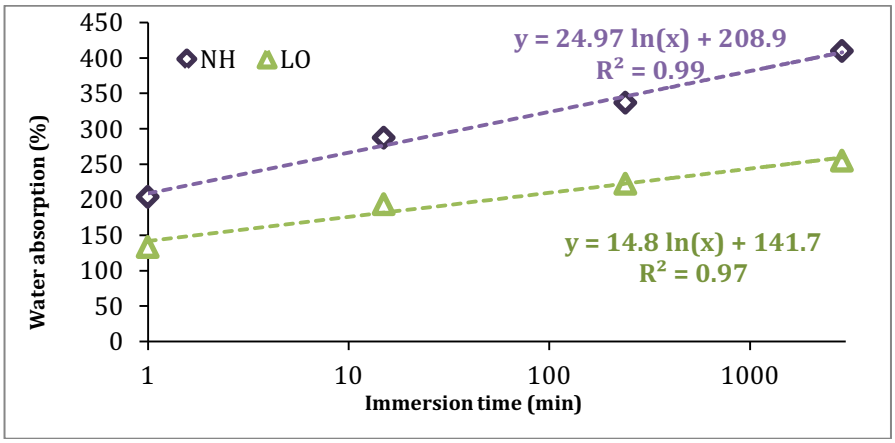

Figure 1: Water absorption of particles in function of time of treated and none-treated hemp shiv

After 1 min of immersion the LO treatment is effective with 133% of water absorption compare to NH aggregates with 204%. After 48 hours the result is the same LO is less absorbent than NH with respectively 255% and 410%.
Water absorption of bio-aggregates is a recurrent problem. The water absorbed by the particles is not available for the binder hydration this is the reason why this investigation is based on aggregates treatments. LO treatment is not just a coating, the treatment infiltrate with polymerisation into the particle and, with this mass addition it blocks particles pore, which avoid water to enter inside the particle.
The bulk density on treated hemp shiv and normal hemp shiv were measured to compare the weight added or not on our samples. Following the process described on previous chapter we have measured the bulk density of three samples for each type of hemp. An average can enable us at the end to obtain the bulk density.
The bulk density obtained for normal hemp (NH) was around 100.9 ± 4.1 kg/m^3. This value is lower than the usual value about 110kg/m^3. This resulted can be explained by the important quantity of fibres contained in the hemp shiv used in this investigation. The bulk density of LO aggregates is almost double of NH one of 186.4 ± 9.1 kg/m^3.

3.2 Autogenous shrinkage

NHV results of autogenous shrinkage of hemp shiv mixes were the lowest one (Fig. 2). The treated mixes with linseed oil for both binder seems to led a high autogenous shrinkage and this can be attributed that there was more water in mix (not absorb by hemp shiv) which hydrated and therefore, led to more autogenous shrinkage. At 50 days, the autogenous shrinkage treated Vicat mix was 5 times higher than none treated and it was almost the same with calcic lime for both mixes NHC and LOC.

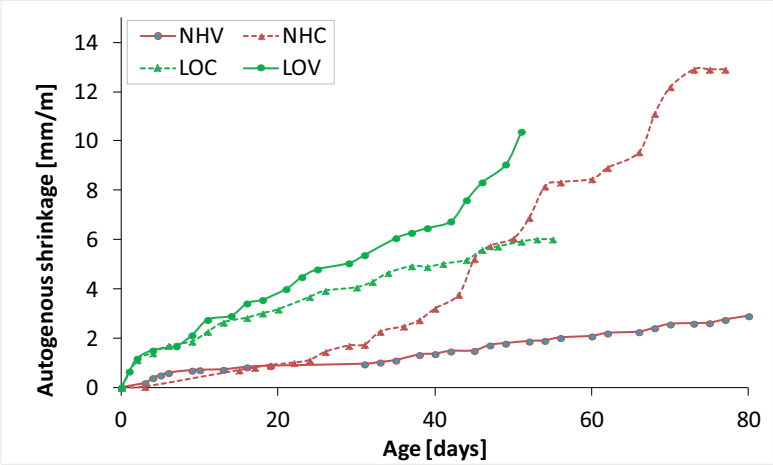

Figure 2: Autogenous shrinkage all mixes

3.3 Effect of treatment with linseed oil on compressive strength

The density has been reduced with age due to the drying of samples in air. The lower reduction is observed for NHC mix with: 374kg/m^3 at 7d and 335 kg/m^3 at 28d (39 kg/m^3 of loss). It can be observed the fact that all mixes with Vicat exhibited the highest densities than those mixes with calcic lime. For example at 28d the difference in percentage represents 9% for NH and 13% for LO between Calcic mix and Vicat mix. LO mixes have the higher density at any age of samples compared to NH mixes, which are quite similar.

Fig. 3 presents the compression strength at 5% of deformation (2.5mm in case of 50mm cubes). At 7 d, LO mixes have the higher compressive strength. However, at 28 d, it is NHV mix which had the highest compressive strength about 0.21 MPa and the f'c of LOV and LOC were 0.17 MPa and 0.20 MPa, respectively. The lowest f'c at 28 d was for NHC (0.14 MPa). Fig. 3 highlights the fact that at 5% of deformation, NHV has the highest compressive strength following by LO mixes. On the other hand, LO treatment enables hemp concrete to be stronger in case of mixed lime, however in average, the compressive values at 14d and 28d of Vicat cement LOV were lower by 5% than NHV.

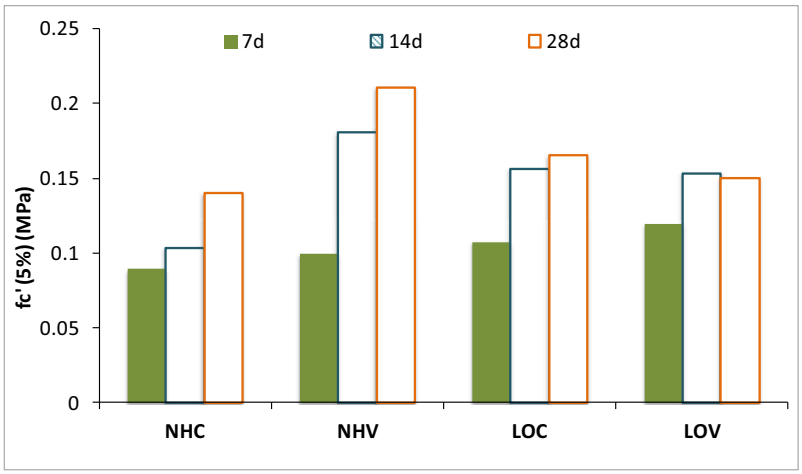

Figure 3: Compressive strength at 5% deformation of all mixes

3.4 Effect of treatment with linseed oil on weathering

Figure 4 represents the water absorption evolution during weathering cycles. It highlights the fact that NH mixes were the most absorbent with a water absorption average included between 60% and 90%. Fig. 5 shows only the wetting cycles and the significant rate increased after the first immersion 60% for NH mixes. After 3 cycles the NHV mix absorbed an average of 80%, NHC is more around 70%, these rates were higher than treated mixes ones. LO mixes were no more than 11% as water absorption during the partial immersion test.

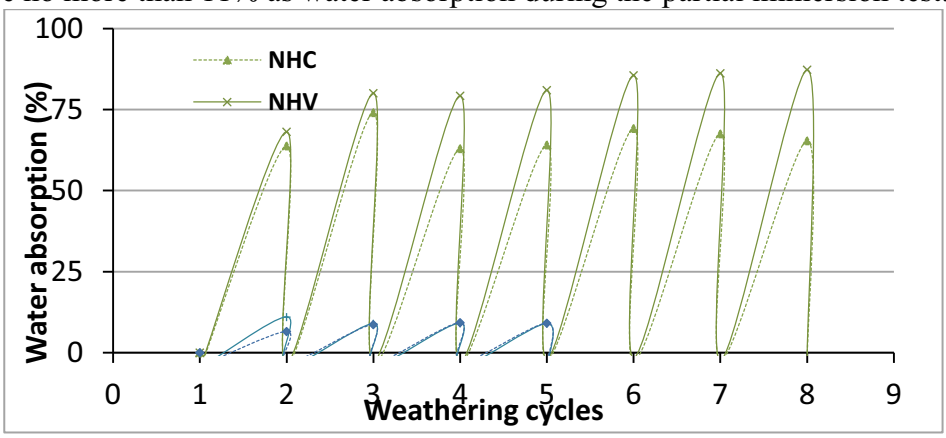

Figure 4: Water absorption rate evolution during partial immersion test

A comparison of partial and full immersion tests are presented in Fig. 5. As expected, it can be observed that the water absorptions of the all mixes in partial immersion were lower than those placed in full immersion. This has been proved to be more efficient for concrete treated with LO for both type of binders.

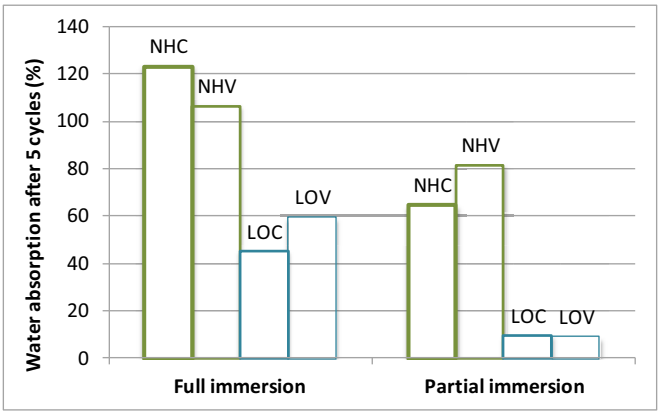

Figure 5: Comparison of water absorption for partial and full immersion test after 5 cycles

Figure 6 highlights the difference of compressive strength between mixes submitted to full immersion and partial immersion. The compressive strength dropped significantly when the samples were subjected to full weathering cycles. Similarly, the compressive strengths were reduced for mixes subjected to partial immersion. As it can be observed, the compressive strength of mixes submitted of full weather are lower than none weathering and when the aggregates were treated, the dropped on compressive is much lower than none-treated. In case of partial immersion, the reduction of compressive strength after 5 cycles of weathering

was lower compared to those full immersions. The full water immersion showed that treated samples with linseed oil are better compared to none-treated. It can be concluded that the treated samples absorbed less water, therefore less degradation and softening of the specimens.

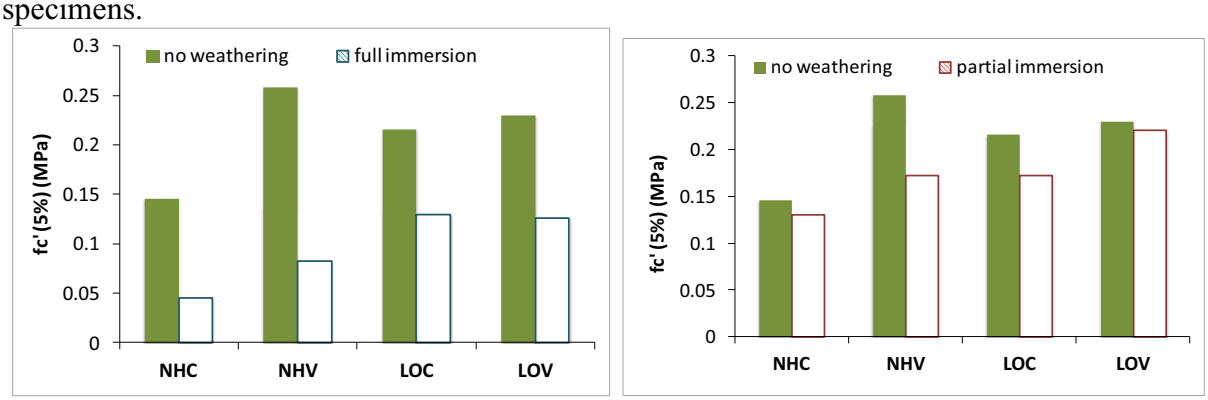

Figure 6: Compressive strength of full and partial immersions

4. Conclusions

Based on the results of this paper, the following conclusions can be drawn:

- The characterisation of hemp shiv particles has highlighted the fact that the LO treatment doubled the density of the aggregates. LO demonstrated a significant decrease by twice of the water absorption of particles. In general, the compressive strength of hemp concrete made with LO has been improved compared to the no-treated concrete.
- Additionally, the sorption coefficient of hemp concrete has been divided by two when LO treatment was used for hemp shiv aggregates.
- Full immersion has shown that treatments significantly decreased the water absorption during cycles. Treatments led to a smaller difference in compressive strength between weathering and no weathering samples.
- Partial immersion demonstrated lower absorption compared to full absorption and it reduced slightly the compressive strength compared to those of full immersion.
- The treated mixes with LO seems to have the highest autogenous shrinkage particularly with Vicat mixes.

References

[1] Amziane, S., Sonebi, M., K. Charlet, Proceedings of the Second International Conference on Bio-Based Building Materials, ICBBM-2017, Proceedings PRO 119, Ed. Amziane, S., Sonebi, M., Clermont-Ferrand (France), RILEM Publications s.a.r.l. (2017)
[2] RILEM STAR of RILEM TC 236-BBM., Bio-aggregates based Building materials, Springer Publisher, (2017)
[3] Amziane, S., Sonebi, M., Proceedings of the First International Conference on Bio-Based Building Materials, ICBBM-2015, Proceedings PRO 99, Ed. Amziane, S., Sonebi, M., Clermont-Ferrand (France), RILEM Publications s.a.r.l. (2015)

SynerCrete'18 International Conference on Interdisciplinary Approaches
for Cement-based Materials and Structural Concrete
24-26 October 2018, Funchal, Madeira Island, Portugal

MECHANICAL PREDICTION OF W.C.C. PROPERTIES: EXPERIMENTAL STUDY AND ANALYTICAL MODELING

Jean Gérard Ndong Engone [(1)], Ahmed El-Moumen [(2)], Chafika Djelal [(3)] Abdellatif Imad [(2)], Yannick Vanhove [(3)]

(1) Laboratoire Matériaux, Géoscan-Structure & Réhabilitation Ingéniérie, 26 rue ampère, F-91430 Igny France
(2) Laboratoire de Mécanique de Lille FRE 3723, Université Lille, F-59655 Villeneuve d'Ascq, France
(3) Univ. Artois, EA 4515, Laboratoire de Génie Civil et géo-Environnement (LGCgE), 62408 Béthune, France

Abstract
The wood industry generates some 12 million tons of waste in France. The reuse of this waste in the most common construction materials (e.g. concrete) may offer a sustainable solution. In this work, an experimental study was performed in order to develop wood cement composite (WCC) based on poplar sawdust by vibrocompaction process and used in concrete masonry blocks. The volume fraction of wood particles in the mixes varies from 23% to 46%. The mechanical properties in compression of these composites are characterized experimentally to determine the breaking stress and the Young's moduli. Thereafter, these Young's moduli are estimated in compression using both analytical homogenization models in order to predict the effective elastic properties of cement-wood composites. The obtained results show a good agreement between the experimental data and analytical calculations up to a 40% volume fraction. The poor models estimation for large volume fractions could be attributed to the experimental sample size, which is no longer representative for large volume fractions. Aside from the effect of specimen size, the physico-chemical phenomena (inhibition of the cement, WP percolation) could be the cause of poor models estimation for large volume fractions.

1. Introduction

Various works have focused on using wood byproducts like sawdust [1], wood chips [2], wood fibers [3] and even wood ash [4] as reinforcement in manufacturing wood-cement composites (WCC). These byproducts originate from deciduous [5] as well as evergreen species [3]. Despite considerable research devoted to WCC, their use in the field of construction remains confined to partition walls and acoustic insulation. This limitation is due

to the drop in mechanical characteristics and the lower durability of these WCC. In the literature, the optimization of WCC generally focuses on experimental studies regardless of mechanical behaviour prediction. The few number of studies actually dedicated to predict the mechanical behaviour of WCC are based on statistical studies of experimental results [6]. This work is focus on the predicting of mechanical behaviour of WCC using the analytical modeling. In this paper, an experimental study has achieved to develop a wood cement composite based on cementitious matrix and sawdust by the vibrocompaction process. The mechanical properties in compression of these composites are characterized experimentally to determine the Young's moduli. Thereafter, these Young's moduli are estimated in compression using an analytical homogenization technique. The experimental and analytical data are compared.

2. Materials

The wood particle (WP) using are wood waste from sawmill. These particles originate from the poplar species. These WP have been used and described by Ndong et al [7]. The mass densities of these WP were determined in accordance with standard NF EN 1097-6. This bulk density is equal to 178 $kg.m^{-3}$. Wood is renowned for its high sensitivity to water; in fact, this material absorbs a quantity of water often exceeding twice its weight. Such water sensitivity has a negative consequence on material properties in both the fresh and hardened states of the composites incorporating these WP. In fact, the water absorption of WP were determined, she is equal to 174%. In this study, the sand with a 0/4 particle grading were used. The cement tested is a CEM I 52.5 N EC CP2 NF.

3. Methods

3.1 Experimental studies

In this work, 7 mix designs were studied (see Tab. 1 for details). These formulations have been studied by Ndong et al [7]. The sand was subsequently replaced by WP. This substitution corresponds to a wood particle volume in the mix varying from 23% (WCC_{23}) to 46% (WCC_{46}). All mix designs are characterized by a cement paste volume of 40%.

Table 1: Various concentrations of wood mortars, $\delta_{(C+W)}$, $\delta_{(Sa)}$ and $\delta_{(Sw)}$ being, the volume ratio of paste (cement+ water), sand and sawdust and the mixture.

	WCC_0	WCC_{23}	WCC_{26}	WCC_{32}	WCC_{35}	WCC_{40}	WCC_{46}
$\delta_{(C+W)}$	40%	40%	40%	40%	40%	60%	0%
$\delta_{(Sa)}$	60%	37%	34%	28%	25%	20%	14%
$\delta_{(Sw)}$	0%	14%	26%	32%	35%	40%	46%

One design composed solely of sand, cement is use as the reference design (WCC_0). The WCC are shaped by vibrocompaction as defined by Xing et al [8]. The samples are cylindrical in shape of 10 cm diameter. They have a height of 20 cm. The vibrocompaction step was carried out with a compactor installed in a temperature-controlled room (T = 20 ± 2°C). The

specimens were stored in a chamber at a temperature of 20 ± 2°C and a relative humidity of 65%. The compression test was conducted using according to standard NF EN 772-1.

3.2 Analytical evaluation

The main objective of this part of study is to analytically simulate the effective's elastic properties of WCC. We have focused on the multiscale analysis of the macroscopic elastic behavior through the knowledge acquired of the mechanical behavior of each phase. Multiscale analysis is based on both of analytical homogenization models. A comparison between experimental data and results of analytical homogenization steps has been drawn. Analytical evaluations of the effective elastic properties of cement-wood composites can be obtained by means of several analytical methods. The proposed estimation typically depends on the inclusion shape and its distribution. These models obviously converge whenever the volume fraction of particles or the contrast between the properties of both phases is too small. Several of analytical homogenization methods can be found and presented in the literature. The following popular approaches will be assessed in the isotropic case namely: the Mori and Tanaka (MT) model [9], the first-order bounds of Voigt [10] and Reuss [11] (VR), and the optimal bounds of Hashin and Shtrikman (HS) [12]. According to these models, elastic properties of composites are determined by knowing those of each phase, "m: matrix" and "i: inclusion", and wood volume fraction "p". Analytical expressions of each model are expressed and given by Equations (1), (2), (3), (4), (5), (8), (9) and (10) as:

- Upper and lower HS bounds, H^{S+} and H^{S-}

$$\begin{cases} K^{HS^-} = k_m + \dfrac{p}{1/(k_i - k_m) + 3(1-p)/(3k_m + 4\mu_m)} \\ K^{HS^+} = k_i + \dfrac{(1-p)}{1/(k_m - k_i) + 3p/(3k_i + 4\mu_i)} \end{cases} \quad (1)$$

$$\begin{cases} \mu^{HS^-} = \mu_m + \dfrac{p}{1/(\mu_i - \mu_m) + 6(1-p)(k_m + 2\mu_m)/5\mu_m(3k_m + 4\mu_m)} \\ \mu^{HS^+} = \mu_i + \dfrac{(1-p)}{1/(\mu_m - \mu_i) + 6p(k_i + 2\mu_i)/5\mu_i(3k_i + 4\mu_i)} \end{cases} \quad (2)$$

HS analytical models obviously propose to calculate the bulk "k" and shear "μ" moduli. It should be pointed out that to derive Young's modulus "E", Equation (5) links all of these elastic properties. Where E^{HS+} and E^{HS-} represent upper and lower Young's modulus, respectively.

$$E^{HS\pm} = \frac{9k^{HS\pm}\mu^{HS\pm}}{(3k^{HS\pm} + \mu^{HS\pm})} \quad (3)$$

- Mori-Tanaka model

$$k^{MT} = k_m\left(1 + \frac{p(k_i - k_m)}{k_m + \alpha(1-p)(k_i - k_m)}\right) \quad (4)$$

$$\mu^{MT} = \mu_m\left(1 + \frac{p(\mu_i - \mu_m)}{\mu_m + \beta(1-p)(\mu_i - \mu_m)}\right) \quad (5)$$

$$\alpha = 3k_m/(3k_m + 4\mu_m) \quad (6)$$

$$\beta = (6(k_m + 2\mu_m))/(5(3k_m + 4\mu_m)) \quad (7)$$

Mori-Tanaka Young's modulus, E^{MT}, is calculated using the following equation:

$$E^{MT} = \frac{9k^{MT}\mu^{MT}}{(3k^{MT} + \mu^{MT})} \quad (8)$$

- VR bounds

$$E^{Voigt} = pE_i + (1-p)E_m \quad (9)$$

$$E^{Reuss} = \frac{E_i E_m}{(1-p)E_i + pE_m} \quad (10)$$

4. Results and discussions

Figure 1 shows the Young's modulus variation as function of wood volume present in the mix at 14 days. The presence of two behavioral fields can be distinguished. In the first field, the decline in Young's modulus is nearly linear until reaching 35% of WP in the mix, at which point its value equals 6.02 GPa (a drop of 51%). This lower Young's modulus in the first field can be attributed to various parameters, including inhibition of the hydration reaction, the mix porosity, the lack of WP stiffness, and distribution of the WP in the mixture. The inhibition of the cement hydration reaction occurs in the fluid state during cement paste / wood particle contact. The alkaline materials stemming from cement dissolution interact with the sugars contained in wood particles [3]. The impact of the wood particles used in this study on the hydration reactions has been demonstrated by several studies [8]. This inhibition plays an even greater role at a greater WP volume in the matrix. The porous WP structure raises the level of composite porosity [8]. During the compression test, this porosity triggers microcracking, which in turn weakens the composite. The effect of these parameters on the composite's mechanical behavior depends on the WP volume in the composite. The WP are arranged randomly, which creates areas of fragility located at different areas in the composite structure. Once the wood volume has reached 35%, another more pronounced decrease is noticed, displaying a value of 1.40 GPa, for a loss of 89%. This rate corresponds to a threshold volume beyond which WP percolates extensively into the composite. This leads to the saturation percolation thereof. This percolation effect modifies the composites' mechanical response. During percolation, the WP are basically entangled, leading to higher composite porosity and creating a vast zone of minimal stiffness. When conducting mechanical tests, these zones behave like pores due to the relatively non-rigid WP; such behavior significantly reduces composite ductility. After WP percolation in the mix, the higher WP volume exerts very little influence on the composite microstructure, hence with only a minimal influence on mechanical behaviour. The analytical results have been compared with experimental data provided by the compression test on specimens. Figure 2 illustrates these results. In the case of a low proportion of aggregates, it appears that the experimental Young's modulus values of WCC systematically lie between the HS bounds, which is in agreement with homogenization theory. It also appears that, both of the MT models and upper HS bounds closely match the experimental results. Beyond a proportion of 35%, the experimental values remain below those of the Reuss model; this limit corresponds to the percolation threshold, as highlighted in figure 1.

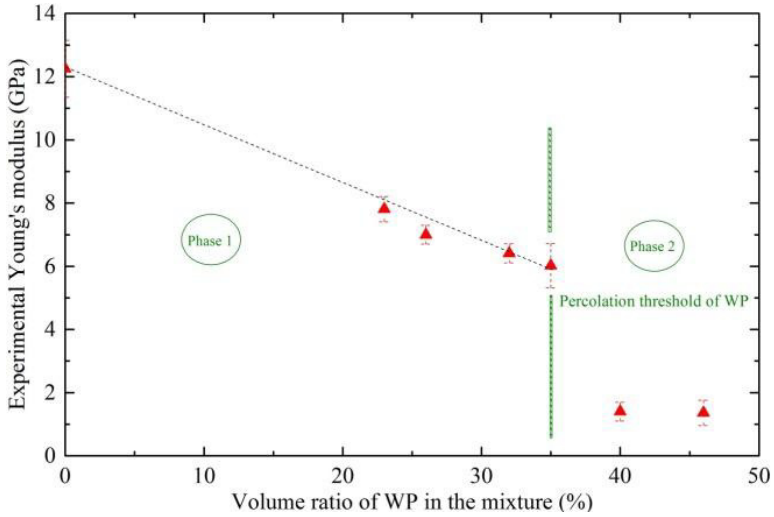

Figure 1: Experimental data of WCC at 14 days.

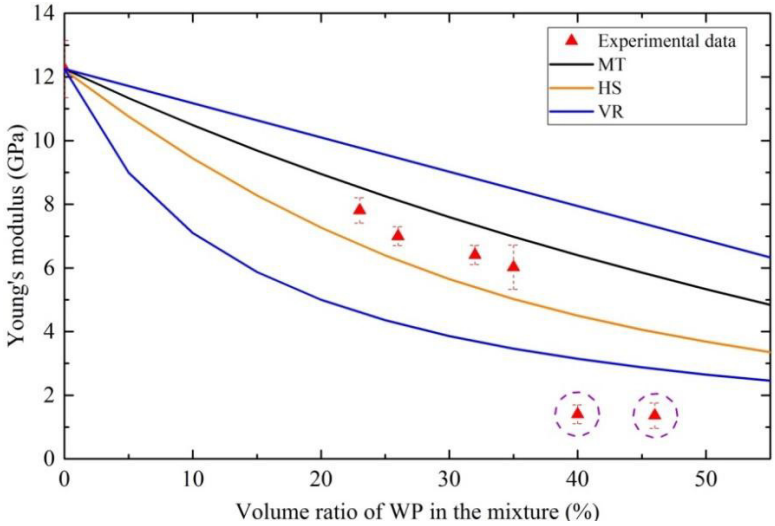

Figure 2: Confrontation between experimental and analytical results

The homogenization models not to have a good estimation of mechanical properties. Methods for estimating effective properties are based on the micromechanics interaction of composite components. In the case of composites of wood, there is a chemical interaction between the WP and the cementitious matrix. This interaction varies depending on the proportion of WP in the mix. For low proportion, the effective properties in the elastic range are weakly impacted. In this study, low impact provides a good estimate of the elastic properties. In the case of high wood proportion, the chemical interaction is high, which could justify the wrong estimation of the actual properties. The mechanical characteristics of the matrix are no longer that of the initial matrix. Homogenization models does not take into account the change in properties of the matrix. Other parts of the percolation phenomenon observed in figure 3 could also be the cause of poor estimation of actual properties. The homogenization theory requires the assumption of inclusion perfectly coated with the matrix. WP percolation invalidates this assumption, which could explain disability the bounds of homogenization. For

the future, numerical modeling based on the homogenization technique will be carried out. The impact of cement phase inhibition will be taken into account.

5. Conclusions

In this study, tests have been conducted to estimate effective properties of WCC by using analytical models. The following conclusions can be drawn; The Young's modulus of wood-cement composites drops with an increase in WP volume. This decline comprises two behavioral fields, one of which remains quasi linear up to a 35% threshold volume, which corresponds to a percolation threshold for WP in the mix; The prediction of Young's modulus by the homogenization analytical method shows that in the case of low proportion of wood particles in the mixture, the Mori-Tanaka model (MT) and upper Hashin and Shtrikman bounds (HS) allow having a good approximation of mechanical properties. Beyond 35% of WP volume in the mixture, conventional homogenization models cannot make a good approximation of mechanical properties. Percolation of WP and significant inhibition of the cement results in poor approximation of mechanical properties.

References

[1] Almir S, Rodrigues de Souza F, and al. Mechanical properties of concrete produced with a composite of water treatment sludge and sawdust. Constr. Build. Mater 25(2001), 2793–2798.
[2] Mohammed B, Abdullahi M, Hoong CK. Statistical models for concrete containing wood chipping as partial replacement to fine aggregate. Constr. Build. Mater 55(2014), 13–19.
[3] Wei YM, Tomita B, Hiramats Y, Fujii T. Study of hydration behaviors of wood-cement mixtures: compatibility of cement mixed with wood fiber strand obtained by the water-vapor explosion process. J. Wood. Sci 48(2002), 365–373.
[4] F. Udoeyop, H. Inyang, DT. Young, EE Oparadu. Potential of wood waste ash as an additive in concrete. J. Mat. Civ. Eng. 18 (2006), 605–611.
[5] Yasuda ES, Ima K, Matsushita Y. Manufacture of wood-cement boards VII: cement-hardening inhibitory compounds of hannoki. J. Wood. Sci 48(2002):242–244.
[6] Chowdhury S, Maniar A, Suganya OM. Strength development in concrete with wood ash blended cement and use of soft computing models to predict strength parameters. J. Adv. Res. 6(2014), 907–1013.
[7] Ndong Engone, J.G., Vanhove, Y., Djelal, C. et al. Optimizing mortar extrusion using poplar wood sawdust for masonry building block. Int J Adv Manuf Technol 95(2018), 3769-3780.
[8] Xing Z, Kada H, Djelal C, Vanhove Y. Wood Waste in Concrete Blocks Made by Vibrocompression. Environ. Process. (2015) 2(Suppl 1), 223-232.
[9] T. Mori and K. Tanaka. Average stress in the matrix and average elastic energy of materials with misfitting inclusions. Acta Metall. 21(1973), 571–574.
[10] Voigt W. Über die beziehung zwischen den beiden elastizitatskonstanten isotroper korper. Wied. Ann 38(1889), 573–587.
[11] Reuss A. Berechnung der fliessgrenz von mischkristellen auf grund der plastizitatsbedingung fur einkristalle. ZAMM 9 (1929), 49–58.
[12] Hashin Z, Shtrikman S. A variational approach to the theory of the elastic behavior of multiphase materials. J. Mech. Phys. Sol. 11(1963), 127–140.

SynerCrete'18 International Conference on Interdisciplinary Approaches
for Cement-based Materials and Structural Concrete
24-26 October 2018, Funchal, Madeira Island, Portugal

RISK ASSESSMENT OF MOLD GROWTH IN HEMP CONCRETE

Dmytro Kosiachevskyi [(1)], Kamilia Abahri [(1)], Mohend Chaouche [(1)], Evelyne Prat [(2)], Anne Daubresse [(2)], Cécile Bousquet [(2)]

(1) LMT, ENS Cachan, CNRS, Université Paris-Saclay, 94235 Cachan, France
(2) Centre d'Innovation Parexgroup, St Quentin Fallavier, France

Abstract
The use of the hemp concrete in the construction sector is interesting due to its hygro-thermal performances, economic and environmental benefits. Nevertheless, these performances can be affected as the hemp aggregate is a perfect substrate for a fungi proliferation. This paper focuses on the evaluation of the risk of mold contamination of the hemp concrete. The main objective is, first, to determine the risks of mold growth in the hemp concrete for durability, and, second, to verify the interconnection between the contamination by the mold of the hemp shiv and of the hemp concrete. Experimentally, a mold identification procedure was used for both samples of hemp shiv and hemp concrete, after being cultured in a Sabouraud culture medium at different conditions in desiccators. In addition, Scanning Electronic Microscope (SEM) observations have been conducted on different contaminated samples to investigate the material degradation and the interaction between the hemp fibers and the concrete. The obtained results have revealed that the fungi from the Aspergillus family are the most common mushrooms present in the material. Their impact on human health has been presented in the paper.

1. Introduction

The use of bio-based building materials is hampered by the lack of a database relating to their intrinsic properties and durability. Nevertheless, the question of their sensibility to several characteristics is still open. The mold growth is one of the most important criterion when assessing the degradation of bio-based materials [1,2,3]. Besides the effect of the degradation of subtract, an exposition to fungi could provoke several adverse health effects as allergic reactions, aggravated rhinitis and asthma [4]. Fungal components, such as spores and hyphal fragments and others volatile particles, may have effects on the health of an exposed

individual because of their size and characteristics [5, 6, 7]. Spores are emitted in the result of the fungal growth that depends on several parameters such us temperature, relative humidity, light, etc.
The fungi are eukaryotic, heterotrophic with septate or siphoned filamentous thallus [8]. They are classified into 5 groups: Chytridiomycota, Zygomycota, Basidiomycota, Ascomycota and Deuteromycota. Unfortunately, there are still a lack of knowledge on the effects of molds on durability of bio-based structures such as the hemp concrete. Particularly, literature presents few works in the field of civil engineering that consider the mold risk on material durability of the building and health of people living there.
That's why, the main objective is, first, to observe and to characterize the mold growth for two different hemp concrete formulations, and, then, to determine the strains and the risk of the mold growth for durability and human health. Since, there is a difference between the samples of two formulations, the results could not be compared. Experimentally, a morphological analysis and interface observation of the mold structures on the contaminated samples have been conducted. Then an identification procedure, that consist to identify them, has been investigated. Overall, the correlation between the contamination of the hemp shiv and the hemp concrete has been studied.

2. Materials and methods

In this part the material formulation and the experimental protocol are presented. For this study one sample of each of two different hemp concrete formulations with two different types of hemp has been used. The HC-B formulation sample was made according to the professional rules of execution of hemp concrete works [9]. It is used as wall insulation. The shiv has the apparent density of about 100 to 110 kg/ m^3. The binder is based on the lime. It is called Batichanvre, produced by French lime producers St. Astier. This binder is a mixture of natural lime from Saint-Astier (Hydraulic lime: NHL and aerial one: CL), cement CEM I 52.5, and different adjuvants to improve rheology and permeability of hemp concretes. Its density is of 500 kg/m^3. The HC-P formulation (produced by ParexGROUP) is made to let an application as a shotcrete. The binder is based on calcic lime, specific binder and specific admixtures. The hemp, used for HC-P, was harvested in the same year in the same region by different farmers, stocked differently but grinded in the same way at different days. Four different types of this hemp have been studied but just one of them (type 4) has been used for a HC-P sample. The two formulations are presented in Tab. 1. The sample of the HC-B formulation of the dimensions of 20,48x20,06x6,29 mm3 has been produced on 31 January 2016. They were conditioned at 23°C and 50% of relative humidity for letting the carbonatation of the binder to diminish the pH level and favour the fungi development. After that, in March 2017 the specimen was put in a desiccator at 94% of relative humidity which is a favourable condition to provoke the mold growth. After one year this sample has been observed using the numerical microscope Keyence VHX-2000. In the case of the HC-P formulation the sample has been taken from real construction site after the mold growth has been visible (after one month, on 28 November 2017). The same numerical microscope observation has been used for the HC-P formulation. The interface and the morphology of the mold structures have been also studied for both formulations using the Hitachi S3400 Scanning Electronical Microscope. The acceleration voltage of 10 kV, the pressure of 50 Pa

for the sample of the HC-B formulation and of 70 Pa for the sample of the HC-P have been chosen for all the observations.

Table 1: Formulation of the studied hemp concretes.

Material	**HC-B**	**HC-P**
Hemp shiv (kg)	10 kg	10 kg
Binder (kg)	25 kg	20 kg
Water (kg)	35 kg	50 kg
Water / binder (-)	1.4	2.5
Binder / hemp shiv (-)	2.5	2

After having observed the mold proliferation the mold types have been determined. It could let us to analyse the risks of such contamination. In this case the experimental protocol consists firstly in sowing contaminated particles separately in Petri dishes to let the mold grow. In order to analyse the mold types present in the hemp concrete, hemp concretes of two formulations have been studied. In order to verify relations between molds from the hemp concrete and the hemp and the dispersion of the contamination four samples of hemp, used for HC-P, have been studied. In this context, the microbiological identification protocol has been used. Electrical burner has been used to protect our samples of bacteria and prevent a possible contamination from outside. The question of repeatability has been studied by seeding contaminated particles twice to be sure in the repeatability. After seeding the particles, Petri dishes were packed with parafilm and put in the closed desiccator to prevent external contamination by the air stream. The temperature of 23 ° C and the relative humidity of 50% was controlled. After 8 days we observed the sampled parts of the mold from these dishes between a microscope slides and cover glasses on the adhesive tape. The identification of mold species was made using the numerical microscope Keyence VHX-2000 based on the morphological characteristics.

3. Results and discussion

3.1 Morphology analysis and interface observation

As expected previously, in this chapter the results of optical and SEM microscopes observation are presented. Hemp concrete has been observed in different scales. So, firstly, we have analysed the numerical microscope images of the hemp concrete before and after the mold contamination (Fig. 1 a and b respectively). They showed that both materials are heterogeneous, porous and represent a big quantity of micro cracks (Fig.1a) in the interface between hemp shives (1) and the cementitious part (2). Additionally, these images give us a better understanding of the procedure of the contamination and the mold growth. On the Fig. 1b we can see the mold on the surface of the contaminated sample (3). As for SEM images Fig. 2 (a and b) represents the photos of one sample of the HC-B formulation. Mold structures such as the filamentous thallus (1) and vesicles (2) are visible on the Fig.2a. Figure 2b shows that the cementitious part (3) covers and protects the hemp shiv (4). The mold net (1) is also visible. The images of the SEM observation of the contaminated sample of the HC-P formulation are presented on the Fig. 3 (a and b).

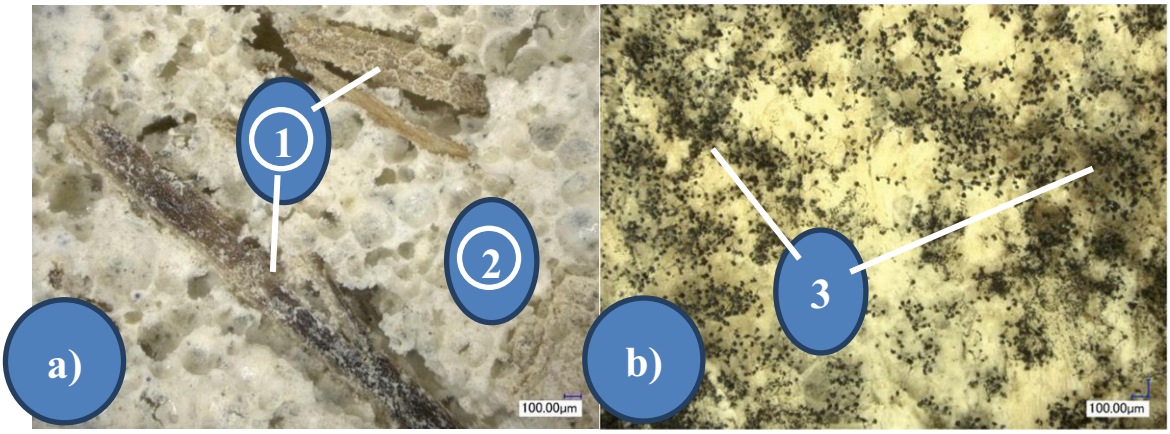

Figure 1: Example of numerical microscope photos of the hemp concrete before (a) and after (b) mold growth: 1 – hemp shiv, 2 - cementitious part, 3 – mold contamination

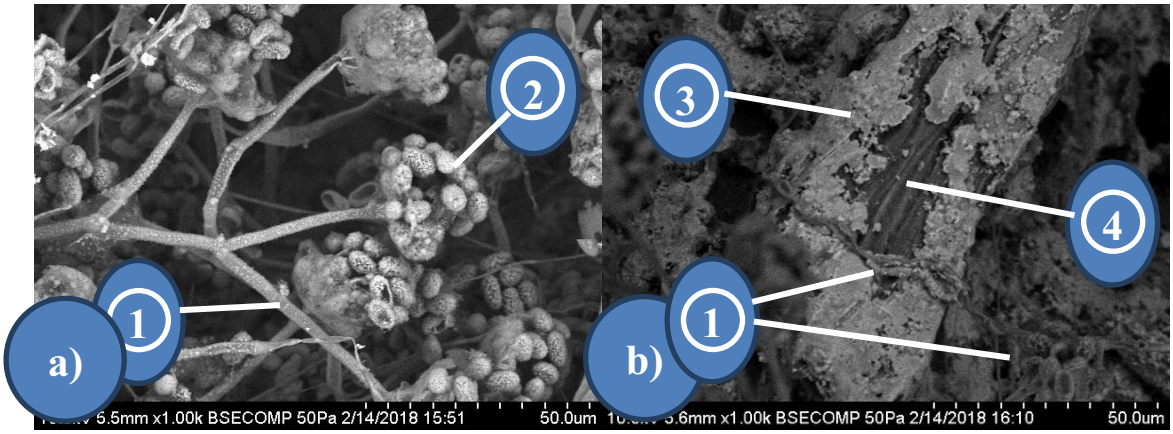

Figure 2: SEM images of the morphological structures of the mold present on the hemp concrete of the HC-B formulation (a and b): 1 - filamentous thallus, 2 – vesicles, 3 - cementitious part, 4 – hemp shiv

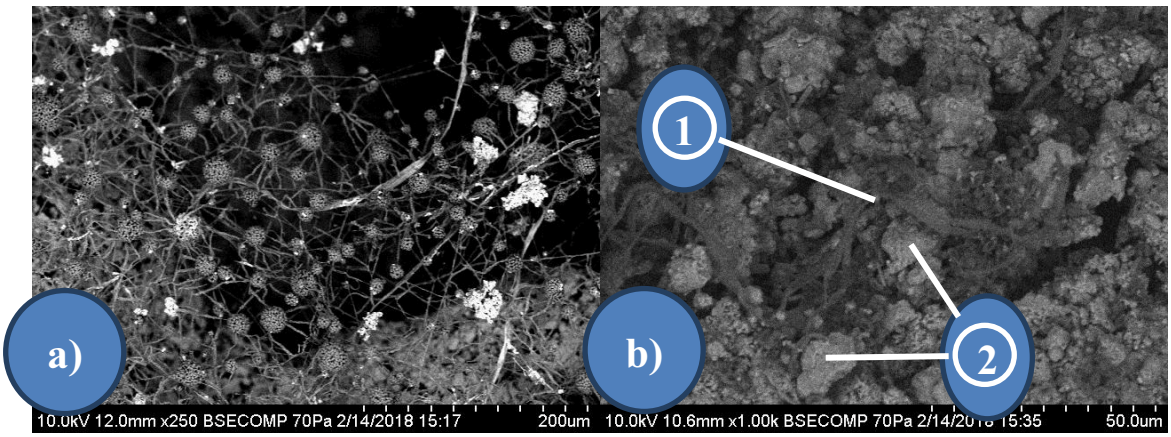

Figure 3: SEM images of the morphological structures of the mold present on the hemp concrete of the HC-P formulation (a and b): 1 - filamentous thallus, 2 - cementitious part

Analogically to the first case, we can see the mold structures with a huge number of the vesicles (Fig. 3a). The mold net (1), that is on the surface of the cementitious part (2) of our sample, is presented on the Fig. 3b. Then we proceeded with the mold identification.

3.2 Mold identification and risk assessment

After cultivating twice molds from two studied formulations of the hemp concrete and four types of the hemp, several types of fungi were identified. Tab. 2 represents all the identified types during this test. Hemp shives could be contaminated at different stage of their life cycle (harvest, storage or implementation). Indeed, all types of hemp particles with the different storage conditions have the similar fungi samples. At the same time, we can see that despite the presence of the dispersion of the contamination there is the consistent pattern of the fungi contamination. Also, we can see that two formulations represent different mold samples that can be explained by the difference of hemp shiv (the main source of fungi spores).

Table 2: Results of the determination of the fungi strains for each type of material.

Type of material		**Mold strains**
Hemp	Hemp type #1	Rhizopus sp, Aspergillus niger
	Hemp type #2	Rhizopus sp, Aspergillus niger
	Hemp type #3	Rhizopus sp, Aspergillus niger
	Hemp type #4	Rhizopus sp.
Hemp concrete	#1 Batichanvre	Aspergillus niger, Aspergillus nidulans
	#2 ParexGroup (hemp type #4)	Rhizopus sp, Aspergillus niger

According to the literature, the toxicity of Aspergillus niger comes from their production of oxalic acid, flavaspérone and aflatoxins [10]. Aspergillus nidulans is toxic through its production of sterigmatocystin, and molecules such as oxalic acid, nidulotoxin or kojic acid. Rhizopus sp. is one of the most isolated species in cerebral and rhinofacial mucormycosis injuries. Patients are often diabetic patients with ketoacidosis, but also leukemic patients, sometimes AIDS patients. More, Rhizopus sp. is dangerous for transplant surgery because of the great risk of the transplant rejection [11].

4. Conclusion

This research lays to examine the risk of mold growth for two different formulations of the hemp concrete. Firstly, optical and SEM microscopic observations of both non-contaminated and contaminated samples have been conducted. Then the mold identification protocol has been used to identify the fungi present in our samples. The favorable microstructure for the mold growth of the hemp concrete has been noticed. Studied hemp concrete represents the difficult heterogeneous microstructure with a high number of micro cracks and pores that facilitate the mold proliferation. Mold growth depends on the contamination of the

components before, during and after the production of a hemp concrete. Several mold strains were determined using the phenotypic method - microscopic observation. At the same time, these tests have demonstrated defects of microscopic identification of strains: (1) under certain conditions certain mold strains do not form structures that make it possible to determine the family of a strain; (2) there is a high possibility of contamination of Petri dishes, which distorts results; (3) due to the effect of synergy some strains may not proliferate which is not representative for the real case; (4) there are some microorganisms in a hemp mortar or hemp itself that probably cannot be identified by this method.

Acknowledgments
The authors acknowledge ParexGroup for financing this project.

References

[1] Arizzi A., Brümmer M., Martín-Sanchez I., Cultrone G. and Viles H. The influence of the type of lime on the hygric behaviour and bio-receptivity of hemp lime composites used for rendering applications in sustainable new construction and repair works, PLoS ONE 10(5): e0125520. doi:10.1371/journal.pone.0125520, 2015
[2] Vereecken E., Roels S. Review of mould prediction models and their influence on mould risk evaluation, Building and Environment 51, 296 -310, 2011
[3] Crawford, B., Pakpour, S., Kazemian, N., Klironomos, J., Stoeffler, K., Rho, D., Denault, J., Milani, A.S. Effect of Fungal Deterioration on Physical and Mechanical Properties of Hemp and Flax Natural Fiber Composites, Materials 2017, Vol. 10, Issue 11, 1252, 2017
[4] Mazur, L.J. and Kim, J., Spectrum of noninfectious health effects from molds. Pediatrics 118(6) (2006), 1909-1926
[5] Górny, R.L., Filamentous microorganisms and their fragments in indoor air - a review. Annals of Agricultural and Environmental Medicine 11(2) (2004), 185-197
[6] Eduard W., Fungal spores: a critical review of the toxicological and epidemiological evidence as a basis for occupational exposure limit setting. Crit Rev Toxicol 39(10) (2009), 799-864
[7] Fischer, G. and Dott, W., Relevance of airborne fungi and their secondary metabolites for environmental, occupational and indoor hygiene. Archives of Microbiology 179(2) (2003), 75-82
[8] Djossou O., Post-harvest Robusta mycoflora and the use of lactic acid bacteria for the control of mycotoxinogenic molds and ochratoxin A, PhD thesis, Paul Cézanne University (2011)
[9] SEBTP. 2012. Professional rules for the execution of hemp concrete works: research development metier, France (2012)
[10] Botton B. et al, Mold, useful and harmful, industrial importance, Collection Biotechnologies, Masson Edition (1990)
[11] Almyroudis N.G., Sutton D.A., Linden P., et al, Zygomycosis in solid organ transplant recipients in a tertiary transplant center and review of the literature. Am J Transplant 6(10) (2006)